Structures 80 (2025) 109750

Contents lists available at ScienceDirect

Structures

journal homepage: www.elsevier.com/locate/structures

Machine learning approach in the quantitative evaluation of the seismic behaviour for 3D reinforced concrete frame structures

Georgiana Bunea [a], Florin Leon [b], Ionuţ-Ovidiu Toma [a,*]

[a] Department of Structural Mechanics, Faculty of Civil Engineering and Building Services, "Gheorghe Asachi" Technical University of Iasi, Iasi 700050, Romania
[b] Department of Computer Science and Engineering, Faculty of Automatic Control and Computer Engineering, "Gheorghe Asachi" Technical University of Iasi, Iasi 700050, Romania

ARTICLE INFO

Keywords:
RC frame structures
Seismic behavior
Non-linear time-history analysis
Neural network prediction
Seismic motion
Structural and seismic influencing parameters

ABSTRACT

The implementation of performance-based seismic design (PBSD) in the design and optimization of the structural system of buildings becomes paramount in view of recent seismic design codes. The large number of simulations and analyses to be conducted for specific types of structures and specific seismic areas are prerequisites of the PBSD methodology. The application of machine learning (ML) techniques proved effective for the development of prediction models that have the potential to significantly minimize the amount of time required for structural damage assessment. Artificial neural networks (ANNs) demonstrated the ability to generalize by accurately predicting output parameters for unseen input parameters not included in the training dataset. In this research, an ANN was used for predicting structural damage parameters corresponding to 3D reinforced concrete frame structure subjected to seismic scenarios and for evaluating the influence of various seismic actions on the structures. A total of 243 3D-reinforced concrete models were generated and subjected to 14 seismic scenarios. Thus, 3402 input-output data sets were obtained and were used for ANN training (80 %) and validation (20 %). A total of 10 input parameters were considered to influence the seismic behaviour and damage levels in the RC frame structures. Out of the 6 input structural parameters, the number of stories, the span width and the width of the column cross-section have the highest impact on the seismic damage of reinforced frame structures. From the 4 input parameters characterizing the seismic motion, the peak ground velocity (PGV) and peak ground acceleration (PGA), were found to be the most important seismic parameters which influenced the damage of the analysed structures. The performance of the ANN was compared against two other machine learning algorithms commonly used in civil engineering applications: Random Forest (RF) and Extreme Gradient Boosting (XGBoost). While these algorithms performed marginally better than ANN in the training and validation stages, they did not manage to be accurate in the testing phase when using newly generated data sets. The considered output parameters were: fundamental period of vibration for the non-damaged and damaged states, final softening index, interstory drift ratio, maximum displacements and maximum absolute accelerations. The ANN was able to accurately predict all output parameters (correlation coefficient larger than 0.85) with the exception of final softening index that may be influence by more complex phenomena that are beyond the scope of this paper. The proposed ANN-based prediction model proves to be a fast and reliable tool for quickly assessing the damage state of 3D reinforced concrete frame structures subjected to different seismic scenarios. It can be further enhanced and extended to include other parameters not considered at this stage of research as well as being included in stacked ML algorithms.

1. Introduction

Seismic activity has resulted in numerous casualties and significant socioeconomic losses in multiple places due to the immense energy released in a matter of seconds. In 2023, two earthquakes originating in Turkey resulted in over 50,000 fatalities in Turkey and Syria, along with significant destruction [1–3]. The damages are not solely structural or economic but also ecological due to the release of harmful compounds into the atmosphere resulting from the partial or total demolition of the buildings [4]. Despite the establishment of seismic codes and substantial

* Corresponding author.
E-mail addresses: georgiana.bunea@academic.tuiasi.ro (G. Bunea), florin.leon@academic.tuiasi.ro (F. Leon), ionut-ovidiu.toma@academic.tuiasi.ro (I.-O. Toma).

https://doi.org/10.1016/j.istruc.2025.109750
Received 10 February 2025; Received in revised form 8 July 2025; Accepted 17 July 2025
Available online 23 July 2025

research on earthquake incidence and seismic wave propagation, earthquakes continue to be among the most devastating natural dangers.

The implementation of performance-based seismic design (PBSD) in the design and optimization of the structural system of buildings becomes more than a recommendation, as stipulated in FEMA:P58–1 [5], FEMA:P58–2 [6] and thoroughly described in FEMA:P58–7 [7]. This methodology allows authorities to accurately ascertain the damage level of a building following an earthquake and to enhance seismic resilience. Nevertheless, its implementation requires, in some cases, a significant change in the national seismic design codes which is challenging to implement in the current state. The large number of simulations and analyses to be conducted for specific types of structures and specific seismic areas are prerequisites of the PBSD methodology. Subsequent to establishing the methodology and guidelines for assessing building damage, an examination is required to evaluate the damages following a seismic event. Considering the limited number of inspectors and the duration necessary for a proper inspection, waiting for such an event is detrimental both to society and the economy. It is possible that the official assessment of structures might take up to a couple of months to complete after a significant seismic event, which can inflict considerable damage to buildings. During this time, the operation of some buildings may be restricted for the purpose of accident prevention. In light of this, it is imperative that solutions be discovered in order to expedite the process of assessing the damage and to restore the operation of the structure as quickly as possible.

Assessing structural integrity, analysing seismic data and reducing earthquake-related risks have all been transformed by the application of machine learning (ML) techniques in earthquake engineering. This expanding discipline uses artificial intelligence to process large and complex datasets, find patterns and make predictions with high levels of efficiency and accuracy [8,9]. According to [9] there are three main types of learning: supervised, unsupervised and reinforcement. Supervised learning is used to create prediction models aimed at mapping a set of inputs (also known as features or characteristics) to one or more outputs (response variables). Supervised learning problems are categorised as pattern recognition, when the response variables are categorical, and as regression when the outputs are numerical variables. Description learning, also known as unsupervised learning, is connected with problems that are considerably less well defined. The objective of this type of learning is to find underlying relationships in the data. Through the utilisation of parametric and nonparametric models, it is possible to accomplish both supervised and unsupervised learning.

The use of ML techniques also demonstrated to be effective for the development of prediction models that have the potential to significantly minimize the amount of time required for structural damage assessment [10–13]. ML methods, such as ANNs, can successfully predict outputs for inputs not included in the training dataset. This is based on the findings of previous structural analyses that were used for training, which consisted of input-output mappings. They are regarded as biologically inspired computational techniques, adapted at modelling complex, nonlinear separable processes [14]. They are best used to address intricate problems that sequential algorithms cannot solve [3]. For this reason, having a tool that is capable of providing the damaged status of a building [15,16] in a timely manner shortly after the occurrence of an earthquake, based on structural and seismic data, would be an extremely useful instrument in the process of strengthening seismic resilience [17].

Using ANNs in seismic analysis research proved efficient in predicting the structural behavior of different types of buildings [18–20]. Several research works focused on predicting the residual drift, seismic limit state capacity and seismic risk assessment of steel moment resisting frames considering soil-structure interaction using machine learning techniques [16,21]. The authors investigated the suitability of several ML algorithms and ranked them based on un performance parameters such as coefficient of determination (R2), mean average error (MAE), mean squared error (MSE) and root mean squared error (RMSE) during both training and testing phases [22]. From the selected algorithms, Artificial Neural Networks (ANN) and Extreme Gradient Boosting (XGBoost) showed quite high performance and high accuracy of the predicting results. In a more recent study [23] a combination of estimator such as ANN and XGBoost, among others, was proposed to create a stacked ML algorithm which showed improved prediction capabilities of interstorey drift (ID) and residual intersotrey drift (RID) for buckling-restrained braced-frames. The obtained results showed that ANNs can estimate the performance of buckling-restrained braced-frame structures with an accuracy higher than 97 %.

The use of ML techniques in assessing the performance of existing reinforced concrete structures was also validated by several studies. Results showed that such an approach could save time, costs and effort spent of seismic assessment practices [3]. ANN algorithm provided a 95.83 % accuracy, while Random Forest (RF) showed a 100 % accuracy. However, in a different study on seismic fragility and seismic vulnerability assessment of reinforced concrete structures [22], RF algorithm ranked below ANN and XGBoost.

While the availability of a predictive program is undeniably beneficial for organizing post-seismic actions, it necessitates a substantial volume of data for effective training, which is challenging to collect. For any ML technique to yield highly accurate predictions, one needs a large pool of data which is often lacking in either the number of entries or accuracy and randomness of data sets [9]. Lack of data, collected or not in small databases, is a pressing issue in many engineering fields. Civil engineering is such an example because the observed phenomena are complex and cannot be accurately described by mathematical models. Moreover, related experiments are very costly because of the size of the specimens and/or cost of equipment. However, small databases did not stop researchers to use parametric numerical simulations of validated models to create additional data entries.

The simplest approach is to utilize finite element (FE) design software. Nonetheless, the FE non-linear analysis of a three-dimensional structure subjected to various seismic scenarios is a laborious task. Consequently, the majority of the research employed simplified models in their analyses. Single degree of freedom SDOF models were used [24] to estimate the nonlinear response of a structure subjected to strong ground motions. As a simplified model, the structural input data was limited, i.e., yield strength, post-yield stiffness ratio, and fundamental period of vibration. Nonetheless, the mean squared error computed during network validation proved the efficiency of ANN prediction. A neural network was also successfully used in a different study [25] for assessing the structural damages registered by a SDOF model after a seismic action. The spectral damage index was considered by the authors as output, whereas the input comprised of both structural and seismic parameters. The efficiency of using neural networks in predicting structural damages in a SDOF model due to seismic actions was also confirmed by [26], [27] and [28]. The maximum inter-story drift ratio (IDR) and the maximum displacement parameters during seismic events corresponding to three simple models, i.e., 3DOF, 4DOF and 6 DOF, were also successfully predicted by using ANNs [20].

Neural networks were used in constructing the fragility curves associated with a 4-story bidimensional reinforced concrete frame building [29], confirming the suitability of ANNs over other traditional methods. Predictive models for bidimensional reinforced concrete frames were also successfully developed using ANNs [30]. The authors considered only the first three natural periods as input, whereas the output comprised several parameters related to both force and displacement. ANNs were also used to predict the results of the pushover analysis for 3-, 6- and 12-story planar steel moment resisting frames [16,31]. The maximum drift responses corresponding to each performance limit were predicted with high accuracy by using the natural periods of the models as input. Additionally, the seismic drift responses were also successfully predicted by using ANN for bidimensional steel moment frames [32]. The authors weighed the importance of the input parameters on the output prediction, i.e., maximum interstory and top drifts.

According to their analysis, the peak ground velocity had a stronger effect on the prediction than the peak ground acceleration. The number of stories was also identified as one of the factors having a high relevance for the output prediction. The importance of the input parameters over the output was also determined for bidimensional reinforced concrete moment frames [33]. The research showed that ground motion intensity had the highest influence on the maximum story drift.

Studies regarding ANN prediction of seismic-induced damages for tri-dimensional structures [34] are seldom found because they are computationally demanding. The non-linear analyses require both powerful computer hardware and are also time consuming. However, such studies are needed, as they consider the tridimensional effects for the seismic energy dissipation through the building, and display a more realistic behavior. One study analysed two models, i.e., a reinforced concrete frame-shear wall structure and a steel frame structure, for which the output was the limit state function corresponding to the structure after seismic loading [35]. The geometrical structural parameters were constant and 100 sets of artificial ground motion data were used in the analysis. The neural network thus trained displayed a good prediction of the output. Another study used ANNs to predict the displacement time history at the top of reinforced concrete and steel structures [36] during a seismic event. Structures having both symmetrical and non-symmetrical plan views were analysed.

This paper seeks to develop a neural network capable of predicting the structural damage state of three-dimensional reinforced concrete models following an earthquake, building on prior research that established the efficacy of neural networks in predicting the seismic response of structures. In contrast to prior research, the present study employed several earthquake events and structural geometry characteristics. The seismic response was assessed utilizing natural vibration periods, seismic damage indices, maximum displacement, and maximum absolute acceleration. Obtaining data on the damage induced on structures of varying geometries or typologies in a markedly reduced timeframe relative to traditional methods is advantageous and enhances seismic resilience in regions susceptible to such hazards. The study categorizes the input parameters based on their impact on the structural damage indices. A total of 243 3D-reinforced concrete models were generated and subjected to 14 seismic scenarios. Thus, 3402 input-output data sets were obtained and were used for ANN training and validation using a 80 %-20 % distribution of data between the training and validation stages, respectively. The number of stories, the span width and the width of the column cross-section are the structural parameters with the highest impact on the seismic damage of reinforced frame structures. The peak ground velocity (PGV) and peak ground acceleration (PGA), as characteristics of the ground motion, were found to be the most important seismic parameters which influenced the damage of the analysed structures. Identifying the significant seismic and structural data for the given structure type could facilitate future improvements to the seismic design codes.

2. Research methodology

A neural network was used for predicting structural damage parameters corresponding to 3D reinforced concrete frame structure subjected to to a series of 14 seismic scenarios and for evaluating the influence of various seismic actions on the structures. An ANN often requires an extensive dataset to achieve high prediction accuracy [22] but, at the same time, it showed its potential even for smaller data sets [34]. For this reason, a series of nonlinear Time-history analysis simulations were carried out in the first step of the research using the finite element software SAP 2000. Each simulation was defined by different input parameter values, and some output parameters related to seismic damage were extracted. The inputs included structural and seismic action parameters. The resulting FE input-output mappings were subsequently used to train and test the neural network.

2.1. Selection of structural parameters

The structural parameters were selected based on the main geometrical characteristics of the building that may influence its behavior under seismic action. Their variation was considered so that it covered a broad range of reinforced concrete frame structures. Certainly, an acceptable limited number of values per each set of input parameters was considered, due to the extensive amount of time and computational power required to obtain the Finite Element Analysis (FEA) results. Table 1 lists the input structural parameters varied throughout the study, for the ANN training stage[37].

Not all combinations of the above presented parameter values were appropriate and some of them had to be excluded from the analysis. For instance, a building having 7 stories and a column cross-section of only 0.30 m width would be unrealistic. Therefore, eventually, 243 structural models were analysed and the results were considered for ANN training purposes. Nonlinear Time-History analyses were carried out for each structural model. Some examples of structural models considered in the analysis are illustrated in Fig. 1.

All the other parameters, such as material properties, intensity of live loads, had fixed values and were not added as inputs to the neural network. Thus, for all structural models, the beams and columns were made of C20/25 concrete, while the slab was made of C16/20 concrete. The concrete class was chosen according to the national seismic norm P100–1/2013 [38] provisions. The steel grades of the reinforcement bars were S355 – for bars of [6…14] mm in diameter - and S345 – for bars of [16…28] mm in diameter. The dimensions of beams and slabs were constant for all models and were computed based on the P100–1/2013 regulations [38]. The beams had a cross-section of 25 × 40 cm, and the thickness of the slab was 13 cm. All structural elements were reinforced considering the minimum required reinforcement, computed according to Eurocode 2 [37,39]. Although there was a small difference between the computed minimum reinforcement area according to the norms and the one computed by considering the standard reinforcement diameters, it was considered acceptable, as it did not impact the final results.

2.2. Selection of seismic action parameters

For predicting the seismic damage of reinforced concrete frame buildings using ANN, the structure was be firstly subjected to a variety of seismic actions. The results were later on used in the ANN training process. For this purpose, 14 accelerograms corresponding to real seismic events were selected and used in the non-linear Time-History analysis in SAP2000. Although the performance-based design approach proposed by FEMA should be generally used worldwide in seismic areas for its feasible solutions [40], its implementation is still difficult in many countries. For this reason, usually, the seismic codes consider mainly the peak ground acceleration (PGA) as being the main parameter used in the seismic design [38]. However, there are other seismic parameters which may prove to have a major influence on the structural behavior. For this study, four seismic parameters were chosen to be considered in the ANN training, as presented in Table 2 [37].

Fig. 2 graphically presents the values of the seismic parameters for each considered action. The minimum and maximum values were

Table 1
Input structural parameters.

ANN Code	Structural parameter	Set of values
I_1	Number of stories	2, 4, 7
I_2	Number of spans in Ox direction	2, 3
I_3	Number of spans in Oy direction	2, 3
I_4	Frame span length	3 m, 4 m, 5 m
I_5	Story height	2.8 m, 3.0 m, 3.5 m
I_6	Width of column cross-section	0.30 m, 0.40 m, 0.50 m, 0.70 m

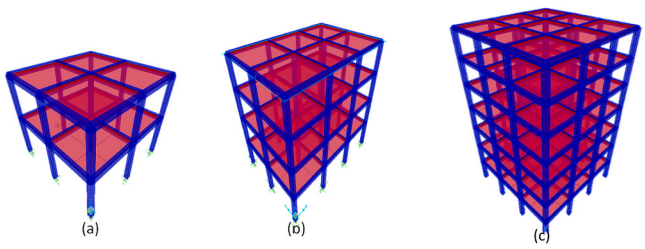

Fig. 1. Structures modelled in SAP 2000: (a) 2 stories; (b) 4 stories; (c) 7 stories.

Table 2
Seismic action parameters.

ANN Code	Seismic parameter	Unit of measurement	Acronym
I_7	Peak ground acceleration	cm/s^2	PGA
I_8	Peak ground velocity	cm/s	PGV
I_9	Peak ground displacement	cm	PGD
I_{10}	Spectral intensity	cm	SI

marked for each parameter.

The national seismic code P100–1/2013 [38] considers the PGV and PGD values only in the calculus of the corner periods, while the PGA value is the base of the building seismic design. The PGA value is established for a medium recurrence period, which was modified with every new version. The changes were made to gradually upgrade the national seismic code to the provisions of the Eurocode 8 [41]. Although the PGA is used in the national codes, it has been proven that PGV is more suitable for assessing the seismic structural damage, as it is associated with the earthquake energy induced in the building [42]. However, neither of these two parameters takes into account the duration of the seismic action or its dominant frequency. According to some studies, Housner's spectral intensity could be successfully used in assessing the structural degradation caused by a seismic action [43–45]. Housner's spectral intensity is computed using Eq. 1 and it defines the damage potential of a seismic action [45,46]:

$$SI_H = \int_{0.1}^{2.5} S_v(T,\xi)dT \tag{1}$$

where $S_v$is the pseudo-velocity response spectrum, T is the natural period of a one-degree of freedom structure and ξ is the damping coefficient. In the current study, the value of the damping coefficient $\xi$was 5 %, according to Eurocode 8 provisions [47].

2.3. Finite element modelling and analysis

Nonlinear Time-History analyses were performed for each of the 243 3D-reinforced concrete models analysed using SAP2000. Each of these structures was subjected to 14 seismic actions, with the main characteristics shown in Fig. 2. Thus, 3402 input-output mappings were obtained and used for ANN training. The Takeda model [48] was used for the hysteresis loop of reinforced concrete, while the selected force-deformation curve followed the Mander model [49]. The moment hinges (M3) for the concrete beams were applied at both ends of the elements. The type selected for the axial force-moment hinges registered in columns was *Fiber P-M2-M3*, being recommended in nonlinear dynamic analyses. As in the case of beams, column hinges were set at both ends of the elements. Fig. 3 presents the nonlinear model considered in the study and the position of hinges in both beams and columns.

Regarding the static loads, except for the self-weight of the elements, the structure was also loaded with an additional permanent load of 3 kN/m^2 – representing the weight of the non-structural elements, and a live load of 1.5 kN/m^2 selected according to SR EN 1991–1–1:2004/NA:2006 [50]. For taking account of the inertial effects, the mass of the structure was computed according to SR EN 1998–1:2004 [41], considering values of the coefficients corresponding to residential buildings. The Direct Integration method was used for the Nonlinear Time-History analysis, which implied the integration of the equations of motion for each considered time interval *dt*. Considering the characteristics of the seismic actions and the large number of nodes and dynamic degrees of freedom, the Hilber-Hughes-Taylor HHT method was selected for the nonlinear analysis.

The models were subjected to seismic actions only in Ox direction. The structural models with different spans were analysed at 0° and 90° in plane rotation, as shown in Fig. 4.

The Final Softening index (FS) was used for assessing the global structural damage state [51]. Its calculus required the computation of the building's fundamental natural period registered after the seismic event. Therefore, following the Nonlinear Time-History analysis, a modal analysis was performed on the damaged structural model for each seismic event.

2.4. Output parameters

The output parameters of the nonlinear analysis, listed in Table 3, were selected so that they point out the structural damage level registered after the occurrence of specific seismic events. Although only O_1 and O_5 parameters are directly assessing the structural damage, other related parameters were also chosen for comparison purposes. Thus, the influence of various seismic actions on the structure can be better analysed for a higher number of seismic damage-related output parameters.

Considering the complexity of the analysis and the large number of structural models, the damage indices were selected so that they were relatively easy to compute and succeeded in describing the global structural damage registered after the occurrence of the seismic event. Two damage indices were calculated: the Final Softening index (FS) and the Interstory Drift Ratio (IDR). The Final Softening index was suggested by [51] and it is computed using Eq. 2:

$$FS = 1 - \frac{T_0^2}{T_{final}^2} \tag{2}$$

where $T_0$is the initial fundamental period of the structure and $T_{final}$is the final fundamental period of the structure, registered after the seismic event.

Following an earthquake, various types of damage such as cracks and plastic hinges, appear in the building, which reduce the rigidity of the individual elements and, consequently, the overall rigidity of the structure. The Final Softening (FS) index is a global damage index that evaluates the decrease of the structural rigidity by comparing the natural period of the structure in the non-damaged and the damage states. The major advantage of using FS in damage assessment is the readiness with which the required parameters are computed employing finite element software [52]. Nonetheless, FS accuracy could be negatively influenced by several factors [53]. Thus, the instantaneous rigidity of the system could be inaccurately computed in the final step of the seismic action [54]. Also, the shape of the natural vibration mode after the seismic action application could change, caused by the shifting to the inelastic domain of some structural elements [55].

The Interstory Drift Ratio (IDR) was the second damage index used in the current analysis. It represents a traditional overall structural damage assessment method, recommended by norms such as FEMA 356 [56]. Some limits of the IDR are given to provide a proper basis for seismic structural design or to evaluate the structural damage level. The IDR is defined as the ratio of the relative horizontal displacement measured between two consecutive levels to the corresponding story height[57, 58]. Eq. 3 presents the mathematical expression used for IDR computation:

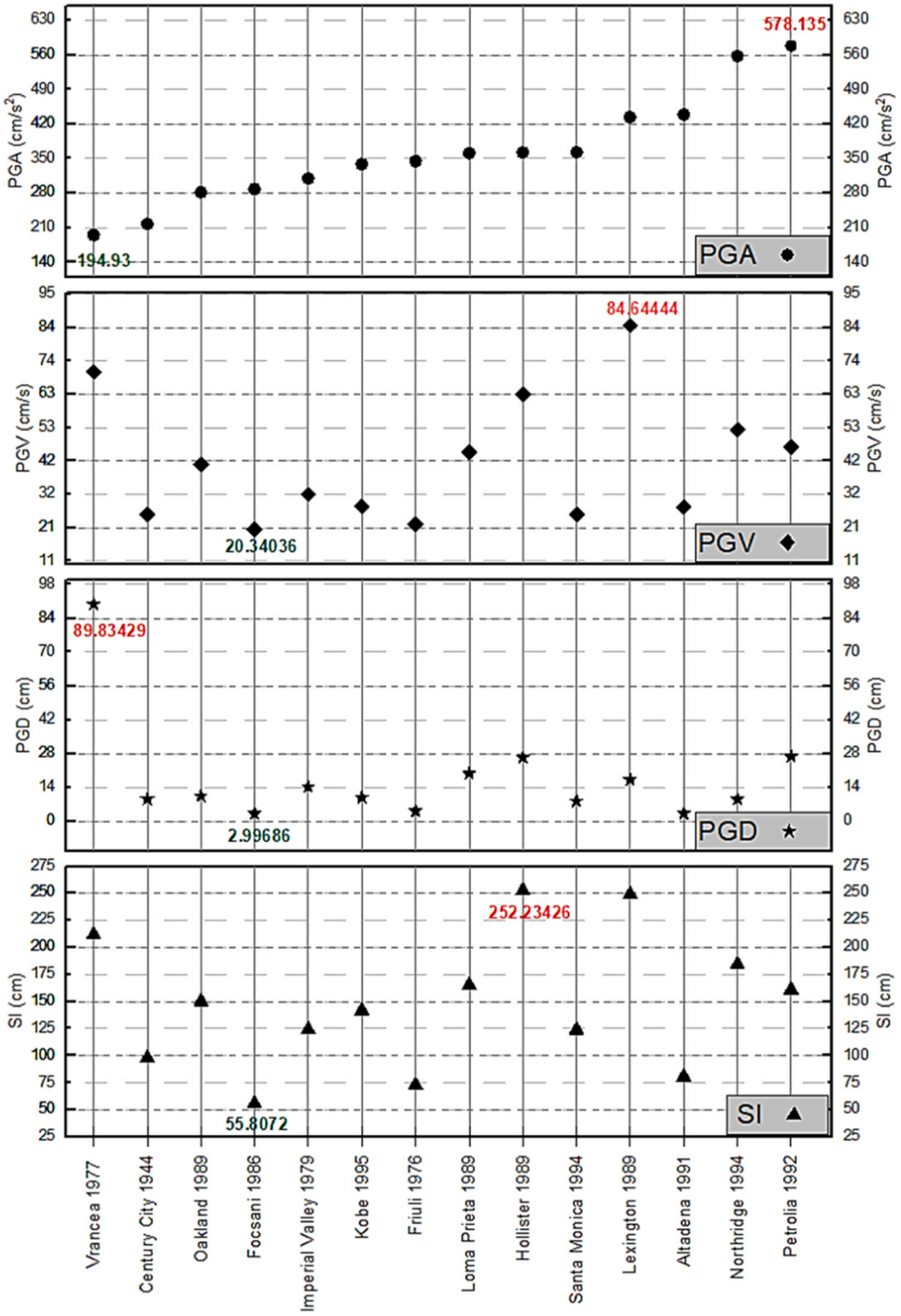

Fig. 2. Seismic action parameter values corresponding to the considered seismic events.

$$IDR = \frac{\delta_i - \delta_{i-1}}{h_i} \quad (3)$$

where $\delta_i$is the lateral displacement associated with level i, δ_{i-1} is the lateral displacement associated with level i-1, and $h_i$is the story height between levels i and i-1 [59].

3. The neural network

3.1. Characteristics of the neural network

The study selected six structural parameters, i.e., I_1-I_6, and 4 seismic action parameters, i.e., I_7- I_{10}, as inputs. Their values were varied to obtain a proper dataset consisting of 3402 entries that were used for the ANN training (80 %) and validation (20 %). The output was defined by 6 parameters, i.e., O_1-O_6, directly or indirectly related to the damage state of the structure. Thus, the neural network was designed to have 10 inputs and 6 outputs.

To minimize errors and account for the output results, a separate ANN was designed for each output parameter. Thus, for outputs O_1, O_2, O_4, O_5 and O_6 the ANN architecture comprises 10 neurons in the input layer, 12 neurons in the intermediate layer and 1 neuron in the output layer. Because of its higher variability, the Final Softening index output O_3 required two intermediate layers: one with 36 neurons followed by

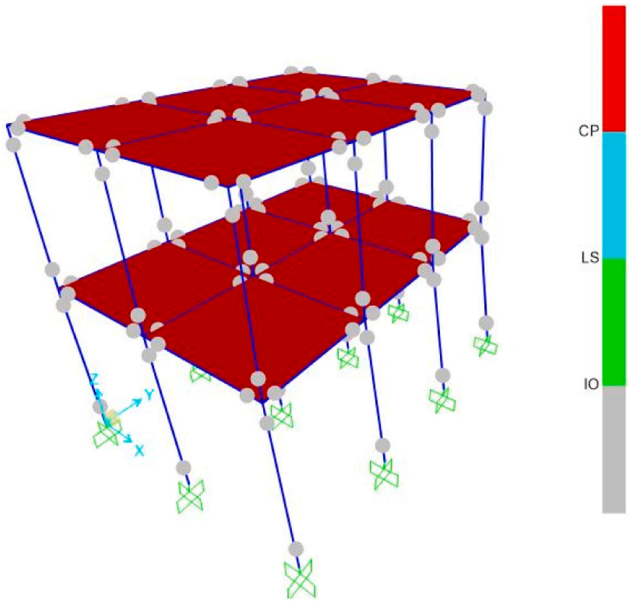

Fig. 3. Nonlinear model with location of the plastic hinges.

another with 12 neurons [37], as presented in Fig. 5. The hyperbolic tangent was used as the activation function.

3.2. Neural network training and correlation coefficient

Following the neural network learning process, a slightly different set of values corresponding to the output parameters is proposed compared to the finite element analysis results. To check the accuracy of the neural network, firstly a comparison had to be made between the ANN final output data and the finite element analysis results. For this purpose, the Pearson correlation coefficient had to be computed, defined by Eq. 5.

$$r = \frac{\sum_{i=1}^{n}(x_i - \overline{x})(y_i - \overline{y})}{\sqrt{\sum_{i=1}^{n}(x_i - \overline{x})^2}\sqrt{\sum_{i=1}^{n}(y_i - \overline{y})^2}} \tag{4}$$

where $\overline{x}$is the average of the dataset represented by $\{x_1, x_2, \ldots, x_i, \ldots, x_n\}$and $\overline{y}$is the average of the dataset represented by $\{y_1, y_2, \ldots, y_i, \ldots, y_n\}$[60–62].

Fig. 6 presents a comparison of the results using ANN and the ones corresponding to the finite element analysis, for each of the six output parameters.

Based on the correlation coefficient evaluation proposed by [63], the ANN proved to have a very strong accuracy when compared to the FEA results. The best correlation was obtained for the fundamental period of vibration of the non-damaged structure T_0 [34]. This result could be explained by the absence of structural non-linearities in the finite element analysis. After the application of the seismic action on the structure, various degradations emerged and the ANN prediction of the fundamental period of vibration of the structure T_{final} became more difficult to be carried out. The lowest accuracy was recorded for the Final Softening index, as presented in Fig. 6. Nonetheless, the coefficient of correlation r still had a high value, i.e., 0.94803, that associates the prediction of this parameter to a high accuracy level.

3.3. Performance of current ANN compared to other ML techniques

In this section, the performance of the previously described Artificial Neural Network (ANN) approach is compared with two widely used machine learning techniques: Random Forest (RF) [64] and Extreme Gradient Boosting (XGBoost) [65]. Both models were trained and evaluated using the same dataset, which consists of ten continuous inputs and six continuous outputs.

Random Forest is an ensemble learning method that builds multiple decision trees during training and outputs the average prediction of these trees for regression tasks. It uses the principle of bagging, i.e., using randomly sampled training instances and random trees that split the data using random features, so that the individual trees within the ensemble are de-correlated. This randomness enhances model generalization and reduces overfitting. Random Forests are particularly effective when the underlying relationship between inputs and outputs is highly nonlinear or the interactions between features are complex. For the current study, the number of estimators considered for Random Forest is 100.

XGBoost, or Extreme Gradient Boosting, is another ensemble method that builds trees sequentially, where each new tree attempts to correct the errors made by the previous ones. It uses gradient descent to minimize a regularized objective function, which balances model accuracy with complexity. As a result, XGBoost shows computational efficiency and scalability. The number of trees considered for XGBoost in the

Table 3
Output parameters [37].

ANN Code	Output parameter	Unit of measure	Symbol
O_1	Fundamental natural period of the non-damaged structure	sec	T_0
O_2	Fundamental natural period of the damaged structure	sec	T_{final}
O_3	Final softening index	-	FS
O_4	Maximum displacement	m	d_{max}
O_5	Interstory drift ratio	%	IDR
O_6	Maximum absolute acceleration	m/s^2	$a_{abs,max}$

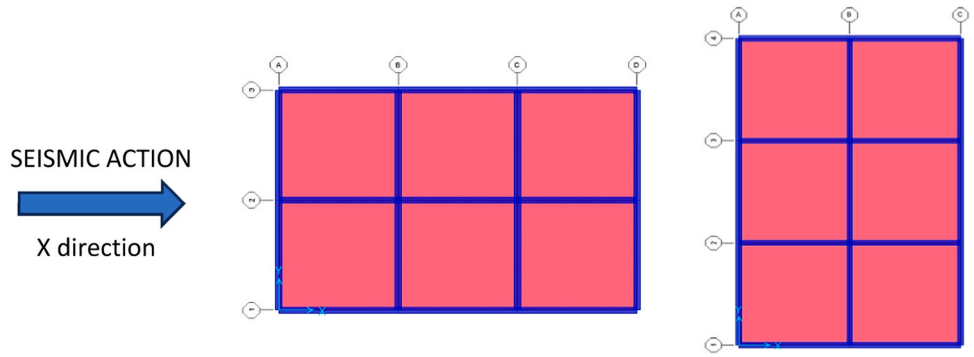

Fig. 4. Models with different number of spans on Ox and Oy directions. Seismic action scenario.

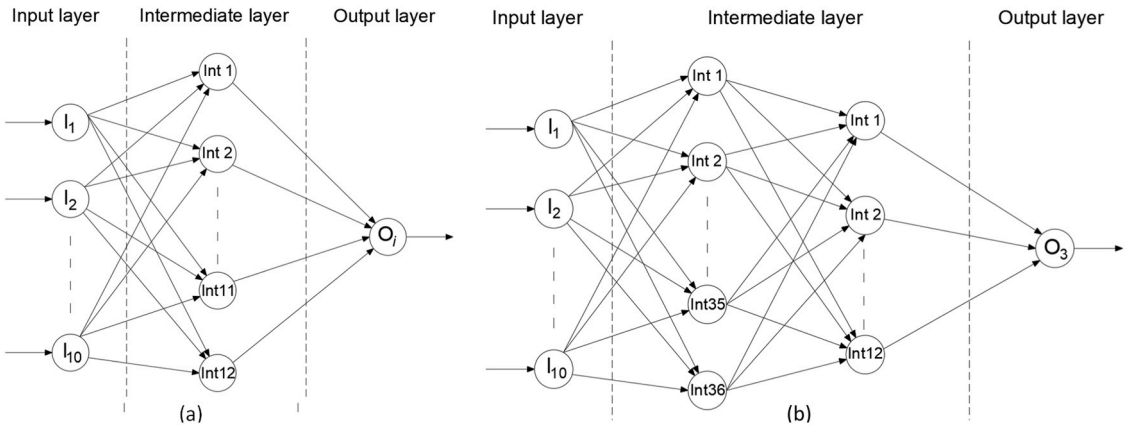

Fig. 5. Neural network architecture for (a) O_1, O_2, O_4, O_5 and O_6 outputs; (b) O_3 output.

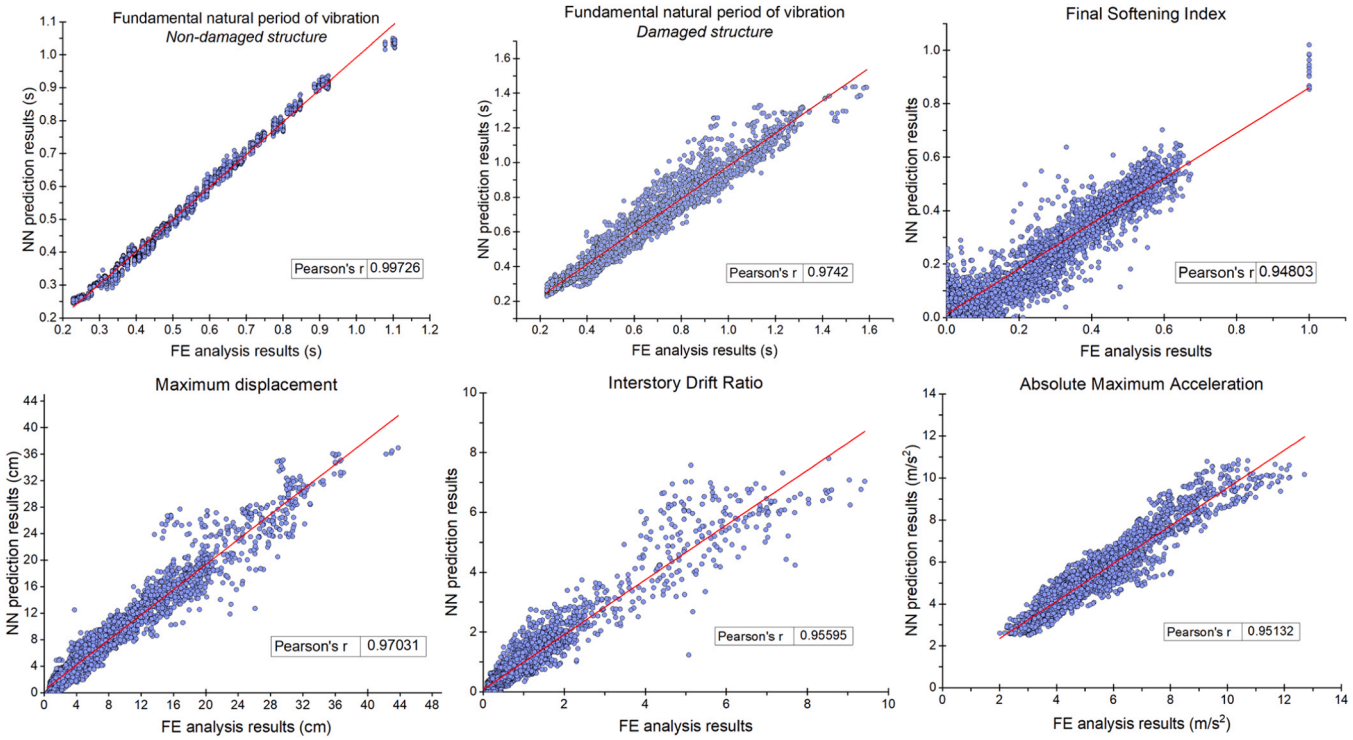

Fig. 6. Linear regression and ANN prediction accuracy analysis.

current analysis is 100, with a learning rate of 0.1 and a maximum depth of 3.

Table 4 shows the comparative performance of the three methods. For both RF and XGBoost, the best results in terms of test correlation coefficient across five runs are included. The table reveals that the ANN consistently generalizes better for most outputs. Random Forest with 100 trees offers good results in some cases, while XGBoost shows signs of overfitting. One of the key observations is that while Random Forest and XGBoost often achieve near-perfect correlation on the training set, their test performance drops more substantially than that of the ANN. This discrepancy points to a possible overfitting tendency in the tree-based models, particularly in XGBoost, which regularly exhibits the largest gap between training and testing correlations. Such behavior may be attributed to its aggressive boosting mechanism and sensitivity to hyperparameter tuning.

Random Forest performs more consistently than XGBoost on the test set and is the best model for O_3 (Final softening index), where ANN notably underperforms. This suggests that O_3 may involve patterns or noise characteristics less amenable to the global function approximation produced by ANNs, but better handled by the localized partitioning structure of decision trees. It may also reflect differences in data complexity or the presence of sharp feature thresholds that decision trees can capture more naturally than artificial neural networks.

The ANN's relatively stable test performance for most outputs suggests a model that has captured the broader structure of the data without relying too heavily on specific features from the training set. Its superior performance, despite lacking perfect training correlations, reinforces its ability to generalize. The one exception, O_3, highlights the value of model diversity in regression tasks, indicating that while ANNs may be preferable overall, tree-based models can offer advantages in specific cases. These findings support the use of ANN as the primary modeling approach in this context, while RF can serve as a valuable alternative for O_3 and O_6. For O_6, however, ANN still performs well.

Unlike RF and XGBoost, which often achieve near-perfect training correlation but exhibit significant drops in test set performance, the ANN maintains a strong balance between fitting the training data and

Table 4
Comparative performance of ANN, Random Forest, and XGBoost in terms of correlation coefficient.

		Train	Test
O_1	ANN	0.9973	0.9795
Fundamental natural period of the non-damaged structure	RandomForest	1.0000	0.8748
	XGBoost	1.0000	0.7376
O_2	ANN	0.9742	0.8743
Fundamental natural period of the damaged structure	RandomForest	0.9986	0.7693
	XGBoost	0.9956	0.6271
O_3	ANN	0.9480	0.5062
Final softening index	RandomForest	0.9860	0.6742
	XGBoost	0.9570	0.4616
O_4	ANN	0.9703	0.9509
Maximum displacement	RandomForest	0.9992	0.8879
	XGBoost	0.9971	0.8266
O_5	ANN	0.9560	0.9200
Interstory drift ratio	RandomForest	0.9976	0.8803
	XGBoost	0.9955	0.8139
O_6	ANN	0.9513	0.8454
Maximum absolute acceleration	RandomForest	0.9988	0.9376
	XGBoost	0.9952	0.8254

preserving predictive accuracy on unseen samples. This suggests that the ANN not only captures complex nonlinear relationships but does so in a way that avoids overfitting. The consistently higher test correlations in five of the six outputs further support the claim that the ANN captures underlying patterns more reliably than the tree-based models, whose test performance is more variable and, in the case of XGBoost, often substantially lower.

4. Influence of the input parameters on the recorded structural damage

The influence of the input parameters on the considered damage parameters, i.e., Final softening index O_3 and Interstory Drift ratio O_5 was determined. For this purpose, the ReliefF algorithm [66] and the SHAP (SHapley Additive exPlanations) technique [67] were used, quantifying the impact each input had on the two considered output parameters.

4.1. Assessment of the influence of the input parameters on the structural damage using RelieF algorithm

The ReliefF algorithm evaluates the importance of input features by assigning them weights. Positive weights indicate that a feature contributes significantly to the predictive performance of the model, with larger positive values representing more influential features. Negative weights suggest that a feature is less relevant or potentially reduces predictive accuracy. Thus, the features with the largest positive weights are the most important for the model.

The advantage of using such an algorithm is to sort the input parameters depending on their influence on the output and determine the ones with a less significant impact. Reducing the number of input parameters to a set composed of only high impact ones may lead to a reduction in the overall error registered by the ANN [68]. Because the input parameters are of two kinds, structural and seismic, the impact analysis focused separately on both types of parameters. However, in the first stage, an overall impact analysis of all input parameters was carried out.

4.1.1. General assessment of the impact of input parameters over the structural damage

Table 5 classifies the input parameters according to their impact on the two damage indices and the corresponding weights are graphically illustrated in Fig. 7.

For both output parameters, the number of stories, i.e., I_1, had a major influence. Conversely, the story height, i.e., I_5, had the smallest

Table 5
Weight of input parameters on the damage indices.

Output No.crt.	Final Softening index O_3		Interstory Drift Ratio O_5	
	Code	Weight	Code	Weight
1	I_1	0.0184942	I_1	0.0524888
2	I_4	0.0064481	I_6	0.051662
3	I_8	0.0041017	I_4	0.0051456
4	I_6	0.0036435	I_3	−0.0000264
5	I_7	0.003367	I_2	−0.0000429
6	I_9	0.0017678	I_9	−0.0086324
7	I_{10}	0.0013924	I_8	−0.0122105
8	I_3	−0.0000323	I_{10}	−0.0173239
9	I_2	−0.0000479	I_7	−0.0244651
10	I_5	−0.0218227	I_5	−0.0382421

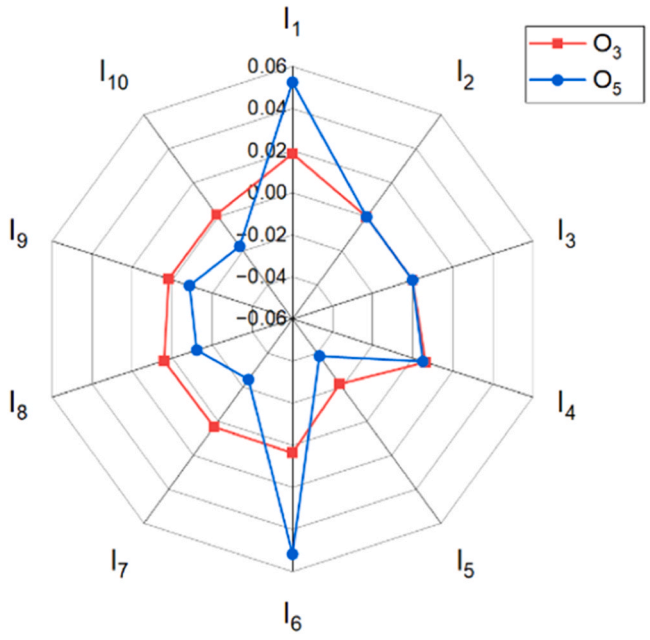

Fig. 7. Comparative graphical representation of FS and IDR parameters.

impact on both FS and IDR parameters. In addition, the impact of the span length I_4 and the column cross-section width I_6 were also relatively high. By comparing the weights corresponding to O_3 and O_5, a certain disparity was observed, which may be explained by the difference in the mathematical formulas associated to each damage index. Thus, the seismic action parameters impact mainly the Final Softening index that was computed by considering the fundamental period of vibration of the damaged and non-damaged structures. They were ranked 3, 5, 6 and 7 in the list, as presented in Table 5. As for the Interstory Drift ratio, computed using the relative lateral story displacement and the story height, the structural parameters were ranked higher in the impact list, i.e., positions 1–5, compared to the seismic action parameters. The impact of the number of spans on Ox and Oy directions, i.e., I_2 and I_3, on O_3 and O_5 outputs varied. Their influence on the Interstory Drift ratio was higher than for the Final Softening index. This result might imply that the mass of the structure impacts with a greater degree the IDR parameter compared to FS.

The ranking of the weights corresponding to the input parameters I_1-I_{10} obtained for the outputs O_3 and O_5 should have been similar, considering that the displacements used in the IDR computation are related to the structural damages, which cause the rigidity decrease in the structure – assessed through the Final Softening index. Nevertheless, the difference in results could be explained by both the structural non-linearities which emerge following a seismic event and the factors which may affect the accuracy of the Final Softening index value, as

presented in Section 2.4. Although the seismic action highly influences the structural response, the characteristics and geometry of the structure are still the primordial parameters.

4.1.2. Influence of seismic parameters on the degree of structural damage

To determine the seismic action impact on the structural damage, it was sufficient to choose a combination of parameters I_1 – I_6, listed in Table 1. The seismic parameters are those associated with the 14 seismic events considered in the analysis, presented in Fig. 2. Considering that I_1 proved to have a high impact on the FS and IDR damage indices, according to the results, the current analysis also focused on varying the number of stories, according to Table 1. Thus, a separate investigation into how the seismic parameters affect the structure for each specific number of stories considered in the analysis was conducted. The impact analysis was carried out for the Final Softening index, i.e., O_3, and the Interstory Drift Ratio, i.e., IDR.

In addition, there was a possibility that the influence of the seismic action parameters would change depending on the rigidity of the structure. To account for this possibility, the combinations of structural parameters were selected to cover various levels of structural rigidity: flexible, medium rigid and rigid structures. The medium rigid structures were chosen to have different number of spans in Ox and Oy directions. Table 6 presents the combinations of structural parameters for which the impact of the seismic action parameters on the seismic damage indices was evaluated. For each I_1 value, a combination of I_2- I_6 values was chosen, which corresponded to the desired structural rigidity level. The values of the seismic parameters varied according to Fig. 2 for each scenario.

Fig. 8 summarizes the results given by ReliefF algorithm. They express the impact of the seismic action parameters on the ANN outputs O_3 and O_5, for structures having different levels of rigidity and different number of stories. The impact was assessed based on the weights computed by ReliefF algorithm corresponding to each seismic action input parameter, i.e., I_7-I_{10}.

The analysis of the impact that seismic action parameters had over the ANN outputs O_3 and O_5 was carried out considering the structural rigidity level, which was also determined by the number of stories. Thus, variations in the degree of influence of the I_7-I_{10} parameters were observed as the structural rigidity level changed. The results indicated that for a flexible structure, as the one corresponding to Scenario 1, the parameter I_8, i.e., PGV, had the highest influence upon the damage of the structure. Conversely, for a rigid structure, I_7, i.e., PGA, was the most detrimental parameter for the building. One single exception was registered for Scenario 2c, in which parameter I_{10}, i.e., SI, had the highest influence on output parameter O_3.

For medium rigid structures, depending on the number of stories, I_7 or I_8 parameters were found in the top of the ranking regarding the impact on the output parameters O_3 and O_5. Thus, the damage registered by the 2-story structures in Scenarios 3.1a and 3.2a was influenced mainly by the input parameter I_7, while for 4- and 7-story structures in Scenarios 3.1b,c and 3.2b,c the highest impact was given by parameter I_8. Only in Scenario 3.2b the highest influence on the output parameter O_3 changed to I_7. However, in this case, the difference between the weights of the two input parameters, i.e., I_7 and I_8, was minor. Based on these observations, it can be stated that the seismic action parameters which had the highest influence on the Final Softening index and Interstory Drift Ratio were PGV for low rigidity structures and PGA for high rigidity structures.

For the considered structures, it was observed that PGD, i.e., I_9, had the lowest influence over the damage indices FS and IDR. Nonetheless, for the flexible structures associated to Scenario 1 the impact of PGA on the structural damage was the smallest among the other seismic action parameters. The spectral intensity, i.e., I_{10}, proved to have a high influence on the structural damage indices, especially in case of small rigidity structures as the ones corresponding to Scenario 1 or the ones having a higher number of stories – Scenarios 3.1b, c and 3.3b, c. This implies that this specific parameter should be considered in the future seismic codes. The degradation of rigid structures was less influenced by the spectral intensity.

When comparing the ranking of the seismic action parameters' impact on the outputs O_3 and O_5, for each scenario, it was observed that the results were similar mainly for highly flexible structures like Scenario 1a,b,c, Scenario 3.1c and Scenario 3.2c. The reason for the discrepancies that emerged in case of high-rigidity structures might be the components of the mathematical expression corresponding to the Final Softening index. As presented in Section 2.4, some errors in the structural instantaneous rigidity might occur. For high-rigidity structures, these errors could have higher values.

4.1.3. Influence of structural parameters on the degree of structural damage

The impact of structural parameters I_1- I_6 on the ANN outputs O_3 and O_5 was evaluated based on specific values for the seismic parameters I_7-I_{10} that were selected and fixed in the ReliefF analysis. Three seismic intensity levels were selected based on the PGA values from the input database: low, medium and high. According to the results presented in Section 4.1, the highest impact on the O_3 and O_5 output parameters was represented by the number of stories I_1. Therefore, the analysis of the impact of structural parameters on the structural damage will focus on the other remaining parameters I_2- I_6. Thus, for each intensity level and each specific number of stories, all possible combinations of structural parameters I_2- I_6 were analysed. Table 7 lists the analysed scenarios, parameters I_2- I_6 varying according to Table 1.

The weights corresponding to each structural parameter I_2- I_6 associated with the outputs O_3 and O_5 are presented in Fig. 9 for three seismic intensity levels. They were computed using ReliefF algorithm. The results were divided based on the number of stories. The impact of structural parameters was given by the ranking of the weights corresponding to each input parameter I_2- I_6, provided by ReliefF algorithm.

Based on the results presented in Fig. 9, the structural parameters with the highest impact on the Final Softening index and the Interstory Drift Ratio were I_4 (span width) and I_6 (column cross-section width). However, according to Scenario 3c, for IDR, the weight of the story height became the most important structural parameter. Thus, by considering IDR, it can be stated that the impact of the story height increases as the seismic action intensity also increases. The number of openings in Ox and Oy directions, parameters I_2 and I_3, proved to have the lowest impact on the structural damage of the building. By comparing these results with the ones obtained in the general analysis presented in Section 4.1, it can be stated that parameters I_4 and I_6 maintained their position at the top of the ranking. Only parameter I_5 did not maintain its position in the ranking of the impact on the structural damage. According to the general analysis, I_5 was placed last, while the results obtained in the current section placed it in the first three places. Nevertheless, the results from the current section could have a higher accuracy considering that each scenario focused on a single seismic recording for the desired intensity level. By reducing the number

Table 6
Structural parameter combinations for assessing the impact of seismic action parameters on structural damage.

Scenario		I_1	I_2	I_3	I_4	I_5	I_6	T_0	Rigidity
1	a	2	2	2	5	3.5	0.3	0.511246	Flexible
	b	4	2	2	5	3.5	0.4	0.745742	
	c	7	2	2	5	3.5	0.7	1.078205	
2	a	2	3	3	3	2.8	0.3	0.251858	Rigid
	b	4	3	3	3	2.8	0.5	0.314365	
	c	7	3	3	3	2.8	0.7	0.539815	
3.1	a	2	2	3	4	3	0.3	0.350161	Medium rigidity
	b	4	2	3	4	3	0.4	0.512238	
	c	7	2	3	4	3	0.7	0.749715	
3.2	a	2	3	2	4	3	0.3	0.350161	
	b	4	3	2	4	3	0.4	0.512238	
	c	7	3	2	4	3	0.7	0.749715	

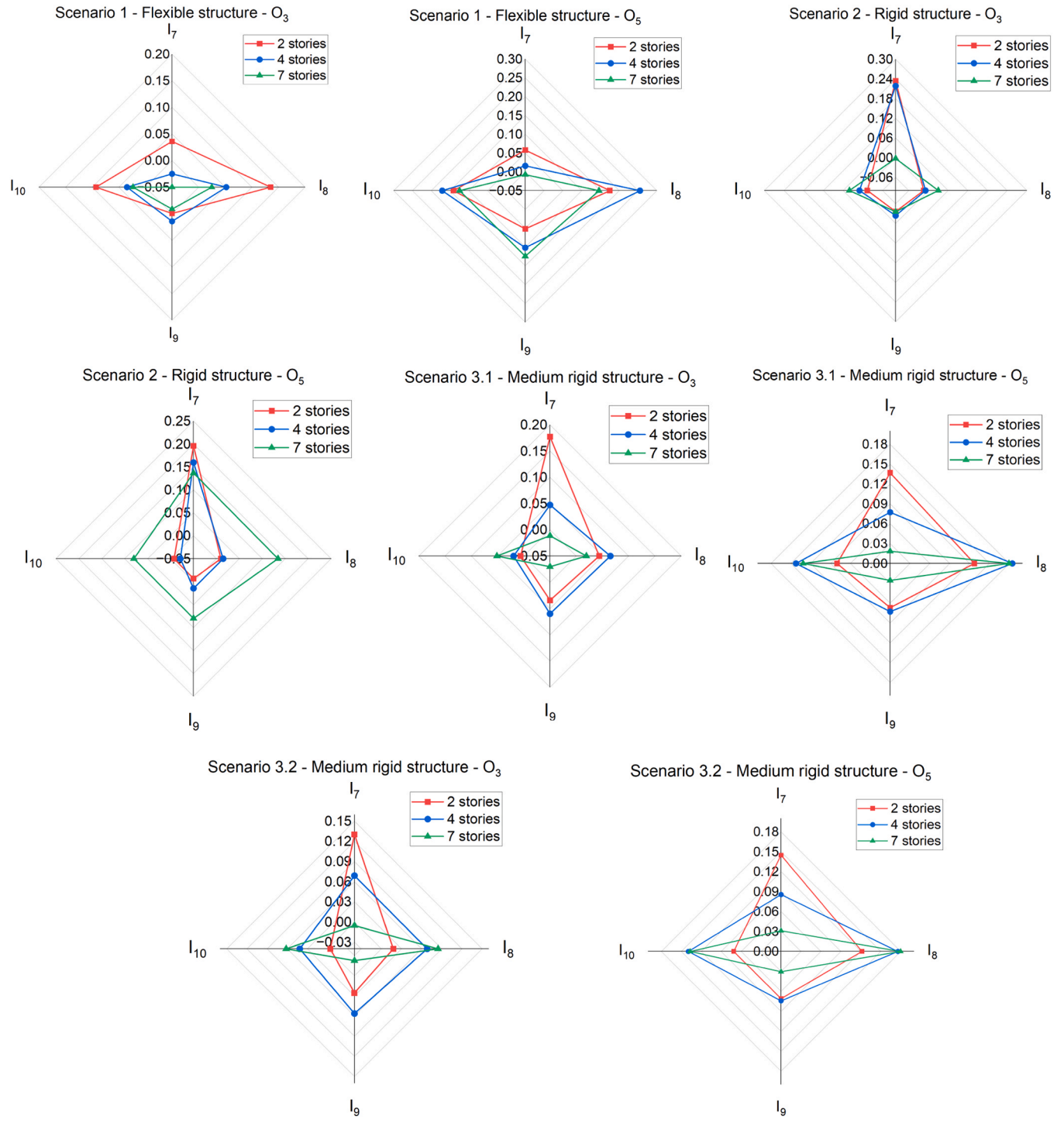

Fig. 8. Influence of seismic action parameters on structural damage (see Annex A, Table A.1).

of parameters to only those of interest, possible errors could be diminished. To sum up, based on the results, it can be stated that the level of seismic intensity does not have a significant impact on the ranking regarding the impact of structural parameters on the structural damage.

When focusing on the number of levels, it can be observed that the ranking between the results corresponding to output O_3 and the ones corresponding to output O_5 slightly changed. However, the differences are small for the 2 stories structures, i.e., Scenarios 1a, 2a, 3a. In all the other cases, although several differences were registered, they were only of maximum one place, except Scenario 2b.

4.2. Assessment of the influence of the input parameters on the structural damage using SHAP technique

SHAP (SHapley Additive exPlanations) [67] is an interpretability technique that explains the output of any machine learning model by quantifying the contribution of each input feature to an individual prediction. It is inspired by the idea of Shapley value from cooperative game theory [69], which aims to allocate credit fairly among contributors, in this case, features. For each prediction, SHAP calculates the change in output when an input is included versus when it is excluded, and averages over all possible combinations of features. This results in a

Table 7
Scenarios used in the analysis of structural parameters impact on the structural damage.

Scenario		I_1	PGA [cm/s^2] In7	PGV [cm/s] In8	PGD [cm] In9	SI [cm] In10	Number of combinations	Seismic intensity level
Scenario 1	a	2	194.93	70.0451	89.8343	211.2727	69	Low
	b	4	194.93	70.0451	89.8343	211.2727	111	
	c	7	194.93	70.0451	89.8343	211.2727	63	
Scenario 2	a	2	433.563	84.6444	17.0825	248.6337	69	Medium
	b	4	433.563	84.6444	17.0825	248.6334	111	
	c	7	433.563	84.6444	17.0825	248.6334	63	
Scenario 3	a	2	578.135	46.3859	26.6627	160.9072	69	High
	b	4	578.135	46.3859	26.6627	160.9072	111	
	c	7	578.135	46.3859	26.6627	160.9072	63	

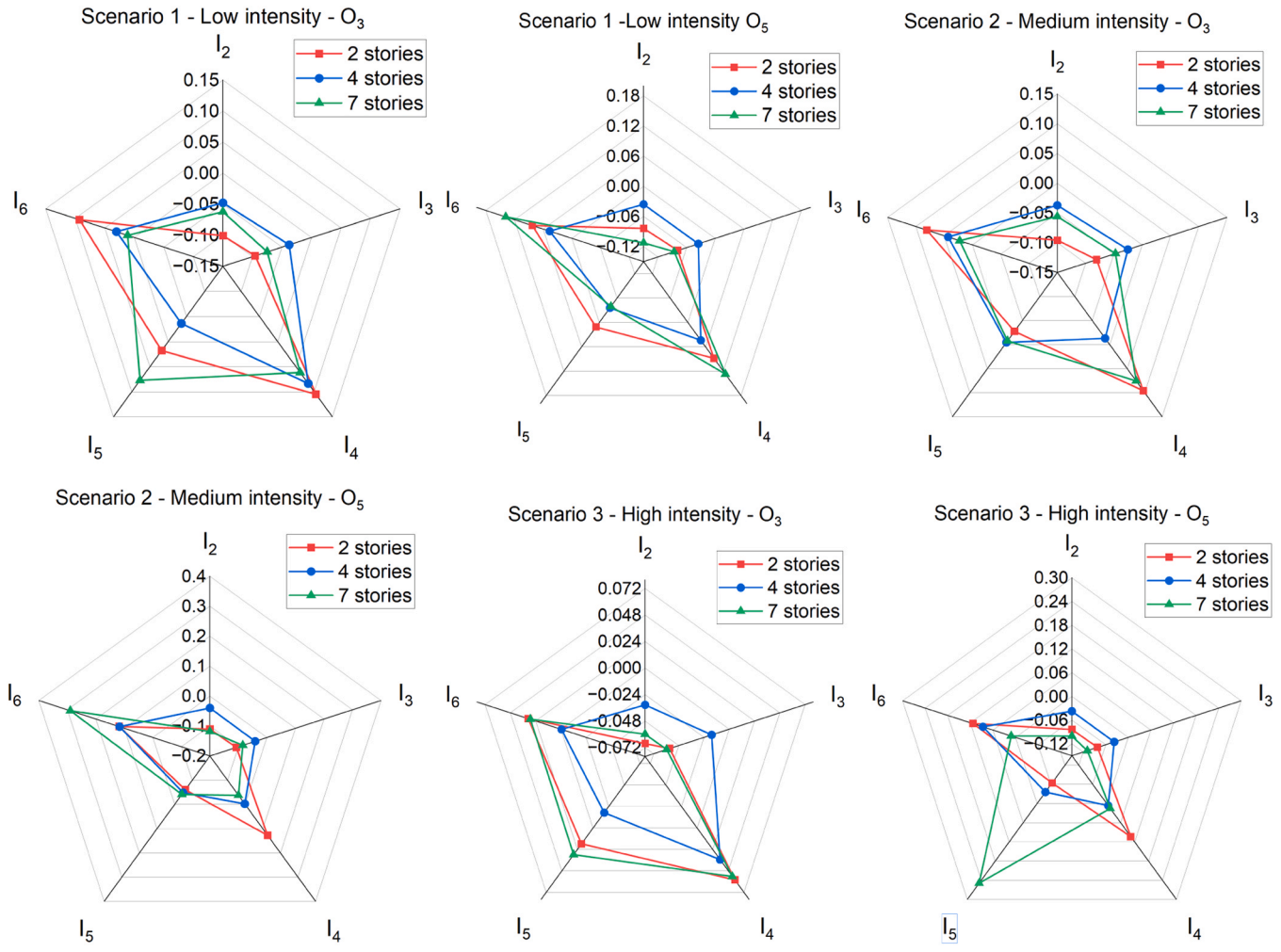

Fig. 9. Impact of structural parameters on the structural damage (see Annex A, Table A.2).

SHAP value for each input, which represents how much it pushes the prediction higher or lower relative to a baseline value, typically the mean prediction. SHAP values are additive and allow for consistent, interpretable breakdowns of model output. By aggregating SHAP values for many samples, one can also assess the global importance of inputs.

The SHAP summary plots (Figs. 10 and 11) for the two outputs related to the damage index provide a detailed picture of how each input feature contributes to the predictions of the model for different outputs.

Output 3 (Final Softening Index) displays a more distributed pattern, with input 8 (Peak ground velocity) as a major factor. Its SHAP values are consistently high for high feature values, which indicates a strong influence. Input 1 (Number of stories), while still active, plays a more balanced role here. This diversified contribution pattern aligns with the earlier finding that Random Forest outperformed ANN for this output, which suggests that the RF model can handle the interactions between features more effectively.

Output 5 (Interstory Drift Ratio) shows a high impact, according to Fig. 11, from input 8 (Peak ground velocity), which indicates a strong nonlinear effect. The wide SHAP spread for inputs 6 (Width of column cross-section) and 10 (Spectral intensity) further supports the presence of key interactions.

The SHAP technique confirms the results of RelieF algorithm presented in Section 4.1. For both damage indices, the number of stories (Input 1) was proven to be important, as well as Inputs 8 (Peak ground

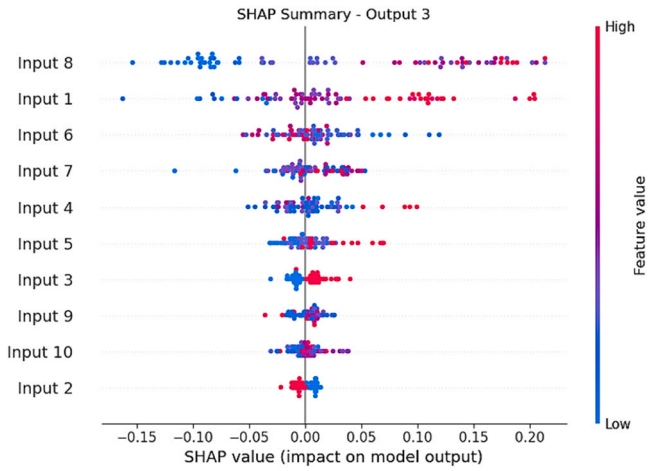

Fig. 10. SHAP value for Output 3 (Final Softening Index).

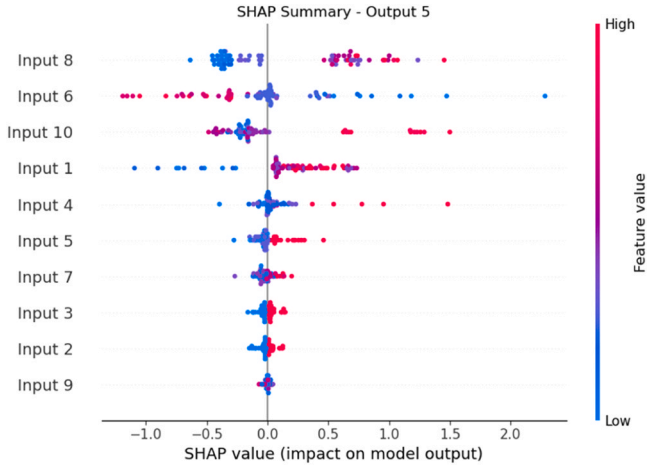

Fig. 11. SHAP value for Output 5 (Interstory Drift Ratio).

velocity) and 6 (width of column cross-section).

4.3. Partial dependence plots (PDPs) of the relationship between inputs and damage indices

Partial Dependence Plots (PDPs) [70] are visualization tools that show the average effect of one or two input features on the predictions of a model. They help to identify whether a relationship between an input and an output is linear, monotonic, or more complex. A PDP varies one input feature across its range while averaging the predictions of the model over all other inputs in the dataset. This isolates the marginal impact of that input feature, assuming it acts independently of others. In regression problems, the y-axis of the PDP represents the predicted output, and the x-axis shows the values of the selected input feature. For example, a steep slope indicates that small changes in the input cause large changes in the prediction, while flat sections imply little to no influence. PDPs are especially useful for identifying thresholds, plateaus, or saturation effects. Though they assume feature independence, they can offer insights into the global behavior of the model with respect to the inputs.

For computing the SHAP values above, the test set was used, because the SHAP values method aims to explain the behavior of the model on data it has not seen during training. This highlights how the model generalizes and which inputs truly influence predictions in real-world or unseen scenarios. Since overfitting is a risk, SHAP values can help to reveal whether the learned patterns hold beyond the training data. In contrast, PDP is designed to show global trends by averaging predictions across the dataset. For this reason, the training set is used here because it contains a full, stable representation of the feature distributions on which the model was trained.

Figs. 12 - 13 show the PDP plots corresponding to the two outputs corresponding to the damage indices (O_3 – Final Softening Index and O_5 – Interstory Drift Ratio). Usually, a common representation of PDPs includes separate graphs for each input. However, here we have 10 inputs, and to save space, we display them on single plots, one for each output, with normalized input values.

For O_3 (Final Softening Index), input 1 (Number of stories) again has the steepest positive slope, meaning that raising this feature leads to a significant boost in output. Inputs 7 (Peak ground acceleration) and 8 (Peak ground velocity) show pronounced nonlinear changes, which indicates complex behavior. For input 7, the partial dependence quickly rises, then shifts downward; mid-range values produce beneficial effects before diminishing returns. Input 8 has abrupt jumps, which suggests that certain intervals drive larger changes than others. These fluctuations reveal thresholds or tipping points where the predictions shift noticeably.

For O_5 (Interstory Drift Ratio), as presented in Fig. 13, input 1 changes its shape: it drives a robust positive impact until mid-range, after which its incremental benefit tapers off. Input 6 (width of column cross-section) begins with a steep negative influence that changes into a more linear decline, suggesting a saturating adverse effect as its values increase. Input 8 shows a distinct threshold; its effect shifts sharply from a modest value to a strong positive impact at mid-range. Meanwhile, input 10 (spectral intensity) remains relatively inactive until the final quarter of its range, where it starts contributing positively to the output.

As seen from these figures, the PDPs show the variable roles of features for each output and highlight key nonlinearities and interactions in the model structure.

5. Neural network testing

To test the neural network, it was run with different input cases, and its predictions were compared with the results from the FE analysis. In a previous paper, research was done on the ANN network for datasets where each input parameter was new to the network compared to the initial input parameters [37]. According to the study, all output parameters were predicted at an acceptable level by the ANN, except the Final Softening index, for which the differences between ANN and FE analysis were so high that the damage level changed.

A different approach was used for the present paper. Instead of modifying all input parameters, the change was done separately on the two types of input parameter sets. Thus, two different analyses were carried out: one in which only structural input parameters were modified and the other in which only the input seismic parameters were modified. When modifying all input parameters, the ANN error should be greater than the one corresponding to the case when only structural or seismic input parameters are modified. However, there might be cases when several input parameters of the considered structure are identical to the ones used in ANN training. The analysis should provide the minimum error when testing the network compared to FE analysis. The maximum error is presented in the above-mentioned study [37].

5.1. ANN testing for distinct input structural parameters

The impact analysis of the structural parameters on the damage indices was considered as a starting point for selecting the parameters to be modified. According to the impact analysis, parameters I_1, I_4 and I_6, representing the number of levels, span opening and column cross-section width, had the highest influence on the FS and IDR damage indices. Therefore, these parameters were selected to be modified for ANN testing purposes. Three scenarios were considered characterized by

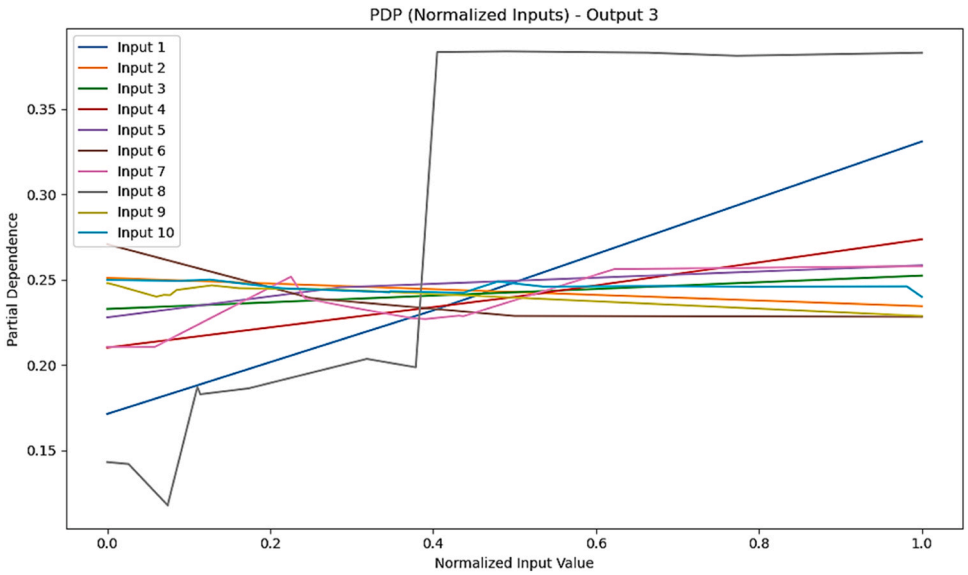

Fig. 12. PDP for Output 3 (Final Softening Index).

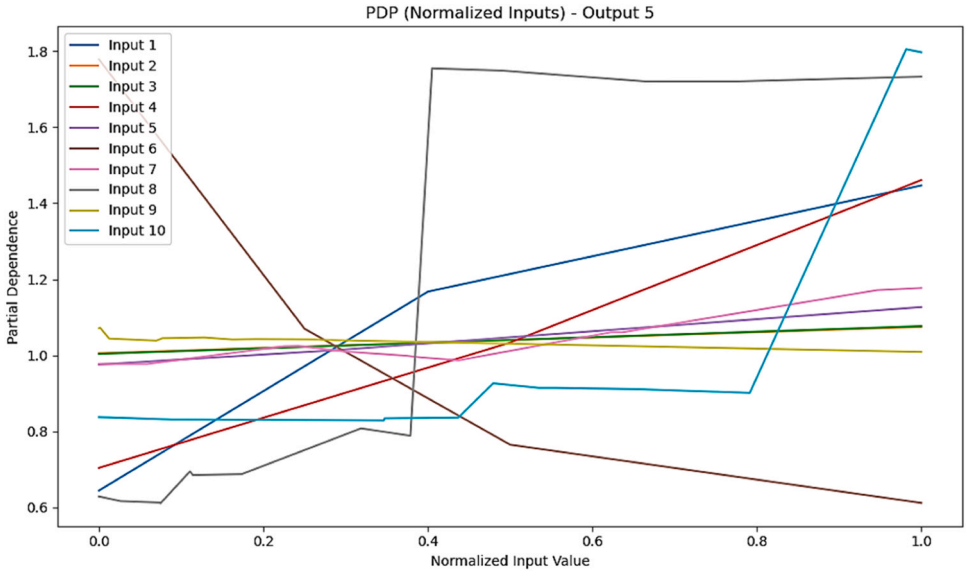

Fig. 13. PDP for Output 5 (Interstory Drift Ratio).

the change of only one parameter from the three mentioned above, as presented in Table 8. The modified parameter is shown in bold. The selection of the base structures was done so that various heights and rigidity levels were covered. In each scenario, the structure was subjected to all 14 seismic events listed in Fig. 2, with a total of 42 new data sets being generated.

The ANN testing was evaluated for all outputs. 42 combinations were analysed and are presented in Annex A, Table A.3 as follows: Scenario A.1 – Combinations 1–14, Scenario B.1 – Combinations 15–28 and Scenario C.1 – Combinations 29–42.

Table 8
Scenarios for ANN testing by varying structural parameters.

	I_1	I_2	I_3	I_4	I_5	I_6
Scenario A.1	**5**	2	3	4	3	0.4
Scenario B.1	4	2	2	**4.2**	3.5	0.4
Scenario C.1	7	3	3	4	2.8	**0.6**

Figs. 14–19 show the differences between ANN and FE analysis results corresponding to Scenarios A.1, B.1 and C.1.

Fig. 14 confirms the previous analysis according to which the number of stories I_1 had the highest influence on the damage indices. The statement could be extended to the fundamental period of vibration of the non-damaged structure, as well. Thus, for Scenario A.1, in which only I_1 parameter was modified, the highest variations between ANN and FEA results were registered, reaching a maximum of 8 %. The variation decreased at a maximum of 4 % for Scenario B.1, where only the span length I_4 was modified. In Scenario C.1 the difference between ANN and FEA continued to decrease to 3 % when the only change was for the cross-sectional width of the column, I_6. To sum up, the neural network accurately predicted the fundamental period of vibration, T_0, for the non-damaged structure.

The comparison between ANN and FEA values regarding the fundamental period of vibration for the damaged structure T_{final} is presented in Fig. 15. No pattern regarding the error distribution could be distinguished. There were combinations, such as Combination 40, where the relative difference between FEA and ANN results reached 19 %. In this case, the T_{final} value computed using FEA was 0.715014 s, while the NN result was 0.857 s. For most combinations, the maximum difference between ANN and FEA results was 11 %, which is an acceptable value due to the benefits the ANN brings compared to the FEA, i.e., reduced computational time.

As shown in Fig. 16, the largest differences in values between ANN and FEA results were obtained for the Final Softening FS index. These important differences were expected because of the lower r value, presented in Fig. 6. However, the importance of damage indices computation is not given by their value, but by its correspondence to a specific performance or damage level. Therefore, the comparison between the FS values given by the ANN and FEA focused not on values but on the corresponding damage levels. The prediction was considered optimum when the damage levels given by ANN and FEA were the same. Based on studies regarding the limits of the FS index [71], the absolute maximum allowed difference between ANN and FEA values was ±0.05. When this value was exceeded, the probability of having different damage levels corresponding to ANN and FEA would be high. There were only 18 combinations for which the absolute difference between ANN and FEA did not exceed ±0.05, representing only 42.9 % of the total number of combinations. Therefore, unlike the other output parameters, the neural network did not succeed in appropriately predicting the FS values, in either of the three considered scenarios.

The output parameter O_4 corresponding to the maximum displacement was satisfactorily predicted by the neural network, as presented in Fig. 17. The largest relative difference between the ANN and FEA values was obtained for Combination 24, i.e., 33.6 %. This absolute difference of only 4.7 cm is high. However, there were only 7 combinations for which the absolute difference between ANN and FEA values was greater than 2.5 cm. Moreover, the absolute differences greater than 1.5 cm were recorded only for structures which had the maximum displacements greater than 10 cm. In those cases, some of the structural elements entered the non-linear domain, which might increase the error value. According to Fig. 13, there are some extreme values recorded for the maximum displacement corresponding to Combinations 9, 11, 23, 25, 37 and 39, which are associated with Lexington 1989 and Hollister 1989 seismic actions. In those cases, the structure yielded, causing large displacements.

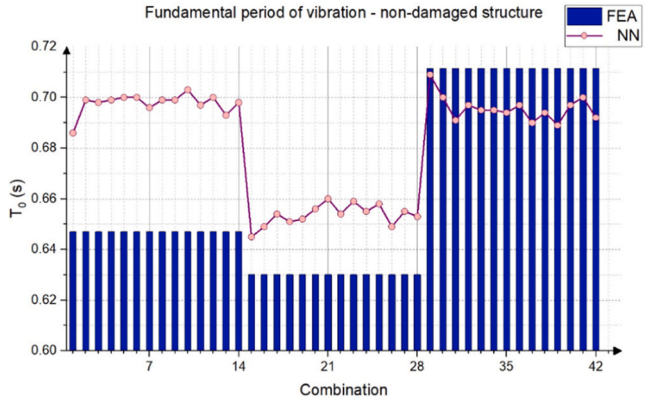

Fig. 14. Comparison between ANN and FEA for the fundamental period of vibration of the non-damaged structure.

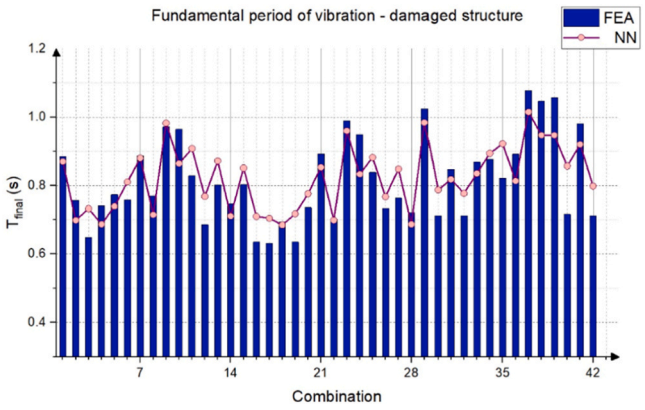

Fig. 15. Comparison between ANN and FEA for the fundamental period of vibration of the damaged structure.

Fig. 16. Comparison between ANN and FEA for the Final Softening Index.

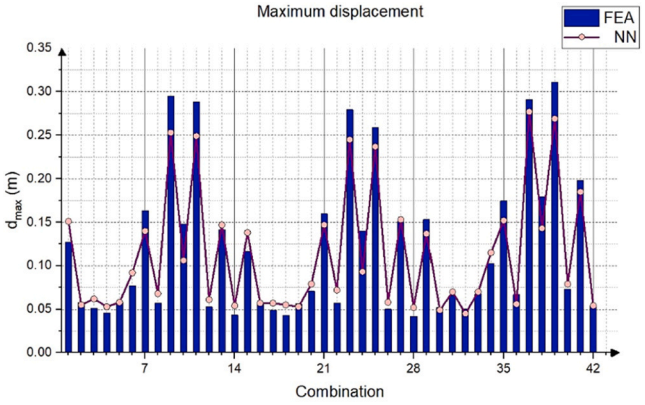

Fig. 17. Comparison between ANN and FEA for the maximum registered displacement.

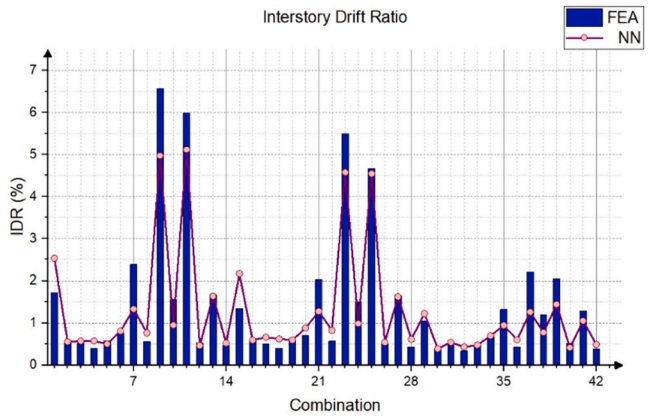

Fig. 18. Comparison between ANN and FEA for the Interstory Drift Ratio.

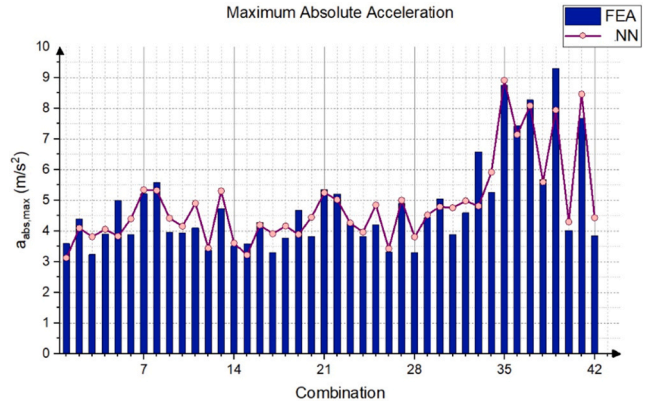

Fig. 19. Comparison between ANN and FEA for the maximum absolute acceleration.

Important differences between ANN and FEA values corresponding to the IDR were obtained, as shown in Fig. 18. However, compared to the ANN prediction of the FS index, IDR prediction exhibited a higher accuracy. The maximum relative difference between the ANN and FEA values for the three scenarios was 61.084 %, corresponding to Combination 15. The maximum absolute difference was registered for Combination 9, i.e., 1.6 %. Nevertheless, compared to the results associated with the FS index, an improvement in the ANN prediction could be seen for IDR. Based on the studies of [71] regarding the relation between the damage levels and IDR, an acceptable absolute difference between the ANN and FEA values was ±0.4 %. There were 12 combinations from a total of 42 that exceeded this limit, representing less than 1/3 of the total number of combinations.

Thus, IDR could be properly estimated using ANN when only one structural parameter was modified. Combinations 9, 11, 23 and 25 associated with Lexington 1989 and Hollister 1989 seismic actions registered the highest IDR values due to the failure of several structural elements.

The ANN prediction of the maximum absolute acceleration recorded by the structure had a high accuracy, as presented in Fig. 19. The highest relative difference between ANN and FEA values was recorded for Combination 33, i.e 26.97 %. However, most of the differences were under 15 %, corresponding to 31 combinations from a total of 42. In addition, Fig. 19 shows an important increase in the maximum absolute acceleration in Scenario C.1 compared to the other two scenarios. This increase could be linked to the number of levels and to the structural mass, which were both higher than in the other scenarios.

5.2. ANN testing for distinct input seismic action parameters

From the input cases used in training the ANN, three combinations of structural parameters I_1 – I_6 were selected, different than the ones used in the previous testing phase, presented in Table 9, and further subjected to other seismic actions than the ones used in training. The seismic recordings were chosen so that the PGA values were found in the minimum-maximum interval marked out in Fig. 2. Fig. 20 presents the characteristics of the seismic actions used in the FEA for testing the prediction capability of the ANN. Thus, a total of 15 new data sets were obtained.

The values of the structural parameters I_1 – I_6 corresponding to the structural models chosen for testing the ANN to other seismic action parameters are presented in Table 9. They were selected from the ANN training combinations.

Each structural model was subjected to the 5 seismic actions presented in Fig. 20. The combinations corresponding to each Scenario are given in Annex A, Table A.4. The comparative analysis between the ANN and FEA values is shown in Figs. 21–26, for each output parameter and each combination.

The fundamental vibration period of the non-damaged structure T_0 did not depend on the seismic action, being computed before its application. Thus, changing the seismic parameters did not influence the results and did not add supplementary errors, as presented in Fig. 21. The maximum relative difference between the ANN and FEA results was 4.3 %. By comparing these results to the ones obtained in the Section 4.5, the importance of geometrical input parameters I_1, I_4 and I_6 was highlighted. When these parameters were not changed, the errors stayed at a minimum value.

The prediction capability of the neural network for the output parameter O_2, i.e., the fundamental vibration period of the damaged structure, was confirmed as presented in Fig. 22. When comparing the ANN and FEA results, the differences were relatively small. The biggest difference relative to the FEA value was recorded for Combination 14, i.e., 32 %. This value was bigger than the maximum difference computed in the previous section for the same output parameter, i.e., 19 %. Nevertheless, only three combinations have significant relative differences (Combinations 2, 13 and 14). The rest had at most 15 % relative differences, which were considered acceptable, their absolute differences being smaller than 0.1 s.

Fig. 23 shows that the neural network did not succeed in accurately predicting FS values for either of the considered scenarios. Based on [71] in which the levels of structural damage are related to certain FS index values, the acceptable maximum absolute difference between ANN and FEA results was 0.05. There were only three combinations for which the absolute difference between ANN and FEA was smaller than 0.05 (Combinations 1, 9 and 10), representing 20 % of the total number of analysed combinations. Thus, using the ANN with the considered architecture for predicting the FS index was not a viable solution.

According to Fig. 24, the maximum displacement d_{max} was satisfactorily predicted by the neural network. The maximum relative difference between ANN and FEA results is approximately 52 % (8.36 cm absolute difference), corresponding to Combination 2. Nevertheless, only 5 combinations had a relative difference greater than 30 %. The rest had an absolute difference between ANN and FEA smaller than 3 cm. It can be also observed that although the combinations were sorted depending on the PGA value, there was no specific evolution of the maximum

Table 9
Scenarios for ANN testing for various seismic action parameters.

	Input					
	I_1	I_2	I_3	I_4	I_5	I_6
Scenario A.2	2	3	3	5	3	0.3
Scenario B.2	4	3	2	4	3	0.4
Scenario C.2	7	3	3	4	3	0.7

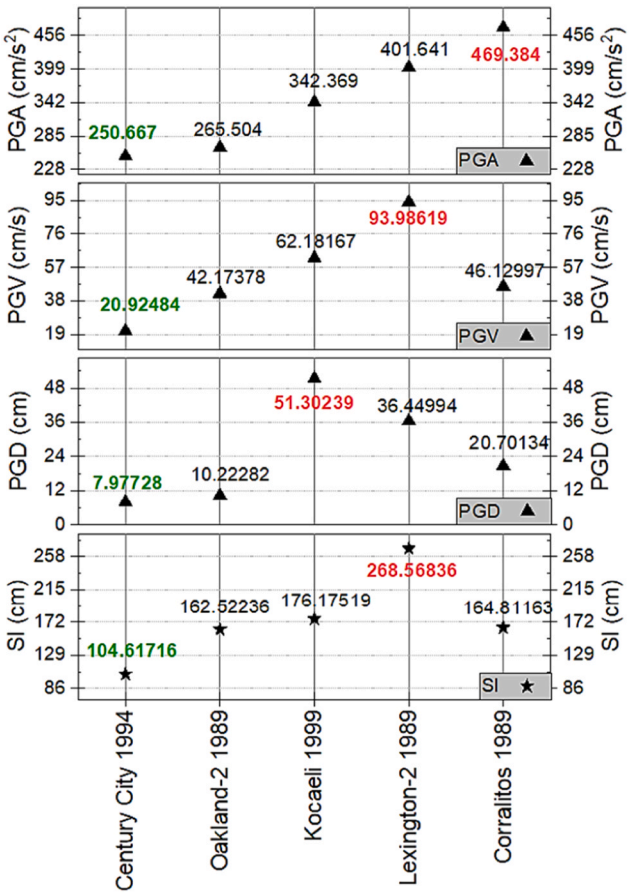

Fig. 20. Seismic action parameter values for ANN testing.

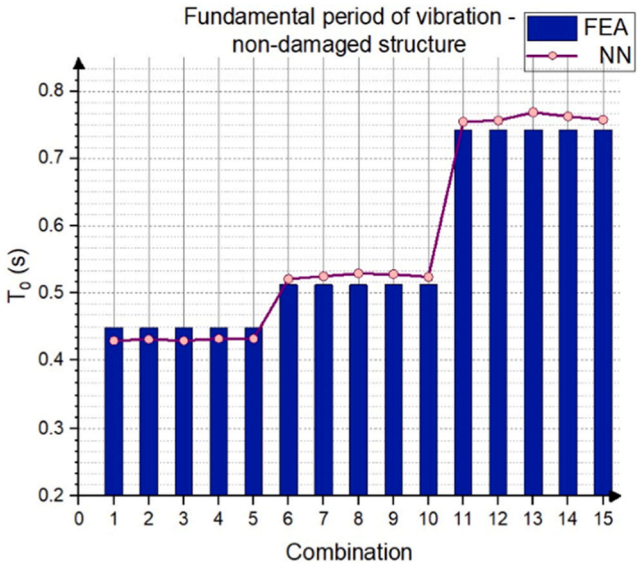

Fig. 21. Comparison between ANN and FEA for the fundamental period of vibration of the non-damaged structure.

recorded displacement (increasing or decreasing). Therefore, the maximum displacement does not depend solely on the PGA value.

According to Fig. 25, the IDR value was predicted at an acceptable level by the ANN, especially when compared to the prediction of FS index. The highest relative difference between ANN and FEA was recorded for Combination 2, i.e., 50.33 %. Only for Combinations 2, 7

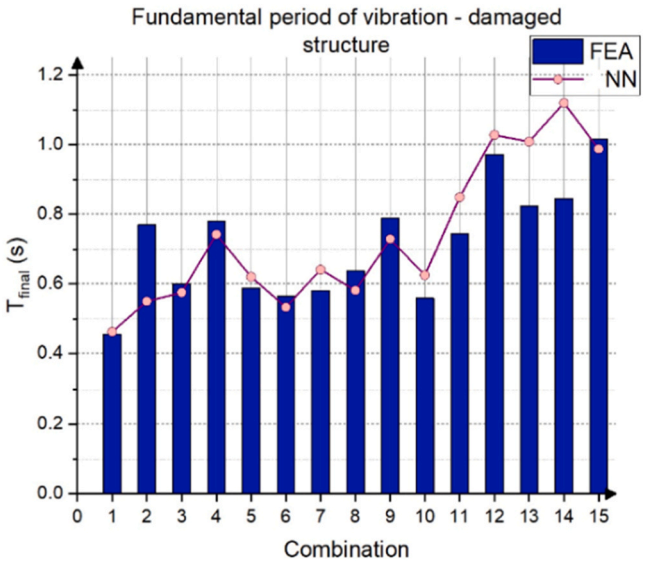

Fig. 22. Comparison between ANN and FEA for the fundamental period of vibration of the damaged structure.

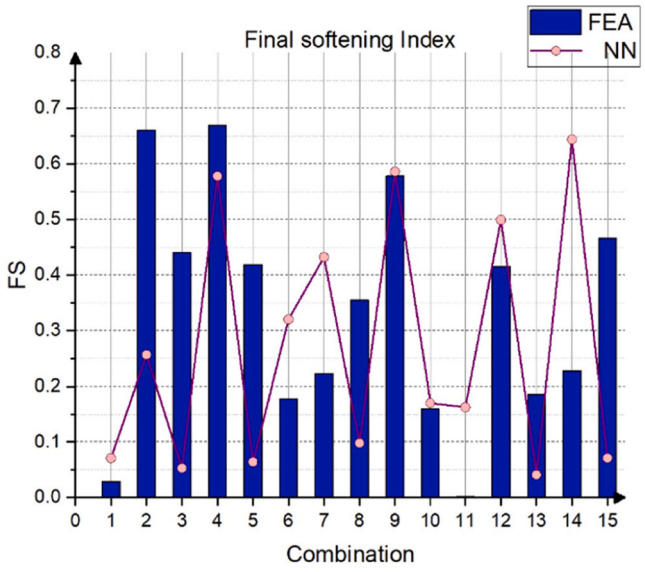

Fig. 23. Comparison between ANN and FEA for the Final Softening Index.

and 10 the relative difference between ANN and FEA values exceeded 30 %. The highest IDR values obtained for Combinations 4 and 9 were associated with Lexington-2 1989. The large IDR values registered for Combinations 2, 4 and 9 could be explained by the failure of the structural elements at a certain level. In the current case, the failure was recorded at the first level.

The maximum relative difference between ANN and FEA values decreased for the current case to 50.33 % compared to the previous analysis. Moreover, the number of combinations for which a maximum absolute difference of 0.4 % was registered between the ANN and FEA results decreased compared to the results obtained when modifying only the structural parameters. Therefore, it can be stated that changing the seismic action parameters results in smaller errors in the IDR calculus than modifying the structural parameters. By considering the damage limit values for IDR based on [71] and setting a maximum absolute difference between ANN and FEA values of ±0.4 %, only 4 combinations overpassed this limit, i.e., Combinations 2, 4, 7 and 10.

The maximum absolute acceleration was predicted at an acceptable

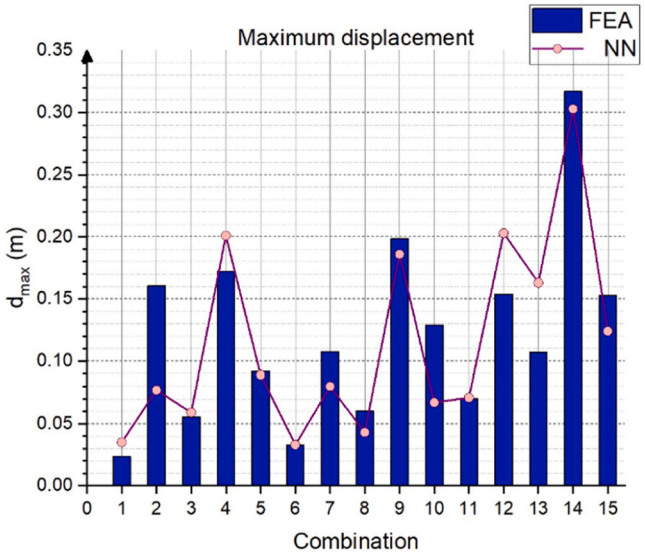

Fig. 24. Comparison between ANN and FEA for the maximum registered displacement.

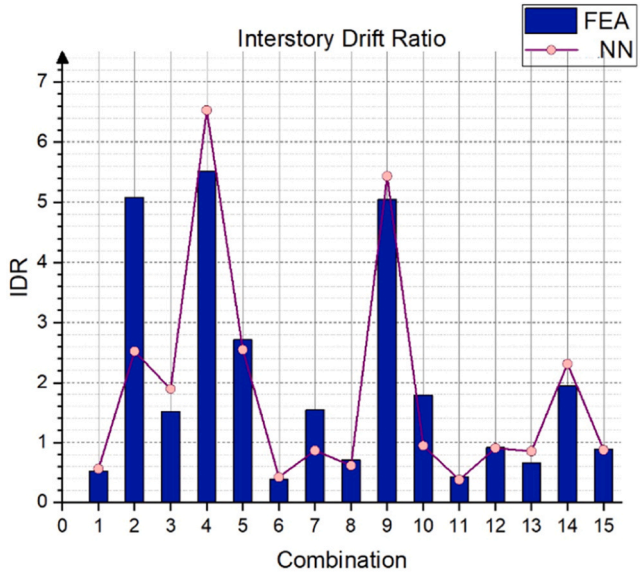

Fig. 25. Comparison between ANN and FEA for the Interstory Drift Ratio.

level, as shown in Fig. 26. Only for Combinations 4 and 13 was the relative difference greater than 25 %. For all other combinations, the absolute difference between ANN and FEA values was less than 1 m/s^2. An increase of the maximum absolute acceleration was observed in case of Scenario C.2, which could be associated with the increase in height. When comparing the results obtained in the previous section, a substantial increase in the maximum relative difference is observed from 26.97 % to 71.67 %. Therefore, only changing the seismic action parameters causes a significant impact on the maximum absolute acceleration, compared to the case when the change is done only to the structural parameters.

5.3. Comparison between ANN and FEA damage levels

Specific levels that correspond to the values of the damage indices were developed to allow for a quick and accurate evaluation of the global damages that may be experienced by a structure. There are several levels proposed by different institutions. For example, the

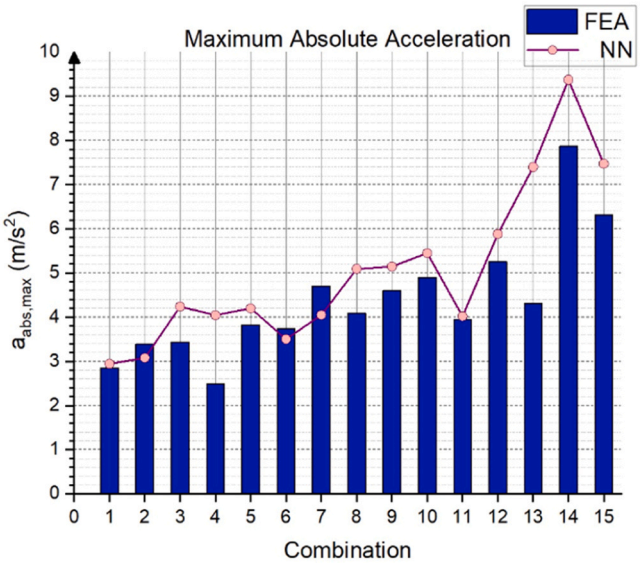

Fig. 26. Comparison between ANN and FEA for the maximum absolute acceleration.

Federal Emergency Management Agency (FEMA) recommends the following building structural performance levels: Immediate Occupancy, Damage control, Life Safety, Limited safety and Collapse prevention [56]. However, FEMA performance levels were found in literature linked to the drift ratio [72], but not to Final Softening index. A common damage scale for both indices would be recommended. Therefore, for the current study, the research provided by [71] was used, given that the damage scale was employed to evaluate both Final Softening and Drift Ratio, as presented in Table 10. The associated performance levels for each damage level given by the drift ration value according to the prescriptions given in FEMA 356 are also presented [56, 73].

Based on the damage levels provided by [71] and the associated Final Softening and Drift Ratio values, an analysis of the correspondence between the damage levels obtained from the FE analysis and those obtained from the ANN was conducted for both training and test sets.

Table 11 shows the differences in the damage level results after training and validation between FEM and ANN for both damage indices, i.e. FS and IDR. For a thorough analysis, when a difference in damage level was registered, the number of levels between FEA and ANN solutions was recorded.

The results show that, after training and validation, the FS index has a high accuracy, recording the same damage level from both FEA and ANN for 70.4 % of all structures. Although when analyzing the IDR results, the number of buildings that reported the same damage level using FEA and ANN was 6.05 % lower than that of FS, the number of structures

Table 10
Damage levels corresponding to Drift Ratio and Final Softening values.

Damage level		Performance level	Final Softening	Drift Ratio [%]
No damage		Immediate Occupancy (IO)	< 0.1	< 0.2
Repairable damage	Light	Damage Control (DC)	0.1–0.15	0.2–0.4
	Moderate	Life Safety (LS)	0.15–0.2	0.4–1.0
Irreparable damage		Life Safety (LS)	0.2–0.4	1.0–1.5
		Collapse Prevention (CP)		1.5–1.8
Severe damage - Life safe -Partial collapse		Collapse Prevention (CP)	0.4–0.6	1.8 – 2.5
		Collapse		2.5–3.0
Collapse		Collapse	> 0.6	> 3.0

Table 11
Damage levels correspondence between ANN and FE analysis after training and validation.

	Final Softening Index		Interstory Drift Ratio	
Difference in damage level	No. of structures	% from total	No. of structures	% from total
No difference	2395	70.40	2189	64.35
1 level	748	21.98	1165	34.24
2 levels	210	6.18	48	1.41
3 levels	49	1.44	-	-

registering differences of more than one damage level was lower compared to FS. As a result, the IDR outperformed the FS index in terms of ANN training success. This statement was confirmed during the testing stage, where the accuracy of the IDR was significantly higher compared to the FS index, as presented in Table 12.

After the testing stage, the accuracy of the IDR was confirmed. For most structures, the damage level was the same according to FEA and ANN. For the rest, a maximum of one level of difference was registered, confirming the utility of the ANN for this damage index. Conversely, for the FS index, the testing stage proved that if the seismic parameters change, the index cannot be used for damage level prediction.

The fast prediction of structural damage levels, after a seismic event is crucial for limiting the number of casualties and the psychological stress of people. After an earthquake, one major problem is the uncertainty regarding the structural safety of the building. For this reason, people tend to sleep outdoors for several days, being afraid to enter their homes. This situation leads not only to discomfort but also to overcrowding in certain areas, which can block important streets or may lead to illnesses because of the lack of sanitization. Experts have to come and assess the structural safety. However, because of the limited number of experts in this field, the time needed to do such a building investigation, in case of a large seismic event, can extend for several days or weeks. A program which may predict the structural damage of a building for that specific seismic action, could prove to be useful. Fig. 27 proposes a damage assessment workflow using the tested neural network for a building.

The workflow presented in Fig. 27 can be extended to several buildings and be used by local institutions to organize people and take fast and resilient decisions. Considering that after a significant seismic action, the building may need strengthening which modifies the buildings characteristics, a real time monitoring system was added to the flowchart, that records the changes and updates the neural network input.

Furthermore, even if the structure does not record severe damages that require at least strengthening interventions and change in structural characteristics, an update of the model will be registered through the real time monitoring system. In this case the real time monitoring system could record various low-level degradations observed within the structure. For this case, the information sent to the neural network regarding the building characteristics will remain unmodified. The real time monitoring system is an optional device and may not be present in all structures, reason for which a dotted line was selected to represent it.

Table 12
Damage levels correspondence between ANN and FE analysis after testing.

	Final Softening Index		Interstory Drift Ratio	
	No. of structures	% from total	No. of structures	% from total
ANN testing for distinct input structural parameters				
No difference	20	47.62	30	71.43
1 level	10	23.81	12	28.57
2 levels	4	9.52	-	-
3 levels	6	14.29	-	-
4 levels	2	4.76	-	-
ANN testing for distinct input seismic parameters				
No difference	4	26.67	9	60
1 level	3	20.00	6	40
2 levels	4	26.67	-	-
3 levels	1	6.67	-	-
4 levels	3	20.00	-	-

6. Prediction improvement for final softening index

Since the predictive performance for the Final Softening Index output was consistently lower than for the other target variables, additional investigations were conducted to see whether combining multiple models could further improve accuracy,as previously reported in the scientific literature (https://doi.org/10.1016/j.engappai.2023.107388). For this purpose a stacked ensemble composed of three regressors was implemented: an Artificial Neural Network, a Random Forest, and an XGBoost model. Each model was trained independently and their predictions were combined through a weighted average to produce the final output.

Neural networks involve a large number of hyperparameters, which makes empirical tuning inefficient and potentially suboptimal. To address this issue, the Optuna library [73] was used to systematically optimize the network architecture and training parameters. Optuna is a software library for hyperparameter optimization that uses Bayesian sampling methods and early stopping to efficiently explore the search space.

To maintain consistency with the evaluation procedure used for other models, 5-fold cross-validation (CV) was applied only on the training set. That is, for each sampled hyperparameter configuration, the network was trained and validated using CV on the training data and the mean Pearson correlation across the validation folds was used as the objective function. This procedure was repeated for 100 trials. The test set remained untouched throughout this process and was used only for the final evaluation.

The ANN configuration identified by Optuna is somewhat different from the typical network design. Rather than using conventional layer sizes, such as powers of two or higher dropout rates for regularization, e.g. 0.5, the selected architecture and hyperparameters reflect an empirically effective configuration. The (near-)optimal architecture consists of 2 hidden layers with 292 and 191 neurons, respectively. The dropout rate applied on the layers is a low value of 1.39×10^{-2}. The network was trained using the Adam optimizer with a learning rate of 1.82×10^{-3}, and an L2 weight decay of 9.93×10^{-5}.

A similar optimization procedure was applied to the RF and XGBoost models using again Optuna for hyperparameters such as tree depth, minimum samples per leaf and learning rate (for XGBoost). However, in both cases, the optimized models did not show improved performance over the simpler configurations previously used in this study, which involved a number of 100 trees or estimators. Thus, the original versions of the RF and XGB models were retrained for the ensemble.

In addition, hyperparameter optimization was conducted for two more popular regression models: k-Nearest Neighbors (kNN) and Support Vector Regression (SVR) with a radial basis function kernel. For kNN, the number of neighbours and distance weighting were tuned, while for SVR, the regularization parameter, kernel width and epsilon margin were varied. Despite these attempts, the performance of both models was consistently inferior to that of the ANN, RF and XGBoost models, both on the training folds and on the test set. As a result, neither kNN nor SVR was included in the final ensemble.

The stacked ensemble model combines the outputs of ANN, RF and XGBoost:

$$\hat{y} = w_1 \cdot \hat{y}_{ANN} + w_2 \cdot \hat{y}_{RF} + w_3 \cdot \hat{y}_{XGB} \quad (5)$$

where the weights w_i are non-negative and sum up to 1.

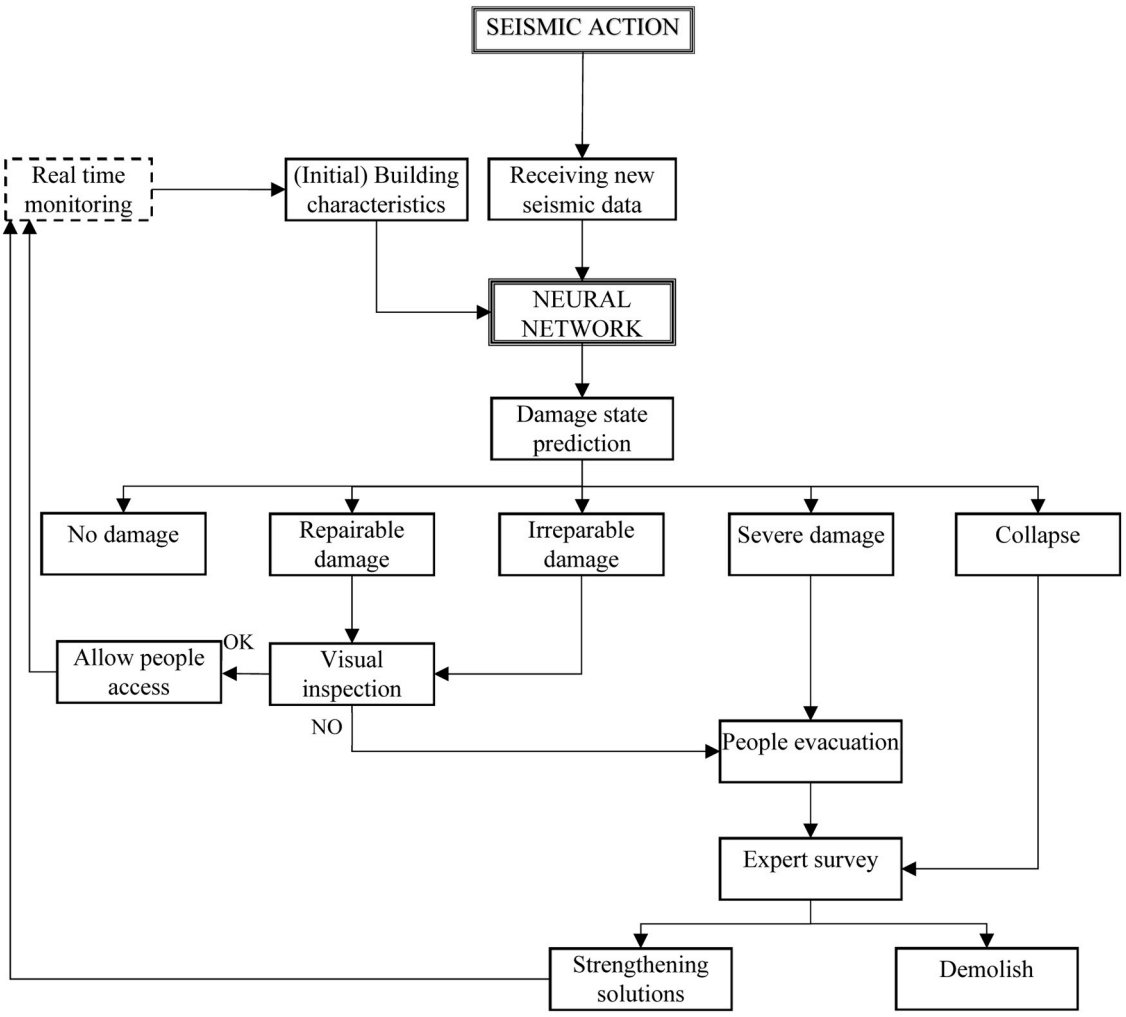

Fig. 27. Proposed damage assessment workflow.

To find whether the ensemble can outperform the individual models, an exhaustive grid search was executed over all possible combinations of weights with a resolution of 0.01. The search evaluated every admissible (w_1, w_2, w_3) tuple and selected the combination that maximized the correlation coefficient. A 5-fold CV strategy to generate out-of-fold predictions from each of the 3 base models was employed. By aggregating the predictions across all folds, full-length out-of-fold predictions for each model were obtained. The final ensemble predictions were aggregated using Eq. 5. The best results were given by the weight vector w = (0.52, 0.48, 0.00) and are presented in Table 13.

They indicate that the ANN and RF models perform comparably well, while the XGBoost model exhibits inferior performance in both error and correlation. During ensemble weight optimization, XGBoost received a weight of zero, which confirms its limited contribution in this setting.

Table 13
Performance summary for the individual models and their ensemble.

Model	Dataset	Mean Squared Error (*MSE*)	Correlation coefficient (*r*)
Artificial Neural Network	Training	0.006858	0.9171
	Testing	0.021974	0.6775
Random Forest	Training	0.001082	0.9887
	Testing	0.024531	0.6703
XGBoost	Training	0.004652	0.9460
	Testing	0.030074	0.5452
Ensemble	Training	0.003220	0.9641
	Testing	0.018291	0.7312

The final ensemble combined only the Neural Network and Random Forest models and produced better test results than any individual model. This can be seen more clearly in Fig. 28, where the correlation coefficient on the test set is represented as a function of the ANN weight w_1.

Since the weight of the XGBoost model (w_3) was zero, and the weights sum up to 1, the weight of the Random Forest model is implicitly $w_2 = 1 - w_1$. The plot illustrates how the ensemble correlation varies along this axis of combinations between the Random Forest (left) and

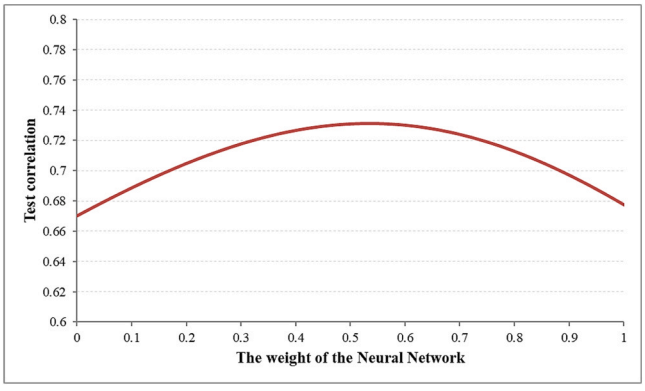

Fig. 28. The correlation coefficient on the test set as a function of Neural Network weight w_1, with $w_2 = 1 - w_1$ and $w_3 = 0$.

the Neural Network (right). A clear maximum is observed around the middle ($w_1 = 0.52$), which demonstrates that a stacked ensemble can lead to more accurate predictions than its individual models.

7. Conclusions

The paper investigates the use of ANNs for predicting structural damage in a reinforced concrete frame structure. Following the analysis of results, the capability of the ANNs to predict the six considered output parameters was verified. The studies presented herein prove the applicability of using the ANNs in assessing the global structural damage of reinforced concrete frame buildings caused by seismic actions. The studies were conducted on three-dimensional structures to obtain realistic results that can later be applied in practical scenarios. The results of ANN regarding the impact of the inputs over the damage indices were also compared to results given by the SHAP technique and similarities were observed. An analysis of the relationship between these indices and the considered input parameters was conducted using the Partial Dependence Plots (PDPs), nonlinearities being registered.

Several remarks can be stated based on the analyses:

- The number of stories, the span width and the width of the column cross-section are the structural parameters with the highest impact on the seismic damage of reinforced frame structures.
- The PGV and PGA were the most important seismic parameters which influenced the damage of the analysed structures. The spectral intensity proved to have a high impact on the damage of low-rigidity structures.
- Based on the comparative analysis between the ANN predictions and FEA values, it can be concluded that the ANN predicts the output parameters at a satisfactory level, except for O_3, which corresponds to the Final Softening Index. In this specific case, the absolute differences between the ANN and FEA values are high enough to modify the structural damage level.
- The stacked ensemble model combining outputs of ANN, RF, and XGBoost succeeded in improving the prediction accuracy of the Final Softening index output but further investigations are necessary for fine tuning the assembling model with considerations of other assembling procedures.

The model does not currently account for material strength variability or multi-directional seismic coupling effects. Its applicability is limited to residential load scenarios defined by codes P100–1/2013 and Eurocode 8. The results of the ANN can be improved by considering additional extensive input parameters that can significantly impact the structural response such as: concrete strength class, different intensities of the live load, arrival angle of the seismic wave, the reinforcement percentage in beams and columns. This can result in an enhanced generalization capability of the model. Moreover, other damage indices could be added to the analysis, which could be better predicted by the ANN, as for example Park-Ang or Roufaiel and Meyer global damage index. Another alternative to improve the accuracy when using stacked ML algorithms, this methods could be used in future studies. The current paper sets the basis for a broader study that aims to predict with reasonable accuracy the degree of damage of a building subjected to a major seismic event.

CRediT authorship contribution statement

Florin LEON: Writing – review & editing, Supervision, Software, Methodology, Formal analysis, Data curation. **Toma Ionut Ovidiu:** Writing – review & editing, Writing – original draft, Validation, Supervision, Investigation, Formal analysis, Data curation. **Georgiana BUNEA:** Writing – original draft, Software, Methodology, Formal analysis, Data curation, Conceptualization.

Declaration of Competing Interest

The authors declare that they have no known competing financial interests or personal relationships that could have appeared to influence the work reported in this paper.

Acknowledgement

This research is supported by the project “Romanian Hub for Artificial Intelligence - HRIA”, Smart Growth, Digitization and Financial Instruments Program, 2021–2027, MySMIS no. 334906.

Appendix A. Supporting information

Supplementary data associated with this article can be found in the online version at doi:10.1016/j.istruc.2025.109750.

References

[1] Jiang X, Song X, Li T, Wu K. Moment magnitudes of two large Turkish earthquakes on February 6, 2023 from long-period coda. Earthq Sci 2023;36:169–74. https://doi.org/10.1016/j.eqs.2023.02.008.
[2] Disel NR, Taskin O, Daglioglu G, Tor B, Secinti S, Devecioglu GF, et al. Factors affecting the mortality of February earthquakes victims in Türkiye. Am J Emerg Med 2024;77:115–20. https://doi.org/10.1016/j.ajem.2023.12.017.
[3] Cosgun C. Machine learning for the prediction of evaluation of existing reinforced concrete structures performance against earthquakes. Structures 2023;50:1994–2003. https://doi.org/10.1016/j.istruc.2023.02.127.
[4] Zanoletti A, Bontempi E. The impacts of earthquakes on air pollution and strategies for mitigation: a case study of Turkey. Environ Sci Pollut Res 2024;31:24662–72. https://doi.org/10.1007/s11356-024-32592-8.
[5] FEMA P58-1. Seismic performance assessment of buildings - volume 1: methodology. Washington, D.C.: 2018.
[6] FEMA P58-2. Seismic performance assessment of buildings - volume 2: Implementation guide. Washington, D.C.: 2018.
[7] FEMA P58-7. Building the performance you need - volume 7: A guide to state-of-the-art tools for seismic design and assessment. Washington, D.C.: 2018.
[8] Cheng K, Ziotopoulou K. Machine Learning Applications in Geotechnical Earthquake Engineering: Progress, Gaps, and Opportunities. Geo-Congress, 2023. Reston, VA: American Society of Civil Engineers; 2023. p. 493–505. https://doi.org/10.1061/9780784484692.050.
[9] Sun H, Burton HV, Huang H. Machine learning applications for building structural design and performance assessment: state-of-the-art review. J Build Eng 2021;33:101816. https://doi.org/10.1016/j.jobe.2020.101816.
[10] Imam MdH, Mohiuddin Md, Shuman NM, Oyshi TI, Debnath B, Liham MdI. MH. Prediction of seismic performance of steel frame structures: a machine learning approach. Structures 2024;69:107547. https://doi.org/10.1016/j.istruc.2024.107547.
[11] Demertzis K, Kostinakis K, Morfidis K, Iliadis L. An interpretable machine learning method for the prediction of R/C buildings' seismic response. J Build Eng 2023;63:105493. https://doi.org/10.1016/j.jobe.2022.105493.
[12] Yavas CE, Chen L, Kadlec C, Ji Y. Improving earthquake prediction accuracy in Los Angeles with machine learning. Sci Rep 2024;14:24440. https://doi.org/10.1038/s41598-024-76483-x.
[13] Bunea G, Leon F, Atanasiu GM. Postdisaster evacuation scenarios using multiagent system. J Comput Civ Eng 2016;30. https://doi.org/10.1061/(ASCE)CP.1943-5487.0000575.
[14] Kazemi F, Asgarkhani N, Shafighfard T, Jankowski R, Yoo D-Y. Machine-learning methods for estimating performance of structural concrete members reinforced with fiber-reinforced polymers. Arch Comput Methods Eng 2025;32:571–603. https://doi.org/10.1007/s11831-024-10143-1.
[15] Arslan MH. An evaluation of effective design parameters on earthquake performance of RC buildings using neural networks. Eng Struct 2010;32:1888–98. https://doi.org/10.1016/j.engstruct.2010.03.010.
[16] Asgarkhani N, Kazemi F, Jankowski R. Machine learning-based prediction of residual drift and seismic risk assessment of steel moment-resisting frames considering soil-structure interaction. Comput Struct 2023;289:107181. https://doi.org/10.1016/j.compstruc.2023.107181.
[17] Tocchi G, Misra S, Padgett JE, Polese M, Di Ludovico M. The use of machine-learning methods for post-earthquake building usability assessment: a predictive model for seismic-risk impact analyses. Int J Disaster Risk Reduct 2023;97:104033. https://doi.org/10.1016/j.ijdrr.2023.104033.
[18] Abdollahzadeh G, Omranian E, Vahedian V. Application of the artificial neural network for predicting mainshock-aftershock sequences in seismic assessment of reinforced concrete structures. J Earthq Eng 2021;25:210–36. https://doi.org/10.1080/13632469.2018.1512062.
[19] Oh BK, Park Y, Park HS. Seismic response prediction method for building structures using convolutional neural network. Struct Control Health Monit 2020;27. https://doi.org/10.1002/stc.2519.

[20] Oh BK, Glisic B, Park SW, Park HS. Neural network-based seismic response prediction model for building structures using artificial earthquakes. J Sound Vib 2020;468:115109. https://doi.org/10.1016/j.jsv.2019.115109.
[21] Kazemi F, Jankowski R. Machine learning-based prediction of seismic limit-state capacity of steel moment-resisting frames considering soil-structure interaction. Comput Struct 2023;274:106886. https://doi.org/10.1016/j.compstruc.2022.106886.
[22] Kazemi F, Asgarkhani N, Jankowski R. Machine learning-based seismic fragility and seismic vulnerability assessment of reinforced concrete structures. Soil Dyn Earthq Eng 2023;166:107761. https://doi.org/10.1016/j.soildyn.2023.107761.
[23] Asgarkhani N, Kazemi F, Jakubczyk-Gałczyńska A, Mohebi B, Jankowski R. Seismic response and performance prediction of steel buckling-restrained braced frames using machine-learning methods. Eng Appl Artif Intell 2024;128:107388. https://doi.org/10.1016/j.engappai.2023.107388.
[24] Kim T, Song J, Kwon O-S. Probabilistic evaluation of seismic responses using deep learning method. Struct Saf 2020;84:101913. https://doi.org/10.1016/j.strusafe.2019.101913.
[25] Gharehbaghi S, Gandomi M, Plevris V, Gandomi AH. Prediction of seismic damage spectra using computational intelligence methods. Comput Struct 2021;253:106584. https://doi.org/10.1016/j.compstruc.2021.106584.
[26] Benbokhari A, Benazouz C, Mebarki A. Artificial Neural Networks for seismic demand prediction of a single degree of freedom. International Conference on Applied Engineering and Natural Sciences. All Sciences Academy; 2023. p. 219–24. https://doi.org/10.59287/icaens.995.
[27] Hadzima-Nyarko M, Nyarko EK, Morić D. A neural network based modelling and sensitivity analysis of damage ratio coefficient. Expert Syst Appl 2011;38:13405–13. https://doi.org/10.1016/j.eswa.2011.04.169.
[28] Wei M, Hu X, Yuan H. Residual displacement estimation of the bilinear SDOF systems under the near-fault ground motions using the BP neural network. Adv Struct Eng 2022;25:552–71. https://doi.org/10.1177/13694332211058530.
[29] Yuan X, Chen G, Jiao P, Li L, Han J, Zhang H. A neural network-based multivariate seismic classifier for simultaneous post-earthquake fragility estimation and damage classification. Eng Struct 2022;255:113918. https://doi.org/10.1016/j.engstruct.2022.113918.
[30] Gharehbaghi S, Yazdani H, Khatibinia M. Estimating inelastic seismic response of reinforced concrete frame structures using a wavelet support vector machine and an artificial neural network. Neural Comput Appl 2020;32:2975–88. https://doi.org/10.1007/s00521-019-04075-2.
[31] Gholizadeh S. Performance-based optimum seismic design of steel structures by a modified firefly algorithm and a new neural network. Adv Eng Softw 2015;81:50–65. https://doi.org/10.1016/j.advengsoft.2014.11.003.
[32] Nguyen HD, Dao ND, Shin M. Prediction of seismic drift responses of planar steel moment frames using artificial neural network and extreme gradient boosting. Eng Struct 2021;242:112518. https://doi.org/10.1016/j.engstruct.2021.112518.
[33] Hwang S-H, Mangalathu S, Shin J, Jeon J-S. Machine learning-based approaches for seismic demand and collapse of ductile reinforced concrete building frames. J Build Eng 2021;34:101905. https://doi.org/10.1016/j.jobe.2020.101905.
[34] Gravett DZ, Mourlas C, Taljaard V-L, Bakas N, Markou G, Papadrakakis M. New fundamental period formulae for soil-reinforced concrete structures interaction using machine learning algorithms and ANNs. Soil Dyn Earthq Eng 2021;144:106656. https://doi.org/10.1016/j.soildyn.2021.106656.
[35] Jia D-W, Wu Z-Y. Structural probabilistic seismic risk analysis and damage prediction based on artificial neural network. Structures 2022;41:982–96. https://doi.org/10.1016/j.istruc.2022.05.056.
[36] Lagaros ND, Papadrakakis M. Neural network based prediction schemes of the non-linear seismic response of 3D buildings. Adv Eng Softw 2012;44:92–115. https://doi.org/10.1016/j.advengsoft.2011.05.033.
[37] Bunea G, Leon F, Atanasiu G-M. Influence of seismic hazard on RC buildings' resilience based on ANN. In: Caspeele R, Taerwe L, Frangopol DM, editors. Life Cycle Analysis and Assessment in Civil Engineering: Towards an Integrated Vision. Ghent, BELGIUM: CRC Press; 2018. p. 1099–106.
[38] Ministerul Dezvoltării Regionale și Administrației Publice MDRAP. Cod de Proiectare Seismică – Partea I - Prevederi de Proiectare pentru Clădiri. Indicativ P100–1/2013. vol. 1. 558 bis/3.09.2013. București, România: Monitorul Oficial al României; 2013.
[39] Asociatia de Standardizare din România (ASRO). SR EN 1992–1-1 Eurocod 2: Proiectarea structurilor de beton. Partea 1–1: Reguli generale și reguli pentru clădiri. 2004.
[40] Applied Technology Council. Guidelines for Performance-Based Seismic Design of Buildings. 2018.
[41] ASRO. SR EN 1998-1:2004 - Eurocod 8: Proiectarea structurilor pentru rezistenta la cutremur. 2004.
[42] Dai R, Lu Q, Chen S, Wang Z, Zhang H. Review of the Correlation between Earthquake Damage of Underground Structures and Ground Motion Parameters. IOP Conference Series: Earth and Environmental Science. 2019, 042036. https://doi.org/10.1088/1755-1315/304/4/042036.
[43] Masi A, Vona M, Mucciarelli M. Selection of natural and synthetic accelerograms for seismic vulnerability studies on reinforced concrete frames. J Struct Eng 2011;137:367–78. https://doi.org/10.1061/(ASCE)ST.1943-541X.0000209.
[44] Chiauzzi L, Masi A, Mucciarelli M, Vona M, Pacor F, Cultrera G, et al. Building damage scenarios based on exploitation of Housner intensity derived from finite faults ground motion simulations. Bull Earthq Eng 2012;10:517–45. https://doi.org/10.1007/s10518-011-9309-8.
[45] Massumi A, Gholami F. The influence of seismic intensity parameters on structural damage of RC buildings using principal components analysis. Appl Math Model 2016;40:2161–76. https://doi.org/10.1016/j.apm.2015.09.043.
[46] Buratti N, Simoni E, Mazzotti C. Post-earthquake estimates of different ground motion intensity measures for the 2012 Emilia earthquake. Earthq Eng Struct Dyn 2023;52:183–203. https://doi.org/10.1002/eqe.3756.
[47] European Committee for Standardization. EN 1998–1:2004 Eurocode 8: Design of Structures for Earthquake Resistance. Part 1: General Rules, Seismic Actions and Rules for Buildings. 2004.
[48] Takeda T, Sozen MA, Nilson NN. Reinforced concrete response to simulated earthquake. J Struct Eng 1970;96:2557–73.
[49] Mander JB, Priestley MJN, Park R. Theoretical stress-strain model for confined concrete. J Struct Eng 1984;114:1804–26.
[50] ASRO. SR EN 1991–1-1 Eurocod 1: Acțiuni asupra structurilor. Partea 1–1: Acțiuni generale - Greutăți specifice, greutăți proprii, încărcări din exploatare pentru construcții. Anexă națională. 2006.
[51] DiPasquale E., Cakmak A.S. On the Relation Between Local and Global Damage Indices. Technical Report NCEER-89-0034, NCEER Contract Number 88-1007, NSF Master Contract Number 86-07591. New York, USA: 1989.
[52] Yi J, Zhao B, Wu D, Zhu H. Softening index-based equivalent linear modeling approach for bolt-connected precast concrete frame. Struct Concr 2024. https://doi.org/10.1002/suco.202401225.
[53] Abou-Elfath HM. Rehabilitation of Nonductile Reinforced Concrete Buildings Using Steel Systems. McMaster University; 1998.
[54] Ghobarah A, Abou-Elfath H, Biddah A. Response-Based Damage Assessment Of Structures, 28. John Wiley & Sons; 1997.
[55] DiPasquale E, Ju J, Askar A, Çakmak AS. Relation between global damage indices and local stiffness degradation. J Struct Eng 1990;116:1440–56. https://doi.org/10.1061/(ASCE)0733-9445(1990)116:5(1440).
[56] FEMA. FEMA 356 - Prestandard and Commentary for the Seismic Rehabilitation of Buildings. Washington, D.C.: 2000.
[57] Rodriguez-Gomez S, Cakmak AS. Evaluation of seismic damage indices for reinforced concrete structures. Tech Rep NCEER900022 Buffalo N Y 1990.
[58] Peng Z, Guo Z, Shen Y, Wang X. Inter-story drift ratio detection of high-rise buildings based on ambient noise recordings. Appl Sci 2023;13:6724. https://doi.org/10.3390/app13116724.
[59] Mosleh A, Rodrigues H, Varum H, Costa A, Arêde A. Seismic behavior of RC building structures designed according to current codes. Structures 2016;7:1–13. https://doi.org/10.1016/j.istruc.2016.04.001.
[60] Berman J.J. Data Simplification: Taming Information With Open Source Tools. 2016. https://doi.org/https://doi.org/10.1016/C2015-0-00783-3.
[61] Heersma HF, Kremer K, van Soolingen D, Hauman J. Setting-Up Intra- and Inter-Laboratory Databases of Electrophoretic Profiles. In: Dijkshoorn L, Struelens M, Towner KJ, editors. New Approaches for the Generation and Analysis of Microbial Typing Data. Elsevier Science; 2001. p. 47–75.
[62] Berman JJ. Indispensable Tips for Fast and Simple Big Data Analysis. In: Berman JJ, editor. Principles and Practice of Big Data. Second Edition. Academic Press; 2018. p. 231–57. https://doi.org/10.1016/B978-0-12-815609-4.00011-X.
[63] Evans JD. Straightforward statistics for the behavioral sciences. Belmont, CA, US: Thomson Brooks/Cole Publishing Co; 1996.
[64] Breiman L. Random forests. Mach Learn 2001;45:5–32. https://doi.org/10.1023/A:1010933404324.
[65] Chen T, Guestrin C. XGBoost: A Scalable Tree Boosting System. Proceedings of the 22nd ACM SIGKDD International Conference on Knowledge Discovery and Data Mining. New York, NY, USA: ACM; 2016. p. 785–94. https://doi.org/10.1145/2939672.2939785.
[66] Kononenko I, Šimec E, Robnik-Šikonja M. Overcoming the myopia of inductive learning algorithms with RELIEFF. Appl Intell 1997;7:39–55. https://doi.org/10.1023/A:1008280620621.
[67] Lundberg S, Lee S-I. A Unified Approach to Interpreting Model Predictions. NIPS'17: Proceedings of the 31st International Conference on Neural Information Processing Systems. 2017. p. 4768–77.
[68] Robnik-Šikonja M, Kononenko I. Theoretical and empirical analysis of ReliefF and RReliefF. Mach Learn 2003;53:23–69. https://doi.org/10.1023/A:1025667309714.
[69] Shapley LS. A Value for n-Person Games. In: Kuhn HW, Tucker AW, editors. Contributions to the Theory of Games, II. Princeton: Princeton University Press; 1953. p. 307–17.
[70] Friedman JH. Greedy function approximation: a gradient boosting machine. Ann Stat 2001;29:1189–232.
[71] Ghobarah A. On Drift Limits Associated with Different Damage Levels. Proceedings of International Workshop on Performance-Based Seismic Design, Department of Civil Engineering. Bled: McMaster University; 2004.
[72] Hueste MBD, Bai J-W. Seismic retrofit of a reinforced concrete flat-slab structure: Part II — seismic fragility analysis. Eng Struct 2007;29:1178–88. https://doi.org/10.1016/j.engstruct.2006.07.022.
[73] Akiba T, Sano S, Yanase T, Ohta T, Koyama M. Optuna: A Next-Generation Hyperparameter Optimization Framework. Proceedings of the 25th ACM SIGKDD International Conference on Knowledge Discovery & Data Mining. New York, NY, USA: ACM; 2019. p. 2623–31. https://doi.org/10.1145/3292500.3330701.

materials

MDPI

Article

Characterization of Self-Compacting Concrete at the Age of 7 Years Using Industrial Computed Tomography

Oana-Mihaela Banu [1], Sergiu-Mihai Alexa-Stratulat [1,*], Aliz-Eva Mathe [2], Giuseppe Brando [3] and Ionut-Ovidiu Toma [1,*]

[1] Faculty of Civil Engineering and Building Services, "Gheorghe Asachi" Technical University of Iasi, 700050 Iasi, Romania; oana-mihaela.banu@academic.tuiasi.ro
[2] Faculty of Civil Engineering, Technical University of Cluj-Napoca, 400641 Cluj-Napoca, Romania; aliz.mathe@mecon.utcluj.ro
[3] Department of Engineering and Geology, University "G. d'Annunzio" of Chieti-Pescara, 66100 Chieti, Italy; giuseppe.brando@unich.it
* Correspondence: sergiu-mihai.alexa-stratulat@academic.tuiasi.ro (S.-M.A.-S.); ionut.ovidiu.toma@tuiasi.ro (I.-O.T.)

Abstract

The pore structure of SCC and of all cement-based materials plays a crucial role on the mechanical and durability characteristics of the material. The pore structure is affected by mix design, water–binder ratio and the incorporation of SCM and/or nanomaterials, all of which can improve mechanical and durability characteristics by decreasing porosity. Computed tomography (CT) is a powerful, non-destructive imaging technique to investigate the internal pore structure of concrete. The main advantage compared to other investigation techniques used to assess the pore structure is in terms of sample size. More specifically, industrial CT can be used to scan large concrete samples and be able to assess the internal pore structure without damaging the specimen. CT provides accurate measurements of pore diameters, volumes and shapes and enables the assessment of the total porosity. The paper presents the results of an experimental program on the characterization of self-compacting concrete (SCC) at a very long age (7 years) in terms of static and dynamic elastic properties and compressive and splitting tensile strength, all of which are correlated with the internal pore structure assessed via the use of an industrial Nikon XTH 450 CT. The results highlight the influence of pore volume, maximum pore diameter and sphericity on the strength and elastic properties of SCC at the age of 7 years. Both the compressive strength and the static modulus of elasticity values tend to decrease with the increase in the internal total porosity, with stronger influence on the former.

Keywords: internal pore structure; dynamic elastic properties; compressive strength; long age

Academic Editor: Carlos Leiva

Received: 17 August 2025
Revised: 26 September 2025
Accepted: 27 September 2025
Published: 29 September 2025

Citation: Banu, O.-M.; Alexa-Stratulat, S.-M.; Mathe, A.-E.; Brando, G.; Toma, I.-O. Characterization of Self-Compacting Concrete at the Age of 7 Years Using Industrial Computed Tomography. *Materials* **2025**, *18*, 4524. https://doi.org/10.3390/ma18194524

1. Introduction

Self-compacting concrete (SCC) is a new kind of concrete that can flow and settle on its own, filling formwork and covering reinforcement without the need for mechanical vibration. It possesses several advantages over the traditional, vibrated concrete, among which the following are worth mentioning: its ability to easily spread and fill the formworks with dense reinforcements, thus improving construction quality and speed [1]; it eliminates the need for mechanical vibrations reducing labor time and costs, noise pollution and

the risk of segregation and/or voids due to improper vibration [2,3]; and its improved durability properties due to its dense microstructure [4,5] and reduced permeability [6].

In much the same way as with vibrated concrete, SCC can incorporate a wide variety of wastes to help reduce its carbon footprint and, at the same time, solve, at least in part, the problem of landfills. When fly ash and slag were used as supplementary cementitious materials (SCMs), a refined pore structure, improved mechanical properties and higher rates of strength gains were obtained [1,7,8]. The use of aeolian sand and recycled aggreges in precise dosages resulted in improved mechanical and durability characteristics of SCC [6]. Coal gangue powder and cement kiln dust were also successfully used as SCMs to obtain SCC with higher values of compressive strength and better microstructure [9].

The pore structure of SCC and of all cement-based materials plays a crucial role on the mechanical and durability characteristics of the material [10,11]. It has been proven that smaller, closely spaced pores are more efficient in relieving pressure due to ice formation during freezing [12], while larger and more distant pores may negatively affect the compressive strength [6]. SCC typically contains a large number of micropores, often in the range of 3–10 μm in diameter [13]. At the same time, it contains various pore types ranging from cylindrical, to ink-bottle shape, to planar interstitial pores [14]. There is a strong negative correlation between the porosity of SCC and its mechanical properties. Among the most significant pore characteristics affecting the properties of SCC are the specific surface area and the average chord length of the pores [15]. The pore structure is affected by mix design, water–binder ratio and the incorporation of SCMs and/or nanomaterials, all of which can improve mechanical and durability characteristics by decreasing porosity and detrimental pore types. Monitoring and optimizing pore structure is crucial for attaining high-performance, durable SCC for structural applications [9,16].

Mercury intrusion porosimetry (MIP) is one of the most popular techniques for determining the distribution of pore sizes. It is based on high-pressure injection of mercury into the sample, and this requires meticulous preparation. At lower pressure values, mercury fills the bigger pores but cannot fill the smaller ones. In order to fill inter- and intra-particle pores, high pressure is needed [17,18]. However, applying MIP to evaluate the pore structure of different media, including concrete, has several drawbacks. Significant differences were found between MIP and other assessment methods, such as helium pycnometry, as highlighted in one of the first studies to compare the two approaches [19]. It was concluded that mercury could not penetrate all the closed pores that helium would otherwise be able to enter. Moreover, subsequent research found that MIP might not be a perfect representation of the actual pore structure. The pore size distribution differed greatly from other approaches, even though the total porosity may have been accurately determined. When using MIP to evaluate the pore structure, several factors must be carefully considered, including the effect of ink bottle pores trapping mercury, the pore connectivity effect and the different contact angles between mercury and the solid portion of the samples during the intrusion and extrusion stages [20]. In addition to the very small material samples required to conduct the test, pore structure may potentially be harmed due to the very high pressure [21].

Low-field nuclear magnetic resonance (NMR) relaxometry is an advanced, non-invasive technique for characterizing the pore structure of porous media, including cement-based materials [22]. It is based on the differences in relaxation times of liquid molecules (typically water) within various pore environments, enabling detailed insights into pore size distribution and dynamics during material hydration [23,24]. Different pore sizes and types (gel pores, capillary pores, macropores) produce distinct relaxation signatures, allowing for the identification and quantification of multiple pore classes within the material. NMR has several advantages over MIP, such as the fact that it does not damage the sample

and avoids the high pressures and toxic mercury used in MIP [25]; the samples can be analyzed in their native state, without the need for drying, cutting, or other preparation steps that might alter the pore structure [23]; it can be applied to fresh, hydrating cement pastes, enabling the study of pore development and water consumption as hydration progresses [22]; and the non-destructive nature allows for repeated measurements on the same sample over time. However, it also has some limitations that need to be acknowledged: precise assessment of absolute pore diameters necessitates the calibration of the pore surface relaxivity parameter, usually accomplished through comparison with MIP or scanning electron microscopy (SEM) data [26,27]; it is assumed that pores are fully saturated with water during measurements [23]; and similar to MIP, the tests are conducted on small scale samples, which makes generalizations rather difficult.

Computed tomography (CT) is a powerful, non-destructive imaging technique to investigate the internal pore structure of concrete [28,29] and aggregate size, shape and distribution, as well as fiber distribution [30,31]. The main advantage with respect to the above-mentioned methods is in terms of sample size. Unlike destructive techniques or laboratory-scale micro-CT, which are generally restricted to small specimens and may not represent the behavior of structural elements, industrial CT enables the scanning of large concrete specimens without damaging them. The distinction is paramount, as it allows pores to be characterized in samples closer to real casting conditions, bridging the gap between laboratory-scale determinations and the performance in a structural-scale situation. Industrial CT measurements provide the possibility to make quantitative assessments of pore diameter, volume, shape and total porosity. Given that the technique involves the 3D image analysis of a specimen that can be used in other tests (mechanical or otherwise), there is great opportunity to study the underlying impact of pore networks in durability and transport phenomena [32,33]. Moreover, total porosity has been deemed insufficient for explaining macroscopic properties, with pore morphology, size and distribution playing an important role [11], providing more incentive to further develop the full-scale CT analysis on concrete specimens. The 3D image analysis quantifies the complexity and interconnectivity of the pore networks, which are critical for understanding fluid transport and durability [29,34]. There are also limitations of the CT approach, which are mostly related to the scanning resolution and differentiating between pores and solid phases, which can be a challenge, especially for pores filled with water or other low-density materials [35]. It has been pointed out that the present technology is not a more important restriction than information interpretation and data processing. Even if traditional techniques are more apt, at the moment, in resolving pores smaller than air voids (under 10 μm), the possibilities offered by CT scanning might prove far greater [36].

Since the development of strength on concrete is strongly related to the pore structure, irrespective of the considered age, the present study brings its contribution to the assessment of strength and elastic properties of self-compacting concrete at a long age, 7 years, in close relationships to the pore structure. Previous studies showed that concrete mechanical properties improve over time and there is a tendency of pores to be filled by hydration products, thus reducing the number of large pores and the total porosity and modifying the pore shape [37–39]. The latter were assessed by means of industrial CT and the 3D reconstruction, which was conducted using the Dragonfly 3D World 2024.1 software. Although CT has been increasingly used in imaging cement-based materials, most existing studies have focused on small laboratory specimens or early-age concrete, most often relying on micro-CT or destructive testing [40–42]. The use of an industrial CT scanning equipment meant that entire concrete cylinders could be scanned [30], thus offering a broader image on the pore distribution inside the concrete specimens. This large-scale, non-destructive imaging approach allows a more representative evaluation of pore distribution, volume,

diameter and sphericity, while preserving specimens for complementary mechanical testing. Three-dimensional reconstructions were performed using the Dragonfly software, enabling quantitative correlation between pore characteristics and static/dynamic elastic properties, compressive strength and splitting tensile strength.

2. Materials and Methods

2.1. Materials

A CEM II/A-LL 42.5R rapid hardening cement, produced by Heidelberg Cement (Bicaz, Romania), complying to currently available norms [43], was used in this research. It contains 80–94% clinker and 6–20% limestone filler, which prevents bleeding and ensures a proper hydration of the cement, and 0 ÷ 5% of other minor additional constituents. The chemical composition of the cement is presented in Table 1.

Table 1. Chemical composition of CEM II/A-LL 42.5R (expressed in %).

CaO	SiO_2	Al_2O_3	Fe_2O_3	MgO	SO_3	Na_2O	K_2O	MgO	TiO_2
61.54	18.92	4.86	2.5	1.9	3.1	0.25	0.98	1.89	0.17

Limestone filler was also used as a mineral additive to increase the paste volume and avoid the use of viscosity modifying admixtures [44–46]. Natural river aggregates, from a local supplier, were used in the concrete mix as highlighted in [47]. The particle distributions for the aggregates are presented in [47].

The considered mix proportions, complying with guidelines for self-compacting concrete [48,49], are presented in Table 2. A Sika ViscoCrete—19 HE (Sika Romania, Bucharest, Romania) high range water reducer (HRWR), a polycarboxylate-ether based superplasticizer, was used as 0.5% by the cement mass. It has a specific gravity of 1.06 ± 0.02 g/cm^3 and, according to the technical specifications, should be used in 0.3–2.5% by mass of the cement.

Table 2. Mix proportions for self-compacting concrete [47].

Concrete Mix	Cement	Sand [0–4 mm]	Aggregates [4–16 mm]	Limestone Filler	Water/Cement	Water/Powder *	HRWR
	[kg/m^3]	[kg/m^3]	[kg/m^3]	[kg/m^3]	-	-	[L/m^3]
SCC 1	320	814	881	160	0.53	0.35	4.5
SCC 2	340	809	876	150		0.38	5.1
SCC 3	360	809	876	130		0.34	5.1

* cement + limestone filler.

A constant 0.53 water/cement ratio was adopted for all 3 mixes, as seen in Table 1. The water-to-cement ratio of 0.53 was selected as a practical compromise to achieve the target self-compactability (slump-flow/passing ability) for the materials and superplasticizer dosages available in this study, while maintaining acceptable mechanical and permeability performance. Values of w/c between 0.4 and 0.55 were frequently reported in the scientific literature referring to self-compacting concrete [50,51]. Trial mixes were cast employing various combinations between w/c ratio and percentage of superplasticizer so that all 3 mixes will fall within the same slum flow class and V-funnel class [52].

2.2. Methods

A similar testing procedure reported in [53] was also adopted in this study. After casting, the 100 mm × 200 mm cylinders (diameter × height) were demolded 24 h later and cured in water for 28 days. Fourteen specimens for each mix proportion shown in Table 1

were further kept in laboratory conditions (23 ± 2 °C and 40–50% relative air humidity) until the day of testing, 7 years later.

The fresh properties of the SCC [47] were assessed by means of a slump flow test and T_{500} test [54], V-funnel test [55] and L-box test [56]. A higher slump flow diameter means the concrete spreads more freely, indicating better flowability. At the same time, a shorter T_{500} time signifies faster flow. A shorter flow time obtained from the V-funnel test suggests a more fluid and workable SCC mix that can easily flow and fill forms. The L-box test on the other hand assesses its passing ability, which is its capacity to flow through obstacles like reinforcement bars without blocking or segregating [57].

The open porosity of SCC mixes was obtained on 3 specimens from each mix presented in Table 1, following the guidelines of ASTM C642-21 [58]. The concrete cylinders were oven dried until constant mass (e.g., difference between two successive measurements would not differ by more than 0.5%). Afterwards, they were placed in water for no less than 48 h and their mass was measured again until constant mass in saturated conditions. The third step consisted in boiling the specimens for 5 h, cooling the specimens to room temperature while immersed in water, followed by their weighing. The volume of permeable pores (open porosity) was then computed.

The static modulus of elasticity was determined in accordance with SR EN 12390-13 [59]. In order to correctly set the stress limits mentioned in the code, 1 sample was loaded in compression until failure. Cyclic loading was applied to each of the remaining 9 specimens and three individual values were obtained for each concrete cylinder. The obtained values were compared to each other in order not to differ by more than 1% from one-another for the same concrete cylinder.

The longitudinal dynamic modulus of elasticity, the dynamic shear modulus and dynamic Poisson's ratio were determined according to ASTM C215-19 [60]. The two dynamic moduli are based on the first resonant frequency (longitudinal and torsional frequencies, respectively) obtained from the Impact Echo Method. As presented in [53], the dynamic modulus of elasticity for the SCC, E_d, was computed based on Equation (1):

$$E_d = D \times m \times f_{ln}^2 \quad (1)$$

where m is the mass of the cylinder, expressed in kg, f_{ln} is the fundamental longitudinal frequency of vibration, expressed in Hz, and D is a shape coefficient that depends on the dimensions of the sample, as shown in Equation (2):

$$D = 5.093 \times \frac{L}{d^2} \quad (2)$$

in which L is the length of the cylinder, in meters, and d is the diameter, given in meters.

On the other hand, the dynamic shear modulus, G_d, was based on the fundamental torsional frequency of vibration, and was computed based on Equation (3):

$$G_d = B \times m \times f_t^2 \quad (3)$$

where f_t is the fundamental torsional frequency of vibration, expressed in Hz, and B is a shape coefficient that depends on the geometrical characteristics of the sample, as shown in Equation (4):

$$B = \frac{4LR}{A} \quad (4)$$

with R being a shape factor equal to 1 [60], and A is the cross-sectional area of the cylinder, expressed in m^2.

The two dynamic moduli were then used to compute the dynamic Poisson's ratio, μ_d, by means of Equation (5):

$$\mu_d = \frac{E_d}{2G_d} - 1 \quad (5)$$

The compressive and splitting tensile strength values were determined in accordance with SR EN 12390-3 [61] and SR EN 12390-6 [62], respectively. The compressive strength was determined of 5 samples whereas the splitting tensile strength was determined from the remaining 4 samples. The applied loading rates were 0.6 MPa/s (4.71 kN/s), for the determination of the compressive strength, and 0.05 MPa/s (1.7 kN/s), for the determination of the splitting tensile strength.

Two specimens of each mix were investigated through industrial computed tomography (CT) using a Nikon XTH 450 with 340 kV voltage and 240 µA current using a 3 mm copper filter. The detector had 2000 pixels × 2000 pixels and the pixel size was 40 µm, with a magnification factor of 2.27 and a white level of 60,000. The magnification factor represents the ratio of the image size to the actual object size or, equivalently, the ratio of the Source-to-Image-Distance (SID) to the Source-to-Object-Distance (SOD) [63]. The magnification factor is a phenomenon caused by the diverging nature of the X-ray beam, which spreads out from the source. The magnification factor was proven to significantly influence the quality of x-ray scans as compared to sampling resolution, which may result in higher computation effort and longer times to reconstruct scanned objects [64].

The scanned samples were in dry conditions as pore water substantially impacts CT results by affecting image density, pore connectivity and the distribution of air–water phases within the scanned material. Its presence may induce imaging artefacts, complicating the precise characterization of pore structures [65]. Scan results were analyzed using the Dragonfly software, version 3D World 2024.1, which is specifically designed for 3D reconstruction of CT images, as well as for computing various parameters: porosity, sphericity of pores, volume and mean radius of pores and others. The procedure applied for the analysis of each specimen started with denoising the original CT result by applying a Gaussian filter [66]. Subsequently, the space surrounding the specimen was removed, as this is considered a pore by the software. This step results in also removing any surface or open pores (connected to the outside), so that only internal pores are left to be addressed [35]. An example of internal pore distribution within the specimen, along with different perspectives, is presented, in Figure 1.

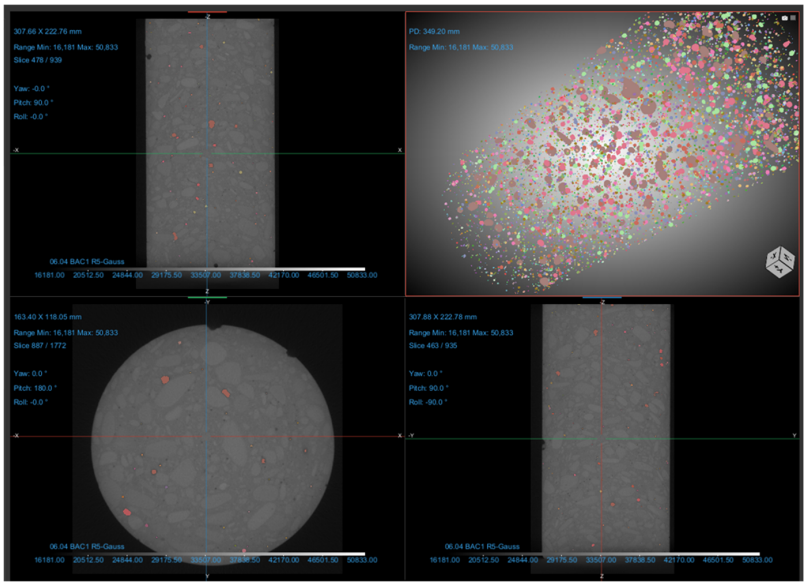

Figure 1. Determining internal pore structure and pore distribution in concrete cylinders.

The spacing in each direction (X, Y and Z) was 0.119591 mm for each of the specimens. The next step consisted in the segmentation procedure, in order to identify the pores. For this reason, the lower Otsu range was applied to the histogram. Given the resolution limitations, pores with a volume lower than 27 voxels ($3 \times 3 \times 3$ voxels) were eliminated. The focus was thus on pores that can be accurately distinguished, limiting the analysis to the air voids. These pores were further taken into consideration, as regions of interest (ROIs), for computing the amount that they represent out of the whole material volume [10,67]. Several parameters were extracted during the analysis: equivalent spherical diameter, mean pore radius, sphericity and volume.

3. Results

3.1. Fresh Properties of SCC

There is a strong, generally inverse correlation between slump flow and T_{500} time in self-consolidating concrete (SCC); as slump flow increases, T_{500} time (a measure of viscosity) typically decreases. A larger slump flow indicates better flowability (lower interparticle friction), while a longer T_{500} time signifies higher viscosity, meaning greater resistance to flow and a more cohesive mix. [9,68–70]. The fresh properties of the considered mixes are summarized in Table 3 [71].

Table 3. Fresh properties of the SCC mixes.

Concrete Mix	Sump Flow	T_{500}	V-Funnel	L-Box
	[mm]	[s]	[s]	
SCC 1	680	4.2	14.4	0.84
SCC 2	690	4.1	11.3	0.88
SCC 3	720	2.9	9.2	0.93

It can be observed that all considered SCC mixes belong to the slump flow class SF2 and V-funnel class VF2. Moreover, they all comply to the European Guidelines for Self-Compacting Concrete [48], with a slump flow of 600–750 mm and T_{500} time of 3.5–6.0 s.

3.2. Bulk Density and Open Porosity

The bulk density was determined on all 14 specimens considered for each mix. The dimensions of the cylinders were measured using a digital caliper with an accuracy of 0.01 mm. Six values for the diameter and three values for the height were measured in order to compute the volume of each specimen. The mass was determined to an accuracy level of 0.01 g. The obtained results, as average of 14 values for each mix, are presented in Table 4.

Table 4. Bulk density and open porosity values.

Concrete Mix	Bulk Density	StDev	COV	Open Porosity
	[kg/m^3]	[kg/m^3]	[%]	[%]
SCC 1	2278	11.05	0.49	12.9
SCC 2	2291	7.10	0.31	11.08
SCC 3	2300	11.99	0.52	8.54

At the same time, the open porosity was obtained as the average of three determinations, following the guidelines of ASTM C642-21 [58]. Similar values were reported in the scientific literature, although for earlier ages of SCC [16,72].

3.3. Static and Dynamic Elastic Properties

The static and dynamic moduli of elasticity were determined on nine specimens for each SCC mix, as shown in Table 2. Figure 2 presents the static longitudinal modulus of elasticity in compression, Young's modulus, for the SCC mixes. It can be observed that there is a gradual increase in the values of Young's modulus with the increase in cement content.

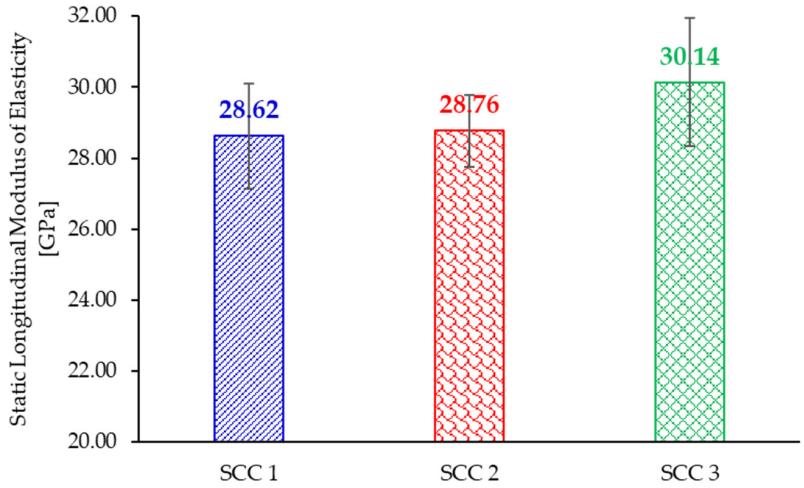

Figure 2. Static longitudinal modulus of elasticity for the considered SCC mixes.

The dynamic moduli of elasticity, as well as the values of Poison's ratio, are presented in Figure 3. The dynamic moduli of elasticity were determined based on the fundamental frequency of vibration, as presented in Table 5.

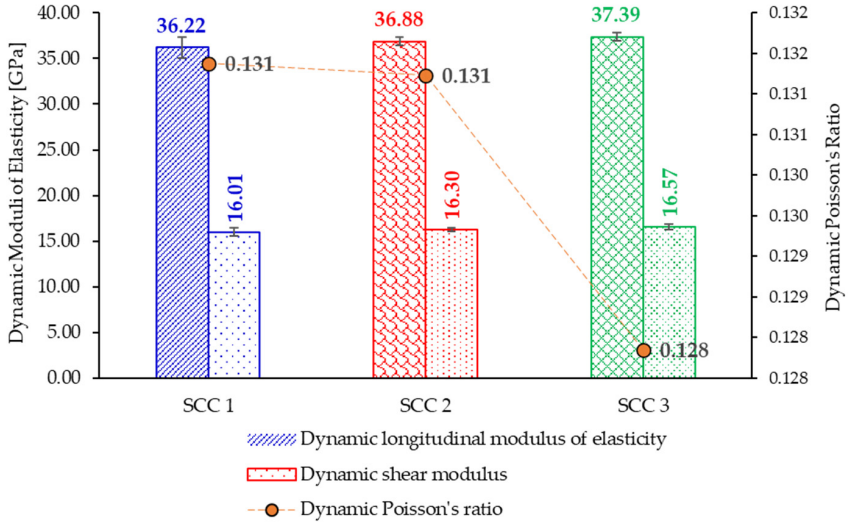

Figure 3. Dynamic elastic properties of the considered SCC mixes.

Table 5. Fundamental frequency of vibration (longitudinal and torsional) [60].

Concrete Mix	Longitudinal Frequency of Vibration	StDev	COV	Torsional Frequency of Vibration	StDev	COV
	[Hz]	[Hz]	[%]	[Hz]	[Hz]	[%]
SCC 1	9954.9	142.98	1.44	6628	79.04	1.19
SCC 2	10,030.3	53.73	0.54	6668.4	45.41	0.68
SCC 3	10,082	99.12	0.98	6712.4	40.26	0.6

3.4. Compressive and Splitting Tensile Strength

The values of the compressive and splitting tensile strengths, determined at the age of 7 years, are presented in Figure 4. They represent the average of five and four determinations, respectively. The values of the mechanical properties follow the similar trend observed for the elastic properties, namely, the increase in the cement content resulted in an increase in the values of both compressive and splitting tensile strength.

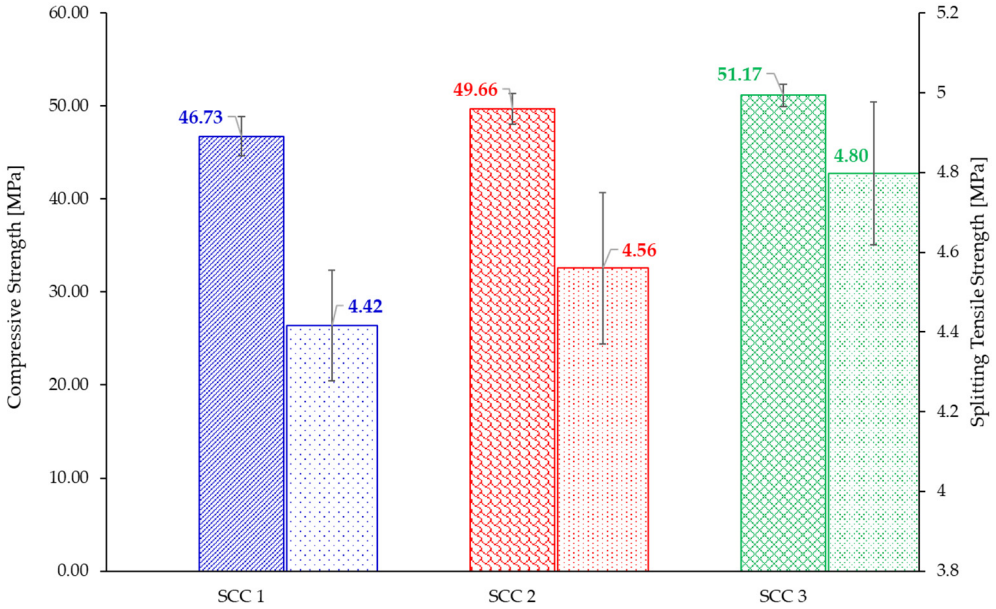

Figure 4. Mechanical properties of the considered SCC mixes at the age of 7 years.

However, the rate of increase in terms of compressive strength values is different than the increase in the splitting tensile strength values. An increase in the cement content and decrease in the aggregate mass, from SCC 1 to SCC 2, resulted in a 6.26% increase in the compressive strength and only a 3.26% increase in the splitting tensile strength. Further increasing the cement content while keeping the same aggregate mass and slightly decreasing the limestone filler, resulted in a further 3.06% increase in the values of the compressive strength and 5.22% increase in the values of the splitting tensile strength.

3.5. Internal Pore Structure

The internal pore structure for each of the considered SCC mixes is shown in Figure 5. It can be observed that the total volume of the internal pores is decreasing with the increase in the cement content. A similar observation can be made for the particle radius value. The higher the cement content, the lower the particle radius due to the partial or total filling of the pores with hydration products [16,72]. Mechanisms that might explain this behavior, that are supported by experimental observations across several studies, relate to: (i) formation of fewer capillary pores; (ii) a denser structure of the hydration products; (iii) the filling of the voids between aggregates and paste; and (iv) a denser, less porous cement matrix [40,73].

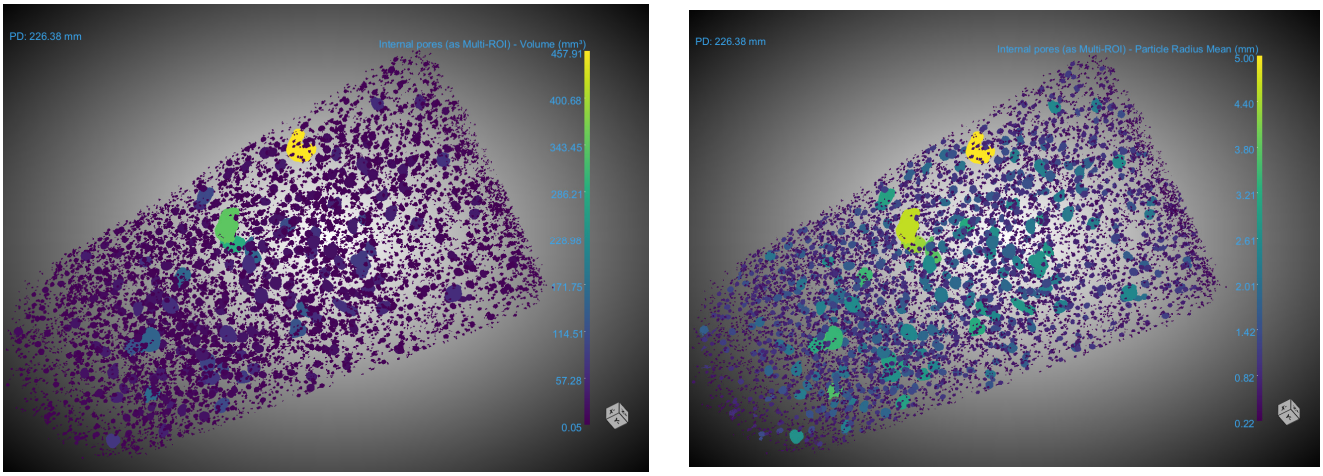

SCC 1 (maximum internal pores volume = 457.91 mm^3; maximum particle radius = 5 mm)

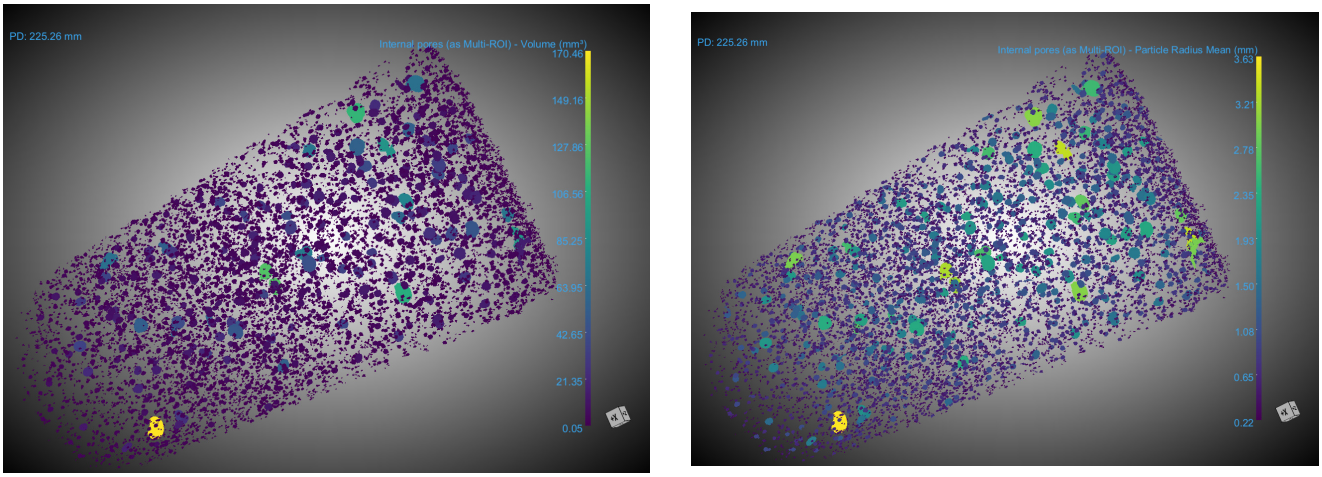

SCC 2 (maximum internal pores volume = 170.46 mm^3; maximum particle radius = 3.63 mm)

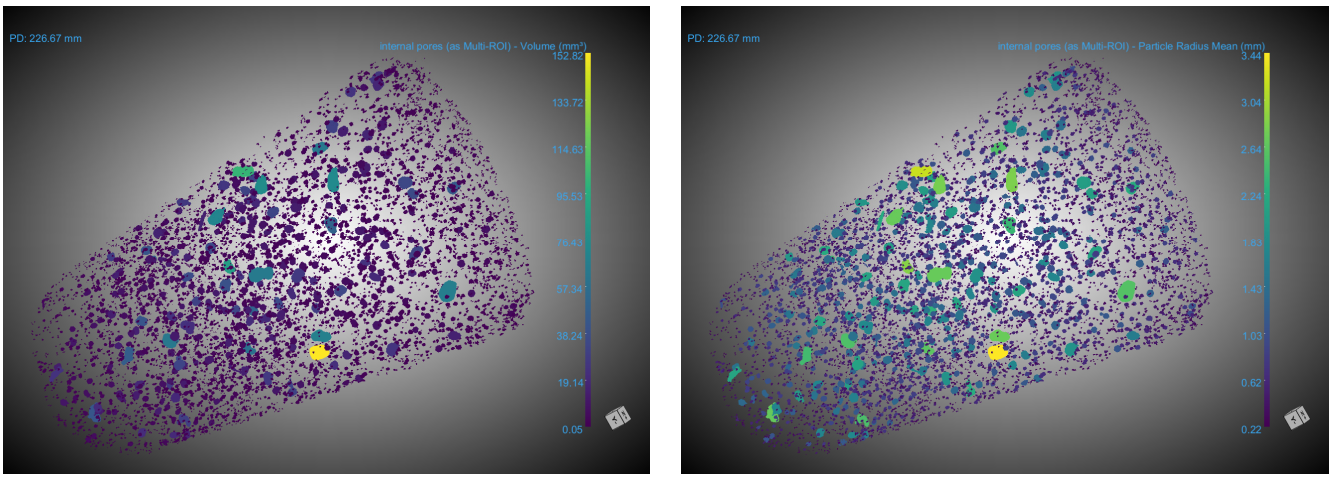

SCC 3 (maximum internal pores volume = 152.82 mm^3; maximum particle radius = 3.44 mm)

Figure 5. Internal pore structure of the considered SCC mixes at the age of 7 years.

4. Discussion

The changes in the mix proportions did not result in large variations of SCC density at the age of 7 years (less than 1%). This was also proven by the similar open porosity percentages of each considered SCC mix. Considering the long age, any differences that could have existed were gradually reduced due to the continuous hydration of the cement particles, thus creating additional hydration products [38,69].

4.1. Static and Dynamic Elastic Moduli

The evaluation of the dynamic modulus of elasticity offers the benefit of a non-destructive approach and can typically be conducted on-site. For design and technical evaluation, the static modulus of elasticity values were utilized, prompting the proposal of conversion equations. Previous studies [53,74] highlighted the suitability of several conversion formulas from the dynamic modulus of elasticity to the static one [75–77].

The obtained results are summarized in Figure 6. It can be observed that both equations proposed by Popovics [75] and Lydon and Balendran [76] slightly overestimate the experimental results by 2.85–5.28% and 3.92–6.42%, respectively. On the other hand, the conversion equation currently available in the design code [77] tends to underestimate the experimental data by 5.79–8.18%.

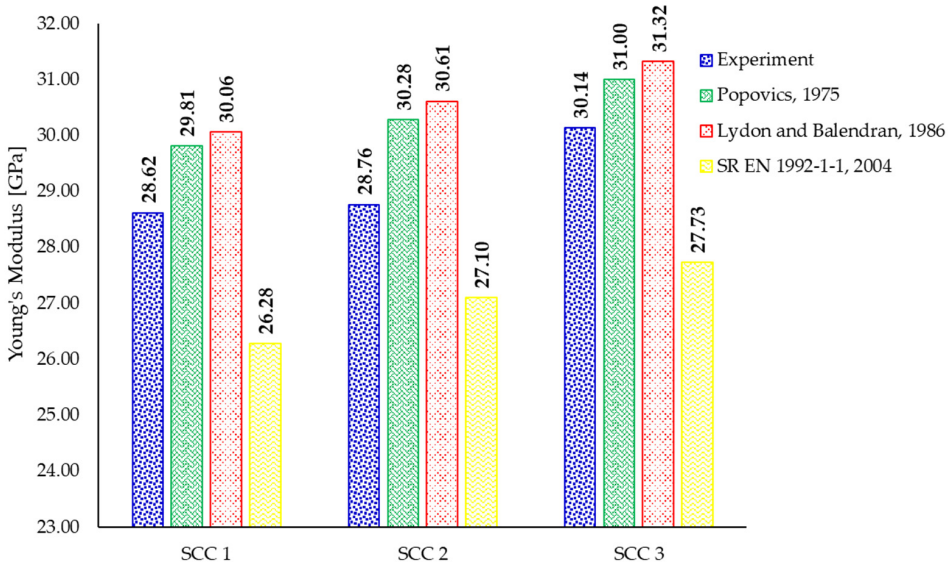

Figure 6. Prediction of the static modulus of elasticity by currently available equations [75–77].

4.2. Compressive Strength

The evolution of the compressive strength from the standard age of 28 days [47] up to 7 years is presented in Figure 7. As generally expected, the strength characteristics of concrete tend to improve over time due to continuous hydration of the cement particles. However, strength evolution is highly dependent on the storage/environmental conditions.

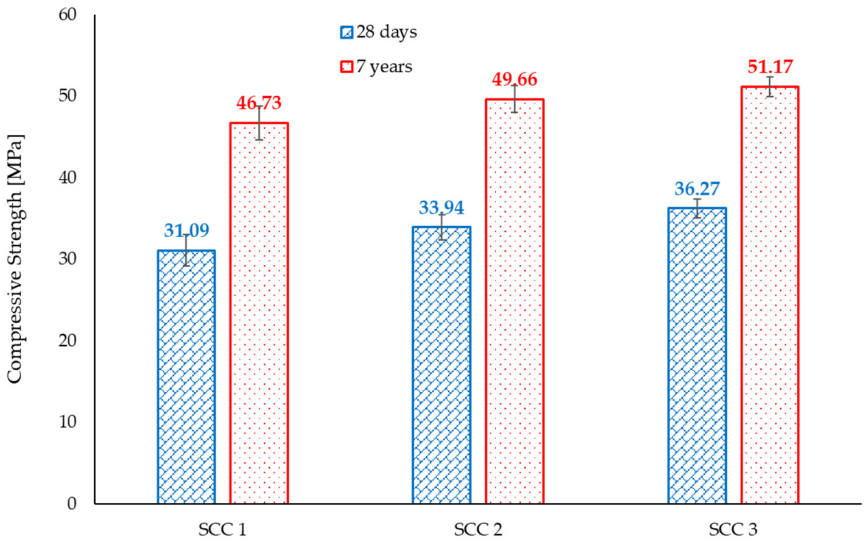

Figure 7. Evolution of the compressive strength.

It can be observed that although the values of the compressive strength increased for all three SCC mixes, the rate of increase was not similar, ranging from a 50.3% increase for SCC1 to a 41.09% increase for SCC 3. Limestone filler interacts with the hydration products of cement, mainly via a filler effect and nucleation, as well as through chemical interactions [78,79]. These interactions can influence the initial strength development, microstructure, and long-term durability of the concrete [80]. However, at higher limestone contents, the dilution effect may become more prominent and may influence the long-term strength gains of concrete.

4.3. Pore Structure

Current CT technology predominantly emphasizes the precise identification of internal pores or cracks within concrete. Nonetheless, it is crucial to acknowledge that exterior pores and cracks on the surface exposed to the environment can considerably influence material strength. Although there is a significant number of research works addressing the porosity of cement based materials [11], it is still challenging to characterize such materials solely based on the total porosity [81–83].

One other significant parameter is the sphericity of the pores, that is, how close the pores are to the shape of a perfect sphere [84]. This perfect spherical shape of the pores helps reducing the stress concentrations under loading conditions. From the results obtained via the use of the Dragonfly software, it resulted that for each of the three considered SCC mixes, more than 95% of the identified pores had a sphericity of 0.99, that is they are very close in shape to a perfect sphere (sphericity = 1). A sphericity close to one for all mixes suggests that the detected pores are almost perfect spheres. This is to be expected in self-compacting concrete, given its very good fluidity, use of a superplasticizer and minimal external deformation during casting. These observations are consistent with recent studies showing that surface tension dominates deformation of air voids [85,86].

Figure 8 presents the distribution of particle radius, sphericity and volume of pores for all considered SCC mixes. It can be observed that increasing the cement content results in a denser matrix [11], with a decrease in the pore radius of the considered mix. While the large majority of detected pores in the SCC1 mix had a radius of up to 3 mm, for both the SCC2 and SCC3 mixes it was reduced to 2.5 mm and 2.00 mm, respectively [87].

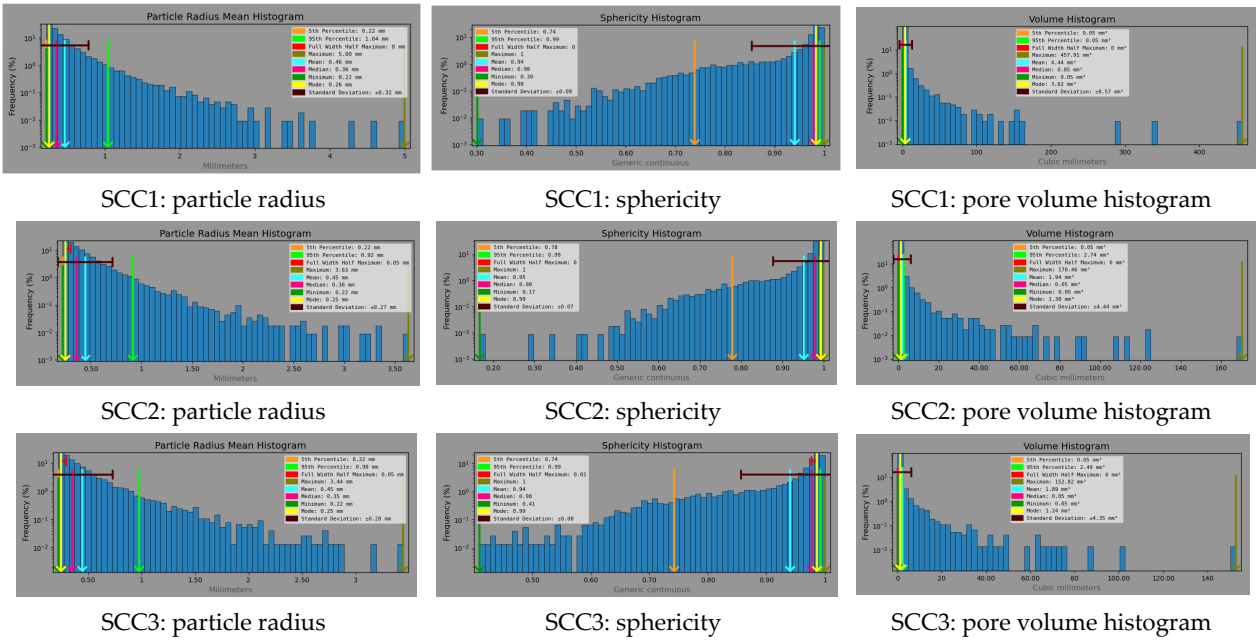

SCC1: particle radius | SCC1: sphericity | SCC1: pore volume histogram

SCC2: particle radius | SCC2: sphericity | SCC2: pore volume histogram

SCC3: particle radius | SCC3: sphericity | SCC3: pore volume histogram

Figure 8. Internal pore structure characterization.

At the same time, it can be seen that the values of pore sphericity increase with the increase in cement content.

At the same time, considering the data presented in Figure 5, it can be concluded that with the increase in the cement content of SCC, which leads to an increase in the values of the mechanical properties, the volume, as well as the maximum pore diameter, of the pores at the age of 7 years decreases. This could be explained by the fact that more hydration products are generated due to both higher cement content and due to the nucleation site effect of limestone filler.

Total internal porosity (φ) was computed as the void volume fraction relative to the full volume. Two classical porosity–strength models were evaluated and fitted by linear regression on logarithmically transformed variables. The results are summarized in Table 6 for compressive strength, static modulus of elasticity and dynamic modulus of elasticity.

Table 6. Properties of the SCC versus internal porosity.

Concrete Mix	Internal Porosity	Compressive Strength	StDev	COV	Static Modulus of Elasticity	StDev	COV
	[%]	[MPa]	{MPa]	[%]	[GPa]	[GPa]	[%]
SCC 1	0.9	46.73	2.11	4.51	28.62	1.47	5.14
SCC 2	0.7	49.66	1.65	3.33	28.76	1.02	3.54
SCC 3	0.635	51.17	1.19	2.33	30.14	1.81	6.01

The change in the elastic and mechanical property values of the SCC as a function of total internal porosity is presented in Figures 9 and 10 for the compressive strength and static modulus of elasticity, respectively. However, given the small number of data sets, the presented results should be regarded as representing the trends. Further investigations are deemed necessary to correctly assess the influence of the internal porosity on the mechanical characteristics of the SCC.

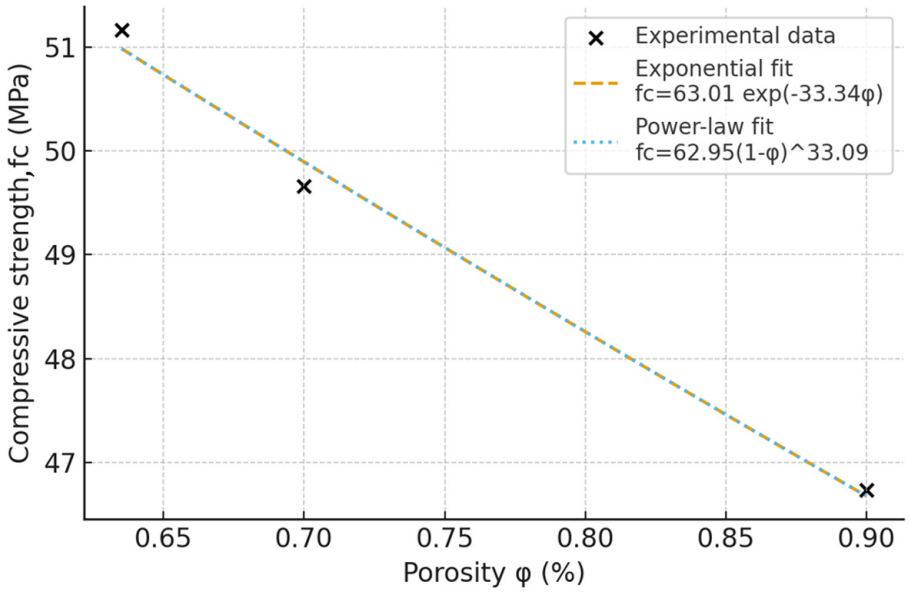

Figure 9. Influence of total internal porosity on the compressive strength.

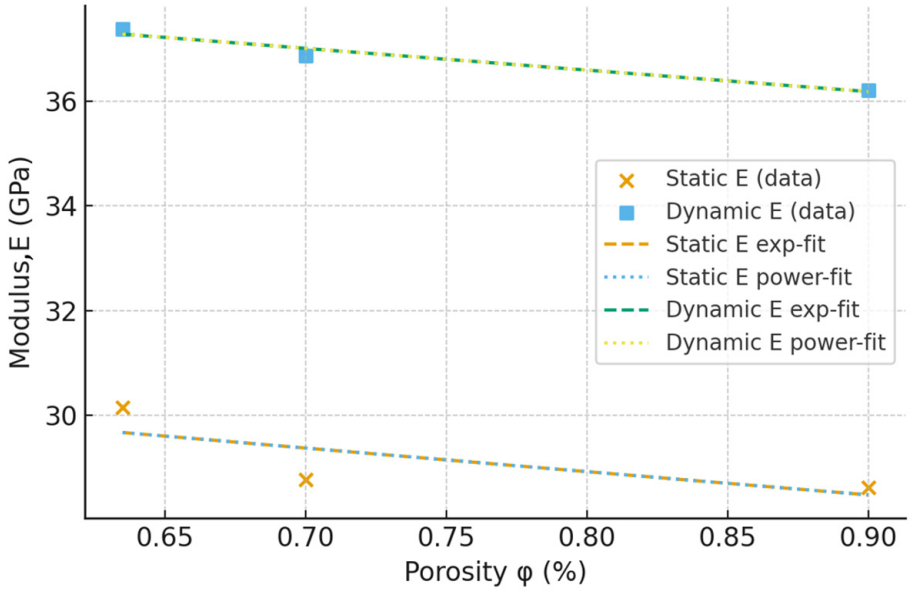

Figure 10. Influence of total internal porosity on the static modulus of elasticity.

5. Conclusions

The paper presents the results obtained on the characterization of self-compacting concrete at a long age (7 years) by using industrial computed tomography to assess the internal pore structure. Based on the obtained results, the following conclusions can be drawn.

1. There is little difference between the bulk density values of the considered SCC mixes at the long age. At the same time, the open porosity ranges from 8.54% to 12.9% and it is influenced by the cement content of the mix.
2. Compressive strength values increase compared to the standard testing age of 28 days. The increase rate is, however, inversely proportional to the cement content.
3. There is a good correlation between the conversion equations from the dynamic modulus of elasticity to the static one. Some of the existing equations tend to slightly overestimate the experimental results, while others underestimate the results.
4. The increased cement content and lower aggregate volume results in a lower volume of internal pores, as well as lower maximum pore radius, as determined through industrial CT scanning on the intact SCC cylinders. At the same time, the sphericity of the internal pores does not seem to be significantly influenced by the SCC mix proportion. Increasing the cement content above 340 kg/m^3 has little influence on the internal pore structure of the SCC.
5. The total internal porosity has a more significant influence on the compressive strength of SCC mixes than on the static modulus of elasticity. The values of the latter decrease at a much lower rate with respect to increasing internal porosity compared to the compressive strength.

Author Contributions: Conceptualization, O.-M.B., A.-E.M. and S.-M.A.-S.; methodology, I.-O.T. and S.-M.A.-S.; software, A.-E.M. and S.-M.A.-S.; validation, I.-O.T., O.-M.B., A.-E.M. and S.-M.A.-S.; formal analysis, I.-O.T., G.B. and S.-M.A.-S.; investigation, I.-O.T. and O.-M.B.; resources, I.-O.T.; data curation, A.-E.M. and S.-M.A.-S.; writing—original draft preparation, A.-E.M. and I.-O.T.; writing—review and editing, O.-M.B., S.-M.A.-S. and G.B.; visualization, I.-O.T.; supervision, I.-O.T. and S.-M.A.-S.; and project administration, I.-O.T. All authors have read and agreed to the published version of the manuscript.

Funding: This research received no external funding.

Institutional Review Board Statement: Not applicable.

Informed Consent Statement: Not applicable.

Data Availability Statement: The raw data supporting the conclusions of this article will be made available by the authors on request.

Acknowledgments: The authors are grateful to Phinia Romania, Iasi Headquarters, for providing access to the industrial CT equipment used to scan the concrete samples. The partnership between Phinia Romania and "Gheorghe Asachi" Technical University of Iasi is gratefully acknowledged. The research was also supported by the Boosting Ingenium for Excellence (BI4E) project, funded by the European Union's HORIZON-WIDERA-2021-ACCESS-05-01-European Excellence Initiative under the Grant Agreement No. 10107132.

Conflicts of Interest: The authors declare no conflicts of interest.

References

1. Yang, Z.; Liu, S.; Yu, L.; Xu, L. A Comprehensive Study on the Hardening Features and Performance of Self-Compacting Concrete with High-Volume Fly Ash and Slag. *Materials* **2021**, *14*, 4286. [CrossRef]
2. Rudnicki, T. Design of Self-Compacting Concrete with Reduced Cement Content by Aggregate Packing Method. *Materials* **2024**, *18*, 4. [CrossRef]
3. Fares, G.; El-Sayed, A.K.; Alhozaimy, A.M.; Al-Negheimish, A.I.; Albidah, A.S. Lightweight SCC Development in a Low-Carbon Cementitious System for Structural Applications. *Materials* **2023**, *16*, 4395. [CrossRef]
4. Zitouni, K.; Djerbi, A.; Mebrouki, A. Study on the Microstructure of the New Paste of Recycled Aggregate Self-Compacting Concrete. *Materials* **2020**, *13*, 2114. [CrossRef] [PubMed]
5. Anjos, M.A.S.D.; Camões, A.; Malheiro, R.; Maia Pederneiras, C.; Peixoto, L.K.S. Experimental Study of Carbonation and Chloride Resistance of Self-Compacting Concretes with a High Content of Fly Ash and Metakaolin, with and Without Hydrated Lime. *Materials* **2025**, *18*, 422. [CrossRef] [PubMed]
6. Zheng, S.; Liu, Q.; Han, F.; Liu, S.; Zhang, G.; Zhu, J. Impermeability and Durability of Self-Compacting Concrete Prepared with Aeolian Sand and Recycled Coarse Aggregate. *Materials* **2023**, *16*, 7279. [CrossRef] [PubMed]
7. Salih, M.A.; Ahmed, S.K.; Alsafi, S.; Abullah, M.M.A.B.; Jaya, R.P.; Abd Rahim, S.Z.; Aziz, I.H.; Thanaya, I.N.A. Strength and Durability of Sustainable Self-Consolidating Concrete with High Levels of Supplementary Cementitious Materials. *Materials* **2022**, *15*, 7991. [CrossRef]
8. Klemczak, B.; Gołaszewski, J.; Smolana, A.; Gołaszewska, M.; Cygan, G. Shrinkage Behaviour of Self-Compacting Concrete with a High Volume of Fly Ash and Slag Experimental Tests and Analytical Assessment. *Constr. Build. Mater.* **2023**, *400*, 132608. [CrossRef]
9. Murtaza, M.; Zhang, J.; Yang, C.; Cui, X.; Su, C.; Ramadan, A.N. Performance Analysis of Self Compacting Concrete by Incorporating Fly Ash, Coal Gangue Powder, Cement Kiln Dust and Recycled Concrete Powder by Absolute Volume Method. *Constr. Build. Mater.* **2024**, *431*, 136601. [CrossRef]
10. Monteiro, P.J.M.; Geng, G.; Marchon, D.; Li, J.; Alapati, P.; Kurtis, K.E.; Qomi, M.J.A. Advances in Characterizing and Understanding the Microstructure of Cementitious Materials. *Cem. Concr. Res.* **2019**, *124*, 105806. [CrossRef]
11. Xiao, J.; Lv, Z.; Duan, Z.; Zhang, C. Pore Structure Characteristics, Modulation and Its Effect on Concrete Properties: A Review. *Constr. Build. Mater.* **2023**, *397*, 132430. [CrossRef]
12. Łaźniewska-Piekarczyk, B. Examining the Possibility to Estimate the Influence of Admixtures on Pore Structure of Self-Compacting Concrete Using the Air Void Analyzer. *Constr. Build. Mater.* **2013**, *41*, 374–387. [CrossRef]
13. Bao, L.; Xu, G.; Li, H.; Xin, C.; Li, H.; He, M.; Liu, C. The Study of the Three-Parameter Normal Distribution Characteristics of the Pore Structure in C80 High-Performance Self-Compacting Concrete (HPSCC). *J. Compos. Sci.* **2024**, *8*, 510. [CrossRef]
14. Xu, G.; He, M.; He, L.; Chen, Y.; Duan, L.; Jiao, W. A Study on the Relationship Between the Pore Characteristics of High-Performance Self-Compacting Concrete (HPSCC) Based on Fractal Theory and the Function of the Water–Binder Ratio (W/C). *J. Compos. Sci.* **2025**, *9*, 66. [CrossRef]
15. Zhang, P.; Shi, D.; Han, P.; Ma, Z. Study on the Mechanical Properties and Pore Structure of Granulated Blast Furnace Slag Self-Compacting Concrete Based on Grey Correlation Theory. *J. Asian Archit. Build. Eng.* **2024**, *23*, 634–648. [CrossRef]
16. Wang, H.; Li, P.; An, X.; Wang, D.; Ji, G. The Evolution of Microstructure and Compressive Strength of Self-Compacting Concrete Affected by Early-Age Loading: Experiments and Multi-Scale Coupling Model. *Constr. Build. Mater.* **2025**, *482*, 141614. [CrossRef]
17. Morales-Cantero, A.; Cuesta, A.; De La Torre, A.G.; Mazanec, O.; Borralleras, P.; Weldert, K.S.; Gastaldi, D.; Canonico, F.; Aranda, M.A.G. Portland and Belite Cement Hydration Acceleration by C-S-H Seeds with Variable w/c Ratios. *Materials* **2022**, *15*, 3553. [CrossRef]

18. Pinheiro, D.G.L.; Sousa, M.I.C.; Pelisser, F.; Da Silva Rêgo, J.H.; Moragues Terrades, A.; Frías Rojas, M. Physical and Chemical Effects in Blended Cement Pastes Elaborated with Calcined Clay and Nanosilica. *Materials* **2023**, *16*, 1837. [CrossRef]
19. Beaudoin, J.J. Porosity Measurement of Some Hydrated Cementitious Systems by High Pressure Mercury Intrusion-Microstructural Limitations. *Cem. Concr. Res.* **1979**, *9*, 771–781. [CrossRef]
20. Hasanuzzaman, M.; Rashid, A.R.M.H.; Olabi, A.G. Characterization of Porous Glass and Ceramics by Mercury Intrusion Porosimetry. In *Reference Module in Materials Science and Materials Engineering*; Elsevier: Amsterdam, The Netherlands, 2017; ISBN 978-0-12-803581-8.
21. Yao, Y.; Liu, D. Comparison of Low-Field NMR and Mercury Intrusion Porosimetry in Characterizing Pore Size Distributions of Coals. *Fuel* **2012**, *95*, 152–158. [CrossRef]
22. Toma, I.-O.; Stoian, G.; Rusu, M.-M.; Ardelean, I.; Cimpoeşu, N.; Alexa-Stratulat, S.-M. Analysis of Pore Structure in Cement Pastes with Micronized Natural Zeolite. *Materials* **2023**, *16*, 4500. [CrossRef] [PubMed]
23. Ardelean, I. The Effect of an Accelerator on Cement Paste Capillary Pores: NMR Relaxometry Investigations. *Molecules* **2021**, *26*, 5328. [CrossRef] [PubMed]
24. Rusu, M.M.; Vilau, C.; Dudescu, C.; Pascuta, P.; Popa, F.; Ardelean, I. Characterization of the Influence of an Accelerator upon the Porosity and Strength of Cement Paste by Nuclear Magnetic Resonance (NMR) Relaxometry. *Anal. Lett.* **2023**, *56*, 303–311. [CrossRef]
25. Saleh, F.K.; Teodoriu, C.; Sondergeld, C. Review of NMR Studies for Oilwell Cements and Their Importance. *ChemEngineering* **2021**, *5*, 18. [CrossRef]
26. Naber, C.; Kleiner, F.; Becker, F.; Nguyen-Tuan, L.; Rößler, C.; Etzold, M.A.; Neubauer, J. C-S-H Pore Size Characterization Via a Combined Nuclear Magnetic Resonance (NMR)–Scanning Electron Microscopy (SEM) Surface Relaxivity Calibration. *Materials* **2020**, *13*, 1779. [CrossRef]
27. Radica, F.; Casarin, A.; Iezzi, G.; Bravo, M.; De Brito, J.; Galderisi, A.; Brando, G.; Nazzari, M.; Scarlato, P. Cement vs Aggregates and Textures of Aggregates in a Mortar: Comparative Image Analysis Methods and Analytical Protocols. *Constr. Build. Mater.* **2024**, *453*, 139033. [CrossRef]
28. Ren, D.; Xu, J.; Su, S.; Tian, G.; Chen, X.; Zhang, A.; Ai, C. Characterization of Internal Pore Size Distribution and Interconnectivity for Asphalt Concrete with Various Porosity Using 3D CT Scanning Images. *Constr. Build. Mater.* **2023**, *400*, 132751. [CrossRef]
29. Jadala, S.; Biligiri, K.P.; Abdulrahman, F.; Zeiada, W.A. A Novel Approach to Assess Internal Pore Structure and Quantify Tortuosity of Clogged Pervious Concrete through Image Analysis Techniques. *Int. J. Pavement Eng.* **2024**, *25*, 2410939. [CrossRef]
30. Balázs, G.L.; Lublóy, É.; Földes, T. Evaluation of Concrete Elements with X-Ray Computed Tomography. *J. Mater. Civ. Eng.* **2018**, *30*, 06018010. [CrossRef]
31. Zhang, Y.; Zhu, X. Evaluation of Pore and Fiber Distribution Characteristics of Hybrid Fiber Reinforced Lightweight Aggregate Concrete Using X-Ray Computed Tomography. *J. Build. Eng.* **2023**, *80*, 108105. [CrossRef]
32. Promentilla, M.; Cortez, S.; Papel, R.; Tablada, B.; Sugiyama, T. Evaluation of Microstructure and Transport Properties of Deteriorated Cementitious Materials from Their X-Ray Computed Tomography (CT) Images. *Materials* **2016**, *9*, 388. [CrossRef]
33. Zhang, Y.; Xu, S.; Gao, Y.; Guo, J.; Cao, Y.; Zhang, J. Correlation of Chloride Diffusion Coefficient and Microstructure Parameters in Concrete: A Comparative Analysis Using NMR, MIP, and X-CT. *Front. Struct. Civ. Eng.* **2020**, *14*, 1509–1519. [CrossRef]
34. Luo, Q.; Zhao, L.; Wu, M. Microstructural Damage Characterization of NC-UHPC Composite under Salt Freeze-Thaw Cycles Based on Ex-Situ X-Ray Computed Tomography. *Constr. Build. Mater.* **2024**, *414*, 134980. [CrossRef]
35. Rossi, E.; Governo, S.; Shakoorioskooie, M.; Zhan, Q.; Mundra, S.; Mannes, D.; Kaestner, A.; Angst, U. X-Ray Computed Tomography to Observe the Presence of Water in Macropores of Cementitious Materials. *RILEM Tech. Lett.* **2024**, *8*, 165–175. [CrossRef]
36. Vicente, M.A.; Mena, Á.; Mínguez, J.; González, D.C. Use of Computed Tomography Scan Technology to Explore the Porosity of Concrete: Scientific Possibilities and Technological Limitations. *Appl. Sci.* **2021**, *11*, 8699. [CrossRef]
37. Revilla-Cuesta, V.; Faleschini, F.; Zanini, M.A.; Skaf, M.; Ortega-López, V. Porosity-Based Models for Estimating the Mechanical Properties of Self-Compacting Concrete with Coarse and Fine Recycled Concrete Aggregate. *J. Build. Eng.* **2021**, *44*, 103425. [CrossRef]
38. Silva, Y.F.; Delvasto, S.; Izquierdo, S.; Araya-Letelier, G. Short and Long-Term Physical and Mechanical Characterization of Self-Compacting Concrete Made with Masonry and Concrete Residue. *Constr. Build. Mater.* **2021**, *312*, 125382. [CrossRef]
39. Bai, W.; Ye, D.; Yuan, C.; Guan, J.; Xie, C.; Cao, K. The Effect of Curing Age on Mechanical Properties and Mesoscopic Damage Mechanism of Recycled Aggregate Concrete Modified with Zeolite Powder. *J. Build. Eng.* **2024**, *85*, 108694. [CrossRef]
40. He, Y.; Mote, J.; Lange, D.A. Characterization of Microstructure Evolution of Cement Paste by Micro Computed Tomography. *J. Cent. South Univ.* **2013**, *20*, 1115–1121. [CrossRef]
41. Chung, S.-Y.; Kim, J.-S.; Stephan, D.; Han, T.-S. Overview of the Use of Micro-Computed Tomography (Micro-CT) to Investigate the Relation between the Material Characteristics and Properties of Cement-Based Materials. *Constr. Build. Mater.* **2019**, *229*, 116843. [CrossRef]

42. Bachofner, W.; Suza, D.; Müller, H.S.; Kollegger, J. Long-Term Shrinkage Measurements on Large-Scale Specimens Exposed to Real Environmental Conditions. *Materials* **2023**, *16*, 7305. [CrossRef]
43. *SR EN 197-1*; Cement. Part I: Composition, Specifications and Conformity Criteria for Normal Use Cements. ASRO Romanian Standards Association: Bucharest, Romania, 2011.
44. Valcuende, M.; Marco, E.; Parra, C.; Serna, P. Influence of Limestone Filler and Viscosity-Modifying Admixture on the Shrinkage of Self-Compacting Concrete. *Cem. Concr. Res.* **2012**, *42*, 583–592. [CrossRef]
45. Palm, S.; Proske, T.; Rezvani, M.; Hainer, S.; Müller, C.; Graubner, C.-A. Cements with a High Limestone Content—Mechanical Properties, Durability and Ecological Characteristics of the Concrete. *Constr. Build. Mater.* **2016**, *119*, 308–318. [CrossRef]
46. Belov, V.; Kuliaev, P. Limestone Filler as One of the Cheapest and Best Additive to Concrete. *IOP Conf. Ser. Mater. Sci. Eng.* **2018**, *365*, 032054. [CrossRef]
47. Bradu, A.; Mihai, P.; Budescu, M.; Banu, O.-M.; Taranu, N.; Florea, N. The Comparative Study of the Self-Compacting Concrete and of Vibrated Concrete Properties Including the Complete Characteristic Curve under Compression. *Rom. J. Mater.* **2017**, *47*, 379–386.
48. The European Project Group (EPG). *The European Guidelines for Self-Compacting Concrete—Specifications, Production and Use*; The European Project Group (EPG): Prague, Czech Republic, 2005.
49. *ACI PRC-237-07*; Self-Consolidating Concrete (Reapproved 2019). American Concrete Institute: Farmington Hills, MI, USA, 2007.
50. Kou, S.C.; Poon, C.S. Properties of Self-Compacting Concrete Prepared with Coarse and Fine Recycled Concrete Aggregates. *Cem. Concr. Compos.* **2009**, *31*, 622–627. [CrossRef]
51. Nikbin, I.M.; Beygi, M.H.A.; Kazemi, M.T.; Vaseghi Amiri, J.; Rahmani, E.; Rabbanifar, S.; Eslami, M. A Comprehensive Investigation into the Effect of Aging and Coarse Aggregate Size and Volume on Mechanical Properties of Self-Compacting Concrete. *Mater. Des.* **2014**, *59*, 199–210. [CrossRef]
52. Petit, J.-Y.; Wirquin, E.; Helnan-Moussa, B. Effect of W/C and Superplasticizer Type on Rheological Parameters of SCC Repair Mortar for Gravitational or Light Pressure Injection. *Cem. Concr. Compos.* **2011**, *33*, 1050–1056. [CrossRef]
53. Alexa-Stratulat, S.-M.; Mihai, P.; Toma, A.-M.; Taranu, G.; Toma, I.-O. Influence of Concrete Strength Class on the Long-Term Static and Dynamic Elastic Moduli of Concrete. *Appl. Sci.* **2021**, *11*, 11671. [CrossRef]
54. *SR EN 12350-8*; Testing Fresh Concrete—Part 8: Self-Compacting Concrete—Slump-Flow Test. Romanian Standards Association (ASRO): Bucharest, Romania, 2019.
55. *SR EN 12350-9*; Testing Fresh Concrete—Part 9: Self-Compacting Concrete—V-Funnel Test. Romanian Standards Association (ASRO): Bucharest, Romania, 2010.
56. *SR EN 12350-10*; Testing Fresh Concrete—Part 10: Self-Compacting Concrete—L Box Test. Romanian Standards Association (ASRO): Bucharest, Romania, 2010.
57. Nguyen, T.L.H.; Roussel, N.; Coussot, P. Correlation between L-Box Test and Rheological Parameters of a Homogeneous Yield Stress Fluid. *Cem. Concr. Res.* **2006**, *36*, 1789–1796. [CrossRef]
58. *ASTM C642-21*; Standard Test Method for Density, Absorption, and Voids in Hardened Concrete. C09 Committee ASTM International: West Conshohocken, PA, USA, 2022. [CrossRef]
59. *SR EN 12390-13*; Testing Hardened Concrete. Part 13—Determination of Secant Modulus of Elasticity in Compression. ASRO Romanian Standards Association: Bucharest, Romania, 2021.
60. *C215-19*; Test Method for Fundamental Transverse, Longitudinal, and Torsional Resonant Frequencies of Concrete Specimens. ASTM—C09 Committee ASTM International: West Conshohocken, PA, USA, 2019. [CrossRef]
61. *SR EN 12390-3*; Testing of Hardened Concrete. Part 3—Compressive Strength of Test Specimens. ASRO Romanian Standards Association: Bucharest, Romania, 2019.
62. *SR EN 12390-6*; Testing of Hardened Concrete. Part 6—Splitting Tensile Strength of Test Specimens. ASRO Romanian Standards Association: Bucharest, Romania, 2010.
63. Brisard, S.; Serdar, M.; Monteiro, P.J.M. Multiscale X-Ray Tomography of Cementitious Materials: A Review. *Cem. Concr. Res.* **2020**, *128*, 105824. [CrossRef]
64. Thompson, A.; Senin, N.; Maskery, I.; Leach, R. Effects of Magnification and Sampling Resolution in X-Ray Computed Tomography for the Measurement of Additively Manufactured Metal Surfaces. *Precis. Eng.* **2018**, *53*, 54–64. [CrossRef]
65. Liu, Z.; Li, M.; Wong, T.N.; Tan, M.J. Determine the Effects of Pore Properties on the Mechanical Performances of 3D Concrete Printing Units with Experimental and Numerical Methods. *J. Build. Eng.* **2024**, *92*, 109730. [CrossRef]
66. Tao, Y.; Wang, Z.; Hadigheh, S.A. Enhancing X-Ray Micro-CT Analysis for Detecting Voids and Carbon Fibre Features in Fibre-Reinforced Cementitious Composites Using Advanced 3D Gaussian Filtering. *Measurement* **2025**, *249*, 117018. [CrossRef]
67. Wang, C.-H.; Hao, B.-B.; Liu, S.-W.; Yuan, L.-Z. Influence of Early Freezing on the Pore Structure Characteristics of Concrete and Its Correlation with Mechanical Properties. *Buildings* **2023**, *14*, 47. [CrossRef]
68. Islam, G.M.S.; Akter, S.; Reza, T.B. Sustainable High-Performance, Self-Compacting Concrete Using Ladle Slag. *Clean. Eng. Technol.* **2022**, *7*, 100439. [CrossRef]

69. Zhao, H.; Sun, W.; Wu, X.; Gao, B. Sustainable Self-Compacting Concrete Containing High-Amount Industrial by-Product Fly Ash as Supplementary Cementitious Materials. *Env. Sci. Pollut. Res.* **2022**, *29*, 3616–3628. [CrossRef]
70. Alami, M.M.; Erdem, T.K. Effects of Mix-Design Variables on the Workability, Rheology and Stability of Self-Consolidating Concrete. *Rev. Construcción* **2022**, *21*, 703–716. [CrossRef]
71. Stratulat, S.; Bradu, A.; Toma, I.O. Dynamic and Environmental Assessment of Self-Compacting Concrete. *Bull. Polytech. Inst. Jassy. Constr. Archit. Sect.* **2020**, *66*, 27–40.
72. Guessoum, M.; Boukhelf, F.; Khadraoui, F. Full Characterization of Self-Compacting Concrete Containing Recycled Aggregates and Limestone. *Materials* **2023**, *16*, 5842. [CrossRef]
73. Vicente, M.A.; Mínguez, J.; González, D.C. Variation of the Pore Morphology during the Early Age in Plain and Fiber-Reinforced High-Performance Concrete under Moisture-Saturated Curing. *Materials* **2019**, *12*, 975. [CrossRef]
74. Toma, I.-O.; Alexa-Stratulat, S.-M.; Mihai, P.; Toma, A.-M.; Taranu, G. Experimental Investigations on the Long Term Material Properties of Rubberized Portland Cement Concrete. *Appl. Sci.* **2021**, *11*, 10868. [CrossRef]
75. Popovics, S. Verification of Relationships between Mechanical Properties of Concrete-like Materials. *Mat. Constr.* **1975**, *8*, 183–191. [CrossRef]
76. Lydon, F.D.; Balendran, R.V. Some Observations on Elastic Properties of Plain Concrete. *Cem. Concr. Res.* **1986**, *16*, 314–324. [CrossRef]
77. *SR EN 1992-1-1*; Eurocode 2: Design of Concrete Structures—Part 1-1: General Rules and Rules for Buildings. Romanian Standards Association (ASRO): Bucharest, Romania, 2004.
78. Jiang, Z.; Yang, Q.; Wang, B.; Li, C.; Zhang, J.; Ren, Q. Limestone Filler as a Mineral Additive on the Compressive Strength and Durability of Self-Compacting Concrete with Limestone Manufactured Sand. *J. Build. Eng.* **2024**, *94*, 109965. [CrossRef]
79. Boutlikht, M.; Douadi, A.; Khitas, N.E.H.; Messai, A.; Hebbache, K.; Belebchouche, C.; Smarzewski, P.; Tawfik, T.A. Optimizing of Self-Compacting Concrete (SCC): Synergistic Impact of Marble and Limestone Powders—A Technical and Statistical Analysis. *Buildings* **2025**, *15*, 1043. [CrossRef]
80. Ouyang, X.; Koleva, D.A.; Ye, G.; Van Breugel, K. Insights into the Mechanisms of Nucleation and Growth of C–S–H on Fillers. *Mater. Struct.* **2017**, *50*, 213. [CrossRef]
81. She, W.; Zhao, G.; Cai, D.; Jiang, J.; Cao, X. Numerical Study on the Effect of Pore Shapes on the Thermal Behaviors of Cellular Concrete. *Constr. Build. Mater.* **2018**, *163*, 113–121. [CrossRef]
82. Li, D.; Li, Z.; Lv, C.; Zhang, G.; Yin, Y. A Predictive Model of the Effective Tensile and Compressive Strengths of Concrete Considering Porosity and Pore Size. *Constr. Build. Mater.* **2018**, *170*, 520–526. [CrossRef]
83. Martínez-García, R.; Sánchez De Rojas, M.I.; Jagadesh, P.; López-Gayarre, F.; Morán-del-Pozo, J.M.; Juan-Valdes, A. Effect of Pores on the Mechanical and Durability Properties on High Strength Recycled Fine Aggregate Mortar. *Case Stud. Constr. Mater.* **2022**, *16*, e01050. [CrossRef]
84. Kruger, J.; Van Der Westhuizen, J.-P. Investigating the Poisson Ratio of 3D Printed Concrete. *Appl. Sci.* **2023**, *13*, 3225. [CrossRef]
85. Liu, C.; Zhang, Z.; Jia, Z.; Cao, R.; Wang, W.; Banthia, N.; Chen, C.; Xiong, Y.; Chen, Y.; Zhang, Y. Quantitative Characterization of Bubble Stability of Foam Concrete throughout Extrusion Process: From Yield Stress, Viscosity and Surface Tension Point of View. *Compos. Part B Eng.* **2024**, *284*, 111724. [CrossRef]
86. Zeng, X.; Lan, X.; Zhu, H.; Liu, H.; Umar, H.A.; Xie, Y.; Long, G.; Ma, C. A Review on Bubble Stability in Fresh Concrete: Mechanisms and Main Factors. *Materials* **2020**, *13*, 1820. [CrossRef]
87. Liu, D.; Šavija, B.; Smith, G.E.; Flewitt, P.E.J.; Lowe, T.; Schlangen, E. Towards Understanding the Influence of Porosity on Mechanical and Fracture Behaviour of Quasi-Brittle Materials: Experiments and Modelling. *Int. J. Fract.* **2017**, *205*, 57–72. [CrossRef]

Construction and Building Materials 438 (2024) 137229

Contents lists available at ScienceDirect

Construction and Building Materials

journal homepage: www.elsevier.com/locate/conbuildmat

Effect of expanded perlite aggregates and temperature on the strength and dynamic elastic properties of cement mortar

Sergiu-Mihai Alexa-Stratulat, George Taranu, Ana-Maria Toma *, Ioana Olteanu, Cristian Pastia, Georgiana Bunea, Ionut-Ovidiu Toma *

The "Gheorghe Asachi" Technical University of Iasi, Faculty of Civil Engineering and Building Services, Iasi, Romania

ARTICLE INFO

Keywords:
Expanded perlite aggregate mortar
Dynamic modulus of elasticity
Flexural strength
Compressive strength
Elevated temperature

ABSTRACT

The residential market consumes nearly half of the world's concrete production, and it is anticipated that 68 % of the global population will reside in urban areas by 2050. Researchers have focused their efforts on exploring alternative options to natural aggregates in concrete and mortar. In line with the principles of circular economy, construction and demolition waste has been repurposed for the manufacture of cement-based materials. Volcanic products, which are abundant but underutilized, have been identified as an alternative to recycled aggregates. They offer several advantages over natural river aggregates, including reduced weight, enhanced thermal and acoustic insulation, improved fire resistance and pozzolanic characteristics. While there has been a significant amount of research on the use of expanded perlite as a supplementary cementitious material, studies involving the use of expanded perlite aggregates (EPA) in cement-based construction materials are relatively limited. This paper seeks to address this knowledge gap by investigating the use of EPA in cement-based mortar at both room and elevated temperatures. The study examines the impact of varying replacement percentages (10 %, 20 % and 30 % - by volume) of natural sand with EPA having a maximum grain size of 4 mm, and the exposure temperature of mortar prisms at the age of 28 days. Specifically, temperatures of 100ºC, 150ºC and 200ºC were selected for analysis. The impact of these parameters on the flexural and compressive strength of mortar, as well as its dynamic elastic properties, was experimentally determined. The findings indicate that, at room temperature, higher replacement percentages of natural sand by EPA result in decreased flexural and compressive strengths, by as much as 50 % and 30.71 %, respectively. However, the dynamic moduli values for replacement percentages up to 20 % are similar to those of the reference mix. Conversely, when subjected to temperatures up to 200ºC, significant improvements were observed in the flexural strength values, e.g. over 20 % for temperatures of 150°C and 200°C, with only marginal improvements in compressive strength, 3 % ÷ 20 % for temperatures of 150°C and 200°C, compared to values obtained at room temperature.

1. Introduction

Concrete is the most widely used construction material with a total worldwide production of 14 billion cubic meters in 2020, according to Global Cement and Concrete Association [1]. Nearly half of this quantity served the residential sector. Projections indicate that 68 % of the world's population will inhabit urban areas by 2050, leading to an estimated annual concrete production of 20 billion cubic meters. Given that aggregates constitute 60 %-75 % of the total concrete volume, it follows that the demand for natural resources will increase substantially. It is estimated that approximately 50 % of the world's raw material consumption is necessary to sustain this demand [2].

Finding alternative solutions to natural aggregates has been actively pursued by many researchers. The use of ferrochrome waste slag aggregates in limestone-calcined clay cement mortar resulted in an increase in both tensile strength (up to 22.2 %) and compressive strength (up to 71 %), as the percentage of natural sand replacement increased [3]. In addition, when natural sand was completely replaced with ferrochrome waste slag aggregates, the water absorption coefficient decreased by 16 %. In line with the principles of circular economy,

* Corresponding authors.
E-mail addresses: sergiu-mihai.alexa-stratulat@academic.tuiasi.ro (S.-M. Alexa-Stratulat), george.taranu@academic.tuiasi.ro (G. Taranu), ana-maria.toma@academic.tuiasi.ro (A.-M. Toma), ioana.olteanu@academic.tuiasi.ro (I. Olteanu), cristian.pastia@academic.tuiasi.ro (C. Pastia), georgiana.bunea@academic.tuiasi.ro (G. Bunea), ionut.ovidiu.toma@tuiasi.ro (I.-O. Toma).

https://doi.org/10.1016/j.conbuildmat.2024.137229
Received 7 December 2023; Received in revised form 13 June 2024; Accepted 24 June 2024
Available online 26 June 2024

construction and demolition waste has been repurposed as a resource for cement-based materials production. A recent study used recycled aggregates to substitute natural sand in mortar at rates of 25 %, 50 %, 75 %, and 100 %.Apart from demonstrating their effectiveness in structural applications, such as masonry elements, completely replacing natural with recycled aggregates with particle size smaller than 2.4 mm resulted in a 64 % reduction of CO_2 emissions associated with production processes. However, after considering both the strength properties and carbon footprint, it was concluded that optimal replacement percentage was 50 % [2].

The use of recycled aggregates from construction and demolition waste in concrete typically results in a decrease in mechanical properties. This is primarily attributed to the quality of the aggregates, which weakens the interfacial transition zone between the porous mortar adhering to the surface of the recycled aggregates and the fresh cement paste [4,5]. A possible solution to this issue involves treating the recycled aggregates with a silica fume slurry. This yielded a notable 16 %-26 % increase in concrete compressive strength at various curing ages, with complete replacement of natural aggregates. The inclusion of carbon fibers resulted in a 38 % increase in the flexural strength of concrete with recycled aggregates and a 34 % increase in the modulus of elasticity [6]. In a separate study, different combinations of recycled aggregates and nano-silica were examined to assess their impact on the mechanical and durability properties of concrete. Researchers employed gene expression programming to predict the compressive strength of concrete incorporating recycled aggregates and nano-silica as a pozzolan [7]. The proposed optimal mix comprised a 26 % replacement of natural coarse aggregates with recycled aggregates and 4 % nano-silica. According to the mathematical model, this mix demonstrated the highest flexural and compressive strength, modulus of elasticity and, simultaneously, the lowest water absorption coefficient.

An alternative to recycled aggregates has been identified in the form of volcanic products, which, despite their substantial potential, are not fully exploited. Volcanic rocks such as pumice, lapillus, tuff, zeolites, and perlite offer several advantages over natural river aggregates, including their lightweight nature, improved thermal and acoustic insulation properties, fire resistance, and pozzolanic properties [8]. The use of volcanic scoria, a type of volcanic rock formed by rapid cooling of lava in air, in concrete led to a 15 % reduction of bulk density and a 22.3 % increase in modulus of elasticity. Furthermore, due to secondary pozzolanic reactions, the compressive strength increased between 28 and 90 days by 15.23 %-22.3 %. However, the obtained values were approximately 70 %-75 % of the compressive strength obtained for the reference mix [9]. The use of zeolites as lightweight aggregates in concrete proved to be advantageous from the point of view of self-weight reduction. Additionally, a smaller interfacial transition zone between the aggregates and the cement paste was achieved, depending on the type of cement used in the concrete mix [10]. High quantities of ettringite and calcium hydroxide (CH) at early ages, and correspondingly high levels of calcium silicate hydrates (CSH) at later ages, were identified as the main factors influencing the quality of the interfacial transition zone, with a pronounced dependence on cement dosage and water-to-cement ratio.

Perlite, an amorphous aluminosilicate volcanic glass, has the ability to expand approximately 5–20 times its original volume when heated to its softening temperature, ranging between 900ºC and 1200ºC [11]. This expansion process, caused by the water trapped inside the perlite ore, results in a lightweight, cellular aggregate with bulk densities ranging from 80 kg/m^3 to 240 kg/m^3 [12]. Expanded perlite, with its high surface area, low sound transmission, low thermal conductivity [12,13] and chemical inertness, finds a wide range of applications, from horticulture to pharmaceutical and filtering applications in municipal drainage systems. In the construction industry, it has been used as a replacement for cement [14] and/or aggregates [11]. Taking into account the many applications of perlite, its worldwide production steadily increased during the last decade, as shown in Fig. 1.

One of the earliest uses of perlite in the construction industry has been in the development of building insulation materials, such as renders and mortars. Considering that approximately 40 % of a building's total energy consumption is dedicated to maintaining a comfortable indoor climate [12,16], there has been a growing demand for improved insulating materials and more efficient cooling and heating systems. Laboratory investigations and numerical analyses have demonstrated that panels composed of a mixture of cement, expanded perlite and pumice exhibit superior thermal performance in both standard (no vegetation) and green roof scenarios compared to reference panels [12]. Combining perlite powder with a sodium hydroxide solution and a foaming agent result in an ultra-lightweight foam concrete-like material, with enhanced thermal properties and fire performance. Heat treatment, particularly at a curing temperature of 850ºC, was identified as an important parameter, yielding the best results in terms of density and thermal conductivity [13]. Additionally, owing to the pozzolanic activity of perlite, a denser and stronger structure of renders and mortars is obtained [17]. A similar densification effect has been observed in the case of a magnesium potassium phosphate cement-expanded perlite composite, used as a fire-resisting coating. The presence of perlite

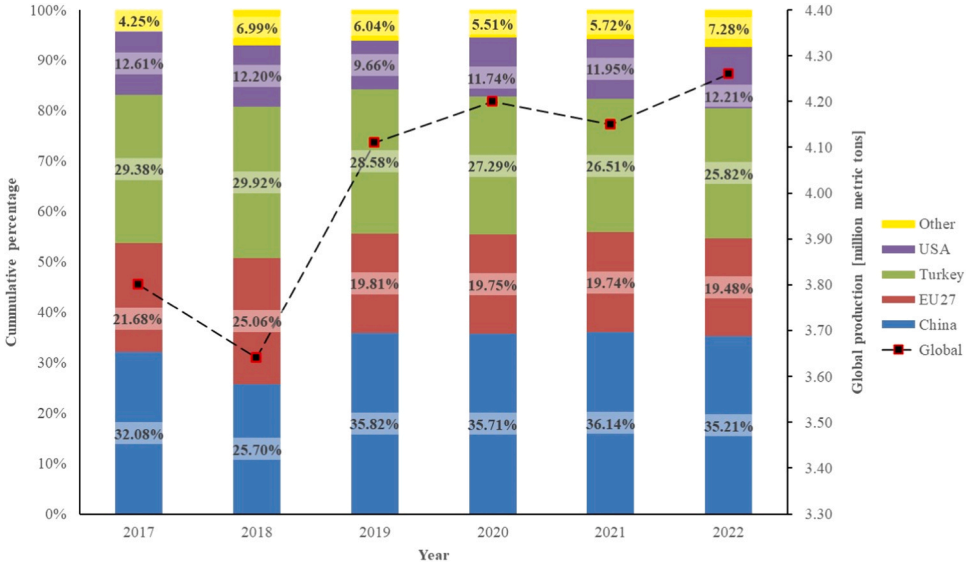

Fig. 1. Worldwide perlite ore production (based on data from USGS [15]).

increased residual bond strength after the fire test and reduced the occurrence of visible cracks on the coating surface [18].

The production of cement is a significant contributor to greenhouse gas (GHG) emissions in the construction industry, accounting for approximately 5 % - 7 % of the global CO_2 emissions [19,20]. To address this environmental impact, the use of supplementary cementitious materials (SCMs) has been proposed as a feasible solution. SCMs can be classified based on their source into industrial wastes, such as silica fume and fly ash, and natural pozzolans, such as pumice, metakaolin, perlite, zeolite and others. Natural pozzolans are aluminosilicate materials capable of reacting with calcium hydroxide (CH) to form calcium silicate hydrates (CSH) gels, contributing to a denser structure in cementitious materials and enhancing strength and durability properties [21]. Research has shown that using perlite powder in self-compacting concrete (SCC) requires an increase in superplasticizer content to achieve similar workability to the reference mix. Compressive strength values were found to be nearly identical to the reference mix at the age of 91 days, with significant improvements observed with increasing the fineness of perlite powder from the age of 28 days [22]. The use of perlite powder in SCC resulted in improved mechanical properties when exposed elevated temperatures, up to 600ºC, with reduced spalling [23]. Replacing cement with high percentages of perlite powder, such as 20 % and 30 %, had a detrimental effect on concrete protection of reinforcement to corrosion in aggressive environments [24]. However, a 40 % replacement of cement by expanded perlite powder yielded comparable 28-day compressive strength values in ultra-high performance concrete (UHPC) but slightly reduced the chloride ion penetration resistance of concrete [25].

In an effort to prevent the depletion of natural resources used in concrete production, researchers have explored alternatives to conventional aggregates. Other forms of natural aggregates, such as expanded perlite, zeolites, and volcanic tuff, were identified, and their impact on the mechanical properties of concrete were evaluated. A recent study focused on the replacement of coarse natural aggregates with perlite aggregates concluded that concrete density is significantly reduced due to perlite porous structure [26]. However, as perlite possesses lower strength than traditional aggregates, the compressive strength of concrete decreased with increasing replacement percentage. Conversely, concrete with expanded perlite aggregates (EPA) demonstrated higher compressive strength values at both 7 and 28 days compared to other lightweight concrete mixes based on pumice aggregates [27]. Moreover, replacing natural sand with EPA in proportions of 75 %-100 % resulted in obtaining ultra-high performance concrete with similar fluidity, mechanical strength and durability properties as conventional UHPC [25].

The existing scientific literature contains a significantly higher number of studies dedicated to perlite as a supplementary cementitious material compared to those investigating expanded perlite as an aggregate substitute. This paper seeks to address this knowledge gap by investigating the use of EPA in cement-based mortar at both room temperature and after exposure to elevated temperatures. Previous research has shown that concrete incorporating powdered perlite exhibited enhanced mechanical properties at temperatures up to 300ºC [23,28]. Therefore, this study focused on evaluating the impact of replacing natural sand with EPA, with a maximum grain size of 4 mm, at varying percentages (10 %, 20 % and 30 % by volume) as well as subjecting mortar prisms to temperature exposure at 28 days. The temperatures selected for the experiment were 100ºC, 150ºC and 200ºC. Experimental determinations were made regarding the impact of both parameters on the flexural and compressive strength of mortar, and on its dynamic elastic properties.

The results indicate that, at room temperature, an increase in replacement percentage of natural sand with EPA leads to decreased flexural strength and compressive strength. However, replacement percentages of up to 20 % exhibit dynamic moduli values similar to those of the reference mix. Conversely, when exposed to temperatures up to 200ºC, there are significant improvements in the flexural strength and minimal gains in compressive strength, compared to the values obtained at room temperature. The most substantial increases were observed at 150ºC.

2. Materials and methods

2.1. Materials

A CEM II B-M (S-LL) 42.5 R cement (StructoPlus), complying with SR EN 197–1:2011 [29] guidelines, was considered in this research. It is widely available on the market, and it comprises 65 %-79 % clinker and a 21 %-35 % combination of blast furnace slag and limestone. The chemical composition of the cement, as provided by the manufacturer (HOLCIM, Romania), is detailed in Table 1. According to Favier et al. [30], CEM II cement is the predominant type in Europe, holding a 47 % market share in 2015.

The aggregate used in this study was river sand with a maximum grain size of 4 mm and a specific weight of 2.69. Expanded perlite, having a specific weight of 0.129 and complying to SR EN 1097–3:2002 [31] and SR EN 933–2:2020 [32], was selected as a substitute for the natural sand, with replacement volumes of 10 %, 20 % and 30 %. Table 1 provides the chemical composition of the expanded perlite, as supplied by the manufacturer (ProcemaPerlit). The sieve analysis of the two types of aggregates is presented in Fig. 2. It can be observed that EPA had almost 60 % of its volume consisting of grains larger than 1 mm [33], whereas in case of sand the percentage was significantly lower, 18.16 %. However, since EPA aggregates have a lower Mohs hardness compared to natural sand, it is expected that particle size distribution of EPA will change during mixing, namely the volume of fine grains to increase, as previously reported [33]. The percentage shown in Fig. 3 for 0.125 mm sieve corresponded to even lower than 0.063 mm sieve, which basically falls in the category of powders. In case of sand, the corresponding percentage was only 3.4 %.

Based on the specifications provided by ASTM C618:2022 [34], expanded perlite falls in the category of natural pozzolans due to the combined content of SiO_2, Al_2O_3 and Fe_2O_3 exceeding 70 % [35]. Fig. 3a depicts the porous structure of expanded perlite. When further magnified, the microstructure shows a series of flakes/sheets [36] separated by gaps, as shown in Fig. 3b. These features contribute to the thermal insulation and water absorption properties of expanded perlite [37].

2.2. Mix proportion

A reference mortar mix ratio of 1:4:0.6 (cement:sand:water) by volume was employed. Table 2 shows the proportions, per cubic meter, for all mixes used in the study. For mortars modified by EPA, a higher water/cement ratio was required to achieve a consistency similar to that of the reference mix [14]. In other previous studies, superplasticizer was used in order to keep the same water/cement ratio [33]. However, according to earlier findings, there are large compatibility issues between various superplasticizers and natural pozzolans [38]. For similar water/binder ratio it was found that there is a need to increase the superplasticizer content by as much as 50 % to counteract the loss of slump caused by the use of zeolite (having similar chemical composition to perlite). Moreover, different superplasticizers required different dosages in order to achieve similar workability of mortar.

Aside of the reference, the mixtures were labeled by EPA (expanded perlite aggregate) and a number indicating the percentage of sand replacement. For each mix outlined in Table 2, twelve standard prisms, each measuring 40 mm×40 mm×160 mm in height, width, and length respectively [39], were cast. This resulted in a total of 48 specimens. The prismatic steel molds were mount on a jolting table (drop height of 15 mm) and vibrated in accordance with specifications of SR EN 196–1:2016 [39]. After vibration, there was no bleeding water visible on the surface of the mortar prisms.

The mortar prisms were demolded after 24 hours from casting and

Table 1
Chemical composition of CEM II cement and expanded perlite (expressed in %).

	CaO	SiO_2	Al_2O_3	Fe_2O_3	MgO	SO_3	Na_2O	K_2O	Cl
CEM II	58.49	16.32	4.83	2.24	1.39	2.85	0.34	0.46	0.035
	CaO	**SiO_2**	**Al_2O_3**	**Fe_2O_3**	**MgO**	**SO_3**	**Na_2O+K_2O**		**Cl**
Expanded Perlite	1.3–1.7	74–77	12–15	1.1–1.6	0.1–0.7	-	5.0–8.0		-

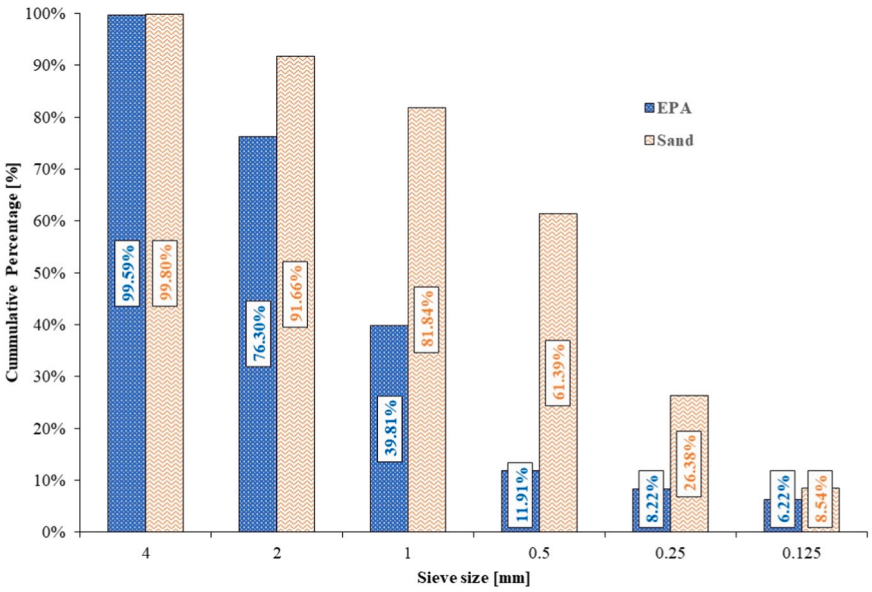

Fig. 2. Sieve analysis of EPA and natural sand.

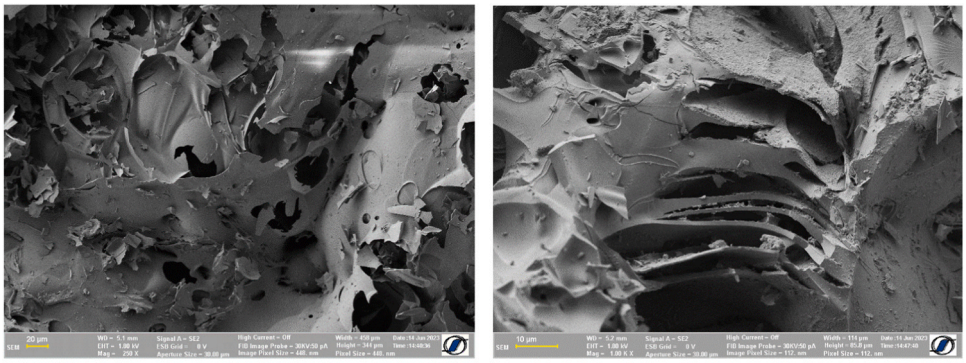

a) porous structure b) flake-like microstructure

Fig. 3. SEM images of expanded perlite.

Table 2
Mix proportions of mortars used in this study.

Mix designation	Cement [kg/m^3]	Sand [kg/m^3]	EPA [kg/m^3]	Water / Cement -
Ref	380	1550	-	0.60
EPA10		1395	7.42	0.65
EPA20		1240	14.85	
EPA30		1085	22.28	

stored in water at 22°C±1°C for 27 days, until the day of testing. Prior to storing the mortar prisms in water, their geometrical dimensions were measured, as presented in Section 2.3.2, to check for compatibility with the dimensions of the steel mold. Additionally, there were no large voids on the surface of the mortar prisms, suggesting that the mortar fully filled the steel mold.

2.3. Methods

2.3.1. Slump test

The slump was assessed using a mini-slump test with a cone of dimensions 100 mm×70 mm×60 mm (bottom diameter × top diameter × height) [40,41]. Once the cone was lifted and the spread of the mortar ceased, the average of three measured diameters was taken into account. In addition, the height reduction was measured relative to the height of the cone.

2.3.2. Dimensions and mass

At the age of 28 days, the mortar prisms were taken out of the water, wiped clean with a thick cloth to remove the excess of water. Afterwards, they were weighed, using a digital scale with an accuracy of 0.01 g, and then measured with the digital caliper, accuracy of 0.01 mm, to check for dimensional stability and also to be able to compute the bulk

density of the obtained mortars. Measurements were recorded for both length (four values) and width/height (six values) of the prisms.

2.3.3. Dynamic moduli of elasticity

The dynamic moduli of elasticity were determined in accordance with ASTM C215:19 specifications [42]. The determination of longitudinal dynamic modulus of elasticity and dynamic shear modulus were based on the first resonant frequencies in longitudinal and transversal directions, respectively, obtained by means of Impact Echo Method (Fig. 4).

The dynamic longitudinal modulus of elasticity was calculated on the basis of Eq. 1 [42]:

$$E_{dyn} = D \cdot M \cdot (n')^2 \quad (1)$$

where: M is the mass of specimen (kg), n' is the fundamental longitudinal frequency of vibration (Hz) and $D = \frac{4 \cdot L}{b \cdot t}$ is a coefficient ($\frac{N \cdot s^2}{kg \cdot m^2}$) that depends on the length L (m) and the cross sectional dimensions b(m) and t (m) of the specimen.

The dynamic shear modulus was calculated using Eq. 2 [42]:

$$G_{dyn} = B \cdot M \cdot (n'')^2 \quad (2)$$

where: M is the mass of specimen (kg), n'' is the fundamental torsional frequency of vibration (Hz) and $B = \frac{4 \cdot L \cdot R}{A}$ is a coefficient ($\frac{N \cdot s^2}{kg \cdot m^2}$) that depends on the length L (m), of the specimen the cross-sectional area A (m^2) and the shape factor R which takes the value of 1.183 for a square cross-section prism [42].

The experimental arrangement depicted in Fig. 4a was used to record the longitudinal free vibration response of all specimens. The signal for each prism consisted of at least 10 impact responses, as exemplified in Fig. 5a for the Ref mix. This signal underwent the Fast Fourier Transform (FFT) analysis, and the frequency spectrum was obtained (Fig. 5b). The fundamental longitudinal frequency was identified by applying a Pseudo-Voigt fitting function on the FFT spectrum (Fig. 5c). The dynamic modulus of elasticity was calculated using Eq. 1.

A similar method was applied to obtain the torsional vibration frequency, employing the set-up outlined in Fig. 4b. Upon obtaining the FFT spectra, two main peaks, closely positioned, were observed, as depicted in Fig. 6a for the Ref mix. Consequently, the fundamental transversal frequency of vibration was also measured, employing the set-up presented in Fig. 4c. This frequency was then neglected in the analysis of the torsional response, which was fitted with the same Pseudo-Voigt function (Fig. 6b). The fundamental torsional frequency was then used to compute the dynamic shear modulus of each prism using Eq. 2.

The dynamic Poisson ratio was computed by means of Eq. 3:

$$\nu_{dyn} = \frac{E_{dyn}}{2G_{dyn}} - 1 \quad (3)$$

where E_{dyn} is the dynamic modulus of elasticity and G_{dyn} is the dynamic shear modulus determined based on Eqs. (1) and (2), respectively.

2.3.4. Temperature

Cement-based materials, such as mortar, concrete and reinforced concrete, may be exposed to severe environmental conditions, including high temperatures. Under extreme circumstances, fire incidents may occur either due to natural disasters or human error. Exposure to high temperatures triggers a series of internal changes in the material that negatively impact its mechanical properties. Previous research indicates that the cement paste is the most vulnerable component or mortar or concrete to high temperatures [43,44]. When exposed to temperatures higher than 900°C the cement paste loses 80 % of its strength [45]. The initial effect is the loss of free and capillary water, with the evaporation process starting at approximately 100ºC. However, given the pore pressure inside the cement-based material, this process takes place within the 100ºC-140ºC temperature range [46]. While the loss of water may lead to shrinkage in the cement paste, its impact on the dimensional stability of elements is generally counteracted by the expansion of non-hydrated products, such as un-hydrated cement grains and calcium hydroxide [47].

The dehydration of ettringite occurs between 80ºC and 150ºC, while the decomposition of gypsum takes place at 150ºC-170ºC. The dehydration process of calcium silicate hydrate (CSH) initiates around 200ºC [48]. Previous studies indicated that cement-based materials do not experience substantial strength reduction when exposed to temperatures up to 300ºC. Any strength loss that occurs is reversible, due to the rehydration process occurring during and after the cooling phase [49].

The selection of temperature values was based on previously mentioned studies on concrete, coupled with the findings of Castellote et al. [50] on cement pastes. Considering the information presented above, the temperature thresholds chosen for this study were 100ºC (marking the onset of evaporation of free and capillary water), 150ºC (indicating the end of free and capillary water evaporation, as well as the dehydration of ettringite) and 200ºC (concluding gypsum decomposition and the beginning of CSH dehydration, but still well below 300ºC). For the purpose of this study, the prisms were placed in an oven, heated to the target temperature, and maintained at that temperature for 4 hours. Once the heating process was terminated, the prisms were allowed to cool gradually to room temperature inside the oven at a cooling rate of 0.5 °C/min. The temperature increase rate was consistent for all specimens, at 6ºC per minute, as shown in Fig. 7.

After being exposed to elevated temperature, the specimens were measured to check for any changes in the geometrical dimensions and weighted to account for the mass loss due to evaporation processes. The dynamic elastic properties were determined following the procedure outlined in Section 2.3.3.

2.3.5. Flexural-tensile strength and compressive strength

The flexural tensile strength and compressive strength of all mortar prisms were assessed in compliance with SR EN 196–1:2016 [39]. Three-point bending test, with a loading rate of 50 N/s, was used to determine the flexural tensile strength. The resulting broken parts of the prism were examined for signs of visible cracks and then subjected to uniaxial compression test with a loading rate of 2400 N/s.

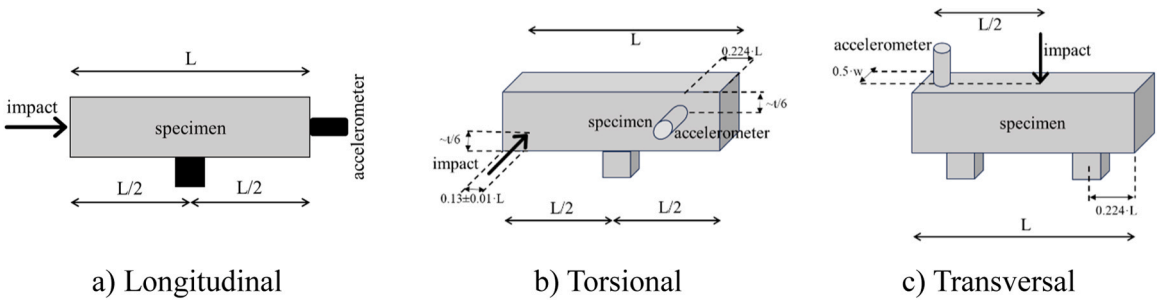

Fig. 4. Set-up for determination of fundamental frequency of vibration [42].

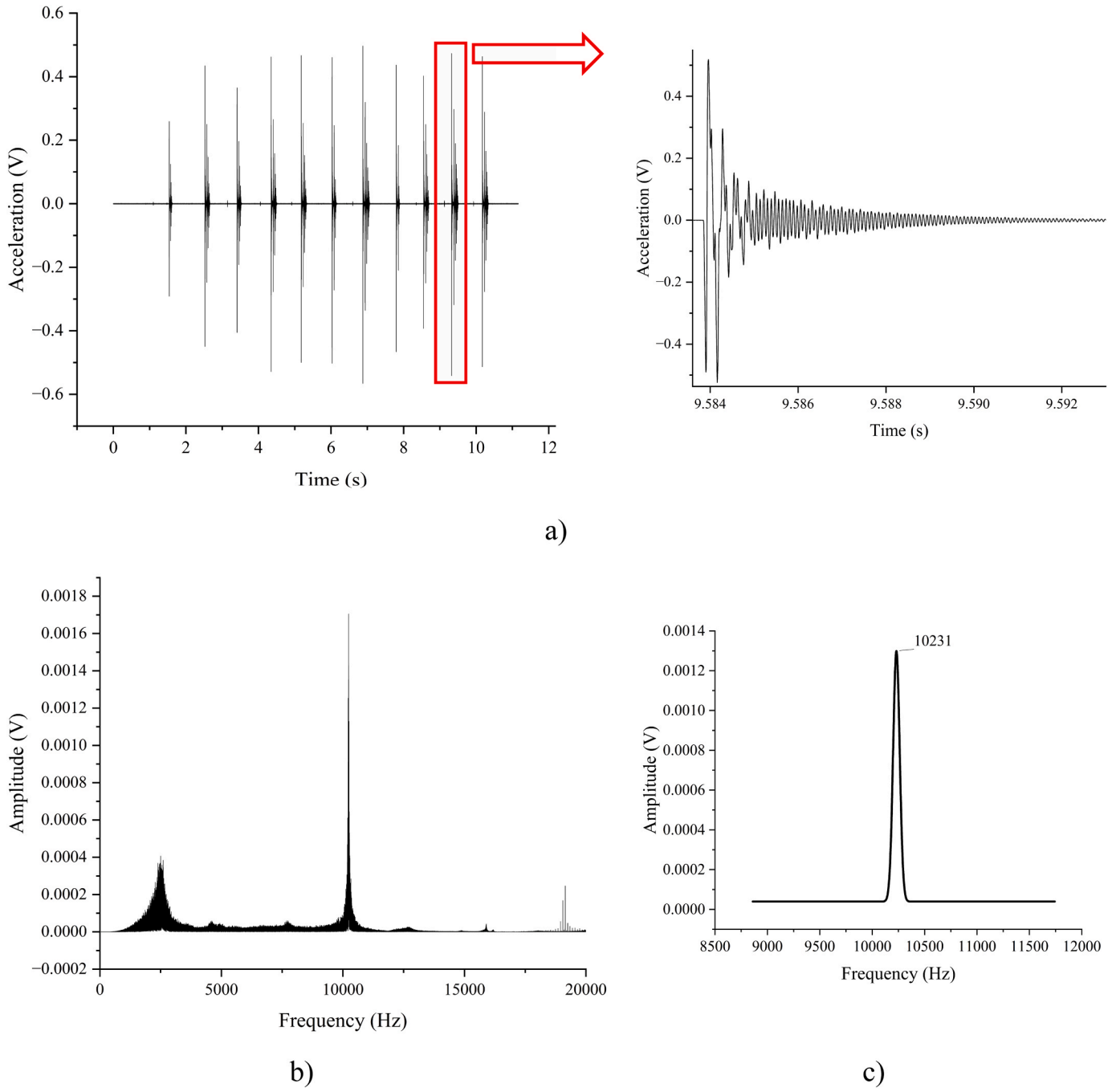

Fig. 5. Procedure for the determination of the fundamental longitudinal frequency of vibration of a prism belonging to the Ref mix: a) Free vibration response (longitudinal impact), b) Overlapped FFT spectra for a single prism, c)Fitting result of the FFT analysis of a longitudinal impact response.

The final values of the flexural strength for the mixes presented in Table 2 were obtained by averaging three measurements for each set of prisms, categorized according to the temperature they were previously exposed to (room temperature, 100ºC, 150ºC and 200ºC). Similarly, the final values of the compressive strength were calculated by averaging six measurements for each set of prisms.

3. Results and discussions

3.1. Effect of EPA

3.1.1. Mortar slump

Workability and consequently, the slump, are influenced by the water content of the mix. A high water/cement ratio results in more workable mortar/concrete but it leads to increased chance of segregation, during casting and vibration, and a decrease in the values of mechanical properties. On the other hand, a stiff mix, results in poor compaction, leading also to a decrease in strength [51].

The results obtained from the mini slump cone [52,53] are summarized in Table 3. The replacement of natural sand by EPA did not result in significant changes of the cone base diameter. The EPA10 mix showed identical behavior with the Ref mix, the same base diameter of the mini cone and the same slump, even though the water/cement ratio was increased. However, increasing the replacement percentage to 20 % and 30 % resulted in higher values of the slump even for marginal changes of the base diameter and without visible swelling of the mortar cone.

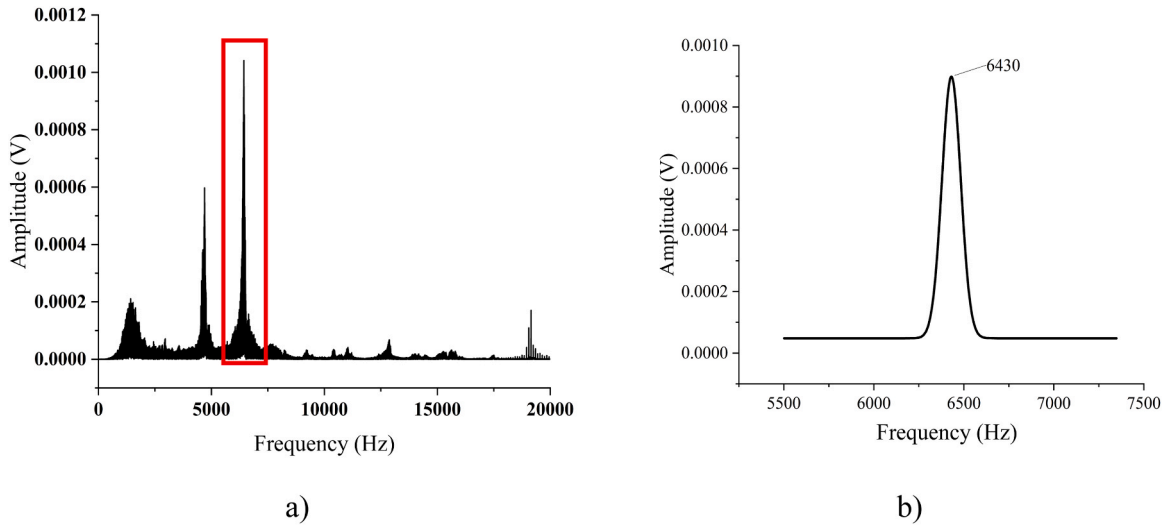

Fig. 6. Determination of the fundamental torsional frequency of vibration of a prism belonging to the Ref mix: a) Overlapped FFT spectra for a single prism, b) Fitting result of a FFT of the torsional impact response.

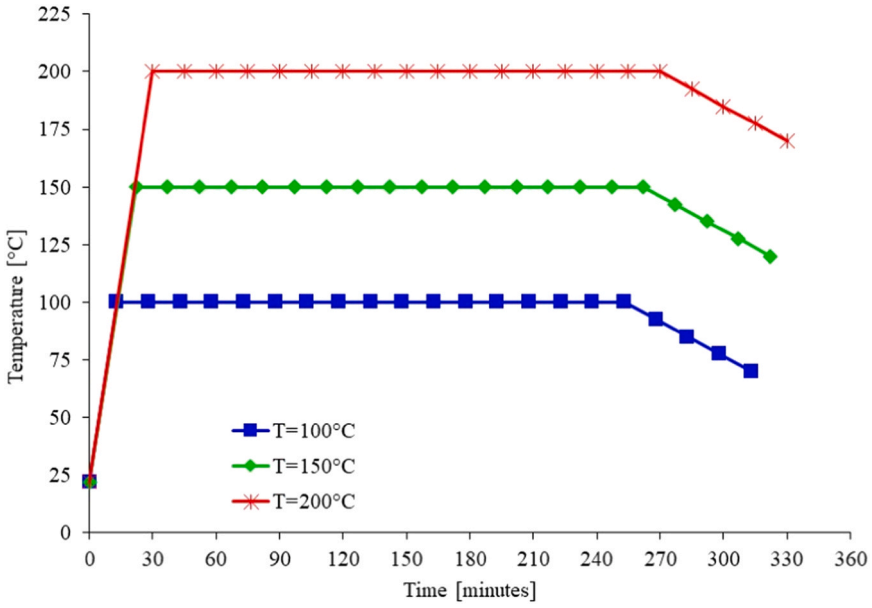

Fig. 7. Temperature-time history.

Table 3
Properties of fresh mortar.

Mix	Ref	EPA10	EPA20	EPA30
	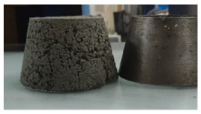	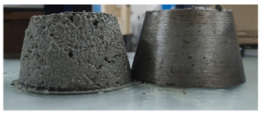	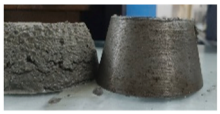	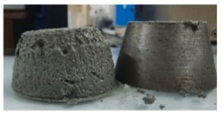
Diameter at the base [mm]	100	100	102	103
Slump [mm]	1	1	13	15

All mixes exhibited similar workability as perceived during casting the specimens. A similar approach of increasing the water/cement ratio to obtain similar workability was previously reported [54], although additives were also used, in fixed percentages for all considered mixes, to adjust the water retentivity of EPA.

3.1.2. Bulk density

The variation of density with the replacement percentage of natural sand by EPA, at the age of 28 days, is presented in Fig. 8.

A decrease in density can be observed with the increase of the replacement percentage. Compared to the reference mix, the EPA30 mix exhibited a 7.73 % reduction in density. The substitution of natural sand

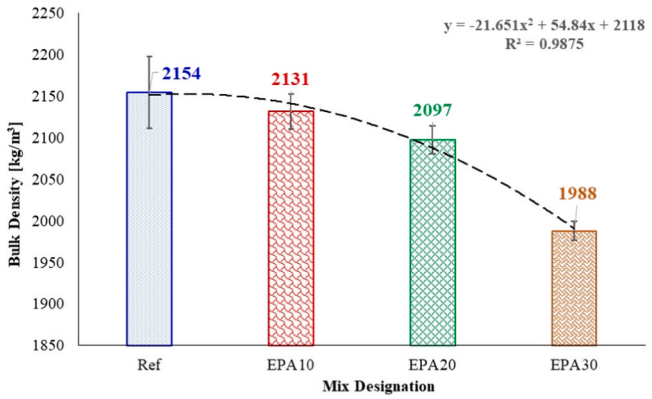

Fig. 8. Variation of density with EPA content.

with EPA led to a 1.06 % and 2.65 % decrease in density values for the EPA10 and EPA20 mixes, respectively. This downward trend appears to follow a quadratic equation, as depicted in Fig. 8.

Similar trends were reported in the scientific literature either in the case of using perlite as cement substitution in mortar [55–57] or as aggregates in lightweight concrete [26].

3.1.3. *Dynamic elastic properties*

The graphs in Fig. 9 illustrate the distribution of dynamic modulus of elasticity values, relative to the median, for all 12 prisms of each mix show in Table 2. It can be observed that Ref, EPA10 and EPA20 mixes exhibit a good distribution of the values, falling within one standard deviation from the median. In contrast, the EPA30 mix displays scattered results, with some values lying outside the standard deviation interval. These values were excluded from computing the dynamic elasticity modulus median value. The dispersion could be the result of the higher replacement percentage, considering the high porosity of EPA

The distribution of the values of the dynamic shear modulus, with respect to the median, is presented in Fig. 10 for all 12 prisms of each mix shown in Table 2. It can be observed that all mixes exhibit good distribution of the values of the modulus of elasticity, within one standard deviation from the median.

The influence of sand replacement by EPA on the dynamic elastic

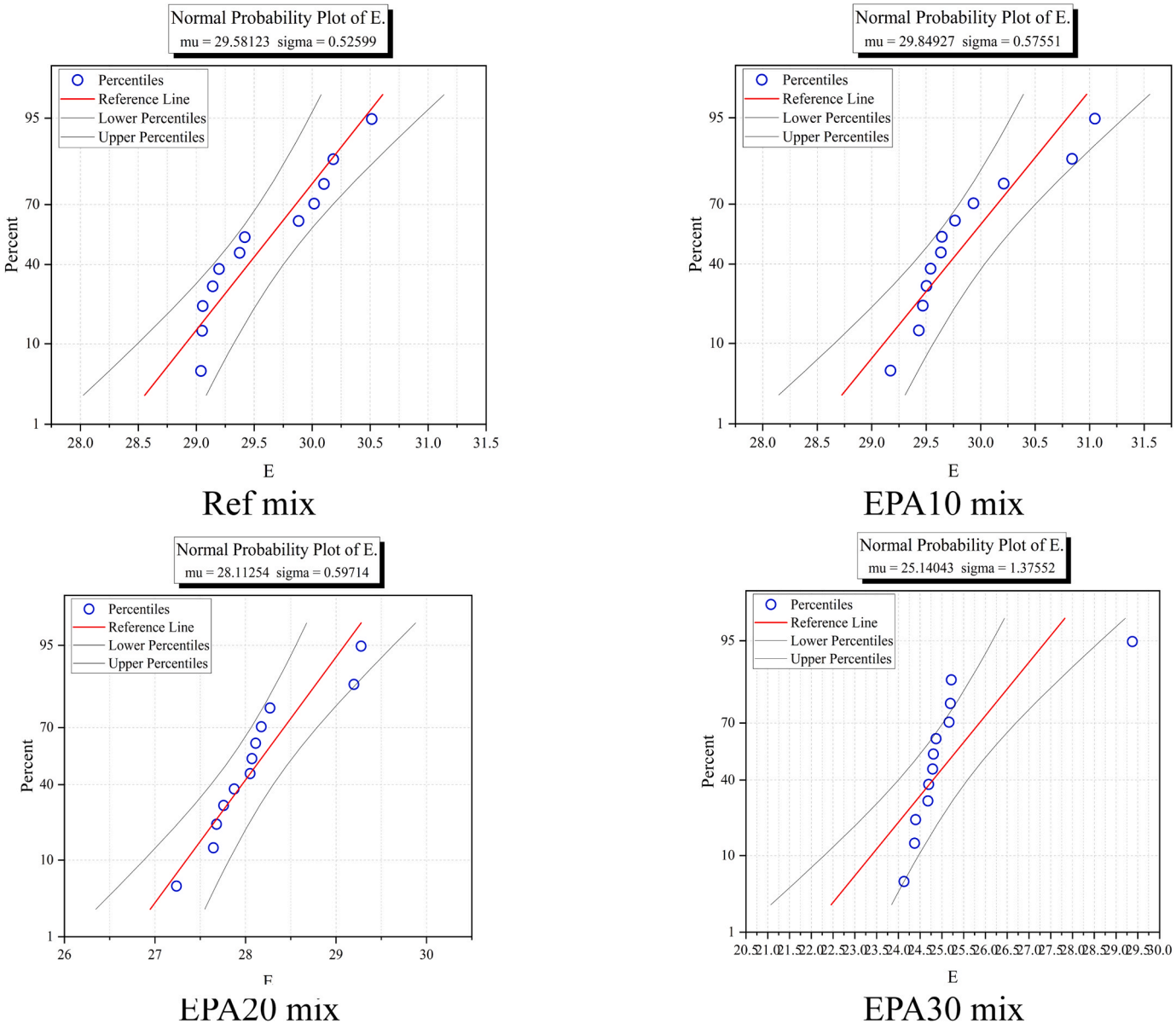

Fig. 9. Distribution of dynamic modulus of elasticity values with respect to the median.

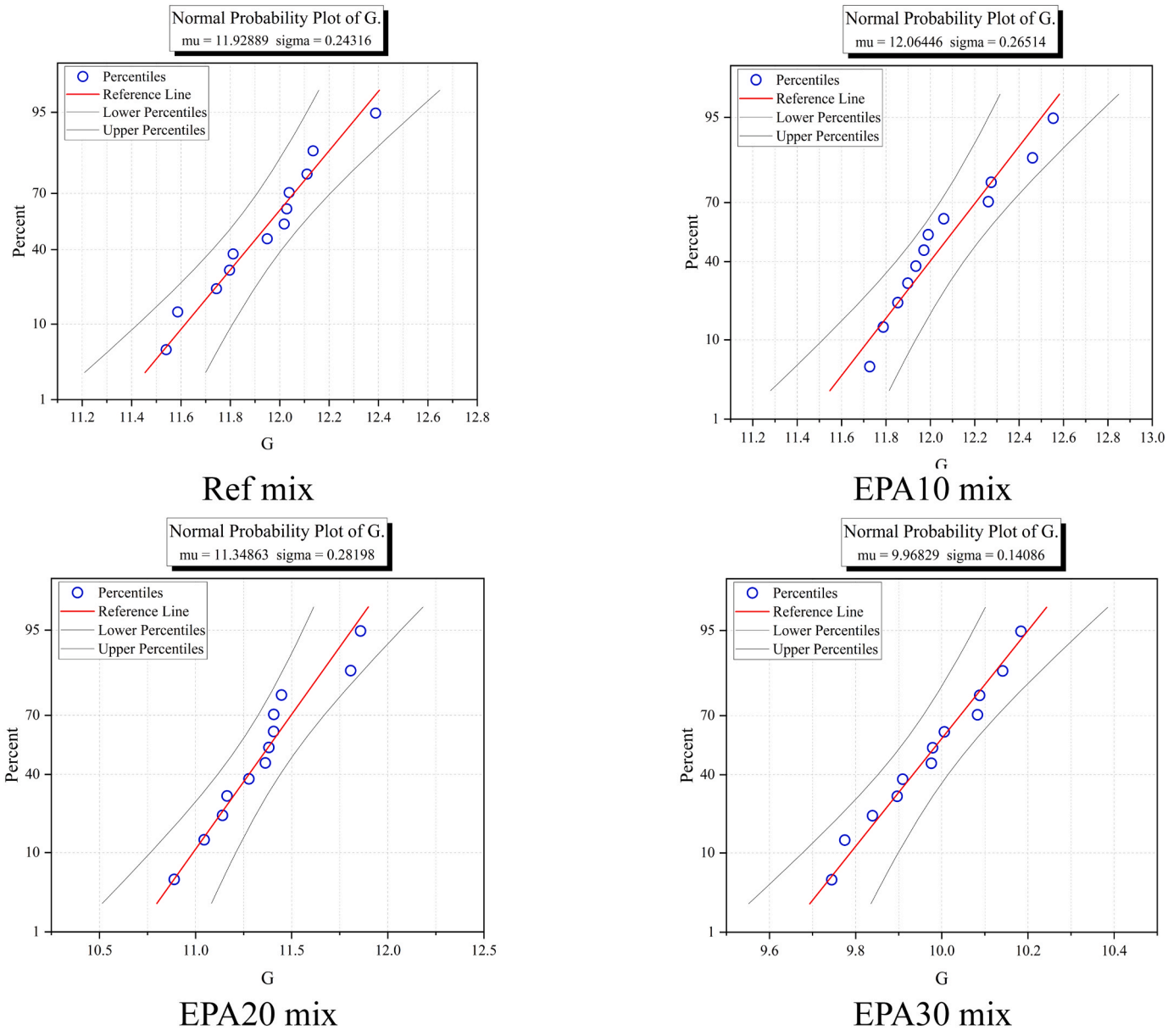

Fig. 10. Distribution of dynamic shear modulus values with respect to the median.

properties of mortar is presented in Fig. 11.

Taking into account Eqs. (1) and (2) for the calculation of the two dynamic elastic moduli, the observed trend in Fig. 11 is consistent with the data presented in Fig. 8. Since the bulk density of the mix did not change significantly, Fig. 8, and D and B coefficients from Eq. (1) and Eq. (2), respectively, are based on the geometrical dimensions of the samples, it follows that the values of the fundamental frequency of vibration for all specimens could be similar to one another. Although sand was replaced by EPA, the mass was also similar among the mixes, with small variations and showing a slight decreasing trend with increasing replacement percentage. This could be attributed to the fact that all prisms were stored in water. The data is summarized in Table 4, as average of 12 values corresponding to the 12 prisms for each mix.

The values of longitudinal (Edyn) and shear (Gdyn) dynamic moduli increased slightly when replacing 10 % of sand by EPA. For higher substitution amounts, the values for these parameters are decreasing. Nevertheless, it can be observed that the Poisson's ratio is directly proportional with the perlite quantity. This implies that Young's modulus is less affected than shear modulus, especially for over 20 % replacement percentages, suggesting a decrease in the transversal deformability

3.1.4. *Flexural tensile strength*

The substitution of natural sand with EPA led to a significant reduction, ranging between 40 % and 51 %, in the flexural tensile strength values. Three prisms from each mix were tested following the procedure presented in Section 2.3.5. The results of the tests are presented in Fig. 12. Similar decreasing trends have been reported in previous research [58] although, in most cases, this was observed in specimens where perlite powder replaced Portland cement rather than sand [55,59].

3.1.5. *Compressive strength*

The decrease in compressive strength values was less pronounced compared to flexural strength when natural sand was replaced by EPA. The reduction ranges from 18.33 % for EPA10 to 30.71 % for EPA30, as shown in Fig. 13. Three prisms from each mix were tested, following the procedure presented in Section 2.3.5. Similar behavior regarding

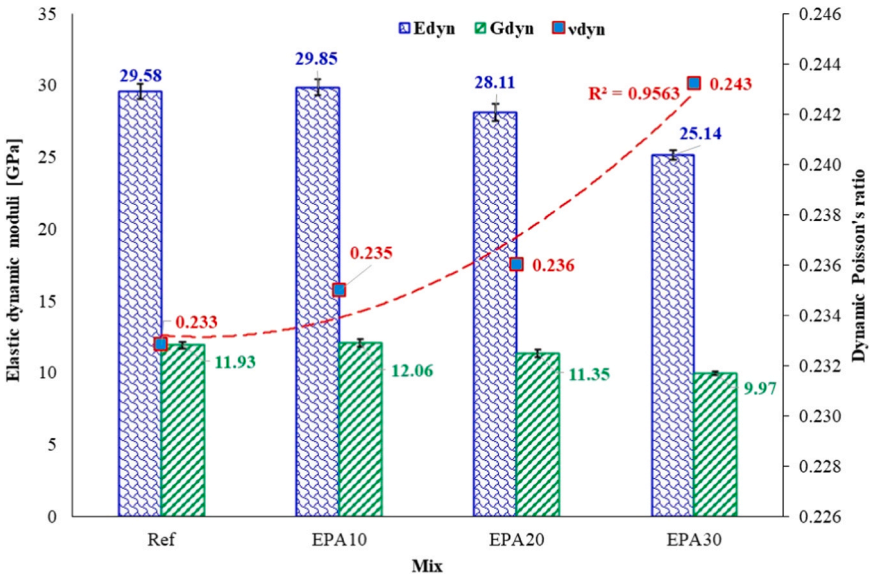

Fig. 11. Influence of EPA replacement percentage on the dynamic elastic properties of mortar.

Table 4
Dynamic characteristics of considered mixes (average values of 12 data sets).

Mix	Mass [kg]	n' (Eq. 1) [Hz]	E_{dyn} (Eq. 1) [GPa]	n'' (Eq. 2) [Hz]	G_{dyn} (Eq. 2) [GPa]	ν_{dyn} (Eq. 3) -
Ref	0.568	11523	**29.58**	6728	**11.93**	**0.233**
EPA10	0.561	11684	**29.85**	6829	**12.06**	**0.235**
EPA20	0.543	11440	**28.11**	6682	**11.35**	**0.236**
EPA30	0.532	11102	**25.14**	6429	**9.97**	**0.243**

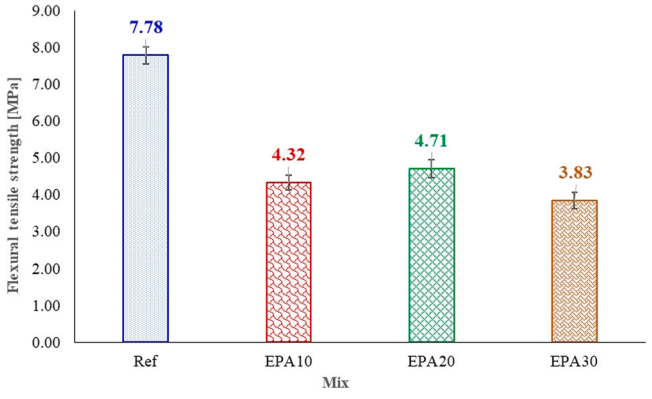

Fig. 12. Influence of EPA replacement percentage on the flexural tensile strength of mortar.

compressive strength was reported previously [58] but mostly for specimens with perlite powder replacing Portland cement instead of sand [55,59].

From the analysis of the obtained data, in terms of average values, an equation linking the dynamic longitudinal modulus of elasticity (E_{dyn}) and the compressive strength (f_c) of mortar with EPA aggregates was proposed, as shown in Eq. (4).

$$f_c = 9.08e^{-4} \cdot E_{dyn} \quad (4)$$

where both the compressive strength and the dynamic longitudinal modulus of elasticity are expressed in MPa. The accuracy of the proposed formula is checked against the experimental obtained values for the compressive strength of mortar mixes. The obtained results are

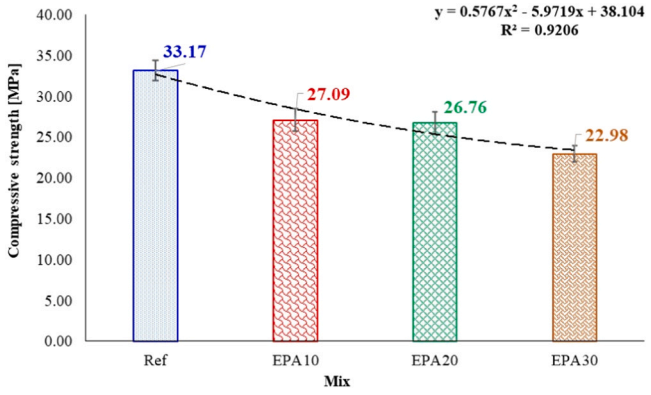

Fig. 13. Influence of EPA replacement percentage on the compressive strength of mortar.

shown in Fig. 14, in terms of average values, and in Fig. 15 in terms of individual values obtained on mortar prisms for each mix containing EPA.

From Fig. 14 it can be observed that there is a very good correlation between the values of the compressive strength given by the proposed

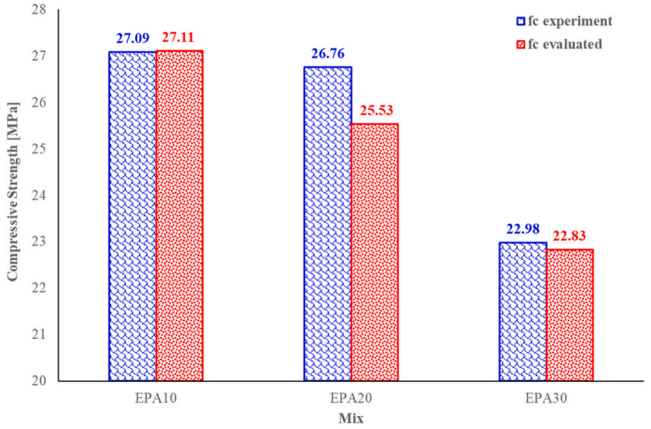

Fig. 14. Analytical vs. experimental results for the compressive strength of mortar mixes (average values).

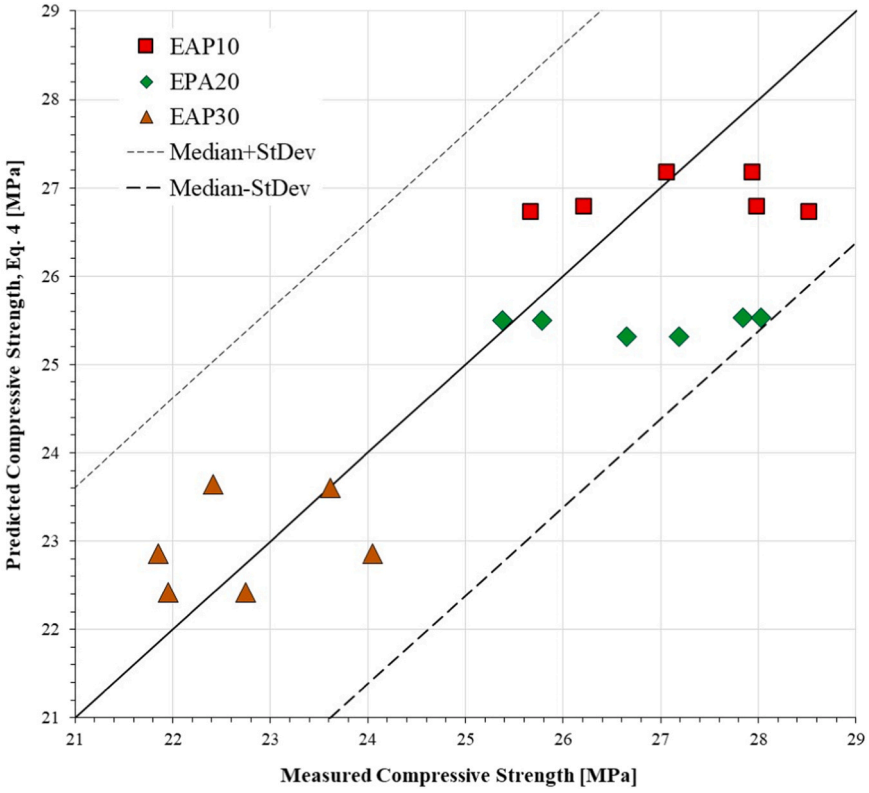

Fig. 15. Distribution of predicted/measured compressive strength values with respect to the median.

formula and the experimentally obtained data. The largest difference was obtained for EPA20 mix, 4.59 %. All other values where less than 1 % apart from the laboratory test values. The data shown in Fig. 15, obtained for individual prisms of each mix, shows that the results obtained from Eq. (4) fall within ±1 standard deviation from the median. There is an underestimation tendency of the experimental results for 20 % and 30 % replacement rates whereas for 10 % EPA content using Eq. (4) leads to slightly overestimated results.

Surveying of the scientific literature revealed no other studies that present both dynamic elastic properties and compressive strength of mortars with EPA, thus the proposed equation could not be validated against other data sets. It is important to note that, upon further validation, the significance of the proposed equation lies in its ability to directly and accurately determine the compressive strength of mortar with EPA once the dynamic modulus of elasticity is known. This could potentially eliminate the need for destructive tests.

The proposed equation has limitations, since it was derived for a specific cement/sand volumetric ratio, a water/cement ratio and a certain cement type. Further investigations are necessary in order to improve this equation, as reported by similar studies investigating the properties of cement-lime laying mortar [60].

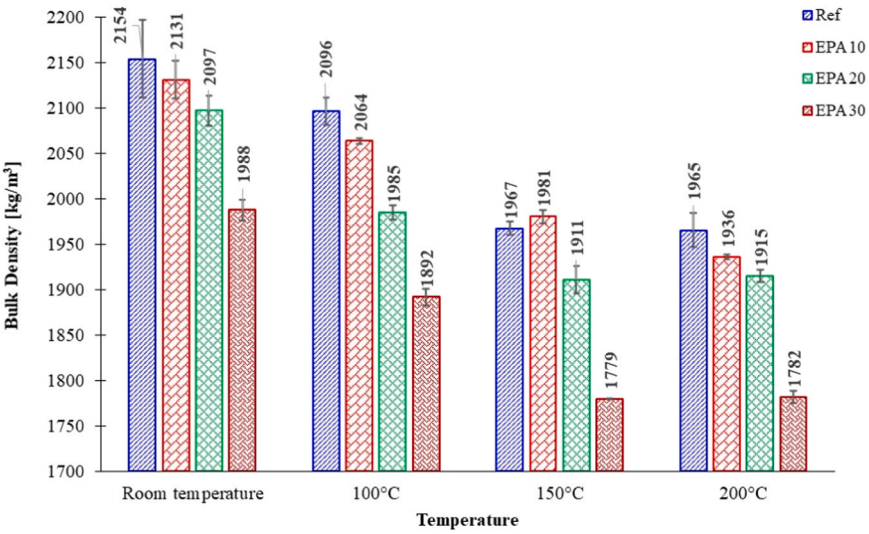

Fig. 16. Influence of temperature on the bulk density of considered mortar mixes.

3.2. Effect of temperature

As outlined in Section 2.3.4, the prismatic specimens were heated up to temperatures of 100ºC, 150ºC and 200ºC at a rate of 6ºC per minute. Subsequently, they were kept for 4 hours and then gradually cooled down back to room temperature. Specimens were analyzed in terms of density, dynamic moduli, and flexural and compressive strength.

3.2.1. Bulk density

After the thermal treatment, specimens were measured again to check for dimensional stability and weighed to account for changes in mass due to water loss. Bulk density values are presented in Fig. 16.

It can be observed that exposure to higher temperatures resulted in lower values for bulk density. Reference, EPA20 and EPA30 mixes appear to stabilize at 150ºC, since exposure at 200ºC does not have a notable impact on density values. EPA10 mix displays an almost linear decrease for density with the increase in temperature.

Fig. 17 illustrates the mass loss resulting from the evaporation process for each mortar mix under consideration. At 100ºC, all EPA mixes exhibited a lower mass loss (4.35 %-4.56 %) compared to the reference (5.25 %). When specimens were exposed to 150ºC, both EPA20 and EPA30 mix showed a higher mass loss than Ref by 0.85 % and 1.56 %, respectively. The EPA10 mix registered the lowest mass loss at this temperature. At 200ºC, the reference mix, EPA10 and EPA20 exhibited nearly identical mass loss values (8.77 %, 9.10 % and 9.20 %). In contrast, EPA30 experienced the highest mass loss of 10.93 %.

The variation of mass loss with temperature can be divided into two intervals: from room temperature to 150ºC, and from 150ºC to 200ºC. In the first range of temperatures, Ref and EPA10 mixes exhibit similar trends, with a steeper slope up to 100ºC, followed by a reduced rate between 100ºC and 150ºC. On the other hand, EPA20 and EPA30 mixes demonstrated a higher rate of mass loss from 100ºC to 150ºC. This phenomenon could be attributed to the increased porosity of specimens with higher percentages of EPA.

Within the temperature range of 150ºC to 200ºC, Ref, EPA20 and EPA30 showed little mass loss variation. This observation is supported by bulk density values depicted in Fig. 16. EPA10 exhibited an almost identical slope to the previous interval.

The observed trends can be explained by considering the internal structure of mortar. EPA are highly porous, as depicted in Fig. 3. Their use in mortar is expected to result in the formation of internal pores that are either closed or open. During heating, capillary water and water from open pores evaporates, accounting for most of the overall mass loss. It was previously reported that ettringite undergoes thermal decomposition at 90ºC, while CSH begins dehydrating between 200ºC and 450ºC, corroborating earlier findings [47]. Additionally, excessive shrinkage of the cement paste was reported at temperatures higher than 200°C with detrimental effects in terms of strength and durability [48]. While ettringite dehydrates between 80ºC and 150ºC, gypsum decomposes at 150ºC-170ºC and CSH starts to dehydrate at 200ºC [48]. Partially saturated internal, sealed pores, resulted from water consumption during the hydration of cement grains, allow the remaining water to transform into vapors. Simultaneously, they provide enough space to prevent vapor pressure from damaging the mortar matrix. A similar phenomenon was reported in earlier research works on EPP (expanded perlite powder) used to suppress the alkali-silica reaction in cement mortar [61,62].

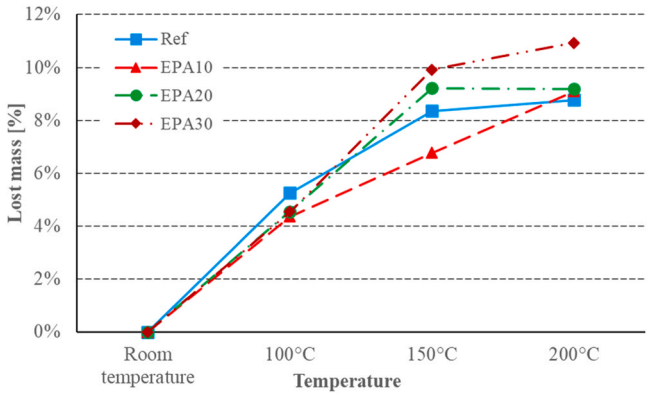

Fig. 17. Lost mass of mortar prisms as function of temperature.

3.2.2. Dynamic elastic properties

Upon cooling to room temperature, the prisms were used to determine dynamic moduli, as outlined in Section 2.3.3. For each considered temperature, 3 specimens were tested, resulting in a total of 30 data sets per mix for the computation of the dynamic modulus of elasticity and the dynamic shear modulus. Results are presented in Fig. 18.

It can be observed that as the temperature increases, the values for the dynamic moduli decrease. Similar to results at room temperature, EPA10 exhibited higher dynamic elasticity modulus compared to Ref, showing improvements of 5.6 %, 5.48 % and 3.85 % at 100ºC, 150ºC and 200ºC, respectively. The dynamic shear modulus of EPA10 showed the highest improvement, with respect to Ref, at 150ºC (6.05 %). Improvements in both moduli, compared to Ref, can be seen only for EPA20 at 150ºC, but they are half the ones observed for the EPA10 mix. Compared to the reference, the EPA30 mix showed consistently lower values, for both E and G, by as much as 14 %.

Values for both moduli decrease almost linearly with temperature for all mixes, as it can be seen in Fig. 19. For both E and G, the temperature of 100ºC represents a threshold corresponding to the most significant decrease. At this temperature, values are reduced for all mixes with percentages between 18.71 % for EPA10 and 20.86 % for Ref. Another important observation is that the EPA20 mix is the least affected by exposure at 150ºC in comparison to 100ºC.

Considering the pozzolanic nature of expanded perlite, if can be inferred that smaller pores were present in mortars with EPA [14,44]. Also, given the porous nature of EPA, modified mortars are expected to exhibit a higher total porosity compared to Ref. Nevertheless, considering bulk density values and the observed temperature effects, pore size and quantity would represent a reasonable underlying mechanism. While using 10 % EPA has a beneficial effect on elastic properties, higher percentages prove detrimental, possibly due to the availability of calcium hydroxide (CH) in the cementitious matrix [63].

3.2.3. Flexural tensile strength

The impact of temperature exposure on the flexural tensile strength of all mortar mixes is shown in Fig. 20. It can be observed that all EPA mixes exhibit lower values than Ref, at both room temperature and 100ºC. Conversely, at higher temperatures all EPA mortars show higher tensile strengths, compared to both the reference mix and to lower treatment temperature values.

At the same time, it can be seen that while the flexural tensile strength of the Ref mix exhibits a decreasing trend with the increase in temperature, EPA mixes showed an opposite behavior. All recorded values of the flexural tensile strength at 100ºC, 150ºC and 200ºC were higher than the value obtained at room temperature. EPA10 and EPA20 mixes registered a peak increase at 150ºC while the value for the EPA30 mix continuously increased with the increase in the exposure temperature, although only a 3.5 % increase was observed from 150ºC to 200ºC.

Tensile strength values of EPA mortars at all temperatures, normalized to the Ref value at each temperature, are presented in Fig. 21. The EPA10 can be seen to exhibit a steeper increase compared to the other two mixes. Comparing Fig. 20 and Fig. 21, it can be inferred that EPA20 and EPA30 display similar trends in both absolute and normalized values. On the other hand, normalized values of EPA10 are seen to continuously increase, suggesting that flexural strength is more affected for Ref than for EPA10, when increasing the temperature from 150ºC to 200ºC.

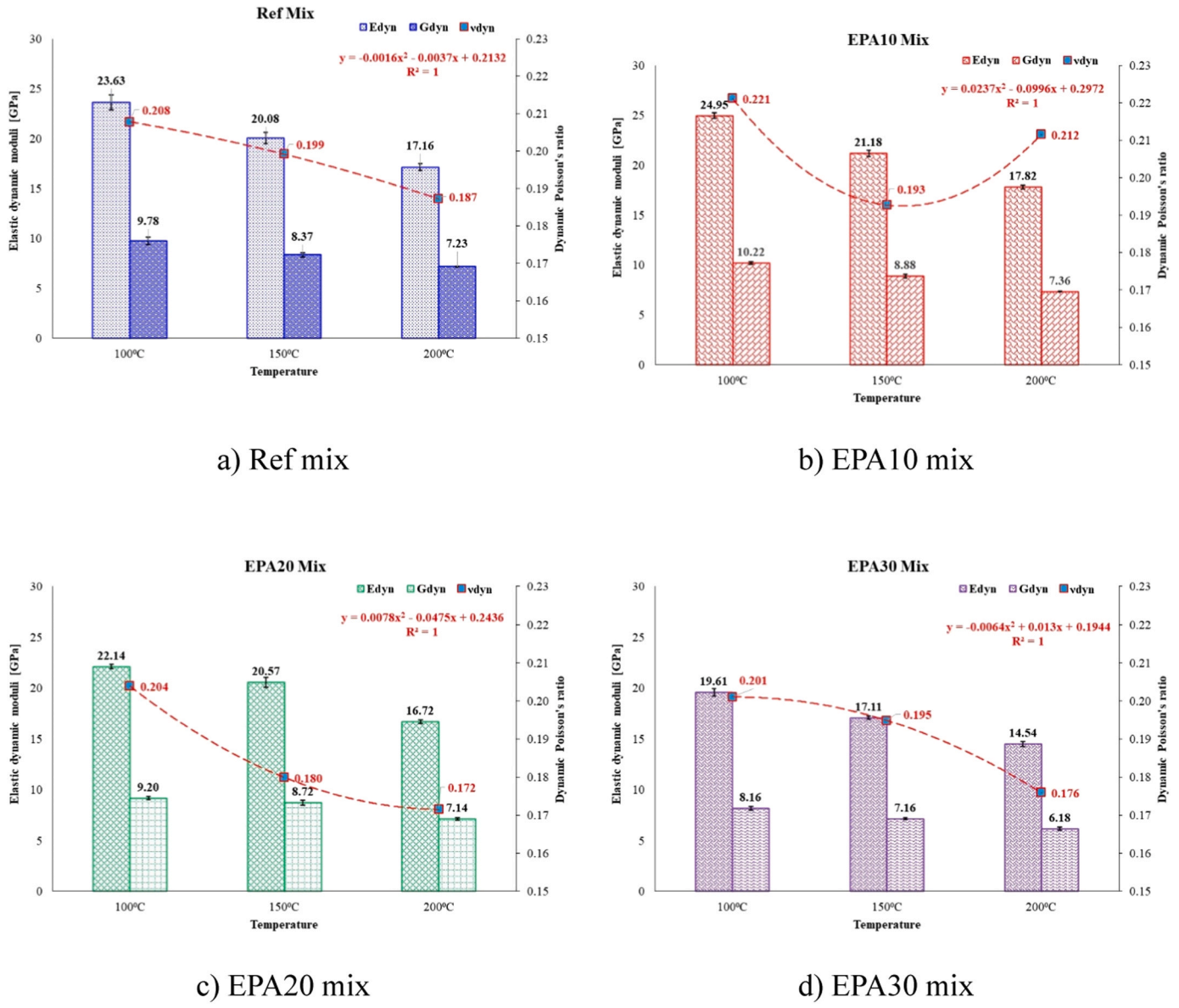

Fig. 18. Temperature influence on the dynamic elastic properties of mortars.

A possible explanation of the obtained results may reside in the pozzolanic nature of expanded perlite aggregates. Recent studies confirmed that, due to pozzolanic activity, the larger pores in the cement matrix are transformed into smaller pores because of the hydration products [44,64,65]. At the same time, no deteriorations in the cementitious matrix were reported for temperatures up to 400ºC [44]. However, pozzolanic reaction needs time and requires a higher activation energy than the case of using Portland cement alone. This accounts for the lower early age mechanical properties in cement-based materials with various pozzolans. One method to accelerate the rate of pozzolanic activity is to increase the curing temperature. However, this approach was reported to influence the degree of crystallinity of the resulting CSH [63]. On the other hand, when subjecting cement-based mortar to elevated temperature, lower mass losses were reported for mixes with calcined perlite [66]. This implies that the presence of expanded perlite positively influences the behavior of mortar at elevated temperatures.

3.2.4. *Compressive strength*

The effect of exposure temperature on compressive strength for all mortar mixes is presented in Fig. 22. An increase in temperature resulted in decreasing values of the Ref compressive strength, with a steep decrease of 19.35 % at 100ºC, and additional reductions of 4 % for 150ºC and 200ºC. The compressive strength values of EPA10 and EPA20 mixes decreased when exposed to 100ºC. However, at 150ºC and 200ºC, both mixes showed higher values compared to both the Ref mix at the same temperature and to their room temperature values. This suggests that a lower content of EPA led to an improved internal structure, potentially related to lower porosity. Additionally, subjecting the EPA specimens to higher temperatures and subsequent cooling to room temperature may have promoted an acceleration of the pozzolanic reaction [44,63–66] and the rehydration of cement grains [49].

The substitution of natural sand by EPA resulted in higher normalized values of the compressive strength with respect to the Ref mix, Fig. 23, compared to the flexural strength, Fig. 21. At the same time, the compressive strength gains when subjected to elevated temperature are lower than in the case of flexural strength for all EPA mixes. This may be attributed to a different CSH crystallinity, due to the promotion of pozzolanic reaction at elevated temperatures, that had a more significant influence on the values of the compressive strength. Similar trends as the ones shown in Figs. 21 and 23 were previously reported [67],

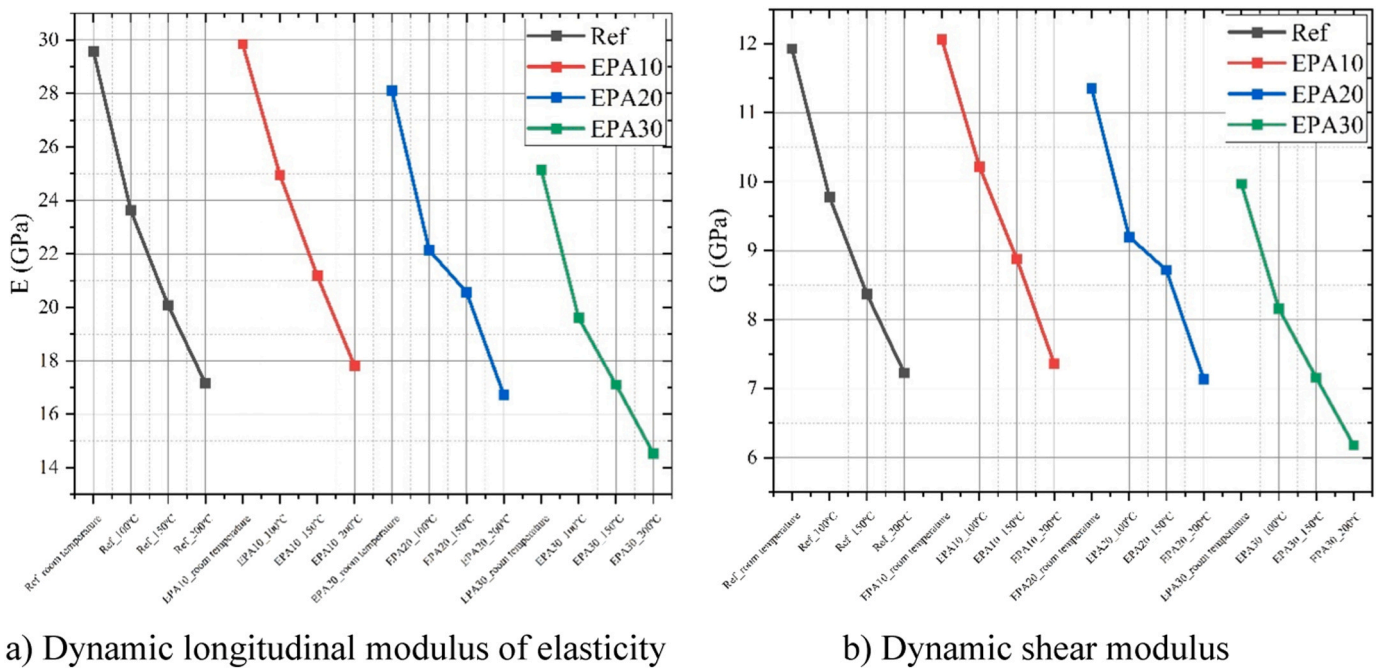

Fig. 19. Decreasing trends of the two dynamic moduli as function of temperature.

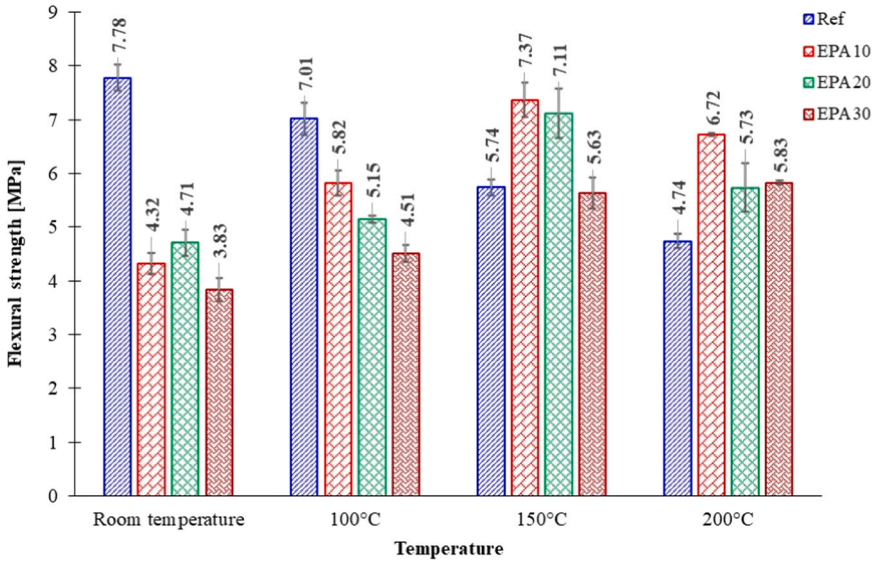

Fig. 20. Influence of temperature on the flexural tensile strength values.

although for higher temperatures and higher replacement percentages [68].

4. Conclusions

The present paper aims at bringing its contribution to narrowing the knowledge gap on the use of EPA in cement-based mortar, both at room and at temperatures up to 200°C. Previous studies reported improvements in the mechanical properties of concrete containing powder perlite for temperatures up to 300°C. Therefore, the parameters considered in this research were: the replacement percentage (10 %, 20 % and 30 % by volume) of natural sand by EPA with a maximum grain size of 4 mm and the temperature treatment of mortar prisms at the age of 28 days. The selected temperatures were 100°C, 150°C and 200°C. The influence of both parameters on the flexural and compressive strength of mortar as well as dynamic elastic properties were experimentally determined. Based on the results presented in the paper, the following conclusions can be drawn:

1. Substituting sand by expanded perlite aggregates, by volume, results in a decrease in the values of density, flexural strength and compressive strength at the age of 28 days. The higher the substitution percentage, the higher the decrease.
2. When substitution percentage of sand by EPA is 10 % or 20 %, very little influence is observed from the point of view of dynamic longitudinal modulus of elasticity and shear modulus of prismatic specimens.
3. An empirical equation is proposed to obtain the compressive strength of mortar with EPA aggregates when the dynamic longitudinal modulus of elasticity (E_{dyn}) is known. The proposed equation shows

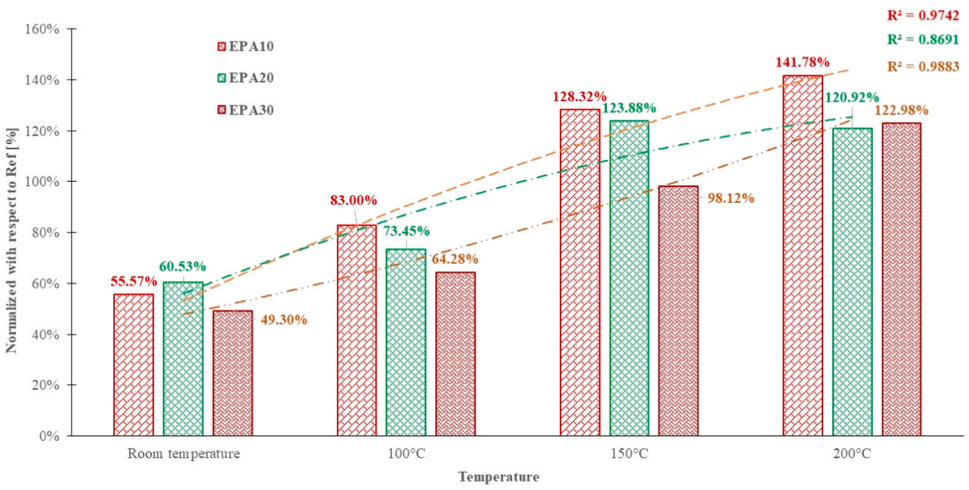

Fig. 21. Flexural tensile strength of EPA mixes normalized with respect to the Ref mix.

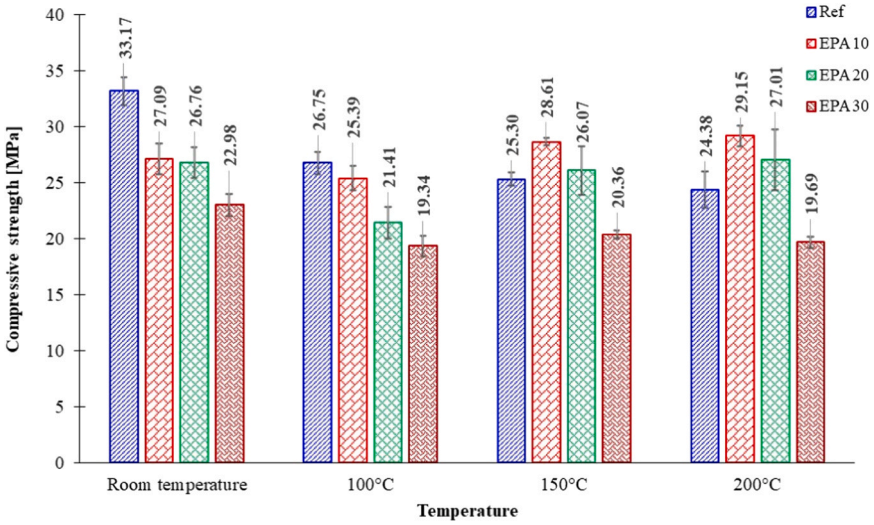

Fig. 22. Influence of temperature on the compressive strength values.

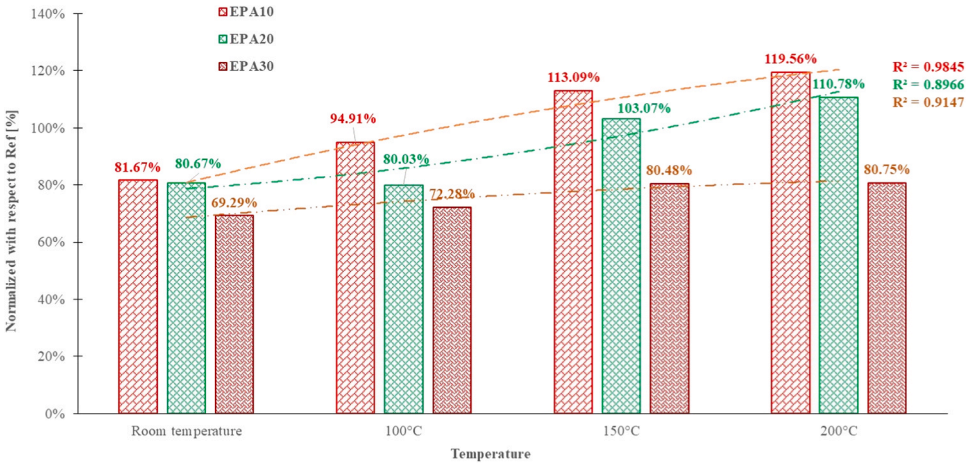

Fig. 23. Compressive strength of EPA mixes normalized with respect to the Ref mix.

good accuracy of the predicted values when compared to experimental data. While further validation is necessary, the scientific literature currently lacks reports on these parameters for cement mortar with EPA.

4. Exposing the specimens to temperatures of 100ºC, 150ºC and 200ºC results in a decrease in the values of bulk density due, mostly, to the evaporation process of capillary water. Expanded perlite mortar mixes exhibit a more pronounced density reduction due to the porous nature of these aggregates.
5. Similar decreasing trends are reported for the values of dynamic moduli of all considered mortar mixes. However, for EPA10 and EPA20 mixes, higher values are reported compared to the Ref mix, without expanded perlite aggregates. This can be attributed to smaller internal pores dimensions. However, further research is necessary to confirm this hypothesis by either computed tomography (CT) or mercury intrusion porosimetry (MIP).
6. While the flexural tensile strength of Ref mix decreased with the increase in temperature, all EPA mixes show higher values after being subjected to selected temperatures compared to the one obtained at room temperature. The highest values are obtained for the EPA10 and EPA20 mixes at 150ºC. The obtained values are also higher than the one obtained for the Ref mix at the considered temperature
7. A similar conclusion can be drawn from the point of view of the compressive strength of mortar mixes. The highest values are obtained for EPA10 and EPA20 mixes at 200ºC, although the increase is only marginal. At both 150ºC and 200ºC the compressive strength of EPA10 and EPA20 mixes are higher than the Ref mix.
8. When taking into account both the temperature and the replacement percentage of natural sand by EPA, the optimum combinations are obtained for 10 % and 20 % replacement percentages at temperatures between 100ºC and 150ºC for the dynamic moduli of elasticity. The same replacement percentages result in improved flexural and compressive strength values at 150ºC. Higher replacement percentages, e.g. 30 % as considered in this research, results in consistently lower values for the investigated parameters, with the exception of flexural strength, at both room and temperatures up to 200°C.

CRediT authorship contribution statement

Ana-Maria Toma: Writing – original draft, Validation, Methodology, Conceptualization. **Ioana Olteanu:** Writing – original draft, Methodology, Investigation, Formal analysis. **George Taranu:** Writing – review & editing, Methodology, Investigation, Formal analysis. **Ionut-Ovidiu Toma:** Writing – original draft, Supervision, Resources, Project administration, Methodology, Investigation, Funding acquisition, Formal analysis, Data curation, Conceptualization. **Cristian Pastia:** Writing – review & editing, Methodology, Investigation, Formal analysis. **Georgiana Bunea:** Writing – review & editing, Visualization, Methodology, Investigation, Formal analysis. **Sergiu-Mihai Alexa-Stratulat:** Writing – original draft, Validation, Supervision, Software, Methodology, Investigation, Formal analysis, Data curation.

Declaration of Competing Interest

The authors declare that they have no known competing financial interests or personal relationships that could have appeared to influence the work reported in this paper.

Data availability

Data will be made available on request.

Acknowledgment

The research presented in this paper was conducted as part of the PN-III-P2–2.1-PED-2021-0677 research grant “Sustainable Concrete for Energy Efficient Buildings” funded by Executive Agency for Higher Education, Research, Development and Innovation Funding – UEFISCDI.

References

[1] GCCAssociation, Cement and Concrete Around the World, Glob. Cem. Concr. Assoc. (2020). https://gccassociation.org/concretefuture/cement-concrete-around-the-world/.
[2] P.M. Borges, J.Z. Schiavon, S.R. da Silva, E. Rigo, A. Neves Junior, E. Possan, J.J. de O. Andrade, Mortars with recycled aggregate of construction and demolition waste: mechanical properties and carbon uptake, Constr. Build. Mater. 387 (2023) 131600, https://doi.org/10.1016/j.conbuildmat.2023.131600.
[3] H. Shoukry, P. Perumal, A. Abadel, H. Alghamdi, M. Alamri, H.A. Abdel-Gawwad, Performance of limestone-calcined clay cement mortar incorporating high volume ferrochrome waste slag aggregate, Constr. Build. Mater. 350 (2022) 128928, https://doi.org/10.1016/j.conbuildmat.2022.128928.
[4] P. Matar, J. Barhoun, Effects of waterproofing admixture on the compressive strength and permeability of recycled aggregate concrete, J. Build. Eng. 32 (2020) 101521, https://doi.org/10.1016/j.jobe.2020.101521.
[5] U. Chandru, B. A, S. R, Systematic comparison of different recycled fine aggregates from construction and demolition wastes in OPC concrete and PPC concrete, J. Build. Eng. (2023) 106768, https://doi.org/10.1016/j.jobe.2023.106768.
[6] M.J. Ashraf, M. Idrees, A. Akbar, Performance of silica fume slurry treated recycled aggregate concrete reinforced with carbon fibers, J. Build. Eng. 66 (2023) 105892, https://doi.org/10.1016/j.jobe.2023.105892.
[7] F. Rezaei, A. Memarzadeh, M.-R. Davoodi, M.-A. Dashab, M. Nematzadeh, Mechanical features and durability of concrete incorporating recycled coarse aggregate and nano-silica: experimental study, prediction, and optimization, J. Build. Eng. 73 (2023) 106715, https://doi.org/10.1016/j.jobe.2023.106715.
[8] L. Barbieri, F. Altimari, F. Andreola, B. Maggi, I. Lancellotti, Characterization of volcano-sedimentary rocks and related scraps for design of sustainable materials, Materials 16 (2023) 3408, https://doi.org/10.3390/ma16093408.
[9] W.H. Juimo Tchamdjou, T. Cherradi, M.L. Abidi, L.A. Pereira-de-Oliveira, Mechanical properties of lightweight aggregates concrete made with cameroonian volcanic scoria: destructive and non-destructive characterization, J. Build. Eng. 16 (2018) 134–145, https://doi.org/10.1016/j.jobe.2018.01.003.
[10] M. Pekgöz, İ. Tekin, Microstructural investigation and strength properties of structural lightweight concrete produced with Zeolitic tuff aggregate, J. Build. Eng. 43 (2021) 102863, https://doi.org/10.1016/j.jobe.2021.102863.
[11] A.M. Rashad, A synopsis about perlite as building material – a best practice guide for Civil Engineer, Constr. Build. Mater. 121 (2016) 338–353, https://doi.org/10.1016/j.conbuildmat.2016.06.001.
[12] S. Celik, R. Family, M.P. Menguc, Analysis of perlite and pumice based building insulation materials, J. Build. Eng. 6 (2016) 105–111, https://doi.org/10.1016/j.jobe.2016.02.015.
[13] M. Davraz, M. Koru, A.E. Akdağ, Kılınçarslan, Y.E. Delikanlı, M. Çabuk, Investigating the use of raw perlite to produce monolithic thermal insulation material, Constr. Build. Mater. 263 (2020) 120674, https://doi.org/10.1016/J.CONBUILDMAT.2020.120674.
[14] E. Kapeluszna, Ł. Kotwica, W. Nocuń-Wczelik, Comparison of the effect of ground waste expanded perlite and silica fume on the hydration of cements with various tricalcium aluminate content – comprehensive analysis, Constr. Build. Mater. 303 (2021) 124434, https://doi.org/10.1016/j.conbuildmat.2021.124434.
[15] United States Geological Survey (USGS), Mineral commodity summaries 2023, 2023. doi:10.3133/mcs2023.
[16] M. Zukowski, G. Haese, Experimental and numerical investigation of a hollow brick filled with perlite insulation, Energy Build. (2010), https://doi.org/10.1016/j.enbuild.2010.03.009.
[17] M. Vyšvařil, M. Pavlíková, M. Záleská, A. Pivák, T. Žižlavský, P. Rovnaníková, P. Bayer, Z. Pavlík, Non-hydrophobized perlite renders for repair and thermal insulation purposes: influence of different binders on their properties and durability, Constr. Build. Mater. 263 (2020) 120617, https://doi.org/10.1016/j.conbuildmat.2020.120617.
[18] Y. Fang, X. Yin, P. Cui, X. Wang, K. Zhuang, Z. Ding, F. Xing, Properties of magnesium potassium phosphate cement-expanded perlite composites applied as fire resistance coating, Constr. Build. Mater. 293 (2021) 123513, https://doi.org/10.1016/j.conbuildmat.2021.123513.
[19] S.M. Motahari Karein, P. Vosoughi, S. Isapour, M. Karakouzian, Pretreatment of natural perlite powder by further milling to use as a supplementary cementitious material, Constr. Build. Mater. (2018), https://doi.org/10.1016/j.conbuildmat.2018.08.012.
[20] H. Li, L. Wang, Y. Zhang, J. Yang, D.C.W. Tsang, V. Mechtcherine, Biochar for sustainable construction industry. in: Curr. Dev. Biotechnol. Bioeng., Elsevier, 2023, pp. 63–95, https://doi.org/10.1016/B978-0-323-91873-2.00015-7.
[21] Ł. Kotwica, W. Pichór, E. Kapeluszna, A. Różycka, Utilization of waste expanded perlite as new effective supplementary cementitious material, J. Clean. Prod. 140 (2017) 1344–1352, https://doi.org/10.1016/j.jclepro.2016.10.018.
[22] S.M.M. Karein, A. Joshaghani, A.A. Ramezanianpour, S. Isapour, M. Karakouzian, Effects of the mechanical milling method on transport properties of self-compacting concrete containing perlite powder as a supplementary cementitious material, Constr. Build. Mater. 172 (2018) 677–684, https://doi.org/10.1016/j.conbuildmat.2018.03.205.

[23] S. Alexander, S. Juhi Manohar, S. Shino John, K. Varun Teja, T. Meena, Mechanical and micro-structural properties of perlite powder incorporated SCC, Mater. Today Proc. 45 (2021) 3374–3382, https://doi.org/10.1016/j.matpr.2020.12.776.
[24] D. Fodil, M. Mohamed, Compressive strength and corrosion evaluation of concretes containing pozzolana and perlite immersed in aggressive environments, Constr. Build. Mater. 179 (2018) 25–34, https://doi.org/10.1016/j.conbuildmat.2018.05.190.
[25] X. Wang, D. Wu, Q. Geng, D. Hou, M. Wang, L. Li, P. Wang, D. Chen, Z. Sun, Characterization of sustainable ultra-high performance concrete (UHPC) including expanded perlite, Constr. Build. Mater. 303 (2021) 124245, https://doi.org/10.1016/J.CONBUILDMAT.2021.124245.
[26] M. Bakhshi, A. Dalalbashi, H. Soheili, Energy dissipation capacity of an optimized structural lightweight perlite concrete, Constr. Build. Mater. 389 (2023) 131765, https://doi.org/10.1016/j.conbuildmat.2023.131765.
[27] R. Demirboğa, I. Örüng, R. Gül, Effects of expanded perlite aggregate and mineral admixtures on the compressive strength of low-density concretes, Cem. Concr. Res. (2001), https://doi.org/10.1016/S0008-8846(01)00615-9.
[28] M. Abed, J. de Brito, Evaluation of high-performance self-compacting concrete using alternative materials and exposed to elevated temperatures by non-destructive testing, J. Build. Eng. 32 (2020) 101720, https://doi.org/10.1016/j.jobe.2020.101720.
[29] ASRO (Romanian Standards Association), SR EN 197–1: Cement. Part I: Composition, specifications and conformity criteria for normal use cements, (2011).
[30] A. Favier, C. De Wolf, K. Scrivener, G. Habert, A Sustainable Future for the European Cement and Concrete Industry, Zurich, 2018. ⟨https://europeanclimate.org/wp-content/uploads/2018/10/AB_SP_Decarbonisation_report.pdf⟩.
[31] ASRO (Romanian Standards Association), SR EN 1097-2:2002 Tests for mechanical and physical properties of aggregates - Part 2: Methods for the determination of resistance to fragmentation, (2020). ⟨https://magazin.asro.ro/ro/standard/274070⟩.
[32] ASRO (Romanian Standards Association), SR EN 933-2:2020 Tests for geometrical properties of aggregates. Determination of particle size distribution. Test sieves, nominal size of apertures, (2020). ⟨https://magazin.asro.ro/ro/standard/274810⟩.
[33] S. Grzeszczyk, G. Janus, Lightweight reactive powder concrete containing expanded perlite, Materials 14 (2021) 3341, https://doi.org/10.3390/ma14123341.
[34] ASTM International, ASTM C618-22: Standard Specification for Coal Fly Ash and Raw or Calcined Natural Pozzolan for Use in Concrete, (2022). doi:10.1520/C0618-22.
[35] ASTM International, ASTM C 618: Standard Specification for Coal Fly Ash and Raw or Calcined Natural Pozzolan for Use in Concrete, (2022). ⟨https://www.astm.org/c0618-22.html⟩.
[36] D. Adi Darmawan, A. Wahyudi, H. Eric Mamby, I. Suherman, Characterization of perlite and expanded perlite from West Sumatera, Indonesia, IOP Conf. Ser. Earth Environ. Sci. 882 (2021) 012010, https://doi.org/10.1088/1755-1315/882/1/012010.
[37] M. Lanzón, F.J. Castellón, M. Ayala, Effect of the expanded perlite dose on the fire performance of gypsum plasters, Constr. Build. Mater. 346 (2022) 128494, https://doi.org/10.1016/j.conbuildmat.2022.128494.
[38] H. AzariJafari, A. Kazemian, B. Ahmadi, J. Berenjian, M. Shekarchi, Studying effects of chemical admixtures on the workability retention of zeolitic Portland cement mortar, Constr. Build. Mater. 72 (2014) 262–269, https://doi.org/10.1016/j.conbuildmat.2014.09.020.
[39] ASRO (Romanian Standards Association), SR EN 196–1:2016, Methods of testing cement - Part 1: Determination of Strength, (2016).
[40] H. Dilbas, Effect of cement type and water-to-cement ratio on fresh properties of superabsorbent polymer-modified cement paste, Materials 16 (2023) 2614, https://doi.org/10.3390/ma16072614.
[41] I.-O. Toma, G. Stoian, M.-M. Rusu, I. Ardelean, N. Cimpoeşu, S.-M. Alexa-Stratulat, Analysis of pore structure in cement pastes with micronized natural zeolite, Materials 16 (2023) 4500, https://doi.org/10.3390/ma16134500.
[42] ASTM International, ASTM C215-19 - Standard Test Method for Fundamental Transverse, Longitudinal, and Torsional Resonant Frequencies of Concrete Specimens, (2019).
[43] D.P. Thanaraj, A.N., P. Arulraj, K. Al-Jabri, Investigation on structural and thermal performance of reinforced concrete beams exposed to standard fire, J. Build. Eng. 32 (2020) 101764, https://doi.org/10.1016/j.jobe.2020.101764.
[44] M. Sarıdemir, A. Yıldırım, Effect of elevated temperatures on properties of high strength mortars containing ground calcined diatomite with limestone sand, J. Build. Eng. 56 (2022) 104748, https://doi.org/10.1016/j.jobe.2022.104748.
[45] S. Alani, M.S. Hassan, A.A. Jaber, I.M. Ali, Effects of elevated temperatures on strength and microstructure of mortar containing nano-calcined montmorillonite clay, Constr. Build. Mater. 263 (2020) 120895, https://doi.org/10.1016/j.conbuildmat.2020.120895.
[46] I. Fletcher, S. Welch, J. Torero, R. Carvel, A. Usmani, Behaviour of concrete structures in fire, Therm. Sci. 11 (2007) 37–52, https://doi.org/10.2298/TSCI0702037F.
[47] J. Piasta, Heat deformations of cement paste phases and the microstructure of cement paste, Mater. Struct. 17 (1984) 415–420, https://doi.org/10.1007/BF02473981.
[48] I. Hager, Behaviour of cement concrete at high temperature, Bull. Pol. Acad. Sci. Tech. Sci. 61 (2013) 145–154, https://doi.org/10.2478/bpasts-2013-0013.
[49] P. Sikora, K. Cendrowski, E. Horszczaruk, E. Mijowska, The effects of Fe3O4 and Fe3O4/SiO2 nanoparticles on the mechanical properties of cement mortars exposed to elevated temperatures, Constr. Build. Mater. 182 (2018) 441–450, https://doi.org/10.1016/j.conbuildmat.2018.06.133.
[50] M. Castellote, C. Alonso, C. Andrade, X. Turrillas, J. Campo, Composition and microstructural changes of cement pastes upon heating, as studied by neutron diffraction, Cem. Concr. Res. 34 (2004) 1633–1644, https://doi.org/10.1016/S0008-8846(03)00229-1.
[51] M. Vijayalakshmi, A.S.S. Sekar, G. Ganesh prabhu, Strength and durability properties of concrete made with granite industry waste, Constr. Build. Mater. 46 (2013) 1–7, https://doi.org/10.1016/j.conbuildmat.2013.04.018.
[52] F. Šoukal, L. Bocian, R. Novotný, L. Dlabajová, N. Šuleková, J. Hajzler, O. Koutný, M. Drdlová, The effects of silica fume and superplasticizer type on the properties and microstructure of reactive powder concrete, Materials 16 (2023) 6670, https://doi.org/10.3390/ma16206670.
[53] H. Varela, G. Barluenga, I. Palomar, A. Sepulcre, Synergies on rheology and structural build-up of fresh cement pastes with nanoclays, nanosilica and viscosity modifying admixtures, Constr. Build. Mater. 308 (2021) 125097, https://doi.org/10.1016/j.conbuildmat.2021.125097.
[54] M. Lanzón, P.A. García-Ruiz, Lightweight cement mortars: advantages and inconveniences of expanded perlite and its influence on fresh and hardened state and durability, Constr. Build. Mater. 22 (2008) 1798–1806, https://doi.org/10.1016/J.CONBUILDMAT.2007.05.006.
[55] F. Guenanou, H. Khelafi, A. Aattache, Behavior of perlite-based mortars on physicochemical characteristics, mechanical and carbonation: case of perlite of Hammam Boughrara, J. Build. Eng. 24 (2019) 100734, https://doi.org/10.1016/j.jobe.2019.100734.
[56] D. Kramar, V. Bindiganavile, Impact response of lightweight mortars containing expanded perlite, Cem. Concr. Compos. 37 (2013) 205–214, https://doi.org/10.1016/j.cemconcomp.2012.10.004.
[57] A. Łagosz, D. Olszowski, W. Pichór, Ł. Kotwica, Quantitative determination of processed waste expanded perlite performance as a supplementary cementitious material in low emission blended cement composites, J. Build. Eng. 40 (2021) 102335, https://doi.org/10.1016/j.jobe.2021.102335.
[58] V. Akyuncu, F. Sanliturk, Investigation of physical and mechanical properties of mortars produced by polymer coated perlite aggregate, J. Build. Eng. 38 (2021) 102182, https://doi.org/10.1016/j.jobe.2021.102182.
[59] K. Şengül, S.T. Erdoğan, Influence of ground perlite on the hydration and strength development of calcium aluminate cement mortars, Constr. Build. Mater. 266 (2021) 120943, https://doi.org/10.1016/j.conbuildmat.2020.120943.
[60] G.H. Nalon, M.A. Alves, L.G. Pedroti, J.C. Lopes Ribeiro, W.E. Hilarino Fernandes, D. Silva de Oliveira, Compressive strength, dynamic, and static modulus of cement-lime laying mortars obtained from samples of various geometries, J. Build. Eng. 44 (2021) 102626, https://doi.org/10.1016/j.jobe.2021.102626.
[61] F. Bektas, L. Turanli, P.J.M. Monteiro, Use of perlite powder to suppress the alkali–silica reaction, Cem. Concr. Res. 35 (2005) 2014–2017, https://doi.org/10.1016/j.cemconres.2004.10.029.
[62] R. Chihaoui, H. Siad, Y. Senhadji, M. Mouli, A.M. Nefoussi, M. Lachemi, Efficiency of natural pozzolan and natural perlite in controlling the alkali-silica reaction of cementitious materials, Case Stud. Constr. Mater. 17 (2022) e01246, https://doi.org/10.1016/j.cscm.2022.e01246.
[63] H. Maraghechi, M. Maraghechi, F. Rajabipour, C.G. Pantano, Pozzolanic reactivity of recycled glass powder at elevated temperatures: reaction stoichiometry, reaction products and effect of alkali activation, Cem. Concr. Compos. 53 (2014) 105–114, https://doi.org/10.1016/j.cemconcomp.2014.06.015.
[64] M.R. Karim, F.I. Chowdhury, H. Zabed, M.R. Saidur, Effect of elevated temperatures on compressive strength and microstructure of cement paste containing palm oil clinker powder, Constr. Build. Mater. 183 (2018) 376–383, https://doi.org/10.1016/j.conbuildmat.2018.06.147.
[65] I. Garcia-Lodeiro, P.M. Carmona-Quiroga, R. Zarzuela, M.J. Mosquera, M. T. Blanco-Varela, Chemistry of the interaction between an alkoxysilane-based impregnation treatment and cementitious phases, Cem. Concr. Res. 142 (2021) 106351, https://doi.org/10.1016/j.cemconres.2020.106351.
[66] S. Çelikten, M. Sarıdemir, K. Akçaözoğlu, Effect of calcined perlite content on elevated temperature behaviour of alkali activated slag mortars, J. Build. Eng. 32 (2020) 101717, https://doi.org/10.1016/j.jobe.2020.101717.
[67] Z. Li, X. Zhou, B. Shen, Fiber-cement extrudates with perlite subjected to high temperatures, J. Mater. Civ. Eng. 16 (2004) 221–229, https://doi.org/10.1061/(ASCE)0899-1561(2004)16:3(221).
[68] I.E. Ariyaratne, A. Ariyanayagam, M. Mahendran, Bushfire-resistant lightweight masonry blocks with expanded perlite aggregate, Fire 5 (2022) 132, https://doi.org/10.3390/fire5050132.

Engineering Structures 307 (2024) 117885

Contents lists available at ScienceDirect

Engineering Structures

journal homepage: www.elsevier.com/locate/engstruct

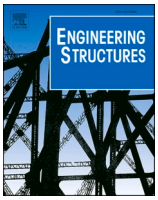

Behaviour of short columns made with conventional or FRP-confined rubberised concrete: An experimental and numerical investigation

Imad El Khouri [a], Reyes Garcia [b,*], Petru Mihai [c], Mihai Budescu [c], Nicolae Taranu [c,d], Ionut Ovidiu Toma [c], Maurizio Guadagnini [a], David Escolano-Margarit [e], Ioana Sorina Entuc [c], Gabriel Oprisan [c], Iman Hajirasouliha [a], Kypros Pilakoutas [a]

[a] Dept. of Civil and Structural Engineering, The University of Sheffield, UK
[b] Civil Engineering Stream, School of Engineering, The University of Warwick, UK
[c] Faculty of Civil Engineering and Building Services, Technical University "Gheorghe Asachi", Iasi, Romania
[d] The Academy of Romanian Scientists, Bucarest, Romania
[e] Depto. de Mecánica de Estructuras e Ingeniería Hidráulica, University of Granada, Granada, Spain

ARTICLE INFO

Keywords:
Short columns
Confined rubberised concrete
FRP confinement
Shear behaviour
Numerical analysis

ABSTRACT

Failure of short columns in concrete buildings has been extensively reported during past earthquakes. Assessing the behaviour of short columns is challenging and often requires using time-consuming advanced numerical modelling. This article presents a new and practical Short Column Macro Element (SCME) that predicts accurately the behaviour of concrete short columns. A 1/3-scale one-storey building with short columns is subjected to lateral loading tests until failure. The experimental results from the building are then used to calibrate a numerical model in Abaqus®. It is shown that the numerical model matches well the experimental results. The experimental crack patterns and stress distribution from Abaqus® are then used to determine the load path within the short column. Based on these data, a new strut-and-tie SCME is proposed and implemented in OpenSees software to simulate accurately (within 5% accuracy) the behaviour of the short columns of the tested building. Subsequently, the frame models calibrated in OpenSees and Abaqus® are modified to examine numerically the effectiveness of highly deformable FRP-confined rubberised concrete (FRP CRuC) at increasing the deformability of short columns with different levels of FRP confinement (1, 2 or 3 layers). The numerical results show that whilst the tested building failed at a small displacement of 5.4 mm (0.43% drift ratio), the use of FRP CRuC short columns with minimal confinement (1 layer of AFRP only) increased the building's displacement by almost seven times to 37 mm (3.0% drift ratio). This also enabled more redistribution of forces to other structural members of the building. This article contributes towards the development of practical design/analysis models for short columns made of conventional concrete and FRP CRuC, which are scarce in the existing literature.

1. Introduction

Current seismic codes (e.g. ACI 318–14 [1], and Eurocode 8 [2]) aim to design reinforced concrete buildings that can meet desired performance levels in terms of ductility and energy dissipation capacity. However, these two structural properties are limited by the deformation (strain) capacity of concrete columns and connections. Although a target ductility can be achieved by confining concrete with properly detailed steel reinforcement, large amounts of lateral reinforcement (links/stirrups) are often required to increase the inherently low strain capacity of concrete in compression to acceptable values. Reinforcement congestion can complicate the construction process and therefore increase the overall costs of construction. In recent years, Rubberised Concrete (RuC) has been proven to increase the strain capacity of concrete, thus emerging as an alternative material to increase the deformability of columns. In RuC, recycled rubber aggregates from waste tyres replace a fraction of the mineral aggregates in the concrete mix. While the inclusion of rubber aggregates often reduces the compressive strength and the Young's modulus of concrete, RuC can develop higher axial strains than conventional concrete (CC) for the same level of

* Corresponding author.
E-mail address: reyes.garcia@warwick.ac.uk (R. Garcia).

https://doi.org/10.1016/j.engstruct.2024.117885
Received 18 July 2023; Received in revised form 12 February 2024; Accepted 17 March 2024
Available online 23 March 2024

applied stress. Most notable is the ability of RuC to expand laterally, up to four times more than CC [3]. This property can be exploited to increase the axial capacity and deformability of RuC through the use of external Fibre Reinforced Polymer (FRP) confinement.

Previous studies have investigated the behaviour of Confined RuC (CRuC) cylinders and columns. For instance, Youssf et al. [4] reported high axial compressive strengths (up to 112.5 MPa) in RuC cylinders confined with Carbon FRP (CFRP) jackets. However, since only 20% of rubber replaced the sand volume in their tests, the maximum axial strains (1.8%) reported by Youssf et al. were comparable to those achieved in normal FRP-confined concrete [5]. This indicates that high volumes of rubber replacement (>50–60%) are necessary to increase deformability. Likewise, Duarte et al. [6] reported a 50% increase in ductility by confining RuC columns with cold-formed steel tubes, although a lower confinement effectiveness was achieved due to the lower dilation angle of RuC [7]. More recent research [8,9] has also proven the effectiveness of Glass (GFRP) and CFRP jackets at enhancing the axial capacity and deformability of square/circular RuC elements. Past research has also shown that flexural-dominated structural elements incorporating RuC and CRuC can develop higher ductility, damping and energy dissipation capacity compared to CC counterpart elements [10–14]. Whilst most of the research to date has examined isolated structural elements, much less research has focused on the shear behaviour of buildings made of RuC or CRuC. A recent study [15] has shown that an increase of rubber replacement levels leads to a decrease in the shear strength of RuC, but also to a better post-peak softening behaviour at relatively high rubber contents (about 60% replacement). In addition, tests by the authors [16] proved that the use of a minimal external confinement (one layer of Carbon FRP (CFRP)) can enhance both the shear deformations (up to forty times) and shear strength (two times) over RuC counterparts.

In buildings located in seismic-prone areas, the geometry of structural elements and their relative stiffnesses significantly affect the load distribution paths and can limit structural performance. For instance, short columns are typical examples where the relatively high stiffness of the element can lead to catastrophic failures [17]. Short columns are columns where the shear ratio α_s is defined as $\alpha_s = \frac{M}{Vl} \leq 2.5$, where M is the end moment, V is the shear force, and l is the width of the column [18–21]. Whilst design codes advise to avoiding the use of short columns in buildings, many times these are necessary due to architectural requirements in parts of the buildings (e.g. in partially buried basements, stair and platform connections, mezzanine floors, and buildings on sloping grounds). Short columns can also be created unintentionally when non-structural partial infill walls or parapets are added between columns. The behaviour of short columns is dominated by shear and therefore (if inadequately detailed) brittle failures can occur, with limited yielding and force redistribution. If short columns are necessary, the use of construction materials able to develop high deformation and rotational capacity (such as CRuC) is expected to promote a better force redistribution and a higher energy dissipation. However, further research is needed to verify the potential of CRuC at improving the shear behaviour of short columns subjected to lateral load. Moreover, conventional seismic analysis tools based on fibre element cannot account for the shear dominated behaviour of short columns, and therefore there is also a need for the development of practical tools to analyse buildings with short columns.

This article proposes a new and practical Short Column Macro Element (SCME) that predicts accurately the behaviour of concrete short columns. The first part of the article presents lateral loading tests on a 1/3-scale one-storey concrete building with short columns. The results from the tested building were used to calibrate a finite element model in Abaqus® software, which provided a thorough insight into the structural behaviour of the short columns. The results from Abaqus® (crack patterns and stress distribution) were subsequently used to develop a new practical Short Column Macro Element (SCME) adopting a strut-and-tie approach to determine its geometry. The SCME was then implemented in OpenSees [22] to simulate the behaviour of the short columns of the tested building. Next, both frame models calibrated in OpenSees and Abaqus® were modified to examine numerically the effectiveness of highly deformable FRP CRuC at increasing the deformability of short columns with different levels of FRP confinement (1, 2 or 3 layers of FRP). This article contributes towards the development of practical design/analysis models for short columns made of conventional concrete and FRP CRuC, which in turn is expected to promote the use of CRuC in shear applications. This study is part of the EU-funded multi-partner project Anagennisi that aimed to develop new RuC and CRuC applications to reuse all tyre components in concrete [23].

2. Experimental programme

2.1. Characteristics of tested building

A one-bay one-storey 1/3 scaled-down concrete building was built and tested at the Technical University "Gheorghe Asachi" of Iasi, Romania, as part of the EU-funded project Anagennisi [24]. The scaled-down building is deemed to represent part of a typical school building, which often have one floor and one bay in one direction. Moreover, numerous school building in past earthquakes have experienced damage or collapse due to short column failures. The building had a storey height of 1360 mm, total length of 2550 mm in the direction of loading (X direction), and a width of 1950 mm in the other direction (see Fig. 1a). The primary consideration in the design of the building was to produce a local shear failure in the short columns, and therefore the column flexural capacity was higher than its shear capacity. Moreover, in order to attain a shear failure in the short columns, the beams were intentionally over strengthened, and the columns' shear reinforcement consisted of mild steel. The four columns had a cross-section of 150 × 150 mm (Fig. 1b) and an effective height of 1100 mm. The base of the columns was bigger (220 ×220 mm) and this was embedded in a rigid steel foundation for a depth of 400 mm. The rigid steel foundation was in turn bolted to the strong floor of the laboratory. The beams measured 150 × 260 mm (Fig. 1b). The columns' longitudinal reinforcement consisted of six 14 mm diameter bars, and these were bent at the ends at a 90° for anchoring. The columns' shear reinforcement consisted of closed stirrups of 4 mm diameter spaced at 100 mm centres. Stirrups were also provided in the beam-column joints. The longitudinal reinforcement of beams in the X (direction of loading) and Y directions consisted of six 12 mm and four 10 mm diameter bars, respectively. The beams had 6 mm diameter stirrups spaced at 200 mm centres in the midspan of the beam, and spaced at 100 mm centres at the ends. The longitudinal steel bars of the beams were anchored at a 90° angle. The slab had a thickness of 60 mm and it was reinforced with a mesh of 6 mm diameter bars at 100 mm centres (Fig. 1a). The clear concrete cover was 20 mm in all structural elements. It should be noted that the corners of the short columns were rounded off (radius = 25 mm) since the short columns of a twin building were to be confined with FRP jackets, and both buildings were cast at the same time.

The columns were intentionally designed to fail in shear at the top region just below the beams, where two braced steel frames (placed along axes 1 and 2) formed a short column (Fig. 1c). The columns had a theoretical flexural yield capacity of 23 kNm, an ultimate flexural capacity of 25 kNm, and a maximum shear capacity of 28 kN for the concrete alone according to Eurocode 2 (EC2) [25]. The shear stirrups of the column provided an additional 6.9 kN resistance. Therefore, at the total (theoretical) shear resistance of 34.9 kN, the bending moment of the short column was only 5.2 kNm, which was well below the flexural yield capacity of 23 kN. The ultimate flexural capacities of the longitudinal beams (X direction) and transverse beams (Y direction) were 46 and 22 kNm, respectively.

The structural elements of the building were identified based on their

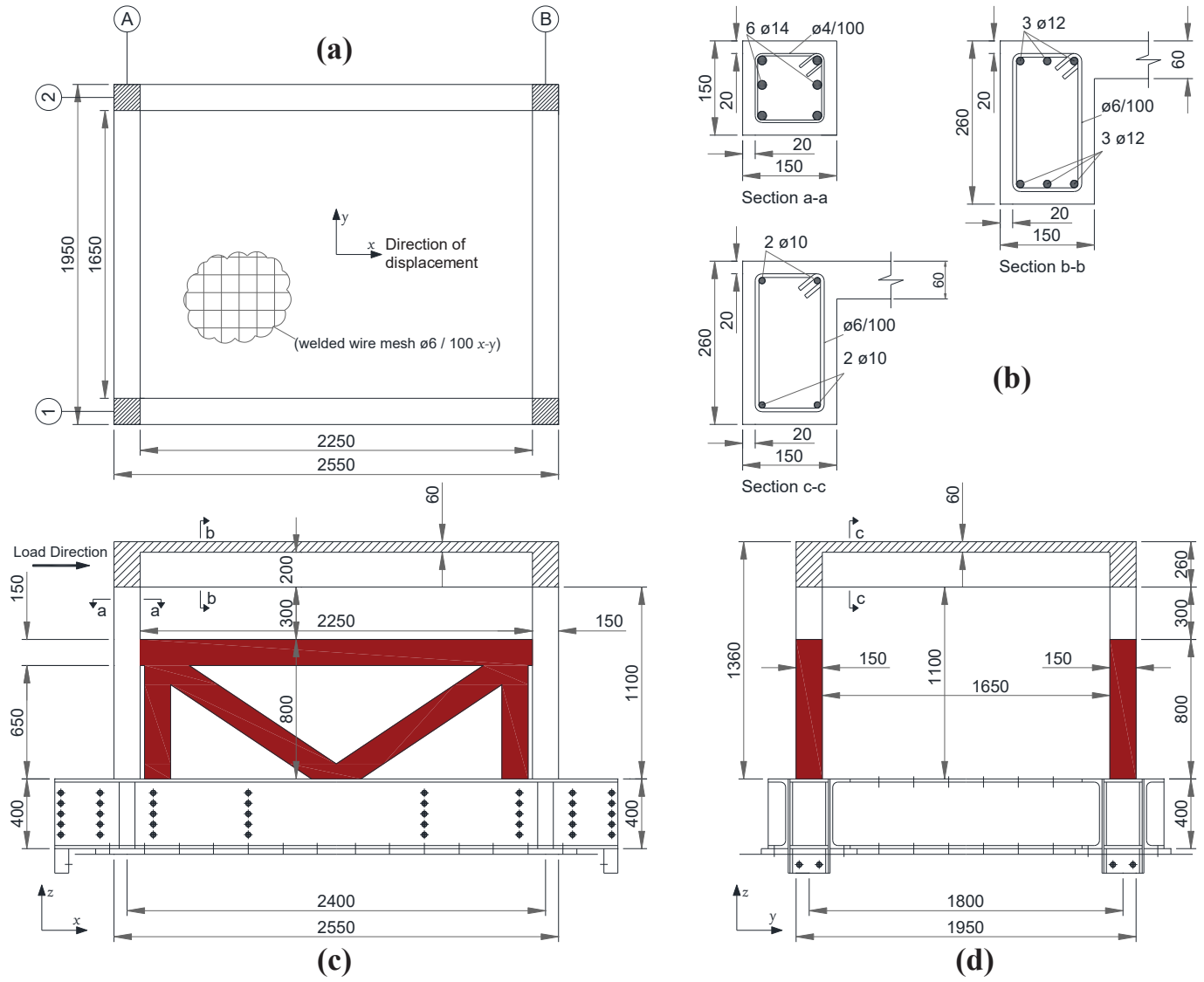

Fig. 1. Geometry and details of tested building (a) plan view, (b) cross sections of elements, (c) elevation showing loading direction and braced steel frames, and (d) elevation in transverse direction.

type, location, and orientation. The first letter of the ID indicates the type of structural element (C=column, J=beam-column joint), while the next digit and letter represent the location of the element based on the intersection of the corresponding axes shown in Fig. 1a. The fourth letter, if used, determines the direction being referred to. For example, J1A-X refers to the joint situated at the intersection of axes 1 and A, and the face being observed is parallel to the X-axis.

2.2. Material properties

A single concrete mix with water/cement ratio $w/c = 0.4$ was used to cast the building. The mechanical properties of the concrete were determined by testing five 150 × 300 mm standard cylinders according to EN 12390–3 [26], which resulted in a mean compressive strength f_{cm} = 37 MPa and a Young's modulus E_c = 30 GPa. The tensile strength of the concrete was obtained from three standard cylinders and was f_{ct} = 3.3 MPa. The longitudinal bars of beams and columns had yield and ultimate strengths of f_{ly} = 513 MPa and f_{lu} = 626 MPa, respectively. These values were obtained from five direct tensile coupons tested according to EN 10080 [27]. The smooth steel wire used for the stirrups and steel mesh of the slab had a yield strength of f_{sy} = 255 MPa, according to the producer's data.

2.3. Test setup, instrumentation, and load sequence

Two braced steel frames restrained the columns in the X-direction and simulated partial infill masonry walls. Such restraining steel frames were bolted to the bottom steel foundation and forced the development of a short column mechanism within the top region of columns C1A and C2A. The clear shear span of the short column was 300 mm, which results in a shear ratio α_s = 1. Ten concrete blocks (total = 36 kN) were bolted to the slab to simulate axial load, thus resulting in an axial load of 9 kN per column, or approximately 1% of the column's axial capacity. Such relatively low axial load was applied due to the limited availability of blocks in the laboratory. Additionally, this test was needed to inform future shake-table tests on a similar building, where the maximum overturning moment was limited to the capacity of the shake table.

The building was instrumented in the X direction with eight horizontal linear variable differential transformers (LVDTs) shown as Ln1 to Ln8 in Fig. 2. These LVDTs were located at the top and bottom of the short columns. Four diagonal LVDTs (Incl1 to Incl4 in Fig. 2) placed at an angle of 45° measured the relative rotation between beams and columns.

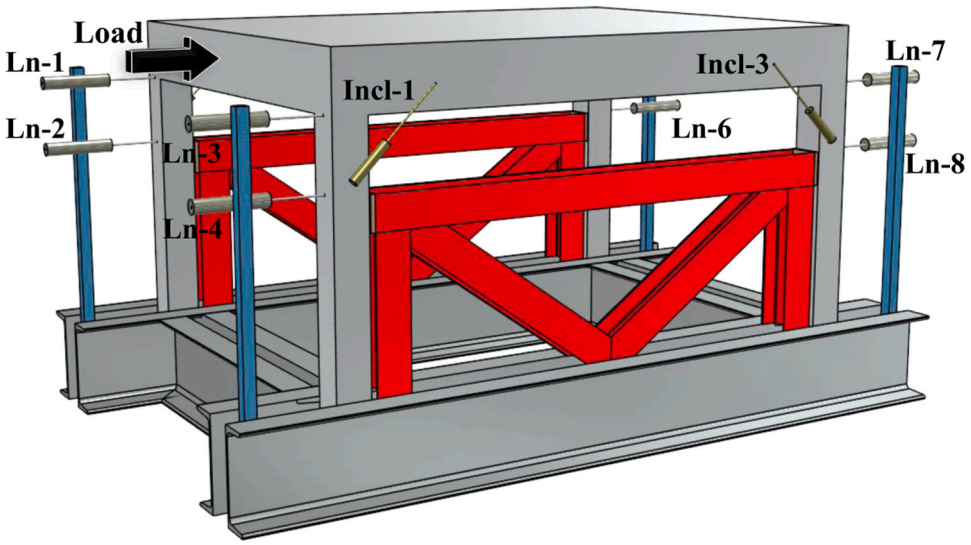

Fig. 2. Schematic view of test setup and instrumentation of tested building.

The lateral load was applied monotonically on the transverse beam via a hydraulic actuator and a stiff transfer steel plate. The test was performed in load control at a rate of 6 kN/min. The building was subjected to three sets of three cycles each: i) set 1 performed at 40 kN to capture the first flexural crack, ii) set 2 performed at 60 kN, and iii) set 3 performed at 100 kN to capture the diagonal shear cracking. This was followed by a final monotonic load up to failure of the short columns. The test was halted when the maximum load recorded during the test dropped by 20%. Fig. 3a shows the experimental model and setup. The lateral actuator applied the force directly on the building using a stiff steel plate to transfer the load (Fig. 3b).

2.4. Test results and discussion

Fig. 4 shows the lateral load vs displacement of the building. The displacements are the average of four horizontal transducers (Ln-1, 3, 5, and 7). In this figure, the top horizontal axis also shows the drift ratio of the unrestrained column (centreline height of 1230 mm).

The results in Fig. 4 indicate that the first flexural crack occurred at joints J1A and J2A during the first loading cycle (set 1) at a lateral force of 37 kN. The cracks propagated at an angle of 45° and 70° from the horizontal for J1A-X and J2A-X, respectively. The cracks further propagated through the joints during the subsequent cycles performed at 40 kN (set 1) and 60 kN (set 2). A few hairline flexural cracks appeared along columns C1A-X and C2A-X during set 3 at 100 kN. At a lateral

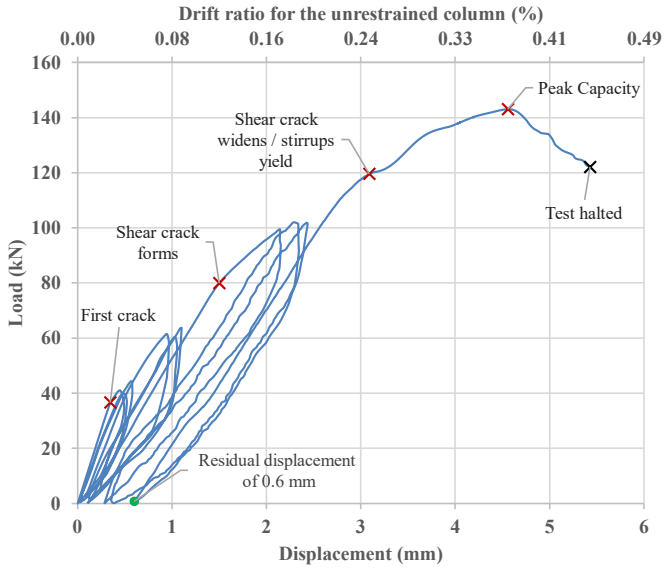

Fig. 4. Load vs displacement curve of tested building.

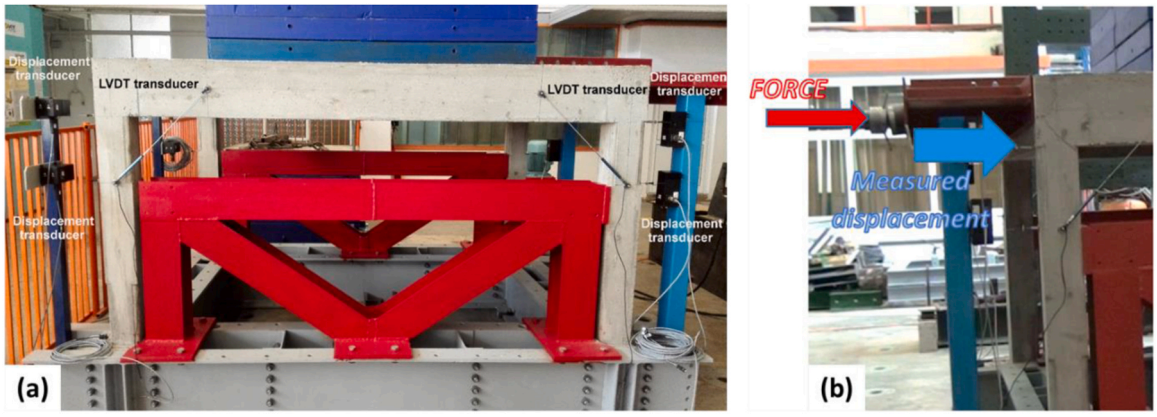

Fig. 3. (a) General test setup, and (b) actuator and stiff transfer plate to apply load.

force of 82 kN, shear cracking occurred in the top portion of both columns C1A-X and C2A-X. The shear crack propagated at an approximate angle of 17° from the vertical along the direction connecting the externally applied load to the internal restraining system as the main load transfer mechanism relied on the formation of a diagonal compression strut. Failure of the building occurred at a small displacement of 5.4 mm (0.43% drift ratio) of the unrestrained column. Figs. 5a-b show, respectively, damage experienced at the short columns and joints J1A and J2A after the test.

Flexural cracking in columns C1B-X and C2B-X initiated during the second cycle at 100 kN (set 3) at approximately 98 kN. The maximum lateral load capacity of the building (143 kN) occurred at a lateral displacement of 4.55 mm. Failure was deemed to occur at a displacement of 5.4 mm (121 kN) following excessive concrete spalling at the top of columns C1A-X and C2A-X. No damage was observed in the slab or the beams. No torsion was recorded as the displacements measured by the LVDTs were similar on both sides of the building. The initial stiffness of the building was 107 kN/mm, measured experimentally from the slope of the load-displacement data up to a load of 30 kN. The stiffness at the start of set 3 was 48 kN/mm (i.e. only 45% of the initial stiffness in set 1).

Fig. 6 shows the beam-column relative rotation at axis-A (θ_A) and axis-B (θ_B) recorded during the test. The first stiffness change (due to flexural cracking) is observed in the rotation at axis-A (marked with an ×). However, the rotation at axis-B does not show any significant stiffness change since the columns and joints at axis B only showed signs of damage at a lateral load of 98 kN. In the next section, the results from these tests are used to study in more detail the structural response and failure mode of the short columns of the building.

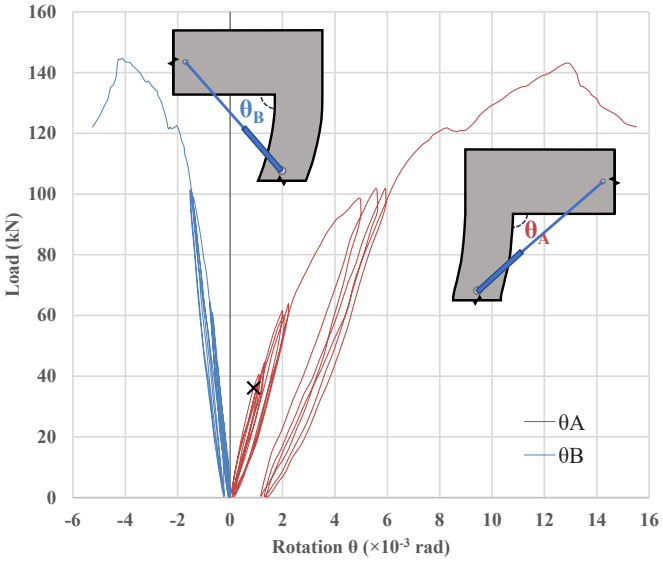

Fig. 6. Average beam-column relative rotation at axis A (joint opening) and axis B (joint closing).

3. Numerical modelling of building in Abaqus®

3.1. Geometry and loading protocol

To study in more detail the response and failure mode of the short columns, the tested building was modelled in Abaqus® [28] software. Due to symmetry and absence of in-plan torsion during the test, the building was modelled as a 2D frame. The geometry of the model

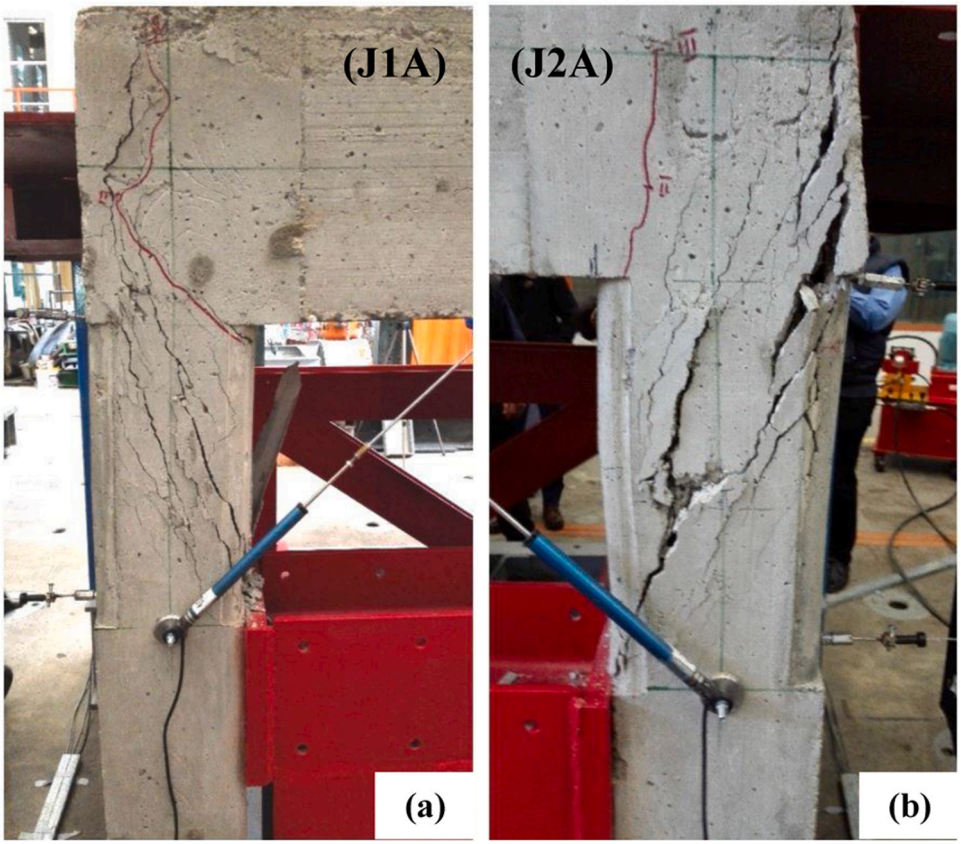

Fig. 5. Shear cracks along short columns and damage of joints (a) J1A, and (b) J2A (excessive spalling in column C2A occurred after peak capacity).

corresponds to that shown in Figs. 1a-d. The bottom 400 mm of the columns were fully restrained along the sides to simulate the fixity provided during the tests by the rigid steel foundation. The braced steel frame was modelled as a 3D analytical rigid body. The interaction between this rigid body and the concrete column was simulated by a surface-to-surface hard contact (with no friction), but allowing separation after contact. The gravity load was applied as concentrated forces on reference points (control nodes). Increasing displacements were imposed on a reference point connected to joint J1A. The reference points were connected to their corresponding transfer steel plate via a Multiple Point Constraint (MPC) tie. Abaqus/Standard was used to perform a static analysis with viscoplastic regularisation, using a viscosity parameter of value of 1E-5. The frame was pushed monotonically until failure as done in the test. The model was built in Abaqus/Standard (Implicit) using a general static analysis.

3.2. Concrete and steel reinforcement models

The built-in concrete damage plasticity model (CDP) in Abaqus/Standard was used in the analysis with the following plasticity parameters: dilation angle $\psi = 37°$; eccentricity $\epsilon = 0.1$; stress ratio $\sigma_{b0}/\sigma_{c0} = 1.16$; and shape factor of the yield surface $K_c = 0.667$. The value of the dilation angle was determined based on a sensitivity analysis (as reported by El Khouri [29]), whereas the parameters ϵ, σ_{b0}/σ_{c0}, and K_c were taken as the default values given by Abaqus®. The compressive stress-strain behaviour was defined according to the Krätzig and Pölling [30] elasto-plastic damage model, whereas the tensile softening function was defined based on the stress-crack opening relation by Hordijk [31]. The CDP damage parameters (for both compression and tension) were defined using the damage evolution model proposed by Alfarah et al. [32]. The adopted framework implements a fracture energy-based regularisation and ensures mesh-independent results. The fracture energy G_F (in N/m) of concrete was calculated using Eq. (1) [33]:

$$G_F = 2.5\alpha_0 \left(\frac{f_{cm}}{0.051}\right)^{0.46} \left(1 + \frac{d_a}{11.27}\right)^{0.22} \left(\frac{w}{c}\right)^{-0.3} \quad (1)$$

where α_0 is 1 for round aggregates; d_a is the maximum aggregate size; and w/c is the water-cement ratio by weight.

In this study, round aggregates of maximum size 15 mm were used in the concrete used to cast the tested building. Likewise, a compressive strength $f_{cm} = 37$ MPa was obtained from the tested cylinders (see Section 2.2). Adopting $\alpha_0 = 1.0$, $f_{cm} = 37$ MPa, $d_a = 15$ mm, and $w/c = 0.4$ (according to the concrete mix in Section 2.2), the fracture energy was calculated as 82 N/m. The crushing energy G_C was taken to be 100 times the fracture energy, as suggested in previous studies [34]. All the concrete parts of the model were meshed with an 8-node linear 3D brick element with reduced integration (C3D8R) as past research [35] proved that this is the most suitable element for 3D models with regular geometry.

The longitudinal steel bars and stirrups were modelled as 2-node linear 3D truss elements (T3D2) assuming an elastic-perfectly plastic behaviour. All reinforcement was fully embedded in the concrete assuming perfect bond. This is reasonable as no debonding of bars was observed during the test. The transfer steel plates used for loading were modelled as 3D solid C3D8R elements with an elastic behaviour.

3.3. Numerical results and discussion

A mesh sensitivity analysis was performed using a different number of elements (4, 5, 6 or 8) across the width of the column, thus resulting in mesh sizes of 37.5, 25, 30, and 18.75 mm, respectively. Fig. 7 compares the lateral load vs displacement results obtained for each element size, as well as the envelope of the experimental results. Whilst some minor differences can be observed in terms of both peak load and

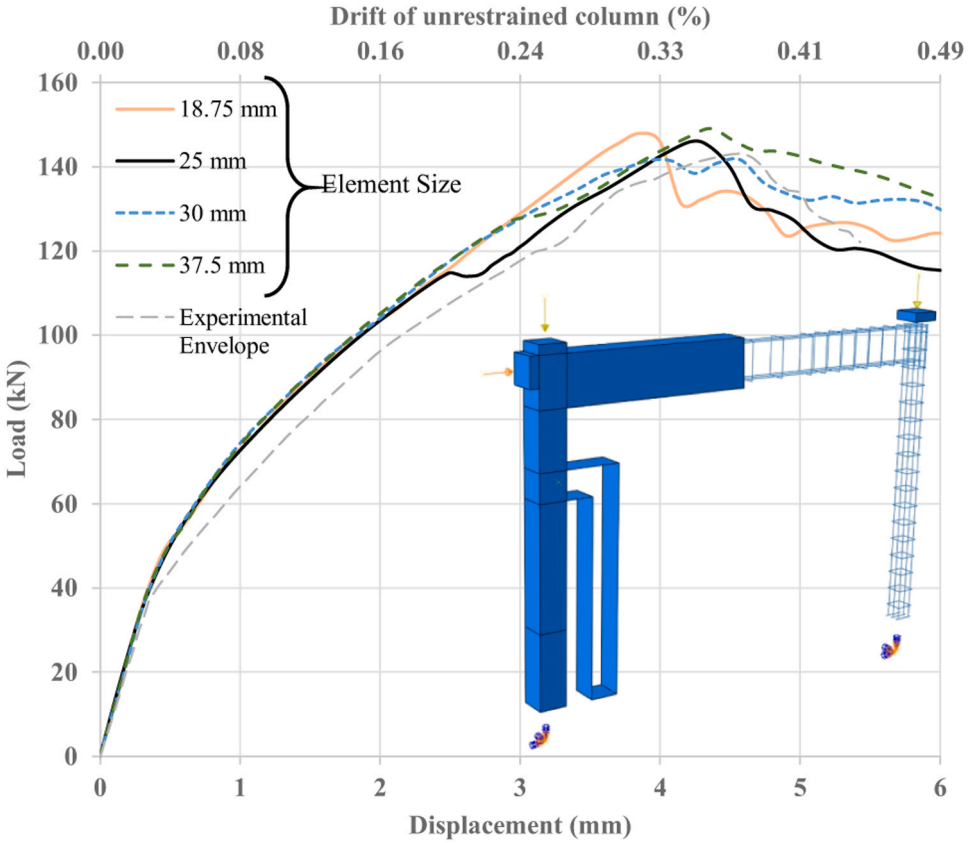

Fig. 7. Load vs displacement for mesh sensitivity analysis in Abaqus® frame model.

displacement, the initial stiffness and subsequent degradation of all models are similar regardless of the mesh size. The results from the 25 mm mesh are considered to best fit the experimental results and are discussed herein. The peak lateral capacity and displacement predicted by the model were 146 kN and 4.2 mm, respectively, which compare well with the experimental values 143 kN and 4.55 mm. The initial stiffness of the model (120 kN/mm) was 12% higher than the initial experimental stiffness (107 kN/mm). The higher stiffness of the Abaqus® model can be attributed to minor unintended cracking caused to the building while positioning it on the testing rig with a crane. At a load of 43 kN, flexural cracking occurred simultaneously in joint J1A-X and along the external face of column C1A-Y (at the level of the braced steel frame) and this is well captured by the model. However, the stiffness reduction after 43 kN was less severe than that in the test, which led to a slightly stiffer response. A sudden increase in lateral displacement was observed at 114 kN, which can be attributed to yielding of the top stirrups in column C1A just below the joint. Such increase in lateral displacement was also observed at 110–130 kN in the other models with different mesh sizes, although the displacement is much less noticeable. Moreover, it is also possible that the difference in mesh size for the same viscosity parameter adopted in the analysis could have led to minor conversion issues in the model with a 25 mm mesh. Accordingly, it is considered that yielding of the stirrups occurred in this short column. However, the longitudinal column bars remained elastic both in the test and the numerical analysis.

The minimum principal stress field along the column and the joint at a displacement of 3.75 mm (see Fig. 8) shows the compressive force path within the short column. The results show that the analytical stress distribution agreed very well with the experimental cracking pattern. Consequently, the 2D frame model in Abaqus® can provide details of the evolution of the main load transfer mechanism within the short columns. Based on the experimental evidence and numerical results, it is possible to conclude that a diagonal concrete strut connecting the bottom of the beam at the loading side to the top of the braced frame clearly formed at a displacement of about 1.2 mm. The dimensions of the nodes of such strut were estimated from the numerical model to be 65 mm and 45 mm for the top and bottom nodes, respectively. These dimensions, which agree well with cross-section analysis calculations, defined the geometry of nodes and strut used to develop the new model proposed in the following section.

4. New Short Column Macro Element (SCME) and OpenSees analysis

Whilst the finite element model of the building (Section 3) matched well the experimental results, such type of analysis is computationally demanding and therefore somehow inconvenient to analyse large buildings and/or dynamic loading effects. Consequently, this section presents a new and practical analytical model to analyse buildings with short columns. The model is implemented in OpenSees [22] software for comparisons with the finite element model.

4.1. Frame geometry and element type

The tested building was modelled as a single 2D frame made of displacement type beam-column elements. The cross-section of the elements was discretised with fibres of three materials (see Fig. 9a): i) unconfined concrete (concrete cover), ii) confined concrete (core concrete) modelled based on Chang and Mander's confinement model [36], and iii) steel (reinforcing bars). Six strut and tie elements (Fig. 9a) were used to model the shear load-transfer mechanism within the short column, as detailed below.

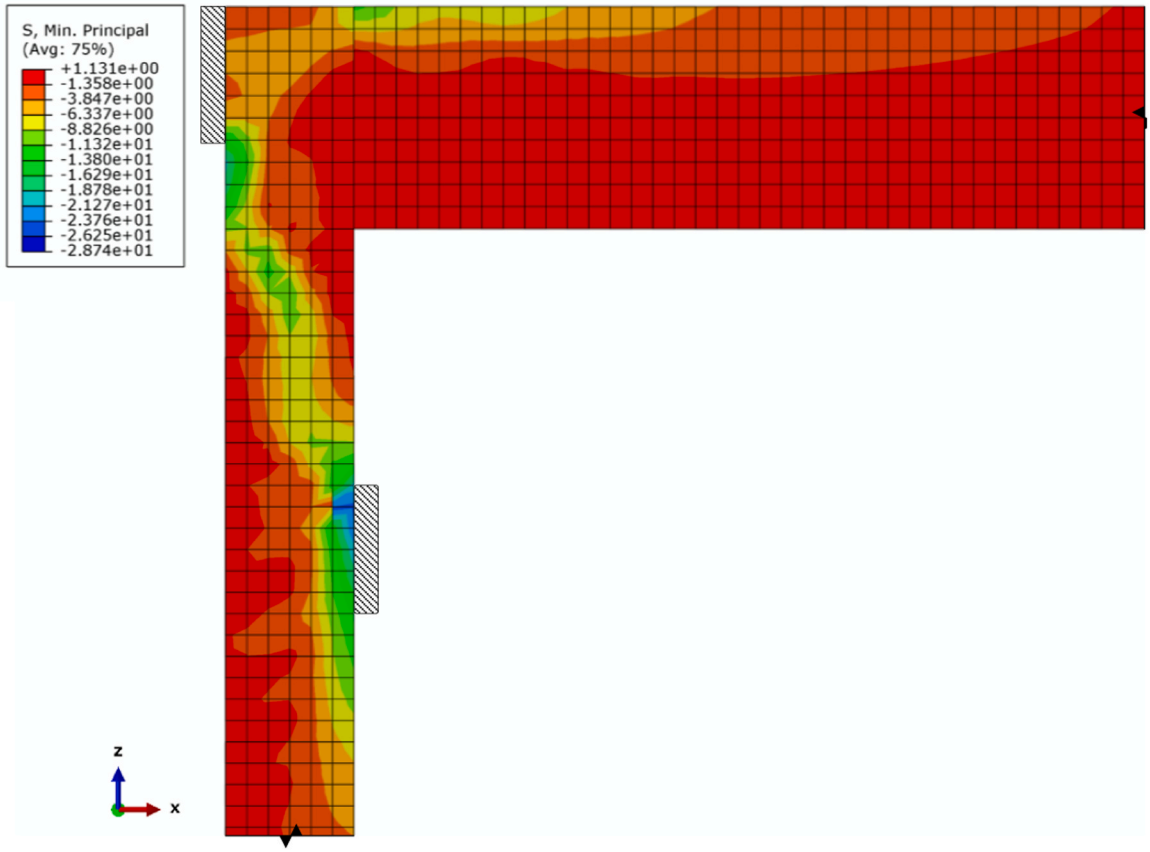

Fig. 8. Minimum principal stress field along short column and joint (displacement = 3.75 mm).

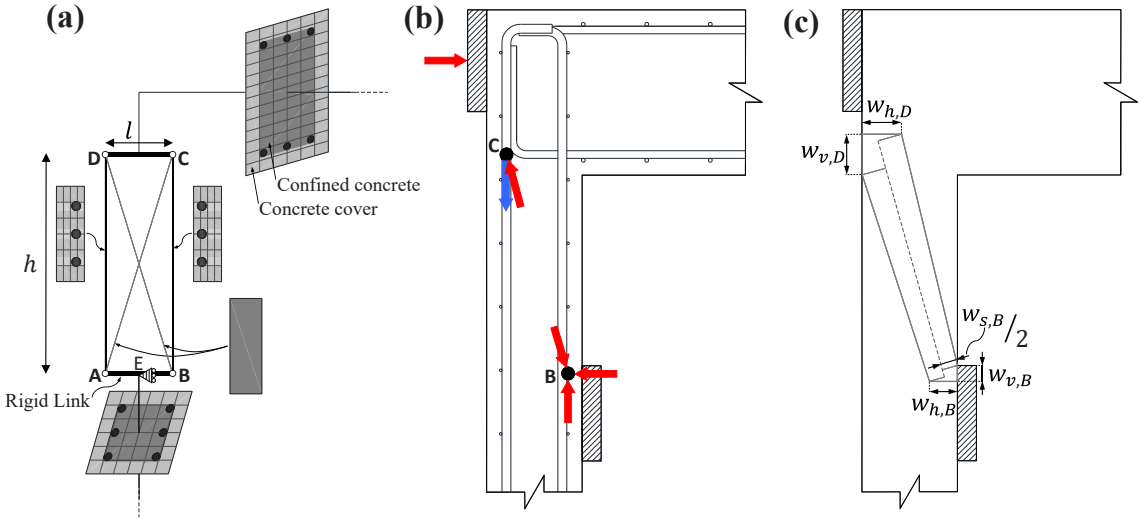

Fig. 9. New Short Column Macro Element (SCME) to model shear-flexure behaviour of short columns (a) SCME topology, (b) force distribution, and (c) strut and node formation.

4.2. New SCME

In this study, a new Short Column Macro Element (SCME) is proposed to model the behaviour of concrete short columns, as shown in Fig. 9a. The geometry of the SCME was defined using a strut-and-tie approach, as well as the experimental observations and numerical analyses of crack patterns and principal stress paths presented in Section 3.3.

In Fig. 9a, the bottom right node B is a CCC node created by the three compression forces shown in Fig. 9b: the reaction at the bearing face, the cross-sectional force at the back-face, and the force imposed by the strut. The width of the bearing face (see $w_{v,B}$ in Fig. 9c) was taken to be 25 mm based on the stress distribution at the interface between the column and the short-column boundary condition, as determined from the finite element analysis. Whilst the effect of the width of the bearing face on the strut angle and its size is minimal, the width of the bearing face was considered in the analysis to get a more precise location of the centroid of node B. For design, a more straightforward approach can be considered by assuming a negligible $w_{v,B}$, hence the node centroid would be at the bottom of the clear height of the short column (in this case at 300 mm down from the beam).

Likewise, the width of the back face $w_{h,B}$ (see Fig. 9c) was chosen to be equal to the neutral axis depth (i.e. 44 mm) at the yielding moment of the column, based on the centre of gravity of the compressive stress of the section. This is because the neutral axis depth represents the region in compression at that location. The width of the strut at node B ($w_{s,B}$ in Fig. 9c) was taken as the width normal to the centreline, according to Eq. (2):

$$w_{s,B} = w_{h,B}\sin\alpha + w_{v,B}\cos\alpha = 50 \text{ mm} \tag{2}$$

where $\alpha = \tan^{-1}h/l$ is the inclination angle of the strut, and h and l are the height and width of the SCME, respectively.

The width of the back face of the bottom left node A ($w_{h,A}$) of the SCME was equal to $w_{h,B}$. The width of the strut between points AC ($w_{s,A}$) was taken as the projection of $w_{h,A}$ onto the axis perpendicular to the strut:

$$w_{s,A} = w_{h,A}\sin\alpha \tag{3}$$

The top left node D (Fig. 9a) is a CCT node, created by the compression from the external load, the compression imposed by the strut, and the tension along the column's longitudinal reinforcement (Fig. 9b). Node D was located at the intersection of the centrelines of the column and beam's (bottom) longitudinal reinforcement of the tested building. The width of the horizontal ($w_{h,D}$) and vertical ($w_{v,D}$ in Fig. 9c) faces of node D was taken as twice the distance from the centreline of the reinforcement to the concrete face. Accordingly, $w_{h,D}$ = 62 mm and $w_{v,D}$ = 64 mm for the tested building. A constant strut width equal to the minimum width (i.e. $w_{s,C}$ = 50 mm) was considered in the analysis, as this captures the maximum resistance of the compressive strut. The depth of all SCME elements was equal to the column depth (150 mm in this case).

4.3. Material and element assignment for SCME

The diagonal struts AC and BD were modelled as truss elements made of plain concrete, using a *ConcreteCM* material in OpenSees. The negative effect of transverse tension on the concrete strength was considered using the approach included in Eurocode 2 [25], as defined by Eq. 4:

$$f_c^e = 0.6\left(1 - \frac{f_{cm}}{250}\right)f_{cm} \tag{4}$$

where f_c^e is the effective concrete compressive strength in the strut (in MPa). To account for the effect of confinement provided by the stirrups, the effective strength of the confined concrete (f_{cc}^e) was calculated using Mander et al.'s model [36] (Eq. 5):

$$f_{cc}^e = \varphi f_c^e \tag{5}$$

where φ is a confined strength ratio, found to be 1.10, which resulted in a value f_{cc}^e. = 21.0 MPa.

The post peak stress-strain behaviour of the strut was modified to consider its aspect ratio [37–39]. The Chang and Mander concrete model in OpenSees allows for the post peak branch to be adjusted by defining a shape factor r_c, which was originally proposed based on Tsai's uniaxial compressional model [40,41]. The factor r_c was calibrated based on the relationship proposed by Palmquist and Jansen [37], and its value was found to be r_c = 10 according to the calculations presented in Appendix A.

The two vertical elements AD and BC of the SCME (see Fig. 9a) were modelled as truss elements made of reinforced concrete, with widths $w_{h,A}$ and $w_{h,B}$, respectively. The concrete in these elements was modelled using the *ConcreteCM* material defined in OpenSees. The effect of the stirrup confinement was ignored for these edge vertical elements and therefore the concrete compressive and tensile strengths were taken as

$f_{cm} = 37.0$ MPa and $f_{ct} = 3.3$ MPa, respectively. Each element had three reinforcing bars according to the cross section of the columns. The bars were modelled using a *Steel02* material model with material properties as described in the experimental section of this study.

The horizontal elements AB and DC of the SCME were modelled as rigid links (see Fig. 9a) to allow the transference of moments and forces from the building to the SCME.

4.4. Analysis of tested building in OpenSees

4.4.1. Load and boundary conditions

The bottom of the columns was modelled as fully fixed. To simulate the short column, node E (located at the middle of the bottom rigid link of the SCME, Fig. 9a) was restrained against displacement in the X direction. A gravity nodal load of 13 kN (including self-weight) was applied at the top of each column under load control. A lateral pushover analysis was performed under displacement control via a nodal force at the top node of the left column, up to a maximum displacement of 6.0 mm.

4.4.2. Results and discussion

Fig. 10 compares the load vs displacement results obtained from OpenSees and Abaqus® models, as well as the backbone curve obtained from the tests on the building. The results indicate that the 2D frame modelled in OpenSees had an initial stiffness of 119 kN/mm, which is similar to that obtained from the finite element model on Abaqus®. The model reached a peak load of 142 kN at a displacement of 4.48 mm. Failure of the OpenSees model was due to the compressive failure of strut DC, which agrees well with the experimental observations. The results also show that, compared to Abaqus®, the load-displacement curve obtained from OpenSees matches better the experimental envelope. However, since the shear stirrups were not explicitly modelled in OpenSees, the horizontal shift in displacement recorded during the test and captured by Abaqus® at the onset of stirrup yielding could not be reproduced by the OpenSees model.

In the new SCME, the shear deformation is a function of the stiffness of the shear transfer mechanisms acting within the SCME. Fig. 11 shows the proportion of shear displacement δ_s (as % of the local short column deformation) within the short column for both OpenSees and Abaqus® models. In this figure, the shear displacements δ_s were decoupled from the flexural displacements using Massone and Wallace's model [42]. The

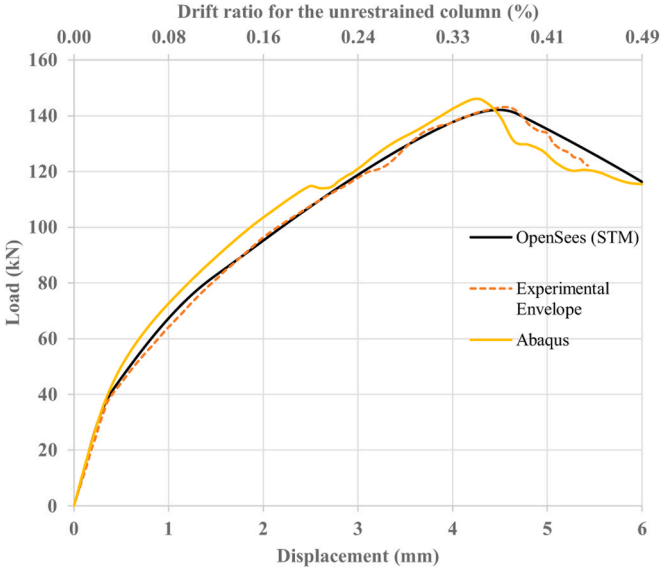

Fig. 10. Load vs displacement results from OpenSees, Abaqus® and experimental envelope results from tested building.

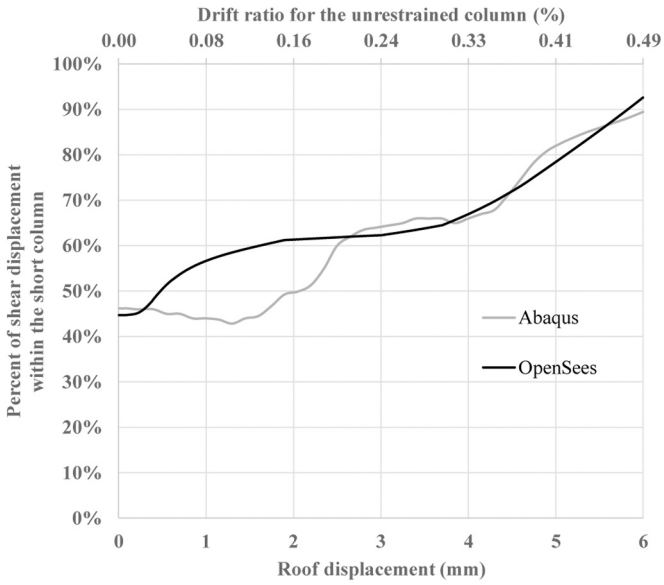

Fig. 11. Decomposition of shear-flexural displacement of short column (conventional concrete).

results in Fig. 11 show that both OpenSees and Abaqus® models calculate the initial δ_s to be 45% of the short column's total deformation. It is also shown that δ_s increases faster in the SCME (in OpenSees) as the global lateral displacement of the frame increases. This is because the SCME was specifically designed to deform in shear from the start of the analysis, whereas the strut and tie mechanism in Abaqus® can only form after the structure has undergone an initial amount of deformation. At higher displacements (>2.6 mm), however, both models calculate similar shear and flexural components of deformation. Moreover, the running time for the OpenSees simulation was only two minutes, whereas that of Abaqus® took an average of five hours to give results. This indicates that the new SCME proposed in this article can predict accurately the load-displacement behaviour of short columns throughout the entire load history (including the elastic behaviour, first cracking, peak capacity, and post-peak softening up to failure) with much less computational time. The results in Fig. 11 also indicate that the deformation capacity of the short columns was very limited, which results from the premature shear failure of the element.

4.4.3. Model validation

To investigate the accuracy of the new SCME at predicting results from short columns with different geometries and materials, the experimental results from short columns (Specimens 1 and 7) reported by Moretti and Tassios [18] were used. Specimen 1 had an aspect ratio of 1.0 ($l = 250$ mm, $h = 500$ mm), whereas Specimen 7 had an aspect ratio of 2.0 ($l = 250$ mm, $h = 1000$ mm). The two Specimens were tested in double curvature until failure. The unconfined concrete compressive strength of both Specimens was 36.0 MPa. Further details of the validation strategy are summarised in Appendix B. Figs. 12a-b compare the load vs displacement results obtained from the OpenSees model with the new SCME, as well as the backbone curve from Specimens 1 and 7 tested by Moretti and Tassios [18]. The results confirm that the proposed SCME captures well the behaviour of short columns, particularly for Specimen 1 that had a smaller aspect ratio. This is reasonable since the new SCME proposed in this study was explicitly developed for columns with short aspect ratio with predominantly shear-dominated behaviour.

The good agreement in results confirmed that the boundary conditions and general behaviour adopted in the new SCME replicate well the behaviour of short concrete columns of buildings. However, it is evident that the deformation capacity of the short columns was very limited. Accordingly, the following section uses the 2D frame model developed

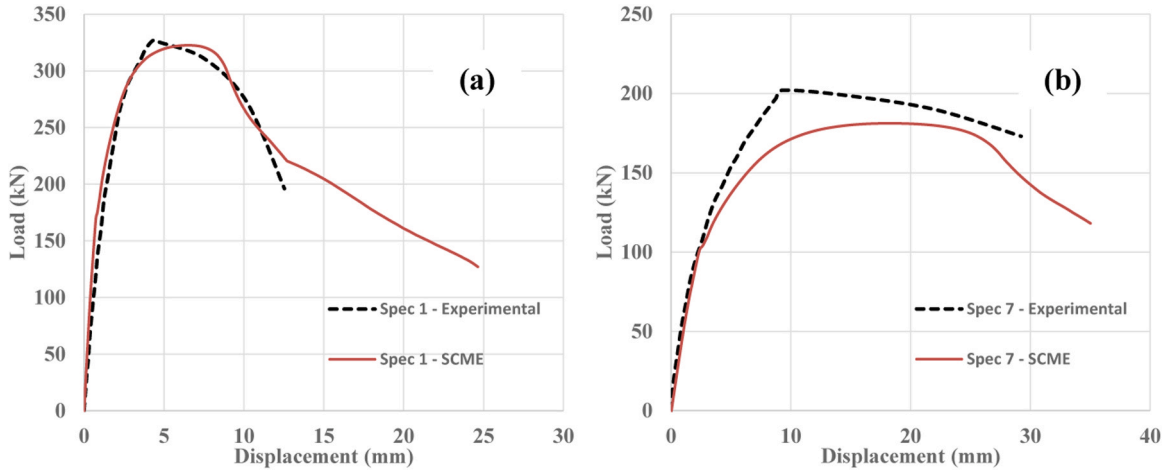

Fig. 12. Load vs displacement results from OpenSee and experimental envelope results from (a) Specimen 1 and (b) Specimen 7 tested by Moretti and Tassios [18].

in OpenSees and Abaqus® to examine numerically the feasibility of using highly deformable FRP CRuC to increase the deformability of short columns. It should be noted that whilst the results from the OpenSees model agree well with the test results and the numerical results from Abaqus®, further research should validate the applicability of the new SCME to other cases studies with different geometry to the short columns presented in this article.

5. Numerical investigation on highly deformable FRP CRuC short columns

Further numerical analyses on OpenSees and Abaqus® examined the behaviour of buildings with short columns made of FRP CRuC. A rubber content of 60% in the CRuC was assumed in the investigation. Previous studies by the authors [43] indicate that such level of aggregate replacement proved suitable to ensuring a high deformability in concrete, while also maintaining a good compressive strength for structural use. Aramid FRP (AFRP) confining jackets were chosen as these provide a good tensile strength at higher ultimate elongation compared to other confining materials [3]. In the analysis, the rupture strain of the AFRP jackets was taken as 65–70% of the ultimate sheet strain given by the manufacturer. This is justified as such values were found to match well actual sheet strains measured on AFRP CRuC cylinders tested in compression, as reported in a previous study by the authors [3]. The reduced ultimate strain of the jackets is lower than the uniaxial rupture strain of the sheet due to the fact that the jacket might have imperfections and stress concentrations, as demonstrated in previous research [23].

5.1. Numerical simulation of FRP CRuC short columns in Abaqus®

The Abaqus® model described in Section 3 was modified to carry out this analysis. The first modification included the separate modelling of: i) the short column using RuC instead of normal concrete, and ii) the addition of external AFRP jackets as confinement. The stress-strain behaviour of RuC was obtained from the constitutive model proposed by Bompa et al. [44], who used similar materials and percentage of rubber replacement as those use in the tested building. Table 1 summarises the material properties of the RuC adopted in the analysis. The dilation angle in the CDP model was increased to $\psi = 45^{\circ}$ to consider the high lateral dilation of RuC, as suggested in previous research [4,6].

The AFRP confinement was modelled as a shell-membrane, with a user-defined *Lamina* material model. Table 1 provides the material properties of the dry AFRP sheets as provided by the producer. A tie constraint was used to connect the AFRP jacket to the concrete surface, assuming perfect bond between the two surfaces.

Table 1
Material properties of RuC proposed by Bompa et al.'s model and AFRP properties.

Conventional concrete	f_{cm}	-	-	-	-	-
Benchmark concrete [44]	63	-	-	-	-	-
RuC	ρ_{vr} (%)	λ	E_{rc}	f_{rc}	ε_{rc}	$f_{rc,t}$
60% rubber replacement	60	2.9	9.2	6.7	0.105	0.92
AFRP CRuC	f_{cr}	ε_{cr}	f_{crc}	ε_{crc}	f^{e}_{crc}	ε^{e}_{crc}
1L (1 Layer of AFRP)	8	0.14	28	3.00	26	2.77
2L (2 Layers of AFRP)	10	0.17	47	4.34	44	4.00
3L (3 Layers of AFRP)	12	0.19	66	5.42	61	5.00
Aramid FRP	t (mm)	E_f	f_u	ε_{fu}	-	-
S&P A120/290	0.2	116	2400	2.5	-	-

Strength f in (MPa), Young's modulus E in GPa, and strain in %

In Table 1, ρ_{vr} is the percentage of rubber replacement by volume; λ is a factor for the type of rubber used (λ=2.9 for a coarse and fine rubber); whereas E_{rc}, f_{rc}, ε_{rc}, and $f_{rc,t}$ are the Young's modulus, peak compressive strength, strain at peak compressive strength, and peak tensile strength for unconfined rubberised concrete, respectively. The latter variables and corresponding values were adopted from Bompa et al.'s model [44]. For the AFRP CRuC part of the table, f_{cr} and ε_{cr} are the critical stress and strain, respectively [45]; f_{crc} and ε_{crc} are the ultimate compressive strength and strain of AFRP CRuC, respectively; f^{e}_{crc}, and ε^{e}_{crc} are the effective ultimate compressive strength and strain of AFRP CRuC, respectively, which account for the inclination of the strut in the new SCME model. Note that the critical stress f_{cr} and corresponding strain ε_{cr} represent the start of unstable crack propagation and concrete expansion, which in turn activate the confining jacket and change the gradient of the stress-strain constitutive curve of AFRP CRuC (see Figure C1 in Appendix C). Full details of the AFRP CRuC constitutive model can be found in Raffoul et al. [45].

In Table 1, the dry AFRP properties t, E_f, f_u, and ε_{fu}, are the dry sheet thickness, Young's modulus, ultimate rupture strength, and strain at rupture, respectively, as given by the AFRP producer.

Based on the above material properties, three frames were modelled assuming AFRP jackets with 1, 2 or 3 layers around the short columns. Such three frame models are identified in Table 1 and in subsequent sections/tables as 1L, 2L, and 3L, respectively. A lateral displacement was imposed at the top of the column until "failure" of the frame model occurred.

5.1.1. Results and analysis of numerical simulations

Fig. 13 compares the load vs displacement curves obtained from Abaqus® for models 1L, 2L, and 3L. The figure also includes the envelope load-displacement curve of the building tested in this study (made

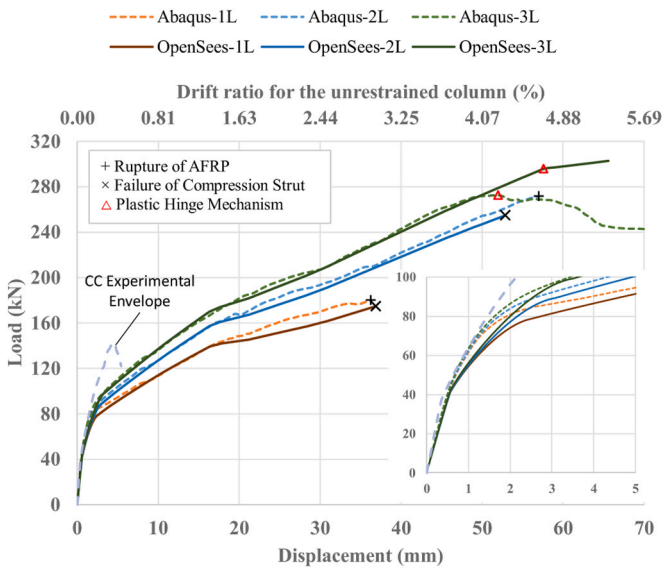

Fig. 13. Load vs displacement of frame models with AFRP CRuC short columns, results from Abaqus® and OpenSees with new SCME.

of CC), as well as OpenSees results to be discussed later in Section 5.2. The behaviour of the three frame models shown in Fig. 13 can be described by four distinctive phases:

1) *Elastic Phase I*, which is not affected by the level of confinement as the AFRP is not yet activated at this stage. The initial stiffness of all frames was around 83 kN/mm.
2) *Transition Phase II*, where the loss in stiffness is due to the development of cracking at the short column/beam interface. At the onset of this phase, the compressive stresses developed within the short column cause its lateral expansion, which in turn activates the AFRP jackets. This phase ends when the RuC reaches its peak strength, which occurs at higher strain values for increasing values of confinement stiffness. This phase ends at a lateral load of 83 kN, 94 kN, and 102 kN for frames 1L, 2L and 3L, respectively.
3) *Linear hardening Phase III*, which stiffness is determined by the level of confinement along with the strength from all other structural elements. The stiffness of this branch was 4.3, 5.4, and 6 kN/mm for frames 1L, 2L and 3L, respectively.
4) A further reduction in stiffness (*Phase IV*) is observed due to yielding of the longitudinal reinforcement at the bottom of unrestrained column C1B (hinge formation), which occurs after a lateral displacement of approximately 19 mm for all three confinement levels.

Phase IV ends with the failure of the frame model. Models 1L and 2L failed when the AFRP reached its rupture strain of 1.75%, which occurred at lateral displacements of 36 mm (2.9% drift ratio) and 57 mm (4.6% drift ratio), respectively. Conversely, frame 3L failed following the formation of a plastic hinge mechanism when the longitudinal reinforcement in column C1A yielded at the short column restraint level, which occurred at a frame displacement of 52 mm and a lateral load of 272 kN. At this stage, the strain in the AFRP was 1.3%.

It should be noted that the load-displacement behaviour described above is in line with that observed by Wang et al. [16] (see Figure C2 in Appendix C). Indeed, Wang et al. proved that the load-displacement behaviour of rectangular prisms confined with FRP CRuC tested in shear also presented four characteristic phases, as discussed by El Khouri [29]. The results from Abaqus® confirm that whilst the behaviour of the frame was dominated by the short column effects, the replacement of conventional concrete with AFRP CRuC improved the frame's performance by increasing the deformability of the short column.

Fig. 14 shows the strain profile vs displacement obtained from Abaqus® for the three frame models 1L, 2L, and 3L. The results were obtained at the centre of the AFRP sheet along the faces of the column both parallel (X direction) and perpendicular (Y direction) to the loading direction. It is shown that, as expected, the FRP strains in the loading direction were higher than the strains in the transverse direction as the fibres resisted the development of diagonal cracking. Moreover, the FRP strains decreased as the amount of FRP layers increased, which in turn led to a more uniform distribution of strains around the column perimeter. For example, at a drift ratio of 2.44% for the unrestrained column (30 mm frame displacement), the strain in the AFRP along the loading direction reached 1.4% for model 1L, while strain levels of 1.03%, and 0.82% were recorded for models 2L and 3L, respectively.

5.2. Modelling FRP CRuC short columns using the proposed SCME in OpenSees

The proposed SCME was modified to model the AFRP CRuC short column in OpenSees. Accordingly, the constitutive model developed by Raffoul et al. [45] was used here to i) define the uniaxial compressive behaviour of AFRP CRuC, which implicitly considers the effect of different confinement stiffnesses (i.e. different jacket thickness and type of FRP), and to ii) determine the relevant parameters of the *Concrete02* material model in OpenSees.

Since the fibres of the AFRP jacket around the short column were assumed as horizontal (i.e. perpendicular to the column axis), and because the strut is inclined at an angle of $\alpha = \tan^{-1} h/l$ as per Eq. 2, the effectiveness of the confinement to the compressive strut had to be reduced. To account for the reduced effectiveness of the confinement due to the relative inclination between the confining FRP fibres and the strut, the ultimate strength f^{e}_{crc} of the AFRP CRuC was reduced using Eq. 6.

$$f^{e}_{crc} = (f_{crc} - f_{cr})\sin^2\alpha + f_{cr} \tag{6}$$

where f_{crc} and f_{cr} are defined as the compressive strength and critical stress of the AFRP CRuC, respectively [45] (see Figure C1 in Appendix C).

Consequently, the ultimate strain, ε_{crc}, was also reduced at a ratio that maintains the second linear stiffness of the AFRP CRuC stress-strain relationship (Table 1). The material properties of the vertical elements of the SCME (AD and BC in Fig. 9a) were not reduced. The same

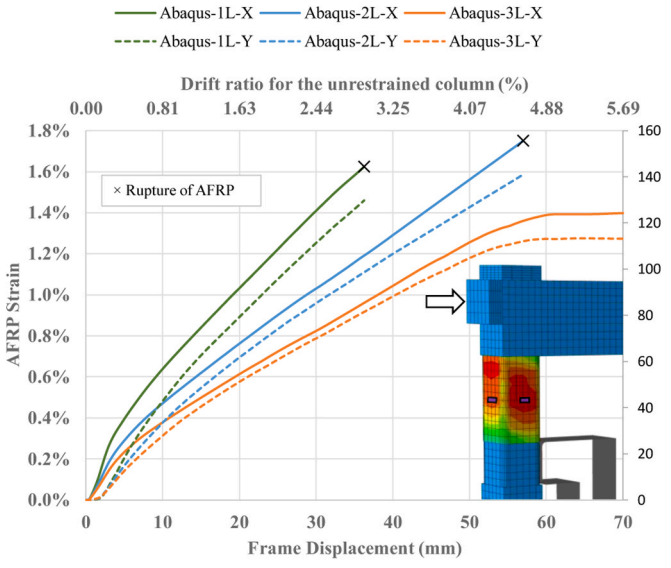

Fig. 14. Numerical lateral strains at centre of AFRP jacket in directions parallel (X) and perpendicular (Y) to loading direction, results obtained from Abaqus®.

boundary conditions and dimensions of the SCME with conventional concrete were also used for the AFRP CRuC SCME.

5.2.1. Results and analysis of the AFRP CRuC SCME simulations

Fig. 13 compares the load vs displacement curves of frames 1L, 2L and 3L with the AFRP CRuC SCME obtained from OpenSees. The results show that the *transition Phase II* was slightly softer in OpenSees than in Abaqus®. However, up to the peak strength of the RuC, the OpenSees results agreed well with those from the more advanced analysis in Abaqus®. The elastic stiffness for all three frames was around 77 kN/mm, whereas the stiffness of the *linear hardening Phase III* was 4.4, 5.2, and 5.6 kN/mm for frames 1L, 2L and 3L, respectively. At a lateral frame displacement of 16.8 mm, the steel at the bottom of the unrestrained column yielded for all three frame models, thus indicating the start of *Phase IV*. Frame models 1L and 2L failed when the strut reached its maximum strength, corresponding to the theoretical rupture of the AFRP jacket at a lateral displacement of 37 mm (3.0% drift ratio) and 52 mm (4.2% drift ratio), respectively. These results indicate that the use of FRP CRuC in the short column was very effective at increasing the deformation capacity of the building. Indeed, whilst the tested building failed at a small displacement of 5.4 mm (0.43% drift ratio), the use of FRP CRuC short columns with minimal confinement (one layer of AFRP only) increased the building's displacement by almost seven times to 37 mm (3.0% drift ratio).

On the other hand, frame model 3L failed due to the formation of a plastic hinge mechanism (which is consistent with the Abaqus® results) at a displacement of 57 mm and a lateral load of 295 kN. The results in Fig. 13 also confirm that the SCME in OpenSees simulated accurately the four-phase load-displacement behaviour observed in shear tests on rectangular prisms confined with FRP CRuC [16]. This provides further confidence on the suitability of the new SCME at predicting the behaviour of short columns made of FRP CRuC. The ductility of the frames was assessed based on the bilinear idealisation of the force-displacement curve according to FEMA 356 [46]. The displacement ductility values obtained from OpenSees were 18.9, 22.9, and 22.3 for the frame models 1L, 2L and 3L, respectively, which are somehow similar to those obtained from the analyses in Abaqus®.

Whilst the AFRP jacket was not explicitly modelled in the SCME in OpenSees, it was possible to estimate the lateral strain of the jacket using the uniaxial compressive strain levels of the strut obtained from the OpenSees results, and the equation of the adopted constitutive model for AFRP CRuC [45,47]. Fig. 15 compares the AFRP strains obtained from the SCME in OpenSees and those obtained from Abaqus®. The results in the figure show that the two curves are very similar up to the theoretical rupture strain of the AFRP jacket. This confirms that the new SCME is very effective at capturing the confining effect of the AFRP jacket.

5.3. Comparison between frame models with CC and CRuC short columns

The results in previous sections proved that short columns made of FRP CRuC can develop higher deformability than CC counterparts. This in turn led to a better utilisation of materials in the frame models since damage distributed more unfirmly among other structural elements, rather than being concentrated only in the short columns. For instance, while using CC in the short column limited the deformability of the frame model and prevented yielding of the longitudinal reinforcement, yielding occurred in the longitudinal bars of column C1B for all three models 1L, 2L and 3L. The higher ductility of the three AFRP CRuC frame models can be attributed to the unique mechanical properties of FRP CRuC, which enabled large shear deformations in the short column [16].

Fig. 16 shows the shear-flexure displacement decomposition of the AFRP CRuC short column for model 3L. Both results from Abaqus® and OpenSees with the new SCME are included. It is shown that the shear deformation of the short column accounts for 80–90% of the total frame deformations after a global displacement > 5 mm (0.4% drift ratio), i.e. once the frame model enters the *transition Phase II* that activates the AFRP jackets.

The numerical investigation presented in this article confirms that FRP CRuC can be used in high shear demand regions of buildings, which in turn can lead to a more ductile behaviour when compared to conventional concrete (CC) counterparts. However, since the proposed model SCME was calibrated with CC short columns, further research should verify experimentally the applicability of the new SCME to RuC and FRP CRuC. Moreover, research on FRP CRuC elements subjected to shear is scarce in the literature, and therefore future research should validate the accuracy of the model using other experimental datasets that include different types of FRP materials (such as Glass or Basalt FRP). A thorough parametric analysis is also necessary to assess the validity of the proposed numerical models in relation to the assumed modelling parameters.

It should be finally mentioned that the authors have also carried out shake table tests on buildings with short columns made of conventional

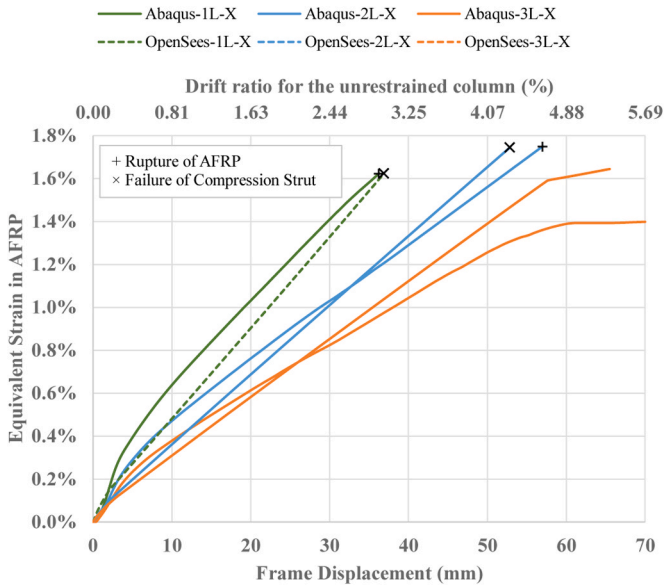

Fig. 15. Lateral strain in AFRP jackets for frame models with AFRP CRuC short columns, results from Abaqus® and OpenSees with new SCME.

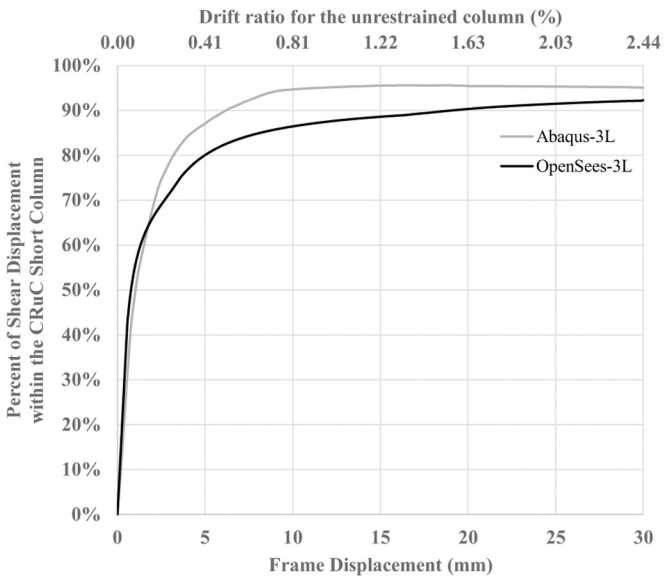

Fig. 16. Decomposition of the shear-flexural displacement of short column (CRuC-3L up to 30 mm lateral displacement of the frame).

concrete or FRP CruC [48]. The geometry, detailing, material properties and number of AFRP jackets examined in these tests were similar to those of frame model 3 L, discussed in Section 5 of this study. The results from these shake table tests confirmed that the use of highly deformable AFRP CRuC increased the drift capacity of the short columns by a factor of 3 over a counterpart frame with conventional short concrete columns. These experimental results are thus fully aligned with the numerical findings discussed in Section 5 of this study. Due to space limitations, the results of these shake table tests will be reported in a forthcoming article.

6. Summary and conclusions

This article proposed a new and practical Short Column Macro Element (SCME) that predicts accurately the behaviour of short concrete columns. A 1/3-scale one-storey building with short columns made of conventional concrete was subjected to lateral loading tests until failure. The experimental results from the building are then used to calibrate a numerical model in Abaqus®. The experimental crack patterns and stress distribution from Abaqus® were used to determine the load path within the short column. Based on this information, a new strut-and-tie SCME was proposed and implemented in OpenSees. Subsequently, the frame models calibrated in OpenSees and Abaqus® were modified to examine numerically the effectiveness of highly deformable FRP CRuC at increasing the deformability of short columns with different levels of FRP confinement (1, 2 or 3 layers). Based on the results of this study, the following conclusions can be drawn:

- Failure of the tested building made of conventional concrete was dominated by the brittle shear failure of the short columns. Failure occurred at a small displacement of only 5.4 mm (0.43% drift ratio) for the unrestrained column. The building did not develop any ductility as the longitudinal reinforcement of all elements remained withing the elastic range.
- The 2D model of the building in Abaqus® was effective at providing details of the evolution of the main load transfer mechanism within the short columns. The analytical stress distribution obtained from the numerical analyses agreed very well with the experimental cracking pattern. It also provided insight into the evolution of the main load transfer mechanism within the short columns.
- The new SCME captured accurately the behaviour of the short columns of the tested building modelled in OpenSees. For the tested building, the OpenSees results predicted accurately the load-displacement behaviour of short columns throughout the entire load history (elastic behaviour, first cracking, peak capacity, and post-peak softening up to failure). Compared to Abaqus®, the load-displacement curve obtained from the OpenSees model matched better the experimental envelope of the building. Moreover, the adoption of the SCME in OpenSees significantly reduced computational time to minutes rather than hours for the analysed building. The new SCME also predicted well the results from short columns with different geometries and materials reported in the literature.
- The proposed SCME was modified to account for the use of highly deformable FRP CRuC in short columns. The numerical results show that FRP CRuC short columns have a four-phase load-displacement behaviour consistent with previous shear tests on FRP CRuC prisms. This confirmed the suitability of the new SCME at predicting the behaviour of short columns made of FRP CRuC.
- The use of highly deformable FRP CRuC in short columns significantly improved the performance of the frame models analysed in OpenSees. Whilst the tested building failed at a small displacement of 5.4 mm (0.43% drift ratio), the numerical analysis showed that use of FRP CRuC short columns with minimal confinement (one layer of AFRP only) increased the building's displacement by almost seven times to 37 mm (3.0% drift ratio). This also enabled more redistribution of forces to other structural members.

CRediT authorship contribution statement

Imad El Khouri: Conceptualization, Data curation, Formal analysis, Investigation, Methodology, Software, Validation, Visualization, Writing – original draft. **Reyes Garcia:** Conceptualization, Funding acquisition, Investigation, Methodology, Supervision, Validation, Visualization, Writing – original draft, Writing – review & editing. **Petru Mihai:** Formal analysis, Investigation, Methodology, Software, Supervision. **Mihai Budescu:** Funding acquisition, Investigation, Project administration, Resources, Supervision. **Nicolae Taranu:** Conceptualization, Funding acquisition, Investigation, Methodology, Project administration, Resources. **Ionut Ovidiu Toma:** Funding acquisition, Investigation, Methodology, Project administration, Supervision. **Maurizio Guadagnini:** Conceptualization, Formal analysis, Investigation, Project administration, Supervision, Writing – original draft. **David Escolano-Margarit:** Formal analysis, Investigation, Software, Validation. **Ioana Sorina Entuc:** Formal analysis, Validation. **Gabriel Oprisan:** Formal analysis, Validation. **Iman Hajirasouliha:** Conceptualization, Formal analysis, Funding acquisition, Methodology, Project administration, Supervision, Validation, Writing – review & editing. **Kypros Pilakoutas:** Conceptualization, Funding acquisition, Investigation, Methodology, Project administration, Supervision, Writing – review & editing.

Declaration of Competing Interest

The authors declare that they have no known competing financial interests or personal relationships that could have appeared to influence the work reported in this paper.

Data availability

No data was used for the research described in the article.

Acknowledgments

The research leading to these results has received funding from the European Union Seventh Framework Programme [FP7/2007–2013] under grant agreement n° 603722. The authors would like to thank the technical staff at the Civil Engineering Laboratory at the Technical University Gheorghe Asachi (Iasi, Romania) for their support to conduct the tests reported in this article.

Appendix A. Calibration of the shape factor r_c in Chang and Mander's concrete stress-strain model

Eq. A1, developed by Tsai and implemented in Chang and Mander's model, gives the stress-strain relation for unconfined concrete:

$$y = \frac{nx}{1 + \left(n - \frac{r_c}{r_c - 1}\right)x + \frac{x^{r_c}}{r-1}} \tag{A1}$$

$$x = \frac{\varepsilon_c}{\varepsilon_{cm}} \tag{A2}$$

$$y = \frac{\sigma_c}{f_{cm}} \tag{A3}$$

where ε_c and σ_c are the compressive strain and stress, respectively; ε_{cm} is the compressive strain at peak stress; n and r_c are parameters that control the shape of the stress-strain curve and are defined by Chang and Mander as follows:

$$n = \frac{7.2}{f_{cm}^{3/8}} \tag{A4}$$

$$r_c = \frac{f_{cm}}{5.2} - 1.9 \tag{A5}$$

Eqs. A1-A5 provide the full stress-strain curve of a concrete cylinder as a function of the peak strength and strain.

Palmquist and Jansen developed Eqs. A6 - A8 to calculate the post-peak strain taking into account the aspect ratio of the element under compression:

$$\varepsilon = \left(\varepsilon_{cm} + \frac{\sigma_c - f_{cm}}{E_c}\right)\frac{H_B}{H} + \frac{1}{V}\left(\frac{f_{cm}}{\sigma_c} - N\right)^M \frac{H_D}{H} \tag{A6}$$

$$H_B = H - H_D \tag{A7}$$

$$H_D = W\left(2 - \frac{\sigma_c}{f_{cm}}\right) \tag{A8}$$

where H is the height of the specimen; H_D is the height of the damage zone in the specimen; and $H_B$is the height of the bulk zone beyond the damage zone (see Figure A1). Likewise, M, N and V in Eq. A6 are empirical constants calibrated for each type of concrete based on the full stress-strain curve.

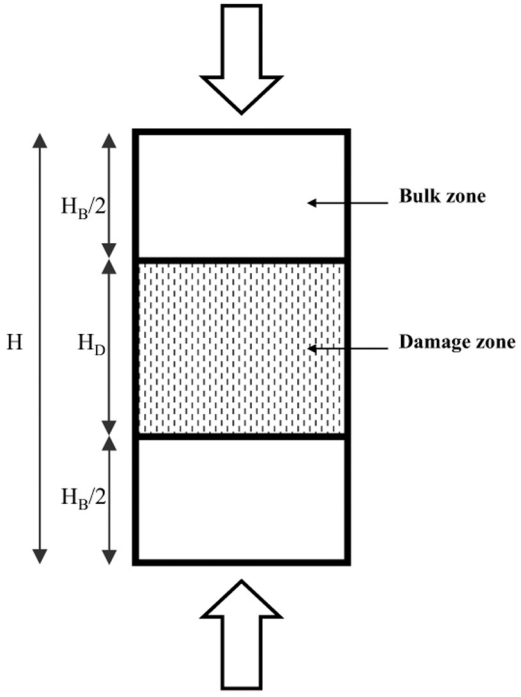

Fig. A1. Definition of the compression damage zone according to Palmquist and Jansen. [37].

Palmquist and Jansen's post-peak strain model was calibrated to fit the stress-strain curve of Chang and Mander for a standard 100 × 200 mm cylinder tested in compression (see Figure A2, for an initial shape factor $r_c = 5.2$). The empirical constants were found to be equal to 0.145, 0.992, and 225 for M, N and V, respectively.

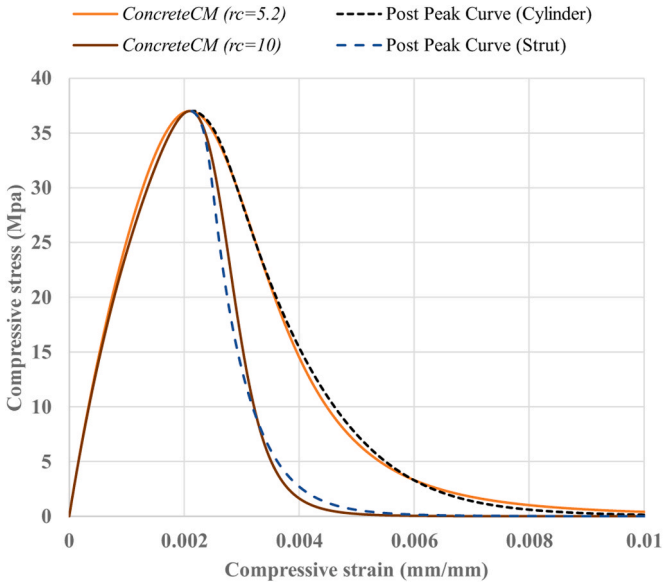

Fig. A2. Calibration of the Shape Factor r_c in Chang and Mander's compressive stress-strain model to account for the slenderness ratio of a concrete strut [40].

The post-peak behaviour was then modified according to the aspect ratio of the strut, which was calculated based on the equivalent diameter of the rectangular area (equal to 97 mm) and an element length of 358 mm. The shape factor r_c was then calibrated to fit the new post-peak behaviour for the strut (see Figure A2), which resulted in a shape factor $r_c = 10$.

Appendix B. Validation of new SCME

The validation was done using Specimens 1 and 7 tested by Moretti and Tassios [18]. The experimental programme involved columns of same cross-section but varying length. Specimen 1 had an aspect ratio equal to 1 (width of 250 mm, length of 500 mm) and somehow similar to the short column in the scaled-down building presented in this article. Specimen 7 had an aspect ratio equal to 2 (with of 250 mm, length of 1000 mm). The columns were reinforced with eight 14 mm longitudinal bars (Figure B1a) which had yield and ultimate strengths of $f_{ly} = 480$ MPa and $f_{lu} = 740$ MPa, respectively. The shear reinforcement consisted of one tie and two cross-ties at a spacing of 50 mm, having a yield strength of $f_{sy} = 300$ MPa. The columns were tested in a double curvature as shown in Figure B1b.

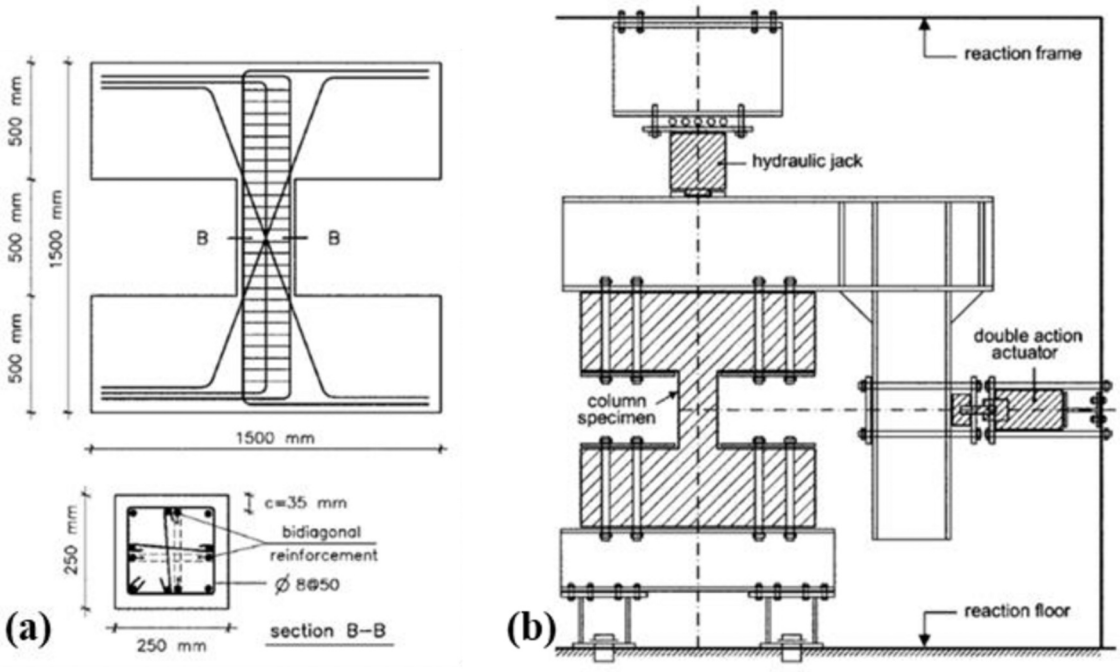

Fig. B1. (a) Specimen cross-section and reinforcement, and (b) test setup [18].

Using the same topology described in Section 4.2 (as shown in Figure B2), the geometry of the SCME for the validation on OpenSees was obtained as described below.

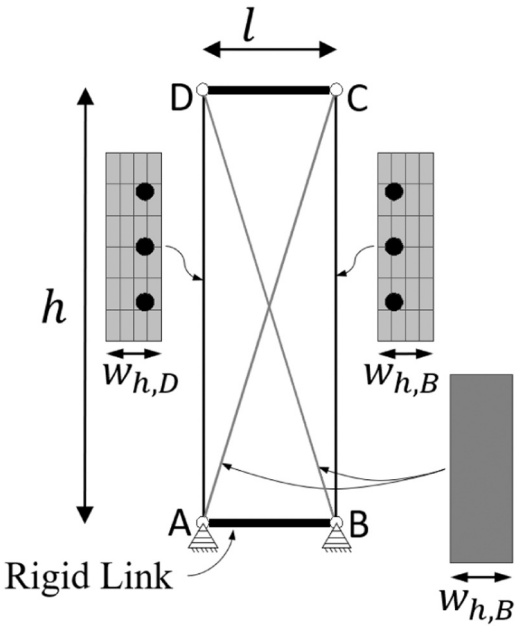

Fig. B2. SCME topology and boundary conditions used to model Specimens 1 and 7 in OpenSees.

The width of the node face $w_{h,B}$ at node B was chosen to be equal to the neutral axis depth (calculated to be 67 mm) at the yielding moment of the column, based on the centre of gravity of the compressive stress of the section. The neutral axis was calculated using a moment-curvature analysis. Due to symmetry of the cross-section, the following values were taken $w_{h,B} = w_{h,A} = w_{h,D} = w_{h,C}$. In the case of double curvature bending tests, there are no vertical nodes or strut supports, which simplifies the dimensioning of the struts, as mentioned in the main text. The width of the diagonal struts is simply taken as the width of the nodes (67 mm). The depth of all SCME elements was equal to the column depth of 250 mm.

The diagonal struts AC and BD were modelled as truss elements made of plain concrete, using *ConcreteCM* material in OpenSees. The effective concrete compressive strength in the strut was calculated to be 18.5 and 19.3 MPa for Specimens 1 and 7, respectively. Based on Mander et al.'s confinement model, the confined strength ratio φ was 1.4. The effective strength of the confined strut was 26 and 27 MPa for Specimens 1 and 7, respectively. The shape factor r_c was calibrated to be 12.

The two vertical elements AD and BC of the SCME were modelled as truss elements made of reinforced concrete with material definitions as given by Moretti and Tassios [18].

The model boundary conditions were set to force a double curvature, and a monotonic increasing displacement was applied to reach failure. The results from the validation are discussed in Section 4.4.3 of the article.

Appendix C. Axial, lateral, and shear stress-strain behaviour of FRP CRuC

Figure C1 shows the stress-strain model adopted for the analysis of FRP CRuC concrete. The constitutive model was extensively calibrated with results from cylinders confined with Carbon and Aramid FRP CRuC under uniaxial compression [3,23,45].

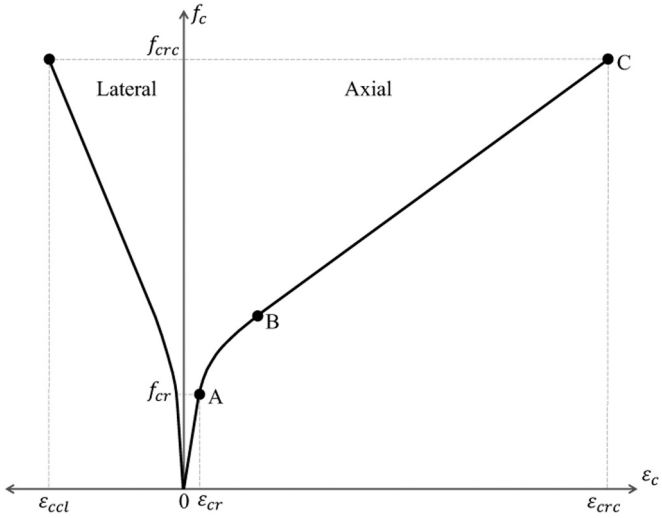

Fig. C1. Schematic axial and lateral stress-strain behavior of CRuC.

Figure C2 shows the shear stress-strain model adopted from Wang et al. [16]. The three phases of the shear stress-strain documented by

Wang match the results obtained in the short column lateral behaviour. The additional fourth phase shown in the figure describes the case of no-rupture of FRP and yielding of the structure that would exhibit a ductile yielding.

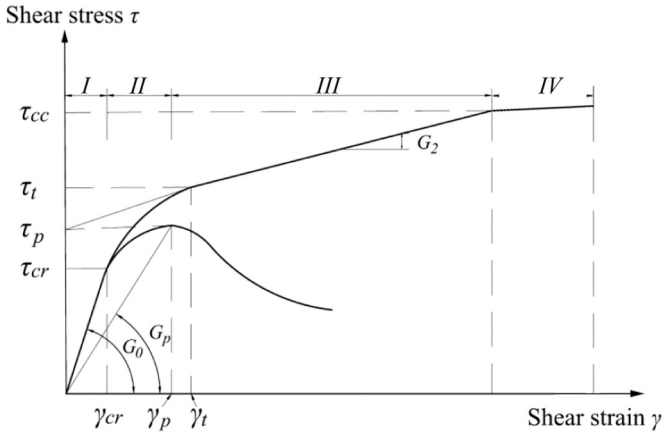

Fig. C2. Schematic shear stress-strain behavior of CRuC adopted from Wang et al. [16].

References

[1] ACI Committee 318. Building Code Requirements for Structural Concrete (ACI 318–14) and Commentary, Farmington Hills, MI, 2014, 519 pp.
[2] EN 1998–1. Eurocode 8: Design of structures for earthquake resistance - Part 1: General rules, seismic actions and rules for buildings, Comité Européen de Normalisation (CEN), Brussels Belgium, 2004.
[3] Raffoul S, Garcia R, Escolano-Margarit D, et al. Behaviour of unconfined and FRP-confined rubberised concrete in axial compression. Constr Build Mater 2017;V. 147:388–97.
[4] Youssf O, Elgawady MA, Mills JE, et al. An experimental investigation of crumb rubber concrete confined by fibre reinforced polymer tubes. Constr Build Mater 2014;V. 53:522–32.
[5] Lam L, Teng JG. Design-oriented stress–strain model for FRP-confined concrete. Constr Build Mater 2003;17:471–89.
[6] Duarte APC, Silva BA, Silvestre N, De Brito J, Júlio E, Castro JM. Tests and design of short steel tubes filled with rubberised concrete. Eng Struct 2016;112:274–86.
[7] Raffoul S, Escolano-Margarit D, Garcia R, Guadagnini M, Pilakoutas K. A new cyclic model for FRP-confined rubberized concrete. Struct Concr 2023;24(1):1627–41.
[8] Cao Y, Liu Y, Li X, Wu Y. Axial stress strain behavior of FRP-confined rectangular rubber concrete columns with different aspect ratio. Eng Struct 2023;297:116987.
[9] Skyrianou I, Valiakou EI, Koutas LN, Papakonstantinou CG. Behaviour of carbon or glass FRP-confined rubberised concrete under monotonic compression. Constr Build Mater 2023;406:133287.
[10] Elghazouli A, Bompa D, Xu B, et al. Performance of rubberised reinforced concrete members under cyclic loading. No. November 2017 Eng Struct 2018;V. 166: 526–45.
[11] Ismail MK, and, Hassan AAA. Performance of full-scale self-consolidating rubberized concrete beams in flexure. ACI Mater J 2016;V. 113(No. 2):207–18.
[12] Son KS, Hajirasouliha I, and, Pilakoutas K. Strength and deformability of waste tyre rubber-filled reinforced concrete columns. Constr Build Mater 2011;V. 25(No. 1): 218–26.
[13] AbdelAleem BH, and, Hassan AAA. Influence of rubber content on enhancing the structural behaviour of beam–column joints. Mag Concr Res 2018;V. 70(No. 19): 984–96.
[14] Bompa DV, and, Elghazouli AY. Behaviour of confined rubberised concrete members under combined loading conditions. Mag Concr Res 2021:1–19.
[15] Xu B, Bompa DV, Elghazouli AY, et al. Behaviour of rubberised concrete members in asymmetric shear tests. Constr Build Mater 2018;V. 159:361–75.
[16] Wang Z, Chen L, Guadagnini M, et al. Shear Behavior Model for FRP-Confined and unconfined rubberized concrete. J Compos Constr 2019;V. 23(No. 5):04019039.
[17] Yamada, M., and Furui, S. Research on the shear resistances of reinforced concrete members subjected to axial load, 1966.
[18] Moretti ML, Tassios TP. Behavior and ductility of reinforced concrete short columns using global truss model. Acids Struct J 2006;V. 103(No. 3):319–27.
[19] Yamada, M., and Furui, S. Shear resistance and explosive cleavage failure of reinforced concrete members subjected to axial load. Final report, 8th international congress IABSE, 1968. pp. 1091–1102.
[20] Wakabayashi, M., and Minami, K. An experimental study on hysteretic characteristics of reinforced concrete columns failing in shear. Proceedings of the 18th national symposium on bridge and structural engineering, 1972. pp. 97–112.
[21] Zhou W, Hong HP. Modeling error of strength of short reinforced concrete columns. Acids Struct J 2000;V. 97(No. 3):427–35.
[22] Mazzoni, S., McKenne, F., Scott, M.H., et al. Open System for Earthquake Engineering Simulation User Manual, Version 2.0, 2009.
[23] Raffoul S, Margarit DE, Garcia R, Guadagnini M, Pilakoutas K. A new cyclic model for FRP-confined rubberized concrete. Struct Concr 2023;V. 24(No. 1):1627–41.
[24] Anaggenisi: Innovative Reuse of All Tyre Components in Concrete, A Europear Commission Seventh Framework Programme, Grant agreement ID: 603722 https://cordis.europa.eu/project/id/603722.
[25] EN 1992–1-1. Eurocode 2: Design of concrete structures - Part 1–1: General rules and rules for buildings, Brussels Belgium, Comité Européen de Normalisation (CEN), 2004, 225 pp.
[26] EN 12390–3. Testing hardened concrete Part 3: Compressive strength of test specimens, Comité Européen de Normalisation (CEN), 2019.
[27] EN 10080. Steel for the reinforcement of concrete: Weldable reinforcing steel, General, Comité Européen de Normalisation (CEN), 2009.
[28] Dassault Systèmes SIMULIA. ABAQUS Software and Documentation, Ver 6.14, 2017.
[29] El Khouri, I. Highly deformable confined rubberised concrete elements for seismic applications, PhD thesis, Dept. of Civil and Structural Engineering, The University of Sheffield, 2021.
[30] Krätzig WB, and, Pölling R. An elasto-plastic damage model for reinforced concrete with minimum number of material parameters. Comput Struct 2004;V. 82(Nos. 15–16):1201–15.
[31] Hordijk DA. Tensile and tensile fatigue behaviour of concrete; experiments, modelling and analyses. Heron 1992;37(1):1–79.
[32] Alfarah B, López-Almansa F, and, Oller S. New methodology for calculating damage variables evolution in plastic damage model for RC structures. Eng Struct 2017;V. 132:70–86.
[33] Bažant ZP, and, Becq-Giraudon E. Statistical prediction of fracture parameters of concrete and implications for choice of testing standard. Cem Concr Res 2002;V. 32 (No. 4):529–56.
[34] Nana WSA, Bui TT, Limam A, et al. Experimental and numerical modelling of shear behaviour of Full-scale RC slabs under concentrated loads. Structures 2017;V. 10: 96–116.
[35] Genikomsou AS, Polak MA. Finite element analysis of punching shear of concrete slabs using damaged plasticity model in ABAQUS. Eng Struct 2015;V. 98:38–48. https://doi.org/10.1016/j.engstruct.2015.04.016.
[36] Mander JB, Priestley MJN, and, Park R. Theoretical stress-strain model for confined concrete. J Struct Eng 1988;V. 114(No. 8):1804–26.
[37] Palmquist SM, Jansen DC. Postpeak strain-stress relationship for concrete in compression. ACI Mater J 2001;V. 98(No. 3):213–9.
[38] Watanabe K, Niwa J, Yokota H, et al. Experimental study on stress-strain curve of concrete considering localized failure in compression. J Adv Concr Technol 2004; V. 2(No. 3):395–407.
[39] Tung ND, Tue NV. Post-peak behavior of concrete specimens undergoing deformation localization in uniaxial compression. Constr Build Mater 2015;V. 99: 109–17.
[40] Chang G.A., and Mander, J.B. Seismic energy based fatigue damage analysis of bridge columns: Part I - Evaluation of seismic capacity. Technical Report NCEER-94–0006, New York, 1994.
[41] Tsai WT. Uniaxial compressional stress-strain relation of concrete. J Struct Eng 1988;V. 114(No. 9):2133–6.
[42] Massone LM, Wallace JW. Load-deformation responses of slender reinforced concrete walls. ACI Struct J 2004;V. 101(No. 1):103–13.
[43] Raffoul S, Garcia R, Pilakoutas K, et al. Optimisation of rubberised concrete with high rubber content: an experimental investigation. Constr Build Mater 2016;V. 124:391–404.

[44] Bompa DV, Elghazouli AY, Xu B, et al. Experimental assessment and constitutive modelling of rubberised concrete materials. Constr Build Mater 2017;V. 137: 246–60.
[45] Raffoul S, Escolano-Margarit D, Garcia R, et al. Constitutive model for rubberized concrete passively confined with FRP laminates. J Compos Constr 2019;V. 23(No. 6):04019044.
[46] FEMA, ASCE. Prestandard and Commentary on the Seismic Rehabilitation of Buildings. Report No. 356. Federal Emergency Management Agency; 2000.
[47] Papastergiou, P. A confinement model for concrete wrapped or pretensioned with FRP. PhD thesis, Dept. of Civil and Structural Engineering, The University of Sheffield, 2010.
[48] El Khouri I., Garcia R., Taranu N., Petru M., Toma I.O., Budescu M. et al. Shake Table Tests on Frames Made with Normal and FRP-Confined Rubberised Concrete. Proceedings of the 16th European Conference on Earthquake Engineering (16ECEE). Thessaloniki, Greece, 18 - 21 June, 2018.

Construction and Building Materials 413 (2024) 134910

Contents lists available at ScienceDirect

Construction and Building Materials

journal homepage: www.elsevier.com/locate/conbuildmat

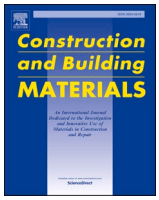

Assessing the effect of adding TiO_2 and calcined montmorillonite clay nanoparticles on the mechanical properties of cement mortar☆

Georgiana Bunea [a], Ionuţ-Ovidiu Toma [a,*], Sergiu-Mihai Alexa-Stratulat [a], Petru Mihai [a], Nicanor Cimpoeşu [a], Bogdan Istrate [a], George Stoian [b]

[a] "Gheorghe Asachi" Technical University of Iași, Iași 700050, Romania
[b] National Institute of Research and Development for Technical Physics, Iași 700050, Romania

ARTICLE INFO

Keywords:
Titanium dioxide
Montmorillonite
Combination
Cement mortar
Mechanical properties

ABSTRACT

The study analyses the influence on the mechanical strength of titanium dioxide TiO_2 and calcined montmorillonite (CMMT) particles added individually and combined to cement mortar mixes. Having both similar and complementary properties, the combined solution of TiO_2 and CMMT nanoparticles can induce positive effects on the overall properties of cementitious composites. However, this combination has been tackled only in a couple of studies, with different approaches regarding the design mix, but without comparing the results with the individual-nanomaterial mixes. In this study, the bulk density, flexural strength, compressive strength, and material microstructure were analyzed at 28 days of curing, for an addition of 0.5 wt% and 0.75 wt% TiO_2, of 1 wt%, 1.5 wt% and 2 wt% calcined montmorillonite (CMMT), and of nanomaterial combinations. From the flexural strength point of view, the CMMT-modified cement mortar mix registered the highest value of all modified mixes for a cement replacement of 1.5 wt%, reaching a 10.27% improvement compared to the reference mix. The highest compressive strength was recorded for the mix comprised of 1 wt% CMMT and 0.75 wt% TiO_2, with an increment of 3.19% compared to the reference mix. The obtained results were confirmed by means of Scanning Electron Microscopy (SEM) investigations showing that the highest amount of CSH was observed for 1% wt% CMMT and 0.75% wt% TiO_2, corresponding to the highest compressive strength value.

1. Introduction

Nanomaterials have become a subject of interest in the civil engineering field, as they improve the mechanical and physical properties of composite construction materials. Several nanomaterials were extensively studied, as they proved their efficiency when added to composite materials such as concrete or mortar [1–5]. For example, nanosilica has been proven to have positive effects on the mechanical properties and durability of both concrete [6,7] and cement mortar [8]. Its pozzolanic properties combined with their nanoscale dimensions succeeded in improving the properties of cementitious composites [9]. An increase in the mechanical strength of concrete and cement mortar was also registered when carbon nanotubes were added to the cement matrix [10,11]. Moreover, CNTs also had a positive influence on the electrical properties [12], on the corrosion rates of reinforcement [13] and on the permeability of cementitious composites [14]. Other studies used graphene oxide [15], ferric oxide (Fe_2O_3) [16], or alumina (Al_2O_3) [17] to improve the properties of cementitious composites. Unlike nanosilica or carbon nanotubes, the research on the impact of titanium dioxide, TiO_2, and montmorillonite clay MMT nanoparticles on the cement mortar and concrete mechanical properties is in its earlier stages.

The use of TiO_2 in building materials has already begun, but the focus was on one special property – the photocatalysis reaction that develops under ultraviolet light [18–21]. Later on, researchers discovered that, due to its nano-scale size, TiO_2 nano-particles act as a non-reactive filler, succeeding in decreasing the porosity of cement-based composite materials. Thus, the mechanical strength of the composite is improved both due to the filler effect and to the high specific surface area of the nano-particles, acting as nucleation sites for the formation of Calcium-Silicate-Hydrate CSH crystals [22–24]. Some studies include additives in their cement mortar mix, such as superplasticizer [25], fly ash [26], ground granulated blast furnace slag [27],

* Corresponding author.
E-mail address: ionut.ovidiu.toma@tuiasi.ro (I.-O. Toma).

https://doi.org/10.1016/j.conbuildmat.2024.134910
Received 23 August 2023; Received in revised form 7 December 2023; Accepted 3 January 2024
Available online 9 January 2024
0950-0618/

or silica fume [25], providing better workability for the material, at low water to binder, w/b, ratios, i.e. 0.35–0.485. Due to the insertion of different additives in the mixture and different w/b ratios, the optimum percentage for the modified-cement mortar as well as the maximum strength values vary from one study to another. For example, the maximum compressive strength when adding 30% fly ash as an admixture, with a w/b ratio of 0.485, was obtained for 3 wt% TiO_2 addition – approximately 36.50 MPa [26]. In contrast, when adding only superplasticizer, for a w/b ratio of 0.40, the maximum compressive strength was approximately 46 MPa, for an addition of 6 wt% TiO_2 to the cement matrix. However, for the flexural strength, the maximum value was recorded for an addition of 3 wt% TiO_2 in the mix. Afterward, the flexural strength registered an important decrease, as the quantity of TiO_2 was increased from 3 to 6 wt%. The 6 wt% TiO_2 mix recorded a flexural strength decrease with about 1.10 MPa compared to the 3 wt% TiO_2 sample [27]. When no other admixtures were present in the cement mortar, except the TiO_2 nanoparticles, the optimum TiO_2 percentage for obtaining the maximum compressive/flexural strength varies from 0.1 wt% [28] to 10 wt% [21]. This wide interval regarding the used TiO_2 quantity may be explained by economic reasons, taking into account the relatively high price of the nanomaterial. Thus, the study may focus on finding the lowest quantity of TiO_2, for which a certain improvement strength is acquired compared to the reference mix, and for the lowest cost increment. Doko et al. [28] based their study on Chinese standards and considered a very low w/c ratio, i.e. 0.32 [28], while Chen et al. [21] considered the ASTM provisions and a w/c ratio of 0.485. The nanomaterial quantity percentage increment in [21] is 5% - a very high increment considering the nano-size scale of the TiO_2 particles, which may be misleading. The results in [24] confirm the above remark, as the authors obtained an optimum percentage of 5 wt% TiO_2 nanoparticles for the maximum compressive strength of 48.80 MPa, which is close to the 49.00 MPa given in [21] – for 10 wt%.

Unlike TiO_2 nanoparticles, montmorillonite MMT nanoparticles have been proven to exhibit a certain level of pozzolanic behavior, depending on their type and the treatments to which they have been subjected [29–31]. This characteristic added to the high specific surface area of the MMT particle makes MMT a good candidate as a supplementary cementitious material for improving the strength and durability of cement mortar. Its efficiency has been confirmed by several studies conducted in the past years [32–36]. Compared to the TiO_2-modified cement mortar, the optimum percentages when adding MMT clay, corresponding to the maximum strength, are significantly lower, i.e. 0.5–2% per weight of cement [31,37–39]. However, the strength values vary depending on the treatments to which the MMT clay has been subjected. The hydrophilic natural MMT lead to the smallest strength values compared to the treated MMT clay, reaching only 41 MPa for the compressive strength and 7.80 MPa for the flexural strength for a 2 wt% of cement. The study considered a w/c ratio of 0.55 and no additives. The specimens were cured in lime-saturated water for 28 days [37]. On the other hand, a maximum compressive strength of 55 MPa was recorded for a cement replacement of 0.5 wt% organo-MMT nanoclay, with 22.2% higher than the reference mix. A maximum flexural strength of 9.80 MPa was registered for a cement replacement of 1 wt% organo-MMT nanoclay - 3.16% higher compared to the reference mix. For curing purposes, the specimens were submerged in water at 23 ± 2 °C for 28 days [38].

By comparing the properties of the two above-mentioned nanoparticles, it was observed that MMT nanoparticles are larger than TiO_2 ones, having usually a medium size of 200–400 nm [40–42], depending on the duration of ultrasonication, while TiO_2 particles reach to sizes of 15 nm [43,44]. MMT nanoparticles were proven to have a certain degree of pozzolanic activity, developed especially after calcination [45–47], while TiO_2 nanoparticles are known for their inert character [48,49]. TiO_2 particles have photocatalytic properties, during which process water molecules are generated [50,51]. MMT is known for its hydrophilic character and good adsorption performance [52], inducing also self-healing properties to cementitious materials, when water is absorbed [53]. Due to their complementary properties, a combination of TiO_2 and MMT nano-particles added in cementitious composites is auspicious for improving both the strength and the durability of cementitious composite materials. Nevertheless, there are few studies on this subject, which do not continue their research afterward, although the results were promising. In one study, a solution of nano-MMT clay, TiO_2, and water was prepared, which replaced 1, 2, and 3 wt% of cement in a cement mortar mix. The optimum percentage of nanomaterial admixture, for the maximum compressive and flexural strength, was 1%. Still, the authors discuss the need for preliminary ultrasonication of the nanomaterial solution, which was not used in the study [54]. The same method of adding the combined nanoclay - TiO_2 solution into the cement mortar matrix was used by Matějka et al. [55], but for metakaolin nanoclay particles. When used in concrete, the nanoclay (metakaolin) – TiO_2 combination produced a maximum increase of the compressive strength by 21.83% and flexural strength increased by 15%, compared to the control sample, at 28 days of curing. The optimum combination was 3 wt% nanoclay and 2 wt% TiO_2 cement replacement [56].

The use of nano-materials in combination with other supplementary cementitious materials was previously investigated for both MMT and TiO_2. The use of nano-MMT in foamed paste with high volume of fly ash binder (70% replacement of Portland cement, by mass) resulted in improved strength values and lowest thermal conductivity [57]. In another study, it was shown that the use of nano-MMT, together with sepiolite, improved the tixotropic behavior of cementitious materials used for 3D printing, especially for those containing fly-ash [58]. The influence of nano bentonite clay together with nano fly ash on the mechanical and durability properties of concrete was recently investigated [59]. Both nano materials were used as cement replacement. Incorporating these materials into a slurry resulted in significant amounts of CH that occupied the pores of the mix. This resulted in a reduction of pore volume and pore sized due to subsequent formation of CSH gels which lead to a denser and more compact microstructure [59]. In a similar manner, nano-TiO_2 was used was used in conjunction with an epoxy resin to improve the microstructure of alkali activated slag/flv ash pastes [60]. Improvements in flexural-compressive strength ratio, reduced shrinkage and decreased capillary sorptivity were reported which makes the new alkali activated slag/flv ash binders a good alternative to Portland-cement based counterparts. A subsequent study demonstrated similar effects on mechanical and bonding properties of cement-based mortars [61]. A novel TiO_2-graphene composite was used to enhance the mechanical and durability properties of alkali-activated slag mortar [62]. Lower capillary sorptivity coefficients, chloride penetration depth and migration coefficients were reported for TiO_2-graphene composite owing to the hydration process and refined the microstructure of alkali-activated slag binding matrix.

This paper discusses the influence on the mechanical properties of adding combined calcined montmorillonite clay and titanium dioxide nanoparticles to cement mortar. Considering the advantages that both nanoparticles proved to have on cementitious composites and the lack of studies on this nanoparticle combination, the current study offers new insights on this subject. Moreover, all previous works have emphasized the need of a more extensive research on the use of combined TiO_2 and MMT nanoparticles in cementitious composites. The current study continues the existent research with some slight modifications, based on the authors proposals in the studies [54] and the physical-chemical properties of the nanomaterials. For example, Selvasofia et al. [63] replaced the aggregates with MMT particles and cement with TiO_2. However, in the current study the inert property of TiO_2 was considered and these nanoparticles replaced the aggregates, while the pozzolanic calcined MMT replaced the cement.

2. Materials and experimental procedure

2.1. Materials

A type II Portland cement CEM II/B-M 42,5 R was used in the current study, which complies with the European Standard SR EN 197–1:2011 [64]. This type of cement was selected based on the availability of the product on the market. Table 1 lists the main characteristics of the cement, according to the information provided by the manufacturer.

A hydrophilic bentonite nanoclay powder (CAS Number 1302–78-9, Nanomer® PGV, chemical formula: $Al_2O_3 \bullet 4SiO_2 \cdot H_2O$) was used in the study. There were no previous treatments applied to the supplied nanoclay. According to the manufacturer, the material consists mostly of montmorillonite clay, with an average particle size of 12 μm. Montmorillonite consists of clay layer stacks, each layer having a thickness of approximately 1 nm. When water is added, due to the hydrophilicity of the material, montmorillonite MMT clay layers dissociate into nano-sized particles [65,66]. Some chemical and physical properties of the used nanoclay, provided by the manufacturer, are presented in Table 2.

Due to their hydrophilicity, MMT particles tend to agglomerate in clusters, leading to a low homogeneity within the composite. Moreover, increased hydrophilicity of the MMT is detrimental to the cement matrix, as they decrease the cohesion between aggregates and the cement matrix, due to the fact that the nanoclay particles attract water around them [67,68]. For limiting this phenomenon and to increase the pozzolanic reactivity, the MMT was first calcined by subjecting it to a temperature of 800 °C for 3 h [69–71]. Throughout the study, the calcined MMT particles are denoted as CMMT.

Titanium Dioxide, Anatase powder (CAS Number 1317–70-0) was used as a non-reactive nano-filler. According to the certificate of analysis provided by the manufacturer, the material is characterized by the following properties listed in Table 3.

The natural river aggregates used in the mixtures are proper for concrete structures and have a particle size in the interval of 0–4 mm, complying with SR EN 12620 +A1:2008 [72] norm.

The XRD analysis of the raw materials confirms the presence of the anatase phase in the TiO_2 sample and a mix of Montmorillonite and Pyrophyllite in the commercially purchased MMT. Also, the mineralogical analysis confirms the decomposition of the hydrated phases due to calcinations. Accordingly, in the CMMT sample, the presence of hydrated Pyrophyllite was not found since this hydrous aluminium silicate will release the water from its composition around 800 °C [73] resulting in Pyrophyllite-1TC (a mineral with the chemical formula $Al_2O_{11}Si_4$). The XRD patterns of all the analysed samples show some humps, which are related to the presence of amorphous phases [74,75]. Fig. 1 presents the XRD patterns for all raw materials used in the analysis.

From a chemical point of view, montmorillonite is a hydrated sodium calcium aluminium magnesium silicate hydroxide having the formula $(Na,Ca)_{0.3}(Al,Mg)_2(Si_4O_{10})(OH)_2 \bullet nH_2O$. The SEM micrographs of CMMT, MMT and TiO2 are presented in Fig. 2. It can be observed that the surface of the montmorillonite particles does not change after calcination.

Table 1
Composition of Type II Portland cement used in the current study. Physical and mechanical properties.

Composition (mass %)	
Clinker	65-79
Blast furnace slag, fly ash, lime	21-35
Other components	0-5
Physical properties	
Initial setting [minutes]	min. 60
Stability (expansion) [mm]	max. 3
Mechanical properties	
Initial compressive strength – 2 days [MPa]	min. 20
Standard compressive strength – 28 days [MPa]	min. 42.5 max. 62.5

Table 2
Chemical and physical properties of the hydrophilic bentonite used in the current study.

Characteristic	Result
Formula weight [g/mol]	180.1
Appearance (color)	beige
Appearance (form)	powder
Bulk density [kg/m^3]	779
Loss on drying [%]	10.8
Average particle size [micron]	12

Table 3
Chemical and physical properties of the titanium dioxide used in the current study.

Characteristic	Result
Formula weight [g/mol]	79.87
Appearance (color)	White
Appearance (form)	powder
Purity [%]	99.7
Surface Area [m^2/g]	50
Average particle size [nm]	20

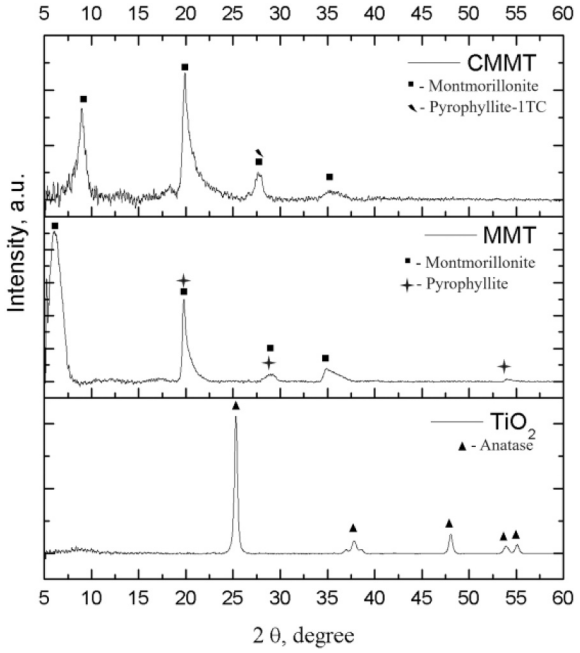

Fig. 1. XRD patterns of the raw materials.

The particle size distribution of CMMT and TiO_2 was obtained from image analyses using Particle Analysis Mode of VegaTC software [76]. Each analysis was conducted several times on batches of 200 particles and the obtained results were averaged.

In case of TiO_2 powder, the minimum measured diameter was 19.3 nm, the maximum one 49.95 nm with an average value of 31.1 nm, larger than the mean values provided by the manufacturer. On average, from the analysis of 200 particles it was observed that 2 particles were between 10 and 20 nm in diameter, 104 particles between 20 and 30 nm in diameter, 78 particles between 30 and 40 nm in diameter and 16 larger particles between 40 and 50 nm in diameter.

In case of CMMT, the minimum measured diameter was 4.5 μm, the maximum one 40.52 μm with an average value of 11.71 μm. The obtained value was very close to the mean particle size diameter provided by the manufacturer. On average, from the analysis of 200 particles it

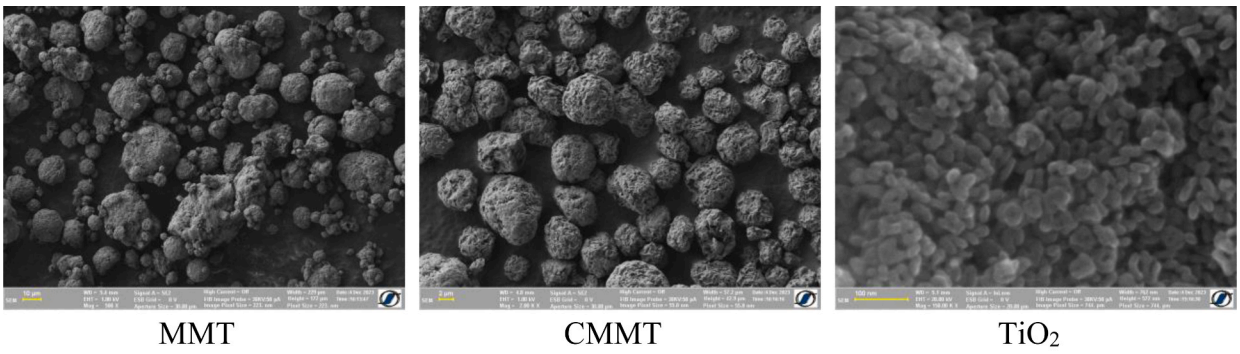

Fig. 2. SEM micrographs of used powders.

was concluded that 96 particles had a diameter between 1–10 μm, 82 particles between 10 and 20 μm, 20 particles between 20 and 30 μm and 2 particles with diameter bigger than 30 μm.

The chemical composition of CMMT and TiO_2 was obtained by means of SEM-EDS analyses. The spectra are presented in Fig. 3, whereas the chemical composition, expressed in atomic percentage, are summarized in Table 4.

2.2. Mixture details

The experimental study consisted of two major phases. In the first phase, the analysis focused on the separate influence that CMMT and TiO_2 have on the mechanical properties of the cement mortar. At first, the effect of CMMT was analyzed by adding 1%, 1.5%, and 2% CMMT by weight of cement into the mix. During this phase, several stages had to be considered. Taking into account that although the hydrophilicity of the MMT particles was decreased by calcination, they still tended to agglomerate. Therefore, ultrasonication was used to provide a higher homogeneity within the cement matrix. The corresponding quantity of CMMT for each mix was mixed with water and ultrasonicated for 5 min. Separately, the cement and sand were drily mixed. Subsequently, the solution comprising water and nanoparticles was added to the cement-sand mix along with the remaining water, and the newly obtained composite was mechanically mixed, according to ASTM C305 [77] regulations.

For the TiO_2-modified cement mortar mix, 0.5% and 0.75% TiO_2 by weight of cement were added to the mix, replacing the corresponding aggregate quantity. For this study, TiO_2 was chosen to replace the aggregate instead of the cement, because these nanoparticles are inert and do not promote pozzolanic reactions, as CMMT does. A solution composed of TiO_2 and water was prepared, for each studied formula. It was manually stirred to ensure the spread of particles in the liquid. After the cement and sand were drily mixed, this solution and the remaining water quantity were added to the mix. The new composite was mechanically mixed, as per ASTM C305 specifications [77]. The corresponding component quantities for each mix, where CMMT and TiO_2 particles were added individually are presented in Table 5. As can be observed, the water quantity had to be increased for CMMT and TiO_2 samples due to the decrease in workability, registered when these nanoparticles were added.

In the second stage, the two nanomaterials were combined and then added to the mix. For combinations, the following nanoparticle percentages were used: 1% and 1.5% for CMMT, and 0.5% and 0.75% for TiO_2, by weight of cement. Considering the increase in nanoparticle quantity, as well as the interactions that may occur between them, the mixing stage was slightly modified to prevent possible agglomerations. Hence, a solution of CMMT and water was prepared and ultrasonicated for 3 min. Afterward, the corresponding quantity of TiO_2 was added and the newly obtained solution was ultrasonicated for another 5 min. During this time, the cement and aggregates were drily mixed. The nanomaterial solution is added to the cement-aggregate mix together with the remaining water and the composite was mechanically mixed, according to ASTM C305 provisions [77]. Table 6 lists the quantities used during the mixing stage of combined CMMT/ TiO_2-modified cement mortar samples.

2.3. Sample preparation and curing conditions

The used mixer is designed to mix mortars and cement pastes to the requirements of the IS:10890 [78], EN 196–1 [79] and EN 196–3 [80]. For each mixture, three samples were prepared for strength testing, which were cast into 40 × 40 × 160 mm prismatic molds. After 24 h they were demolded and stored in water for 28 days. Following this period, they were taken out of the water, naturally dried for 24 h in a

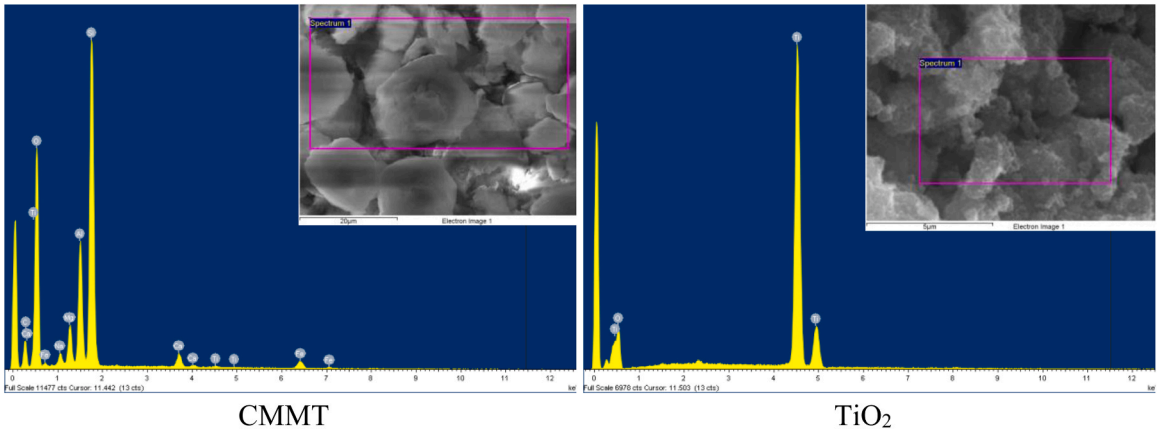

Fig. 3. SEM-EDS spectra for chemical composition analysis.

Table 4
Chemical composition of CMMT and TiO_2 (expressed in atomic percentage).

Spectrum	C	O	Na	Mg	Al	Si	Ca	Ti	Fe
CMMT	28.46	52.84	0.69	1.69	3.95	11.29	0.48	0.06	0.52
TiO_2	-	65.37	-	-	-	-	-	34.63	-

Table 5
Cement mortar mix quantities for samples with individual addition of nanoparticles.

Mix	Cement [kg/m^3]	Aggregate [kg/m^3]	Water [l/m^3]	w/b ratio	CMMT [kg/m^3]	TiO_2 [kg/m^3]
M – Control sample	380	1550	228	0.6	-	-
CMMT 1	376.2	1550	247	0.65	3.8	-
CMMT 1.5	374.3	1550	247	0.65	5.7	-
CMMT 2	372.4	1550	247	0.65	7.6	-
TiO_2 0.5	380	1548.1	247	0.65	-	1.9
TiO_2 0.75	380	1547.15	247	0.65	-	2.85

normal temperature and humidity environment, and then tested.

2.4. Testing methodology

For each sample, the flexural and compressive strength test was carried out according to SR EN 196–1 [79], at a loading rate of 0.05 kN/s for flexural strength and 2.4 kN/s for compressive strength. The results were registered and the average strength values were computed for each considered mix.

For the microstructural analysis using Scanning Electron Microscopy (SEM), a Carl Zeiss NEON 40EsB Cross-Beam system with thermal Schottky field emission emitter and accelerated Ga ions column was used when the mortar samples reached the age of 28 days.

The X-Ray Diffraction Analysis (XRD) analysis was conducted at 28 days of curing using a true representative sample of each type of raw material has been analyzed. The modified cement mortar mixes were evaluated based on some fragments left from the mechanical tests, which were crushed down to a powder state. The diffraction patterns were collected using X'Pert Pro MPD equipment (Malvern Panalytical Ltd., Eindhoven, Netherlands) with a CuK source at 45 kV/40 mA. The radiation was recorded between 5° and 60° 2θ at a step of 0.013°. The identification of the phases was conducted using the *QUALX2.0 software* [81].

3. Results and discussions

3.1. Bulk density

Before placing the samples in water for curing purposes and before testing them at the age of 28 days, the bulk density of each of them was determined and a mean value was considered for each batch, for comparison purposes. Fig. 4 presents the variation of density depending on the type and quantity of nanomaterials used in the mix.

For the calcined montmorillonite CMMT-modified cement mortar samples, an increase in density was registered, for both considered ages, compared to the mean density value of the control specimen, as shown in Fig. 4a. Two reasons could explain this behavior. The first one was related to the filling effect that the CMMT nanoparticles had and the second one to the hydrophilicity of the particles. The maximum density was registered for the CMMT 1.5 sample. As more nanomaterials were added, the density slightly decreased by 1.06%, which may be due to some agglomerations of nanoparticles and a non-homogeneous dispersion within the matrix. Similar results were obtained in the case of nanoclay-modified concrete specimens, where, as the nanoclay nanoparticle quantity increased to 1 wt% [82], a decrease in flexural strength was registered. Thus, there is an optimum limit for MMT addition in the cementitious composites and it is related to the porosity of the sample. As the pores are filled with MMT, the excess surrounds cement aggregates and blocks cement hydration. As cement particles hydrate only partially, the strength decreases [82].

Table 6
Cement mortar mix quantities for samples with combined nanoparticle addition.

Mix abbreviation	Mix details	Cement [kg/m^3]	Aggregate [kg/m^3]	Water [l/m^3]	w/b ratio	CMMT [kg/m^3]	TiO_2 [kg/m^3]
COMB1	1% CMMT + 0.5%TiO_2	376.2	1548.1	247	0.66	3.8	1.9
COMB2	1% CMMT + 0.75%TiO_2	376.2	1547.15	247	0.66	3.8	2.85
COMB3	1.5% CMMT + 0.5%TiO_2	374.3	1548.1	247	0.66	5.7	1.9
COMB4	1.5% CMMT + 0.75%TiO_2	374.3	1547.15	247	0.66	5.7	2.85

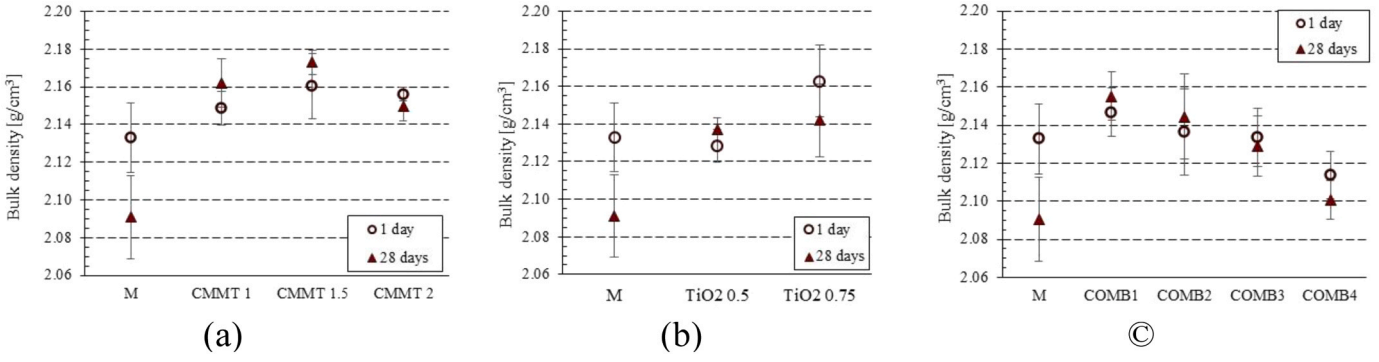

Fig. 4. Bulk density variation at 1 and 28 days of curing for control cement mortar specimens and (a) CMMT-modified samples; (b) TiO_2-modified samples; (c) combined CMMT and TiO_2-modified samples.

At 1 day of curing the density value reached 2.16 g/cm^3 – with an increase of 1.28% relative to the control specimen value. At 28 days of curing, the density of CMMT 1.5 was 2.17 g/cm^3, with an increment of 3.92% compared to M-mix. Therefore, as the hydration process developed, the density of the CMMT 1.5 mix increased compared to the M-mix. This trend was observed also in the case of the CMMT 1 mix, as presented in Fig. 4a.

In addition, in the case of the control specimen at 28 days of curing, the density was lower by 1.97% compared to the 1-day of curing value. However, for the CMMT-modified samples, the density at 28 days increased compared to the 1-day initial density value, by approximately 0.60%. As the free water evaporated from the voids of the cement mortar sample, the density of the specimen should decrease, as was the case of the M-sample. Still, the calcined montmorillonite particles preserved a certain degree of hydrophilicity, given both by their internal properties and by the high specific surface area. Therefore, after they were placed in water for curing, the CMMT nanoparticles attracted more water molecules, needed for continuing the hydration process and the promotion of CSH. This phenomenon resulted in a decrease in free water quantity and an increase in physically bonded water. Consequently, after 24 h left to naturally dry in normal conditions, CMMT-modified samples preserved a larger amount of water compared to both control and 1-day CMMT-modified samples.

As for the TiO_2-modified samples, the filling effect due to their nano-size dimension led to an increase in density at both 1 day and 28 days of curing, compared to the control mix. Their smaller hydrophilicity compared to the CMMT-modified samples, was observed based on the results illustrated in Fig. 4b. A greater density was registered at 28 days compared to the 1-day record only in the case of TiO_2 0.5-modified mix. However, the difference was only 0.40%, smaller than in the case of CMMT 1.5. For the TiO_2 0.75-modified samples, after 28 days of curing, the density value decreased by 0.96% compared to the one at 1 day. The maximum density at 28 days was registered for the TiO_2 0.75-modified mix – larger by 2.44% than the control mix density.

Fig. 4c presents the density variation for the combination CMMT/ TiO_2-modified cement mortar samples. Similar to the CMMT mixes, the density variation between the 1-day value and the 28-day one, for the combined CMMT/ TiO_2-modified mixes was insignificant, the maximum being reached for the 1.5B 0.75 T mix – 0.62%. Although the variation was small and can be considered to be in the error interval, the results confirm the general physical behavior of both nanomaterials and cement mortar mix. The highest density value was obtained for the COMB1 mix, i.e. 2.155 g/cm^3, whereas the smallest density value, corresponding to the modified specimens, was registered for the COMB2 mix – 2.101 g/cm^3. As the CMMT quantity increased to 1.5 wt% in COMB3 and COMB4 samples, and more cement was replaced, the density at 28 days of curing registered a slight drop. Since the percentage of nanoparticles increased in the specimen, the density decreased, due to the smaller density values of the two nanoparticles compared to cement and aggregate.

As a general remark, when combining CMMT with TiO_2 particles, for the 1 wt% CMMT combinations, i.e. COMB1 and COMB2, the final density value at 28 days of curing was between the density values corresponding to the individual nanomaterial-modified samples. Nevertheless, as the quantity of CMMT increased to 1.5 wt%, the density registered a decrease in value relative to the individual nanomaterial-modified mixes. Considering the lower bulk density value of both CMMT and TiO_2 compared to the cement particle and to the aggregate respectively, this decrease in density for the combination samples was expected.

Although the bulk density variations are small, the analysis of this parameter is important considering that few studies discuss this topic [83], and the results are conflicting, taking into account the various types of densities that are computed. However, an increase in the density, compared to the control specimen, for organo-modified montmorillonite cement paste was also previously reported [84,85] and hydrophilic bentonite concrete [36]. Increases in density value have been registered also for titanium dioxide addition in hardened cement mortar mix [86,87]. Correlating the results with the mechanical properties of the cement mortar samples, a better report on the material could be achieved.

3.2. Flexural strength

The flexural strength of the nanomaterial-modified cement mortar specimens has been determined for each specimen at 28 days of curing. Based on the results, the average of the flexural strength has been computed for each mix, together with the corresponding standard deviation. The graphical representation of both the calcined montmorillonite CMMT and TiO_2 mixes is presented in Fig. 5. To connect the density variation with the flexural strength, the density was also represented.

The maximum flexural strength value, i.e. 4.94 MPa, was registered when the cement mortar was modified with 1.5 wt% CMMT. Compared to the control mix M, the strength for CMMT 1.5 increased by 10.27%. The result was consistent with the maximum density value. Therefore, the optimum mix at 28 days of curing was CMMT 1.5. By superposing the flexural strength with the density values, a similarity in variation could be observed. Thus, the minimum flexural strength was registered for the CMMT 2 mix, corresponding to the lowest density value. Although inferior to CMMT 1.5, CMMT 1 and CMMT 2 flexural strength values were still higher than the control mix M values by 7.95% and 8.46% respectively. Despite the fact that the CMMT particles replaced cement particles, they still had a positive effect on the flexural strength due to their higher pozzolanic properties, they still had a positive effect on flexural strength.

The increase in flexural strength for all CMMT-modified mixes was doubled by an increase in density compared with the control mix M, as illustrated in Fig. 5a.

Based on the results, the CMMT addition to cement mortar improved the flexural strength of the composite. It should be noted that although the w/b ratio had to be increased for all CMMT mixes (Table 5), compared to the control mix M, the flexural strength values increased. The result may be explained by the pozzolanic reactions associated with CMMT, together with the large specific surface area of these nanoparticles, which promoted the hydration of CH crystals into CSH.

Although there were scarce results in the literature regarding the flexural strength of MMT-modified cement mortar, without any other supplementary materials, they were consistent with the results of the current study. For example, a hydrophilic MMT clay, with no treatments, and a w/b ratio of 0.55 led to a maximum increase in flexural strength of 5.4% relative to the control specimen, for 2 wt% nanomaterial replacement by weight of cement [32,37]. An organo-modified MMT clay added to a cement matrix with a w/c ratio of 0.5, increased the flexural strength of the composite to a maximum of 5% increment relative to the control specimen, for a cement replacement of 1 wt% with MMT [38].

Compared to the CMMT-modified cement mortar mixes, TiO_2-modified mixes exhibited a smaller flexural strength at 28 days, as presented in Fig. 5b. Although TiO_2 nanoparticles were introduced in the cement matrix and increased the average density of the mix, compared to the control mix M, as presented in Fig. 4b, the flexural strength value decreased under the level of the control mix, as illustrated in Fig. 5b. If for 0.5 wt% TiO_2 there was a relatively small decrease of only 0.08 MPa, for 0.75 wt% cement replacement the decrease was 0.60 MPa.

A similar variation was found in other studies. A decrease in flexural strength at 28 days of curing, when adding up to 1 wt% TiO_2 nanoparticles was registered also for self-compacting concrete [44] and cement mortar without additives [28]. Another study reported a gradual decrease in flexural strength as the cement mortar was modified with 0.5, 1, 2.5 and 5 wt% TiO_2 by weight of cement [88]. No improvement in flexural strength was registered for 1 wt% TiO_2 cement replacement,

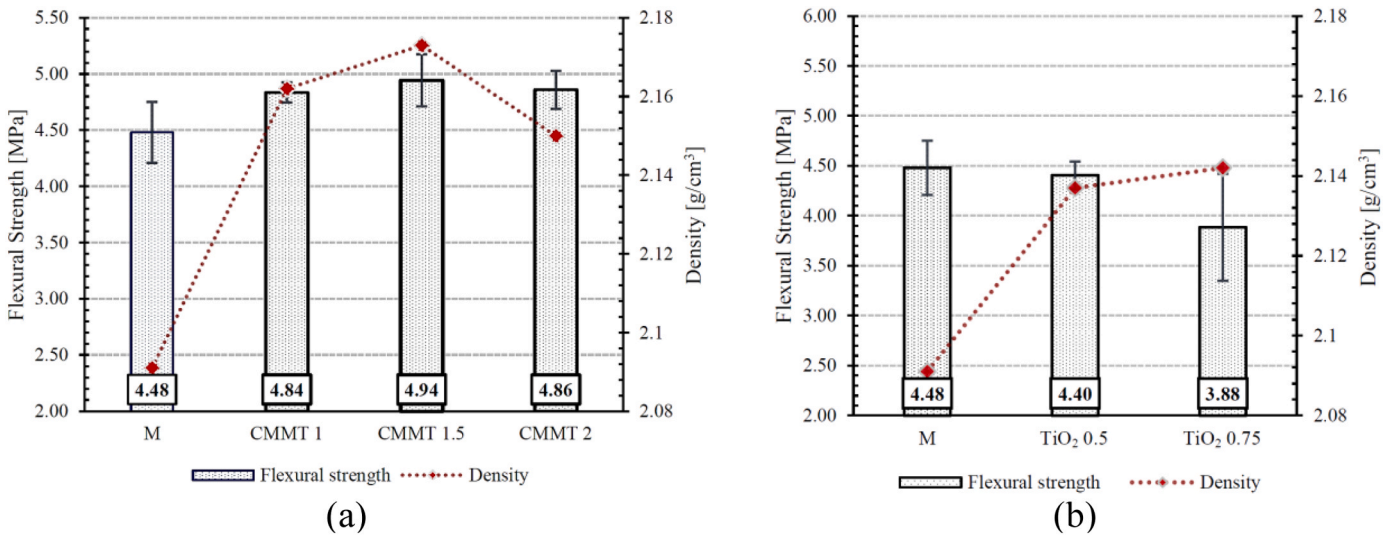

Fig. 5. Variation of flexural strength and density for (a) CMMT- modified cement mortar samples; (b) TiO_2 - modified cement mortar samples.

when adding 30 wt% fly ash to the cement mortar composite, according to Siang et al. [26].

The lack of pozzolanic properties of TiO_2 particles might be the cause of the flexural strength decrease, although the cement quantity did not change. In addition, adding TiO_2 particles might disrupt the hydration process of cement particles, as they attract water molecules due to their high specific surface area. The pore-filling ability of TiO_2 particles, given by their small size, increased the density of the specimens compared to the control sample. Furthermore, the increased water content could also be related to the high-density of the sample.

However, after 28 days of curing, the hydration process continues at a relatively high rate. As the TiO_2 nanoparticle had a high specific surface area, the water absorption increased during the curing stage, leading to high water content, compared to the reference mix. More nucleation sites were made available for the CH crystals to hydrate, compared to the reference sample – effect due to the high specific surface area of the TiO_2 particle. The combined above mentioned characteristics, lead to a prolonged hydration process, as the water content was higher in the sample and the number of CH hydration reactions were also higher [89]. The moisture within the TiO_2-modified cement mortar sample can be visually observed in Fig. 6 (inside the green polygon).

Practically, the TiO_2-modified cement mortar mixes at 28 days had a higher density given by pore infilling and high-water content, but a lower flexural strength, compared to the control sample. Nevertheless, the flexural strength is expected to increase, after the completion of the hydration process, as all the CH crystals become hydrated [87,90,91].

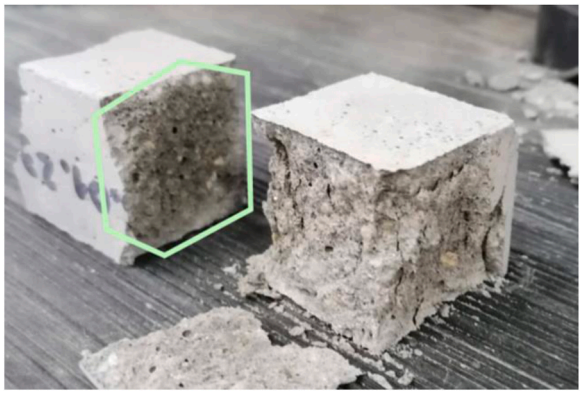

Fig. 6. Cross-section of nanomaterial-modified cement mortar sample after testing.

When comparing the flexural strength results of CMMT and TiO_2 addition, it could be noted that their different properties strongly influenced the final result. The larger pozzolanic CMMT particles succeeded in increasing the flexural strength at 28 days of curing, while the smaller, inert, TiO_2 particles hindered the strength increase. Although they have a higher specific surface area and they fill better the voids due to their smaller size, the TiO_2 nanoparticles lack pozzolanic properties. CMMT particles, although with a smaller specific surface area compared to TiO_2 nanoparticles, work in two directions at early ages for promoting CSH crystals and increasing flexural strength: the pozzolanic reactions and the filling of voids.

Fig. 7 presents the flexural strength variation for the considered nanomaterial combinations, at 28 days of curing.

All nanomaterial combination-modified mixes recorded higher flexural strength values compared to the control specimen. The highest increment in flexural strength value relative to the control mix was obtained for the COMB4 mix – 4.69%. The second highest value was recorded for the COMB1 mix, as shown in Fig. 7. The smallest increment in flexural strength – of only 0.45% relative to the control sample corresponds to the COMB3 mix.

The increase in flexural strength could be related to the increase in specific surface area, due to the nano-size dimension of bentonite and titanium dioxide. With the increase in specific surface area, the promotion of CSH crystal production expands. As more CHS crystals are formed, the bond between particles improves and the flexural strength increases.

On the other hand, adding both TiO_2 and CMMT nanoparticles in the cement mortar mix improved the filling of micro-pores. Thus, although both particles were smaller than cement ones, the TiO_2 particle was considerably smaller than the CMMT particle, succeeding in better filling the pores. Titanium dioxide lacked pozzolanic behavior, but it was balanced with the addition of CMMT in the cement mix. Therefore, the best formula could be considered to be the one associated with COMB4, in which CMMT accelerated the promotion of CSH crystals due to its pozzolanic properties and TiO_2 filled better the micro-pores.

The important flexural strength value corresponding to the COMB1 sample compared to COMB4 could point out the need for better ultrasonication. Adding more nanomaterials in the mix increased the risk of particle agglomeration, which affected the general homogeneity of the samples, induced weak points and decreased the mechanical properties.

Although the variations were small, up to a maximum of 4.70% relative to the control sample, they are expected to increase in time, considering the increased quantity of physically bound water in the modified mixes compared to the control mix, as presented in Section 3.1.

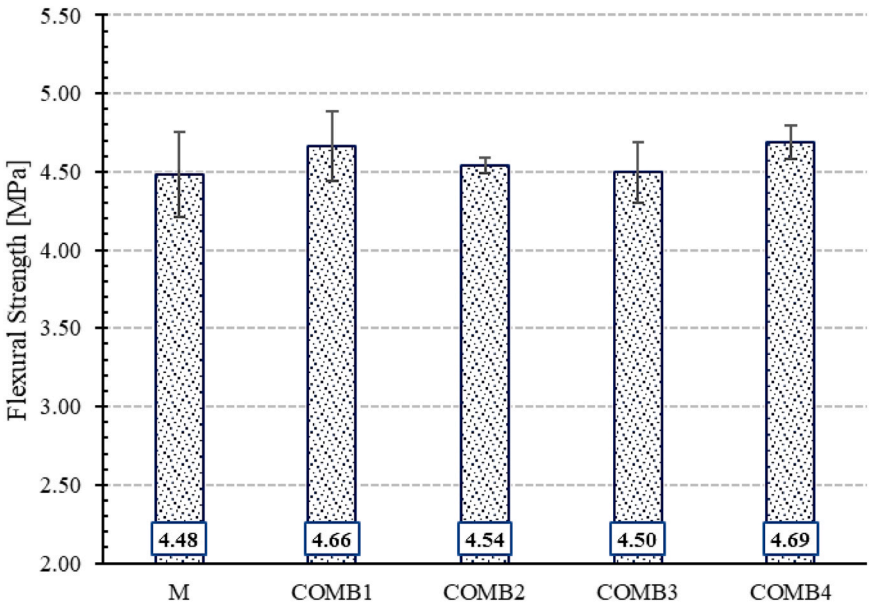

Fig. 7. Variation of flexural strength for CMMT and TiO_2-modified cement mortar mixes.

Despite the pozzolanic property of CMMT, which should promote the formation of CSH crystals, these types of reactions may be delayed at early ages because of the fly ash presence in the cement composition [92,93].

According to the results presented in Figs. 5 and 7, the flexural strength value corresponding to the combined CMMT and TiO_2 samples was in between the extreme values of the individual nanomaterial-modified cement mortar mixes. The registered flexural strength value for the COMB samples was higher than the TiO_2-modified cement mortar samples. The pozzolanic effect and the hydrophilicity of CMMT prevailed but the inert nanoparticles of TiO_2 decreased the final strength of the combination samples. Therefore, the result regarding the flexural strength for the combination nanomaterial samples was consistent with the individual nanomaterial mixes and no improvement was registered at 28 days of curing when using the two nanomaterials combined.

3.3. Compressive strength

The compressive strength of the cement mortar mixes modified with calcined montmorillonite CMMT and TiO_2 nanoparticles was determined for each sample, at 28 days of water curing. The uniaxial compression test was conducted on the end portions of the broken prisms, as described in Section 2.4. The average of the compressive strength values was computed and the results are graphically presented in Fig. 8.

Unlike the flexural strength results, CMMT samples register a decrease in compressive strength compared to the control mix M. When adding only 1 wt% of CMMT in the cement matrix, i.e. CMMT 1, the compressive strength decreases by 9.07%, as illustrated in Fig. 8a. The minimum compressive strength was obtained for CMMT 1.5, with a 15.22% decrease compared to the control mix M. Conversely, the density corresponding to all CMMT-modified samples had a significant increase compared to the control mix, the maximum increment being associated with CMMT 1.5. The difference in variation between the two parameters might be explained by the presence of bound water within the specimen. CMMT is known for its hydrophilicity, which increases water absorption during the water curing period. As the water was absorbed by CMMT particles, the density of the specimen increased but the cohesion between the cement matrix and aggregates decreased [92,94]. The final result was a decrease in compressive strength in contrast with the control mix. Based on this observation and the hydrophilic character of CMMT, as presented in Section 3.1, the existence of

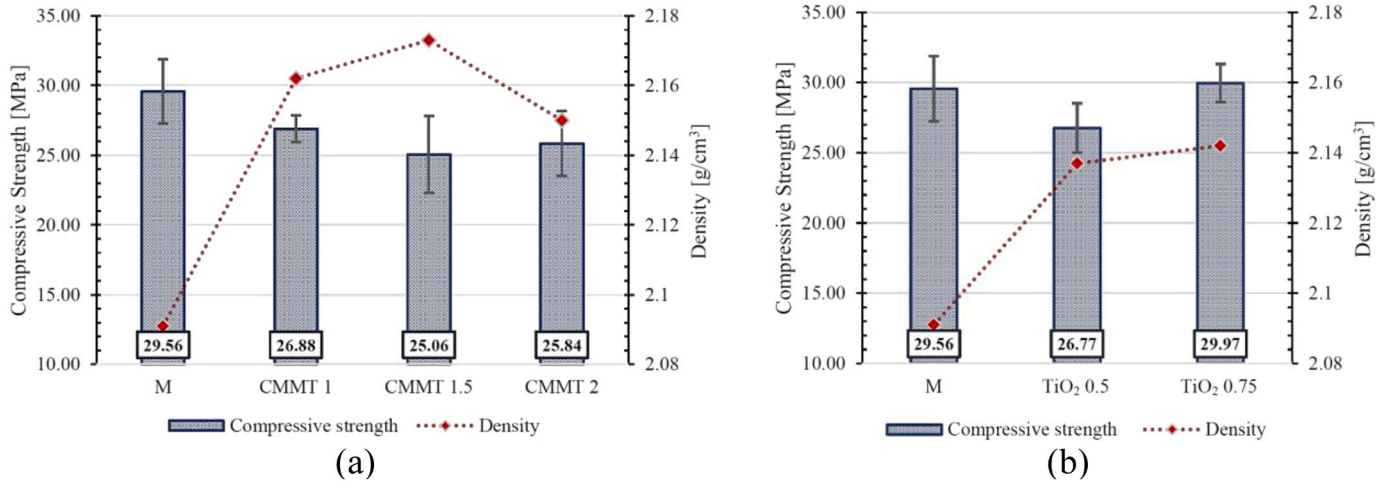

Fig. 8. Variation of compressive strength for (a) CMMT- modified cement mortar samples; (b) TiO_2 - modified cement mortar samples.

physically bound water was detrimental for the specimen under compressive actions. The existent water found in the pores created cracks during the compressive loading, which accelerated the failure of the sample.

Some researchers also reported a decrease in the compressive strength of cement mortar modified with various MMT percentages, at 28 days of curing [92,95]. Other authors registered only one compressive strength value, corresponding to the MMT-modified samples, above the control specimen [96,97]. On the other hand, other studies pointed out that as the curing period increased and more hydration products were generated from the ongoing reactions, the compressive strength improved. The negative difference compared to the control specimen was reduced and, for some MMT percentages, the compressive strength value increased above the value corresponding to the control mix [92, 95].

By contrast, titanium dioxide particles, had a better performance on the compressive strength of the cement mortar. Although TiO_2 particles were added as a supplement in the cement matrix and in smaller quantities compared to CMMT, the density value of TiO_2-modified samples was smaller, as shown in Fig. 4b. Nevertheless, the compressive strength for both TiO_2-modified mixes was higher than the CMMT mixes. For the TiO_2 0.75 mix, the compressive strength was slightly higher than the control mix by 1.39%. The difference in compressive strength between CMMT- and TiO_2 – mixes might be due to the smaller particle size of TiO_2. With a particle size of only 20 nm, they succeeded in filling both micro- and nano-pores, leading to improved mechanical and durability properties of cement mortar [86,88,98]. Moreover, the lower density value associated with TiO_2-modified mixes could be a cue for the lower water quantity present in these samples, compared to the CMMT-modified mixes.

Similar results were reported in a previous study [88] but for a maximum compressive strength corresponding to 1 wt% TiO_2 cement replacement, followed by a decrease in strength compared to the control sample for the 0.5, 2.5 and 5 wt% TiO_2 cement replacement. Other researchers registered decreases in compressive strength compared to the control specimen, for 0.5, 1 and 1.5 wt% TiO_2 cement replacement [99]. The compressive strength for TiO_2-modified cement mortar samples is expected to increase at 56 days of curing, after the consumption of more $Ca(OH)_2$ and the formation of CSH crystals.

To sum up, CMMT- and TiO_2-modified cement mortar mixes showed different behaviors under compressive strength. Unlike the flexural strength tests, where CMMT proved to be a better solution as supplementary cementitious material than TiO_2, for the compressive strength tests, the results reversed. Although TiO_2 lacks pozzolanic properties, the decrease in water quantity and the total porosity due to the smaller TiO_2 particles led to higher compressive strength values [88].

Fig. 9 illustrates the compressive strength value variation, at 28 days of curing, corresponding to the cement mortar mixes containing both CMMT clay and TiO_2 nanoparticles.

The compressive strength results regarding the nanomaterial combinations followed a different trend than the flexural strength ones, presented in Fig. 7. As the quantity of CMMT increased to 1.5 wt% by mass of cement, the compressive strength registered an important drop in the value by 8.96% for the COMB3 mix and 11.51% for the COMB4 one, compared to the control mix. The decrease in strength could be related to the presence of water inside the specimen. As it was presented in Section 3.1, MMT nanoparticles still maintain their hydrophilicity after calcination. During the 28 days of curing, free water bonds physically and more water is absorbed, which limits its evaporation during the 24 h set for drying. Therefore, a larger amount of water is found in the COMB3 and COMB4 mortar mixes, compared to the control, COMB1 and COMB2 mixes. Knowing that water is incompressible when the specimens were subjected to compression, the water present in the sample caused the occurrence of cracks, which led to a decrease in load-carrying capacity and hence a decline in compressive strength.

The maximum compressive strength was registered for the COMB2 mix. A smaller amount of CMMT, which decreased the quantity of water in the mix compared to the COMB3 and COMB4 mixes, together with a larger amount of TiO_2, succeeded in filling up the pores, leading to this result. The compressive strength increment for the COMB2 mix, relative to the control mix was 3.19%. Comparing the compressive strength values corresponding to the COMB1 and COMB2 mixes, the importance of TiO_2 in filling up the composite pores was pointed out.

In contrast to the flexural strength results, the use of combined CMMT and TiO_2 in the cement mortar mix had a positive influence on the compressive strength values at 28 days of curing, when compared to the mixes containing only CMMT or TiO_2 nanoparticles. Particularly, the COMB1 and COMB2 mixes had higher compressive strength values than

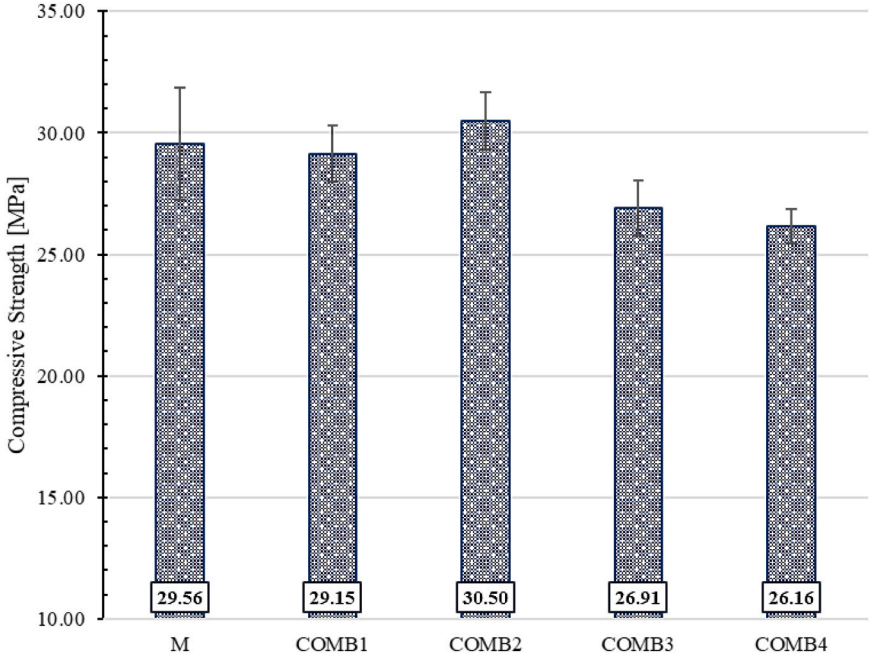

Fig. 9. Variation of compressive strength for the combined CMMT and TiO2 - modified cement mortar samples.

the individual-nanomaterial-modified mixes. There was only one exception for COMB1, for which the strength value was 2.73% smaller compared to the TiO_2-modified cement mortar mix. COMB1 – composed of 1 wt% CMMT and 0.5 wt% TiO_2 – had a 16.3% higher compressive strength than the CMMT 1.5 mix, although the nanomaterial percentage in the mix was the same. In addition, COMB1 registered a 12.81% higher compressive strength compared to the CMMT 2 mix. COMB2 showed the highest compressive strength compared to all individual nanomaterial mixes. Relative to CMMT 1, the compressive strength value was higher by 13.77% and relative to TiO_2 0.75 – by 1.77%.

COMB3 and COMB4 registered a decrease in compressive strength values compared to the control mix although the values were still above the one obtained for the CMMT-modified mortar mix. As more nanomaterials were added to the mix, particle agglomeration might occur, which led to an uneven distribution and a decrease in strength. As CMMT preserved a certain level of hydrophilicity, the probability of agglomeration was higher when it was supplemented in the mix.

As stated in Section 3.2, because the hydration process develops and the CSH crystals are formed, it is expected that the compressive strength will increase at later ages for all nanomaterial-modified mixes. Therefore, the difference between the TiO_2 and COMB2 mixes is expected to increase with time, due to the pozzolanicity and hydrophilicity of CMMT particles combined with the inert character of TiO_2.

3.4. Microstructural analysis

3.4.1. Scanning electron microscopy (SEM)

The impact of individually adding calcined montmorillonite CMMT and TiO_2 nanoparticles to the cement mortar mix has been analyzed using SEM images, as presented in Fig. 10. The microstructural analyses were performed at 28 days of curing.

The microstructure evolved depending on the quantity and the type of nanoparticles which was introduced in the mix. The control mix, illustrated in Fig. 10a, has an apparent non-uniform aspect, which was improved when adding CMMT and TiO_2 nanoparticles. Comparing Fig. 10a)-d), an increase in CSH quantity was observed as more CMMT was added to the mix. The largest area distribution of CSH particles was reported for 1.5 wt% CMMT, as presented in Fig. 10c), compared to Fig. 10b) and d). In addition, there were smaller voids compared to the control mix and the 2 wt% mix. The result corresponded also to the highest flexural strength value, discussed in Section 3.1. As the quantity of CMMT increased to 2 wt%, cracks began to develop and the quantity of CSH decreased compared to the 1.5 wt% sample. As more CMMT was added to the mix, given its hydrophilicity, it absorbed the water around the cement particles, and CH particles were left unhydrated. It resulted in a decrease in flexural strength for the 2 wt% CMMT compared to the 1.5 wt% CMMT.

The promotion of CSH crystals was smaller in the case of 0.5 wt% TiO_2 addition to the mortar mix, presented in Fig. 10 e), compared to the 1.5 wt% CMMT. More voids were observed and the structure had a non-uniform aspect, still displaying CH crystals. Conversely, 0.75 wt% TiO_2-modified cement mortar mix was defined by a uniform microstructure, with higher quantities of CSH compared to 0.5 wt% TiO_2 and higher quantities of CH compared to 1.5 wt% CMMT. Voids were still present in this sample. However, they were in a smaller number than the 1.5 wt% CMMT specimen. The uniform aspect, the high quantity of CSH crystals and the presence of smaller and fewer voids led to the highest compressive strength values, as discussed in Section 3.3.

SEM analysis was performed also on the cement mortar specimens modified with combined CMMT and TiO_2 nanoparticles, at 28 days of curing, and the results were presented in Fig. 11.

The presence of primary ettringite was observed in all cement mortar samples modified with combined CMMT and TiO_2 nanoparticles, which was beneficial for strength development during the early stages [100]. The largest distribution of ettringite was observed in the case of COMB2 and COMB4 mixes, where the highest quantity of TiO_2 was used. Being a product of hydration, its presence was related to the level of hydration achieved by a specimen, which influenced the mechanical strength. The

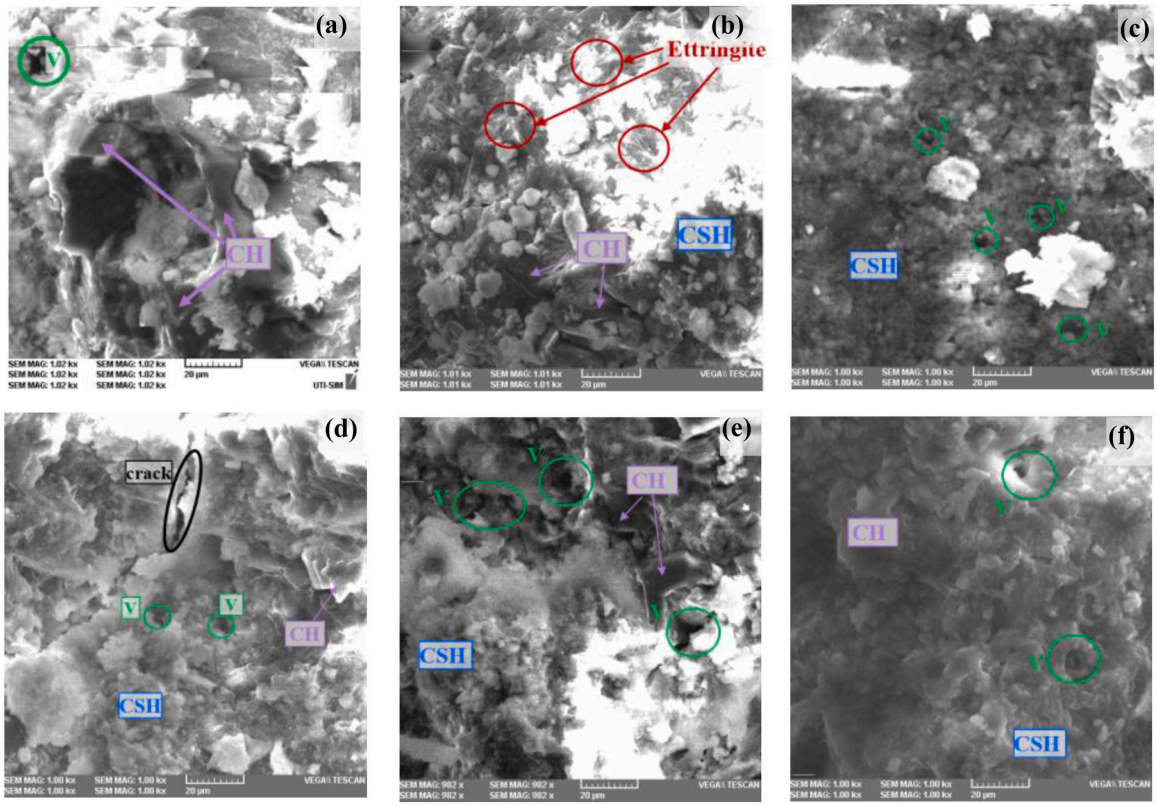

Fig. 10. SEM images for cement mortar modified with (a) 0% nanomaterials; (b) 1% CMMT; (c) 1.5% CMMT; (d) 2% CMMT; (e) 0.5% TiO_2; (f) 0.75% TiO_2.

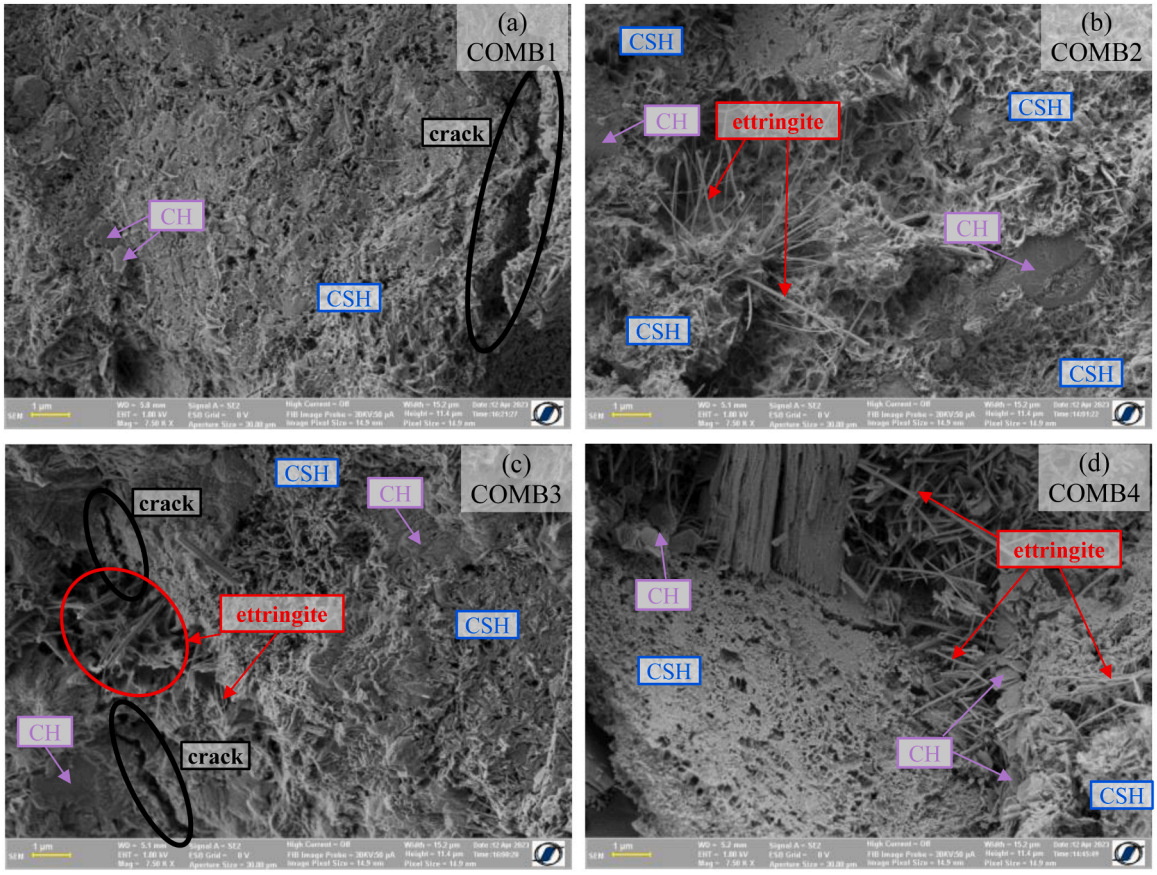

Fig. 11. SEM images for cement mortar modified with (a) 1% CMMT and 0.5% TiO_2; (b) 1% CMMT and 0.75% TiO_2; (c) 1.5% CMMT and 0.5% TiO_2; (e) 1.5% CMMT and 0.75% TiO_2.

combination between CSH and ettringite was the most dominant in Fig. 11b, corresponding to the COMB2 mix. Although the hydration process was not completed, given the presence of CH in the mix, the highest quantity of CSH was registered, compared to the records of the other mixes. Therefore, the SEM images confirm the compressive strength results, represented in Fig. 9.

3.4.2. *X-ray diffraction analysis (XRD)*

The X-ray diffraction XRD analysis was carried out for both cement mortar mixes modified separately with calcined montmorillonite CMMT and TiO_2 and the mixes modified with combinations of the two considered nanomaterials. All were compared with the control mix [81]. Firstly, XRD analysis was conducted to observe the influence of CMMT addition on the phase transition during cement hydration. The XRD patterns of the cement mortar mixes with up to 2 wt% addition of CMMT and the control mix are presented in Fig. 12.

The control mix showed clear peaks specific to quartz and other phases which confirmed the hydration process of calcium. Next to the clear peaks specific for Portlandite, some humps can be identified on the spectra, which confirm the presence of amorphous phases such as CSH gel, ettringite and monosulfate [101,102]. The presence of these phases in ordinary cementitious composites and also in modified with nanoclay ones was also observed [103]. Additionally, the peak around 29° 2θ, was confirmed as tobermorite and seemed constant in intensity despite the amount of CMMT [104].

The peak with the highest intensity from all samples was detected around 26° 2θ and confirmed the presence of quartz. Around 18°, 27° and 34° 2θ Portlandite phase was confirmed, as also identified by Tang et al. [105]. The same previous study also identified Montmorillonite at similar positions to those detected in the samples with CMMT addition. Clear peaks, but with different intensities that are related to CMMT content in the sample, were identified around 6°, 11°, 28° and 35° 2θ. The increase in CMMT content produced a decrease in the strength of the peaks specific to calcium-rich phases. This phenomenon could be related to the consumption of CH due to the carbonation of CO_2 and the pozzolanic reactions of CMMT [105–107].

As CMMT dosage increased in the mixes, the intensity of the new phases, detected around 27° 2θ as anorthite and albite, increased, which is normal considering the Al content of CMMT [101].

The phase composition of the cement mortar samples after TiO_2 addition is illustrated in Fig. 13. The XRD analysis confirms the presence of the anatase phase through two new peaks positioned around 25° and 46° 2θ, as also previously reported in [108] and [109].

The XRD analysis of the samples modified with both CMMT and TiO2 nanoparticles confirmed that a mixture of phases took place when the two types of nanoparticles were combined. Fig. 14 illustrates the phase composition of the composite when both nanoparticles are added to the matrix.

Based on Fig. 14, it was observed that no new phases were detected following the combining of CMMT and TiO_2. Mostly, the intensity of the peaks could be correlated with the amount of one or the other component but there were some discrepancies, which could be related to the samples collected and prepared for XRD analysis. Considering the very low amount that is subjected to this analysis, along with the low amount of TiO_2 and NC in the composition, it is quite understandable that the differences between the samples are not strictly related to the composition of the mixtures.

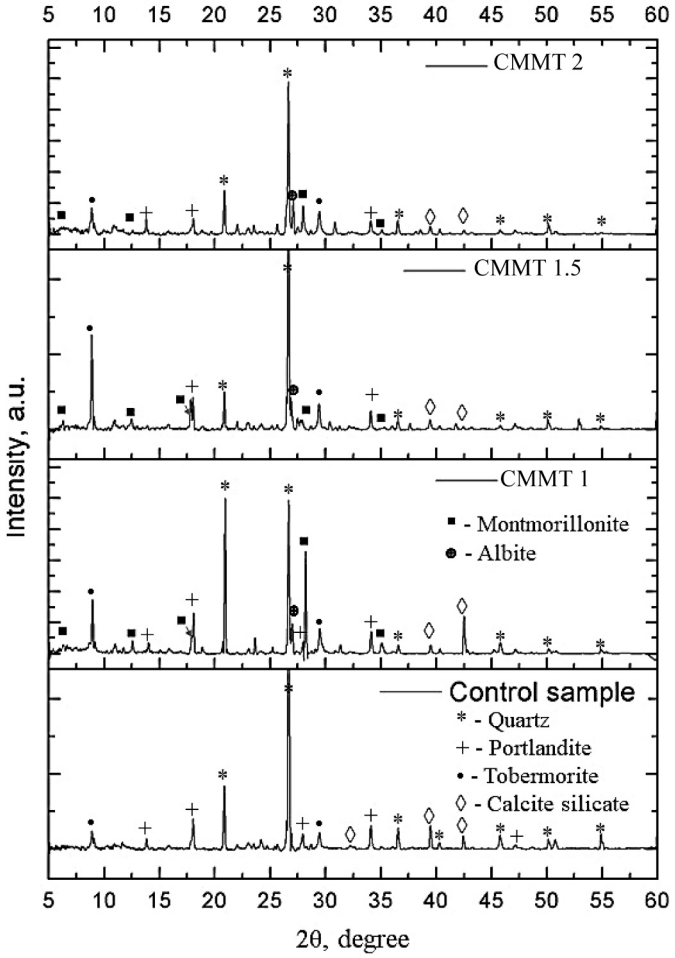

Fig. 12. XRD patterns of cement mortar specimens with different CMMT content.

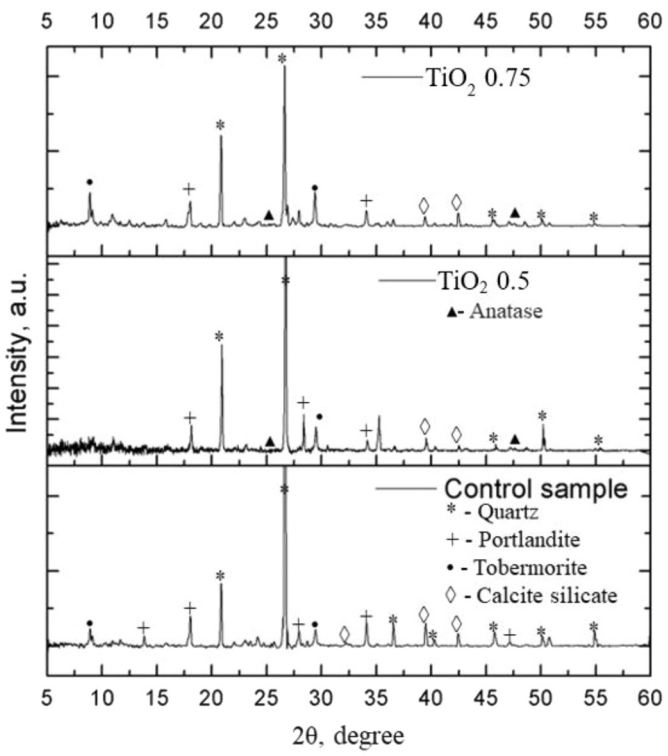

Fig. 13. XRD patterns of cement mortar specimens with different TiO_2 content.

4. Conclusion

The article tackles the use of combined calcined montmorillonite and titanium dioxide nanoparticles in the composition of cement mortar, regarding the mechanical characteristics at 28 days of curing. Based on the analyses developed in the study, the following conclusions are drawn:

- All CMMT-modified cement mortar mixes have a higher flexural strength than the control mix, with a maximum reached for a 1.5 wt % CMMT cement replacement. At the same time, the TiO_2-modified mixes register a decrease in flexural strength compared to the control mix.
- Combining CMMT and TiO_2 nanoparticles in the cement mortar mix does not increase the flexural strength beyond the upper value set by CMMT-modified mortar samples. The result can be explained by the high quantity of water that is still present inside the pores at 28 days of curing, causing a decrease in the adherence between cement and aggregates. Increasing the quantity of nanomaterials implies an increase in water demand during the hydration process. However, after 28 days, this process is still under way. Thus, when subjected to bending, the cement and aggregates are easier to be separated, leading to crack occurrence.
- When combining CMMT and TiO_2 nanoparticles in the cement mortar mix, an improvement in the compressive strength value is registered, compared to the individual nanoparticle-modified samples. The maximum compressive strength is recorded for COMB2, with 3.19% higher than the control specimen. The filler effect of both nanomaterials and the pozzolanic property of CMMT can increase the strength above values corresponding to the control and individual-modified samples.

To conclude, the combination of CMMT and TiO_2 proves to have a positive influence on the cement mortar mix, from the mechanical strength point of view. Nevertheless, considering the slower hydration process of the cement mortar modified with CMMT, compared to the plain cement mortar, it is recommended to study the mechanical behavior of the modified samples at later ages, as an increase in strength is expected. Hence, as the hydration process develops, more CSH is produced and the matrix strengthens. In addition, the water quantity decreases, improving the ITZ and, as consequence, could lead to an increase in flexural strength.

Funding

This research was funded by the Romanian Government through the Ministry of Research, Innovation and Digitalization, grant number PN III 27PFE/2021.

CRediT authorship contribution statement

Cimpoesu Nicanor: Visualization, Software, Investigation, Formal analysis, Data curation. **Istrate Bogdan:** Software, Methodology, Investigation, Formal analysis. **Alexa-Stratulat Sergiu-Mihai:** Validation, Methodology, Investigation, Data curation. **Mihai Petru:** Writing – review & editing, Validation, Supervision, Methodology, Formal analysis. **Stoian George:** Software, Methodology, Investigation, Formal analysis. **Bunea Georgiana:** Writing – original draft, Validation, Supervision, Project administration, Methodology, Investigation, Funding acquisition, Data curation, Conceptualization. **Toma Ionut-Ovidiu:** Writing – review & editing, Writing – original draft, Visualization, Validation, Supervision, Methodology, Investigation, Formal analysis,

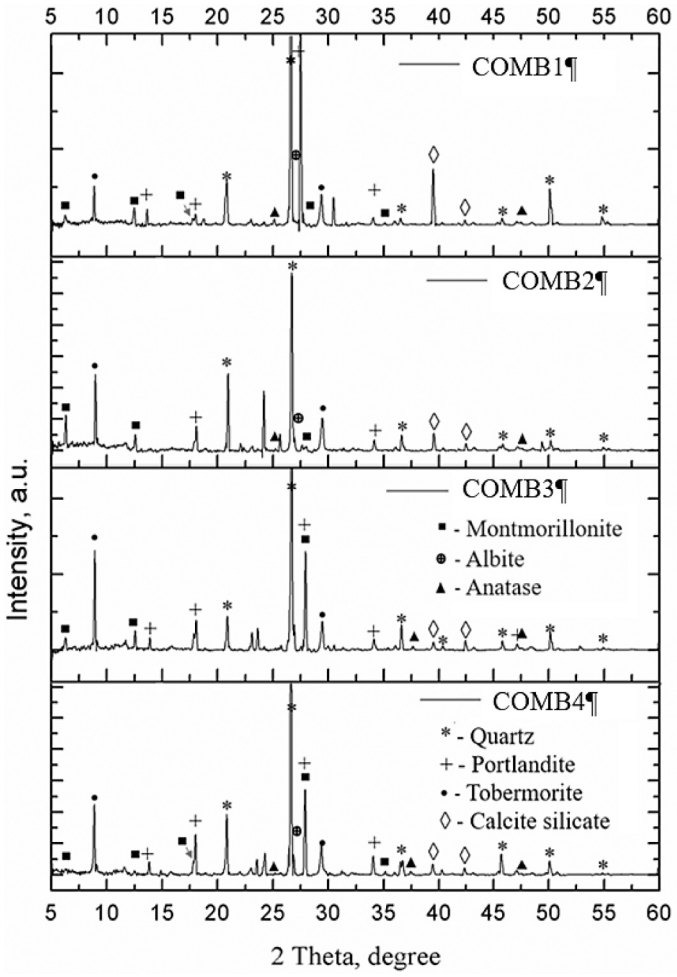

Fig. 14. XRD patterns of cement mortar specimens modified with CMMT and TiO2 nanoparticles.

Data curation, Conceptualization.

Declaration of Competing Interest

The authors declare that they have no known competing financial interests or personal relationships that could have appeared to influence the work reported in this paper.

Data Availability

Data will be made available on request.

Acknowledgments

This research was accomplished with the support of COMPETE 2.0 Project nr. 27PFE/2021, financed by the Romanian Government, Ministry of Research, Innovation and Digitalization. This research was also supported by "Gheorghe Asachi" Technical University from Iaşi (TUIASI), through the Project "Performance and excellence in post-doctoral research 2022".

References

[1] P. Sikora, M. Abd Elrahman, D. Stephan, The influence of nanomaterials on the thermal resistance of cement-based composites-a review, Nanomaterials 8 (2018), https://doi.org/10.3390/nano8070465.

[2] H. Saleem, S.J. Zaidi, N.A. Alnuaimi, Recent advancements in the nanomaterial application in concrete and its ecological impact, Materials 14 (2021), https://doi.org/10.3390/ma14216387.

[3] G.F. Huseien, A review on concrete composites modified with nanoparticles, J. Compos. Sci. 7 (2023), https://doi.org/10.3390/jcs7020067.

[4] G. Goel, P. Sachdeva, A.K. Chaudhary, Y. Singh, The use of nanomaterials in concrete: a review, Mater. Today Proc. 69 (2022) 365–371, https://doi.org/10.1016/j.matpr.2022.09.051.

[5] B.B. Jindal, R. Sharma, The effect of nanomaterials on properties of geopolymers derived from industrial by-products: a state-of-the-art review, Constr. Build. Mater. 252 (2020), https://doi.org/10.1016/j.conbuildmat.2020.119028.

[6] C. Liu, X. Su, Y. Wu, Z. Zheng, B. Yang, Y. Luo, J. Yang, J. Yang, Effect of nano-silica as cementitious materials-reducing admixtures on the workability, mechanical properties and durability of concrete 10 (2021) 1395–1409, https://doi.org/10.1515/ntrev-2021-0097.

[7] F.T. Isfahani, E. Redaelli, F. Lollini, W. Li, L. Bertolini, Effects of nanosilica on compressive strength and durability properties of concrete with different water to binder ratios, Adv. Mater. Sci. Eng. 2016 (2016), https://doi.org/10.1155/2016/8453567.

[8] B. Behnia, H. Safardoust-Hojaghan, O. Amiri, M. Salavati-Niasari, A. Aali Anvari, High-performance cement mortars-based composites with colloidal nano-silica: synthesis, characterization and mechanical properties, Arab. J. Chem. 14 (2021), https://doi.org/10.1016/j.arabjc.2021.103338.

[9] S. Gupta, Application of nano-silica in cement mortar and concrete, in: M.S. Liew, P. Nguyen-Tri, T.A. Nguyen, S. Kakooei (Eds.), Smart Nanoconcretes and Cement-Based Materials, 27, Elsevier, 2020, pp. 601–617, https://doi.org/10.1016/B978-0-12-817854-6.00027-1.

[10] N.G. Muradyan, H. Gyulasaryan, A.A. Arzumanyan, M.M. Badalyan, M. A. Kalantaryan, Y.V. Vardanyan, D. Laroze, A. Manukyan, M.G. Barseghyan, The effect of multi-walled carbon nanotubes on the compressive strength of cement mortars, Coatings 12 (2022), https://doi.org/10.3390/coatings12121933.

[11] A. Hassan, S. Galal, A. Hassan, A. Salman, Utilization of carbon nanotubes and steel fibers to improve the mechanical properties of concrete pavement, Beni Suef Univ. J. Basic Appl. Sci. 11 (2022) 121, https://doi.org/10.1186/s43088-022-00300-5.

[12] Y. Liu, X. Cheng, Effect of carbon nanotube size on electrical properties of cement mortar under different temperatures and water content, Geofluids 2022 (2022) 7237049, https://doi.org/10.1155/2022/7237049.

[13] A. Hassan, H. Elkady, I.G. Shaaban, Effect of adding carbon nanotubes on corrosion rates and steel-concrete bond, Sci. Rep. 9 (2019) 6285, https://doi.org/10.1038/s41598-019-42761-2.

[14] M.O. Mohsen, M.S. Al Ansari, R. Taha, N. Al Nuaimi, A.A. Taqa, Carbon nanotube effect on the ductility, flexural strength, and permeability of concrete, J. Nanomater 2019 (2019) 6490984, https://doi.org/10.1155/2019/6490984.

[15] K. Sreeja, T. Naresh Kumar, Effect of graphene oxide on fresh, hardened and mechanical properties of cement mortar, Mater. Today Proc. 46 (2021) 2235–2239, https://doi.org/10.1016/j.matpr.2021.03.574.

[16] E. Najafi Kani, A.H. Rafiean, A. Alishah, S. Hojjati Astani, S.H. Ghaffar, The effects of Nano-Fe2O3 on the mechanical, physical and microstructure of cementitious composites, Constr. Build. Mater. 266 (2021), https://doi.org/10.1016/j.conbuildmat.2020.121137.

[17] R. Gowda, H. Narendra, D. Rangappa, R. Prabhakar, Effect of nano-alumina on workability, compressive strength and residual strength at elevated temperature of cement mortar, Mater. Today Proc. 4 (2017) 12152–12156, https://doi.org/10.1016/j.matpr.2017.09.144.

[18] A. Zhao, J. Yang, E.H. Yang, Self-cleaning engineered cementitious composites, Cem. Concr. Compos 64 (2015) 74–83, https://doi.org/10.1016/J.CEMCONCOMP.2015.09.007.

[19] P.G. Moradeeya, A. Sharma, M.A. Kumar, S. Basha, Titanium dioxide based nanocomposites – current trends and emerging strategies for the photocatalytic degradation of ruinous environmental pollutants, Environ. Res 204 (2022) 112384, https://doi.org/10.1016/J.ENVRES.2021.112384.

[20] M. Janczarek, Ł. Klapiszewski, P. Jędrzejczak, I. Klapiszewska, A. Ślosarczyk, T. Jesionowski, Progress of functionalized TiO2-based nanomaterials in the construction industry: a comprehensive review, Chem. Eng. J. 430 (2022) 132062, https://doi.org/10.1016/J.CEJ.2021.132062.

[21] J. Chen, S. Kou, C. Poon, Hydration and properties of nano-TiO2 blended cement composites, Cem. Concr. Compos 34 (2012) 642–649, https://doi.org/10.1016/j.cemconcomp.2012.02.009.

[22] M. Xu, Y. Bao, K. Wu, H. Shi, X. Guo, V.C. Li, Multiscale investigation of tensile properties of a TiO2-doped engineered cementitious composite, Constr. Build. Mater. 209 (2019) 485–491, https://doi.org/10.1016/J.CONBUILDMAT.2019.03.112.

[23] T.S. Mustafa, M.O.R. El Hariri, M.A. Nader, W.M. Montaser, Enhanced shear behaviour of reinforced concrete beams containing nano-titanium, Eng. Struct. 257 (2022) 114082, https://doi.org/10.1016/J.ENGSTRUCT.2022.114082.

[24] M. Daniyal, S. Akhtar, A. Azam, Effect of nano-TiO2 on the properties of cementitious composites under different exposure environments, J. Mater. Res. Technol. 8 (2019) 6158–6172, https://doi.org/10.1016/J.JMRT.2019.10.010.

[25] N. Farzadnia, A.A. Abang Ali, R. Demirboga, M.P. Anwar, Characterization of high strength mortars with nano Titania at elevated temperatures, Constr. Build. Mater. 43 (2013) 469–479, https://doi.org/10.1016/J.CONBUILDMAT.2013.02.044.

[26] D. Siang Ng, S.C. Paul, V. Anggraini, S.Y. Kong, T.S. Qureshi, C.R. Rodriguez, Q. feng Liu, B. Šavija, Influence of SiO2, TiO2 and Fe2O3 nanoparticles on the

properties of fly ash blended cement mortars, Constr. Build. Mater. 258 (2020), https://doi.org/10.1016/j.conbuildmat.2020.119627.
[27] A.Qudoos Atta-ur-Rehman, H.G. Kim, J.S. Ryou, Influence of titanium dioxide nanoparticles on the sulfate attack upon ordinary Portland cement and slag-blended mortars, Materials 11 (2018), https://doi.org/10.3390/ma11030356.
[28] V.K. Doko, S.P. Hounkpe, S.O. Kotchoni, L. Hui, A.T. Datchossa, Changing mechanicals characteristiques of cementitious materials using titanium dioxide, Mater. Sci. Appl. 12 (2021) 297–313, https://doi.org/10.4236/msa.2021.126020.
[29] S. Papatzani, E.G. Badogiannis, K. Paine, The pozzolanic properties of inorganic and organomodified nano-montmorillonite dispersions, Constr. Build. Mater. 167 (2018) 299–316, https://doi.org/10.1016/J.CONBUILDMAT.2018.01.123.
[30] T.P. Chang, J.Y. Shih, K.M. Yang, T.C. Hsiao, Material properties of portland cement paste with nano-montmorillonite, J. Mater. Sci. 42 (2007) 7478–7487, https://doi.org/10.1007/s10853-006-1462-0.
[31] M.R. Irshidat, M.H. Al-Saleh, Thermal performance and fire resistance of nanoclay modified cementitious materials, Constr. Build. Mater. 159 (2018) 213–219, https://doi.org/10.1016/J.CONBUILDMAT.2017.10.127.
[32] M.R. Irshidat, M.H. Al-Saleh, Thermal performance and fire resistance of nanoclay modified cementitious materials, Constr. Build. Mater. 159 (2018) 213–219, https://doi.org/10.1016/J.CONBUILDMAT.2017.10.127.
[33] S. Alani, M.S. Hassan, A.A. Jaber, I.M. Ali, Effects of elevated temperatures on strength and microstructure of mortar containing nano-calcined montmorillonite clay, Constr. Build. Mater. 263 (2020), https://doi.org/10.1016/j.conbuildmat.2020.120895.
[34] M. Chi, R. Huang, Effect of montmorillonite as additive on the properties of cement-based composites, Sci. Eng. Compos. Mater. 19 (2012) 45–54, https://doi.org/10.1515/secm-2011-0129.
[35] M.A. Kafi, A. Sadeghi-Nik, A. Bahari, A. Sadeghi-Nik, E. Mirshafiei, Microstructural characterization and mechanical properties of cementitious mortar containing montmorillonite nanoparticles, J. Mater. Civ. Eng. 28 (2016), https://doi.org/10.1061/(asce)mt.1943-5533.0001671.
[36] W. Asim, M. Hussain, N.R. Kadhim, A.T. Abdulrasool, S.A. Alhabeeb, S.S. Mohammed, Influence of Using Nano-Clay Hydrophilic Bentonite on Mechanical Properties of Concrete, 2022. ⟨http://journalppw.com⟩.
[37] M.R. Irshidat, M.H. Al-Saleh, Influence of nanoclay on the properties and morphology of cement mortar, KSCE J. Civ. Eng. 22 (2018) 4056–4063, https://doi.org/10.1007/s12205-018-1642-x.
[38] S.J. Lee, S. Kawashima, K.J. Kim, S.K. Woo, J.P. Won, Shrinkage characteristics and strength recovery of nanomaterials-cement composites, Compos Struct. 202 (2018) 559–565, https://doi.org/10.1016/J.COMPSTRUCT.2018.03.003.
[39] W.Y. Kuo, J.S. Huang, C.H. Lin, Effects of organo-modified montmorillonite on strengths and permeability of cement mortars, Cem. Concr. Res 36 (2006) 886–895, https://doi.org/10.1016/j.cemconres.2005.11.013.
[40] S. Gea, M. Firmansyah, T. Hidayat, Marpongahtun, Y.A. Hutapea, The preparation and characterization of bentonite nanoparticle from Bener Meriah, Indonesia, in: J Phys Conf Ser, Institute of Physics Publishing, 2018. https://doi.org/10.1088/1742–6596/1116/4/042011.
[41] D. RKh, A. SKh, A. Ma-v, I. M-am, Surface Characteristics of Nanosized Bentonite Suspensions as a Modifying Component of Cement Composites, 2018.
[42] R.M. Waqas, F. Butt, A. Danish, M. Alqurashi, M.A. Mosaberpanah, B. Masood, E. E. Hussein, Influence of bentonite on mechanical and durability properties of high-calcium fly ash geopolymer concrete with natural and recycled aggregates, Materials 14 (2021), https://doi.org/10.3390/ma14247790.
[43] A. Nazari, S. Riahi, S. Riahi, S. Fatemeh Shamekhi, A. Khademno, Assessment of the effects of the cement paste composite in presence TiO2 nanoparticles, 2010. ⟨http://www.americanscience.orgeditor@americanscience.org⟩.
[44] A. Nazari, S. Riahi, The effect of TiO2 nanoparticles on water permeability and thermal and mechanical properties of high strength self-compacting concrete, Mater. Sci. Eng.: A 528 (2010) 756–763, https://doi.org/10.1016/J.MSEA.2010.09.074.
[45] S. Papatzani, E.G. Badogiannis, K. Paine, The pozzolanic properties of inorganic and organomodified nano-montmorillonite dispersions, Constr. Build. Mater. 167 (2018) 299–316, https://doi.org/10.1016/j.conbuildmat.2018.01.123.
[46] T.P. Chang, J.Y. Shih, K.M. Yang, T.C. Hsiao, Material properties of portland cement paste with nano-montmorillonite, J. Mater. Sci. 42 (2007) 7478–7487, https://doi.org/10.1007/s10853-006-1462-0.
[47] R. Fernandez, F. Martirena, K.L. Scrivener, The origin of the pozzolanic activity of calcined clay minerals: a comparison between kaolinite, illite and montmorillonite, Cem. Concr. Res 41 (2011) 113–122, https://doi.org/10.1016/j.cemconres.2010.09.013.
[48] G. Diamantopoulos, M. Katsiotis, M. Fardis, I. Karatasios, S. Alhassan, M. Karagianni, G. Papavassiliou, J. Hassan, The role of titanium dioxide on the hydration of portland cement: a combined NMR and ultrasonic study, Molecules 25 (2020), https://doi.org/10.3390/molecules25225364.
[49] D.P. Rawski, Pulp and Paper: Nonfibrous Components, in: K.H.J. Buschow, R. W. Cahn, M.C. Flemings, B. Ilschner, E.J. Kramer, S. Mahajan, P. Veyssière (Eds.), Encyclopedia of Materials: Science and Technology, Elsevier, Oxford, 2001, pp. 7908–7910, https://doi.org/10.1016/B0-08-043152-6/01423-6.
[50] A.M. Castro-Hoyos, M.A. Rojas Manzano, A. Maury-Ramírez, Challenges and opportunities of using titanium dioxide photocatalysis on cement-based materials, Coatings 12 (2022), https://doi.org/10.3390/coatings12070968.
[51] F. Hamidi, F. Aslani, Tio2-based photocatalytic cementitious composites: materials, properties, influential parameters, and assessment techniques, Nanomaterials 9 (2019), https://doi.org/10.3390/nano9101444.
[52] Z.U. Zango, A. Garba, Z.N. Garba, M.U. Zango, F. Usman, J.-W. Lim, Montmorillonite for adsorption and catalytic elimination of pollutants from wastewater: a state-of-the-arts review, Sustainability 14 (2022), https://doi.org/10.3390/su142416441.
[53] D. Luo, J. Wei, Upgrading sodium montmorillonite into a reactive internal curing agent for sustainable cement composites through non-ionic functionalization, Compos B Eng. 242 (2022) 110076, https://doi.org/10.1016/j.compositesb.2022.110076.
[54] A. Sadeghi-Nik, J. Berenjian, A. Bahari, A.S. Safaei, M. Dehestani, Modification of microstructure and mechanical properties of cement by nanoparticles through a sustainable development approach, Constr. Build. Mater. 155 (2017) 880–891, https://doi.org/10.1016/j.conbuildmat.2017.08.107.
[55] V. Matějka, P. Kovář, P. Bábková, J. Přikryl, K. Mamulová-Kutláková, P. Čapková, Utilization of Photoactive Kaolinite/TiO2 Composite in Cement-Based Building Materials, in: Z. Bittnar, P.J.M. Bartos, J. Němeček, V. Šmilauer, J. Zeman (Eds.), Nanotechnology in construction 3, Springer Berlin Heidelberg, Berlin, Heidelberg, 2009, pp. 309–314.
[56] S.D.A. Selvasofia, E. Sarojini, G. Moulica, S. Thomas, M. Tharani, P. T. Saravanakumar, P.M. Kumar, Study on the mechanical properties of the nanoconcrete using nano-TiO2 and nanoclay, Mater. Today Proc. 50 (2022) 1319–1325, https://doi.org/10.1016/J.MATPR.2021.08.242.
[57] Z. Li, J. Gong, S. Du, J. Wu, J. Li, D. Hoffman, X. Shi, Nano-montmorillonite modified foamed paste with a high volume fly ash binder, RSC Adv. 7 (2017) 9803–9812, https://doi.org/10.1039/C6RA26968K.
[58] E.M. Aydin, B. Kara, Z.B. Bundur, N. Ozyurt, O. Bebek, M. Ali Gulgun, A comparative evaluation of sepiolite and nano-montmorillonite on the rheology of cementitious materials for 3D printing, Constr. Build. Mater. 350 (2022) 128935, https://doi.org/10.1016/j.conbuildmat.2022.128935.
[59] D.K. Das, A.K. Tiwary, Influence of nano bentonite clay and nano fly ash on the mechanical and durability properties of concrete, Clean. Technol. Environ. Policy (2023), https://doi.org/10.1007/s10098-023-02610-3.
[60] J. Ren, S.-Y. Guo, T.-J. Zhao, J.-Z. Chen, R.S. Nicolas, L. Zhang, Constructing a novel nano-TiO2/Epoxy resin composite and its application in alkali-activated slag/fly ash pastes, Constr. Build. Mater. 232 (2020) 117218, https://doi.org/10.1016/j.conbuildmat.2019.117218.
[61] S.-Y. Guo, X. Zhang, J. Ren, J.-Z. Chen, T.-J. Zhao, T.-W. Li, L. Zhang, Preparation of TiO2/epoxy resin composite and its effect on mechanical and bonding properties of OPC mortars, Constr. Build. Mater. 272 (2021) 121960, https://doi.org/10.1016/j.conbuildmat.2020.121960.
[62] S.-L. Zhang, X.-Q. Qi, S.-Y. Guo, J. Ren, J.-Z. Chen, B. Chi, X.-C. Wang, Effect of a novel hybrid TiO2-graphene composite on enhancing mechanical and durability characteristics of alkali-activated slag mortar, Constr. Build. Mater. 275 (2021) 122154, https://doi.org/10.1016/j.conbuildmat.2020.122154.
[63] S.D.A. Selvasofia, E. Sarojini, G. Moulica, S. Thomas, M. Tharani, P. T. Saravanakumar, P.M. Kumar, Study on the mechanical properties of the nanoconcrete using nano-TiO2 and nanoclay, Mater. Today Proc. 50 (2022) 1319–1325, https://doi.org/10.1016/J.MATPR.2021.08.242.
[64] European Committee for Standardization, Cement, Part 1: Composition, specifications and conformity criteria for common cements SR EN 197–1:2011, n. d. www.asro.ro (accessed March 24, 2023).
[65] C. Zhou, D. Tong, W. Yu, Smectite nanomaterials: preparation, properties, and functional applications, Nanomater. Clay Miner.: A N. Approach Green. Funct. Mater. (2019) 335–364, https://doi.org/10.1016/B978-0-12-814533-3.00007-7.
[66] E.P. Grishina, L.M. Ramenskaya, N.O. Kudryakova, K.V. Vagin, A.S. Kraev, A. V. Agafonov, Composite nanomaterials based on 1-butyl-3-methylimidazolium dicianamide and clays, J. Mater. Res. Technol. 8 (2019) 4387–4398, https://doi.org/10.1016/j.jmrt.2019.07.050.
[67] P. Yu, Z. Wang, P. Lai, P. Zhang, J.P. Wang, Evaluation of mechanic damping properties of montmorillonite/organo-modified montmorillonite-reinforced cement paste, Constr. Build. Mater. 203 (2019) 356–365, https://doi.org/10.1016/J.CONBUILDMAT.2019.01.110.
[68] G. Bunea, S.-M. Alexa-Stratulat, P. Mihai, I.-O. Toma, Use of clay and titanium dioxide nanoparticles in mortar and concrete—a state-of-the-art analysis, Coatings 13 (2023) 506, https://doi.org/10.3390/coatings13030506.
[69] G. Wakoya, E.T. Quezon, W. Ararsa, J. Chimdi, G.D. Lemu, Effect and suitability of calcined montmorillonite clay powder and waste khat husk ash in the strength and durability of C-25 concrete and its benefits cost analysis, J. Sustain. Constr. Mater. Proj. Manag. 1 (2021). ⟨https://www.scipedia.com/public/Review_135425093121⟩.
[70] N. Garg, J. Skibsted, Heated montmorillonite: structure, reactivity, and dissolution, in: K. Scrivener, A. Favier (Eds.), Calcined Clays for Sustainable Concrete, Springer Netherlands, Dordrecht, 2015, pp. 117–124, https://doi.org/10.1007/978-94-017-9939-3_15.
[71] N. Garg, J. Skibsted, Thermal activation of a pure montmorillonite clay and its reactivity in cementitious systems, J. Phys. Chem. C. 118 (2014) 11464–11477, https://doi.org/10.1021/jp502529d.
[72] European Committee for Standardization, Aggregates for concrete SR EN 12620+A1:2009, 2009. ⟨www.asro.ro⟩.
[73] G. Li, J. Zeng, J. Luo, M. Liu, T. Jiang, G. Qiu, Thermal transformation of pyrophyllite and alkali dissolution behavior of silicon, Appl. Clay Sci. 99 (2014) 282–288, https://doi.org/10.1016/j.clay.2014.07.011.
[74] J. Cuevas, M.Á. Cabrera, C. Fernández, C. Mota-Heredia, R. Fernández, E. Torres, M.J. Turrero, A.I. Ruiz, Bentonite powder XRD quantitative analysis using rietveld refinement: revisiting and updating bulk semiquantitative mineralogical compositions, Minerals 12 (2022), https://doi.org/10.3390/min12060772.

[75] V.A. Lebedev, D.A. Kozlov, I.V. Kolesnik, A.S. Poluboyarinov, A.E. Becerikli, W. Grünert, A.V. Garshev, The amorphous phase in titania and its influence on photocatalytic properties, Appl. Catal. B 195 (2016) 39–47, https://doi.org/10.1016/j.apcatb.2016.05.010.
[76] H. Bresch, V.-D. Hodoroaba, A. Schmidt, K. Rasmussen, H. Rauscher, Counting small particles in electron microscopy images—proposal for rules and their application in practice, Nanomaterials 12 (2022) 2238, https://doi.org/10.3390/nano12132238.
[77] ASTM International, Standard Practice for Mechanical Mixing of Hydraulic Cement Pastes and Mortars of Plastic Consistency ASTM 305–06, n.d. www.astm.org.
[78] IS 10890: Specification for planetary mixer used in tests of cement and pozzolana, New Delhi, 1984.
[79] European Committee for Standardization, Test Methods for Cement, Part 1: Mechanical Strength Test SR EN 196–1:2006, (n.d.).
[80] European Committee for Standardization, Methods of testing cement. Part 3, Determination of setting time and soundness. SR EN 196–3:2005, BSI, 1995.
[81] A. Altomare, N. Corriero, C. Cuocci, A. Falcicchio, A. Moliterni, R. Rizzi, QUALX2.0: a qualitative phase analysis software using the freely available database POW-COD, J. Appl. Crystallogr 48 (2015) 598–603, https://doi.org/10.1107/S1600576715002319.
[82] G. Shafabakhsh, A.M. Janaki, O.J. Ani, Laboratory investigation on durability of nano clay modified concrete pavement, Eng. J. 24 (2020) 35–44, https://doi.org/10.4186/ej.2020.24.3.35.
[83] V.A. Franco-Luján, F. Montejo-Alvaro, S. Ramírez-Arellanes, H. Cruz-Martínez, D. I. Medina, Nanomaterial-reinforced portland-cement-based materials: a review, Nanomaterials 13 (2023) 1383, https://doi.org/10.3390/nano13081383.
[84] M.K. Moraes, E. Maria da Costa, Effect of adding organo-modified montmorillonite nanoclay on the performance of oil-well cement paste in CO_2-rich environments, Cem. Concr. Compos 127 (2022) 104400, https://doi.org/10.1016/J.CEMCONCOMP.2021.104400.
[85] A. Hakamy, F.U.A. Shaikh, I.M. Low, Characteristics of nanoclay and calcined nanoclay-cement nanocomposites, Compos B Eng. 78 (2015) 174–184, https://doi.org/10.1016/j.compositesb.2015.03.074.
[86] P. Jędrzejczak, A. Parus, S. Balicki, K. Kornaus, M. Janczarek, K.A. Wilk, T. Jesionowski, A. Ślosarczyk, Ł. Klapiszewski, The influence of various forms of titanium dioxide on the performance of resultant cement composites with photocatalytic and antibacterial functions, Mater. Res Bull. 160 (2023), https://doi.org/10.1016/j.materresbull.2022.112139.
[87] M.J. Kadhim, R.S. Al-Jadiri, M.A. Al Wahab Ali, Study the Effect of Addition nano-TiO2 by Dispersion Method on the Some Mechanical Properties and Durability of Cement Mortar, in: IOP Conf Ser Mater Sci Eng, Institute of Physics Publishing, 2019. https://doi.org/10.1088/1757–899X/518/3/032027.
[88] S.S. Lucas, V.M. Ferreira, J.L.B. De Aguiar, Incorporation of titanium dioxide nanoparticles in mortars - influence of microstructure in the hardened state properties and photocatalytic activity, Cem. Concr. Res. 43 (2013) 112–120, https://doi.org/10.1016/j.cemconres.2012.09.007.
[89] M. Daniyal, S. Akhtar, A. Azam, Effect of nano-TiO2 on the properties of cementitious composites under different exposure environments, J. Mater. Res. Technol. 8 (2019) 6158–6172, https://doi.org/10.1016/J.JMRT.2019.10.010.
[90] A. Joshaghani, Evaluating the effects of titanium dioxide (TiO2) and carbon-nanofibers (CNF) as cement partial replacement on concrete properties, MOJ Civ. Eng. 4 (2018) 29–38, https://doi.org/10.15406/mojce.2018.04.00094.
[91] V. Francioso, C. Moro, I. Martinez-Lage, M. Velay-Lizancos, Curing temperature: a key factor that changes the effect of TiO2 nanoparticles on mechanical properties, calcium hydroxide formation and pore structure of cement mortars, Cem. Concr. Compos 104 (2019) 103374, https://doi.org/10.1016/J.CEMCONCOMP.2019.103374.
[92] V.K. Karunarathne, S.C. Paul, B. Šavija, Development of nano-SiO2 and bentonite-based mortars for corrosion protection of reinforcing steel, Materials 12 (2019), https://doi.org/10.3390/ma12162622.
[93] G.L. Golewski, The role of pozzolanic activity of siliceous fly ash in the formation of the structure of sustainable cementitious composites, Sustain. Chem. 3 (2022) 520–534, https://doi.org/10.3390/suschem3040032.
[94] S.S. Mousavi, C. Bhojaraju, C. Ouellet-Plamondon, Clay as a sustainable binder for concrete—a review, Constr. Mater. 1 (2021) 134–168, https://doi.org/10.3390/constrmater1030010.
[95] S. Ahmad, S.A. Barbhuiya, A. Elahi, J. Iqbal, Effect of Pakistani bentonite on properties of mortar and concrete, Clay Min. 46 (2011) 85–92, https://doi.org/10.1180/claymin.2011.046.1.85.
[96] H.H. Lee, C.W. Wang, P.Y. Chung, Experimental study on the strength and durability for slag cement mortar with bentonite, Appl. Sci. (Switz.) 11 (2021) 1–13, https://doi.org/10.3390/app11031176.
[97] H.H. Lee, C.W. Wang, Experimental study on cement mortar with bentonite, : Adv. Mat. Res. (2013) 1741–1744, https://doi.org/10.4028/www.scientific.net/AMR.671-674.1741.
[98] D. Shafaei, S. Yang, L. Berlouis, J. Minto, Multiscale pore structure analysis of nano titanium dioxide cement mortar composite, Mater. Today Commun. 22 (2020), https://doi.org/10.1016/j.mtcomm.2019.100779.
[99] J. Szymanowski, Ł. Sadowski, The influence of the addition of tetragonal crystalline titanium oxide nanoparticles on the adhesive and functional properties of layered cementitious composites, Compos Struct. 233 (2020), https://doi.org/10.1016/j.compstruct.2019.111636.
[100] Z. Yang, H. Ye, Q. Yuan, B. Li, Y. Li, D. Zhou, Factors influencing the hydration, dimensional stability, and strength development of the opc-csa-anhydrite ternary system, Materials 14 (2021), https://doi.org/10.3390/ma14227001.
[101] G. Regmi, B. Indraratna, L.D. Nghiem, L. Banasiak, Evaluating waste concrete for the treatment of acid sulphate soil groundwater from coastal floodplains, Desalin. Water Treat. 32 (2011) 126–132, https://doi.org/10.5004/dwt.2011.2687.
[102] M. Singh, R. Sidddique, S.S. Setia, G. Singh, Recycling of waste bagasse ash in concrete for sustainable construction, Asian J. Civ. Eng. 22 (2021) 831–842, https://doi.org/10.1007/s42107-021-00349-0.
[103] S. Hoshino, T. Yamaguchi, T. Maeda, M. Mukai, T. Tanaka, S. Nakayama, Mineralogical changes of cement and bentonite accompanied with their interactions, MRS Online Proc. Libr. 1193 (2009) 445, https://doi.org/10.1557/PROC-1193-445.
[104] J. Qin, X. Pang, H. Li, Z. Zhang, Mechanism of long-term strength retrogression of silica-enriched Portland cement assessed by quantitative X-ray diffraction analysis, Front Mater. 9 (2022), https://doi.org/10.3389/fmats.2022.982192.
[105] B. Tang, W. Cui, B. zeng Zhang, Z. an Jiang, The macroscopic mechanical characteristics and microscopic evolution mechanism of plastic concrete, Constr. Build. Mater. 391 (2023), https://doi.org/10.1016/j.conbuildmat.2023.131898.
[106] F.J. Shi, S.J. Feng, Q.T. Zheng, X.L. Zhang, H.X. Chen, Effect of polyanionic cellulose modification on properties and microstructure of calcium bentonite, Appl. Clay Sci. 228 (2022), https://doi.org/10.1016/j.clay.2022.106633.
[107] M. Liu, Y. Hu, Z. Lai, T. Yan, X. He, J. Wu, Z. Lu, S. Lv, Influence of various bentonites on the mechanical properties and impermeability of cement mortars, Constr. Build. Mater. 241 (2020) 118015, https://doi.org/10.1016/j.conbuildmat.2020.118015.
[108] S. Feng, J. Song, F. Liu, X. Fu, H. Guo, J. Zhu, Q. Zeng, X. Peng, X. Wang, Y. Ouyang, F. Li, Photocatalytic properties, mechanical strength and durability of TiO2/cement composites prepared by a spraying method for removal of organic pollutants, Chemosphere 254 (2020), https://doi.org/10.1016/j.chemosphere.2020.126813.
[109] X. Yu, C. Zhang, Q. Yang, S. Kasap, Enhancement of hardness in nanostructured CuO/TiO2–cement composites, SN Appl. Sci. 2 (2020), https://doi.org/10.1007/s42452-020-2428-6.

coatings

MDPI

Review

The Use of Natural Zeolites in Cement-Based Construction Materials—A State of the Art Review

Sergiu-Mihai Alexa-Stratulat [1], Ioana Olteanu [1], Ana-Maria Toma [1], Cristian Pastia [1,*], Oana-Mihaela Banu [1], Ofelia-Cornelia Corbu [2] and Ionut-Ovidiu Toma [1,*]

[1] Faculty of Civil Engineering and Building Services, The "Gheorghe Asachi" Technical University of Iasi, 700050 Iași, Romania; sergiu-mihai.alexa-stratulat@staff.tuiasi.ro (S.-M.A.-S.); ioana.olteanu@academic.tuiasi.ro (I.O.); ana-maria.toma@academic.tuiasi.ro (A.-M.T.); oana-mihaela.banu@academic.tuiasi.ro (O.-M.B.)

[2] Faculty of Civil Engineering, Technical University of Cluj-Napoca, 400114 Cluj-Napoca, Romania; ofelia.corbu@staff.utcluj.ro

* Correspondence: cristian.pastia@academic.tuiasi.ro (C.P.); ionut.ovidiu.toma@tuiasi.ro (I.-O.T.); Tel.: +40-232-701455 (I.-O.T.)

Abstract: Natural zeolite is a honeycomb-structured aluminosilicate mineral with an open crystalline structure which makes it suitable for a variety of applications. Given the beneficial effects of zeolites on the properties of cementitious materials, the present paper aims to summarize the recent findings reported in the scientific literature on the use of zeolites in cement-based construction materials. This paper limits the analysis to natural zeolites. The influence of natural zeolites on the workability and setting time of cement-based construction materials revealed that increasing the zeolite content led to a reduction in workability compared to the control mixes. At the same time, the initial and final setting times of cement pastes showed a decreasing trend with an increase in the replacement percentage. The slow pozzolanic reaction of clinoptilolite zeolite results in lower flexural strength and compressive strength values of mortars at the age of 28 days. Blending zeolites with other supplementary cementitious materials resulted in improved values of the mechanical properties of mortar and concrete. The findings regarding the impact of zeolite on the durability of concrete suggest that zeolite shows promise as a viable alternative to cement, with positive effects on various aspects of durability. The majority of the durability factors are interconnected. The presence of conflicting findings is particularly significant in this context, highlighting the need for a comprehensive approach to address these challenges in the future.

Keywords: natural zeolite; cement-based materials; workability; strength; durability

Citation: Alexa-Stratulat, S.-M.; Olteanu, I.; Toma, A.-M.; Pastia, C.; Banu, O.-M.; Corbu, O.-C.; Toma, I.-O. The Use of Natural Zeolites in Cement-Based Construction Materials—A State of the Art Review. *Coatings* **2024**, *14*, 18. https://doi.org/10.3390/coatings14010018

Academic Editor: Qiao Dong

Received: 24 November 2023
Revised: 20 December 2023
Accepted: 21 December 2023
Published: 23 December 2023

1. Introduction

Natural zeolite is a honeycomb-structured aluminosilicate mineral with an open crystalline structure which makes it suitable for a variety of applications. The term "zeolite" was proposed by the Swedish mineralogist A. F. Cronstedt in 1756 [1] and it stems from the Greek words "zeo", meaning "to boil", and "lithos", meaning "stone". Hence, the meaning of "zeolite" is literally "boiling stone" and was attributed to it based on the observations of Cronstedt, who discovered that rapidly heating this mineral produced steam from the water that was previously absorbed by the material.

Nowadays, there are more than 50 types of known natural zeolites and more than 150 types of synthetic zeolites, with different applications in various industries. In the construction industry, especially when referring to cement-based materials, natural zeolites are mostly known for replacing Portland cement due to their pozzolanic nature [2]. The large percentages of SiO_2 and Al_2O_3 found in zeolites can react with $Ca(OH)_2$ produced during the hydration process of cement and form additional phases of calcium–silicate–hydrate (C-S-H) [2–4]. This results in a denser structure of the cementitious matrix, leading

to improved strength and durability characteristics of the material [5]. According to several studies, clinoptilolite, heulandite and faujasite are the most used types of natural zeolites in the construction industry [3,6] because of their cation exchange capacity.

Due to their internal structure, consisting of a network of tetrahedral crystals with extremely small pores and channels, zeolites have a very high total specific surface of 34–45 m^2/g [2] and are able to easily absorb and desorb water. Clinoptilolite zeolites have the advantage of not changing their dimensions during the absorption and desorption phases [5] and are, therefore, preferred to other natural zeolites when used in cement-based materials. However, their pozzolanic effect is, sometimes, considered to be slow compared to other types of natural zeolites and their effect can continue for longer periods of time than the standard age of 28 days for assessing mortar/concrete mechanical properties [3,7].

While the pozzolanic properties of zeolites make them suitable as supplementary cementitious materials, leading to improved mechanical properties of cement-based construction materials [8], their high porosity and the configuration of their internal structure, as shown in Figure 1, leads to two different effects. In the fresh state, zeolites containing cementitious materials exhibit a lower workability, as reported by several recent studies [3–5,9], but without significant influence on the setting time [4,10]. In the hardened state, the water absorbed by the zeolites is gradually desorbed and contributes to the long-term hydration of the cement particles, thus acting as an internal curing agent [5,8]. At the same time, zeolites significantly reduce the autogenous shrinkage of cement-based materials [8,11].

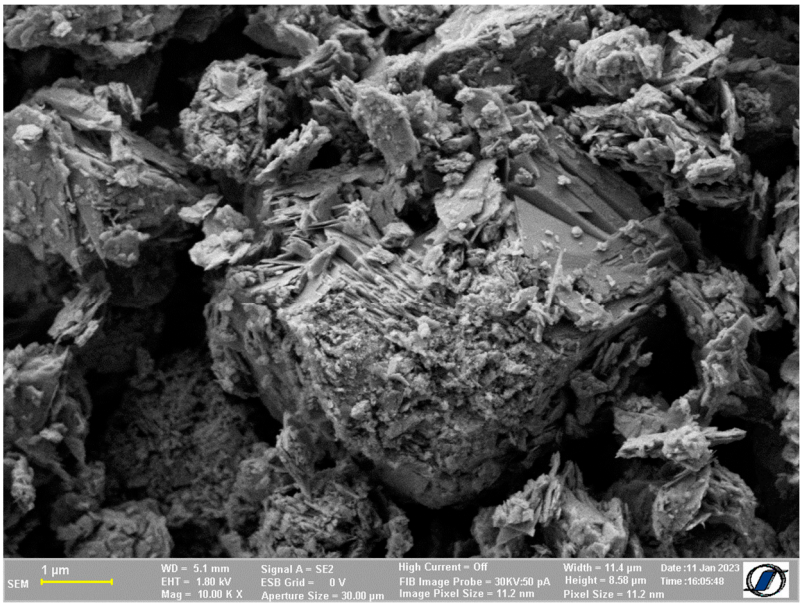

Figure 1. Microstructure of clinoptilolite zeolite.

Considering the large number of research papers investigating the effect of zeolites on the properties of cement-based materials, an attempt was made to summarize the findings and draw some generally valid conclusions [12]. The study highlighted the pozzolanic effect of natural zeolites, when used as a substitute for Portland cement, their internal curing capabilities, as well as their use as aggregates in lightweight concrete (as air entraining agents). A 12% improvement in the compressive strength value was reported for replacement percentages up to 20%. Higher replacement values resulted in a decline in the strength characteristics. Moreover, improvements in terms of chloride penetration, water penetration, frost resistance and shrinkage of concrete were also reported.

Given the beneficial effects of zeolites on the properties of cementitious materials, the present paper aims to summarize the recent findings reported in the scientific literature on the use of zeolites in cement-based construction materials. This paper limits the analysis

to natural zeolites. Both fresh- and hardened-state characteristics are presented as the use of zeolites has influences on both of these phases/states of cement-based materials. The findings are summarized in terms of strength (compressive and flexural strength) and durability properties (freeze–thaw, chloride diffusivity, acid attack resistance, water transport properties, carbonation, electrical resistivity and drying shrinkage) for cement paste, mortar and concrete. Where applicable, differences will be highlighted between the use of natural zeolites as supplementary cementitious materials and their use as aggregates, although their use as aggregates is rather limited. A short discussion on the underlying mechanisms leading to the reported results in the scientific literature coupled with limitations on the use of natural zeolites and future challenges is also provided.

2. Fresh-State Properties

The influence of natural zeolites on the workability and setting time of cement-based construction materials was also investigated. The workability while in the plastic state can affect the hardened properties of cement-based materials. A stiff mix may require excessive vibration to fully and evenly fill the formwork, which may lead to segregation. On the other hand, a fluid mix may result in segregation and water bleeding. Both these extreme scenarios should be avoided and careful investigations should be conducted in designing a cohesive mix but with sufficient workability.

A recent study investigated the influence of clinoptilolite zeolite on the slump and setting time values of mortar and cement paste, respectively. Increasing the zeolite content to 10% resulted in a 25% reduction in workability compared to the control mix [3]. At the same time, the initial and final setting times of the cement pastes showed a decreasing trend with the increase in the replacement percentage. One possible explanation could be the higher specific area of zeolite particles coupled with the porous nature of zeolites, which results in part of the mixing water being absorbed. The effect of zeolites on the fresh properties of the investigated cement-based materials was more pronounced compared to other supplementary cementitious materials used in the study: metakaolin, ground granulated blast furnace slag and type C fly-ash.

In another study conducted on the pore structure of cement pastes containing natural zeolites, it was reported that the initial setting time values decreased with the increase in zeolite content, while the final setting time values increased. The considered cement replacement percentages by clinoptilolite zeolite were 10%, 20% and 30%, by mass. A rather high water/binder ratio of 0.6 was chosen, which could explain the longer final setting time values. Moreover, the initial setting time values did not change with the increase in the replacement percentage, while higher percentages than 20% had no influence on the final setting time. The flow, however, decreased with the increase in the zeolite content in an almost linear manner [4].

Different results were reported in [10] in terms of initial and final setting time values of cement pastes containing zeolites. The authors concluded that the variation between the setting time values of all considered mixes was small and, therefore, the zeolite content did not play a significant role. However, a 13.79% increase in the initial setting time value was reported for a replacement percentage of 20%. An interesting conclusion was drawn in terms of the volume stability of zeolite mixes, especially for replacement percentages equal to and higher than 10%. These mixes showed a better volume stability compared to the reference mix, which could be attributed to the volume stability of zeolite particles [5] and to the significantly reduced shrinkage provided by the presence of zeolites [11].

Calcination of zeolites to 600 °C and 800 °C results in a lower demand for superplasticizer, at a constant water/binder ratio of 0.33. The calcination leads to lower water demand because the porosity of zeolites is greatly reduced [13]. At the same time, while the amorphous content of zeolites increases with calcination temperature, their pozzolanic activity, porosity and surface area greatly reduced [13,14].

The use of natural zeolites together with limestone powder as substitutes for cement in self-compacting mortar resulted in a higher dosage of water-reducing admixture coupled

with longer times for the mortar to reach spread diameters of 250 mm and 300 mm [15]. The study concluded that the combined use of zeolites with limestone powder in equal parts, at a constant water/cement ratio of 0.42 and a similar water/binder ratio of 0.336, resulted in overall better characteristics of self-compacting mortar than all other blends of supplementary cementitious materials investigated in the study.

In a different study, the cement was replaced by zeolite at rates of 5%, 10%, 15% and 20%, by volume. The results showed an increase in the flowability of mortar with up to 10% replacement, compared to the reference mix. Higher replacement percentages resulted in lower flowability values but all zeolite-containing mixes exhibited larger values compared to the control mix [9]. The porous nature of zeolite coupled with its high specific area were considered as the main influencing factors for the obtained results for replacement percentages higher than 10%. A previous study also indicated that another possible cause could be the angular shape of zeolite particles, which may result in increased friction forced between the particles of the mix [16].

In an earlier study, it was found that replacing Portland cement by amounts of 5%, 10%, 15% and 20%, by mass, resulted in a higher dosage of superplasticizer in order to obtain a similar slump with the reference concrete mix. At the same time, the air content of the mix increased with the increase in the replacement percentage due to the porous nature of zeolites [2].

Similar results were reported in [17] for 10% and 15% replacement percentages by mass of cement. Increasing the water/binder (w/b) ratio from 0.35 to 0.5 resulted in lower dosages of water-reducing admixture. However, the increased content of water-reducing admixture after increasing the replacement percentage was reported for all considered w/b ratios.

A summary of the presented results can be found in Table 1. The information was sorted first on the type of material, from cement paste to mortar and finally to concrete. The second sorting criterion was the water/binder ratio.

Table 1. Influence of zeolite content on the fresh properties of cement-based materials.

Material	Water/Binder Ratio	Replacement Percentage	Findings	Ref.
Paste	0.4	5%, 10% by mass	The initial and final setting time decreased by 20–35 min and 15–35 min, respectively, compared to the control mix.	[3]
Paste	0.45, 0.5, 0.55, 0.6, 0.65, 0.7	5%, 10%, 15%, 20% by mass	*flow spread* increased with increase in w/b but decreased with increase in zeolite content; *packing density* increased with increase in zeolite content; *water film thickness* increased with increase in w/b but decreased with increase in zeolite content.	[18]
Paste	0.5	5%, 10%, 15%, 20% not specified	*water demand* increased with zeolite content; *volume expansion* was halved with more than 5% zeolite; initial/final *setting time* showed little variations.	[10]
Paste	0.6	10%, 20%, 30% by mass	initial *setting time* decreased and final *setting time* increased when using zeolite; *flow* of cement paste decreased with increase in zeolite content.	[4]
Mortar	0.33	15%, 30% by mass	higher dosage of *superplasticizer* required when using zeolite; *slump* increased after zeolite calcination.	[13]

Table 1. *Cont.*

Material	Water/Binder Ratio	Replacement Percentage	Findings	Ref.
Mortar	0.336	10% by mass	higher *water-reducing admixture* content. highest times for mortar to reach *spread diameters* of 250 mm and 300 mm.	[15]
Mortar	0.485	5%, 10% by mass	the use of up to 10% zeolite *decreased the workability* by approximately 25% compared to the control mix.	[3]
Mortar	0.5	5%, 10%, 15%, 20% by volume	the flowability increased up to 10% replacement and then decreased; porosity was higher than control mix and highest for 10% replacement.	[9]
Concrete	0.4	5%, 10%, 15%, 20% by mass	Increased dosage of superplasticizer to obtain a similar slump to the control mix; air content increased with the increase in the replacement percentage.	[2]
Concrete	0.35, 0.4, 0.45, 0.5	10%, 15% by mass	higher dosage of water-reducing admixture was required with the increase in the zeolite content in order obtain similar slump values with the control mix; increasing the w/b ratio resulted in lower dosages of water-reducing admixture.	[17]
Concrete	0.48	5%, 10%, 15% by mass	slump decreased with an increase in zeolite percentage; The increase in the crumb rubber content resulted in a further decrease in the slump.	[19]

3. Mechanical Properties

This section summarizes recent findings in terms of the compressive strength, flexural strength and modulus of elasticity of cement-based construction materials. The information is presented and discussed in terms of influencing factors such as the role of natural zeolites as supplementary cementitious materials or aggregates, the replacement percentages of Portland cement or traditional aggregates and the water/cementitious binder ratio, as well as the curing age of tested specimens. Where applicable, the use of natural zeolites together with other pozzolans will be presented and discussed.

3.1. Cement Paste

There are not many studies addressing the mechanical properties of cement pastes with zeolites. Still, the findings are similar to the ones reported for mortars and concrete.

In a comprehensive research work, six different water/binder ratios, four replacement percentages of cement by natural zeolite and three different curing ages were considered for cement pastes in order to assess the compressive strength [18], as summarized in Table 2. The highest gain in compressive strength values were obtained from 7 days to 28 days, irrespective of zeolite content or water/binder ratio. However, the strength gain from 28 days to 70 days was more pronounced for zeolite-containing pastes than for the reference ones. This gain was mostly governed by the zeolite content, whereas the w/b ratio had little effect. This confirmed the slow pozzolanic reaction of clinoptilolite zeolite reported in other studies [3,7].

There was no clear increasing or decreasing trend in terms of compressive strength values up to the age of 28 days for pastes containing zeolites compared to the reference mix. However, at the age of 70 days, all pastes with zeolites showed consistently larger values compared to the reference mixes.

Table 2. Influence of zeolite content on the compressive strength of cement paste.

Water/Binder Ratio	Replacement Percentage	Age [Days]	Findings	Ref.
0.45, 0.5, 0.55, 0.6, 0.65, 0.7	5%, 10%, 15%, 20% by mass	7, 28, 70	Increasing the w/b ratio decreases the compressive strength irrespective of age or replacement percentage; The compressive strength decreases with the increase in zeolite content compared to reference mix; At the age of 70 days, all zeolites containing pastes showed higher values compared to the reference mix, irrespective of w/b ratio.	[18]

3.2. Mortar

In the case of mortars, the mechanical properties are determined on 40 mm × 40 mm × 160 mm prisms. The specimens are subjected to three-point loading tests to determine the flexural tensile strength. The compressive strength is determined from the uniaxial compression tests conducted either on the resulting half prisms from the bending test or on cube specimens.

The slow pozzolanic reaction of clinoptilolite zeolites results in lower flexural strength and compressive strength values of mortars at the age of 28 days. When samples are subjected to elevated temperatures (200 °C, 300 °C, 400 °C, 650 °C and 800 °C), the presence of zeolites increases the possibility of higher hydration production occurrence due to water release from the porous structure of the zeolite coupled with internal pore pressure, which leads to the so-called autoclave curing [20]. This effect was observed especially at temperatures higher than 400 °C.

Researchers looked for alternatives to improve the effect of zeolites as supplementary cementitious materials. There are currently two main approaches: milling, to decrease the particle size, and calcination, which helps in reducing their porous structure and, consequently, decreasing the water demand [13,21]. According to a recent study, calcination of natural zeolites resulted in marginal improvements over non-calcined zeolites in terms of compressive strength at either early age or 28 days. Milling pre-treatment, on the other hand, resulted in significantly improved values of the compressive strength of zeolites containing mortars, compared to the natural, non-treated zeolite mortar. The combination between milling and calcination pre-treatments resulted only in marginal gains that could not justify the embed energy consumption [21].

According to a recent study, the use of zeolites blended with other supplementary cementitious materials, at water/binder ratios lower than 0.45, resulted in improved values of mechanical properties [15]. The TGA analysis showed that blending limestone powder with natural zeolites resulted in better hydration compared to the control mix, although the cement content was lower.

The use of nano-silica in cement-based mortar promotes the acceleration of cement hydration. Using blends of nano-silica and zeolites to replace the cement not only results in higher compressive strength values at early ages but also beyond 28 days when the pozzolanic reaction of zeolites starts contributing [22]. The small dimensions of nano-silica create a nucleation site inside the matrix and lead to the formation of a denser structure. Hence, it has been hypothesized that calcium hydroxide crystals have less space to grow which results in smaller dimensions but larger numbers [23,24]. This leads to an increase in the lateral surface of CH crystals, accelerating the pozzolanic reaction. Therefore, it can be assumed that the use of nano-silica together with zeolites, or any other natural pozzolan, has a synergistic effect because their beneficial effects are augmented by the presence of the nano-silica.

The use of zeolites as a replacement for aggregates, e.g., sand, in engineering cementitious composites was considered from the point of view of the zeolite's internal curing properties [25] rather than the strength gains of the resulting material. A successful decrease

in the 28 day shrinkage was obtained at the cost of a 10% reduction in compressive strength for a 30% replacement, by mass, of quartz sand by natural zeolite.

A summary of individual findings in terms of using natural zeolites and their effect on the mechanical properties of mortars can be found in Table 3.

Table 3. Influence of zeolite content on the flexural tensile strength and compressive strength of mortar.

Water/Binder Ratio	Replacement Percentage	Age [Days]	Findings	Ref.
0.5	5%, 10%, 15%, 20% not specified replaces cement	2, 7, 28, 56	early age (2 and 7 days) *flexural strength* decreased with increase in zeolite content; at 28 and 56 days, *flexural strength* of mortars with 5% and 10% zeolite was similar to the reference; higher percentages resulted in lower values; *compressive strength* followed a similar trend.	[10]
0.5	30%, 40%, 50% by mass of cement	1, 3, 7, 28	lower *compressive strength* for all mortar mixes with zeolite; increase in replacement percentages resulted in lower values; *compressive strength* was slightly improved by calcination of zeolite; *compressive strength* was significantly improved by milling of zeolite; milling and calcination did not show improvements in *compressive strength* over milling alone.	[21]
0.485	15% by mass of cement	3, 7, 28, 90	*compressive strength* of mortar with zeolite increased with the curing age; early age *compressive strength* is lower for zeolite mortars compared to the reference; at 28 and 90 days, *compressive strength* is higher for zeolite mortars; when used together with nano-silica (3%, 4%), *compressive strength* is consistently higher than the one obtained for control.	[22]
0.4	5%, 10%, 15%, 20% by volume of cement	90	*flexural tensile strength* decreased when zeolite was used; smallest decrease recorded for 10% zeolite; *compressive strength* marginally higher for 10% and 15% zeolite use compared to control; the other two mixes showed up to 12% decrease.	[9]
0.336	10% by mass of cement	7, 28	*compressive strength* increased for both ages compared to control (additionally, 10% of cement was replaced by limestone powder); highest increase, of 26%, obtained at 28 days.	[15]
Not specified	10%, 20% by mass of cement	28	*compressive strength* at room temperature was 5% lower, on average, when using zeolite; with increasing temperature, the decrease was up to 10.53%; *flexural tensile strength* at room temperature was similar to the reference for the 10% zeolite mix and 12.57% lower for the 20% mix; exposure to temperatures up to 800 °C resulted in an average decrease of 3.45%.	[20]
0.2	15%, 20%, 30% by mass of sand	28	*compressive strength* was lower at 28 days when using zeolite, both natural and calcined; *compressive strength* reduced by 2.24% for 15% zeolite use (either natural or calcined) and by 5% for 20% calcined zeolite use; increasing zeolite content resulted in 10% decrease in *compressive strength*.	[26]

3.3. Concrete

In the case of concrete, studies revealed that a smaller zeolite particle size resulted in higher compressive strength values, irrespective of the considered curing age of concrete [27]. A lower w/b ratio resulted in a better performance of zeolites containing self-compacting concrete, which had higher compressive strength values compared to the reference mix [28]. The obtained results are in line with previously reported trends [29].

The increase in the compressive strength of zeolites containing concrete could be attributed to the active SiO_2 and Al_2O_3 present in the zeolite, promoting its pozzolanic activity [30].

After 90 days of curing, the hydration of 20% zeolite concrete resulted in a compact microstructure of the matrix, as demonstrated by means of mercury intrusion porosimetry (MIP) results. The total porosity was lower than that of the control mix. Increasing the replacement percentage resulted in large capillary pores and cracks occurring in the concretes [31].

A summary of the individual findings in terms of elastic and strength properties of concrete using zeolites is presented in Table 4.

Table 4. Influence of zeolite content on the compressive strength (f'_c), splitting/flexural tensile strength (f_t) and modulus of elasticity (E) of concrete.

Water/Binder Ratio	Replacement Percentage	Age [Days]	Investigated Properties: f'_c, f_t, E	Findings	Ref.
0.48	5%, 10%, 15% by mass of cement	7, 28	f'_c, f_t, E	*compressive strength* and *splitting tensile strength* at 28 days increased with increasing zeolite content for all crumb rubber percentages; *modulus of elasticity* was influenced by the crumb rubber content rather than zeolite.	[19]
0.45	2.5%, 5%, 7.5%, 10% by mass of cement	7, 28	f'_c	*compressive strength* of all zeolite mixes was higher than the reference; increasing zeolite percentage resulted in a lower increase in *compressive strength* during curing.	[30]
0.42, 0.46	5%, 10%, 15% by mass of cement	7, 28, 90	f'_c, f_t	higher w/b resulted in lower values of mechanical properties; early age *compressive strength* was lower with increasing zeolite content; *compressive strength* at 90 days was higher for zeolite concrete for all w/b; 10% zeolite use resulted in highest *compressive strength*, irrespective of w/b; similar results were obtained for *flexural tensile strength*.	[32]
0.41	5%, 10%, 15%, 20% by mass of cement	7, 28, 90, 180	f'_c, f_t, E	*compressive strength* was lower for all concrete mixes containing zeolite at all ages; mechanical properties were highly affected by cement type; *tensile splitting strength* was lowest for 10% zeolite use, irrespective of cement type; *tensile strength* was higher for higher replacement percentages; *modulus of elasticity* was not significantly influenced by zeolite or cement type.	[33]
0.4	5%, 10%, 15%, 20% by mass of cement	3, 7, 28, 90	f'_c	*compressive strength* was higher for all zeolite concrete at all ages; *compressive strength* decreased with increasing zeolite content, up to 28 days; significantly higher *compressive strength* was obtained at 90 days compared to the reference.	[2]

Table 4. *Cont.*

Water/Binder Ratio	Replacement Percentage	Age [Days]	Investigated Properties: f'_c, f_t, E	Findings	Ref.
0.4	10%, 15% by mass of cement	28, 90, 236	f'_c	*compressive strength* was higher for all zeolite concrete at all ages; increasing volcanic tuff content improved the *compressive strength* values; concrete with 10% zeolite performed slightly better than the 15% mix.	[34]
0.4	10%, 20%, 30% by mass of cement	7, 28	f'_c	*compressive strength* decreased with increase in zeolite content; at 7 days, the 10% zeolite concrete mix showed higher *compressive strength* than the control; at 28 days, both 10% and 15% zeolite concrete mixes showed higher *compressive strength* than the control.	[35]
0.38, 0.45	5%, 10%, 15%, 20% by mass of cement	3, 7, 14, 28, 90	f'_c, f_t	*compressive strength* increased with the age of concrete and with reduction in w/b; higher rate of *compressive strength* development with age was recorded for zeolites containing self-compacting concrete; *splitting tensile strength* at 28 days decreased with increasing zeolite content.	[28]
0.35	5%, 7.5%, 10% by mass of cement	7, 28, 90	f'_c, f_t	*compressive* and *splitting tensile strength* at all ages were improved by increasing the zeolite percentage; mechanical properties were further improved by adding fibers.	[36]
0.3	20%, 40%, 60% by mass of cement	7, 28, 90	f'_c	*compressive strength* of zeolite concrete was lower than the reference at 7 and 28 days; 20% zeolite use resulted in the highest *compressive strength* at 90 days; higher percentages resulted in lower *compressive strength* compared to the control.	[31]
0.18	5%, 10%, 15% by mass of cement	3, 7, 28, 90	f'_c	*compressive strength* increased for all zeolite concrete at all ages, compared to the reference; early age (3 and 7 days) *compressive strength* was highest for the 5% zeolite mix; at 28 days and later, the 10% zeolite mix exhibited the highest *compressive strength*.	[27]
-	7%, 14%, 21% by mass of cement	N.A.	f'_c, f_t	*compressive strength* of autoclave aerated concrete was significantly improved by zeolite; *compressive* and *splitting tensile strength* increased with increasing the zeolite content.	[37]
0.2	15%, 30% by mass of sand	3, 7, 28	f'_c	*compressive strength* decreased with increasing the zeolite content at all ages; zeolite calcination had a positive effect after 90 days, though *compressive strength* was slightly lower than the reference; calcination pre-treatment was not effective at early ages.	[38]

4. Durability

Due to the widespread application of concrete in civil engineering, enhancing its durability emerges as a crucial element in the development of sustainable structures characterized by increased life-span and lowered carbon footprint. Zeolite has the potential to be a significant factor towards achieving this goal. In addition to its pozzolanic activity, which makes it a desirable substitute for cement, the structure and characteristics of zeolite make it attractive for its use in cementitious materials. Natural zeolites exhibit intriguing

properties related to ion exchange and water transport, which are derived from their framework-like structure [12,39].

The durability of concrete denotes its capacity to withstand and resist the action of different factors that can affect its structural integrity and functional performance. Enhancing this property will contribute to increasing the resilience of structures in line with sustainable construction practices, thereby reducing the environmental impact. In the following description, the discussion will take into consideration the most important and widely researched mechanisms regarding durability and the manner in which they are impacted by the presence of zeolites.

4.1. Freeze–Thaw Resistance

The ability of concrete to withstand frost effects is a critical characteristic as the material possesses a specific pore structure and water content. The repeated freezing and thawing cycles, as well as the presence of de-icing salts, can lead to the deterioration of the material [40]. Specific mechanisms have been suggested, stemming from the increase in volume of around 9% that the water undergoes upon freezing. Internal stresses will appear due to the hydraulic pressure inside the pores, while repeated freezing and thawing will lead to additional water in the capillary pores as well [41]. Following this process, which starts at the surface and propagates inwards, the microstructure can be severely affected.

Zeolites have been studied in relation to their potential for enhancing the frost resistance of concrete. Substituting 10% of the cement mass with natural zeolites reduces the percentage of strength loss after 150 cycles, when compared to the initial value, by over 30% [7]. Additionally, the study indicated that incorporating an air-entraining agent further enhanced resistance in both zeolite and control mixes, with the zeolite showing a positive impact in this comparison as well.

Several replacement percentages of cement with natural zeolite (10, 20, 30 and 40%) were investigated in [42]. It was found that only specimens with 10% and 20% replaced cement have a higher frost resistance coefficient when compared to the control. The study also found the same behavior for the mass loss due to de-icing salts. Weight loss during freezing–thawing was also found to be reduced by over 80% when using 15% zeolite instead of cement [43].

Research on mortars revealed that only 5% cement replacement results in better values than the reference [44], while in another study it was found that 10% increases frost resistance [45]. Both studies agree that superior replacement values will lead to poor resistance to the freezing–thawing of mortars. The researchers explain this on the basis of the pozzolanic activity of zeolite, which will lead to a densification of the microstructure, thus prohibiting expansion of ice crystals and subsequent damage.

The main findings are summarized in Table 5.

Table 5. Influence of zeolite content on the freeze–thaw behavior of mortar and concrete.

Material	Replacement Percentage	Measurement	Findings	Ref.
Concrete	10% by mass of cement	strength loss	lower *strength loss* percentage (25.6 vs. 37.9 after 150 cycles).	[7]
Concrete	10%, 20%, 40%, 60% by mass of cement	strength loss	10% and 20% zeolite use resulted in better results when compared to reference, in both *compression* and *bending*.	[42]
Concrete	10%, 20%, 40%, 60% by mass of cement	mass loss (de-icing salts)	*mass loss* was reduced by 50% for 10% and 20% zeolite use, compared to control; *mass loss* was increased 2–3 times by 40% and 60% zeolite use.	[42]
Concrete	15% by mass of cement	mass loss (de-icing salts)	four times less *mass loss* when using zeolite; obs.: lime was also used in all mixes.	[43]

Table 5. *Cont.*

Material	Replacement Percentage	Measurement	Findings	Ref.
Mortar	5%, 10%, 15%, 20%, 30% by mass of cement	mechanical properties	increase in zeolite content resulted in better *mechanical properties* compared to the reference before freeze–thaw cycles; after 50 freeze–thaw cycles, 5% zeolite use resulted in better values of *mechanical properties*.	[44]
Mortar	10%, 20%, 30% by mass of cement	Compressive strength	*compressive strength* for all mixes decreased after 50 freeze–thaw cycles; 10% zeolite use resulted in the highest freeze–thaw performance.	[45]

4.2. Chloride Diffusion Resistance

Chloride ions are mainly dangerous for reinforced concrete, with reinforcing bars being subjected to corrosion. Depletion of the passive layer will lead to the oxidation of steel, which leads to its volume expanding and, consequently, to the cracking of concrete due to internal stresses [46]. Several studies have indicated that zeolite can effectively decrease the diffusion of chloride ions.

It was found that replacements of 15% and 30% cement by natural zeolites significantly reduce chloride ion permeability compared to control, with values reduced by around 90% at an age of 90 days [11]. In another study where lower concentrations of zeolites were used (10% and 15%), chloride resistance was found to decrease, but with a maximum of 70% [34]. However, the authors simultaneously substituted volcanic tuff for the fine aggregates while also replacing cement.

In a more detailed study, chloride profiles and the total and surface chloride concentration, as well as the apparent chloride diffusion coefficient, were investigated [47]. These were tested in splash, tidal and laboratory conditions. Zeolites were used in percentages of 10%, 15% and 20% replacing cement. The chloride profiles were all steeper (for all types of tests and all concentrations) than those obtained for control. In tests under laboratory and tidal conditions, the total chloride contents at 10mm were similar for all zeolite concretes and the values were lower by around 20% than the reference, while, under splash conditions, only the specimens with 20% zeolites showed a reduction of over 50%. The apparent diffusion coefficient was markedly lower for all zeolite specimens, while the surface chloride concentration was lower only for the 20% replacement level.

Another study on the same replacement levels of 10%, 20% and 30% of cement with zeolites determined that the diffusion coefficient was lowered by more than 50% in modified concrete mixes [48]. It was also found that 10% and 20% zeolite use as a cement replacement leads to a decrease in the diffusion coefficient of more than 100%, as highlighted in [49]. Ahmadi replacement levels of 10%, 15% and 20% reduce the apparent diffusion coefficient by up to 66%, while 5% cement substitution shows almost no change [2].

The positive influence of zeolites regarding chloride diffusion can be altered by other factors, such as the water to binder ratio (w/b) and temperature and age of the specimens.

Tests performed on high cement replacement percentages, namely 30% and 40%, applied on mixes with w/b of 0.3 and 0.4, showed that only the lower w/b value had reduced chloride diffusivities [50]. In this case, 30% showed a greater chloride diffusivity reduction than 40% (38% vs. 21%) did compared to control. A similar approach was taken by other researchers, who tested various w/b (0.3, 0.35, 0.4 and 0.45) with cement replacement levels of 10% and 15% [17]. Irrespective of water or zeolite content, all modified concrete mixes showed reduced chloride permeability, with higher zeolite levels showing more improvement.

The influence of curing age was also investigated for a 15% cement replacement percentage with natural zeolite [43]. The migration coefficient up to 365 days and the behavior of control, which was quite different compared to the zeolite-containing concrete,

were measured. The reference had a more linear drop in the migration coefficient with age, while the modified concrete showed a more abrupt change during the first 28 days. The final value for the reference was also 3 times higher at the end of the 365 day experiment. The same type of experiment was performed in [51] for 10% and 15% zeolite content. The same abrupt change in the migration coefficient was observed in both mixes, with slightly different slopes but with final values being similar at 365 days. The difference between the control and modified recipes is also similar to the previous study, with the control's migration coefficient being around 3 times higher than that of the zeolite concretes.

The temperature influence was also measured in a research work trying to replicate, as much as possible, the real life exposure conditions of concrete [52]. Cement was replaced in amounts of 10%, 15% and 20% with natural zeolite, and the temperatures used in the study were: 22 °C, 35 °C and 50 °C. At every temperature, the apparent diffusion coefficient was reduced more with the increasing zeolite content. At the same time, the coefficient grew with increasing temperature for all specimens, but the increase was smaller for the zeolite concretes than the reference. The smallest increase was shown to happen for the 15% replacement.

A summary of the findings can be found in Table 6.

Table 6. Influence of zeolite content on the chloride diffusion resistance of concrete.

Material	Replacement Percentage	Measurement	Findings	Ref.
Concrete	15%, 30% by mass of cement	rapid chloride penetration test	values were lowered by up to 85% and 93% for 15% and 30%, respectively, after 90 days of curing.	[11]
Concrete	30%, 40% by mass of cement	rapid chloride penetration test	zeolite mixes showed low *chloride permeability* for low w/b (0.3), while reference had a moderate one; zeolite had no impact at higher w/b (0.4).	[50]
Concrete	10%, 15% by mass of cement	rapid chloride penetration test	higher w/b resulted in higher *chloride penetration* for the reference; similar behavior was observed for zeolite concrete for w/b ratios of 0.35, 0.4 and 0.45; 10% zeolite reduced *chloride permeability* by 43%, 57%, 59% and 54% for w/b of 0.35, 0.4, 0.45 and 0.5; 15% zeolite reduced *chloride permeability* by 51%, 58%, 65% and 70% for w/b of 0.35, 0.4, 0.45 and 0.5.	[17]
Concrete	10%, 20%, 30% by mass of cement	accelerated chloride penetration test	zeolite use increased resistance to *chloride diffusion*; 20% zeolite presented the best results in splash conditions.	[47]
Concrete	10%, 20%, 30% by mass of cement	accelerated chloride penetration test	*chloride penetration* was lower in zeolite specimens and it reduced with zeolite percentage.	[48]
Concrete	10%, 20% by mass of cement	accelerated chloride penetration test	*diffusion coefficient* decreased more than 2 times compared to control	[49]
Concrete	15% by mass of cement	non-steady-state chloride migration	the *diffusion coefficient* value at day 7 is the same for reference and zeolite-containing mix; during aging, zeolite mix showed a more pronounced reduction; after 365 days, zeolite mix showed a value 3 times lower than the control.	[43]

Table 6. *Cont.*

Material	Replacement Percentage	Measurement	Findings	Ref.
Concrete	10%, 15% by mass of cement	non-steady-state chloride migration	*migration coefficient* decreased more abruptly during curing to 365 days when zeolite was used; values were 2.3 and 2.9 times lower than control; *penetration depth* decreased by ~30% for zeolite mixes when tested after 230 days of saline solution immersion; *diffusion coefficient* was reduced to half for zeolite mixes.	[51]
Concrete	10%, 20%, 30% by mass of cement	apparent diffusion coefficient	*diffusion coefficient* decreased ~2 times when zeolite was used; exposure temperature (22, 35, 50 °C) increased the *diffusion coefficient*, but growth rate was slower for zeolite concrete.	[52]
Concrete	5%, 10%, 15%, 30% by mass of cement	apparent diffusion coefficient	*diffusion coefficient* decreased with zeolite percentage; 5% zeolite mix was similar to control, while 30% zeolite resulted in ~66% reduction.	[2]
Concrete	10%, 15% by mass of cement	standard chloride diffusion test	zeolite use decreased the *diffusion coefficient*, proportional to zeolite percentage.	[34]

4.3. Acid Attack Resistance

Concrete is particularly susceptible to the action of acid environments, due to its alkaline nature. In general, any acid will firstly react with calcium hydroxide and soluble calcium salts will be formed. These are easily removed from the cement matrix, thus lowering its resistance [53]. The resulting calcium salts can be either very soluble, in the case of aggressive acids, or of lower solubility, when interaction with less aggressive acids occurs. One of the most aggressive and damaging instances of acid attack is represented by the interaction of concrete with sulfuric acid. This is due to the fact that the resulting salt, namely calcium sulfate (gypsum), will further react with calcium silicate hydrate (CSH), causing serious structural damage, or with calcium aluminate, which results in ettringite, that has a larger volume than gypsum and will induce micro-cracks [54,55].

Scientific literature findings vary in their assessment of the impact of zeolite utilization on the acid attack resistance of concrete, tending to predominantly indicate a detrimental effect. When testing concrete specimens with 15% and 30% cement substitution by natural zeolite [11], the results indicated that while the weight of the control mix increased during a 300-day immersion period, the mass of the zeolite concrete specimens initially decreased and then returned close to the initial value. However, the residual compressive strength was significantly affected by acid attack in the presence of zeolite. The initial strength was reduced by 20.8% (15% zeolite) and 23.3% (30% zeolite), which was considerably higher than the loss experienced by the control mix (5.5%).

Strength loss after sulfuric acid immersion was also obtained for higher zeolite contents, replacing 30% and 40% of cement [50]. Two water to binder (w/b) ratios: 0.3 and 0.4, were considered and the strength loss was more pronounced for the higher w/b for all mixes. The zeolite specimens exhibited a greater reduction in compressive strength compared to the reference, with the difference being more pronounced for w/b = 0.4. Additionally, it was found that the mass loss was lower for the 30% mixture compared to the reference for both w/b values, while the 40% mixture was more adversely affected in comparison to the control.

In the case of lower concentrations of zeolite in concrete (10% and 15%), it was found that, in relation to sulfuric acid, using zeolite increased the depth of erosion. Results indicated loss in both mass and strength proportional to the amount of zeolite [34]. The

authors also performed tests with hydrochloric acid, for which zeolite imposed a similar trend of mass loss, albeit at lower reduction values.

For the same cement substitution amounts of 10% and 15%, opposing results after performing sulfuric acid immersion for 8 weeks were obtained in a different study [56]. In this case, the weight loss of 10% zeolite concrete was similar to the reference mix, while the 15% zeolite specimens presented a 40% lower weight loss. The same trend was observed in the results showing load loss by splitting. The 10% mix showed similar results to the control mix after 4 weeks immersion, but the loss was 35% smaller after 8 weeks. In contrast, the 15% zeolite mix demonstrated a load loss at 4 weeks that was 10 times smaller than that of the reference and nearly 4 times smaller at 8 weeks. These findings are consistent with the results reported in [57], where positive outcomes for specimens containing 20% cement replacement were observed. This study focused on resistance measurements that indicated a lower potential for corrosion for the zeolite mixes.

The highlights of this subsection are presented in Table 7.

Table 7. Influence of zeolite content on the acid attack resistance of concrete.

Material	Replacement Percentage	Measurement	Findings	Ref.
Concrete	15%, 30% by mass of cement	strength loss	after H_2SO_4 immersion for 300 days, zeolite concrete showed a higher *strength loss* (20.8% and 23.3%) than control (5.5%).	[11]
Concrete	10%, 15% by mass of cement	strength loss	after 180 days immersion in H_2SO_4, *strength loss* increased with zeolite content.	[34]
Concrete	10%, 15% by mass of cement	strength loss	after H_2SO_4 immersion for 8 weeks, zeolite concrete behaved better compared to the reference; 10% zeolite use resulted in minor improvement of *strength loss*, and 15% zeolite use reduced *strength loss* by over 70%.	[56]
Concrete	30%, 40% by mass of cement	strength loss	after H_2SO_4 immersion, zeolite concrete exhibited a higher *strength loss*.	[50]
Concrete	15%, 30% by mass of cement	mass loss	reference concrete *mass* increased during immersion; zeolite modified concrete *mass* firstly decreased and then increased, almost reaching the initial value.	[11]
Concrete	10%, 15% by mass of cement	mass loss	after 180 days immersion in either HCl or H_2SO_4, mass loss increased with zeolite content.	[34]
Concrete	10%, 15% by mass of cement	mass loss	after 8 weeks immersion in H_2SO_4, specimens with 10% zeolite were very similar to the control; 15% zeolite use reduced mass loss by over 37%.	[56]
Concrete	30%, 40% by mass of cement	mass loss	after H_2SO_4 immersion for 56 days, 30% zeolite mix reduced *mass loss* for w/b = 0.3 and w/b = 0.4; for higher w/b, mass loss is lower; *mass loss* was higher than the reference for 40% zeolite mix, irrespective of w/b.	[50]
Concrete	20% not specified	electrochemical impedance spectroscopy	*resistance* was higher for zeolite specimens during exposure to H_2SO_4, indicating a lower corrosion potential.	[57]

4.4. Water Transport Properties

The movement of water within concrete is a critical factor in determining its long-term durability as it influences the penetration and distribution of chemical substances. The consequences of water ingress and permeation can be either advantageous or detrimental. For instance, the saturation of capillary pores due to water penetration can result in reduced

resistance to frost. Additionally, the transport of water within concrete can act as a barrier against harmful gases, while also serving as a medium for the movement of various ions. Moreover, the presence of water may lead to its absorption by ettringite and alkali silica gel, causing volume expansion.

In most situations, the replacement of cement with zeolite has been demonstrated to enhance the performance of concrete in terms of water transport properties.

Water penetration is primarily influenced by the microstructure of the material, particularly the pore structure or network. Literature reports indicate that using zeolite decreases this parameter. When testing mixes with zeolite substituting 15% and 30% cement, it was found that water penetration depth decreased by up to 26% with increasing zeolite content at both 28 and 90 days when compared to the reference mix [11]. Similarly, in another study, higher decreases in water penetration values, tested at 28 days, when using 10% and 15% zeolite, with differences of 55% and 65%, respectively, were reported [51]. Using the same replacement values of 10% and 15% and changing the w/b ratio (0.35, 0.40, 0.45, 0.50), it was found that the penetration depth decreased with increasing zeolite content, while the w/b ratio had the opposite effect [17]. A smaller decrease was found when replacing 10% of the cement with zeolite, for which the water penetration depth reduced by only 13% [7]. Nevertheless, in this study, the reference mix already had a very low penetration depth. All of these results consistently indicated a relationship between reduced water penetration depth and other durability factors related to pore structure, including frost resistance and chloride diffusion/migration.

There is a more substantial body of research regarding the water absorption properties of mixtures incorporating zeolite, yielding a range of findings. However, the majority of studies tend to support the beneficial impact of zeolite use on water absorption.

An increase in water absorption of around 20% when using 15% and 30% cement replacement percentages was found. This behavior was assumed to be caused the higher absorption properties that zeolite particles have compared to cement [11]. Similarly, a nearly 23% increase in water absorption when substituting 10% of cement was reported in [7]. In a long-term study on concrete with zeolite-replaced cement in amounts of 10% and 15%, it was concluded that modified concrete presented higher water absorption than the control mix [51]. The authors tested the behavior of specimens in two circumstances: after immersion and after immersion and boiling. The results showed that at 365 days, absorption was higher by around 12% and 25% for 10% and 15% zeolite, respectively, in both scenarios. The findings correlated to permeable pores measurements that presented a similar behavior to water absorption.

Reports of water absorption decreasing with zeolite use are, nevertheless, more numerous. In this context, a decrease of up to 35% when cement was replaced with zeolite at levels of 10% and 15% was observed [34]. In this study, a part of fine aggregates was also replaced by tuff. The authors attributed this decrease to the pozzolanic activity of zeolite, which modified the capillary pore structure. The findings also had a good correlation with chloride diffusion measurements. A non-linear relation between cement replacement values with zeolite (10%, 20% and 30%) and water absorption was reported in [48]. Zeolite in amounts of 10% and 20% showed a slight increase in water absorption, with values close to the reference. Nevertheless, the replacement value of 30% proved to lower water absorption by around 15%. Water absorption measurements demonstrated a similar behavior to results obtained for the volume of voids. Lower substitution values (5%, 10%, 15%, 20%) were considered and all zeolite concrete mixes exhibited similar values of water absorption, which were around 20% lower than the reference [2]. The same replacement values but using two w/b ratios: 0.38 and 0.45, were considered in a different study [28]. Water absorption values at 90 days for high w/b = 0.45 were in good agreement with the previous study, with the variation in zeolite percentage having little impact. Nonetheless, using a lower w/b of 0.38 leads to a constant decrease in water absorption with zeolite content, reaching a reduction of almost 50% compared to control in the case of 20% zeolite use. A reduction in water absorption was also observed when using 10% and 20% zeolite

instead of cement [49]. A higher zeolite percentage resulted in a slightly higher decrease in water absorption of about 20%. Lower zeolite concentrations, replacing cement with 2.5%, 5%, 7.5% and 10% zeolite, were also considered [30]. While 2.5% and 5% zeolite use yielded similar values to control, water absorption was significantly reduced when using 7.5% and 10%, by over 50%.

Sorptivity represents a durability factor that defines the absorption by capillary forces which can also be related to other durability parameters. Overall, zeolite use as cement replacement helps reduce this type of transport, albeit up to a certain concentration. This was demonstrated in tests using 10%, 20% and 30% replacement levels [48]. While sorptivity increased with increased zeolite content, 10% and 20% zeolite use provided smaller values than the reference mix. The reduction in capillary absorption observed in specimens with 15% cement replaced by natural zeolite was attributed to the pozzolanic activity of zeolite, leading to the formation of secondary CSH [43,51]. Additionally, when the w/b ratio was varied, a diminished benefit from zeolite usage was reported with the increase in the w/b ratio.

A summary of the findings is presented in Table 8.

Table 8. Influence of zeolite content on the water transport properties of concrete.

Material	Replacement Percentage	Measurement	Findings	Ref.
Concrete	15%, 30% by mass of cement	water penetration	*water penetration* decreased with increasing zeolite content; the effect of zeolite percentage is more pronounced at the age of 90 days.	[11]
Concrete	10%, 15% by mass of cement	water penetration	*penetration depth* was decreased by 55% and 65% for 10% and 15% zeolite use, respectively.	[51]
Concrete	10% by mass of cement	water penetration	15% decrease in *water penetration* compared to reference mix	[7]
Concrete	10%, 15% by mass of cement	water penetration	28 days: 10% (15%) zeolite use reduced the maximum permeability by 18% (30%), 15% (42%), 16% (29%) and 28% (44%) for w/b ratios of 0.35, 0.4, 0.45 and 0.5 90 days: 10% (15%) zeolite use reduced maximum permeability by 12% (22%), 26% (36%), 12% (36%) and 10% (21%) for w/b ratios of 0.35, 0.4, 0.45 and 0.5	[17]
Concrete	15%, 30% by mass of cement	water absorption	*water absorption* increased for zeolite mixes; age and replacement percentage had little impact.	[11]
Concrete	5%, 10%, 15%, 20% by mass of cement	water absorption	initial and final *absorption* for w/b = 0.45 decreased linearly with zeolite content at 28 and 90 days; initial and final *absorption* for w/b = 0.38 was lowered for all zeolite mixes, with similar values at 90 days.	[28]
Concrete	10%, 15% by mass of cement	water absorption	*water absorption* decreased with increasing zeolite content.	[34]
Concrete	10%, 20%, 30% by mass of cement	water absorption	*water absorption* decreased for 30% zeolite use compared to control and was similar for other mixes.	[48]

Table 8. *Cont.*

Material	Replacement Percentage	Measurement	Findings	Ref.
Concrete	10%, 15% by mass of cement	water absorption	*water absorption* after immersion increased by up to 12.5% and 25% for 10% and 15% zeolite use, respectively, after 365 days of curing; *water absorption* after immersion and boiling was higher than the control by 11.7% and 23.5% for 10% and 15% zeolite use, respectively.	[51]
Concrete	10% by mass of cement	water absorption	*water absorption* increased by 23% compared to reference mix.	[7]
Concrete	10%, 20% by mass of cement	water absorption	~20% reduction in *water absorption* when using zeolite.	[49]
Concrete	2.5%, 5%, 7.5%, 10% by mass of cement	water absorption	*water absorption* decreased with increasing zeolite percentage; 2.5% and 5% zeolite use resulted in values close to the control; 7.5% and 10% zeolite use resulted in values less than half of the control.	[30]
Concrete	5%, 10%, 15%, 20% by mass of cement	water absorption	zeolite lowered *water absorption* with a similar percentage for all specimens (20%).	[2]
Concrete	10%, 20%, 30% by mass of cement	sorptivity	*sorptivity* decreased compared to control for 10% and 20% zeolite use.	[48]
Concrete	15% by mass of cement	sorptivity	*capillary absorption* decreased at various ages up to 365 days; values were 1.33–1.63 times lower than control.	[43]
Concrete	10%, 15% by mass of cement	sorptivity	sorptivity decreased with increasing zeolite content (by 25% and 42%)	[51]
Concrete	10%, 15% by mass of cement	sorptivity	*capillary absorption* (measured at 28, 90 and 270 days) was improved by zeolite use; reduction percentages were between 20% and 53%.	[17]

4.5. Carbonation Resistance

The phenomenon of carbonation is the chemical process initiated by the interaction of cement paste with carbon dioxide. This reaction has the potential to corrode reinforcement by lowering the pH of concrete to levels as low as 8.3, which is below the depassivation threshold [58]. Due to carbonation, the porosity of cement pastes is bound to change and dissolution of certain cement phases is expected. At the same time, structural changes in C-S-H may result in strength increases, followed by carbonation cracking. Carbon dioxide affects both calcium hydroxide and CSH gels, leading to a reduction in porosity [59].

Accelerated carbonation tests were conducted on cement replacement levels of 10% and 15%, revealing a significant rise in carbonation depth with the incorporation of zeolite [17]. The measurements were performed at 28, 90 and 270 days, indicating a substantial reduction in carbonation depth after 90 days for all samples. Additionally, various w/b ratios of 0.35, 0.40, 0.45 and 0.50 were employed, demonstrating that an increase in w/b ratio correlates with higher carbonation depth. The findings were assumed to be related to the consumption of CH due to the pozzolanic reaction of natural zeolite. This significantly reduced the reaction between the carbon dioxide and the available CH and resulted in a larger carbonation depth.

Similar tests were conducted on the same cement substitution rates (10%, 15%), as reported in another study [56]. Their investigation demonstrated that zeolite concrete mixes exhibited increased carbonation depths under accelerated carbonation conditions, with values directly correlated to the extent of cement replacement. Additionally, the study

included an assessment of natural carbonation effects, which indicated that only the 15% zeolite substitution level resulted in a measurable carbonation depth.

The main findings are summarized in Table 9.

Table 9. Influence of zeolite content on the carbonation resistance of concrete.

Material	Replacement Percentage	Measurement	Findings	Ref.
Concrete	10%, 15% by mass of cement	accelerated carbonation	10% zeolite use increased *carbonation depth* by 105%–253% for w/b between 0.35 and 0.5; 15% zeolite use increased *carbonation depth* by 163%–495% for w/b between 0.35 and 0.5.	[17]
Concrete	10%, 15% by mass of cement	accelerated and natural carbonation	*carbonation depth* (accelerated test) increased 4 times and 9 times for 10% and 15% zeolite use, respectively; *mass gain* (accelerated test) was 3 times larger for 15% zeolite mix compared to reference; *carbonation depth* (natural) increased only for 15% zeolite use (7 mm).	[56]

4.6. Electrical Resistivity

Instead of serving as a parameter, electrical resistivity functions as an indicator of concrete durability, reflecting the ease of ion transportation within the material being measured. This property is linked to several durability factors, including carbonation, frost resistance, acid attack, and corrosion of reinforcement [60].

The findings from various studies indicate that the substitution of cement with zeolite results in an increase in resistivity and resistance values. It was observed that concrete mixes containing 10%, 20% and 30% zeolite in place of cement exhibited higher resistivity compared to the reference mix at both 28 and 365 days [48]. The highest resistivity value was recorded for the mix with 30% zeolite, showing a four-fold increase compared to the control mix. Similarly, a 3.5-fold increase in resistivity when 15% zeolite was used instead of cement was reported in another study [43]. Laboratory investigations on concrete incorporating lime and 10% and 15% zeolite as cement replacements showed resistivity increases of 2 and 2.75 times compared to the reference mix at 365 days [51]. It is noteworthy that measurements of permeable pores exhibited a similar trend to electrical resistivity.

The impact of zeolite replacement at 10% and 20% levels was also assessed [49]. After 90 days, the measurements indicated that the resistivity of the specimens was 3.5 and 6 times higher than the control group, respectively. Different zeolite percentages were considered, 10% and 15%, for which a significant increase in resistivity with age for these samples up to 270 days, compared to a smaller increase in the control group, was observed [17]. Additionally, their findings suggested that a higher zeolite content led to greater resistivity. Furthermore, the study revealed a general decrease in resistivity with an increase in the water-to-binder ratio for all specimens. In a study encompassing a broader range of cement replacement percentages (5%, 10%, 15%, 20%), it was found that all specimens containing zeolites exhibited higher resistivity values compared to the control, with the 5% zeolite mix closely resembling the reference [2].

It is important to note that there exists a minimum resistivity threshold that serves as a critical limit for the onset of reinforcement corrosion. Consequently, a resistivity level above 20kΩ·cm is considered adequate for safeguarding against corrosion [49]. It is noteworthy that the electrical resistivity results for the zeolite mixes mentioned earlier all surpass the minimum value required for cement replacement percentages, exceeding 5%. Some of the presented reports indicate that certain control mixes do not meet this criterion.

The data are summarized in Table 10.

Table 10. Influence of zeolite content on the electrical resistivity of concrete.

Material	Replacement Percentage	Measurement	Findings	Ref.
Concrete	10%, 20%, 30% by mass of cement	AC Impedance Spectrometry	the 28 days *resistivity* increased with increasing zeolite content (up to ~3.5 times compared to reference); The 365 days *resistivity* increased 3 times (10% and 20% zeolite) and 4 times (30% zeolite).	[48]
Concrete	10%, 20% by mass of cement	AC Impedance Spectrometry	*resistivity* increased by 3.5 to 6 times with increase in zeolite content.	[49]
Concrete	5%, 10%, 15%, 20% by mass of cement	AC Impedance Spectrometry	*resistivity* during aging increased more with increasing zeolite percentage; at 90 days, *resistivity* of 20% zeolite mix is 3 times higher than control.	[2]
Concrete	15% by mass of cement	electrical resistivity of water-saturated concrete	*resistance* increased by zeolite use and age; 365 days value was 3.5 times larger for zeolite mix compared to reference.	[43]
Concrete	10%, 15% by mass of cement	electrical resistivity of water-saturated concrete	the 365 days *resistivity* was 2 times and 3 times larger for 10% and 15% zeolite use, respectively, compared to control.	[51]
Concrete	10%, 15% by mass of cement	electrical resistivity of water-saturated concrete	the 28 days *resistance* increased for 10% (15%) zeolite use compared to control, for w/b of 0.35, 0.4, 0.45 and 0.5, with 82%–159% (96%–200%); at 90 days and 270 days, *resistance* increased more, with up to 200%–300%.	[17]

4.7. Drying Shrinkage

The presence of a moisture gradient in concrete, caused by uneven drying, induces internal stresses in the material, which can lead to cracking in certain circumstances [61]. While this issue has been extensively researched in conventional concrete for more than five decades, there is limited documentation on its occurrence in zeolite-containing concrete.

Najimi et al. conducted a study to investigate the impact of replacing 15% and 30% of cement with natural zeolite on the drying shrinkage of concrete [11]. The specimens were cured in water for 28 days, and the drying shrinkage was subsequently measured. The results revealed a reduction of 16% and 36% in drying shrinkage for the concrete samples with 15% and 30% zeolite replacement, respectively, compared to the control group at 90 days. This difference was further amplified at 120 days. The observed outcomes were found to be closely associated with the decrease in moisture content.

A more consistent decrease was observed in a study where 10% cement was substituted with zeolite [7]. The modified concrete exhibited nearly three times lower drying shrinkage compared to the control, and a similar strong association with water loss was noted.

Similar studies were conducted on high-performance and ultra-high-performance concrete. The internal curing capabilities of zeolites contributed towards a significant reduction in the autogenous shrinkage [5,26,62].

A brief summary of the main findings is presented in Table 11

Table 11. Influence of zeolite content on the shrinkage of cement-based materials.

Material	Replacement Percentage	Measurement	Findings	Ref.
Mortar	10% by mass of cement	Early age shrinkage	*shrinkage* decreased by 5% compared to control when a blend of limestone powder and zeolite powder was used.	[15]
Mortar	15%, 30% by mass of cement	Drying shrinkage	*shrinkage* was increased by natural zeolite by up to 48.69%; calcination of zeolite did not improve the *shrinkage* behavior.	[13]
Concrete	10% by mass of cement	Drying shrinkage	*drying shrinkage* was ~3 times lower when using zeolite compared to reference.	[7]
Concrete	15%, 30% by mass of cement	Drying shrinkage	*drying shrinkage*, measured at 90 days, was 84% and 64% of the control value for 15% and 30% zeolite specimens, respectively.	[11]
High performance concrete	5%, 10%, 15% by mass of cement	Autogenous shrinkage	early age *autogenous shrinkage* was reduced with increasing zeolite percentage; long-term *autogenous shrinkage* decreased for lower zeolite percentage (5%); both short-term and long-term *autogenous shrinkage* decreased with increasing zeolite particle size.	[27]
Ultra-high performance concrete	25%, 50%, 75%, 100% by mass of silica fume	Autogenous shrinkage	*autogenous shrinkage* of ultra-high performance concrete was significantly reduced with increasing zeolite content.	[5]

5. Discussions

According to a recent study [63], the research works investigating the use of natural zeolites in cement-based materials originate from various countries and employ various sources of zeolites. Although the chemical composition is mainly the same, there are small variations between the percentages of various components that may lead to different, sometimes contradictory, results. Some of these results are also presented in this paper. A summary of the chemical compositions of the employed natural zeolites in the studies that served as sources of information for the present paper is shown in Table 12.

Table 12. Chemical composition of natural zeolites from surveyed scientific literature.

CaO	SiO_2	Al_2O_3	Fe_2O_3	MgO	Na_2O	K_2O	SO_3	LOI	Reference(s)
1.68	67.79	13.66	1.44	1.2	2.04	1.42	0.52	10.23	[11,16,31,34,36,38,48,52]
1.33	66.70	11.48	0.9	0.22	1.8	3.42	3.43	14.10	[3]
1.22	71.50	11.30	2.05	0.17	1.24	4.55	-	-	[5]
3.3	72.5	12.5	1.7	0.6	0.2	3.6	-	5.6	[9]
1.77	64.44	8.3	1.66	0.07	2.3	2.24	0.04	18.95	[10]
2.18	70.11	11.45	1.89	1.62	0.77	2.36	0.03	9.52	[13]
7.97	68.7	13.59	2.43	1.12	3.03	2.69	-	-	[14]
3.48	75.04	12.85	2.38	0.8	0.5	4.86	-	-	[14]
5.91	68.8	14.06	2.56	0.97	3.84	2.83	-	-	[14]
2.58	76.55	12.76	1.47	0.95	0.77	4.86	-	-	[14]
2.74	76.93	14.68	1.39	0.79	1.23	2.07	-	-	[14]
2.71	62.87	13.46	1.35	2.38	-	-	-	-	[18]

Table 12. *Cont.*

CaO	SiO_2	Al_2O_3	Fe_2O_3	MgO	Na_2O	K_2O	SO_3	LOI	Reference(s)
3.04	71.29	11.43	2.16	1.11	1.72	0.95	0.05	7.69	[21]
3.1	66.5	11.8	1.3	0.8	2.03	2.1	0.52	9.85	[22]
1.99	64.27	12.7	0.68	0.46	2.30	2.90	0.34	14.18	[26]
4.11	60.25	18.45	1.9	1.12	1.66	1.18	-	11.33	[27]
1.51	68.4	12.5	1.32	1.4	2.2	1.3	0.45	-	[28]
2.10	71.35	13.10	0.9	1.07	0.8	2.45	-	-	[30]
3.67	66.98	19.88	1.21	0.49	-	0.06	0.71	4.71	[31]
5.50	59.81	14.32	1.04	0.83	5.76	1.36	-	7.47	[33]
2.24	69.2	15.28	3.01	1.4	2.2	2.1	0.45	-	[34]
3.56	69.28	10.43	0.49	0.5	0.73	1.27	0.005	12.97	[36]
4.34	68.28	12.30	0.08	1.05	0.26	0.94	-	-	[12]
3.28	74.69	14.99	1.53	0.653	0.834	3.6	-	5.32	[42]
3.6	63.32	11.7	0.32	1.2	-	-	0.088	8.49	[49]
3.97	68.85	11.71	1.29	1.06	0.29	2.19	0.18	10	[57]
9.20	50.89	9.00	1.18	7.68	1.03	2.43	0.04	18.17	[64]
9.73	60.9	11.0	7.91	-	-	8.89	-	-	[64,65]

The chemical composition of zeolites is an important indicator of their contribution on the overall behavior of cement-based materials. According to an earlier study [10], a high content of silica is more effective on the development of the compressive strength. As can be seen from the data presented in Table 12, all natural zeolites considered in the research work have a Si/Al ratio larger than 4. It is therefore expected that the use of zeolites as a partial replacement of cement is beneficial from the point of view of mechanical properties. The pozzolanic reactions between SiO_2 and Al_2O_3 in natural zeolites and CH lead to the formation of calcium–silicate–hydrate (CSH) and calcium–aluminate–hydrate (CAH) gels, which further contribute to increasing the density of concrete and improve its mechanical and durability properties [12], as shown in previous sections. However, severe penalties in terms of strength values were reported for high replacement percentages of cement by natural zeolites [42].

The evolution of the compressive strength of cement pastes with different percentage replacements of cement with natural zeolite is shown in Figure 2. It can be observed that at early ages, 2 and 7 days, the pastes with lower replacement percentages and higher water/binder ratios exhibited compressive strength values larger than the reference mix, shown in Figure 2a. At the age of 28 days, a similar pattern can be seen but the influence of the zeolite particle's size becomes a significant influencing factor [18], as shown in Figure 2b. At the age of 70 days, the use of superfine zeolite results in an improved compressive strength compared to the reference mix, irrespective of the replacement percentage, Figure 2c. This trend could be explained by the slower pozzolanic reaction of clinoptilolite natural zeolite, as reported in previous studies [3,7].

A similar trend can be observed in the case of concrete with different replacement percentages of Portland cement with natural zeolite, shown in Figure 3. The conclusions that can be drawn at early ages are limited by the rather small number of data sets available, as shown in Figure 3a. The water/binder ratio seems to play a defining role, similar to the zeolite content. At the age of 28 days, shown in Figure 3b, both aforementioned parameters seem to equally influence the compressive strength. However, for higher zeolite contents, with a higher than 20% cement replacement, the compressive strength value is significantly reduced. This was attributed to the so-called dilution effect [32]. This effect occurs in cases

of high replacement percentages and more significantly impacts the compressive strength values at 90 days and beyond, shown in Figure 3c. This effect is mainly caused by the lower amount of CH that is able to react with the pozzolanic material [31].

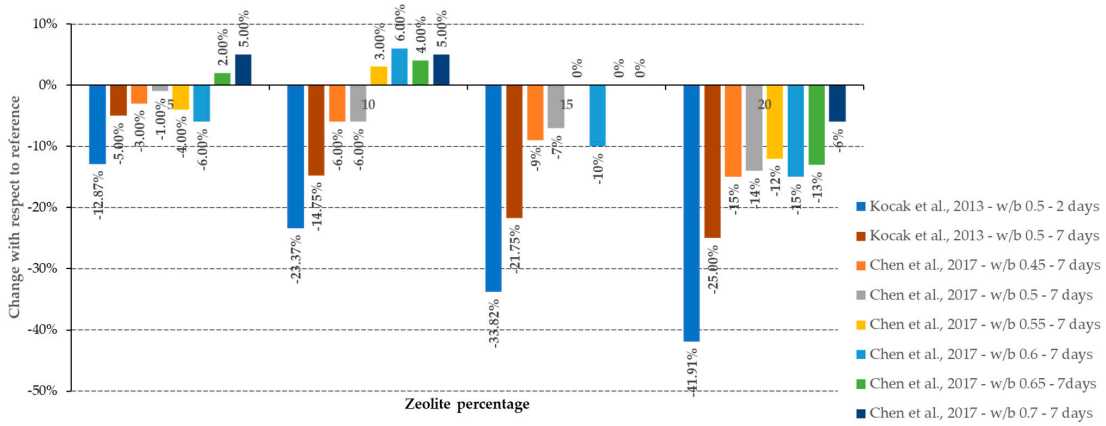

(**a**)

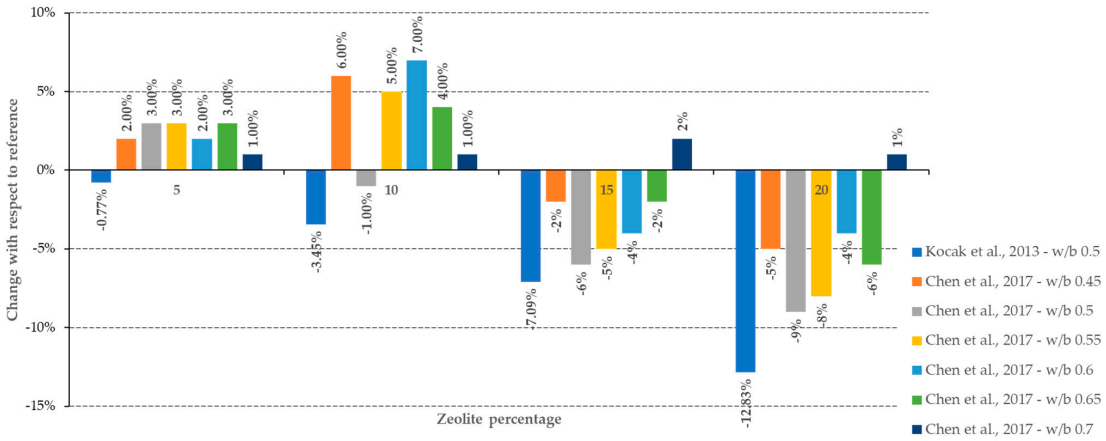

(**b**)

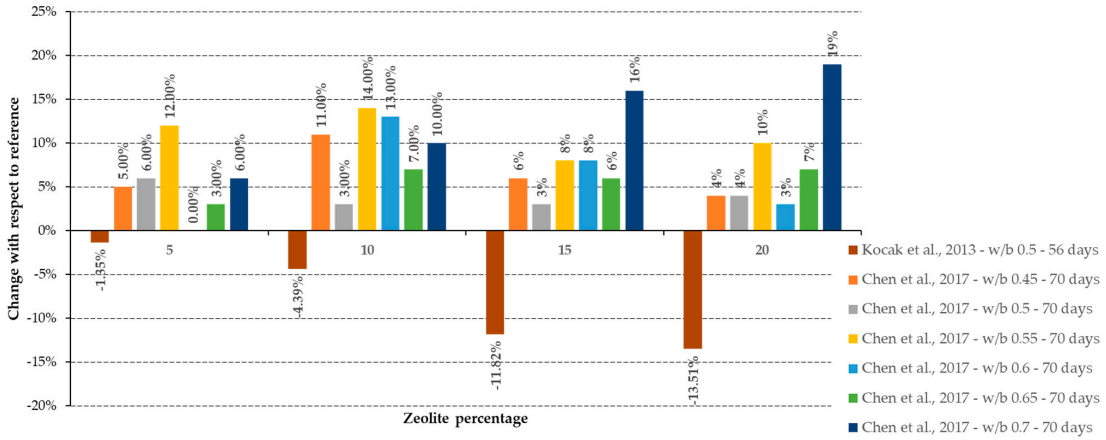

(**c**)

Figure 2. Variation of cement paste compressive strength with curing age, water/binder ratio and zeolite content (using data from [10,18]). (**a**)compressive strength values at early ages (2 and 7 days, normalized); (**b**) compressive strength values at 28 days (normalized) and (**c**) Compressive strength values at 56 and 70 days (normalized).

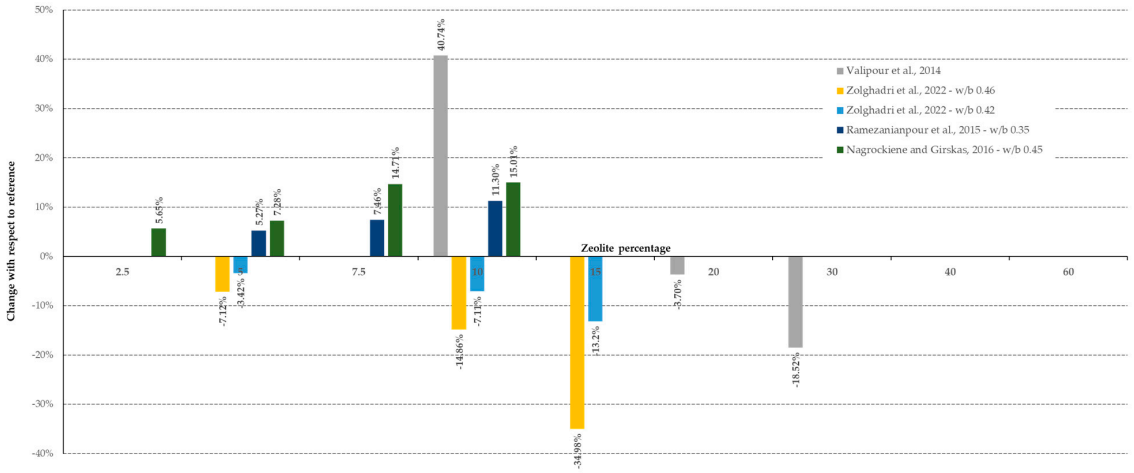

(**a**)

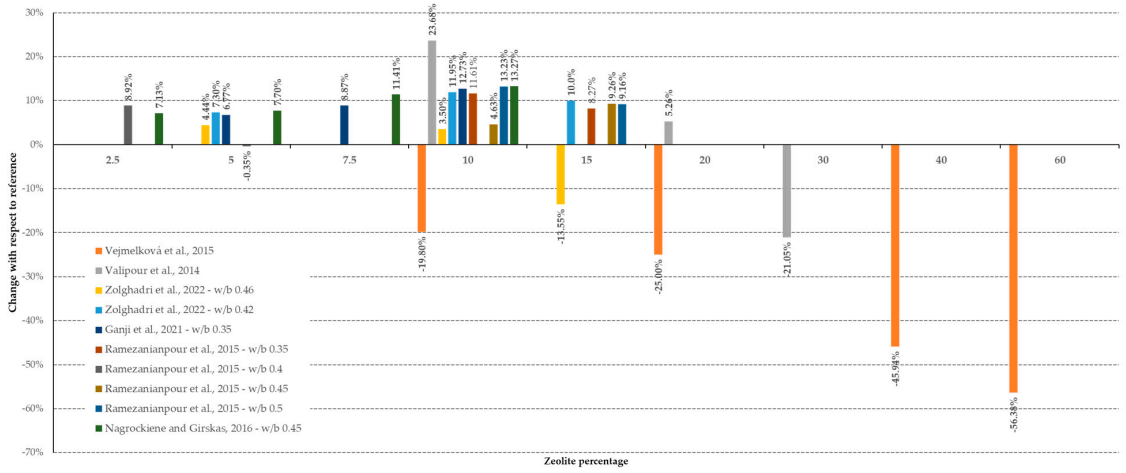

(**b**)

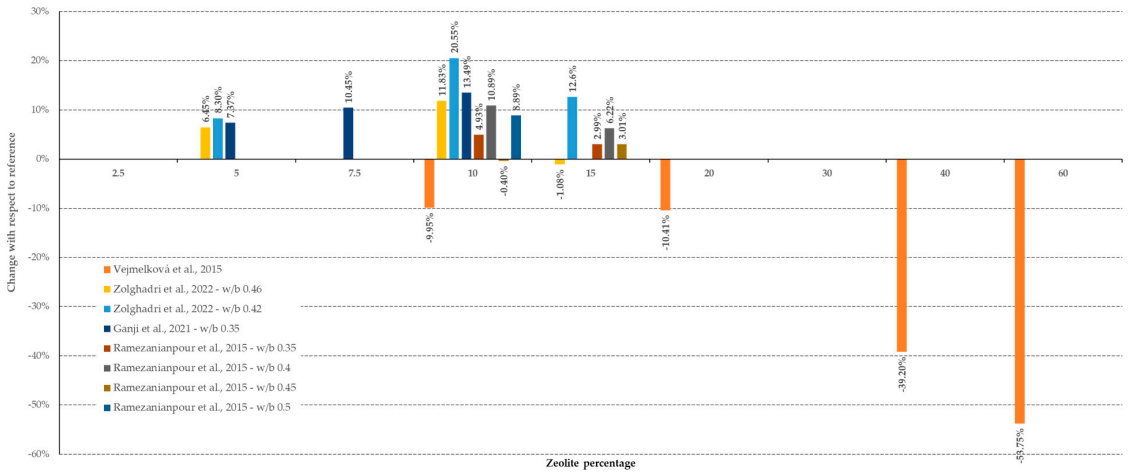

(**c**)

Figure 3. Variation of concrete compressive strength with curing age, water/binder ratio and zeolite content (using data from [17,30,32,35,36,42]). (**a**) compressive strength values at early ages (7 days, normalized); (**b**) compressive strength values at 28 days (normalized) and (**c**) compressive strength values at 90 days (normalized).

It is generally agreed that due to the low amount of CH produced at the early ages of cement hydration, the pozzolanic reaction of natural zeolite and, consequently, the secondary formation of CSH [4] is limited. This leads to lower values of mechanical properties of cement-based materials with natural zeolites at early ages [32]. There are, however, conflicting results reported in the scientific literature because the mechanism of zeolite interaction with cement hydration products is still unclear and under debate and requires more research in order to be fully understood [49].

Natural zeolites proved to be an efficient pozzolan, although the pozzolanic reaction is rather slow compared to other materials [49]. Moreover, their porous structure leads to some of the mixing water being absorbed by zeolites, resulting in the lower workability of cement-based materials [64]. The high specific surface area coupled with the irregular particle shape of zeolite powder leads to increased internal friction that contributes to further decreasing the workability. On the other hand, the free water absorbed during mixing is released later on, making zeolite a suitable candidate for internal curing [5,8]. This would contribute to improved mechanical and durability properties at later ages.

There are currently three main techniques to optimize the structure of zeolites. The first method involves the immersion of zeolite in acid solution to favor the reaction of dealumination inside the zeolite particles and thus increase their surface area [64]. This would increase the reactivity of zeolite to CH and promote the pozzolanic reaction. Another method frequently employed is calcination. Calcined zeolites have reduced porosity and water absorption properties. However, the benefits of this method on hardened properties of cement-based materials are only marginal and do not justify the high energy demand for calcination [21]. The third method involved milling the zeolite to a finer particle size. So far, this method has proved to be the most efficient from the point of view of energy consumption versus improvements in the mechanical and durability properties of cementitious materials [21].

There are certain drawbacks of using natural zeolites in cement-based mortar and concrete. First and foremost, there is an inconsistency in the reported results from the point of view of mechanical properties. The number of studies reporting improvements in mechanical properties is on par with the number of studies reporting the opposite effect, especially at early ages. The majority of studies concluded that the replacement of Portland cement with natural zeolite up to 20% is generally beneficial. Peak improvements were consistently reported for 10% replacement. Similar conclusions were drawn from the findings in terms of durability properties, with improved freeze–thaw performance, lower chloride permeability, lower water penetration depth and increased electrical resistivity. However, higher replacement percentages resulted in significant loss of compressive and flexural strength values.

The most significant benefits of using natural zeolites reside in a reduced carbon footprint [35] by using lower amounts of cement and improvements in the durability properties of cement-based materials. These benefits can be further enhanced when using natural zeolites together with other pozzolanic materials [48,49]. Nowadays, continuous advancements and technological breakthroughs offer the opportunity to combine natural zeolites with carbon nano-tubes and other nano materials [63].

6. Conclusions

The influence of natural zeolites on the workability and setting time of cement-based construction materials reveals that increasing the zeolite content results in a reduction in workability compared to the control mixes. At the same time, the initial and final setting times of cement pastes show a decreasing trend with the increase in the replacement percentage. Moreover, the increase in zeolite content results in a higher demand for water-reducing admixtures in order to maintain similar workability to the reference mix.

There is no clear increasing or decreasing trend in terms of compressive strength values up to the age of 28 days for pastes containing zeolites compared to the reference mix.

However, at the age of 70 days, cement pastes with zeolites show consistently larger values compared to the reference mixes.

The slow pozzolanic reaction of clinoptilolite zeolite results in lower flexural strength and compressive strength values of mortars at the age of 28 days. The most used alternatives to improve the effect of zeolites as supplementary cementitious materials are milling, to decrease the particle size, and calcination, which helps reduce their porous structure and, consequently, the water demand. The calcination of natural zeolites results in marginal improvements over non-calcined zeolites in terms of compressive strength at either early age or 28 days. Milling pre-treatment, on the other hand, results in significantly improved values of the compressive strength of zeolites containing mortars, compared to natural, non-treated zeolite mortars.

Blending zeolites with other supplementary cementitious materials results in improved values of the mechanical properties of mortar and concrete. Using blends of nano-silica and zeolites to replace the cement not only leads to higher compressive strength values at early ages but also beyond 28 days when the pozzolanic reaction of zeolites starts contributing.

The use of zeolites as a replacement for aggregates, e.g., sand, in engineering cementitious composites was considered from the point of view of zeolite's internal curing properties rather than the strength gains of the resulting material. A successful decrease in the 28 day shrinkage was obtained at the cost of reduced compressive strength.

The findings regarding the impact of zeolite on the durability of concrete suggest that zeolite shows promise as a viable alternative to cement, with positive effects on various aspects of durability. However, challenges have been observed in terms of resistance to acid and carbonation. It is important to note that carbonation may not be entirely detrimental and ongoing research is investigating its potential to enhance concrete properties.

The majority of durability factors are interconnected. For example, water movement significantly affects concrete's susceptibility to damage during freeze–thaw cycles and the migration of chloride ions within the material. The complexity of these interactions is further complicated by the crucial role of pore size distribution and overall porosity in linking these effects. The presence of conflicting findings is particularly significant in this context, highlighting the need for a comprehensive approach to address these challenges in the future.

Author Contributions: Conceptualization, S.-M.A.-S., A.-M.T. and I.-O.T.; methodology, I.O., A.-M.T. and O.-M.B., literature search, S.-M.A.-S., I.O., A.-M.T., C.P., O.-M.B., O.-C.C. and I.-O.T.; formal data analysis, I.O., A.-M.T., C.P., O.-M.B. and O.-C.C.; writing—original draft preparation, S.-M.A.-S., I.O. and A.-M.T.; writing—review and editing, C.P., O.-M.B., O.-C.C. and I.-O.T.; supervision, I.O., A.-M.T., C.P. and I.-O.T.; project administration, I.-O.T.; funding acquisition, C.P. and I.-O.T. All authors have read and agreed to the published version of the manuscript.

Funding: This research was funded by PN-III-P2-2.1-PED-2021-0677 research grant "Sustainable Concrete for Energy Efficient Buildings" funded by Executive Agency for Higher Education, Research, Development and Innovation Funding—UEFISCDI.

Institutional Review Board Statement: Not applicable.

Informed Consent Statement: Not applicable.

Data Availability Statement: Data are contained within the article.

Conflicts of Interest: The authors declare no conflict of interest.

References

1. Iijima, A. Geology of natural zeolites and zeolitic rocks. *Pure Appl. Chem.* **1980**, *52*, 2115–2130. [CrossRef]
2. Ahmadi, B.; Shekarchi, M. Use of natural zeolite as a supplementary cementitious material. *Cem. Concr. Compos.* **2010**, *32*, 134–141. [CrossRef]
3. Islam, M.S.; Mohr, B.J.; VandenBerge, D. Performance of natural clinoptilolite zeolite in the cementitious materials: A comparative study with metakaolin, fly ash, and blast furnace slag. *J. Build. Eng.* **2022**, *53*, 104535. [CrossRef]

4. Toma, I.-O.; Stoian, G.; Rusu, M.-M.; Ardelean, I.; Cimpoeşu, N.; Alexa-Stratulat, S.-M. Analysis of Pore Structure in Cement Pastes with Micronized Natural Zeolite. *Materials* **2023**, *16*, 4500. [CrossRef] [PubMed]
5. Kazemian, M.; Shafei, B. Internal curing capabilities of natural zeolite to improve the hydration of ultra-high performance concrete. *Constr. Build. Mater.* **2022**, *340*, 127452. [CrossRef]
6. Gottardi, G.; Galli, E. *Natural Zeolites*; Springer: Berlin/Heidelberg, Germany, 1985; Volume 18, ISBN 978-3-642-46520-8.
7. Markiv, T.; Sobol, K.; Franus, M.; Franus, W. Mechanical and durability properties of concretes incorporating natural zeolite. *Arch. Civ. Mech. Eng.* **2016**, *16*, 554–562. [CrossRef]
8. Xuan, Z.; Jun, Z. Influence of zeolite addition on mechanical performance and shrinkage of high strength Engineered Cementitious Composites. *J. Build. Eng.* **2021**, *36*, 102124. [CrossRef]
9. Kriptavičius, D.; Girskas, G.; Skripkiūnas, G. Use of Natural Zeolite and Glass Powder Mixture as Partial Replacement of Portland Cement: The Effect on Hydration, Properties and Porosity. *Materials* **2022**, *15*, 4219. [CrossRef]
10. Kocak, Y.; Tascı, E.; Kaya, U. The effect of using natural zeolite on the properties and hydration characteristics of blended cements. *Constr. Build. Mater.* **2013**, *47*, 720–727. [CrossRef]
11. Najimi, M.; Sobhani, J.; Ahmadi, B.; Shekarchi, M. An experimental study on durability properties of concrete containing zeolite as a highly reactive natural pozzolan. *Constr. Build. Mater.* **2012**, *35*, 1023–1033. [CrossRef]
12. Tran, Y.T.; Lee, J.; Kumar, P.; Kim, K.-H.; Lee, S.S. Natural zeolite and its application in concrete composite production. *Compos. Part B Eng.* **2019**, *165*, 354–364. [CrossRef]
13. Kaplan, G.; Coskan, U.; Benli, A.; Bayraktar, O.Y.; Kucukbaltacı, A.B. The impact of natural and calcined zeolites on the mechanical and durability characteristics of glass fiber reinforced cement composites. *Constr. Build. Mater.* **2021**, *311*, 125336. [CrossRef]
14. Burris, L.E.; Juenger, M.C.G. Effect of calcination on the reactivity of natural clinoptilolite zeolites used as supplementary cementitious materials. *Constr. Build. Mater.* **2020**, *258*, 119988. [CrossRef]
15. Faheem, A.; Rizwan, S.A.; Bier, T.A. Properties of self-compacting mortars using blends of limestone powder, fly ash, and zeolite powder. *Constr. Build. Mater.* **2021**, *286*, 122788. [CrossRef]
16. Rahhal, V.F.; Pavlík, Z.; Tironi, A.; Castellano, C.C.; Trezza, M.A.; Černý, R.; Irassar, E.F. Effect of cement composition on the early hydration of blended cements with natural zeolite. *J. Therm. Anal. Calorim.* **2017**, *128*, 721–733. [CrossRef]
17. Ramezanianpour, A.A.; Mousavi, R.; Kalhori, M.; Sobhani, J.; Najimi, M. Micro and macro level properties of natural zeolite contained concretes. *Constr. Build. Mater.* **2015**, *101*, 347–358. [CrossRef]
18. Chen, J.J.; Li, L.G.; Ng, P.L.; Kwan, A.K.H. Effects of superfine zeolite on strength, flowability and cohesiveness of cementitious paste. *Cem. Concr. Compos.* **2017**, *83*, 101–110. [CrossRef]
19. Jokar, F.; Khorram, M.; Karimi, G.; Hataf, N. Experimental investigation of mechanical properties of crumbed rubber concrete containing natural zeolite. *Constr. Build. Mater.* **2019**, *208*, 651–658. [CrossRef]
20. Abdi Moghadam, M.; Izadifard, R.A. Effects of zeolite and silica fume substitution on the microstructure and mechanical properties of mortar at high temperatures. *Constr. Build. Mater.* **2020**, *253*, 119206. [CrossRef]
21. Florez, C.; Restrepo-Baena, O.; Tobon, J.I. Effects of calcination and milling pre-treatments on natural zeolites as a supplementary cementitious material. *Constr. Build. Mater.* **2021**, *310*, 125220. [CrossRef]
22. Ramezanianpour, A.A.; Mortezaei, M.; Mirvalad, S. Synergic effect of nano-silica and natural pozzolans on transport and mechanical properties of blended cement mortars. *J. Build. Eng.* **2021**, *44*, 102667. [CrossRef]
23. Sobolev, K.; Flores, I.; Torres-Martinez, L.M.; Valdez, P.L.; Zarazua, E.; Cuellar, E.L. Engineering of SiO_2 Nanoparticles for Optimal Performance in Nano Cement-Based Materials. In *Nanotechnology in Construction 3*; Springer: Berlin/Heidelberg, Germany, 2009; pp. 139–148.
24. Said, A.M.; Zeidan, M.S.; Bassuoni, M.T.; Tian, Y. Properties of concrete incorporating nano-silica. *Constr. Build. Mater.* **2012**, *36*, 838–844. [CrossRef]
25. Zhang, J.; Wang, Q.; Zhang, J. Shrinkage of internal cured high strength engineered cementitious composite with pre-wetted sand-like zeolite. *Constr. Build. Mater.* **2017**, *134*, 664–672. [CrossRef]
26. Wang, Q.; Zhang, J.; Ho, J.C.M. Zeolite to improve strength-shrinkage performance of high-strength engineered cementitious composite. *Constr. Build. Mater.* **2020**, *234*, 117335. [CrossRef]
27. Thang, N.C.; Van Tuan, N.; Yang, K.-H.; Phung, Q.T. Effect of Zeolite on Shrinkage and Crack Resistance of High-Performance Cement-Based Concrete. *Materials* **2020**, *13*, 3773. [CrossRef] [PubMed]
28. Ranjbar, M.M.; Madandoust, R.; Mousavi, S.Y.; Yosefi, S. Effects of natural zeolite on the fresh and hardened properties of self-compacted concrete. *Constr. Build. Mater.* **2013**, *47*, 806–813. [CrossRef]
29. Poon, C.S.; Lam, L.; Kou, S.C.; Lin, Z.S. A study on the hydration rate of natural zeolite blended cement pastes. *Constr. Build. Mater.* **1999**, *13*, 427–432. [CrossRef]
30. Nagrockiene, D.; Girskas, G. Research into the properties of concrete modified with natural zeolite addition. *Constr. Build. Mater.* **2016**, *113*, 964–969. [CrossRef]
31. Yu, Z.; Yang, W.; Zhan, P.; Liu, X.; Chen, D. Strengths, Microstructure and Nanomechanical Properties of Concrete Containing High Volume of Zeolite Powder. *Materials* **2020**, *13*, 4191. [CrossRef]
32. Zolghadri, A.; Ahmadi, B.; Taherkhani, H. Influence of natural zeolite on fresh properties, compressive strength, flexural strength, abrasion resistance, Cantabro-loss and microstructure of self-consolidating concrete. *Constr. Build. Mater.* **2022**, *334*, 127440. [CrossRef]

33. Raggiotti, B.B.; Positieri, M.J.; Oshiro, Á. Natural zeolite, a pozzolan for structural concrete. *Procedia Struct. Integr.* **2018**, *11*, 36–43. [CrossRef]
34. Mohseni, E.; Tang, W.; Cui, H. Chloride Diffusion and Acid Resistance of Concrete Containing Zeolite and Tuff as Partial Replacements of Cement and Sand. *Materials* **2017**, *10*, 372. [CrossRef] [PubMed]
35. Valipour, M.; Yekkalar, M.; Shekarchi, M.; Panahi, S. Environmental assessment of green concrete containing natural zeolite on the global warming index in marine environments. *J. Clean. Prod.* **2014**, *65*, 418–423. [CrossRef]
36. Ganji, S.; Sharabiani, H.E.; Zeinali, F. Laboratory investigation on abrasion resistance and mechanical properties of concretes containing zeolite powder and polyamide tire cord waste as fiber. *Constr. Build. Mater.* **2021**, *308*, 125053. [CrossRef]
37. Pachideh, G.; Gholhaki, M. Effect of pozzolanic materials on mechanical properties and water absorption of autoclaved aerated concrete. *J. Build. Eng.* **2019**, *26*, 100856. [CrossRef]
38. Zhang, G.-Z.; Wang, X.-Y. Effect of Pre-Wetted Zeolite Sands on the Autogenous Shrinkage and Strength of Ultra-High-Performance Concrete. *Materials* **2020**, *13*, 2356. [CrossRef] [PubMed]
39. Sobuś, N.; Czekaj, I.; Diichuk, V.; Kobasa, I.M. Characteristics of the structure of natural zeolites and their potential application in catalysis and adsorption processes. *Tech. Trans.* **2020**, *117*, e2020043. [CrossRef]
40. Zhang, H. Concrete. In *Building Materials in Civil Engineering*; Zhang, H., Ed.; Elsevier: Amsterdam, The Netherlands, 2011; pp. 81–423, ISBN 9781845699550.
41. Powers, T.C. A Working Hypothesis for Further Studies of Frost Resistance of Concrete. *ACI J. Proc.* **1945**, *41*, 245–272. [CrossRef]
42. Vejmelková, E.; Koňáková, D.; Kulovaná, T.; Keppert, M.; Žumár, J.; Rovnaníková, P.; Keršner, Z.; Sedlmajer, M.; Černý, R. Engineering properties of concrete containing natural zeolite as supplementary cementitious material: Strength, toughness, durability, and hygrothermal performance. *Cem. Concr. Compos.* **2015**, *55*, 259–267. [CrossRef]
43. Ebrahimi Besheli, A.; Samimi, K.; Moghadas Nejad, F.; Darvishan, E. Improving concrete pavement performance in relation to combined effects of freeze–thaw cycles and de-icing salt. *Constr. Build. Mater.* **2021**, *277*, 122273. [CrossRef]
44. Bilim, C. Properties of cement mortars containing clinoptilolite as a supplementary cementitious material. *Constr. Build. Mater.* **2011**, *25*, 3175–3180. [CrossRef]
45. Milović, T.; Šupić, S.; Malešev, M.; Radonjanin, V. The Effects of Natural Zeolite as Fly Ash Alternative on Frost Resistance and Shrinkage of Blended Cement Mortars. *Sustainability* **2022**, *14*, 2736. [CrossRef]
46. Chakraborty, S.; Mandal, R.; Chakraborty, S.; Guadagnini, M.; Pilakoutas, K. Chemical attack and corrosion resistance of concrete prepared with electrolyzed water. *J. Mater. Res. Technol.* **2021**, *11*, 1193–1205. [CrossRef]
47. Valipour, M.; Shekarchi, M.; Arezoumandi, M. Chlorine diffusion resistivity of sustainable green concrete in harsh marine environments. *J. Clean. Prod.* **2017**, *142*, 4092–4100. [CrossRef]
48. Valipour, M.; Pargar, F.; Shekarchi, M.; Khani, S. Comparing a natural pozzolan, zeolite, to metakaolin and silica fume in terms of their effect on the durability characteristics of concrete: A laboratory study. *Constr. Build. Mater.* **2013**, *41*, 879–888. [CrossRef]
49. Sabet, F.A.; Libre, N.A.; Shekarchi, M. Mechanical and durability properties of self consolidating high performance concrete incorporating natural zeolite, silica fume and fly ash. *Constr. Build. Mater.* **2013**, *44*, 175–184. [CrossRef]
50. Madhuri, P.V.; Kameswara Rao, B.; Chaitanya, A. Improved performance of concrete incorporated with natural zeolite powder as supplementary cementitious material. *Mater. Today Proc.* **2021**, *47*, 5369–5378. [CrossRef]
51. Samimi, K.; Kamali-Bernard, S.; Akbar Maghsoudi, A.; Maghsoudi, M.; Siad, H. Influence of pumice and zeolite on compressive strength, transport properties and resistance to chloride penetration of high strength self-compacting concretes. *Constr. Build. Mater.* **2017**, *151*, 292–311. [CrossRef]
52. Dousti, A.; Rashetnia, R.; Ahmadi, B.; Shekarchi, M. Influence of exposure temperature on chloride diffusion in concretes incorporating silica fume or natural zeolite. *Constr. Build. Mater.* **2013**, *49*, 393–399. [CrossRef]
53. Oueslati, O.; Duchesne, J. Resistance of blended cement pastes subjected to organic acids: Quantification of anhydrous and hydrated phases. *Cem. Concr. Compos.* **2014**, *45*, 89–101. [CrossRef]
54. Chintalapudi, K.; Pannem, R.M.R. Enhanced chemical resistance to sulphuric acid attack by reinforcing Graphene Oxide in Ordinary and Portland Pozzolana cement mortars. *Case Stud. Constr. Mater.* **2022**, *17*, e01452. [CrossRef]
55. Irico, S.; De Meyst, L.; Qvaeschning, D.; Alonso, M.C.; Villar, K.; De Belie, N. Severe Sulfuric Acid Attack on Self-Compacting Concrete with Granulometrically Optimized Blast-Furnace Slag-Comparison of Different Test Methods. *Materials* **2020**, *13*, 1431. [CrossRef] [PubMed]
56. Samimi, K.; Kamali-Bernard, S.; Maghsoudi, A.A. Durability of self-compacting concrete containing pumice and zeolite against acid attack, carbonation and marine environment. *Constr. Build. Mater.* **2018**, *165*, 247–263. [CrossRef]
57. Gerengi, H.; Kocak, Y.; Jazdzewska, A.; Kurtay, M.; Durgun, H. Electrochemical investigations on the corrosion behaviour of reinforcing steel in diatomite- and zeolite-containing concrete exposed to sulphuric acid. *Constr. Build. Mater.* **2013**, *49*, 471–477. [CrossRef]
58. Šavija, B.; Luković, M. Carbonation of cement paste: Understanding, challenges, and opportunities. *Constr. Build. Mater.* **2016**, *117*, 285–301. [CrossRef]
59. Thiery, M.; Villain, G.; Dangla, P.; Platret, G. Investigation of the carbonation front shape on cementitious materials: Effects of the chemical kinetics. *Cem. Concr. Res.* **2007**, *37*, 1047–1058. [CrossRef]
60. Azarsa, P.; Gupta, R. Electrical Resistivity of Concrete for Durability Evaluation: A Review. *Adv. Mater. Sci. Eng.* **2017**, *2017*, 8453095. [CrossRef]

61. Idiart, A.E.; López, C.M.; Carol, I. Modeling of drying shrinkage of concrete specimens at the meso-level. *Mater. Struct.* **2011**, *44*, 415–435. [CrossRef]
62. Lv, Y.; Ye, G.; De Schutter, G. Investigation on the potential utilization of zeolite as an internal curing agent for autogenous shrinkage mitigation and the effect of modification. *Constr. Build. Mater.* **2019**, *198*, 669–676. [CrossRef]
63. Shekarchi, M.; Ahmadi, B.; Azarhomayun, F.; Shafei, B.; Kioumarsi, M. Natural zeolite as a supplementary cementitious material—A holistic review of main properties and applications. *Constr. Build. Mater.* **2023**, *409*, 133766. [CrossRef]
64. Wang, Q.; Xiong, Z.; He, J.; Lai, M.; Ho, J. Effective solution for improving rheological properties of cement paste containing zeolite. *Constr. Build. Mater.* **2022**, *351*, 128780. [CrossRef]
65. Thomas, M.; Osińska, M.; Ślosarczyk, A. Long-Term Behavior of Cement Mortars Based on Municipal Solid Waste Slag and Natural Zeolite—A Comprehensive Physico-Mechanical, Structural and Chemical Assessment. *Materials* **2022**, *15*, 1001. [CrossRef] [PubMed]

materials

MDPI

Article

Analysis of Pore Structure in Cement Pastes with Micronized Natural Zeolite

Ionut-Ovidiu Toma [1,*], George Stoian [2], Mihai-Marius Rusu [3], Ioan Ardelean [3], Nicanor Cimpoeşu [4] and Sergiu-Mihai Alexa-Stratulat [1,*]

[1] Faculty of Civil Engineering and Building Services, The "Gheorghe Asachi" Technical University of Iasi, 700050 Iasi, Romania
[2] National Institute of Research and Development for Technical Physics, 700050 Iasi, Romania; gstoian@phys-iasi.ro
[3] Department of Physics and Chemistry, Technical University of Cluj-Napoca, 400114 Cluj-Napoca, Romania; mihai.rusu@phys.utcluj.ro (M.-M.R.); ioan.ardelean@phys.utcluj.ro (I.A.)
[4] Faculty of Material Science and Engineering, The "Gheorghe Asachi" Technical University of Iasi, 700050 Iasi, Romania; nicanor.cimpoesu@academic.tuiasi.ro
* Correspondence: ionut.ovidiu.toma@tuiasi.ro (I.-O.T.); sergiu-mihai.alexa-stratulat@staff.tuiasi.ro (S.-M.A.-S.); Tel.: +40-232-701455 (I.-O.T.)

Abstract: The continuous development of urban areas around the world led to an increase in construction material use and demand, with concrete seeing significant market uptake. Although significant progress has been made to reduce the environmental impact of concrete, there is still a stringent need for improvement. One of the most widely used methods to reduce the environmental impact of the cement industry and the construction industry alike is the replacement of ordinary Portland cement (OPC) by supplementary cementitious materials (SCM). Aside from by-products of industry, SCMs could also come from natural sources. Taking into account the porous structure of zeolites and their contribution to the improvement of the mechanical and durability properties of cement-based materials, the analysis of pore structure in cement pastes incorporating micronized natural zeolite is deemed necessary. In this research, the OPC was replaced by zeolite in three different percentages: 10%, 20%, and 30% by mass. The evolution of pore structure was investigated by means of nuclear magnetic resonance relaxometry at the curing ages of 1, 7, and 28 days. The microstructure of cement pastes was assessed by scanning electron microscopy investigations at 1, 7, 14, 21, and 28 days. The obtained results show that smaller pore sizes are present in cement pastes containing zeolites during the first 7 days. However, at the age of 28 days, the reference mix exhibits a similar pore structure to the mix containing 10% micronized zeolite due to the presence of larger amounts of hydration products. Increasing the replacement percentage to 30% results in larger pores, as indicated by larger values of the relaxation time.

Keywords: cement paste; micronized natural zeolite; pore structure; scanning electron microscopy (SEM); nuclear magnetic resonance (NMR)

Citation: Toma, I.-O.; Stoian, G.; Rusu, M.-M.; Ardelean, I.; Cimpoeşu, N.; Alexa-Stratulat, S.-M. Analysis of Pore Structure in Cement Pastes with Micronized Natural Zeolite. *Materials* **2023**, *16*, 4500. https://doi.org/10.3390/ma16134500

Academic Editor: Agnieszka Ślosarczyk

Received: 25 May 2023
Revised: 15 June 2023
Accepted: 19 June 2023
Published: 21 June 2023

1. Introduction

The continuous development of urban areas around the world led to an increase in construction material use and demand. The concrete market was forecast to reach 970 billion USD by 2030, with a compound annual growth rate (CAGR) of 4.7%. Consequently, cement production has to keep up, and it will reach a market value of almost half that of concrete by 2029, with a CAGR of 5.1%. Cement reacts with water to create a matrix, which binds the aggregates into a rock-like solid material known as concrete. It is the key component of normal to ultra-high-strength concrete. However, this comes at a cost in terms of greenhouse gas emissions (GHG), with the cement industry responsible for 7% of anthropogenic GHG [1]. Although the GHG associated with cement production has

significantly decreased from 783 kgCO_2/ton of cement [2], it is still a long way until net zero emissions are set as a target for 2050. Moreover, recent reports and statistics indicate a steady rise of 1.5% per year during the 2015–2021 time interval of GHG associated with cement production worldwide, as seen in Figure 1 [3]. Consequently, urgent measures need to be taken to reach the proposed intermediary goal of 472 kgCO_2/ton of cement by 2030 [2], resulting in an annual 3% decrease in CO_2 emissions. While the industry should focus on reducing the clinker/cement ratio, the implementation of innovative technologies for carbon capture and storage, the development of more energy-efficient kilns, and identifying alternative energy sources, the scientific community should intensify its research efforts to contribute to the development of new blended cements and/or cement-free binders [4,5].

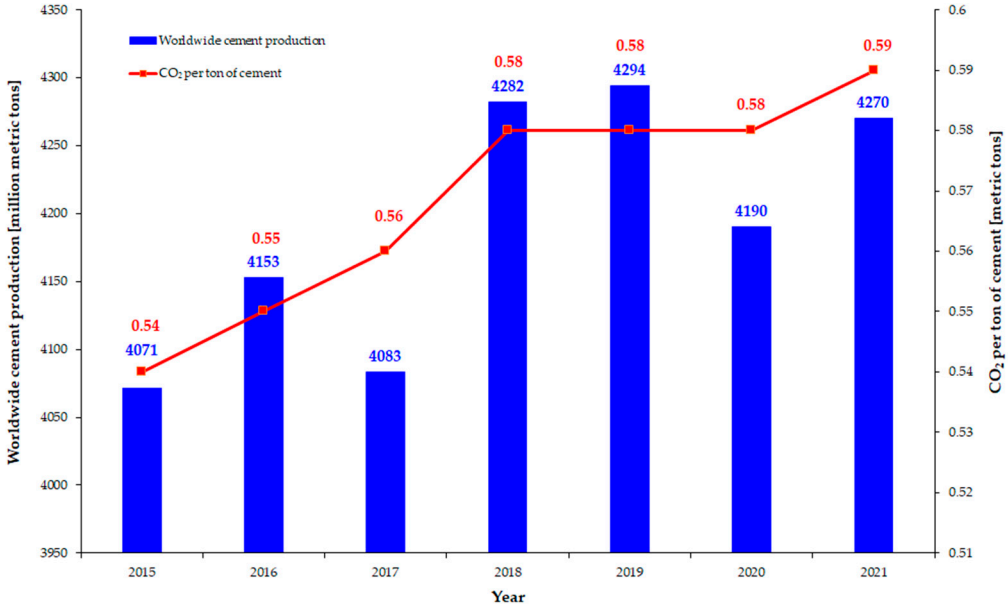

Figure 1. Evolution of worldwide cement production and associated CO_2 emissions per ton of cement (data from [3]).

One of the most widely used methods to reduce the environmental impact of the cement industry and the construction industry alike is the replacement of ordinary Portland cement (OPC) by supplementary cementitious materials (SCM). Due to their pozzolanic activity, the use of SCMs results in a long-term improvement of the mechanical and durability properties of cement-based materials. Fly-ash, a by-product of coal power plants, has been successfully used as a SCM due to the improvements it brings to cement-based materials in terms of strength [6], durability [7,8], and self-healing properties [9]. Ground-granulated blast furnace slag (GGBS) is another frequently used SCM due to its beneficial effect in terms of workability, long-term mechanical properties of mortar and concrete [10], improved pore structure [11], reduced shrinkage, and better durability [12]. The replacement of OPC by phosphogypsum, a by-product of fertilizer manufacturing, has also recently been recognized to have beneficial effects in terms of the elastic, mechanical, and durability properties of mortar and concrete [13–15]. However, in the case of phosphogypsum, a setting retarder is recommended.

Aside from by-products of industry, supplementary cementitious materials could also come from natural sources. Volcanic tuffs are a prime source for pozzolanic materials to be used as a partial replacement for OPC [16,17]. Zeolites, a naturally occurring volcanic rock, are known for their wide range of applications in agriculture, the petrochemical industry, cement industry, and, more recently, in nuclear waste repositories [18]. Being hydrated aluminosilicates, zeolites applications in cement-based construction materials have been intensively studied due to their pozzolanic activity [19]. Their porous structure enables zeolites to adsorb water and gradually release it during the curing period of cement-based

materials, thus reducing autogenous shrinkage and providing a favorable environment for the long-term hydration of cement [19,20]. Zeolites strongly influence the rheological properties of cement pastes, with direct implications for the workability of fresh mortar and concrete [21]. Due to their open crystal structure coupled with a high specific surface area, they absorb some of the free water, thus reducing the workability of fresh cement-based materials (cement paste, mortar, and concrete) [22]. This may adversely affect the mechanical and durability properties of the resulting material if countermeasures are not considered. On the other hand, this apparent drawback becomes an advantage in the long run [19], with better hydration of the cement particles resulting in denser matrices and overall improved material properties. The main advantage consists in the fact that clinoptilolite natural zeolites do not swell or shrink during the process of absorption and desorption of water, being dimensionally stable. However, the porous structure of natural zeolites may adversely influence the pore structure of the cementitious matrix.

The pore structure is a very important parameter that influences the above properties and should, therefore, be correctly assessed. Recent studies have made it evident that the permeability and strength of cement pastes are governed by pore size distribution rather than porosity [23]. The smaller the pore size, the higher the compressive strength and the lower the thermal conductivity [24]. One of the most widely used methods for assessing the pore size distribution is mercury intrusion porosimetry (MIP). It involves careful sample preparation and is based on the high-pressure injection of mercury into the sample. At lower values of pressure, the mercury fills the larger pores but is unable to fill the smaller ones. Increasing the pressure results in mercury filling the smaller pores, both inter- and intra-particle pores [25–27]. There are, however, some limitations to using MIP to assess the pore structure of various media, such as cement pastes, mortar, and concrete. In one of the first studies to compare the results of using MIP with other assessing techniques, e.g., helium pycnometry, in hydrated Portland cement systems, it was concluded that significant results were obtained between the two methods [28]. The assumption was that mercury could not enter all the spaces, or closed pores, that are otherwise available to helium. Additional assessments of pore structure were conducted using methanol as a displacement fluid, and the obtained results confirmed prior findings. Later studies concluded that using MIP may not be entirely representative of the real pore structure. Even though the total porosity may have been correctly assessed, the pore size distribution varied significantly compared with other methods [29]. Various parameters need to be carefully considered when applying MIP to assess the pore structure, such as the varying contact angles between mercury and the solid part of the samples during the intrusion and extrusion stages, the effect of ink bottle pores entrapping mercury, and the pore connectivity effect [30]. A too high pressure applied may also lead to damage to the pore structure of the material [31].

Another technique for assessing the pore structure of porous media is low-field nuclear magnetic resonance (NMR) relaxometry [32]. NMR relaxometry of cement-based materials exploits the difference in relaxation times experienced by liquid molecules filling in different pore reservoirs. The main advantages of this technique over MIP are that it is completely non-invasive and does not require any special sample preparation. Furthermore, it can be applied even during the hydration process of cement-based materials [33]. This makes it possible to highlight the three types of pores inside cement-based mate-rials, during hydration and investigate the effects of different external parameters on them. However, precise absolute dimensions of the pores cannot be obtained without prior calibration of the pore surface relaxivity, and this can be achieved only by comparison with other techniques, such as MIP. The accuracy of the NMR relaxometry technique was highlighted in a recent study by comparing the results with the information acquired by MIP [34]. By using NMR relaxometry, the effect of calcium nitrate on the fresh and hardened properties of cement pastes was investigated and compared with the results extracted via X-ray diffraction (XRD) and scanning electron microscopy (SEM) [35]. It was also studied the influence of

an accelerator on the pore structure development and the correlation with the strength of cement pastes made with CEM-I type of cement [36].

Taking into account the porous structure of zeolites and their contribution to the improvement of the mechanical and durability properties of cement-based construction materials, the analysis of pore structure in cement pastes incorporating micronized natural zeolite is of paramount importance. The OPC was replaced by micronized natural zeolite in three different percentages, 10%, 20%, and 30%, by mass, and the evolution of pore structure was investigated by means of low-field NMR relaxometry at the curing ages of 1 day, 7 days, and 28 days. The microstructure of cement pastes was assessed by SEM investigations. The SEM analyses offer valuable information about the internal structure of the material, e.g., the formation of ettringite, CH and CSH gels. Additionally, when conducted over longer periods of time, SEM investigations can provide information on the hydration processes and hydration products evolution that may explain the macro-properties of the material. The obtained results show that smaller pore sizes are present in cement pastes containing zeolites up to the age of 28 days, when the pore sizes in the cement pastes containing 20% and 30% micronized zeolites were slightly larger compared with the reference mix, as indicated by NMR relaxometry. Additionally, there seems to be a threshold, identified in this study as being 20% of cement replacement, above which the use of zeolites becomes detrimental from the point of view of the durability and strength characteristics of cement-based materials because it leads to an increase in the pore size.

2. Materials and Methods

2.1. Materials

The cement considered in this research was CEM II B-M (S-LL) 42.R, a rapid hardening composite Portland cement readily available on the market (HOLCIM), following the guidelines of SR EN 197-1:2011 [37]. The choice of this type of cement was based on the fact that it contains 65–79% clinker, thus contributing to lower GHG emissions. The remaining 21–35% of its composition consists of a mix of blast furnace slag and limestone. Another reason for considering this type of cement was the fact that it is the most commonly used type of cement in Europe. According to ref. [38], 47% of the cement sold in Europe in 2015 consisted of CEM II cement.

The natural zeolite powder used in the present research is based on Clinoptilolite (87–90%), being thermally stable up to 450 °C, has a pH value of 8.7, and has a mean particle distribution of 26.7 μm. The chemical compositions of the two materials, as supplied by the manufacturers, are shown in Table 1. According to ASTM C 618: 2022 [39], for the zeolite to be considered a natural pozzolan, the total content of SiO_2 + Al_2O_3 + Fe_2O_3 should be at least 70%. Moreover, the SiO_2/Al_2O_3 ratio greater than 4.0 confirms the Clinoptilolite type of the zeolite [40].

Table 1. Chemical composition of cement and natural zeolites (expressed in %).

	CaO	**SiO_2**	**Al_2O_3**	**Fe_2O_3**	**MgO**	**SO_3**	**Na_2O**	**K_2O**	**Cl**
CEM II	58.49	16.32	4.83	2.24	1.39	2.85	0.34	0.46	0.035
Zeolite	2.86–5.2	68.75–71.30	11.35–13.10	1.90–2.10	1.18–1.20	-	0.82–1.30	3.17–3.40	-

The SEM image of the natural zeolite considered in this study is shown in Figure 2. The porous structure can be clearly seen. However, one advantage of the clinoptilolite-based zeolite is that it does not change its structure during the absorption or desorption of water and, therefore, is geometrically stable [19]. This is an important property since it does not create swelling or contractions in the cement matrix, which may lead to the formation of microcracks.

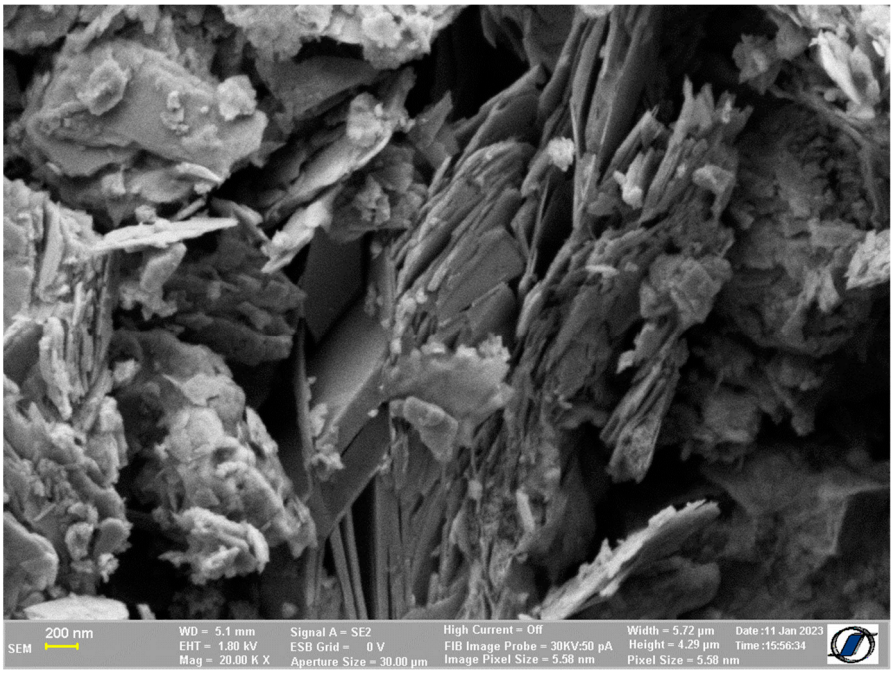

Figure 2. SEM image of clinoptilolite based natural zeolite.

2.2. Methods

The mix proportions considered in this study are presented in Table 2. The water-to-binder ratio was kept at 0.6 for all mixes. The binder consisted of either Portland cement or Portland cement with natural zeolite. Three replacement percentages of CEM II OPC by clinoptilolite-based natural zeolite were selected: 10%, 20%, and 30% by mass of cement. The mixes were named to reflect the replacement percentage, e.g., ZP20 stands for paste with zeolite powder (micronized zeolite), ZP, replacing 20% of cement.

Table 2. Mix proportions.

Mix	Binder		Water/Binder
	CEM II	Micronized Zeolite	
	[%]	[%]	[%]
Ref	100	-	0.6
ZP10	90	10	
ZP20	80	20	
ZP30	70	30	

The pastes were poured into 10 mm diameter glass tubes and sealed to prevent loss of water.

The microstructure of the cement pastes, using a scanning electron microscope, was investigated at 1 day, 7, 14, 21 and 28 days of curing by means of a Carl Zeiss NEON 40EsB Cross-Beam system with thermal Schottky field emission emitter and accelerated Ga ions column.

The pore distribution in the cement pastes was assessed by means of the low-field nuclear magnetic resonance (LF-NMR) relaxometry technique using a Minispec MQ20 (Bruker, Heilderberg, Germany) instrument, operating at a proton resonance frequency of 20 MHz. The LF-NMR relaxometry allows the monitoring of the pore structure evolution and water consumption during the hydration process [32,33]. The Carr-Purcell-Meiboom-Gill (CPMG) [41,42] pulse sequence was applied to record the echo trains of each paste at the ages of 1 day, 7 days, and 28 days. The CPMG echo trains consist of 2000 echoes that were recorded after 32 scans, with an echo time of 80 µs and a recycle delay of 0.5 s. A

numerical Laplace inversion algorithm applied to the recorded echo trains provided the relaxation time, T_2, distributions [43].

The relaxation time can then be used to assess the dimension of the pores using the equation [44]:

$$\frac{1}{T_2} = \rho \frac{S_p}{V_l} \quad (1)$$

where S_p is the surface of the pore in contact with the confined liquid, V_l is the volume of liquid inside the pore, ρ is the relaxivity, and T_2 is the relaxation time. The relaxivity is a constant depending on the magnetic field induction, the pore surface, and the interaction between the molecules inside the pore and the surface of the pore itself (surface affinity). In case of saturated pores, when the liquid fills the entire pore volume, the following is considered $V_l = V_p$ in Equation (1). Assuming spherically shaped pores, Equation (1) becomes:

$$T_2 = \frac{1}{3\rho} \cdot R \quad (2)$$

where R is the radius of the pore. Note that, even if the relaxivity was unknown, the relaxation time distribution still provides information about the relative distribution of the pores.

Two distinct NMR measurements were performed at the age of 28 days. The first measurement considered the cement pastes in their initial condition, e.g., with water still present in the matrix. The second measurement was conducted on the samples after they had been fully immersed in cyclohexane for 4 h. Prior to the immersion stage, the samples were stored in a vacuum for 24 h in order to remove the free water from the capillary pores. Since cyclohexane has a longer relaxation time than water, this would result in a more clear separation between the pores from the gel hydration products and the capillary pores after the post-processing of the CMPG echo trains by numerical Laplace inversion [45].

Fresh properties of the cement paste, such as flowability and setting time, were also determined for each mix shown in Table 2. The flowability was assessed by means of a mini-slump test using a cone having a top and bottom diameter of 70 mm and 100 mm, respectively [46]. After the cone was lifted and the spread of the cement paste stopped, the average of two perpendicular diameters was considered. The initial and final setting times were determined in accordance with SR EN 196-3:2017 specifications [47].

3. Results

3.1. Flowability and Setting Time

The obtained results for the flowability of cement pastes and the initial and final setting times are presented in Figure 3.

It can be observed that the addition of micronized zeolite results in decreased values of the initial setting time compared with the reference mix. On the other hand, the final setting time value was larger compared with the one obtained for the reference mix by 3.85% for the ZP10 mix and 23.08% for ZP20 and ZP30 mixes. Increasing the replacement percentage of cement by micronized zeolite above 20% does not seem to influence the setting times values.

At the same time, replacing cement by micronized natural zeolite has a decreasing effect on the flow of cement paste. The final diameter of the ZP10 mix decreased by 9.09% compared with the reference mix, while increasing the replacement percentage to 20% and 30% resulted in 28.18% and 43.49% decrease, respectively. Similar decreasing trends were previously reported in the scientific literature [21,48].

3.2. SEM Analyses

Investigations on the material structure of the four cement pastes presented in Table 2 were conducted by means of SEM at the ages of 1 day, 7, 14, 21, and 28 days.

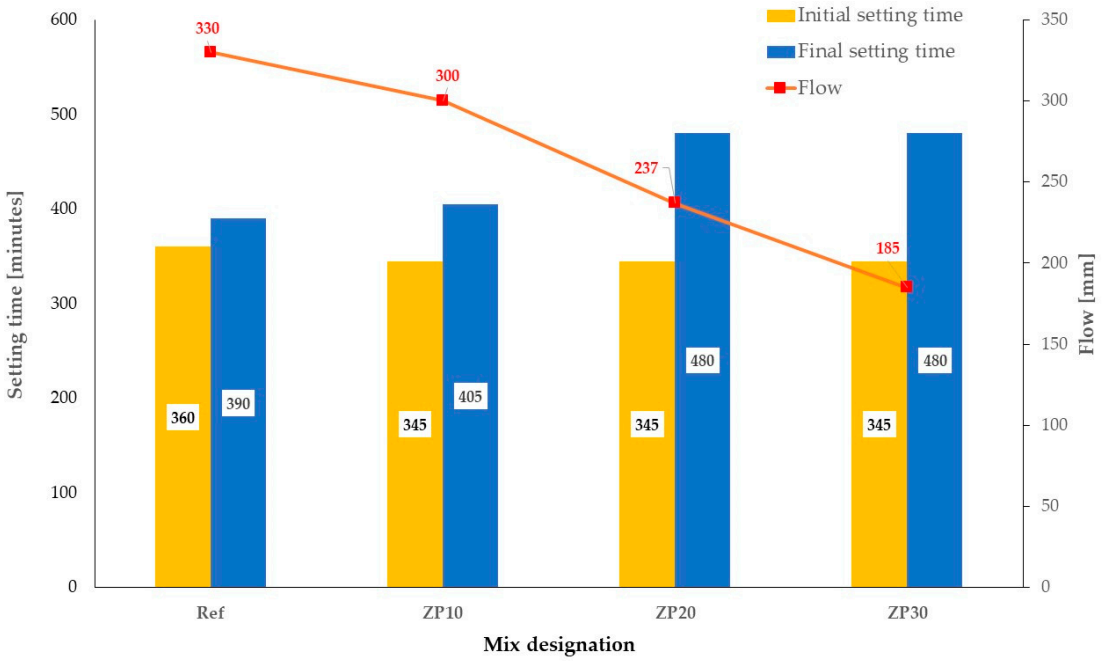

Figure 3. Flowability and setting times for the considered cement pastes.

Figure 4 depicts the SEM images one day after casting. A similar structure can be observed for all cement pastes, with ettringite being the main hydration product. The presence of calcium hydroxide (CH) hexagonal platelets can be observed for the ZP30 mix. Additionally, a more pronounced presence of calcium silicate hydrate (CSH) can be observed in the reference mix compared with other pastes. Calcium silicate hydrates, the main hydration product of OPC and the one responsible for the strength of the cementitious matrix, are heterogenous nanopore materials having an alternate structure of sheets containing calcium, oxygen atoms and silicate tetrahedra. CSH together with un-hydrated cement grains and other hydration products create a complex porous network containing intra-CSH pores, inter-CSH pores and capillary pores [44].

The SEM images of the cement pastes at the age of 7 days are presented in Figure 5. Ettringite formations were still present in all cement pastes, but in a reduced amount. The zeolite particles [49] and the CSH gels due to the pozzolanic reaction of zeolites [50,51] could be clearly seen in the case of the ZP10 mix. Flower-like shapes of hydrated zeolite particles were observed in the ZP20 mix. Previous research works reported similar results for zeolites synthesized using aluminum dross and waste liquid crystal display glass powder [52]. ZP30 showed large amounts of CH formation.

The microstructure of all considered cement pastes at the age of 14 days is shown in Figure 6. The Ref mix showed quite an irregular structure, with "lumps" of CSH being separated by micropores. All micronized zeolite pastes exhibited a more compact structure, although similar microcracks and micropores to the reference mix could also be observed. Calcium hydroxide was still present in the zeolite-containing pastes, e.g., ZP20. This could be due to the pozzolanic reaction of zeolites, as reported in earlier research [53]. A porous honeycomb-like microstructure was observed for the ZP30 mix. This could be attributed to the porous structure of the zeolite combined with the high percentage replacement of OPC [54,55].

More CSH formations could be detected at the age of 21 days for all cement pastes, as shown in Figure 7. The presence of CSH due to the pozzolanic reaction of zeolites [51,54] was detected in the ZP30 mix. Calcium hydroxide crystals were still present in the mixes. The porous structure of zeolites resulted in more micropores in the corresponding mixes, as can be seen from the SEM micrographs presented in Figure 7.

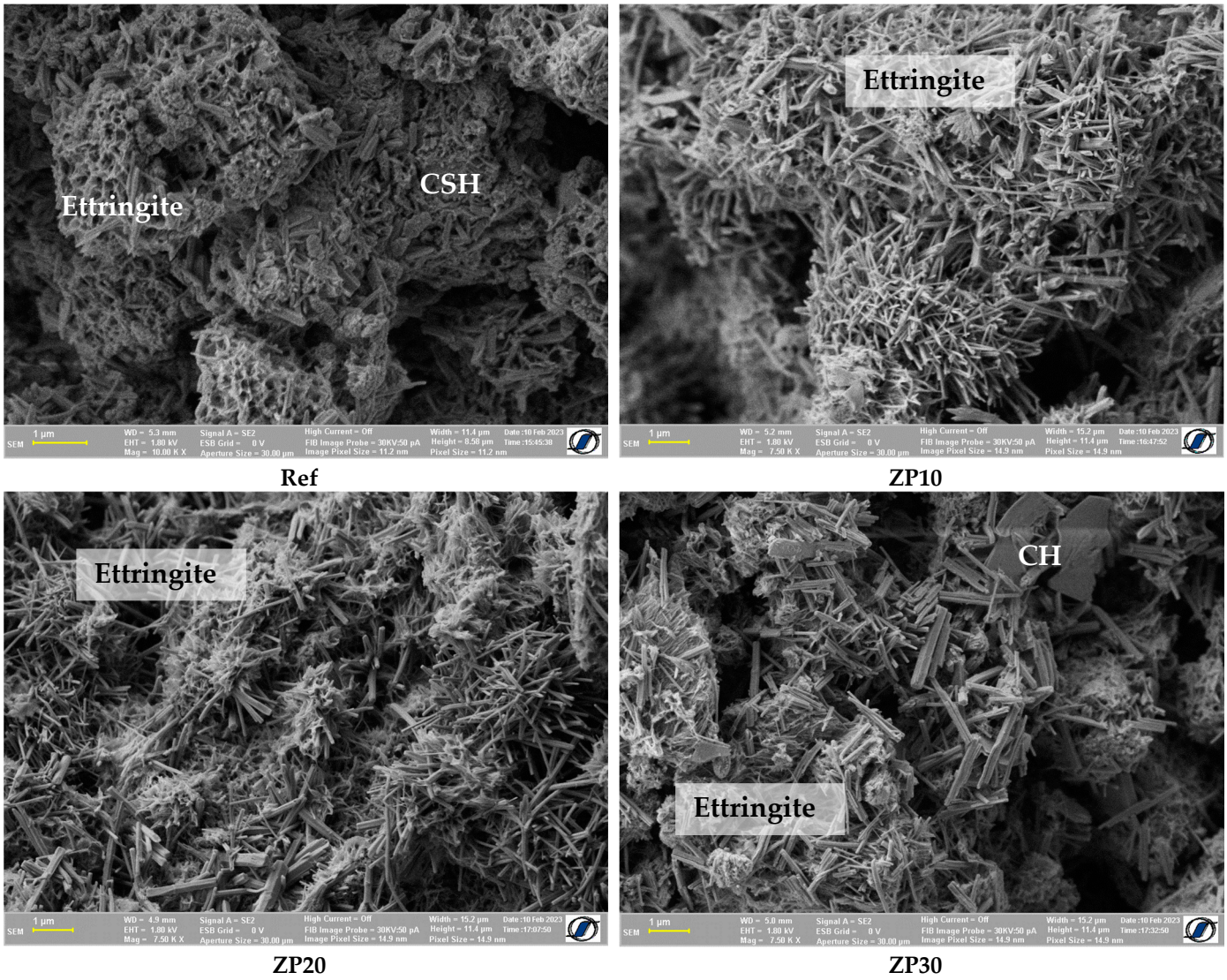

Figure 4. SEM micrographs of cement pastes at the age of 1 day.

Large amounts of CSH could be identified for all cement pastes at the age of 28 days, as shown in Figure 8. It can be observed that all considered mixes exhibited a denser structure compared with earlier ages with the number and size of micropores being smaller. Calcium hydroxide crystals could still be identified in the matrix. However, their dimensions were smaller in the case of ZP20 paste as compared with the reference mix. It can be assumed that the consumption of CH and its transformation into CSH at later ages were due to the presence of micronized zeolite acting as pozzolan [53,56]. In addition, taking into account the porous structure of the zeolite, which results in water absorption during the initial stages of the hydration process and water desorption at later ages, it could be hypothesized that the internal curing property of zeolites and the promotion of hydration reactions at later ages.

3.3. NMR Relaxometry

Figure 9 shows the CPMG echo trains for all cement-based pastes at the ages of 1 day, 7 days, and 28 days. It should be pointed out that these results were obtained while there was still water present in the paste, meaning the hydration of cement was still going on. Consequently, the letter "w" was added to the designation in order to distinguish between different measuring conditions.

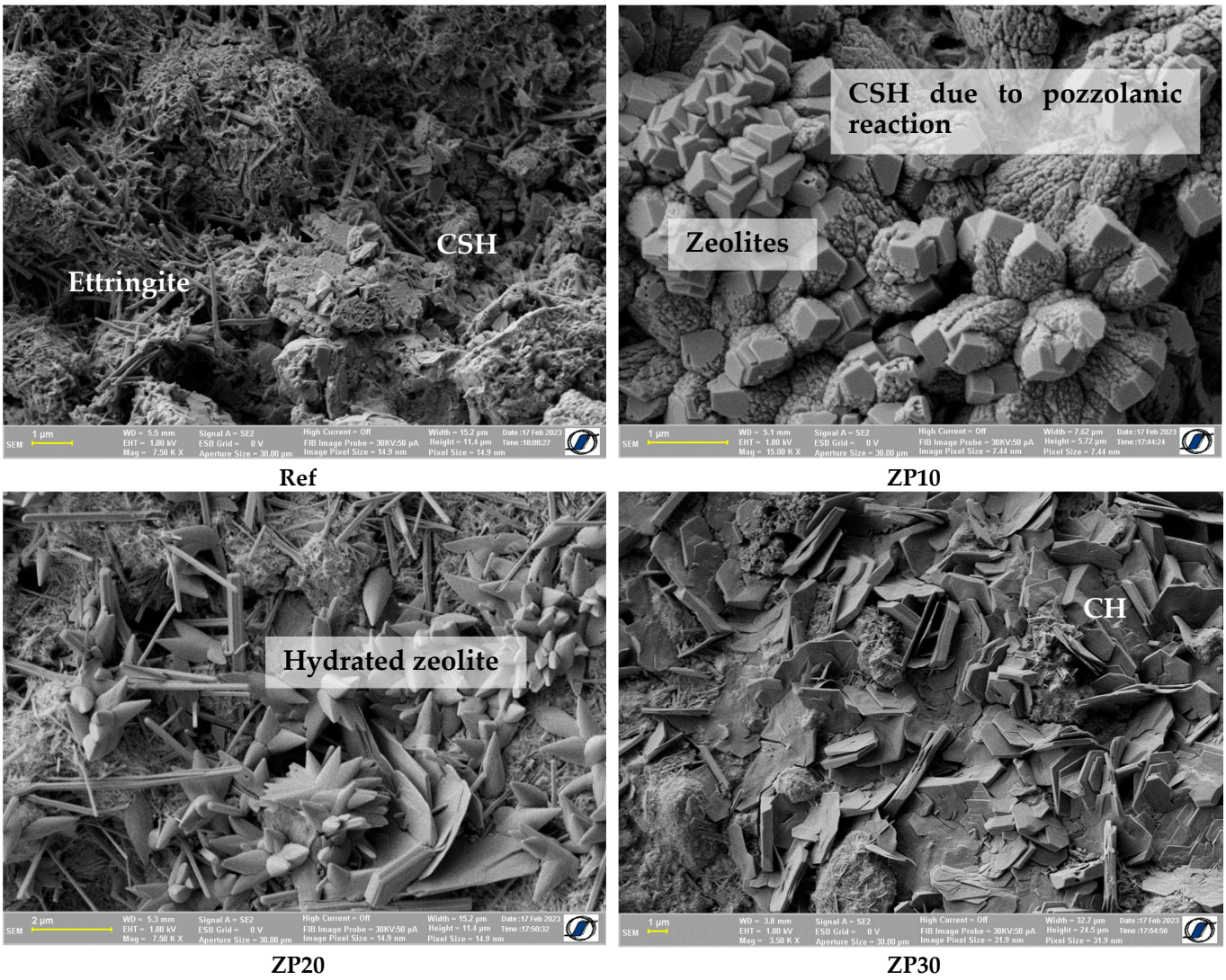

Figure 5. SEM micrographs of cement pastes at the age of 7 days.

It can be observed that for each selected curing age, the initial slope of the echo trains of the pastes containing micronized natural zeolite was steeper than the slope for the reference mix. This could imply that pores with smaller diameters were formed inside pastes with zeolite. While at the age of 1 day, the ZP20 and ZP30 pastes showed almost identical decaying paths, starting from the seventh day, the ZP20 exhibited a steeper slope than all other pastes. The slope of the echo trains could also be a sign of the speed of the hydration processes taking place inside the paste, and the addition of micronized zeolite certainly has an influential role in promoting the formation of hydration products such as ettringite, CH, and CSH, as highlighted in Section 3.2. At the same time, a part of the micronized zeolite may act as a filler during the first day of the hydration process and reduce the volume of the voids between the cement particles. However, this requires more in-depth investigations in order to highlight the hydration process of the cement-zeolite binder during the initial stages.

By applying a numerical Laplace inversion, the transverse relaxation times were obtained. Although the relaxivity was not assessed at this stage of the research, the pore size distribution could be discussed in a more general manner based on Equation (2). The change in the values of the transverse relaxation time for the considered pastes is presented in Figure 10.

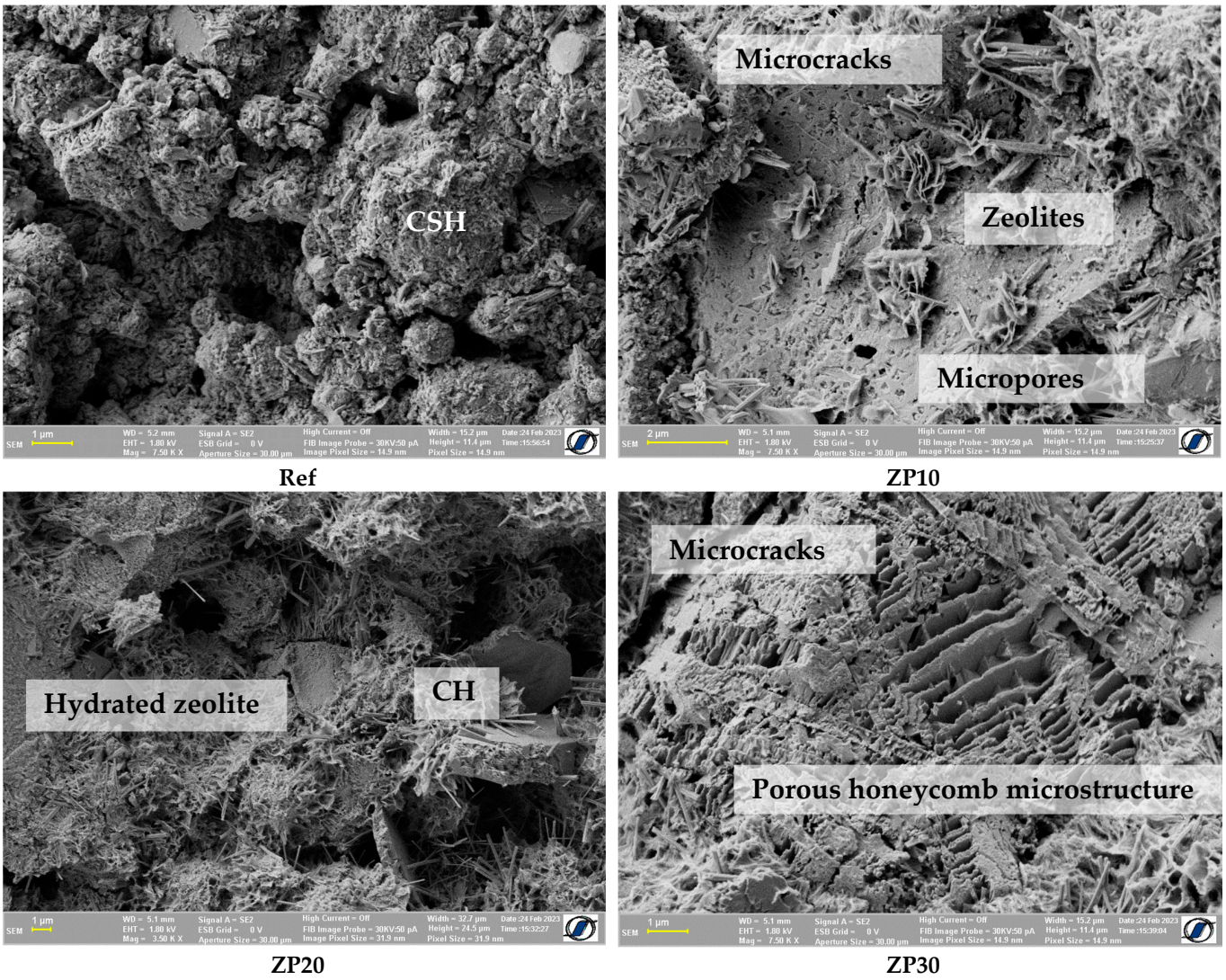

Ref **ZP10**

ZP20 **ZP30**

Figure 6. SEM micrographs of cement pastes at the age of 14 days.

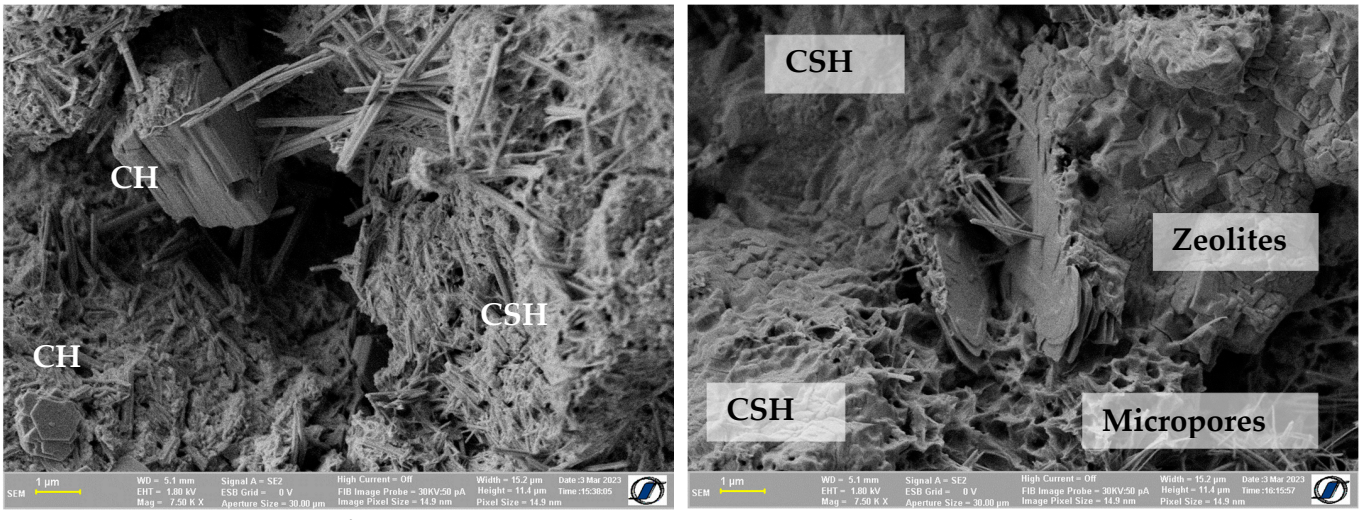

Ref **ZP10**

Figure 7. *Cont.*

ZP20 **ZP30**

Figure 7. SEM micrographs of cement pastes at the age of 21 days.

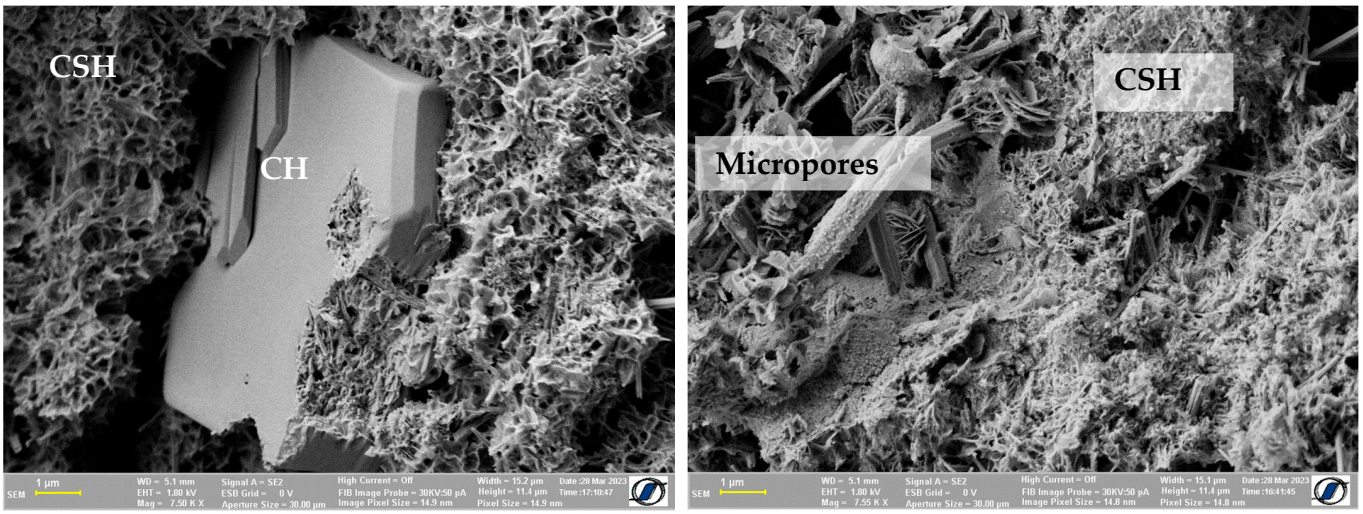

Ref **ZP10**

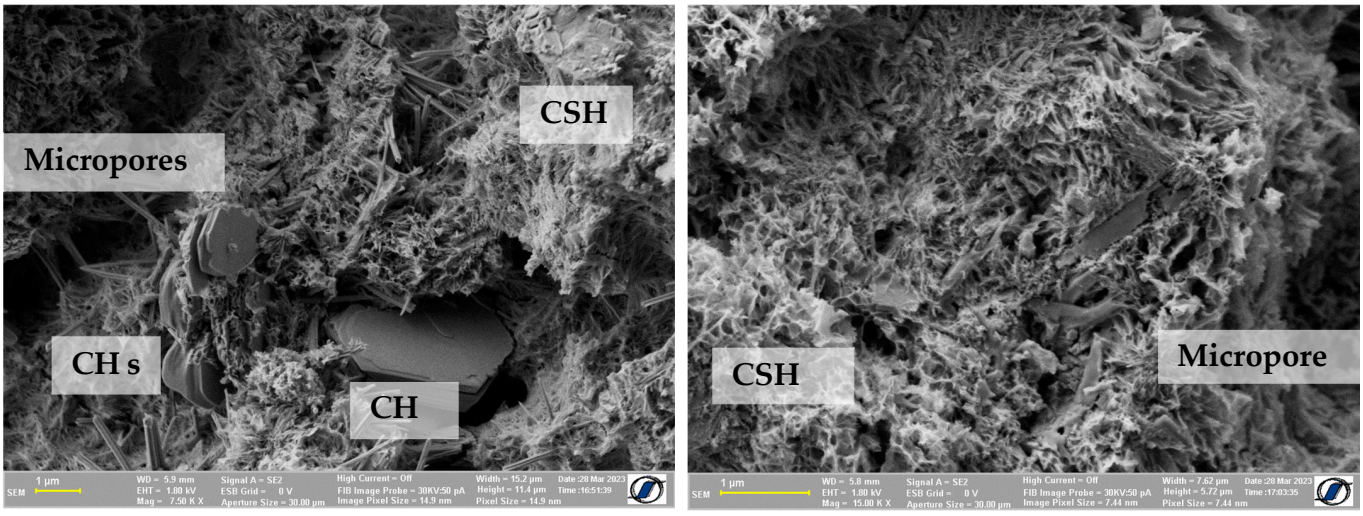

ZP20 **ZP30**

Figure 8. SEM micrographs of cement pastes at the age of 28 days.

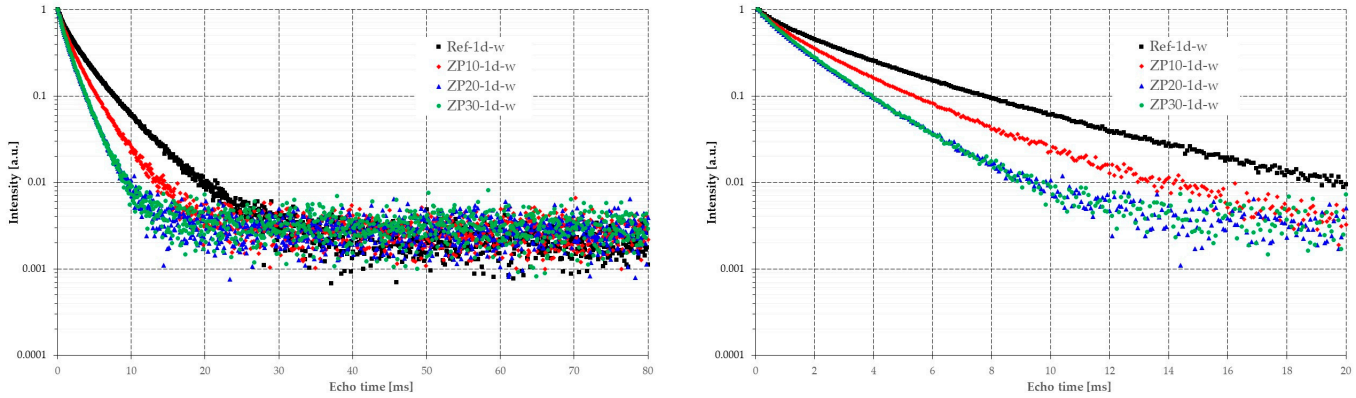

(**a**)

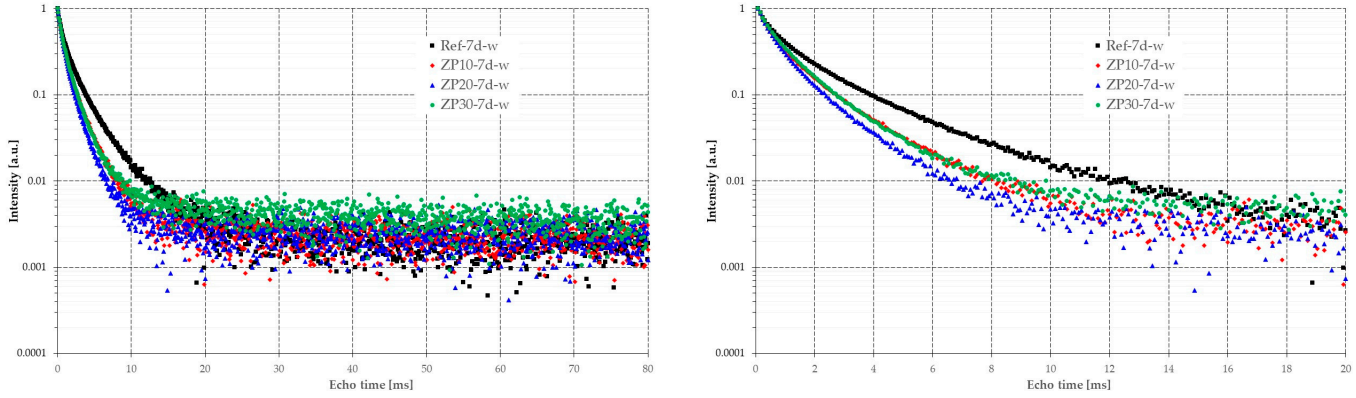

(**b**)

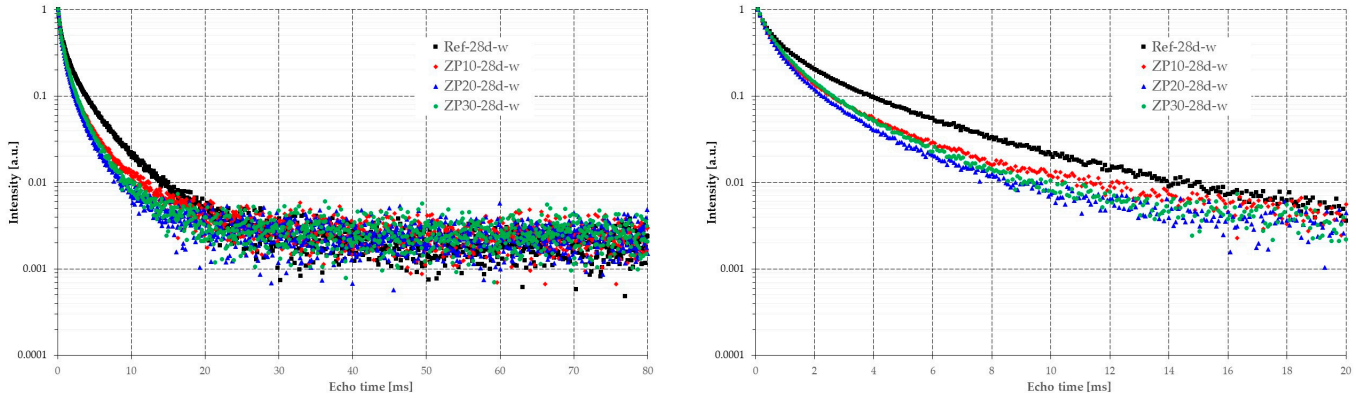

(**c**)

Figure 9. CPMG echo trains at different curing ages: full record (**left**); detail of initial decay slope (**right**). (**a**) 1 day curing; (**b**) 7 days curing; (**c**) 28 days curing.

The relaxation time T_2 corresponding to the larger peaks in Figure 10 could offer qualitative information on the pore size distribution. Lower values of T_2 mean smaller pore sizes, according to Equation (2). The shape of the graph changes from 1 day of curing to 28 days of curing because the pore structure changes due to the hydration reaction of cement particles coupled with the pozzolanic reaction of micronized zeolites. Therefore, larger pores that were initially filled with water gradually change their dimensions because more volume is occupied by the hydration products. The shift in T_2 values towards the left at early ages of 1 day and 7 days means a smaller pore size for pastes containing micronized zeolites. At the age of 28 days, however, the Ref mix showed a smaller pore size structure compared with the mixes with micronized zeolite.

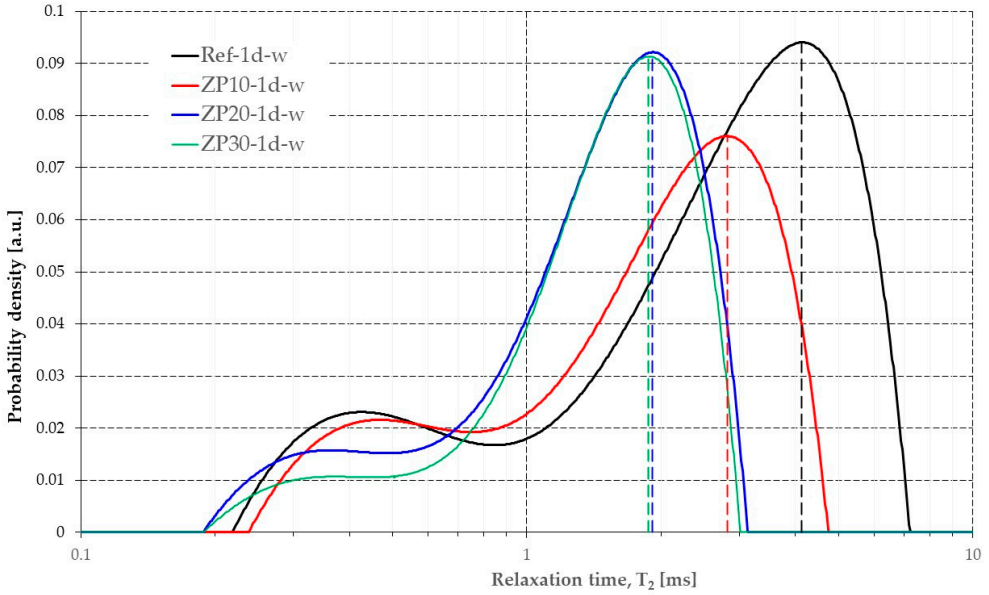

(**a**)

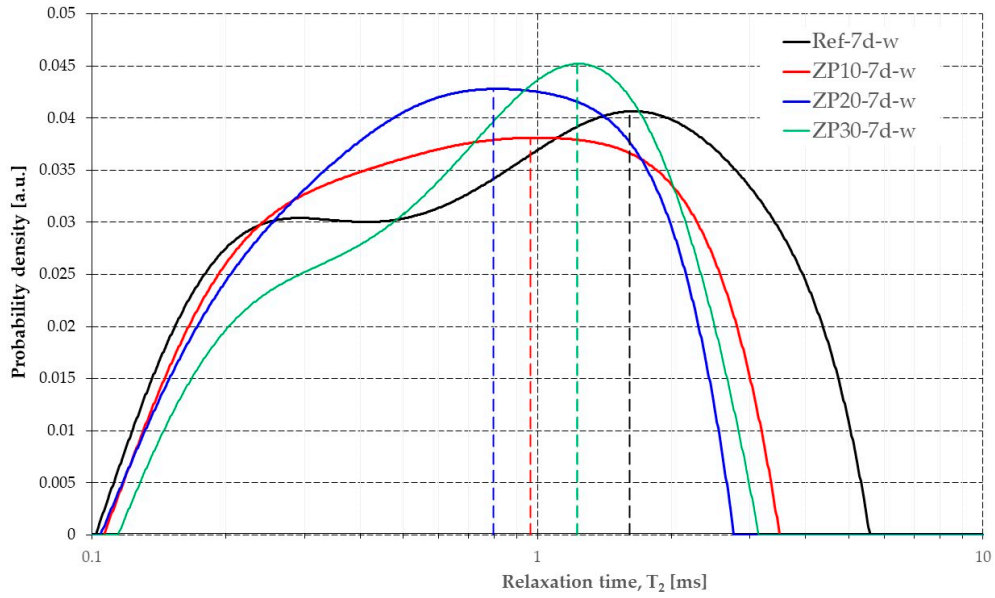

(**b**)

Figure 10. *Cont.*

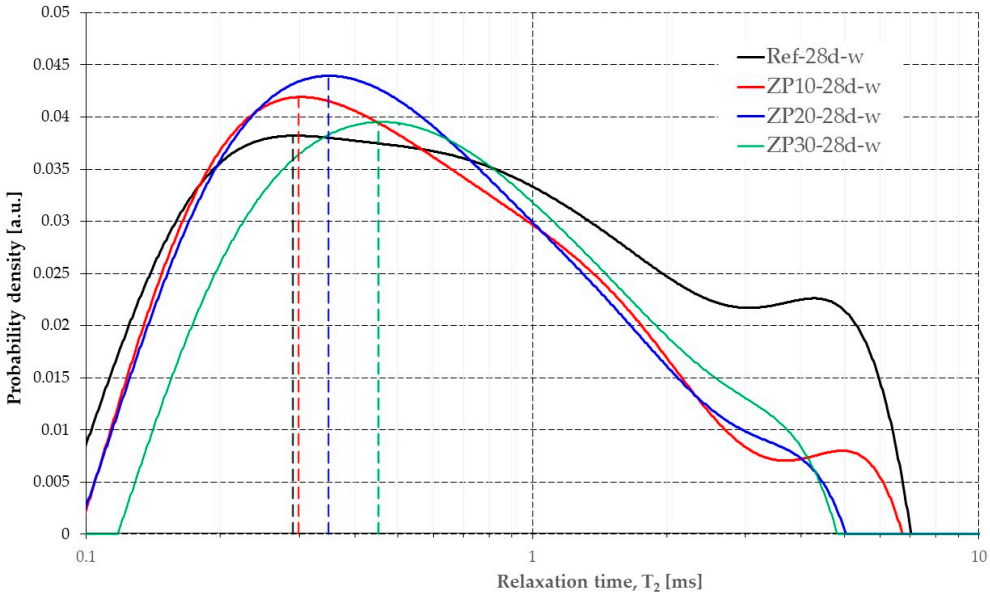

(**c**)

Figure 10. Relaxation time distribution of the considered cement pastes. (**a**) 1 day curing; (**b**) 7 days curing; (**c**) 28 days curing.

4. Discussion

The addition of micronized zeolite resulted in increased friction between the particles in the paste due to small particle size of zeolites and their higher surface area, which resulted in decreased flowability. Similar results were previously reported in the scientific literature, although for smaller water/binder ratios [21,48]. Furthermore, it should be pointed out that zeolites tend to absorb part of the water during the mixing procedure and early stages of cement hydration only to gradually release it at later ages [19].

The high water/binder ratio would result in a higher degree of hydration of the paste, up to 82% [57], which would result in larger amounts of hydration products. The presence of large amounts of CH and CSH at the ages of 21 and 28 days was highlighted by means of SEM investigations, as shown in Figures 7 and 8.

The results obtained from NMR relaxometry are an indication of the pore structure of the cement pastes, Figure 10. At the age of 1 day, most of the water is located in the inter-CSH pores, represented by the higher peak in Figure 10a. The lower peak, at lower values of T_2, corresponds to the intra-CSH pores, which are of smaller dimensions. The obtained results are in line with previously published research [33,35]. The increase in the OPC replacement percentage by micronized clinoptilolite-based zeolite resulted in smaller pore dimensions in the cement paste, as indicated by the shift towards the left in the values of relaxation time. This is supported by the micro-structure of the cement pastes presented in Figure 4. Although more ettringite was present in the case of ZP pastes, the structure was denser compared with Ref mix.

At the age of 7 days, Figure 10b, there was no clear difference between the peaks associated to capillary pores and the intra-CSH pores represented by the relaxation time of water molecules, especially for ZP10 and ZP20 mixes. Only Ref and ZP30 mixes exhibited a slight tendency to differentiate between the two types of pores. While in case of Ref the hydration process is still ongoing, in the case of ZP30 mix it may be still in its initial stage due to the pozzolanic reactivity of zeolites [50]. The pastes containing zeolites in different replacement percentages of OPC exhibited smaller pore sizes which was highlighted by smaller values of relaxation time (Figure 10b).

At the age of 28 days (Figure 10c) most of the water in the capillary pores was consumed by the chemical reactions in the cement matrix. Due to the rapid hardening properties of the CEM II cement, the Ref mix exhibited a denser structure compared with the

ZP mixes. This resulted in lower values for the relaxation time compared with the zeolite-containing mixes. However, taking into account the fact that a composite cement was used (Section 2.1) the presence of CH crystals could be observed (Figure 8) [58].

As previously mentioned, additional NMR investigations were conducted at the age of 28 days, with the samples being fully saturated with cyclohexane. The cement paste samples were placed in a vacuum for 24 h to remove the water from the inter-CSH pores and capillary pores. The water from the intra-CSH pores could not be removed without damaging the sample. The CPMG echo-trains were obtained by applying the same measuring parameters as described in Section 2.2. The obtained results are presented in Figure 11.

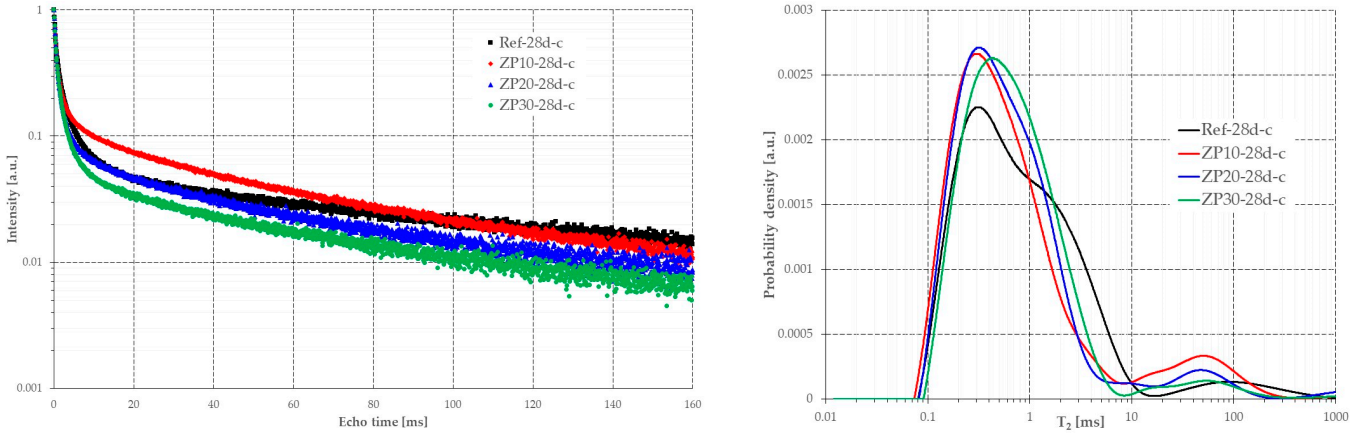

Figure 11. CPMG echo trains (**left**) and relaxation time distribution (**right**) of the considered cement pastes fully saturated with cyclohexane.

The obtained results are in line with the ones presented in Figures 9 and 10 when the samples were still fully or partially saturated with water.

The evolution of the relaxation time, T_2, for all cement pastes at all considered ages is summarized in Figure 12. It can be observed that at early ages, 1 day and 7 days, the Ref mix exhibited larger values of the relaxation time, meaning larger pores were present in the matrix compared with ZP mixes. This fact changed at the age of 28 days when ZP mixes exhibited slightly larger values of T_2 compared with the Ref mix. Taking into account the small differences of 3.4% and 3.5; for the ZP10 and ZP20 mixes, respectively, it can be considered that the pore size distribution was almost similar between the mixes.

On the other hand, a 43.7% increase was recorded for the ZP30 mix compared with Ref mix. This could be attributed to the larger replacement percentage, 30%, of OPC by micronized zeolite. Taking into account the pozzolanic property of natural zeolite coupled with the use of blended cement, some of the chemical reactions in the cement paste would be slowed down [59], resulting in a more porous structure. Previous research showed that increasing the replacement percentage of blended OPC by natural zeolite resulted in smaller values of density, flexural strength, and compressive strength in mortars at an early age [60].

The results in terms of relaxation time obtained using cyclohexane were similar to those obtained on samples saturated with water. The same tendency in pore structure was observed in the case of cyclohexane-saturated samples.

The decreasing trend of relaxation time values for the considered mixes is presented in Figure 13. While Ref, ZP10 and ZP20 mixes showed quadratic variation (2nd degree polynomial) of the relaxation time values with curing age, the ZP30 mix exhibited linear dependency. This could be attributed to slower chemical reactions in the paste due to the high percentage of OPC replacement by zeolite and taking into account the type of cement used in this research.

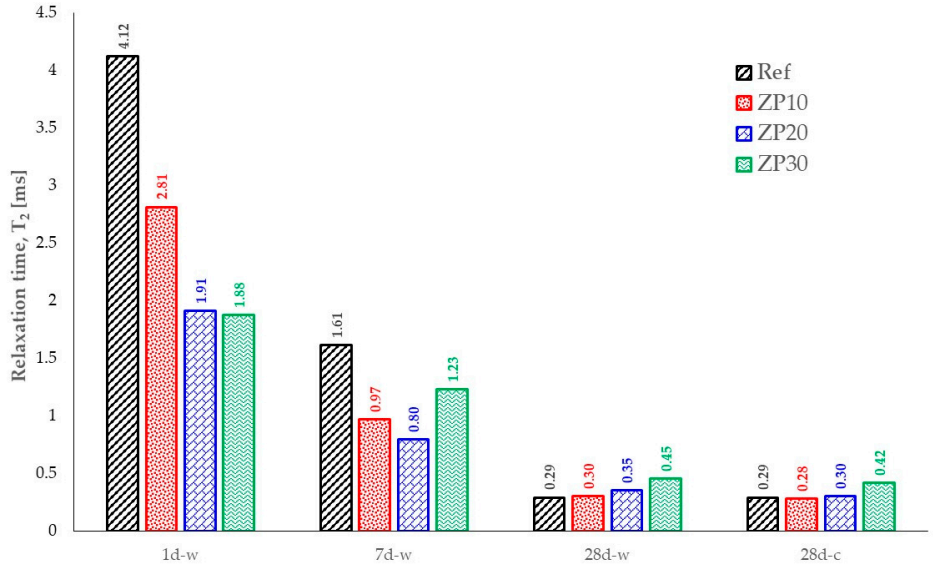

Figure 12. Time dependency of relaxation time for the considered mixes.

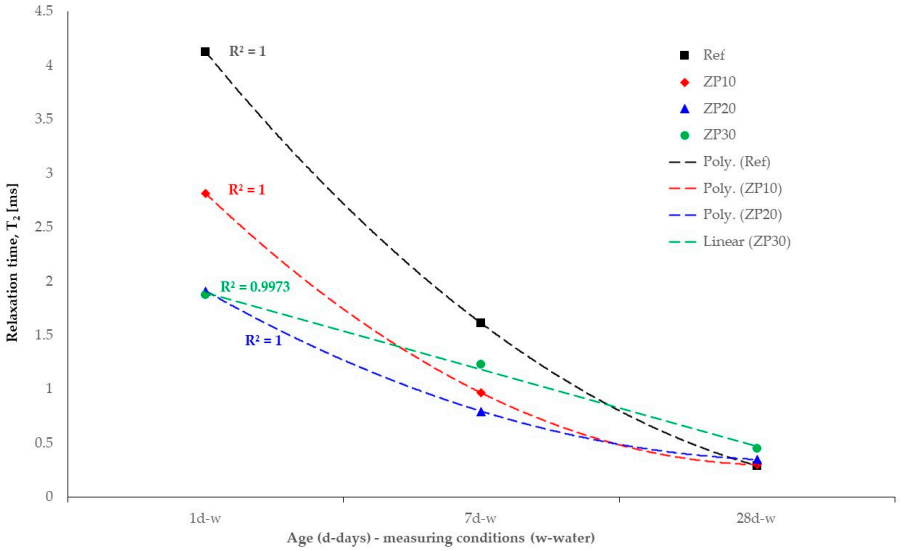

Figure 13. Trend of relaxation time values.

The speed of hydration product formation in the cement pastes could be indicated by the slopes of the decaying curves. Ref mix shows the steepest decay compared with ZP10 and ZP20 mixes [55]. The hydration reaction took place at a higher speed, and the pore sizes decreased faster. This is in line with the SEM micrographs presented in Figures 4–8. There were no notable differences in the microstructure of Ref mix from day 7 to day 28 of curing.

As seen from Figure 13, increasing the zeolite percentage results in a slower decrease in the pore size of the matrix, as shown in Equation (2). Moreover, the increase in the zeolite percentage results in smaller pore diameters at early ages, 1 day and 7 days, compared with the reference mix. At the age of 28 days, however, the ZP30 mix exhibited larger pores, as indicated by the results presented in Figure 11.

5. Conclusions

The paper presents the results obtained during an experimental program aimed at assessing the pore structure in cement pastes with micronized natural zeolites used as cement replacement. The considered percentage replacements were 10%, 20%, and

30% by mass of cement. The pore structure was qualitatively assessed by means of NMR relaxometry, and the obtained results were compared and validated using scanning electron microscopy. Based on the obtained results, the following conclusions can be drawn:

1. The gradual generation of CSH gels with curing age is rendered evident by means of SEM analyses. Moreover, CSH formations due to the pozzolanic reaction of micronized zeolite are also identified. The microstructure of cement pastes becomes more compact and denser with curing age. At the same time, fewer micropores can be identified. A replacement of OPC by natural zeolites in the range of 10–20% by mass of cement is also reported in the scientific literature as leading to the highest improvements in terms of durability properties and long-term strength values of cement-based materials. The microstructure analyses confirm the fact that smaller pores are obtained in cement pastes with a 10% and 20% replacement of OPC by natural zeolite. Increasing the replacement percentage to 30% results in larger pores due to a higher amount of water being absorbed and stored in the porous structure of zeolites.
2. The NMR relaxometry technique is used to qualitatively assess the pore structure of the cement pastes. At an early age, e.g., 1 day, there is a clear distinction between the inter- and intra-CSH pores. The presence of water molecules in the former pores results in larger relaxation time values, whereas the latter yield lower values of the relaxation time. The replacement of OPC by micronized natural zeolites results in a shift towards lower values of relaxation time, which means smaller pores in the cementitious matrix. While at early ages the ZP20 and ZP30 pastes have similar pore structures, as a result of the very close values of relaxation time corresponding to the mixes, at the ages of 7 days and 28 days the values of T_2 corresponding to the ZP20 mix are closer to the ones corresponding to the ZP10 mix. This could indicate that there might be a threshold of cement replacement by micronized zeolite above which the effect might be detrimental in terms of pore structure.
3. At the age of 28 days, the pore structures of the Ref, ZP10, and ZP20 mixes are similar. The T_2 values of the ZP10 and ZP20 mixes are slightly larger than the one of Ref mix by 3.4% and 3.5%, respectively. The ZP30, however, registers a 43.7% increase in the value of relaxation time, indicating the presence of larger-diameter pores. Similar results are obtained when saturating the samples with cyclohexane. The pozzolanic nature of zeolite, coupled with the use of blended cement, leads to slower development of hydration products, e.g., CSH, as demonstrated in the scientific literature. Higher percentages of zeolite result in lower amounts of available CH, leading to decreased formation of CSH gels due to secondary pozzolanic reactions. As a result, the decreased availability of CH results in a lower amount of water needed for chemical reactions, and, therefore, the water absorbed by zeolite during the early stages of hydration remains trapped in the pores. This can have detrimental effects on the durability and strength development of cement-based construction materials in the long run.
4. Although the pore structure of cement pastes containing zeolites as a replacement for OPC in different percentages can be assessed by means of NMR relaxometry, a more in-depth analysis is required to determine the relaxivity constant. The results obtained by NMR should be confirmed by other assessment techniques such as computer tomography (CT).

Author Contributions: Conceptualization, I.-O.T. and I.A.; methodology, S.-M.A.-S., G.S. and N.C.; validation, I.-O.T., I.A. and N.C.; formal analysis, S.-M.A.-S., M.-M.R. and I.A.; investigation, I.-O.T., G.S., M.-M.R., I.A., N.C. and S.-M.A.-S.; resources, I.-O.T., G.S. and I.A.; writing—original draft preparation, I.-O.T., S.-M.A.-S. and G.S.; writing—review and editing, N.C., M.-M.R. and I.A.; supervision, I.-O.T. and I.A.; project administration, I.-O.T.; funding acquisition, I.-O.T. All authors have read and agreed to the published version of the manuscript.

Funding: This research was funded by PN-III-P2-2.1-PED-2021-0677 research grant "Sustainable Concrete for Energy Efficient Buildings" funded by Executive Agency for Higher Education, Research, Development and Innovation Funding—UEFISCDI. The APC was funded by PN-III-P2-2.1-PED-2021-0677 research grant.

Institutional Review Board Statement: Not applicable.

Informed Consent Statement: Not applicable.

Data Availability Statement: Not applicable.

Acknowledgments: The research presented in this paper was conducted as part of the PN-III-P2-2.1-PED-2021-0677 research grant "Sustainable Concrete for Energy Efficient Buildings" funded by Executive Agency for Higher Education, Research, Development and Innovation Funding—UEFISCDI.

Conflicts of Interest: The authors declare no conflict of interest.

References

1. Miller, S.A.; Habert, G.; Myers, R.J.; Harvey, J.T. Achieving net zero greenhouse gas emissions in the cement industry via value chain mitigation strategies. *One Earth* **2021**, *4*, 1398–1411. [CrossRef]
2. The European Cement Association (CEMBUREAU). *Cementing the European Green Deal*; CEMBUREAU: Bruxelles, Belgium, 2023.
3. International Energy Agency (IEA). Cement. 2022. Available online: https://www.iea.org/reports/cement (accessed on 27 April 2023).
4. Salamanova, M.; Murtazaev, S.-A.; Saidumov, M.; Alaskhanov, A.; Murtazaeva, T.; Fediuk, R. Recycling of Cement Industry Waste for Alkali-Activated Materials Production. *Materials* **2022**, *15*, 6660. [CrossRef] [PubMed]
5. Torréns-Martín, D.; Fernández-Carrasco, L.J.; Blanco-Varela, M.T. Up to 100% Replacement of Natural Materials from Residues: Recycling Blast Furnace Slag and Fly Ash as Self-Leveling Cementitious Building Materials. *Materials* **2023**, *16*, 3350. [CrossRef]
6. da Silva, S.R.; de Oliveira Andrade, J.J. Investigation of mechanical properties and carbonation of concretes with construction and demolition waste and fly ash. *Constr. Build. Mater.* **2017**, *153*, 704–715. [CrossRef]
7. Park, B.; Choi, Y.C. Effects of fineness and chemical activators on the hydration and physical properties of high-volume fly-ash cement pastes. *J. Build. Eng.* **2022**, *51*, 104274. [CrossRef]
8. Fu, J.X.; Wang, K.; Wang, J. Internal pore evolution and early hydration characterization of fly ash cement backfill. *J. Build. Eng.* **2023**, *72*, 106716. [CrossRef]
9. Luan, C.; Yuan, L.; Wang, J.; Zhou, Z. Uncovering the Mechanism of the Role of Fly Ash in the Self-Healing Ability of Mortar with Different Curing Ages. *Materials* **2023**, *16*, 3453. [CrossRef]
10. Nicula, L.M.; Manea, D.L.; Simedru, D.; Cadar, O.; Becze, A.; Dragomir, M.L. The Influence of Blast Furnace Slag on Cement Concrete Road by Microstructure Characterization and Assessment of Physical-Mechanical Resistances at 150/480 Days. *Materials* **2023**, *16*, 3332. [CrossRef]
11. Liu, Z.; Takasu, K.; Suyama, H.; Koyamada, H.; Liu, S.; Hao, Q. The Effect of Cementitious Materials on the Engineering Properties and Pore Structure of Concrete with Recycled Fine Aggregate. *Materials* **2022**, *16*, 305. [CrossRef]
12. Ghostine, R.; Bur, N.; Feugeas, F.; Hoteit, I. Curing Effect on Durability of Cement Mortar with GGBS: Experimental and Numerical Study. *Materials* **2022**, *15*, 4394. [CrossRef] [PubMed]
13. Toma, I.-O.; Covatariu, D.; Toma, A.-M.; Taranu, G.; Budescu, M. Strength and elastic properties of mortars with various percentages of environmentally sustainable mineral binder. *Constr. Build. Mater.* **2013**, *43*, 348–361. [CrossRef]
14. Li, P.; Zhang, X.; Zhong, M.; Fan, Z.; Xiong, J.; Zhang, Z. Phosphogypsum-Based Ultra-Low Basicity Cementing Material. *Materials* **2022**, *15*, 6601. [CrossRef] [PubMed]
15. Yang, Q.; Xiang, Z.; Liu, T.; Deng, C.; Zhang, H. Study on the Mechanical Properties of Cast-In-Situ Phosphogypsum as Building Material for Structural Walls. *Materials* **2023**, *16*, 1481. [CrossRef]
16. Barbieri, L.; Altimari, F.; Andreola, F.; Maggi, B.; Lancellotti, I. Characterization of Volcano-Sedimentary Rocks and Related Scraps for Design of Sustainable Materials. *Materials* **2023**, *16*, 3408. [CrossRef]
17. Aissa, Y.H.; Goual, I.; Benabed, B. Mix-design and properties of self-compacting concrete made with calcareous tuff. *J. Build. Eng.* **2020**, *27*, 100997. [CrossRef]
18. Ma, B.; Fernandez-Martinez, A.; Mancini, A.; Lothenbach, B. Spectroscopic investigations on structural incorporation pathways of FeIII into zeolite frameworks in cement-relevant environments. *Cem. Concr. Res.* **2021**, *140*, 106304. [CrossRef]
19. Kazemian, M.; Shafei, B. Internal curing capabilities of natural zeolite to improve the hydration of ultra-high performance concrete. *Constr. Build. Mater.* **2022**, *340*, 127452. [CrossRef]
20. Stocker, K.; Ellersdorfer, M.; Lehner, M.; Raith, J.G. Characterization and Utilization of Natural Zeolites in Technical Applications. *BHM Berg- Und Hüttenmännische Mon.* **2017**, *162*, 142–147. [CrossRef]
21. Wang, Q.; Xiong, Z.; He, J.; Lai, M.; Ho, J. Effective solution for improving rheological properties of cement paste containing zeolite. *Constr. Build. Mater.* **2022**, *351*, 128780. [CrossRef]

22. Kriptavičius, D.; Girskas, G.; Skripkiūnas, G. Use of Natural Zeolite and Glass Powder Mixture as Partial Replacement of Portland Cement: The Effect on Hydration, Properties and Porosity. *Materials* **2022**, *15*, 4219. [CrossRef] [PubMed]
23. Gong, J.; Mao, Z.; Cao, Z.; Huang, X.; Deng, M. Effect of Different Fineness of Cement on the Autogenous Shrinkage of Mass Concrete under Variable Temperature Conditions. *Materials* **2023**, *16*, 2367. [CrossRef] [PubMed]
24. Ding, Z.; Chen, J.; Zheng, S.; Hu, Y.; Fang, Y. Influence of Anhydrite on the Properties and Microstructure of Aluminophosphate Cement. *Materials* **2022**, *15*, 7005. [CrossRef] [PubMed]
25. Morales-Cantero, A.; Cuesta, A.; De la Torre, A.G.; Mazanec, O.; Borralleras, P.; Weldert, K.S.; Gastaldi, D.; Canonico, F.; Aranda, M.A.G. Portland and Belite Cement Hydration Acceleration by C-S-H Seeds with Variable w/c Ratios. *Materials* **2022**, *15*, 3553. [CrossRef]
26. Li, Y.; Luo, Y.; Du, H.; Liu, W.; Tang, L.; Xing, F. Evolution of Microstructural Characteristics of Carbonated Cement Pastes Subjected to High Temperatures Evaluated by MIP and SEM. *Materials* **2022**, *15*, 6037. [CrossRef]
27. Pinheiro, D.G.L.; Sousa, M.I.C.; Pelisser, F.; da Silva Rêgo, J.H.; Moragues Terrades, A.; Frías Rojas, M. Physical and Chemical Effects in Blended Cement Pastes Elaborated with Calcined Clay and Nanosilica. *Materials* **2023**, *16*, 1837. [CrossRef]
28. Beaudoin, J.J. Porosity measurement of some hydrated cementitious systems by high pressure mercury intrusion-microstructural limitations. *Cem. Concr. Res.* **1979**, *9*, 771–781. [CrossRef]
29. Hidalgo, A.; Petit, S.; García Calvo, J.L.; Alonso, C.; Andrade, C. Microstructure of the system calcium aluminate cement-silica fume: Application in waste immobilization. *Stud. Surf. Sci. Catal.* **2007**, *170*, 1617–1628. [CrossRef]
30. Hasanuzzaman, M.; Harunur Rashid, A.R.M.; Olabi, A.-G. Characterization of Porous Glass and Ceramics by Mercury Intrusion Porosimetry. In *Reference Module in Materials Science and Materials Engineering*; Elsevier: Amsterdam, The Netherlands, 2017.
31. Yao, Y.; Liu, D. Comparison of low-field NMR and mercury intrusion porosimetry in characterizing pore size distributions of coals. *Fuel* **2012**, *95*, 152–158. [CrossRef]
32. Ardelean, I. The Effect of an Accelerator on Cement Paste Capillary Pores: NMR Relaxometry Investigations. *Molecules* **2021**, *26*, 5328. [CrossRef] [PubMed]
33. Pop, A.; Ardelean, I. Monitoring the size evolution of capillary pores in cement paste during the early hydration via diffusion in internal gradients. *Cem. Concr. Res.* **2015**, *77*, 76–81. [CrossRef]
34. Xu, J.; Zhan, P.; Zhou, W.; Zuo, J.; Shah, S.P.; He, Z. Design and assessment of eco-friendly ultra-high performance concrete with steel slag powder and recycled glass powder. *Powder Technol.* **2023**, *419*, 118356. [CrossRef]
35. Rusu, M.M.; Vulpoi, A.; Vilau, C.; Dudescu, C.M.; Păşcuţă, P.; Ardelean, I. Analyzing the Effects of Calcium Nitrate over White Portland Cement: A Multi-Scale Approach. *Materials* **2022**, *16*, 371. [CrossRef]
36. Rusu, M.M.; Vilau, C.; Dudescu, C.; Pascuta, P.; Popa, F.; Ardelean, I. Characterization of the Influence of an Accelerator upon the Porosity and Strength of Cement Paste by Nuclear Magnetic Resonance (NMR) Relaxometry. *Anal. Lett.* **2023**, *56*, 303–311. [CrossRef]
37. *SR EN 197-1*; Cement. Part I: Composition, Specifications and Conformity Criteria for Normal Use Cements. ASRO (Romanian Standards Association): Bucharest, Romania, 2011.
38. Favier, A.; De Wolf, C.; Scrivener, K.; Habert, G. *A Sustainable Future for the European Cement and Concrete Industry*; ETH: Zurich, Switzerland, 2018.
39. *ASTM C 618*; Standard Specification for Coal Fly Ash and Raw or Calcined Natural Pozzolan for Use in Concrete. ASTM International: West Conshohocken, PA, USA, 2022.
40. Sáez, P.; Rodríguez, A.; Gómez, J.M.; Paramio, C.; Fraile, C.; Díez, E. H-Clinoptilolite as an Efficient and Low-Cost Adsorbent for Batch and Continuous Gallium Removal from Aqueous Solutions. *J. Sustain. Metall.* **2021**, *7*, 1699–1716. [CrossRef]
41. Carr, H.Y.; Purcell, E.M. Effects of Diffusion on Free Precession in Nuclear Magnetic Resonance Experiments. *Phys. Rev.* **1954**, *94*, 630–638. [CrossRef]
42. Meiboom, S.; Gill, D. Modified Spin-Echo Method for Measuring Nuclear Relaxation Times. *Rev. Sci. Instrum.* **1958**, *29*, 688–691. [CrossRef]
43. Provencher, S.W. CONTIN: A general purpose constrained regularization program for inverting noisy linear algebraic and integral equations. *Comput. Phys. Commun.* **1982**, *27*, 229–242. [CrossRef]
44. Bede, A.; Scurtu, A.; Ardelean, I. NMR relaxation of molecules confined inside the cement paste pores under partially saturated conditions. *Cem. Concr. Res.* **2016**, *89*, 56–62. [CrossRef]
45. Cadar, C.; Cotet, C.; Baia, L.; Barbu-Tudoran, L.; Ardelean, I. Probing into the mesoporous structure of carbon xerogels via the low-field NMR relaxometry of water and cyclohexane molecules. *Microporous Mesoporous Mater.* **2017**, *251*, 19–25. [CrossRef]
46. Dilbas, H. Effect of Cement Type and Water-to-Cement Ratio on Fresh Properties of Superabsorbent Polymer-Modified Cement Paste. *Materials* **2023**, *16*, 2614. [CrossRef] [PubMed]
47. *SR EN 196-3:2017*; Methods of Testing Cement. Determination of Setting Times and Soundness. ASRO (Romanian Standards Association): Bucharest, Romania, 2017.
48. Chen, J.J.; Li, L.G.; Ng, P.L.; Kwan, A.K.H. Effects of superfine zeolite on strength, flowability and cohesiveness of cementitious paste. *Cem. Concr. Compos.* **2017**, *83*, 101–110. [CrossRef]
49. Kocak, Y.; Tascı, E.; Kaya, U. The effect of using natural zeolite on the properties and hydration characteristics of blended cements. *Constr. Build. Mater.* **2013**, *47*, 720–727. [CrossRef]

50. Liguori, B.; Aprea, P.; Gennaro, B.d.; Iucolano, F.; Colella, A.; Caputo, D. Pozzolanic Activity of Zeolites: The Role of Si/Al Ratio. *Materials* **2019**, *12*, 4231. [CrossRef]
51. Ramezanianpour, A.A.; Mousavi, R.; Kalhori, M.; Sobhani, J.; Najimi, M. Micro and macro level properties of natural zeolite contained concretes. *Constr. Build. Mater.* **2015**, *101*, 347–358. [CrossRef]
52. Kang, Y.; Swain, B.; Im, B.; Yoon, J.-H.; Park, K.H.; Lee, C.G.; Kim, D.G. Synthesis of Zeolite Using Aluminum Dross and Waste LCD Glass Powder: A Waste to Waste Integration Valorization Process. *Metals* **2019**, *9*, 1240. [CrossRef]
53. Cornejo, M.H.; Elsen, J.; Baykara, H.; Paredes, C. Hydration process of zeolite-rich tuffs and siltstone-blended cement pastes at low W/B ratio, under wet curing condition. *Eur. J. Environ. Civ. Eng.* **2014**, *18*, 629–651. [CrossRef]
54. Caputo, D.; Liguori, B.; Colella, C. Some advances in understanding the pozzolanic activity of zeolites: The effect of zeolite structure. *Cem. Concr. Compos.* **2008**, *30*, 455–462. [CrossRef]
55. Rudžionis, Ž.; Adhikary, S.K.; Manhanga, F.C.; Ashish, D.K.; Ivanauskas, R.; Stelmokaitis, G.; Navickas, A.A. Natural zeolite powder in cementitious composites and its application as heavy metal absorbents. *J. Build. Eng.* **2021**, *43*, 103085. [CrossRef]
56. Florez, C.; Restrepo-Baena, O.; Tobon, J.I. Effects of calcination and milling pre-treatments on natural zeolites as a supplementary cementitious material. *Constr. Build. Mater.* **2021**, *310*, 125220. [CrossRef]
57. Chen, X.; Wu, S. Influence of water-to-cement ratio and curing period on pore structure of cement mortar. *Constr. Build. Mater.* **2013**, *38*, 804–812. [CrossRef]
58. He, Z.; Cai, R.; Chen, E.; Tang, S. The investigation of early hydration and pore structure for limestone powder wastes blended cement pastes. *Constr. Build. Mater.* **2019**, *229*, 116923. [CrossRef]
59. Shahbazpanahi, S.; Tajara, M.K.; Faraj, R.H.; Mosavi, A. Studying the C–H Crystals and Mechanical Properties of Sustainable Concrete Containing Recycled Coarse Aggregate with Used Nano-Silica. *Crystals* **2021**, *11*, 122. [CrossRef]
60. Toma, I.-O.; Alexa-Stratulat, S.-M.; Mihai, P.; Toma, A.-M.; Venghiac, V.-M. Influence of elevated temperature on the early age properties of cement mortar with zeolite powder. In Proceedings of the 22nd International Multidisciplinary Scientific GeoConference SGEM 2022, Vienna, Austria, 6–8 December 2022; pp. 429–436.

coatings

MDPI

Review

Use of Clay and Titanium Dioxide Nanoparticles in Mortar and Concrete—A State-of-the-Art Analysis

Georgiana Bunea [1,*], Sergiu-Mihai Alexa-Stratulat [1], Petru Mihai [2] and Ionuț-Ovidiu Toma [1,*]

[1] Department of Structural Mechanics, Faculty of Civil Engineering and Building Services, "Gheorghe Asachi" Technical University of Iasi, 700050 Iasi, Romania
[2] Department of Concrete Structures, Building Materials, Technology and Management, Faculty of Civil Engineering and Building Services, "Gheorghe Asachi" Technical University of Iasi, 700050 Iasi, Romania
* Correspondence: georgiana.bunea@academic.tuiasi.ro (G.B.); ionut.ovidiu.toma@tuiasi.ro (I.-O.T.)

Abstract: In the past decades, nanomaterials have become one of the focal points in civil engineering research. When added to cement-based construction materials (e.g., concrete), it results in significant improvements in their strength and other important properties. However, the final mix characteristics depend on many variables that must be taken into account. As such, there is no general consensus regarding the influence upon the original material of certain nano-sized additives, the optimum dosage or the synergistic effect of two or more nano-materials. This is also the case for titanium dioxide (TiO_2) and nanoclay (NC). The paper focuses on reporting the existing research data on the use of the above-mentioned materials when added to mortar and concrete. The collected data is summarized and presented in terms of strength and durability properties of cement mortar and concrete containing either TiO_2 or NC. Both nano-materials have been proven, by various studies, to increase the strength of the composite, at both room and elevated temperature, when added by themselves in 0.5%~12% for TiO_2 and 0.25%~6% for NC. It can be inferred that a combination of the two with the cementitious matrix can be beneficial and may lead to obtaining a new material with improved strength, elastic and durability properties that can be applied in the construction industry, with implications at the economic, social and environmental levels.

Keywords: nanomaterials; nanoclay; titanium dioxide; cementitious material; sustainability

Citation: Bunea, G.; Alexa-Stratulat, S.-M.; Mihai, P.; Toma, I.-O. Use of Clay and Titanium Dioxide Nanoparticles in Mortar and Concrete—A State-of-the-Art Analysis. *Coatings* **2023**, *13*, 506. https://doi.org/10.3390/coatings13030506

Academic Editor: Andrea Nobili

Received: 22 January 2023
Revised: 22 February 2023
Accepted: 23 February 2023
Published: 24 February 2023

1. Introduction

Various global-sized revolutions have changed previously held ideas, encouraging both research and industry. Nowadays, the growth and general evolution within societies is significantly accelerated by technological breakthroughs. This has resulted in new problems which are currently unsolved, namely pollution and the threat of natural resource depletion. In the field of civil engineering, researchers are compelled to mitigate the influence the construction industry has, considering that in 2020 it was responsible for approximately 37% of the global process-related carbon dioxide emissions. Of this percentage, 10% was generated by the manufacturing processes of building materials [1]. Nanotechnology has influenced almost all of nowadays advancements in terms of mechanical properties and durability of materials, construction materials included. The term "nanomaterial" has been defined by the European Union Commission [2] in the Official Journal of the European Union as being an artificially-created or a natural material, of which at least 50% of the particles have one, or more, external dimensions between 1 nm and 100 nm. In cementitious composites, many components fit this description, and their study is now possible due to the progress of material characterization techniques at this level.

To this day, several nanomaterials have been studied with respect to their applications in the construction industry. In addition to strength, other properties were also considered within the framework of nanotechnology. A recent study [3] highlighted the positive

effect of several nanomaterials on the thermal resistance of cementitious composites, of which nano-silica stands out as being one the most studied materials. Additionally, several other nanomaterials were mentioned as increasing the high-temperature strength of the cement-based composites: carbon-based nanomaterials (carbon nanotubes, carbon nanofibers, graphene oxide, graphene nanoplatelets), nanoclay, nano-alumina, nano-iron oxides and nano-titania. Other studies [4,5] focused on the environmental impact of using nanoparticles in concrete, concluding that TiO_2 has a positive influence from this perspective [4].

The present work aims at creating a structured report encompassing the existing information about the impact of titanium dioxide (TiO_2) and nanoclay (NC) on cementitious composites from the point of view of strength enhancements and improvement of durability characteristics. A definite remark upon the influence of nanoclay on cement mortar or concrete is difficult to advance, as the variables change from one study to another. An important change is the type of nanoclay used in the study, the number of curing days or the additives introduced in the mix, e.g., fly ash, polypropylene fibers, superplasticizer, silica fume. These influence the final measured values for the strengths of the composite. Titanium dioxide nanoparticles succeed in improving both mechanical properties and photocatalytic reactions of cement mortar and concrete due to their chemical and physical properties. They are usually used in mortar/concrete mixes combined with superplasticizers in order to obtain a higher workability. Considering that TiO_2 is a non-reactive powder, there are studies in which pozzolans were added with the purpose of promoting the cement hydration reaction, e.g., fly ash, silica fume.

The mechanisms of improving the strength and durability properties of cementitious materials by using each of the two nanomaterials are different from one another but the end results are similar: NC is a highly pozzolanic material with significant influences on strength and durability at later ages while TiO_2 is inert and plays a filler effect. However, due to the very small particle sizes of nano-TiO_2, it serves as nucleation sites in the cement matrix with benefits in terms of strength and durability at earlier ages compared to NC. The information summarized in this work could serve as the starting point for future research works investigating the influence of combining TiO_2 and NC on the strength, elastic and durability properties of cement mortar and concrete.

2. The Influence of Nanoclay on Cementitious Materials

The use of nanoclay as a component of other materials started in the late 20th century when researchers observed that, by using this nanomaterial, the properties of the new composite material improved as compared to the material without the addition of nanoclay [6–9]. Among its first applications were the polymer matrices. The next observable research stage involved combining nanoclays with other materials of the same size (e.g., carbon nano-tubes [10,11]) as well as using them in cementitious mixes [12–14].

Nanoclay is defined as a layered mineral silicate, which, due to its filler and pozzolanic characteristics, succeeds in enhancing the mechanical and durability properties of several types of materials such as polymers or cement-based materials [15–18]. The use of such layered crystals, i.e., clays, in polymer composites resulted in improved physical properties and in the heat deflection temperature mainly due to their high surface area [19]. Moreover, the benefits of using nanoclay did not go unnoticed and their field of application soon extended to construction materials.

2.1. Types of Nanoclay Used in Combination with Cementitious Materials

There are several types of natural clays that were used as raw materials for the manufacturing of nanoclays: bentonite, montmorillonite, kaolin, illite, halloysite. They all have the same base crystalline structure, with the difference coming from the types of bonds between the stacked layers. This leads to different properties with direct effect in terms of the obtained results when added in the composition of another material [20,21]. Most of the research in terms of nanoclays used in cement-based materials is conducted with

montmorillonite or kaolin clays, usually in a modified form, in order to obtain a significant improvement of the physical properties of the resulting material.

Montmorillonite (MMT) nanoclay has a 2:1 layer structure and very weak Van der Waals forces keeping the outer layers together. This means that when combined with water the particles absorb water molecules and the distance between layers increases, leading to swelling [21]. A more detailed explanation of this phenomenon was given in [20]. Based on the available information at that time, one way to decrease the swelling was to add exchangeable cations with a lower hydration energy, thus obtaining a more hydrophobic nano-montmorillonite. Some researchers based their studies on this method and used ammonium cations to decrease the hydrophilicity of MMT obtaining an organo-modified montmorillonite [12,17,22–27]. Other studies prepared the nanoclay particles by subjecting them to very high temperatures, in the range of 750–900 °C for 2 h, obtaining a nano-calcined montmorillonite clay [28–31].

Unlike montmorillonite clays, kaolin ones have hydrophobic properties, as they are composed only of two layers connected not only by Van der Waals forces but also by hydrogen bonds which do not allow water molecules to enter between them [21]. Therefore, no additional treatment is needed before using nano-kaolin particles in the cement-based composites. However, when subjected to high temperatures, due to the calcination process, the hardness of the kaolin clay nano-particles is increased together with their degree of pozzolanicity. The particles change their shape and size, become more hydrophobic, as in the case of MMT nanoclay, and increase their whiteness. Due to its improved afore mentioned properties, the calcined kaolin nanoclay, i.e., metakaolin, became the focus for researchers instead of the raw kaolin nanoclay [32–36].

2.2. Chemical Structure and Properties

Nanoclay is a general term for the nanoparticles, which, as mentioned above, are comprised of layered mineral silicates [37] and, depending on the arrangement of the layers in the crystal lattice and the existing types of bonds, they result in different types. As mentioned before, MMT and kaolin are the most used types of nanoclays in civil engineering. Kaolin is a 1:1- type of clay mineral consisting of one silica tetrahedral sheet connected to the alumina octahedral sheet by means of the hydrogen atoms, having the chemical formula $Al_2Si_2O_5(OH)_4$ [38]. Montmorillonite, on the other hand, is a 2:1-type of clay mineral having a sandwich-like structure and it consists of two silica tetrahedral sheets with a single alumina or magnesium octahedral sheet in between, having the formula $(Na,Ca)_{0.33}(Al,Mg)_2(Si_4O_{10})(OH)_2 \cdot nH_2O$ [17,39]. The dimension of a phyllosilicate sheet is approximately 1 nm, whereas the nanoparticle size is in the interval 30–100 nm [40].

The benefits of using them in combination with cement are two-fold. On one hand, their very small particle size leads to a higher specific surface area than the micro-sized particles, on which the hydration products can form. Moreover, because of this, nanoclay particles succeed in entering the existing voids between the cement paste and the aggregates, at a nanoscale level, thus obtaining a decrease in porosity. Combining the aforementioned phenomena occurring inside the cement-based material, the resulted strength and durability increases [18,37]. On the other hand, the increase in strength is given also by the nanoclay chemical reactivity with calcium hydroxide (CH) during the hydration process. Having in its composition two layers of silica, nanoclay promotes the formation of calcium-silicate-hydrates (CSH) in a pozzolanic reaction. The increase in the concentration of CSH leads to an increased strength of the material [14,41].

2.3. Nanoclay Particles in Cementitious Materials—Technological Flow

Because of their very small size, nanoclay particles behave differently when mixed with water than the micro- or macro-sized particles usually used in civil engineering. The effect of electrostatic attraction is greater in case of nanoparticles leading to the occurrence of flocs. When water is added, the flocculation effect can become more prominent, especially in case of MMT clays, where the water molecules can intercalate with the outer layers of

the crystal and cause swelling [21,42]. This agglomeration of particles within the mortar or concrete has a negative impact upon the strength. Therefore, there is a stringent need for particle dispersion before the start of cement hydration.

The scientific literature gives two main ways in which this dispersion can be performed. The first one, which is the most recommended one, is to introduce the nanoclay particles in the water and then to subject the solution to ultrasonic waves. In this manner, the vibration caused within the molecules due to the impact of ultrasonic waves will prevent nanoclay particles to flocculate and will disperse them. Then the nanoclay-water solution can be used in two different ways to create the mortar or concrete samples: mechanical mixing or ultrasonic mixing. The mechanical mixing follows the steps given in ASTM C305 norm [18,43]. Using the ultrasonic mixing, the dry mixed materials (cement, sand, additives) are added to the nanoclay suspension already obtained and the ultrasonication is started again for the whole mix [44]. A previous study [45] concluded that in case of nanoclay, the sonication process has a positive effect on the final mechanical properties of the concrete samples. They also stated that the maximum allowable percentage of nanoclay used in cement-based materials is 5% [22,45].

The second method of dispersion is a simpler one and does not require any additional equipment than the one needed for preparing the mortar/concrete, namely, the dry mixing method. In this case, the mixing is performed in steps. The cement and the additives are dry mixed together with the nanoclay particles. In this manner, the nanoclay particles can be easily dispersed, due to the lack of a solving agent. Because the quantity of nanoclay is very small compared to that of cement, the distance between the nanoclay particles tends to increase during the dry mixing. This leads to a decrease in the flocculation probability when adding water. Afterwards, the aggregates are added and the mixing is restarted. Finally, the water is introduced in the composite [29,46].

A comparison between the previously mentioned methods of mixing nanoclay with cement-based materials, i.e., ultrasonication and dry mixing, showed that for a substitution of cement of 1–3% nanoclay, no differences were registered in terms of mechanical strengths. It was therefore concluded that both methods were equally reliable in properly dispersing nanoclay particles within the cement matrix [42].

2.4. Results of Laboratory Analyses (Microstructural Analyses)

When analyzing the nanoclay-cement-based material composite, the laboratory results vary depending on several factors, e.g., the nanoclay particle size, the nanoclay/cement ratio, the type of cement, the water/cement ratio, type and quantity of additives, type and size of aggregates. However, there are some common properties which are further discussed in this paper. Taking into account that when using sand or gravel, an important quantity of silica is introduced in the composite and the properties change significantly. The analyses will be presented considering this factor.

2.4.1. Scanning Electron Microscopy (SEM) Analysis

The layered structure of the organo-modified montmorillonite nanoclay (OMMT), obtained by cation exchange with quaternary ammonium cations, was extensively studied by means of SEM analysis [22]. Because MMT has a very high hydrophilicity, when it is introduced in the cement matrix, it begins to absorb the water from the cement matrix. In this manner, at first, the hydration of cement particles is slowed down and the workability is significantly reduced. The advantage of montmorillonite particles is that they begin to release the accumulated water at a later period during the hydration process of cement, leading to an improvement in strength. The phenomenon was later observed in other supplementary cementitious materials, such as zeolites, and it is now known as internal curing. However, the major problem with MMT particles, from this point of view, is that because of the initial occurring phenomenon, they introduce a water to cement ratio gradient near them as the quantity of water increases in that area. By increasing the water, the porosity is automatically increased, reducing the cohesion between the cement matrix

and MMT particles [17]. When adding OMMT instead of MMT the water/cement ratio gradient around the nanoclay particles is decreased and the development of cracks is hindered [17].

The effects of high temperatures on mortar containing 5 wt% nano-calcinated montmorillonite clay (NCMC) was also studied [28] by firstly analyzing the SEM images, presented in Figure 1, for samples with and without NCMC at 25 °C, 250 °C and 900 °C, at 28 days of curing. The investigations highlighted the positive effect the NCMC has on the mortar matrix, especially at the level of the interfacial transition zone (ITZ) between the aggregates and the cement paste (#2 in Figure 1d). It was therefore concluded that by adding NCMC to the mortar, a denser matrix was obtained [28] mainly due to the filler effect of the nanoparticles. Additionally, an increase in the pozzolanic activity was detected. When the temperature was increased to 250 °C, the cement hydration was accelerated and more CSH were obtained in case of NCMC mortar than in case of control mortar (#3 in Figure 1b,e) [28]. After 300 °C, the development of microcracks began and at 450 °C the cracks widened and were clearly visible as Portlandite started to degrade and CSH particles lost their structural integrity [47]. At 900 °C, wide cracks were present in the control sample (#4 in Figure 1c) leading to a significant strength loss. However, when adding NCMC in the mix, the cement matrix experienced fewer cracks (#4 in Figure 1f), thus leading to higher strength values [28].

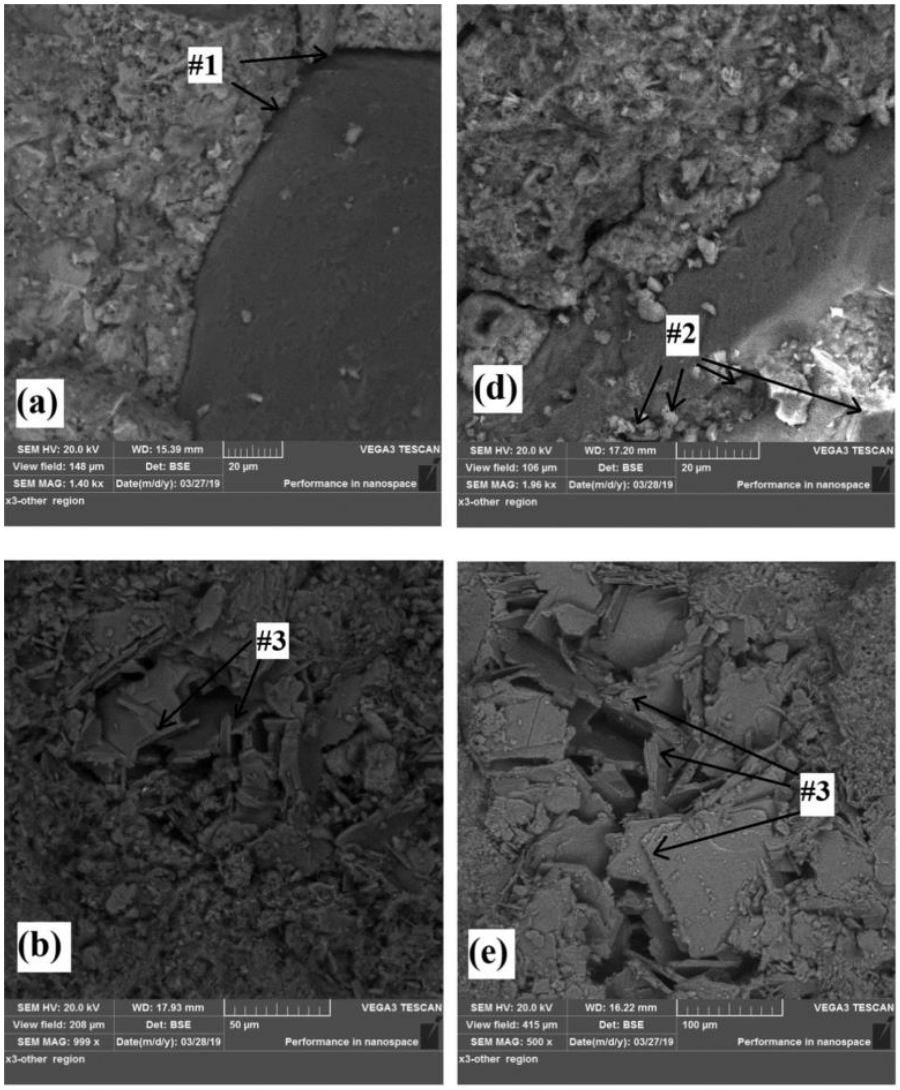

Figure 1. *Cont.*

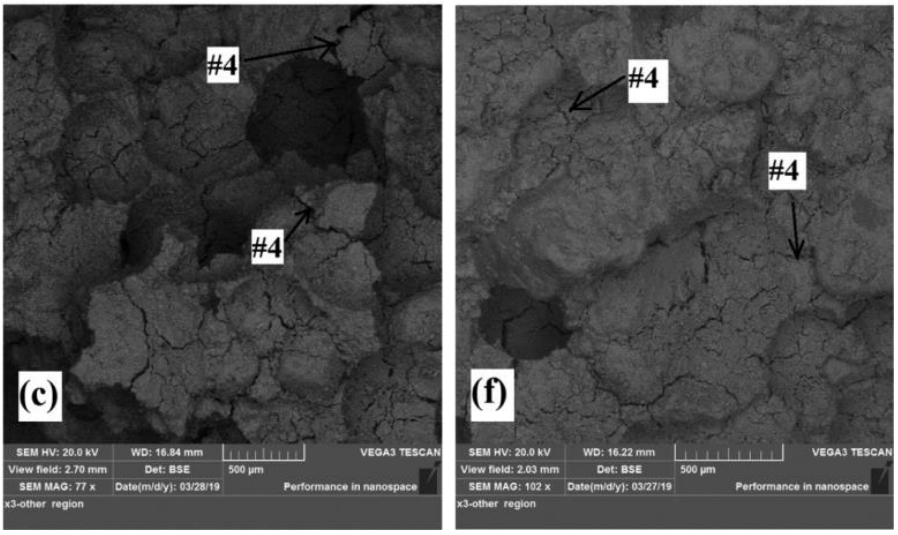

Figure 1. SEM images of fracture surfaces of control and modified mortar [28] (Reprinted/adapted with permission from Ref. [28]. Copyright 2018, ELSEVIER); (**a**) control at 25 °C, (**b**) control at 250 °C, (**c**) control at 900 °C, (**d**) NCMC mortar at 25 °C, (**e**) NCMC mortar at 250 °C, (**f**) NCMC mortar at 900 °C.

2.4.2. Thermogravimetric Analysis (TGA)

TG analysis is used to evaluate the influence of the temperature upon the considered material. Usually, the TGAs are conducted on cement paste samples because the aggregates significantly influence the final result. Generally, aggregates do not vary in weight when subjected to an increase in temperature so including them in the very small samples needed to run TG analysis would only lead to erroneous results [48,49].

Natural hydrophilic montmorillonite in 1% and 2% cement replacement was used to investigate the influence of temperature on the obtained cement paste. The heating rate for the TGA in this test was 30 °C/min. The study revealed that there were two main stages in the weight loss of cement paste: the dehydration of C-S-H at 105 °C and the CH decomposition at 470 °C [18]. The obtained results were in good agreement with the ones previously reported in general study on cement pastes [48]. At approximately 750 °C a third stage could be distinguished, corresponding to the decarbonation of calcium carbonate $CaCO_3$ [48]. It was shown that, as the percentage of nanoclay increases, the weight loss increases, indicating the property of natural montmorillonite to attract water molecules. Therefore, when heated, the samples began releasing the physically bounded water, its quantity being greater in case of samples with MMT compared to the control sample.

In contrast to the results presented in [18], the use of calcined natural montmorillonite clay resulted in a smaller weight loss compared to the control sample [28]. The stages of weight loss depending on the temperature were similar with the ones reported in [18]. However, during the first stage, i.e., 100–110 °C, there was no abrupt change in weight for the NCMC but a more gradual one due to the fact that the NCMC water absorption capacity has been significantly reduced by means of calcination. Between 430 °C and 470 °C the dehydration of weakly bound water from CH and CSH products occurred, followed by a reduction in weight between 580 and 680 °C when the strongly bound water was lost.

Similar results to the ones reported in [28] regarding the nano-calcined montmorillonite clay (CNCC) for 1, 2 and 3 wt% cement replacement were previously reported [29]. The earlier research work continued the study further on, including in the TG analysis samples of 1 wt% cement replacement by nanoclay modified with quaternary ammonium salt (NCC). It was observed that a smaller weight loss occurred when adding CNCC of 1 and 2 wt% than when using 1 wt% NCC. This result proved that nano-montmorillonite calcination has a greater impact on the decreasing the hydrophilicity than adding ammonium cations.

2.4.3. X-ray Power Diffraction (XRD) Analysis

When creating a new composite material, it is very important to know the influence that each component has upon the final result. In this regard, XRD analysis provides an insight regarding the mineralogical changes that occur inside the material, e.g., mortar/concrete, when adding nanomaterials, e.g., nanoclay [50]. Using 2 wt% nanoclay, untreated hydrophilic montmorillonite by weight of cement replacement and subjecting the samples to 25 °C, 200 °C, 400 °C and 600 °C, it was observed that the intensity of CSH is higher for all samples combined with NC, as shown in Figure 2, by comparison with the control samples, which leads to an increase in strength [18]. The increase in CSH crystals quantity became more prominent when increasing the temperature. Thus, for samples subjected to 400 °C and 600 °C, there was a strong peak for the CSH crystals (at 2θ = 28°), while up to 400 °C, the quantity was significantly smaller. Moreover, the intensity of CH (2θ = 18°) decreased with the temperature, as the cement hydration accelerated [18].

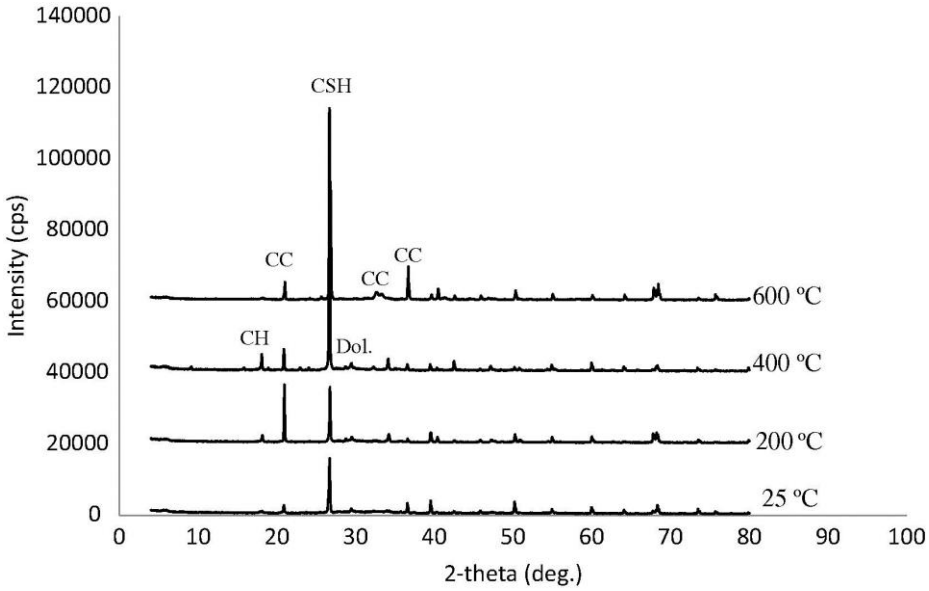

Figure 2. XRD patterns of mortar with 2% untreated hydrophilic montmorillonite nanoclay after exposure to different temperatures [18] (Reprinted/adapted with permission from Ref. [18]. Copyright 2020, ELSEVIER).

In another study, XRD analysis was performed on mortars combined with nano-calcined montmorillonite clay CNC, which lead to the conclusion that the calcined nanoclay had a positive effect upon the strength of the material, as it promoted the consumption of CH crystals and the formation of CSH gel [28]. The researchers used a 5 wt% nanoclay cement replacement and the analyzed samples were previously subjected to temperatures of 25 °C, 150 °C and 900 °C. The authors interpreted the presence of belite in the composite as an indicator for the level of both CH and CSH decomposition. Based on this remark, it can be stated that calcined nano-montmorillonite clay has a positive effect on the material properties, even at elevated temperatures as high as 900 °C. At that temperature, the control sample exhibited an important increase in belite, i.e., 8% higher than nanoclay mortar [28].

Similar results have been previously reported in a study in which the cement was replaced with 1, 2 and 3 wt% CNC and observed a reduction in the CH quantity (approximately 28% compared with control sample) [29]. This was attributed to the pozzolanic reaction which consumed the CH and led to the formation of CSH gel. Moreover, the increasing in the unreacted dicalcium silicate (C_2S) and tricalcium silicate (C_3S), compared with quantities from the control cement paste, confirmed the pozzolanic property of CNC. However, as the percentage of nanoclay introduced in the cement was increased, the reduction of CH crystals decreased. Moreover, a smaller quantity of C_2S and C_3S was obtained

for 3 wt% CNC than for 1 wt% CNC, indicating a decrease in the pozzolanic activity. The XRD patterns for 1% CNC and the ones obtained for 1% cement replacement with montmorillonite nanoclay indicated that the calcined nanoclay led to a higher pozzolanic activity than the organo-modified nanoclay [29].

2.5. Material Strength Improvements

A definite remark upon the influence of nanoclay on cement mortar or concrete is difficult to advance, as the variables from one study to another are changing. An important change is the type of nanoclay used in the study, the number of curing days or the additives introduced in the mix, e.g., fly ash, polypropylene fibers, superplasticizer, silica fume. These influence the final measured values for the strengths of the composite. However, considering the reports from recent studies, the use of nano materials, nanoclay included, results in a denser microstructure of the material with net benefits in terms of strength and durability properties [51–53]. From this perspective, the current paper presents the literature results in a centralized manner identifying the possible influences on the reported results, where they are present. Moreover, the paper extracts from the literature only the results for the cement-based composites, where the main cement replacement material is nanoclay.

2.5.1. Splitting Tensile Strength

Taking into account that concrete/cement mortar elements have a very poor tensile strength and that their main strength develops under compression, the number of studies analyzing the tensile strength for a simple combination of cement-based material and nanoclay is very limited. However, based on the information presented in Sections 2.2 and 2.4 regarding the influence of nanoclay on the chemical and physical properties of the cement composite, an improvement in the tensile strength is expected. The porosity decrease, the prolonged hydration and the higher quantity of CSH crystals, all compared with the plain cement mortar, are all contributing towards a higher value of the tensile strength. Moreover, nanoclay particles attract cement particles and bond them together, thus obtaining a more durable composite [46,54].

It was also observed that the final tensile strength was also influenced by the curing method. Results on samples cured in water and samples cured by plastic wrapping were obtained and compared. Lower values of the tensile strength were obtained, especially after 90 days of curing, by applying the second method as the cement particles did not have enough water to fully hydrate. For 1% cement replacement with montmorillonite nanoclay, the difference between the two methods, in terms of strength, was 0.40 MPa at 90 days of curing [55].

The influence of temperature upon the cement mortar combined with 1 and 2 wt% natural hydrophilic montmorillonite sample was also investigated. It was observed that when the temperature increased up to 200 °C, the value of the tensile strength increased substantially for all samples, including the control sample. In case of 2% nanoclay cement replacement, a maximum difference of approximately 27% was reported between the values obtained for the tensile strength of the control sample and the nanoclay-cement composite, the nanoclay particles proving their efficiency. This increase in the value of the tensile strength was given by the chemical reactions which occurred during sample heating, namely the hydration acceleration, which promoted CSH formation around the nanoclay particles. As the temperature increased to 400 °C, the tensile strength dropped to 1.5–1.9 MPa for all samples. At 600 °C, a maximum value of approximately 0.2 MPa was obtained for the splitting tensile strength of the control mix. However, the nanoclay composite samples maintained consistently better values of the splitting tensile strength than the control one [18].

Table 1 summarizes the values of the tensile strength of mortar or concrete samples combined with different percentages of nanoclay, at room temperature, cured for 28 days in tap water or lime-saturated water.

Table 1. Splitting tensile strength values for different nanoclay-cement matrix samples.

Study	Type of Nanoclay	Type of Sample	Standard	w/b w/c	Additives	NC [%]	Tensile Strength [1] [MPa]
[18,56]	Natural hydrophilic montmorillonite	Cement mortar	ASTM C190	w/b 0.55	-	0	3.20
						0.5	3.30
						1	3.40
						2	3.50
[46]	Metakaolin	Cement mortar	ASTM C307	w/b 0.50	-	0	3.60
						2	4.05
						4	4.48
						6	4.92
						8	5.36
[54]	Metakaolin	Concrete	ASTM C496	w/c 0.42	1.5% polypropylene	0	7.96
						2	8.32
						4	9.54
						6	10.42
						8	11.16
						10	9.63
[55]	Montmorillonite (type not specified)	Concrete	ASTM C496	w/c 0.45	-	0	aprox. 4.30
						1	aprox. 5.80
						2	aprox. 5.50
						3	aprox. 5.10

[1] Some values were approximated from the graphics, associated with the cited scientific research.

All samples registered a growth in the values of the tensile strength as the percentage of nanoclay increased, except for the sample analyzed in [54]. In that case, at 10 wt% NC addition, the value of the strength decreased by 13.70%, compared to those obtained for an 8 wt% NC addition. Taking into account that the nanoclay percentage was very high, obtaining a homogeneous nanoclay dispersion becomes very difficult, leading to flocculation. This automatically creates weak points within the matrix. The values of the splitting tensile strength reported in [54] were higher than those presented in [55] due to the use of polypropylene fibers, which succeed in controlling the occurrence and the propagation of cracks. In the former case, the authors used nanoclay in order to obtain a better bond between the polypropylene fibers and the matrix [54]. Although nanoclay is not able to completely prevent the occurrence and propagation of fractures, the increase in the value of the flexural tensile strength of the composite leads to smaller and fewer cracks inside the material. Therefore, the reinforcement is protected from the ingression of chemical agents and humidity increasing the durability of reinforced concrete elements.

The results obtained for mortar samples follow the same trend as the ones reported for concrete [18,46,56]. The difference of 0.55 MPa for 2 wt% NC can be explained by the smaller water to binder ratio used for the former.

2.5.2. Flexural Tensile Strength

Taking into account that the bending state of loading is present in every civil engineering structure, the researchers had to verify if and to what extent the content of nanoclay would influence the flexural tensile strength of cement mortar or concrete elements. There are several studies on the improvement of the flexural strength regarding the combination between nanoclay and cement-based materials. The focus was on preventing or limiting the occurrence of cracks, which, besides the fact that this leads to the exposure of reinforcement to the outside air, the reinforcement could not benefit from the protection of the concrete cover in case of a fire.

In case of exposure to high temperatures, the same trend observed for the splitting tensile strength was reported in [18] for the flexural tensile strength, for 1 and 2 wt% natural hydrophilic montmorillonite cement replacement, without any treatments. For all

specimens and all temperatures, the 2 wt% NC composites exhibited the highest strength values compared with the control sample. The maximum flexural strength was reached at a temperature of 200 °C, at 11.60 MPa. When subjected to 400 °C, the flexural strength had a major drop in the value, of about 76% for the control sample, considering as reference the value for 200 °C, reaching a value of 2.60 MPa. The influence of nanoclay was evident at 400 °C, as the flexural strength value increased for 2 wt% NC by 138% compared to the control specimen. Unlike the tensile strength, the specimens preserved a certain value of flexural strength after their treatment at 600 °C, although very small—0.8 MPa for the control specimen. Adding 1 wt% NC, in this case, did not lead to flexural strength improvements, but for the 2 wt% NC combination the strength value reached 1.7 MPa [18].

A similar analysis was conducted for 1, 3 and 5 wt% nano-calcined montmorillonite clay [28]. The same trend of flexural strength increase was obtained at 250 °C, reaching the maximum value for 5 wt% nanoclay. At the next temperature stage, i.e., 450 °C, the strength decreased significantly for all specimens. It should be noted that at about 180 °C, polypropylene fibers started to melt and caused an increase in porosity which, in turn, led to smaller flexural strength values than the ones reported in [18].

A comparison was conducted between two types of curing methods applied to specimens with various percentages of nanoclay added in the cement matrix, i.e., water curing and plastic cover curing. The authors of the study observed that, similar to the tensile strength, the flexural strength value was smaller when curing the specimens by plastic wrapping than by immersing them in water. The major difference was obtained at 90 days of curing for 1 wt% NC sample, in which case the flexural strength decreased by approximately 14.9% for the second curing method compare to the traditional, water curing method [55]. This could be explained by the fact that the water cured specimens had enough moisture to continue the hydration process of the cement whereas the same process was significantly slowed down in case of plastic wrapping curing method once the mixing water was consumed.

Table 2 presents the values of the flexural tensile strength, for different inputs, regarding cement mortar and concrete composites with different nanoclay quantities. The values were selected for samples subjected only to room temperature and cured for 28 days in water or lime-saturated water.

Regarding what concerns the flexural strength for both cement mortar and concrete, the values vary significantly from one study to the other. The only common information resulted from these analyses would be the increase in the value of the flexural strength with the increasing nanoclay percentage within the cement matrix. The available data is sometimes conflicting, with some authors [28] reporting smaller values of the flexural tensile strength than others [18,56], although additives were used to improve workability and strength. One possible explanation could be the water to binder ratio. A w/b ratio of 0.55 could provide cement and nanoclay particles enough water to hydrate during mixing and curing period [18,56]. In another study [28], however, a lower w/b ratio was considered but a superplasticizer was used to improve workability. Generally, a small calculated w/b ratio provides a higher strength. However, due to the level of hydrophilicity of nanoclay, a higher amount of water could be needed. Moreover, there were two different types of montmorillonite used: a calcined one which was less hydrophilic and a natural one without treatment which had a high level of hydrophilicity.

Table 2. Flexural strength values for different nanoclay-cement matrix samples.

Study	Type of Nanoclay	Type of Sample	Standard	w/b w/c	Additives	NC %	Flexural Strength [1] [MPa]
[18,56]	Natural hydrophilic montmorillonite	Cement mortar	ASTM C348	w/b 0.55	-	0 0.5 1 2	7.40 7.60 7.60–7.70 7.80
[28]	Calcined hydrophilic montmorillonite clay	Cement mortar	ASTM C348	w/b 0.484	- non-absorbent monofilament polypropylene fibers - naphthalene-sulfonate-based superplasticizer	0 1 3 5	approx. 6.10 approx. 6.20 approx. 6.70 approx. 7.00
[54]	Metakaolin	Concrete	ASTM C293	w/c 0.42	1.95% polypropylene	0 2 4 6 8 10	9.36 9.92 11.24 12.02 12.76 11.50
[55]	Montmorillonite (type not specified)	Concrete	ASTM C78	w/c 0.45	-	0 1 2 3	approx. 5.00 approx. 6.60 approx. 6.30 approx. 5.90
[23]	Organo-montmorillonite clay	Cement mortar	ASTM C348	w/c 0.50	-	0 0.25 0.5 1	approx. 9.50 approx. 9.60 approx. 9.10 approx. 9.80

[1] Some values were approximated from the graphics, associated with the cited scientific research.

A decrease in the value of the flexural tensile strength for a higher percentage nanoclay was reported in [54,55], which may be due to the inhomogeneous specimens given by the large quantity of nanoclay present within the mixture. The values of the flexural tensile strength obtained by [54] on the concrete samples were higher for every nanoclay percentage, mainly because of the 1.5% polypropylene addition, which prevents crack formation and propagation.

The highest value of the flexural tensile strength from all the presented studies was reported by [23], although the authors did not use additives. This may be related to the organo-modified montmorillonite clay, which resulted after a treatment of the natural montmorillonite with dimethyl dehydrogenated tallow and quaternary ammonium chloride.

2.5.3. Compressive Strength

The most important material property of both cement mortar and concrete is their compressive strength.

Considering that there are several studies that investigated the variation in the compressive strength depending on temperature, the analysis within Section 2.5.3 pursues two directions. The first one will debate upon the compressive strength results obtained for specimens stored and tested at room temperature, while the second one will focus only on the studies where the specimens were subjected to elevated temperatures.

Strength Values at Room Temperature

From the data presented so far for splitting and flexural tensile strength, it was concluded that between the water curing and the plastic wrapping curing, the former is the best one to use for cement-based composites with nanoclay additions. The same trend was reported for the case of compressive strength. The latter curing method resulted in lower values of the compressive strength at 90 days, with on average a 14% decrease compared with water curing. As previously explained, cement and nanoclay particles need water to

hydrate and if they do not have enough, the hydration reaction significantly decreases and even stop and no C-S-H gels will be produced anymore, thus limiting the strength increase. The highest difference was observed at 90 days of curing. On the other hand, at the age of 28 days, this difference was very small [55].

In another study, the enhancement of compressive strength due to 1, 2, 3 wt% nanoclay addition in self-consolidating concrete was investigated [42]. The considered curing ages were 3, 7, 14, 28 and 90 days. The obtained results showed that the highest increment in the values of the compressive strength was at 7 and 14 days of curing, compared to the control mix. In that time interval the hydration process reached a maximum level, as the CH particles were consumed and CSH gels were formed. As more nanoclay was added in the cement matrix, the difference between the compressive strength of the control sample and the compressive strength of the nanoclay enriched composite became larger. A maximum was reached for 3 wt% nanoclay addition, the difference between the value of the compressive strength for the control mix and the nanoclay composite at 7 and 14 days of curing being 31% and 14%, respectively. For the 2 wt% nanoclay addition, this difference was 20.70% and 4.70%, respectively [42].

The compressive strength of a nanoclay-concrete composite at 7, 14, 28, 49, 56 and 90 days of curing, for nanoclay percentages of 0.1, 0.3 and 0.5 wt% and two water to cement ratios, i.e., 0.40 and 0.50, was also investigated. A similar trend was observed with the one reported in [42], the largest increase in the value of the compressive strength being during the first 28 days. The study also investigated the influence of water to cement ratio on the values of the compressive strength. The nanoclay percentage for which the maximum compressive strength was obtained changed depending on the w/c ratio. For a w/c ratio of 0.40, the optimum nanoclay percentage was 0.50%, whereas for a w/c ratio of 0.50, it decreased to 0.30% [57].

Table 3 summarizes the findings on the values of the compressive strength for mortar/cement specimens with certain percentages of nanoclay additions, stored at room temperature and cured for 28 days in water or lime-saturated water.

The smallest values for cement mortar reported in [28] can be explained by a non-homogeneous distribution of nanoclay within the cement matrix, the authors resorting to manual mixing of the material. This method can cause nanoclay particles to agglomerate and, eventually, lead to a decrease in strength. The same can be observed in terms of values of the flexural tensile strength obtained in [28] compared to other studies. In case of concrete, the results presented in [57] were very low in comparison with the other studies.

According to [57], for low nanoclay percentages, there was a negative influence upon the compressive strength of the composite. An addition of only 0.1 wt% nanoclay led to a decrease of 14% in the value of the compressive strength, for a w/c ratio of 0.50. However, when increasing the nanoclay content, the compressive strength value exceeded the one of the control specimen but not significantly [57]. For percentages greater than 0.1 wt% nanoclay, the compressive strength value increased with the increase in nanoclay content within the cement matrix. However, a small decrease in the values of the compressive strength at the maximum analyzed nanoclay percentage, of about 5.15%, compared to the previous percentage, was reported in [54,55]. Taking into account the spread of the reported results, it is difficult to provide a reason applicable to all scenarios. On the other hand, as the percentage of nanoclay increases, the distance between nanoclay particles decreases and, as they tend to attract each other, flocculation of nanoparticles may occur, which leads to a decrease in the strength of the material.

Table 3. Compressive strength values for nanoclay—mortar/concrete specimens at room temperature.

Study	Type of Nanoclay	Type of Sample	Standard	w/b w/c	Additives	NC %	Compressive Strength [1] [MPa]
[23]	Organo-montmorillonite clay	Cement mortar	ASTM C109	w/c 0.50	-	0 0.25 0.5 1	approx. 45.50 approx. 49.00 approx. 55.00 approx. 52.50
[28]	Calcined hydrophilic montmorillonite clay	Cement mortar	ASTM C109	w/b 0.48	- non-absorbent monofilament polypropylene fibers - naphthalene-sulfonate-based superplasticizer	0 1 3 5	approx. 21.00 approx. 21.20 approx. 22.00 approx. 24.10
[18,56]	Natural hydrophilic montmorillonite clay	Cement mortar	ASTM C109	w/b 0.55	-	0 0.5 1 2	37.00–37.60 38.00 38.50–39.00 40.30–41.00
[46]	Metakaolin MKC	Cement mortar	ASTM C109	w/b 0.50	-	0 2 4 6 8	approx. 47.20 approx. 47.60 approx. 48.50 approx. 49.70 approx. 50.50
[54]	Metakaolin MKC	Concrete	BS 1881 -Part 116	w/c 0.42	1.5% polypropylene	0 2 4 6 8 10	52.32 53.80 55.90 57.50 58.80 55.60
[55]	Montmorillonite (type not specified)	Concrete	ASTM C470	w/c 0.45	-	0 1 2 3	approx. 45.00 approx. 61.00 approx. 58.00 approx. 55.00
[42]	Montmorillonite (type not specified)	Self-consolidated concrete	-	w/b 0.34	F-type poly-carboxylate-based superplasticizer	0 1 2 3	approx. 49.20 approx. 52.00 approx. 51.00 approx. 54.50
[57]	type not specified	Concrete	-	w/c 0.40 ——— w/c 0.50	-	0 0.1 0.3 0.5 0 0.1 0.3 0.5	approx. 35.00 approx. 34.00 approx. 37.00 approx. 39.40 approx. 34.00 approx. 29.00 approx. 36.00 approx. 35.00

[1] Some values were approximated from the graphics, associated with the cited scientific research.

Strength Values at Elevated Temperatures

When concrete or cement mortar specimens are subjected to high temperatures, a temperature gradient develops inside the elements. The chemical and physical phenomena which occur lead to spalling or fracture development. Therefore, a decrease in strength is registered, the material losing its ability to overtake the induced thermal generated stresses.

Table 4 presents the compressive strength variation for different cement mortar/concrete specimens with nanoclay addition, cured for 28 days in water or lime-saturated water, subjected to various temperatures. Taking into account that the studies which are presented in this section were also reported in Table 3, the given information will focus only on the temperature variation and the corresponding values of the compressive strength.

Table 4. Compressive strength values for nanoclay—mortar/concrete specimens at high temperature.

		[18]			[28]			
Type of Nanoclay		**Natural Hydrophilic Montmorillonite**			**Calcinated Hydrophilic Montmorillonite**			
Nanoclay Content [%]		**0**	**1**	**2**	**0**	**1**	**3**	**5**
Compressive strength [1] [MPa]	25 °C	37.6	38.5	40.3	21	21.2	22	24.1
	200 °C	54.4	56.1	59.7				
	250 °C				22.5	23	24	27
	400 °C	38.9	40.2	41.6				
	450 °C				11	12	14	17
	600 °C	9.2	9.8	10.6	10	10.5	12	13.5
	900 °C				2	2.5	5	5

[1] All values are approximated from the graphics, associated with the cited scientific research.

As temperature reaches 200 °C, the value of the compressive strength increases, according to the data reported in [18] and graphically presented in Figure 3a due to the acceleration of the hydration process and the CSH production. The highest value was obtained for 2% nanoclay cement replacement—59.7 MPa. On the other hand, the rate of increase in the values of the compressive strength for the three considered mixes was between 44.68% for the control mix and 48.14% for the mix containing 2 wt% nanoclay cement replacement. As the temperature increased up to 400 °C, the material lost its strength by about 30% but it still maintained a value higher than the control specimen kept at room temperature. It is interesting to observe that in this case, the highest gain in the value of the compressive strength was obtained by the mix with 1 wt% nanoclay cement replacement, at 4.42%. At 600 °C, all samples registered a very high strength loss of about 75% with respect to the 400 °C samples, the 2% nanoclay combination having the biggest residual compressive strength value, i.e., 10.6 MPa [18].

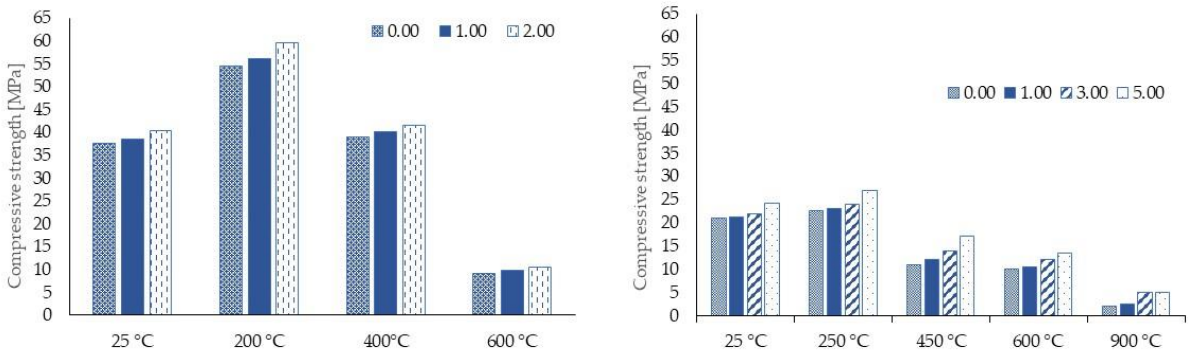

Figure 3. Variation in compressive strength as function of temperature and different percentages of nanoclay. (**a**) results reported in [18]; (**b**) results reported in [28].

Although the values were smaller than those presented in [18], the trend reported in [28] was similar for the cement mortar subjected to high temperatures, as seen in Figure 3b. The authors observed that as the temperature rose to 250 °C, the value of the compressive strength increased as well, as the hydration process is accelerated and more CSH is produced. For that temperature, the optimum nanoclay percentage was 5%. However, at 450 °C, the strength was already diminished significantly by about 37% compared to the 5% nanoclay cement replacement at 250 °C, when CSH was in the decomposing process. For 600 °C, there was an evident strength loss especially for the nanoclay-cement composite reaching a maximum of 20.6%. At 900 °C, the strength loss continued for all specimens but the nanoclay-cement composite still maintained a higher

strength value than the control sample. It should be noted that there was no difference in residual compressive strength between the 3% and 5% nanoclay cement replacement [28].

2.6. Durability Tests

The durability of a material is essential in civil engineering where the structures must have a life cycle of decades and where some of them are subjected not only to external loads but also to water penetration which can lead to corrosion, to frost-thaw cycles, to air with various chemical pollutants, etc. There are several studies that investigated the influence of nanoclay on the long-term durability of cement mortar or concrete.

Gas permeability tests with methanol were used [14] on samples made of cement paste with different quantities of montmorillonite nanoclay. As the curing period increased, the permeability coefficient decreased. There was a pattern emerging from this analysis that is common to all curing periods. The smallest permeability coefficient was registered for 0.4% nanoclay cement replacement, whereas the highest corresponds to the control specimen. The relative decrease was significant, a value of 49.95% being obtained for the 56 days curing period [14]. This result demonstrates the filler effect that nanoclay has on the cement matrix, succeeding in decreasing porosity and blocking outside elements to penetrate inside the cement matrix.

However, the results of the tests on cement pastes could not be confirmed by the results obtained on concrete specimens [41]. Nano-metakaolin was used in the concrete mixes and oxygen permeability tests were conducted. A higher permeability was obtained for nanoclay samples compared to the control samples, with approximately 150% for the 1% nanoclay and 200% for the 2% nanoclay. The difference between the two studies may have several explanations: different types of permeability tests, increased porosity due to the presence of aggregates combined with an insufficiently dispersion of nanoclay particles within the cement matrix, type of nanoclay, etc.

Water penetration and water absorption test are relevant when assessing the probability of water reaching the reinforcement and eventually causing corrosion. Tests were conducted in accordance to the EN 12390-8 norm and it was observed that for 1–3 wt% nanoclay cement replacement, the quantity of water penetrating the concrete samples was less than in case of the control samples, for which a 31 mm depth was registered [55]. The smallest depth of water absorption, i.e., 20 mm, was obtained for the 1 wt% nanoclay. The reasons for the smaller water depth values for concrete combined with nanoclay are the filler effect that nanoclay has coupled with the higher development of CSH gels compared to the control sample resulting in a denser structure of the material. The above results were obtained at the age of 28 days of water curing. In case of plastic wrapping curing, all samples had a higher water absorption than the control sample, which confirms the results obtained for compressive, flexural and tensile strengths [55]. Similar results were obtained for self-consolidated concrete with 1, 2 and 3 wt% nanoclay addition, with 90 days of curing [42]. However, the smallest water penetration depth was registered for 3% nanoclay addition, which was 64.3% smaller than the control specimen [42].

A water absorption test based on ASTM C642 for concrete specimens with 1, 2 and 3% montmorillonite nanoclay was also used [55]. As in the case of water penetration test, all nanoclay specimens had a water absorption percentage smaller than the control specimen. The lowest water absorption percentage corresponded to the 1% nanoclay sample, i.e., 1.46%, 54.3% smaller compared to the control sample [55]. Similar results were reported for self-consolidated concrete samples with 1, 2 and 3% nanoclay addition [42]. In contrast with [55], the lowest water absorption percentage corresponded to the 3% nanoclay mix while the highest was for 2% nanoclay. A possible explanation could be attributed to the effect of shrinkage on the integrity of the mix [42]. For cement mortar on the other hand, the obtained results were different, as the water absorption percentage for a 0.5% nanoclay addition was smaller than the one for the control specimen, but for 1% and 2% nanoclay, the value was higher and has an increasing trend [56]. The authors associated their results with the capillary water absorption test, in which case the specimens were

submerged in water only at 5–10 mm depth, according to BS EN 1015-18 norm. The lowest capillarity absorption coefficient results came from 1% and 2% nanoclay, reaching a value of approximately 0.03 kg/(m^2 min$^{0.5}$), compared with 0.04 kg/(m^2 min$^{0.5}$)—corresponding to the control sample [56].

When water trapped inside the cement matrix starts to evaporate, it creates pressure on the void walls which leads to the development of fine cracks. These cracks have a negative impact both on the strength and on the durability of the material. The influence of adding organo-montmorillonite nanoclay in the cement matrix upon the material plastic shrinkage was evaluated in [23]. It was concluded that nanoclay has a definite positive effect, as the plastic shrinkage value decreased by 70%, even for the lowest analyzed nanoclay quantity, i.e., 0.25 wt% cement replacement [23].

An impressed voltage test was employed to analyze the variation in corrosion current for self-consolidating concrete modified with 1, 2 and 3% nanoclay [42]. It resulted that, as the percentage of nanoclay increases, the deterioration time of the reinforcement extended, meaning that the use of nanoclay leads to a better protection of the steel reinforcement against corrosion mainly due to the denser structure of the cement matrix.

Table 5 summarizes the findings reported in this section of the paper. The information is structured based on the type of durability test, type of material it was conducted on (i.e., mortar or concrete) and nanoclay percentage. The main findings of each referenced study are also included.

Table 5. Durability tests on nanoclay—mortar/concrete specimens.

Measured Parameter	Scientific Paper	Test	Type of Sample	Type of Nanoclay	Nanoclay Percentage	Observation
Permeability coefficient	[14]	Gas permeability test (methanol)	Cement paste	Montmorillonite in liquid form (type not specified)	0; 0.2; 0.4; 0.6; 0.8	- As the curing period increased, the permeability coefficient decreased - The smallest permeability coefficient was registered for 0.4% nanoclay, and the highest for the control sample
	[41]	Oxygen permeability test	Concrete	Nano-metakaolin	0; 1; 2	- Higher permeability for nanoclay samples compared to control samples
Water absorption percentage	[55]	Water absorption test	Concrete	Montmorillonite (type not specified)	0; 1; 2; 3	- The test was carried out at 28 days of curing - Water absorption percentage smaller than the control specimen - The lowest value corresponds to 1 wt% nanoclay - Plastic wrapping curing samples had a higher water absorption than the water curing samples
	[42]	Water absorption test	Self-consolidated concrete	Montmorillonite (type not specified)	0; 1; 2; 3	- The test was carried out at 90 days of curing - Water absorption was reduced when nanoclay was added - The best result was for the 3 wt% nanoclay addition
	[56]	Water absorption test	Cement mortar	Natural hydrophilic montmorillonite clay	0; 0.5; 1; 2	- Water absorption percentage for 0.5% nanoclay was smaller compared to the control specimen - For 1 and 2% nanoclay, the value was higher than the control specimen

Table 5. *Cont.*

Measured Parameter	Scientific Paper	Test	Type of Sample	Type of Nanoclay	Nanoclay Percentage	Observation
Water penetration depth	[55]	Water penetration test	Concrete	Montmorillonite (type not specified)	0; 1; 2; 3	- The test was carried out at 28 days of curing - 1 wt% nanoclay—smallest depth of water absorption (20 mm) - Plastic wrapping curing samples had a higher water absorption than the water curing samples
	[42]	Water penetration test	Self-consolidated concrete	Montmorillonite (type not specified)	0; 1; 2; 3	- The test was carried out at 90 days of curing - The best result was for the 3 wt% nanoclay addition
Capillary water absorption coefficient	[56]	Water absorption test	Cement mortar	Natural hydrophilic montmorillonite clay	0; 0.5; 1; 2	- The lowest capillarity absorption coefficients resulted for 1 and 2% nanoclay
Plastic shrinkage	[23]	Plastic shrinkage test	Cement mortar	Organo-montmorillonite clay	0; 0.25; 0.5; 1	- Nanoclay has a definite positive effect - Plastic shrinkage decreased by 70% for 0.25 wt% nanoclay cement replacement
Corrosion current	[42]	Impressed voltage test	Self-consolidated concrete	Montmorillonite (type not specified)	0; 1; 2; 3	- As the percentage of nanoclay increases, the deterioration time of the reinforcement ex-tended

2.7. Remarks on the Impact of Using Nanoclay in Cement Composites

Nanoclay particles can be used in a modified or unmodified physical state, depending on their properties. From the scientific literature analysis, it can be stated that nanoclay has a positive impact as it succeeds in diminishing some of the weak points characteristic to mortar and concrete, the newly composite being characterized by:

- higher values of tensile, flexural and compressive strength, for both specimens kept at room temperature and subjected to high temperatures
- lower water absorption percentage and water penetration depth
- lower plastic shrinkage
- extended reinforcement deterioration time

The combined physical and chemical properties of nanoclay make this nanomaterial suitable for use in mortar/concrete mixes. Although all results concur to this idea, the values differ from one study to another, especially the ones related to the mechanical properties. At this moment, most of the related studies are focused on the cement paste. Therefore, there is a great gap of knowledge regarding mortar and, especially, concrete modified with nanoclay. Moreover, taking into account the promising values of compressive strength for specimens subjected to high temperatures and the lack of research in this area, more studies should be conducted on this subject.

3. Influence of Titanium Dioxide on Cement-Based Materials

The use of titanium dioxide (TiO_2) in the construction industry did not have a structural purpose in the beginning, but a more architectural and ecological one. Torre de Especialidades from Mexico City and the Jubilee Church in Rome Italy are two of the buildings for which titanium dioxide was used in the concrete formula with the purpose of decreasing the level of pollutants, i.e., nitrogen oxide and nitrogen dioxide. Except the practical application, the esthetics of these buildings stands out not only due to the architecture but also due to their bright whiteness [58–61].

As a nanomaterial, TiO_2 captured the interest of researchers in the fields of building services and electrotechnics. It started to be used in photovoltaic cells, in the composition of semiconductors and even in bio-medical applications and cancer therapy [62]. Moreover, as its properties have the potential to improve the strength and durability of cement mortar and concrete elements, the research in civil engineering is still on-going. The positive influence on both ecology and civil engineering is a material property which is constantly searched for, in view of the new stricter regulations in terms of greenhouse gas emissions. Titanium dioxide combines, at a certain level, these two areas of interest. In addition, TiO_2 is a naturally occurring oxide, being found in the Earth's crust [63], its addition to concrete enhancing the sustainability index of the new material [64].

3.1. Chemical Structure and Properties—Types of TiO_2 Used in Cement Mortar and Concrete

The crystalline structure of titanium dioxide, TiO_2, is found in three main different forms: anatase, rutile and brookite. Both anatase and rutile have a tetragonal crystal structure, while brookite has an orthorhombic crystal structure [63,65,66]. From these three crystal structures, the most commonly used in civil engineering are anatase and rutile. Both are wide band gap semiconductors, meaning that they can resist higher temperatures, unlike brookite [65,67].

Rutile is considered as the most stable form of titanium dioxide but only for a particle size greater than 35 nm. Below that size, the thermodynamic stability decreases. Another characteristic of rutile is its behavior at high temperatures. When the calcination temperature increases, its particle size increases also with a growth rate higher than in case of anatase [63]. Anatase, on the other hand, develops a higher photocatalytic activity than rutile and, thus, was preferred for various element coatings. Moreover, it was demonstrated that it has better success in breaking both inorganic and organic pollutants. On the other hand, it was shown that combining the anatase and rutile phases, leads to an increase in the photocatalytic activity [65,68]. This breaking of pollutants during the photocatalytic process begins when a light with enough energy strikes the material containing TiO_2, i.e., the catalyst, and an oxidation-reduction reaction takes place. During the process, the pollutants are mineralized, but the quantity of TiO_2 is not consumed. However, between 550 °C and 1000 °C anatase transforms into rutile, the transformation temperature depending on the existent impurities and the morphology of the sample [65,66,68].

Several general chemical properties of TiO_2 are listed in [66], with some of them making it adequate for use in mortar and concrete, such as its chemical stability, biocompatibility, low toxicity, and low cost compared with other nanomaterials.

3.2. Input of TiO_2 Particles in Cementitious Materials—Technological Flow

There are two possibilities of using TiO_2 combined with mortar or concrete. The first one is by introducing a certain quantity of nanomaterial in the cement matrix and mixing it. The other one is by coating the element with a special formula in order to protect the element from the exterior polluted environment. This study will focus on the first method, taking into account that the main interest is the material strength. Moreover, there is an important probability that the coating could be damaged during execution or service life [65]. Unlike nanoclay, titanium dioxide does not require any additional special mixing processes before being added to the cement matrix, as it does not have the tendency to flocculate. There are two methods of adding TiO_2 in the cement matrix, namely the wet and the dry mixing procedures.

In the first method, TiO_2 is introduced in water and mixed for several minutes. The cement and aggregates are mixed in dry conditions, separately. Afterwards, the water-nanomaterials solution is added to the dry mix, the rest of the water is added and a final mixing is performed. If there was fiber reinforcement to be added, e.g., PP fibers, it is introduced into the matrix in the final step and mixed again [58,69–71].

In the second method, the aggregates and all the powder materials, including TiO_2, are dry mixed together. The water is gradually introduced, along with the superplasticizer and mixed for 3–5 min until a proper consistency is reached [72–75].

3.3. Structural Influence of TiO_2

Similar to other nanoparticles, titanium dioxide nanoparticles have been used for their high specific surface area which can result in promoting the hydration reaction and for their pore-filling effect. In addition to these benefits, common to this size, TiO_2 has specific properties that make it attractive in its use in cementitious composites, such as its photocatalytic properties and thermal stability.

Titanium dioxide does not possess pozzolanic activity, as shown in several studies [59,76]. Nevertheless, it increases the rate of hydration due to the nanoparticles acting as nucleation sites. This process, together with the small size induced filling effect, creates a denser structure. It has been found that CH is influenced by the presence of these nanoparticles, which decrease the size of CH crystals either by limiting their growth space or by promoting accelerated CSH gels formation [59,76].

Studies on cement paste incorporating TiO_2 nanoparticles used TG analysis in order to render evident the hydration reaction acceleration [77]. It can be inferred that the pure cement specimen contains less non-evaporable water, chemically bound water, than the cement-titanium blend, which is a result of the presence of more hydration products [77].

3.4. Material Strength Improvements

Titanium dioxide nanoparticles succeed in improving the mechanical properties of cement mortar and concrete due to their chemical and physical properties. They are usually used in mortar/concrete mixes combined with superplasticizers in order to obtain a higher workability. Taking into account that TiO_2 is a non-reactive powder, there are studies in which pozzolans were added with the purpose of promoting the cement hydration reaction, e.g., fly ash, silica fume. In addition, in comparison with nanoclay studies, in the case of TiO_2, the number of scientific experiments made on mortars and concrete is significantly larger. This section of the state-of-the-art article presents the strength values of mortar and concrete modified with certain quantities of TiO_2 and other additives. The results will focus on the effect that TiO_2 has on the mortar and cement, with or without supplementary materials.

3.4.1. Splitting Tensile Strength

As in the case of nanoclay, the number of research works focusing on the tensile strength is less than in case of compressive strength. However, this mechanical property is also important, mainly from the point of view of cracks occurrence which must be prevented. Even micro-cracks can lead to an exponential decrease in the concrete and/or reinforced concrete durability. Due to the large specific surface area of TiO_2 particle there is more area available for the cement hydration reaction to occur and to produce more CSH, which leads to an increase in strength [78].

The value of the tensile strength of concrete when the cement was replaced with 1 wt% nano-TiO_2 was compared with the one obtained when the cement was replaced with 1 wt% nano-Fe_3O_4 [79]. The results showed that the TiO_2-modified specimen developed 18% higher values for the tensile strength. It should be noted that adding Fe_3O_4 to the mix results in values of the tensile strength smaller than the ones corresponding to the control specimen.

Other studies focused on the synergistic effect of using two nano-materials, e.g., both TiO_2 nanoparticles and carbon nanofibers (CNF) [80]. By adding only 0.2% and 0.4% of CNF in the cement matrix, the tensile strength values increased at about 3.90 MPa and 4.20 MPa, respectively. Compared with specimens containing only TiO_2, these values were much higher, proving that CNF have a higher efficiency in strength improvement than TiO_2. When introducing both CNF and TiO_2 nanoparticles in the composition, although

the values of the tensile strength were higher compared to the composite with a single type of nanomaterial addition, the dispersion deficiencies and particle agglomeration started to emerge. Thus, for the highest nanoparticle quantity combination considered, i.e., 0.4% CNF and 5% TiO_2, the tensile strength value was smaller than for the 0.4% CNF and 3% TiO_2 at 28 days of curing. Moreover, at 180 days of curing, the tensile strength value for the maximum nanoparticle combination became smaller than the composite having only 0.4% CNF and no TiO_2. Another remark that could be made regarding the values of the tensile strength for the 3% and 5% TiO_2 combination, after 90 days of curing, was that the difference between these values started to decrease slowly and reached almost the same value of 4.8 MPa at 180 days of curing [80].

In another study, ZnO and TiO_2 nanoparticles were used as supplementary materials to improve the mechanical properties of concrete containing 0.6% polypropylene fibers. The focus of the research work was to find the best combination for which a maximum strength was achieved. The cement was replaced with ZnO and TiO_2 in the following percentages: (1%; 0.5%), (2%; 1%), (3%; 1.5%), (4%; 2%), (5%; 2.5%). For the splitting tensile strength, the best combination was (4%; 2%), which proved that both ZnO and TiO_2 have a positive effect on the material properties. However, when the nanomaterials quantities were increased to (5%; 2.5%), a decrease in the values of the tensile strength was registered due to the problems in nanoparticles dispersion [71].

Table 6 lists a series of research works in which various cement mortar or concrete specimens modified with TiO_2 nanoparticles were tested to obtain the values of the tensile strength at 28 days of curing. It should be noted that the list focuses on the research works that used TiO_2 as principal nanomaterial.

Table 6. Splitting tensile strength values mortar/concrete specimens modified with TiO_2 nanoparticles, at room temperature.

Study	Type of TiO_2	Type of Sample	Standard	w/b w/c	Additives	TiO_2 %	Splitting Tensile Strength [3] [MPa]
[78]	Type not specified (probably anatase)	concrete	-	w/c 0.45	Sulphonated naphthalene formaldehyde (superplasticizer)	0 0.5 1 1.5	3.45 3.54 3.76 3.65
[79]	Type not specified (probably anatase/rutile combination)	concrete	-	w/c 0.57	-	1	3.36
[80]	Type not specified (probably anatase)	concrete	ASTM C496	w/c 0.45	Polycarboxylate-based HRWR [1] agent (superplasticizer)	0 3 5	approx. 3.00 approx. 3.60 approx. 3.30
[70]	White powder (probably anatase)	concrete	-	w/c 0.38	15% Silica fume Sika ViscoCrete-3425 superplasticizer	0 0.5 1 1.5	3.37 4.39 4.93 4.76
[81]	Type not specified (probably anatase)	concrete	ASTM C496	w/b 0.40	-	0 0.5 1 1.5 2	1.80 2.60 3.00 2.70 1.90
[82]	Type not specified (probably anatase)	SCC [2]	ASTM C496	w/b 0.40	Polycarboxylate (superplasticizer)	0 1 2 3 4 5	1.60 1.60 2.00 2.50 2.90 2.60

[1] High-range water reducer. [2] Self-compacting concrete. [3] Some values were approximated from the graphics, associated with the cited scientific research.

The main common observation of these studies is that for high nanoparticle quantities, the value of the tensile strength decreased. Two main reasons are given for this phenomenon in the scientific literature. The first one is the dispersion difficulties that emerge when adding high percentages of nanoparticles as it increases the probability of agglomeration occurring. The second one is that if the quantity of TiO_2 was greater than the quantity needed for CH hydration, an excess of silica would be found inside the cement matrix, leading to a decrease in strength [70,81]. This percentage varies, but the majority of the listed research works showed that 1% cement replacement with TiO_2 is the quantity for which a maximum value of the tensile strength was obtained in case of concrete specimens [70,78,81].

The highest values of the tensile strength compared to the other studies was reported in [70]. It this case, the addition of 15% silica fume proved its efficiency [70]. The lowest values were obtained for the self-consolidated concrete specimens and plain concrete, respectively, both modified with various TiO_2 percentages [81,82].

Altogether, the TiO_2 nanoparticle addition in the cement matrix leads to a definite increase in the values of the splitting tensile strength, as the specific surface area increases and CSH particles formation accelerates. However, the increment is not well defined as it depends on a series of variables which are different, usually, from study to study, e.g., additives, water/cement or water/binder ratio, type of cement, type of mixing, particle size etc.

3.4.2. Flexural Tensile Strength

The flexural strength for various combinations of CNF and TiO_2 nanoparticles added in concrete was also investigated [80]. All combinations had a higher strength value than the control sample. However, the specimens containing CNF had superior strength, whereas the 5% TiO_2 mix had the smallest strength value from the modified formula samples. When combining 0.4% CNF with 3% and 5% TiO_2, the highest flexural strength values were obtained. In case of flexural tensile strength, unlike the splitting tensile test results, all CNF mixes, including combinations, led to superior strength values, especially after 180 days of curing. Therefore, the combination 0.2% CNF and 5% TiO_2 registered, at 180 days of curing, a value of the flexural strength smaller than that of the sample with only 3% TiO_2. These results confirm the observations made in the case of splitting tensile strength, that as the quantity of nanoparticle increases above a certain critical level, the strength begins to decrease because silica accumulates within the matrix and particle agglomerations occur [80]. For the flexural strength tests carried out on ZnO and TiO_2 specimens, the best combination was (4%; 2%) [71].

Table 7 summarizes the values for the flexural tensile strength for a series of studies on concrete specimens modified with a certain quantity of TiO_2 nanoparticles, stored at room temperature, after 28 days of curing.

For the TiO_2 modified cement mortar, the values of the flexural tensile strength were higher than in the case of concrete specimens. When adding coarse aggregates, although the compressive strength increased, voids occurred at the interfacial transition zone, which tended to develop under tensile stresses. Therefore, these voids led to smaller values for splitting and flexural tensile strength. However, the nanoscale particles have a filler effect on the matrix due to their reduced size. They can enter these voids and reconstruct the ITZ so that the weak areas are reduced in size and the development of microcracks is either slowed down or completely arrested. This phenomenon was observed by comparing the strength increment when adding TiO_2 nanoparticles in the matrix, in both cement mortar and concrete, respectively. Higher strength differences were registered for concrete specimens when they were modified with TiO_2 compared with the control samples, i.e., greater than 1 MPa [80–82]. However, in case of cement mortar, these improvements in the flexural tensile strength remained smaller than 1 MPa [83–85].

Table 7. Flexural strength values mortar/concrete specimens modified with TiO_2 nanoparticles, at room temperature.

Study	Type of TiO_2	Type of Sample	Standard	w/b w/c	Additives	TiO_2 %	Flexural Strength [3] [MPa]
[80]	Type not specified (probably anatase)	concrete	ASTM C78	w/c 0.45	Polycarboxylate-based HRWR [1] agent (superplasticizer)	0 3 5	approx. 4.00 approx. 5.20 approx. 4.50
[83]	Type not specified (probably anatase)	Cement mortar	ASTM C293	w/b 0.485	30% Fly ash by weight of cement	0 1 3 5	approx. 5.15 approx. 5.15 approx. 5.70 approx. 5.15
[81]	Type not specified (probably anatase)	concrete	ASTM C293	w/b 0.40	-	0 0.5 1 1.5 2	4.40 5.10 5.50 5.40 5.10
[82]	Type not specified (probably anatase)	SCC [2]	ASTM C293	w/b 0.40	Polycarboxylate (superplasticizer)	0 1 2 3 4 5	4.20 4.00 4.90 5.60 6.30 6.00
[84]	anatase	Cement mortar	Chinese standard	w/c 0.32	-	0 0.1 1	10.10 10.80 9.60
[85]	anatase	Cement mortar	ASTM C348	w/b 0.40	GGBFS [2] Polycarboxylate (superplasticizer)	0 3 6 9 12	approx. 5.30 approx. 5.50 approx. 4.40 approx. 4.00 approx. 3.80

[1] High-range water reducer. [2] Ground granulated blast furnace slag. [3] Some values were approximated from the graphics, associated with the cited scientific research.

Experiments conducted based on the Chinese standard resulted in the highest flexural strength values, reaching up to 10 MPa for cement mortar [84]. However, the researchers who used ASTM norms, whether or not additives were used, obtained values in the range of 4.0–6.0 MPa [80–83,85].

Taking into account the variability in TiO_2 percentages from one study to another and the difference in results, there is no optimum percentage which can be clearly defined. Smaller percentage increments, i.e., smaller than 1%, should be selected and the range of their variability should be larger in order to be able to thoroughly analyze the dependency between strength and the quantity of TiO_2 introduced. However, there is a certain trend which is also respected in the case of flexural tensile strength, namely, as the quantity of TiO_2 exceeded a certain level, the value of the flexural strength decreased.

3.4.3. Compressive Strength

The most important material property of both cement mortar and concrete is their compressive strength. As in the case of nanoclay, some studies subjected the specimens to high temperatures while others analyzed the samples only at room temperature. Taking into account that the high temperature tests are conducted in steps, for different temperature levels, corresponding to various physical and chemical phenomena, they are separately presented in the present paper.

Compressive Strength Values Obtained at Room Temperature

In case of compressive strength, a similar trend of the results was obtained as for flexural strength [80]. The CNF modified concrete exhibited the highest values of the compressive strengths compared with the specimens modified only with TiO_2. However, the maximum strength from the analyzed samples corresponds to a concrete specimen modified with both CNF and TiO_2 nanoparticles, i.e., 0.4% CNF and 3% TiO_2. Similar to the flexural tensile strength, the samples of CNF+ TiO_2 having 5% TiO_2 exhibited lower compressive strength value than the corresponding CNF modified concrete samples but without the TiO_2 addition. The trend was maintained at least up to 180 days of curing. Moreover, for the 0.2% CNF and 5% TiO_2, the registered values of the compressive strength was smaller than the 3% TiO_2 mix, at 28 days of curing [80].

Unlike the tensile strength case, the compressive strength of the 1% TiO_2 concrete specimens was lower than for the 1% Fe_3O_4 concrete specimens [79]. TiO_2 was used in combination with ZnO and 0.6% polypropylene fibers PPF to improve the concrete formula [71]. Samples were tested in compression according to the Indian standard IS: 516–1959. For both mixes, with or without PPF, the best nanomaterial combination was (4%; 2%) by weight of cement, the result being applicable for all curing ages (7, 14, 28 and 90 days). For the largest nanomaterial quantity, i.e., 5% ZnO and 2.5% TiO_2, the compressive strength value decreased at all ages below the values corresponding to the control sample [71].

Table 8 summarizes the values of compressive strength for concrete specimens modified with TiO_2 nanoparticles, kept at room temperature, and cured for 28 days.

The importance of TiO_2 nanoparticle dimension on the compressive strength value of cement mortar was demonstrated in [77]. The study employed two types on TiO_2, with dimensions of 21 nm and 350 nm. The mortar modified with larger TiO_2 particles had smaller values for the compressive strengths than the one with 21 nm. As the particle dimension increased, the specific surface area decreased, being promoted less CH for hydration and thus, less CSH in the cement matrix.

All samples registered a decrease in the values of mechanical properties after a certain TiO_2 quantity when the high number of particles increased the probability of flocculation and thus stress concentrations could occur. Moreover, as in the nanoclay case, when introducing a higher quantity of nanomaterial than the one needed for CH hydration, an excess of silica is available, resulting in a deficiency in strength [70]. The TiO_2 optimum percentage, from which this decrease initiated, and emphasized in Table 8, is not well defined when considering all the studies. It varies from 1% to 6% by weight of cement. High compressive strength was also obtained at 10%, according to [77], but there were no higher TiO_2 percentages analyzed, so there is no specific optimum TiO_2 percentage.

On the other hand, a previous study [60] reported that the values of the compressive strength decreased with the increase of TiO_2 percentage. Taking into account that the TiO_2 percentages analyzed in that study were relatively high, i.e., 5% and 10%, there is a high probability that the main cause of the obtained results was the agglomeration of nano particles during the mixing procedure.

To sum up, the compressive strength results presented in Table 8 demonstrate the positive effect that TiO_2 particles have on the cement mortar/concrete compressive strength. Unlike the case of the flexural tensile strength, there is no significant difference between the values of the compressive strength concrete and mortar, due to the fact that, during compression, the voids present in the ITZ tend to close.

Table 8. Compressive strength values mortar/concrete specimens modified with TiO_2 nanoparticles, at room temperature.

Study	Type of TiO_2	Type of Sample	Standard	w/b w/c	Additives	TiO_2 %	Compressive Strength [3] [MPa]
[80]	-	Concrete	ASTM C39	w/c 0.45	Polycarboxylate-based HRWR [1] agent (superplasticizer)	0	approx. 33.00
						3	approx. 42.00
						5	approx. 37.00
[83]	-	Cement mortar	ASTM C109M-16a	w/b 0.485	30% Fly ash by weight of cement	0	approx. 26.50
						1	approx. 33.00
						3	approx. 36.50
						5	approx. 30.70
[81]	-	Concrete	ASTM C39	w/b 0.40	-	0	36.80
						0.5	41.90
						1	43.40
						1.5	42.50
						2	39.30
[82]	-	SCC[2]	ASTM C39	w/b 0.40	Polycarboxylate (superplasticizer)	0	31.60
						1	35.20
						2	38.30
						3	44.50
						4	50.10
						5	48.70
[79]	-	Concrete	-	w/c 0.57	-	1	approx. 31.00
[85]	anatase	Cement mortar	ASTM C109	w/b 0.40	GGBFS [2] Polycarboxylate (superplasticizer)	0	approx. 40.00
						3	approx. 44.00
						6	approx. 46.00
						9	approx. 42.00
						12	approx. 36.00
[77]	75% anatase and 25% rutile (21 nm)	Cement mortar	ASTM C109	w/c 0.485	-	0	approx. 39.50
						5	approx. 47.50
						10	approx. 49.00
	99% anatase (350 nm)					5	approx. 43.00
						10	approx. 44.50
[69]	Rutile and anatase	Cement mortar	-	w/b 0.45	-	0	43.70
						1	47.60
						3	48.20
						5	48.80
[86]	Anatase and rutile—Aeroxide P25	High strength mortar	ASTM C109	w/b 0.35	2% naphthalene sulfonate base superplasticizer 5% silica fume	0	approx. 55.00
						1	approx. 63.00
						2	approx. 64.00
						3	approx. 61.00
[70]	White powder (probably anatase)	Concrete	-	w/c 0.38	15% Silica fume Sika ViscoCrete-3425 superplasticizer	0	49.86
						0.5	55.74
						1	58.79
						15	57.42
[60]	80% anatase and 20% rutile	ECC [1]	ASTM C109	w/c 0.30	PVA [2]	0	66.53
						5	60.05
						10	58.49
[78]	-	Concrete	-	w/c 0.45	Sulphonated naphthalene formaldehyde (superplasticizer)	0	33.00
						05	35.00
						1	38.00
						1.5	30.00
[75]	-	Concrete	BS 1881-part 116	w/c 0.40	Superplasticizer	0	34.00
						2	41.40
						4	44.20
						6	48.40
						8	46.50
[76]	-	Cement mortar	-	w/c 0.50	-	0	approx. 50.00
						1	approx. 50.00
						2	approx. 52.00
						5	approx. 48.00

[1] Engineered cementitious composite. [2] Polyvinyl alcohol fibers. [3] Some values were approximated from the graphics, associated with the cited scientific research.

Compressive Strength Values at Elevated Temperatures

Considering the filler effect that titanium dioxide has upon the cement matrix, along with promoting of the development of hydration compounds, it has been proven that the TiO_2 introduction in the cement matrix succeeded in improving the material strength to

elevated temperatures. Table 9 presents some of the compressive strength results on cement mortar/concrete when the specimen was subjected to elevated temperatures.

Table 9. Compressive strength values for TiO_2—mortar/concrete specimens at high temperature.

		[86]				[87]			
TiO_2 [%]		**0**	**1**	**2**	**3**	**0**	**2**	**4**	**6**
Compressive strength [1] [MPa]	25 °C	55	63	64	61	33	36.3	46.2	48
	100 °C	47	58	62	54				
	200 °C	46	52	58	51	38	43.5	47	54
	300 °C	35	46	51	48				
	400 °C	35	47	49	44	35	42	46	51.5
	600 °C	31	37	35	31	25	31	33.5	38.5
	800 °C	17	17	22	17				
	1000 °C	6	6	7	5				

[1] All values are approximated from the graphics, associated with the cited scientific research.

A high strength mortar was modified with 1%, 2% and 3% Aeroxide P25, i.e., a multiphasic titanium dioxide containing both anatase and rutile. A 5% silica fume and a superplasticizer were added in the mix. The water to binder ratio was maintained at 0.35 [86]. On the other hand, another study focused on heavy concrete samples, having a density greater than 2600 kg/m^3 with magnetite aggregates of 25 mm maximum size. The authors modified the samples by adding 2%, 4% and 6% TiO_2 as a cement replacement [87]. Although the difference between the values obtained in the two studies was expected to occur, the positive influence of TiO_2 is evident in both cases.

However, while a 2% TiO_2 was obtained as the optimum percentage for the compressive strength of, for all temperatures [86], as shown in Figure 4a, the maximum strength was recorded at the maximum nanoparticle addition of 6% [87], as seen in Figure 4b. Taking into account the use of magnetite aggregates, they will have a different behavior to high temperatures than the normal aggregates used in previous studies. Moreover, only fine aggregates were used in [86], thus obtaining a more homogeneous sample with less voids and less disturbances than in [87]. Therefore, a comparison between these two studies can be made only by analyzing the positive variation that TiO_2 had on the samples. Although the compressive strength decreased for the 3% TiO_2 sample, it still remained higher than the one corresponding to the control sample up to 400 °C [86]. After this temperature limit, the compressive strength maintained a value approximately equal with the one associated to the control specimen.

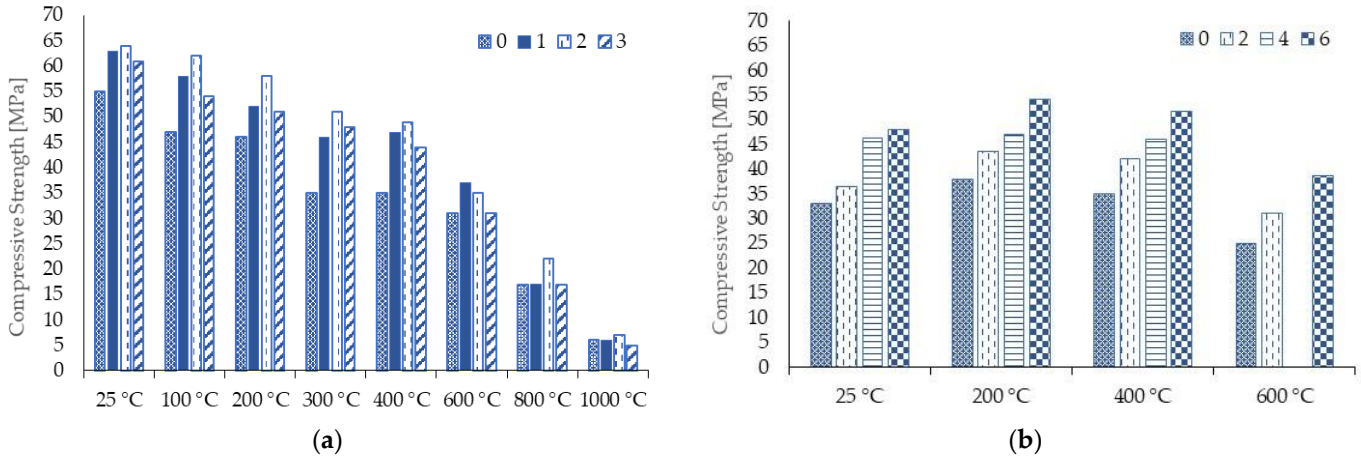

Figure 4. Variation in compressive strength as function of temperature and different percentages of TiO_2. (**a**) results reported in [86]; (**b**) results reported in [87].

3.5. Durability Tests

When the TiO_2 nanoparticles are introduced in the cement matrix, due to their small size, they start filling the existent voids, gathering around them CH compounds and promoting the CH hydration. Thus, the density of the specimen increases and water absorption is expected to decrease. For the anatase-based modified cement mortar used in [85], a constant decrease in water absorption up to the maximum considered TiO_2 percentage, from approximately 9%—for 0 wt% TiO_2, to 7%—for 12 wt% TiO_2 was recorded. These results were confirmed by [82]. A comparison between the influence of 1% Fe_3O_4 and 1% TiO_2 on concrete water absorption was conducted in [79]. From the analysis, nano-titania particles succeeded in restricting the water absorption better than Fe_3O_4, also having a smaller void ratio.

As the water absorption and void ratio decreased, the probability of liquid infiltration was significantly reduced, as the chloride and sulphate exposure analyses proved. A higher level of steel reinforcement corrosion protection was gained by using nano-TiO_2 as supplementary material in concrete, according to [79]. The potentio-dynamic polarization test confirmed the benefits of using TiO_2 in the cement matrix as the reinforcement corrosion rates were lower for all adverse exposure environments studied (tap water, saline water, acidic solution), compared to the control specimen [69].

However, it was recommended that all cementitious materials using nano-titania as additive should be specially designed to sulphate attack, as the expansion rate of the mortar increased with the quantity of TiO_2 and important cracks occur, compared to the control sample [85].

Table 10 summarizes the findings in terms of durability tests on mortar and concrete samples enhanced with TiO_2.

Table 10. Durability tests on TiO_2—mortar/concrete specimens.

Measured Parameter	Scientific Paper	Type of Sample	TiO_2 Percentage	Observation
Water absorption percentage	[85]	Cement mortar	0; 3; 6; 9; 12	- Decrease in water absorption with the increase in TiO_2 content
	[82]	SCC	0; 1; 2; 3; 4; 5	- During the first 2 days, the water absorption percentage increased compared to the control sample - For 7 and 28 days of curing, the water absorption percentage decreased compared to the control sample
	[79]	Concrete	1	- Nano-TiO_2 particles restrict water absorption better than Fe_3O_4
Durability to chloride and sulphate ions (corrosion potential)	[79]	Concrete	1	- Nano-TiO_2 leads to a higher level of steel reinforcement corrosion protection than Fe_3O_4
	[69]	Cement mortar	0; 1; 3; 5	- Reinforcement corrosion rates were lower for all adverse exposure environments studied compared to control samples - The optimum TiO_2 percentage was 5 wt%
Expansion rate	[85]	Cement mortar	0; 3; 6; 9; 12	- The expansion rate of the mortar increases with the quantity of TiO_2 and important cracks occur, compared to control sample

3.6. Remarks on the Impact of Using TiO_2 in Cement Composites

Titanium dioxide is a nanomaterial with multiple benefits, in various areas of interest, which has proven its significance in the field of civil engineering. Its nano-sized structure characterized by a large specific surface area promotes the acceleration of the CH hydration activity. Its filling effect, together with a high quantity of hydration products, i.e., CSH, results in higher values of compressive, flexural and splitting tensile strength compared to the control specimens. The filling effect also decreases the void ratio and the water absorption, increasing the reinforcement protection against tap/saline water or acidic solutions.

4. Conclusions

Nanomaterials have proven their benefits when used in cement mortar or concrete. Their size and chemical properties largely improve the strength and physical characteristics of cementitious composites. Nanoclay acts as a pozzolanic and filler nanomaterial, while titanium dioxide is an inert filler and promotor of nucleation sites for CSH development. Both nanoclay and titanium dioxide nano-particles succeed in promoting CH hydration when added to the cement matrix, thus leading to strength improvements. The water absorption decreases as well as the void ratio, increasing the reinforcement protection to corrosion. For both of them, the behavior is enhanced when subjected to high temperatures, compared with the control samples. Practically, they both improve the mechanical and physical characteristics of cement mortar and/or concrete. However, the manner in which this improvement is manifests varies.

The use of NC definitely influences the values of the splitting tensile strength for both mortar and concrete in a positive manner. However, the magnitude of this improvement greatly varies from one study to another because of the type of NC used and water/binder ratio. However, the use of montmorillonite-based NC shows its influence at lower percentages by weight of cement, for both mortar (2 wt%) and concrete (1 wt%), than metakaolin based NC (8 wt%). Based on the analyzed data, the rate of improvement also greatly depends on the water/binder ratio.

Similar conclusions can be drawn in terms of flexural tensile strength of cement-based mortar and concrete. For mortars, both natural hydrophilic montmorillonite and organo-montmorillonite based NC shown similar rates of improvement, compared to the reference mix, for 2 wt% replacement of cement for natural hydrophilic montmorillonite NC and 1 wt% replacement for organo-montmorillonite based NC. On the other hand, the use of calcinated hydrophilic montmorillonite NC leads to highest values in terms of flexural tensile strength of mortars when used in 5 wt% replacement of cement. For concrete mixes, metakaolin based NC should be used in higher percentages (8 wt% of cement) to obtain the highest values for the flexural tensile strength as compared to montmorillonite NC which leads to the best results at only 1 wt% of cement.

The compressive strength of both mortar and concrete are positively influenced by the addition of nanoclay, but the rate of improvement is different from mortar to concrete. Lower percentages of montmorillonite-based NC are required to obtain the highest values of compressive strength compared to metakaolin based NC. While for the former the highest values of the compressive strength of mortar are obtained at 0.5 wt% in case of organo-montmorillonite and up to 5 wt% in case of calcinated hydrophilic montmorillonite NC, in case of metakaolin based NC a higher percentage is required, 8 wt% of cement. Similar observations can be made for concrete, although the exact type of NC is not clearly specified. For montmorillonite-based NC the percentage varies between 1 wt% and 3 wt%, while for metakaolin based NC the percentage stays unchanged, namely at 8 wt% of cement.

The loss of compressive strength at elevated temperatures is inversely proportional to the percentage of NC in concrete. Based on the available scientific data, the peak performance is reached for 2% natural hydrophilic montmorillonite NC at 200 °C, while a similar trend is observed at 5% calcinated hydrophilic montmorillonite NC at 250 °C.

In case of durability of cement mortar and concrete, the best values are reached for much lower values of NC percentages than in the case of mechanical properties. Most of

the available scientific literature reporting results on durability performance of nanoclay modified mortar and concrete focuses on the use of montmorillonite-based NC. Significant improvements are obtained for percentages as low as 0.4 wt% of cement.

On the other hand, titanium dioxide, with a smaller particle dimension, is only an inert filler which does not have the possibility to promote pozzolanic activity as nanoclay does. The CH hydration, in this case, is accelerated only by the nucleation effect.

Most of the studies related to the use of TiO_2 in cement-based mortar and concrete used anatase based nano TiO_2. Therefore, the scattering of the reported results in terms of the optimum content of TiO_2 is smaller compared to their counterparts using NC.

From the point of view of the splitting tensile strength most of the studies recommend an optimum percentage of 1 wt% of cement in order to obtain the highest increase in performance for regular concrete. Self-compacted concrete, on the other hand, requires a higher percentage of nano TiO_2, up to 4%.

For the flexural tensile strength, the use of nano TiO_2 in 3 wt% of cement results in the highest values both for mortar and concrete. In this case however, there seems to be a large discrepancy of the obtained results depending on the standard applied.

When it comes to the compressive strength, although improvements were reported for both mortar and concrete with nano TiO_2 addition, the reported results in terms of optimum nano-TiO_2 content varies significantly from one study to another. While for concrete the optimum percentage varies from 1 wt% of cement up to 6 wt% of cement, with most of the studies recommending 1% addition of nano TiO_2 for best performance gains, the interval is much larger in case of mortar. In this case, the optimum percentage varies from 2 wt% of cement and up to 10 wt% of cement. It should be pointed out that the larger recommended interval is due to the fact that the input parameters significantly changed from one study to another: supplementary cementitious materials (fly ash, GGBS, silica fume), type of TiO_2 (anatase and combinations of anatase and rutile in different percentages).

The decrease in the compressive strength values of concrete with nano TiO_2 subjected to elevated temperatures followed a similar trend with the one reported for NC. The use of higher percentages of nano TiO_2 resulted in significantly lower strength losses with the increase in temperature compared to the reference mix. The temperature threshold beyond which strength loss become significant is similar to the one reported for NC, namely 400 °C. This suggests that, in case of elevated temperatures, the limitation is related to the behavior of cement rather than the other constituent materials.

In terms of durability performance of mortar and concrete, the optimum percentage varies from one study to another. According to the available data, a 5 wt% of cement leads to the best performance in durability tests. Higher percentages result in slightly better performance but the benefit is not as significant, percentage-wise.

Each of the two nanomaterials presented in this study lack some properties from the other, while having other similar effects on the cementitious materials. Therefore, a combination of these two types of nanoparticles has the potential of improving the mortar and/or concrete properties beyond the level set by each nanomaterial on its own due to their synergistic effect. While the synergistic effect of using TiO_2 in combination with silica fume [70], CNF [80], fly ash [83] and GGBS [85] was rendered evident in some previous studies, the use of TiO_2 in conjunction with nanoclay was not so intensively studied and only recently a very limited number of studies emerged in this direction.

A recent study proved the potential of this combination by adding to concrete 1%, 2%, 3% and 4% nanoclay as fine aggregate and 1%, 2%, 3% and 4% TiO_2 as cement replacement. The best results were obtained for the 2%-TiO_2 and 3%-nanoclay combination, with a compressive strength increment of 48.64% compared to the control sample and 21.83% increment compared to the concrete modified with only 2% TiO_2 [88].

A similar research work investigated the combined used of TiO_2 and NC in fly ash geopolymer concrete [89]. The main difference between this study and the previous one resides in the fact that lower percentages were used; only 1% NC and 1.25% TiO_2, by mass of fly ash. Improvements were observed in the values of splitting tensile and compressive

strengths of investigated mixes. The SEM images revealed the absence of interfacial voids and crack in the ITZ and the formation of needle-like structures at the interface regions between paste and aggregates. Those formations were attributed to pozzolanc interaction between the nanomaterials and the promotion of the nucleation sites.

Both aforementioned studies showed that better material properties can be obtained when TiO_2 and NC are used together, compared to the case when they are individually used and that lower percentages of the two nanomaterials are needed to obtain those improved material properties compared to each nanomaterial used individually. However, there is a lack of research on this combination of nanomaterials, which, taking into account their beneficial potential, should be studied further.

Author Contributions: Conceptualization, I.-O.T. and G.B.; methodology, G.B., S.-M.A.-S., P.M. and I.-O.T.; formal analysis, G.B., S.-M.A.-S. and P.M.; investigation, G.B., S.-M.A.-S., P.M. and I.-O.T.; writing—original draft preparation, G.B. and S.-M.A.-S.; writing—review and editing, P.M. and I.-O.T.; supervision, P.M. and I.-O.T.; project administration, G.B.; funding acquisition, G.B. All authors have read and agreed to the published version of the manuscript.

Funding: This research was funded by the Romanian Government through the Ministry of Research, Innovation and Digitalization, grant number PN III 27PFE/2021; The APC was funded by The "Gheorghe Asachi" Technical University of Iasi.

Acknowledgments: This paper was realized with the support of COMPETE 2.0 Project nr. 27PFE/2021, financed by the Romanian Government, Ministry of Research, Innovation and Digitalization.

Conflicts of Interest: The authors declare no conflict of interest.

References

1. United Nations Environment Programme. *Global Status Report for Buildings and Construction 2021*; United Nations Environment Programme: Nairobi, Kenya, 2021.
2. European Union. EU Commission recommendation of 18 October 2011 on the definition of nanomaterial (2011/696/EU). *Off. J. Eur. Union* **2011**, *275*, 38–40.
3. Sikora, P.; Abd Elrahman, M.; Stephan, D. The Influence of Nanomaterials on the Thermal Resistance of Cement-Based Composites—A Review. *Nanomaterials* **2018**, *8*, 465. [CrossRef] [PubMed]
4. Saleem, H.; Zaidi, S.J.; Alnuaimi, N.A. Recent Advancements in the Nanomaterial Application in Concrete and Its Ecological Impact. *Materials* **2021**, *14*, 6387. [CrossRef] [PubMed]
5. Monteiro, H.; Moura, B.; Soares, N. Advancements in nano-enabled cement and concrete: Innovative properties and environmental implications. *J. Build. Eng.* **2022**, *56*, 104736. [CrossRef]
6. Duquesne, S.; Jama, C.; Le Bras, M.; Delobel, R.; Recourt, P.; Gloaguen, J. Elaboration of EVA–nanoclay systems—Characterization, thermal behaviour and fire performance. *Compos. Sci. Technol.* **2003**, *63*, 1141–1148. [CrossRef]
7. Park, J.H.; Jana, S.C. The relationship between nano- and micro-structures and mechanical properties in PMMA–epoxy–nanoclay composites. *Polymer* **2003**, *44*, 2091–2100. [CrossRef]
8. Xu, L.; Lee, L.J. Effect of nanoclay on shrinkage control of low profile unsaturated polyester (UP) resin cured at room temperature. *Polymer* **2004**, *45*, 7325–7334. [CrossRef]
9. Lee, H.-C.; Lee, T.-W.; Kim, T.-H.; Park, O.O. Fabrication and characterization of polymer/nanoclay hybrid ultrathin multilayer film by spin self-assembly method. *Thin Solid Films* **2004**, *458*, 9–14. [CrossRef]
10. LAU, K.; LU, M.; QI, J.; ZHAO, D.; CHEUNG, H.; LAM, C.; LI, H. Cobalt hydroxide colloidal particles precipitation on nanoclay layers for the formation of novel nanocomposites of carbon nanotubes/nanoclay. *Compos. Sci. Technol.* **2006**, *66*, 450–458. [CrossRef]
11. Lau, K.; Gu, C.; Hui, D. A critical review on nanotube and nanotube/nanoclay related polymer composite materials. *Compos. Part B Eng.* **2006**, *37*, 425–436. [CrossRef]
12. Kuo, W.-Y.; Huang, J.-S.; Lin, C.-H. Effects of organo-modified montmorillonite on strengths and permeability of cement mortars. *Cem. Concr. Res.* **2006**, *36*, 886–895. [CrossRef]
13. He, X.; Shi, X. Chloride Permeability and Microstructure of Portland Cement Mortars Incorporating Nanomaterials. *Transp. Res. Rec. J. Transp. Res. Board* **2008**, *2070*, 13–21. [CrossRef]
14. Chang, T.-P.; Shih, J.-Y.; Yang, K.-M.; Hsiao, T.-C. Material properties of portland cement paste with nano-montmorillonite. *J. Mater. Sci.* **2007**, *42*, 7478–7487. [CrossRef]
15. Dhiman, N.K.; Sidhu, N.; Agnihotri, S.; Mukherjee, A.; Reddy, M.S. Role of nanomaterials in protecting building materials from degradation and deterioration. *Biodegrad. Biodeterior. Nanoscale* **2022**, 405–475. [CrossRef]

16. Ali, S.W.; Basak, S.; Shukla, A. Nanoparticles: A potential alternative to classical fire retardants for textile substrates. *Handb. Nanomater. Manuf. Appl.* **2020**, 265–278. [CrossRef]
17. Yu, P.; Wang, Z.; Lai, P.; Zhang, P.; Wang, J. Evaluation of mechanic damping properties of montmorillonite/organo-modified montmorillonite-reinforced cement paste. *Constr. Build. Mater.* **2019**, *203*, 356–365. [CrossRef]
18. Irshidat, M.R.; Al-Saleh, M.H. Thermal performance and fire resistance of nanoclay modified cementitious materials. *Constr. Build. Mater.* **2018**, *159*, 213–219. [CrossRef]
19. Pavlidou, S.; Papaspyrides, C.D. A review on polymer–layered silicate nanocomposites. *Prog. Polym. Sci.* **2008**, *33*, 1119–1198. [CrossRef]
20. Nehdi, M.L. Clay in cement-based materials: Critical overview of state-of-the-art. *Constr. Build. Mater.* **2014**, *51*, 372–382. [CrossRef]
21. Kawashima, S.; Wang, K.; Ferron, R.D.; Kim, J.H.; Tregger, N.; Shah, S. A review of the effect of nanoclays on the fresh and hardened properties of cement-based materials. *Cem. Concr. Res.* **2021**, *147*, 106502. [CrossRef]
22. Moraes, M.K.; Maria da Costa, E. Effect of adding organo-modified montmorillonite nanoclay on the performance of oil-well cement paste in CO2-rich environments. *Cem. Concr. Compos.* **2022**, *127*, 104400. [CrossRef]
23. Lee, S.J.; Kawashima, S.; Kim, K.J.; Woo, S.K.; Won, J.P. Shrinkage characteristics and strength recovery of nanomaterials-cement composites. *Compos. Struct.* **2018**, *202*, 559–565. [CrossRef]
24. Papatzani, S.; Badogiannis, E.G.; Paine, K. The pozzolanic properties of inorganic and organomodified nano-montmorillonite dispersions. *Constr. Build. Mater.* **2018**, *167*, 299–316. [CrossRef]
25. Kalpokait-Dičkuvien, R.; Lukošiūt, I.; Ččsnien, J.; Baltušnikas, A.; Brinkien, K. Influence of the Organically Modified Nanoclay on Properties of Cement Paste. Available online: https://www.laviosa.com/wp-content/uploads/2015/01/LAVIOSA_Plastic_InfluenceOfTheOrganicallyModifiedNanoclayOnPropertiesOfCementPaste.pdf (accessed on 7 November 2022).
26. Kuo, W.-Y.; Huang, J.-S.; Yu, B.-Y. Evaluation of strengthening through stress relaxation testing of organo-modified montmorillonite reinforced cement mortars. *Constr. Build. Mater.* **2011**, *25*, 2771–2776. [CrossRef]
27. Papatzani, S.; Paine, K. *Nanotechnology in Construction*; Sobolev, K., Shah, S.P., Eds.; Springer International Publishing: Cham, Switzerland, 2015; ISBN 978-3-319-17087-9.
28. Alani, S.; Hassan, M.S.; Jaber, A.A.; Ali, I.M. Effects of elevated temperatures on strength and microstructure of mortar containing nano-calcined montmorillonite clay. *Constr. Build. Mater.* **2020**, *263*, 120895. [CrossRef]
29. Hakamy, A.; Shaikh, F.U.A.; Low, I.M. Characteristics of nanoclay and calcined nanoclay-cement nanocomposites. *Compos. Part B Eng.* **2015**, *78*, 174–184. [CrossRef]
30. Rehman, S.U.; Yaqub, M.; Ali, T.; Shahzada, K.; Khan, S.W.; Noman, M. Durability of Mortars Modified with Calcined Montmorillonite Clay. *Civ. Eng. J.* **2019**, *5*, 1490–1505. [CrossRef]
31. Wakoya, G.; Quezon, E.; Ararsa, W.; Chimdi, J.; Lemu, D.G. Effect and Suitability of Calcined Montmorillonite Clay Powder and Waste Khat Husk Ash in the Strength and Durability of C-25 Concrete and its Benefits Cost Analysis. *J. Sustain. Constr. Mater. Proj. Manag.* **2021**, *1*.
32. Said-Mansour, M.; Kadri, E.-H.; Kenai, S.; Ghrici, M.; Bennaceur, R. Influence of calcined kaolin on mortar properties. *Constr. Build. Mater.* **2011**, *25*, 2275–2282. [CrossRef]
33. Chandrasekhar, S.; Ramaswamy, S. Influence of mineral impurities on the properties of kaolin and its thermally treated products. *Appl. Clay Sci.* **2002**, *21*, 133–142. [CrossRef]
34. Badogiannis, E.; Kakali, G.; Tsivilis, S. Metakaolin as supplementary cementitious material. *J. Therm. Anal. Calorim.* **2005**, *81*, 457–462. [CrossRef]
35. Fadzil, M.A.; Nurhasri, M.S.M.; Norliyati, M.A.; Hamidah, M.S.; Ibrahim, M.H.W.; Assrul, R.Z. Characterization of Kaolin as Nano Material for High Quality Construction. *MATEC Web Conf.* **2017**, *103*, 09019. [CrossRef]
36. Siddique, R.; Klaus, J. Influence of metakaolin on the properties of mortar and concrete: A review. *Appl. Clay Sci.* **2009**, *43*, 392–400. [CrossRef]
37. Mansi, A.; Sor, N.H.; Hilal, N.; Qaidi, S.M.A. The Impact of Nano Clay on Normal and High-Performance Concrete Characteristics: A Review. *IOP Conf. Ser. Earth Environ. Sci.* **2022**, *961*, 012085. [CrossRef]
38. Firoozi, A.A.; Firoozi, A.A.; Baghini, M.S. A Review of Clayey Soils. *Asian J. Appl. Sci.* **2016**, *4*, 1319–1330.
39. Nisticò, R. A Comprehensive Study on the Applications of Clays into Advanced Technologies, with a Particular Attention on Biomedicine and Environmental Remediation. *Inorganics* **2022**, *10*, 40. [CrossRef]
40. Salam, H.; Dong, Y.; Davies, I. Development of biobased polymer/clay nanocomposites. In *Fillers and Reinforcements for Advanced Nanocomposites*; Elsevier: Amsterdam, The Netherlands, 2015; pp. 101–132; ISBN 9780081000823.
41. Patel, K. The Use of Nanoclay as a Constructional Material. *Int. J. Eng. Res. Appl.* **2012**, *2*, 1382–1386.
42. Mirgozar Langaroudi, M.A.; Mohammadi, Y. Effect of nano-clay on workability, mechanical, and durability properties of self-consolidating concrete containing mineral admixtures. *Constr. Build. Mater.* **2018**, *191*, 619–634. [CrossRef]
43. Irshidat, M.R.; Al-Saleh, M.H.; Sanad, S. Effect of Nanoclay on the Expansive Potential of Cement Mortar due to Alkali-Silica Reaction. *ACI Mater. J.* **2015**, *112*, 801–808. [CrossRef]
44. Liu, G.; Zhang, S.; Fan, Y.; Shah, S.P. Study on Shrinkage Cracking Morphology of Cement Mortar with Different Nanoclay Particles under Restraint. *Buildings* **2022**, *12*, 1459. [CrossRef]

45. Noori, A.; Yubin, L.; Saffari, P.; Zhang, Y.; Wang, M. The optimum percentage of nano clay (NC) in both direct-additive and sonicated modes to improve the mechanical properties of self-compacting concrete (SCC). *Case Stud. Constr. Mater.* **2022**, *17*, e01493. [CrossRef]
46. Morsy, M.S.; Alsayed, S.H.; Aqel, M. Effect of Nano-clay on Mechanical Properties and Microstructure of Ordinary Portland Cement Mortar. *Int. J. Civ. Environ. Eng. IJCEE-IJENS* **2010**, *10*, 21–25.
47. Tantawy, M.A. Effect of High Temperatures on the Microstructure of Cement Paste. *J. Mater. Sci. Chem. Eng.* **2017**, *05*, 33–48. [CrossRef]
48. Alarcon-Ruiz, L.; Platret, G.; Massieu, E.; Ehrlacher, A. The use of thermal analysis in assessing the effect of temperature on a cement paste. *Cem. Concr. Res.* **2005**, *35*, 609–613. [CrossRef]
49. Han, B.; Li, Z.; Zhang, L.; Zeng, S.; Yu, X.; Han, B.; Ou, J. Reactive powder concrete reinforced with nano SiO_2-coated TiO_2. *Constr. Build. Mater.* **2017**, *148*, 104–112. [CrossRef]
50. Mohammed, A.; Rafiq, S.; Mahmood, W.; Al-Darkazalir, H.; Noaman, R.; Qadir, W.; Ghafor, K. Artificial Neural Network and NLR techniques to predict the rheological properties and compression strength of cement past modified with nanoclay. *Ain Shams Eng. J.* **2021**, *12*, 1313–1328. [CrossRef]
51. Allalou, S.; Kheribet, R.; Benmounah, A. Effects of calcined halloysite nano-clay on the mechanical properties and microstructure of low-clinker cement mortar. *Case Stud. Constr. Mater.* **2019**, *10*, e00213. [CrossRef]
52. Emamian, S.A.; Eskandari-Naddaf, H. Effect of porosity on predicting compressive and flexural strength of cement mortar containing micro and nano-silica by ANN and GEP. *Constr. Build. Mater.* **2019**, *218*, 8–27. [CrossRef]
53. Zhang, A.; Yang, W.; Ge, Y.; Liu, P. Effect of nanomaterials on the mechanical properties and microstructure of cement mortar under low air pressure curing. *Constr. Build. Mater.* **2020**, *249*, 118787. [CrossRef]
54. Naji, H.F.; Khalid, N.N.; Alsaraj, W.K. Influence of Nanoclay on the Behavior of Reinforced Concrete Slabs. *IOP Conf. Ser. Mater. Sci. Eng.* **2020**, *870*, 012107. [CrossRef]
55. ali Shafabakhsh, G.; Janaki, A.M.; Ani, O.J. Laboratory Investigation on Durability of Nano Clay Modified Concrete Pavement. *Eng. J.* **2020**, *24*, 35–44. [CrossRef]
56. Irshidat, M.R.; Al-Saleh, M.H. Influence of Nanoclay on the Properties and Morphology of Cement Mortar. *KSCE J. Civ. Eng.* **2018**, *22*, 4056–4063. [CrossRef]
57. Wang, W.-C. Compressive strength and thermal conductivity of concrete with nanoclay under Various High-Temperatures. *Constr. Build. Mater.* **2017**, *147*, 305–311. [CrossRef]
58. Shafaei, D.; Yang, S.; Berlouis, L.; Minto, J. Multiscale pore structure analysis of nano titanium dioxide cement mortar composite. *Mater. Today Commun.* **2020**, *22*, 100779. [CrossRef]
59. Francioso, V.; Moro, C.; Martinez-Lage, I.; Velay-Lizancos, M. Curing temperature: A key factor that changes the effect of TiO_2 nanoparticles on mechanical properties, calcium hydroxide formation and pore structure of cement mortars. *Cem. Concr. Compos.* **2019**, *104*, 103374. [CrossRef]
60. Zhao, A.; Yang, J.; Yang, E.-H. Self-cleaning engineered cementitious composites. *Cem. Concr. Compos.* **2015**, *64*, 74–83. [CrossRef]
61. Tokuç, A.; Özkaban, F.F.; Çakır, Ö.A. Biomimetic Facade Applications for a More Sustainable Future. In *Interdisciplinary Expansions in Engineering and Design With the Power of Biomimicry*; InTech: London, UK, 2018.
62. Moradeeya, P.G.; Sharma, A.; Kumar, M.A.; Basha, S. Titanium dioxide based nanocomposites—Current trends and emerging strategies for the photocatalytic degradation of ruinous environmental pollutants. *Environ. Res.* **2022**, *204*, 112384. [CrossRef]
63. Janczarek, M.; Klapiszewski, Ł.; Jędrzejczak, P.; Klapiszewska, I.; Ślosarczyk, A.; Jesionowski, T. Progress of functionalized TiO_2-based nanomaterials in the construction industry: A comprehensive review. *Chem. Eng. J.* **2022**, *430*, 132062. [CrossRef]
64. Jayapalan, A.R.; Lee, B.Y.; Kurtis, K.E. Can nanotechnology be 'green'? Comparing efficacy of nano and microparticles in cementitious materials. *Cem. Concr. Compos.* **2013**, *36*, 16–24. [CrossRef]
65. Hamidi, F.; Aslani, F. TiO_2-based Photocatalytic Cementitious Composites: Materials, Properties, Influential Parameters, and Assessment Techniques. *Nanomaterials* **2019**, *9*, 1444. [CrossRef]
66. Castro-Hoyos, A.M.; Manzano, M.A.R.; Maury-Ramírez, A. Challenges and Opportunities of Using Titanium Dioxide Photocatalysis on Cement-Based Materials. *Coatings* **2022**, *12*, 968. [CrossRef]
67. Albetran, H.M. Thermal expansion coefficient determination of pure, doped, and co-doped anatase nanoparticles heated in sealed quartz capillaries using in-situ high-temperature synchrotron radiation diffraction. *Heliyon* **2020**, *6*, e04501. [CrossRef] [PubMed]
68. Mohamed, H.; Deutou, J.G.N.; Kaze, C.R.; Beleuk à Moungam, L.M.; Kamseu, E.; Melo, U.C.; Leonelli, C. Mechanical and microstructural properties of geopolymer mortars from meta-halloysite: Effect of titanium dioxide TiO_2 (anatase and rutile) content. *SN Appl. Sci.* **2020**, *2*, 1573. [CrossRef]
69. Daniyal, M.; Akhtar, S.; Azam, A. Effect of nano-TiO_2 on the properties of cementitious composites under different exposure environments. *J. Mater. Res. Technol.* **2019**, *8*, 6158–6172. [CrossRef]
70. Mustafa, T.S.; El Hariri, M.O.R.; Nader, M.A.; Montaser, W.M. Enhanced shear behaviour of reinforced concrete beams containing Nano-Titanium. *Eng. Struct.* **2022**, *257*, 114082. [CrossRef]
71. Reshma, T.V.; Manjunatha, M.; Bharath, A.; Tangadagi, R.B.; Vengala, J.; Manjunatha, L. Influence of ZnO and TiO_2 on mechanical and durability properties of concrete prepared with and without polypropylene fibers. *Materialia* **2021**, *18*, 101138. [CrossRef]
72. Moro, C.; Francioso, V.; Velay-Lizancos, M. Nano-TiO_2 effects on high temperature resistance of recycled mortars. *J. Clean. Prod.* **2020**, *263*, 121581. [CrossRef]

73. Nazari, A.; Riahi, S.; Shamekhi, S.F.; Khademno, A. Assessment of the effects of the cement paste composite in presence TiO_2 nanoparticles. *J. Am. Sci.* **2010**, *6*, 43–46.
74. Jalal, M. Durability enhancement of concrete by incorporating titanium dioxide nanopowder into binder. *J. Am. Sci.* **2012**, *8*, 289–294.
75. Nikbin, I.M.; Mohebbi, R.; Dezhampanah, S.; Mehdipour, S.; Mohammadi, R.; Nejat, T. Gamma ray shielding properties of heavy-weight concrete containing Nano-TiO_2. *Radiat. Phys. Chem.* **2019**, *162*, 157–167. [CrossRef]
76. Nochaiya, T.; Chaipanich, A. The effect of nano-TiO_2 addition on Portland cement properties. In Proceedings of the 2010 3rd International Nanoelectronics Conference (INEC), Hong Kong, China, 3–8 January 2010; Volume 2, pp. 1479–1480.
77. Chen, J.; Kou, S.; Poon, C. Hydration and properties of nano-TiO_2 blended cement composites. *Cem. Concr. Compos.* **2012**, *34*, 642–649. [CrossRef]
78. Aravind, R.; Devasena, M.; Sreevidya, V.; Vadivel, M. Dispersion Characteristics and Flexural Behavior of Concrete Using Nano Titanium Dioxide. *Int. J. Earth Sci. Eng.* **2016**, *9*, 443–447.
79. d'Orey Gaivão Portella Bragança, M.; Portella, K.F.; Gobi, C.M.; de Mesquita Silva, E.; Alberti, E. The Use of 1% Nano-Fe_3O_4 and 1% Nano-TiO_2 as Partial Replacement of Cement to Enhance the Chemical Performance of Reinforced Concrete Structures. *Athens J. Technology Eng.* **2017**, *4*, 97–108. [CrossRef]
80. Joshaghani, A. Evaluating the effects of titanium dioxide (TiO_2) and carbon-nanofibers (CNF) as cement partial replacement on concrete properties. *MOJ Civ. Eng.* **2018**, *4*, 29–38. [CrossRef]
81. Nazari, A.; Riahi, S.; Riahi, S.; Shamekhi, S.F.; Khademno, A. Improvement the mechanical properties of the cementitious composite by using TiO_2 nanoparticles. *J. Am. Sci.* **2010**, *6*, 98–101.
82. Nazari, A.; Riahi, S. The effect of TiO_2 nanoparticles on water permeability and thermal and mechanical properties of high strength self-compacting concrete. *Mater. Sci. Eng. A* **2010**, *528*, 756–763. [CrossRef]
83. Siang Ng, D.; Paul, S.C.; Anggraini, V.; Kong, S.Y.; Qureshi, T.S.; Rodriguez, C.R.; Liu, Q.; Šavija, B. Influence of SiO_2, TiO_2 and Fe_2O_3 nanoparticles on the properties of fly ash blended cement mortars. *Constr. Build. Mater.* **2020**, *258*, 119627. [CrossRef]
84. Doko, V.K.; Hounkpe, S.P.; Kotchoni, S.O.; Hui, L.; Datchossa, A.T. Changing Mechanicals Characteristiques of Cementitious Materials Using Titanium Dioxide. *Mater. Sci. Appl.* **2021**, *12*, 297–313. [CrossRef]
85. Qudoos, A.; Kim, H.; Ryou, J.-S. Influence of Titanium Dioxide Nanoparticles on the Sulfate Attack upon Ordinary Portland Cement and Slag-Blended Mortars. *Materials* **2018**, *11*, 356. [CrossRef]
86. Farzadnia, N.; Abang Ali, A.A.; Demirboga, R.; Anwar, M.P. Characterization of high strength mortars with nano Titania at elevated temperatures. *Constr. Build. Mater.* **2013**, *43*, 469–479. [CrossRef]
87. Nikbin, I.M.; Mehdipour, S.; Dezhampanah, S.; Mohammadi, R.; Mohebbi, R.; Moghadam, H.H.; Sadrmomtazi, A. Effect of high temperature on mechanical and gamma ray shielding properties of concrete containing nano-TiO_2. *Radiat. Phys. Chem.* **2020**, *174*, 108967. [CrossRef]
88. Selvasofia, S.D.A.; Sarojini, E.; Moulica, G.; Thomas, S.; Tharani, M.; Saravanakumar, P.T.; Kumar, P.M. Study on the mechanical properties of the nanoconcrete using nano-TiO_2 and nanoclay. *Mater. Today Proc.* **2022**, *50*, 1319–1325. [CrossRef]
89. Jumaa, N.H.; Ali, I.M.; Nasr, M.S.; Falah, M.W. Strength and microstructural properties of binary and ternary blends in fly ash-based geopolymer concrete. *Case Stud. Constr. Mater.* **2022**, *17*, e01317. [CrossRef]

Thin-Walled Structures 182 (2023) 110258

Contents lists available at ScienceDirect

Thin-Walled Structures

journal homepage: www.elsevier.com/locate/tws

Full length article

Shake table test and numerical analyses of a thin-walled Cold-Formed Steel structure: Part 1 — Investigation of the structural skeleton without claddings

George Taranu [a,*], Viorel Ungureanu [b], Zsolt Nagy [c], Mihai-Sergiu Alexa-Stratulat [a], Ionut-Ovidiu Toma [a], Septimiu-George Luca [a]

[a] The "Gheorghe Asachi" Technical University of Iasi, Faculty of Civil Engineering and Building Services, Department of Structural Mechanics, 700050, D. Mangeron no. 1, Iasi, Romania

[b] Politehnica University of Timisoara, Department of Steel Structures and Structural Mechanics, 300224, Ioan Curea no. 1, Timisoara, Romania

[c] Technical University of Cluj-Napoca, Faculty of Civil Engineering, No. 28, Memorandumului Street, Cluj-Napoca, 400114, Romania

ARTICLE INFO

Keywords:
Thin-walled cold-formed steel profiles
Seismic action
Shake table experimental testing
Nonlinear analysis

ABSTRACT

CFS structures are classified as structures with low ductility. Due to this, they are not recommended for medium to high seismic areas. The paper presents the results of a complex experimental program coupled with numerical investigations on the behavior of Cold Formed Steel (CFS) structures under seismic actions. The scaled-down model skeleton was made of DX51D+Z C-shaped 89 × 41 × 12 × 1 mm steel elements connected by 4.8 × 16 mm self-tapping screws (STS) and 5.5 × 25 mm self-drilling screws (SDS). This structure represents a replica of constructive solutions for single-story or one or two-storey structures that are frequently met in South-Eastern Europe, including highly active seismic areas.

The main purpose of the research program is to gather both quantitative and, more importantly, accurate information regarding structural response to dynamic actions characterized by input accelerations equal in amplitude to the maximum values specified in seismic design codes, up to PGA = 0.40 g. The damage of the joints and the reduction in the structural stiffness due to cyclic loads, such as the ones produced by earthquakes, change the structure's eigen period and significantly influence the structure's response to seismic actions. Larger gravitational loads lead to more extensive damage of the joints. The developed numerical model based on the experimentally determined connection axial rigidity can offer accurate results in terms of the fundamental frequency of vibration, relative accelerations and displacements. However, for a more accurate capturing of the local damages and onset of failure mechanisms, more complex numerical models are needed, which take into account non-linear material behavior.

The results presented in this paper help to design these structures as only the skeleton and serve as a starting point for future research work aimed to assess the influence of the sheathing on the global response of CFS structures to seismic actions. Additionally, research in the direction of improved joints with better energy dissipation properties is also pursued by the authors.

1. Introduction

The behavior of civil engineering structures to seismic motions is a continuous matter of investigation for researchers around the world. Besides ensuring the safety of the inhabitants and mitigating the damages to the structures and the stored goods in the framework of performance-based design, buildings also need to become economic and sustainable in the sense that their maximum performance should be obtained with the least material consumption. Currently available seismic design codes, such as EN 1998-1 [1] or the Romanian code [2] include a lot of information and details on the seismic design of steel structures. Based on their specifications, Thin-Walled Cold-Formed Steel Structures (TWCFSS) are classified as having low dissipative capabilities and the verification of structural elements included in Class 4 is made in accordance with EN 1993-1-3 [3], and EN 1993-1-5 [4], respectively. The seismic design codes limit the behavior factor q to 1.5 in [1] and to 1 in [2] because such structural systems without cladding materials have low energy dissipation capabilities. The values of the behavior factor q and the associated ductility classification which are given in the design codes, characterize the balance between resistance and energy-dissipation capacity. "For the design of structures classified as

* Corresponding author.
E-mail addresses: george.taranu@academic.tuiasi.ro (G. Taranu), viorel.ungureanu@upt.ro (V. Ungureanu), zsolt.nagy@dst.utclus.ro (Z. Nagy), mihai-sergiu.alexa-stratulat@staff.tuiasi.ro (M.-S. Alexa-Stratulat), ionut-ovidiu.toma@academic.tuiasi.ro (I.-O. Toma), septimiu-george.luca@academic.tuiasi.ro (S.-G. Luca).

https://doi.org/10.1016/j.tws.2022.110258
Received 24 May 2022; Received in revised form 11 August 2022; Accepted 10 October 2022
Available online 1 November 2022

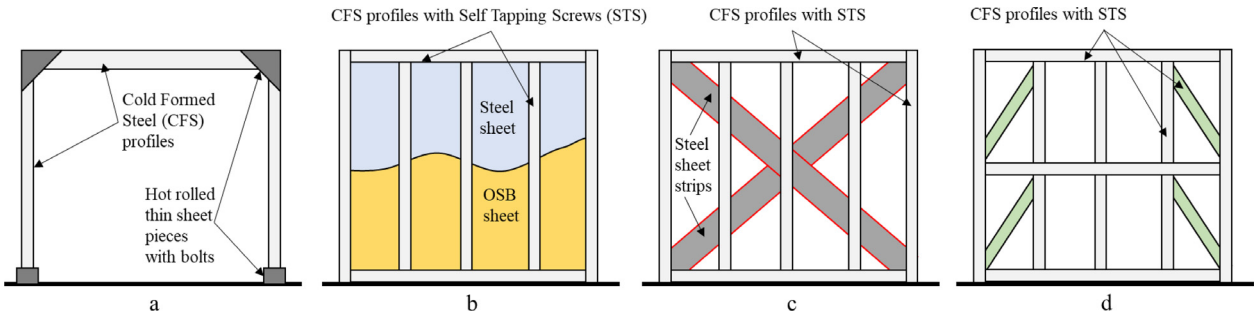

Fig. 1. Structural type systems: (a) frame system; (b) panel; (c) panel with strips diagonal; (d) panel with diagonals system.

Fig. 2. Real House structural systems — personal archive: (a) Romania, 2018, (b) Germany, 2018.

low-dissipative, no account is taken of any hysteretic energy dissipation and the behavior factor may not be taken, in general, as being greater than the value of 1.5 considered to account for overstrengths". "The behavior factor q is an approximation of the ratio of the seismic forces that the structure would experience if its response was completely elastic with 5% viscous damping, to the seismic forces that may be used in the design, with a conventional elastic analysis model, still ensuring a satisfactory response of the structure" [1]. In this study, the behavior factor was not used. Based on the presented results future numerical analyses will be developed in order to determine the appropriate value of the behavior factor for such types of structures.

The seismic behavior of hot-rolled steel structures was the main subject of research until 1990. Several approaches were considered from scaled-down models to structural sub-systems, to individual structural elements. A very powerful equipment used in such experimental investigations, both for hot-rolled and cold-formed steel structures, is the shake table. It is the only equipment that can simulate real seismic motions of either past earthquakes or artificially generated ones. However, due to its high initial and maintenance costs, most experimental works included pseudo-dynamic tests on structural elements or parts of structures that can lead to obtaining similar results. Another alternative would be the use of numerical simulations where various parameters could be changed and many different scenarios could be considered. However, these numerical models should be validated by laboratory tests in order to ensure the accuracy of the obtained results [5,6].

Thin-walled cold-formed steel structures elements started to attract more and more attention from 1990 because of their gradual implementation in civil engineering structures. Their use has seen a continuous grow and a significant number of studies were published in USA [7–13], Italy [14–22], Romania [23–28], Turkey [29], UK [30,31] or Asia [32–43]. Each study considered different CFS profiles, structural system of connectors for joining the elements. The most used structural typologies consisted in 3D frames with built-up cross-sections for the elements or framing elements to form rigid systems for structural applications. Fig. 1 presents 4 of the main CFS structural systems that are currently in use. The solution presented in Fig. 1a is that of a portal frame using built-up cross-sections for the elements. The elements are connected at the nodes by means of hot-rolled steel plates and bolts. These are the so-called moment-resisting frames where the seismic force is dissipated due to the moment–rotation capacity of the joint. On the other hand, in case of framing systems made of shear wall panels, Fig. 1b, sheathing with either Oriented Strand Boards — OSB panels or corrugated steel sheets, the seismic force is dissipated by the panels/sheets and the connectors used to fix the panels onto the steel framing.

In the case of framing systems with vertical studs and diagonal steel strips, as shown in Fig. 1c, the seismic force is resisted by the framing and the diagonal elements. On the other hand, the truss-like framing system with rigid diagonal elements, Fig. 1d, is able to dissipate the seismic energy mainly through the diagonal elements. In either of the presented structural systems, the presence of OSB, corrugated steel sheet or any other sheathing panels greatly contribute to the dissipation mechanism of the seismic force. The efficiency of a scaled down two storey model, using the same structural approach presented in Fig. 1c, to seismic motion was demonstrated in a series of shake table tests conducted in 2009 at the "Gheorghe Asachi" Technical University of Iasi [44]. Additional experimental investigations on different structural typologies were conducted from 2016 to the present day [7,8,20,37,45]. Such research works contribute to the general knowledge on the seismic behavior of steel structural systems and can be used to calibrate numerical models in order to conduct complex parametric investigations.

The structural model used in the present research is based on a framing concept with truss-like diagonal elements located in the marginal panels, as shown in Fig. 1d. Such system is frequently met in practice all over Europe, including in highly seismic active areas. Fig. 2 presents two examples of such structures built in Romania (see Fig. 2a), and Germany (see Fig. 2b), in 2018.

Fig. 3 presents an overview of a ground-floor building made from a combination of thin-walled cold-formed steel lipped channel profiles having the dimensions 89 × 41×12 × 1 mm and plain channel profiles with dimensions of 358 × 78×4 mm.

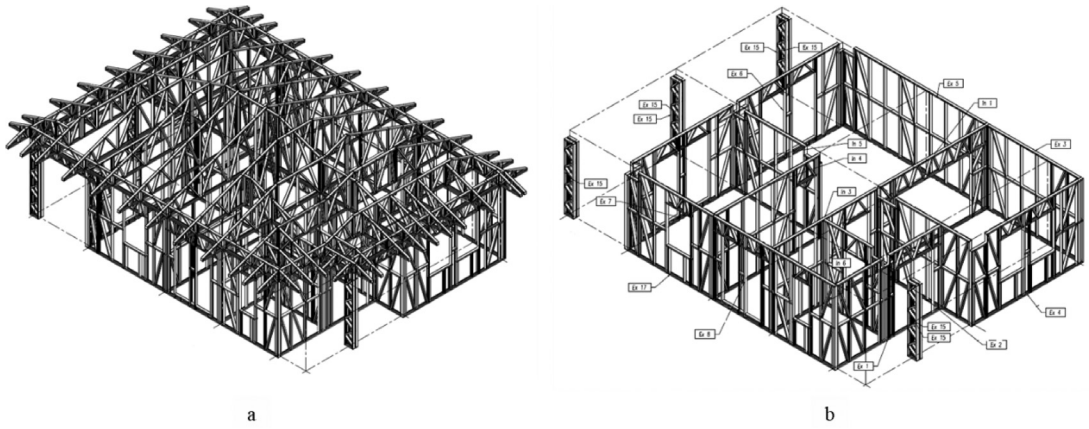

Fig. 3. Axonometry of typical one storey structural systems made of TWS profiles C89x41x12x1: (a) general assembly; (b) wall panel system.

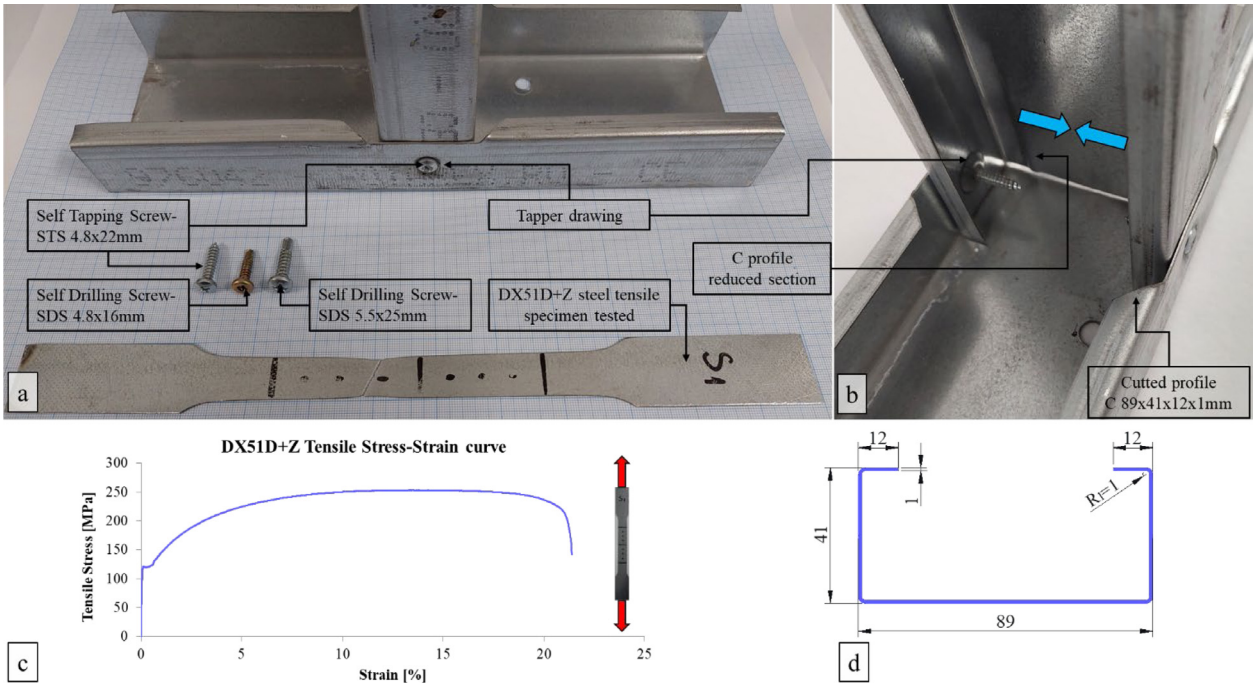

Fig. 4. (a) Materials and typical *T* joint connection; (b) perspective view of the connection with the interior; (c) average experimental tensile stress–strain curve of DX51D+Z steel sheet; (d) C profile section dimensions.

The lipped channels of 89 × 40×12 × 1 mm represents a relatively advantageous solution both for the end-user (beneficiary) and building-contractor due to its small overall dimensions. However, their use in structural elements to resist seismic loads should be considered only after significant experimental work in the laboratory. Such work could offer insightful information that can be used in the design practice. The obtained results are important data to calibrate numerical models based on FEM.

The present paper presents the results obtained from laboratory investigation on the material properties, behavior of T-joints to static and cycling loading scenarios and shake table tests to assess the behavior of the structural system made of CFS frames with truss-like diagonal elements in the central panels. The experimental program is accompanied by numerical simulations in order to create a computer model that is able to simulate, as accurately as possible, the real behavior of the scaled-down model to seismic actions. Both linear and non-linear analyses were conducted to render evident the differences between the two approaches.

2. Materials and methodology

2.1. Structural materials and connectors

The material properties of the steel sheet and connectors are presented in Table 1. The steel sheet used to obtain the steel profiles by cold-forming was DX51D+Z. Self-Tapping Screws (STS) with dimensions of 4.8 × 22 mm were used to connect the elements of the framing whereas Self Drilling Screws (SDS) with dimensions of 5.5 × 25 mm were used to connect the shear walls to each other. Additionally, the diagonal elements were connected by means of 4.8 × 16 mm SDS. The material properties of the steel sheet were experimentally determined by means of direct tensile tests on specimens cut from the profile web [46]. The material properties of the STS and SDS were the ones given by the manufacturer. The average stress–strain curve for the DX51D+Z steel is presented in Fig. 4a and the dimensions of the C-shaped profile are shown in Fig. 4b.

Table 1
Materials properties.

Element	Type	Elastic modulus (GPa)	Tensile yield strength (MPa)	Tensile ultimate strength (MPa)
Steel sheet C profiles — Fig. 4(a)	DX51D+Z	210	120 (exp)	250 (exp)
SDS — Fig. 4 (a) for profile connections ISO 15481 class (5.6) [47]	4.8 × 16 mm	210	300 [48]	500 [48]
SDS — Fig. 4 (a) for panel connections ISO 15481 class (5.6) [47]	5.5 × 25 mm	210	300 [48]	500 [48]
STS — Fig. 4 (a) for profile connections ISO 7049 class (5.6) [49]	4.8 × 22 mm	210	300 [48]	500 [48]

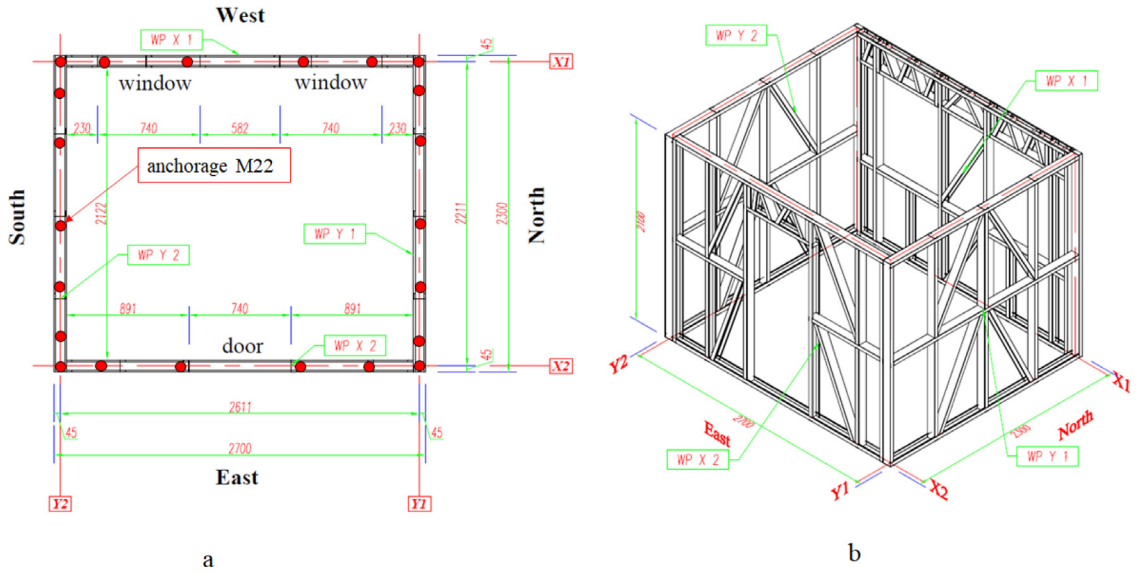

Fig. 5. (a) Plan view of the structural model; (b) Axonometry of the wall panels.

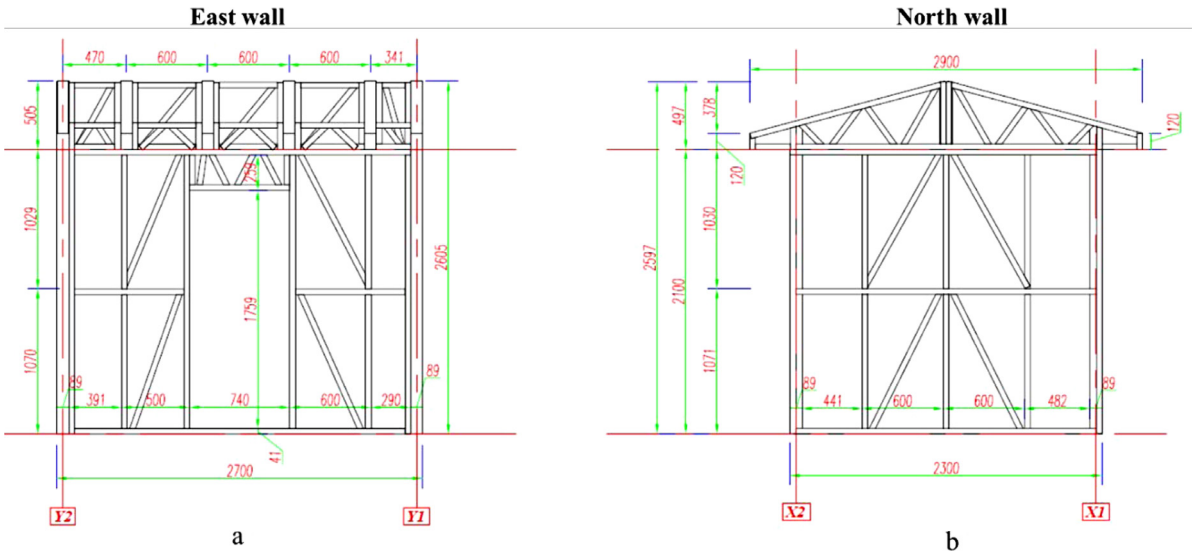

Fig. 6. Front views of the walls: (a) East wall, X1 direction; (b) North wall, Y1 direction.

2.2. Structural model assembly

The scaled-down model, presented in Fig. 5, had the in-plane dimensions of 2700 × 2300 mm, wall height of 2100 mm and the total height (at the ridge) of 2597 mm. The model was made of four panels. The roof was made of trusses with inclined upper chords, as shown in Fig. 6, transversally positioned (Y direction in Fig. 5). The stiffness of the roof was ensured by using truss panels located on top of the longitudinal wall panels (X direction in Fig. 5) and at the middle of transversal wall panels. The longitudinal wall panels had openings for windows and doors.

Fig. 5a presents the in-plane view of the model whereas Fig. 5b presents the axonometric view of the wall panels. The North–South direction of the model coincides with the X axis of the shake table along which the shaking motions will be induced. The East wall has a door opening with the dimensions of 740 × 1759 mm and the opposite, West,

Table 2
Similarity relationship and Cauchy similitude scaling factors.

Parameter	Symbol	Prototype	Model	Scale factor (prototype/ model)	Scale factor value
Length	L	3240 (mm)	2700 (mm)		
Width	w	2760 (mm)	2300 (mm)	$L_p/L_m = \lambda$	1.2
Height	h	3126 (mm)	2605 (mm)		
Steel profile section	sps	C 89 × 40 × 12 × 1 (mm)	C 89 × 40x12 × 1 (mm)	$L_p/L_m = \lambda$	1
Elasticity modulus	E	210000 (N/mm^2)	210000 (N/mm^2)	$e = E_p/E_m$	1
Specific mass	ρ	7850 (kg/m^3)	7850 (kg/m^3)	$\rho = \rho_p/\rho_m$	1
Mass	m	506 (kg)	293 (kg)	$m = m_p/m_m = \lambda^3$	1.728
Displacement	d			$d = d_p/d_m = \lambda$	1.2
Velocity	v			$v = v_p/v_m$	1
Acceleration	a			$a_p/a_m = 1/\lambda$	0.833
Time	t			$t_p/t_m = \lambda$	1.2
Frequency	f			$f_p/f_m = \frac{1}{\lambda}$	0.833

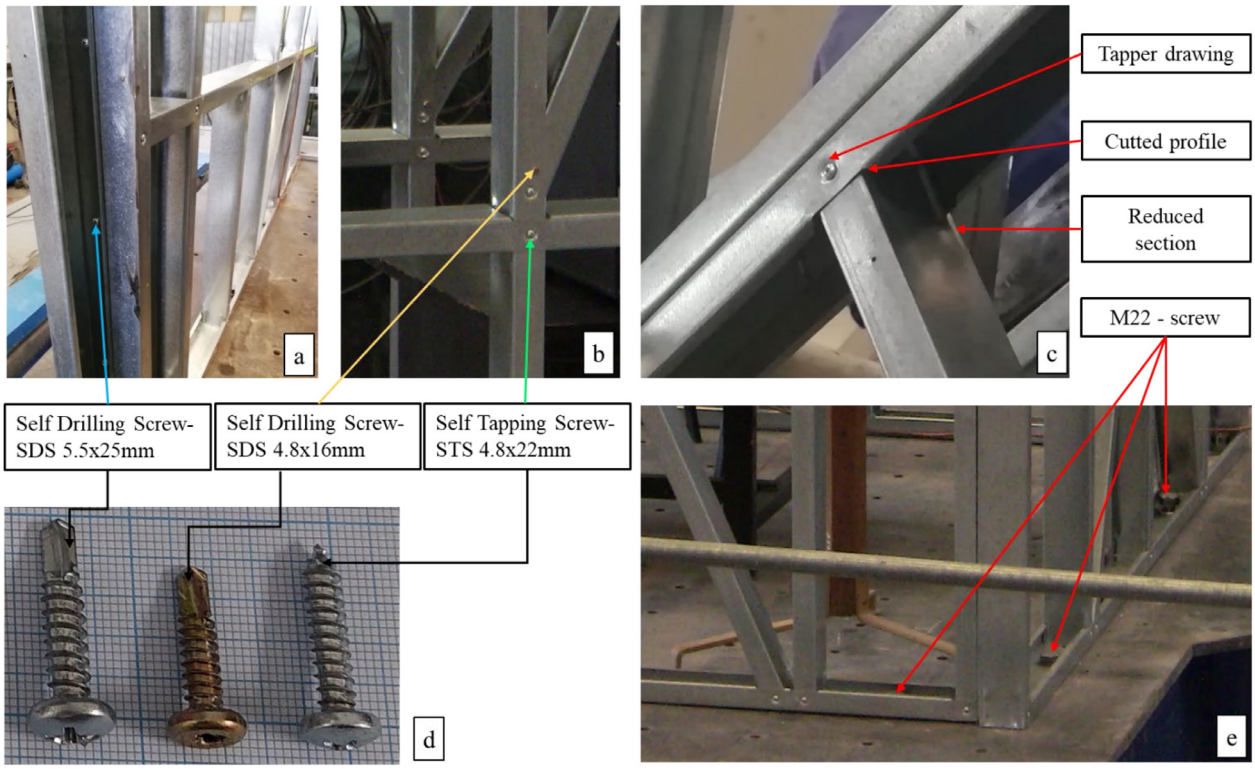

Fig. 7. Connection details: (a) panel intersection connection; (b) current joint of diagonals; (c) upper part T joint connection; (d) screws details; (e) base fixing detail.

wall had two window openings with dimensions of 740 × 1000 mm. The X1 and X2 represent the axes of the longitudinal walls and Y1 and Y2 represent the axes of the transversal walls.

The geometrical dimensions of the East wall and North wall are presented in Fig. 6. North and South wall panels are identical to one another whereas East and West wall panels have different configuration to accommodate the door and window openings. The wall framing panels were obtained by connecting the CFS elements by means of 4.8 × 16 mm STS that fit in the drawings located at the theoretical longitudinal axes of the steel profiles. The model was fixed on the shake table by 14 M22 bolts (4 bolts in both X1 and X2 directions and 3 bolts on both Y1 and Y2 directions).

The scaling down of the model was bound by the dimensions of the ANCO R250 shake table. Table 2 summarizes the values of the scaling factor based on the Cauchy law of similarity [50,51].

The joining of the steel profiles presented drawings, the diagonal members and the struts had reduced cross-sectional height and the clipping of the C-profile flanges was performed for the contour elements. Details of the joint layouts are presented in Fig. 7.

2.3. Test set-up and data acquisition

The experimental program took place at the Department of Structural Mechanics from the "Gheorghe Asachi" Technical University of Iasi. The 3-DOFs ANCO R-250 shake table has the in-plane dimensions of 3000 × 3000 mm. The 600 kN electro-hydraulic actuators are located at 120 degrees, as shown in Fig. 8. The frequency range is between 0–30 Hz whereas the maximum acceleration can reach 3 g. The fixing on the models on the shake table can be done using M22 bolts in a grid having the 200 step-size in both in-plane directions.

The scaled-down model was fitted with 4 PT5 A displacement transducers denoted as $D_{x1} \ldots D_{x4}$ in Fig. 8. The shaking motion was applied in the X direction, as shown in Fig. 8. The response of the model, in terms of accelerations, was recorded by means of four DYTRAN 3202 A accelerometers (A_{x1}, A_{x2}, A_{y1} and A_{y2}) located at the eaves, as shown in Fig. 9. The sampling frequency of the ESAM traveler data acquisition system was set at 50 recordings/ second/ channel.

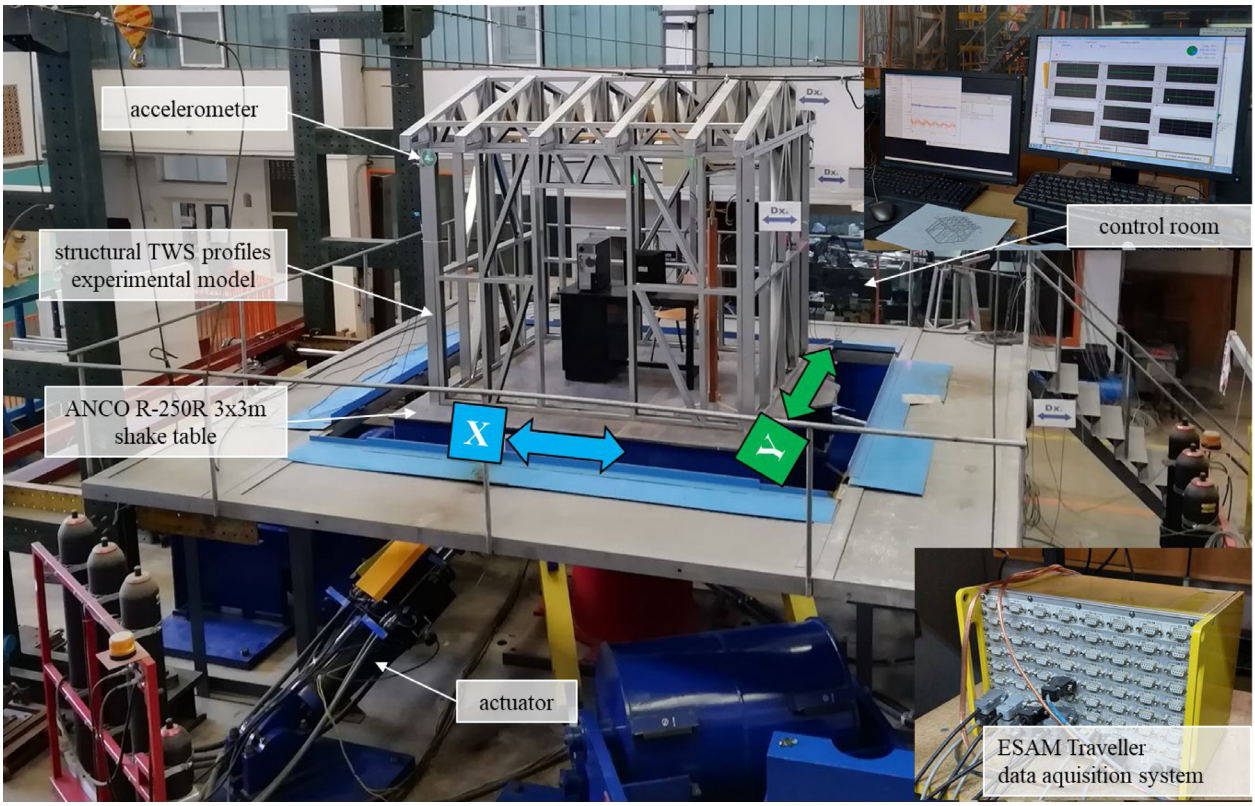

Fig. 8. View of the model on the shake table and instrumentation position.

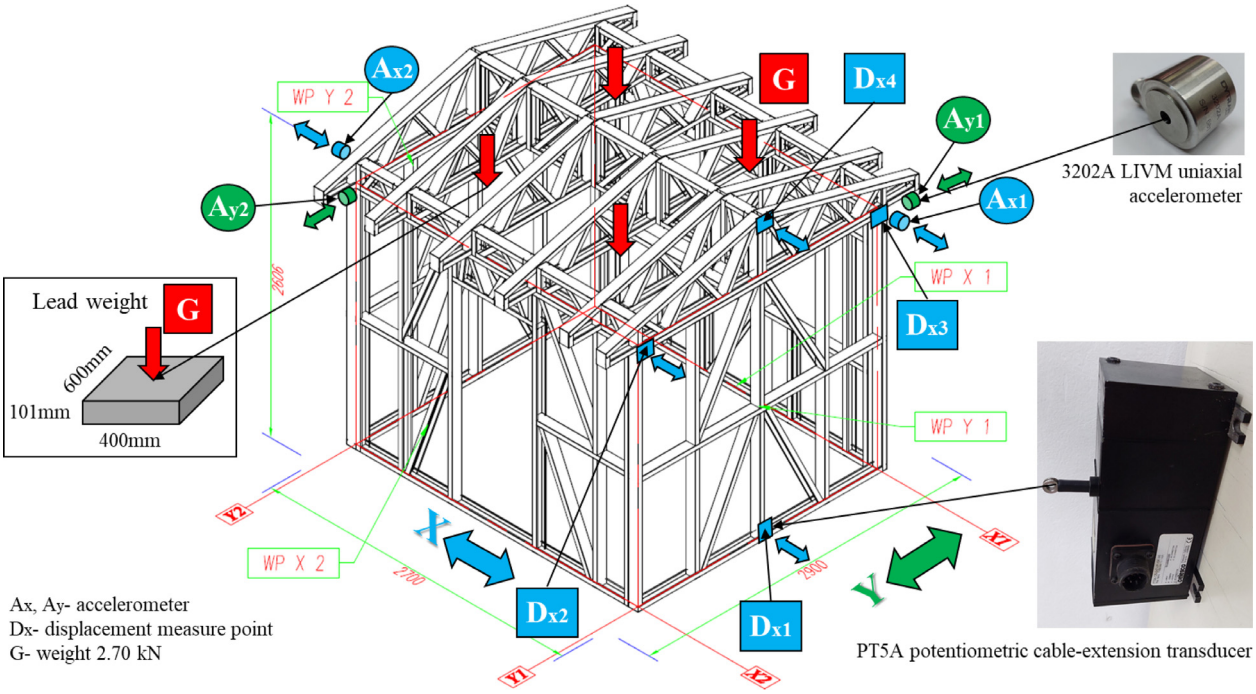

Fig. 9. Axonometry of the structural model with displacement LVDT positions.

3. Experimental program

3.1. Dynamic motions

According to the seismic design codes [1,2] and taking into account the seismic zoning of Romania, shown in Fig. 10, there are three distinct values for the corner/control period T_C: 0.7 s, 1.0 s and 1.5 s. The peak ground acceleration (PGA) in the Vrancea area, epicentral zone, is 0.4 g for a return period of 225 years and a 20% probability of being exceeded in 50 years. Sine beat loading function was chosen with 1 Hz, 1.5 Hz and 6 Hz frequencies and acceleration amplitudes between 0.14 g and 0.71 g.

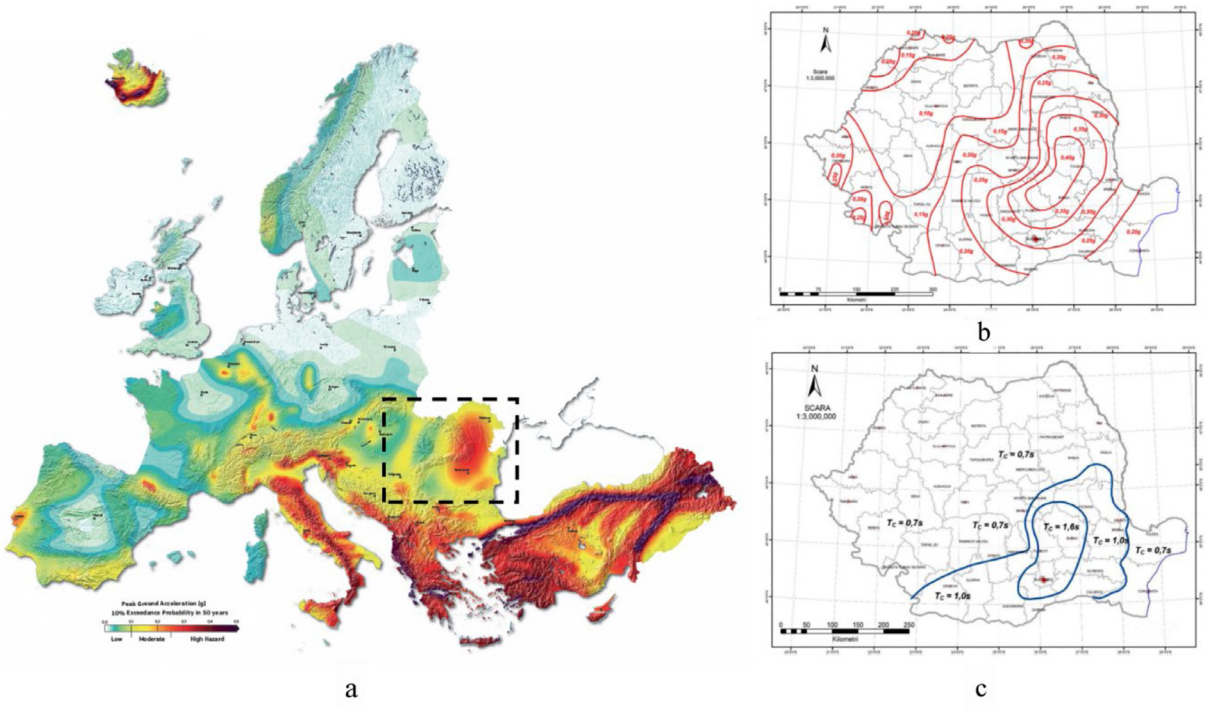

Fig. 10. (a) Europe seismic map [52]; (b) Romania — PGA for a RMI of 225 years and 20% probability of exceedance in 50 years; (c) Zonation of Romania based on the control/corner period T_C, of the response spectrum [2].

3.2. Loading scenarios

The experimental program considered two distinct cases in terms of live loads: bare frame without any additional gravitational loads (Unloaded-UL) and additional masses located at the top part of the walls. The additional masses, shown in Fig. 9, consisted of lead weights, each weighing 275 kg. They were symmetrically located at the ceiling level representing an equivalent load of 1.80 kN/m^2. The dynamic characteristics of the model were firstly determined after which shaking motions were induced following a sine-beat function with different frequencies and different amplitudes of accelerations.

The total load $q = q_1 + q_2 + q_3 + q_4 = 1.80$ kN/m^2 represented the contribution of permanent and partial snow loads considered with their most unfavorable intensities:

- Tile roof $q_1 = 0.75$ kN/m^2;
- Additional steel profiles for cladding: $q_2 = 0.12$ kN/m^2;
- Covering elements: $q_3 = 0.3$ kN/m^2;
- 40% of the snow load with $s = 2.5$ kN/m^2: $q_4 = 0.63$ kN/m^2;

Table 3 summarizes the loading protocol. The different frequencies of the sine-beat function as well as levels of accelerations would offer sufficient data to better understand the behavior of the CFS model to seismic actions.

There are two categories of tests presented in Table 3. The tests denoted with F are those for which the fundamental frequency of vibration was measured in the initial, undamaged state, and after each series of dynamic tests. The tests denoted with T are the test involving the dynamic sine-beat motions. The number in the test designation means the frequency of the shaking motion. Hence, F0-UL-1 Hz represents the test conducted to determine the fundamental frequency of vibration in the initial, unloaded (UL) state. Consequently, T10-L-1 represents test number 10, conducted on the loaded model (L) and the shaking motion had a frequency of 1 Hz.

3.3. Cyclic loading tests on T-joints

The shake table tests were preceded by cyclic loading tests on the T-joints with different configurations in terms of used connectors: type A with 4.8 × 16 mm SDS, type B with 4.8 × 22 mm STS and Tapper drawing and type C using a combination of types A and B. A detailed presentation of the research work can be found in [46]. For the purpose of this study, only type B joints were considered.

In case of structures subjected to seismic motions, the behavior of joints to cycling loads is very important because it can give information related to the possible deformations and decrease of rigidity. The cyclic tests were conducted in accordance with the methodology outlined in [53,54]. Five T-joint specimens were considered. They were first subjected to 20, displacement controlled, cyclic tests with a maximum amplitude of +/−1 mm and a loading rate of 0.083 mm/s. After the 20 cycles, the amplitude was increased to +/−2 mm and the loading rate to 0.167 mm/s and an additional 20 cycling tests were performed. An electro-hydraulic Zwick/Roell 1000SP universal testing machine was used to run this part of the experimental program (see Fig. 11).

4. Experimental results

4.1. Results of cyclic tests on the T-joint

Fig. 12 presents the average load–displacement curves obtained during the cyclic tests. It can be observed that for a maximum displacement of +/−1 mm, Fig. 12a, the stiffness on the tensile part of the test is almost constant with a value of 2300 N/mm and did not decrease significantly after 20 loading cycles. The peak load corresponding to the maximum displacement of 1 mm was 2300 N la 1 mm. On the compression part of the curve however, two different behaviors could be observed: from 0 to −0.5 mm the average value of the stiffness was 2200 N/mm. From −0.5 mm to −1.0 mm the stiffness increased to 8896 N/mm. A more evident decrease in the value of the stiffness can be observed after 20 loading cycles, especially for displacements between −0.5 mm to −1.0 mm. The variation in the applied force amplitude with the number of loading cycles, both in the tensile and compression ranges of the load–displacement curve is presented in Fig. 12c. It can be observed that the intensity of the applied load in the tensile range is almost constant whereas a significant decrease could be seen in the compression range. The value of the secant stiffness,

Table 3
Experimental test.

Current no.	Test label	Description	Dead load (kN/m^2)	Action type	Action frequency (Hz)	Action period (s)	Action max. abs. acceleration (g)	Percent of max. PGA seismic design code (0.4g)	Max. shake table abs. displacement in X direction (mm)
1	F0-UL-1Hz	Unloaded model (UL) tests	0	Sine beat	1	1	-	-	-
2	T1-UL-1						0.21	52.5%	52.44
3	T2-UL-1						0.31	77.5%	73.34
4	T3-UL-1						0.43	107.5%	102.4
5	F1-UL-1Hz				1.5	0.667	-	-	-
6	T4-UL-1.5						0.36	90%	39.88
7	T5-UL-1.5						0.51	127.5%	55.62
8	T6-UL-1.5						0.71	177.5%	76.85
9	F2-UL-1.5Hz				6	0.167	-	-	-
10	T7-UL-6						0.14	35%	1.26
11	T8-UL-6						0.23	57.5%	2.56
12	T9-UL-6						0.33	82.5%	3.87
13	F3-UL-6Hz						-	-	-
14	F4-L-1Hz	Loaded model (L) tests	1.80	Sine beat	1	1	-	-	-
15	T10-L-1						0.22	55%	52.92
16	F5-L-1Hz						-	-	-
17	T11-L-1 (FEM correlation)						0.31	77.5%	72.89
18	F6-L-1Hz						-	-	-
19	T12-L-1 (collapse)						0.46	115%	100.49

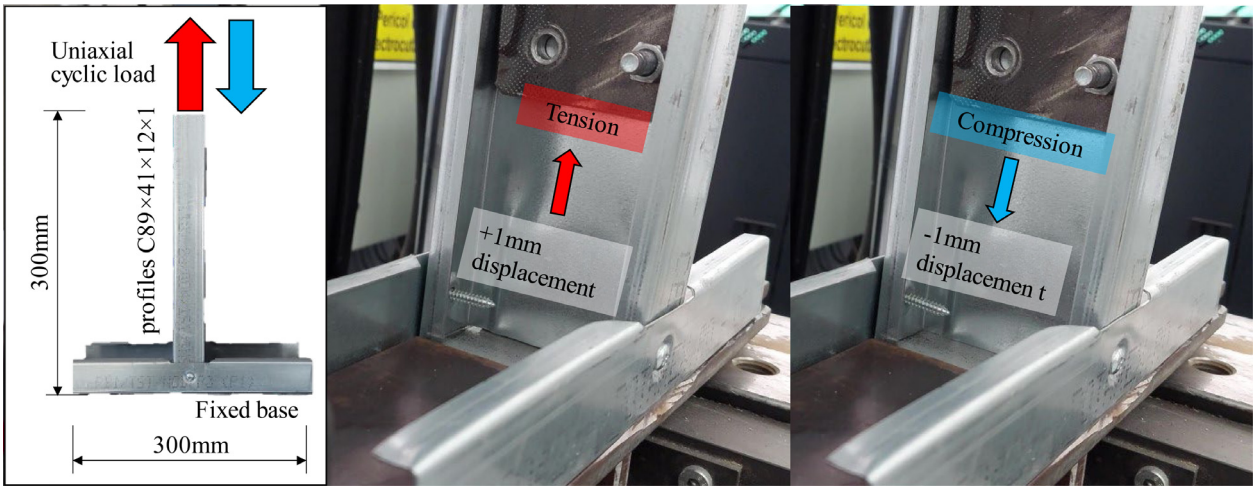

Fig. 11. Tension–Compression cyclic loading experimental test +/−1 mm @0.083 mm/s.

after 20 loading cycles, stabilized around de 2300 N/mm. After the initial test, a second round of cyclic tests were conducted on the same samples of T-joints with double the amplitude of the displacement: +/−2 mm. This resulted in a decrease in the values of the secant stiffness by approximately 30%, Fig. 12b, and almost constant intensity of the applied load both in tension and a smaller decrease of the load in compression, Fig. 12d.

4.2. Dynamic properties of the scaled down-model

The fundamental frequency of vibration for the unloaded, undamaged model was determined using the free-vibration decay method. The scaled-down model was then subjected to a first set of seismic motions at a motion frequency of 1 Hz (tests T1–T3 from Table 3). The fundamental frequency of vibration was then measured again at the end of the first series of tests. The experimental program continued with a second series of seismic motions with a motion frequency of 1.5 Hz. After a third determination of the fundamental frequency, the bare frame model was subjected to a third series of shake table test with a frequency of 6 Hz (tests T7–T9, Table 3). The change in the fundamental frequency of vibration from one series of tests to another, for the bare frame, is presented in Fig. 13a. The model was then loaded, as described in Section 3.2. The addition of masses changed the fundamental frequency from 8.09 Hz to 2.98 Hz, a 278% decrease. For the loaded model only one test was conducted for the motion frequency of 1 Hz but with different amplitudes (tests T10–T12, Table 3). The change in the fundamental frequency for the loaded model is presented in Fig. 13b

Based on the obtained data it can be concluded that the model exhibited some slight damages which is reflected in a decrease of the fundamental frequency from 8.28 Hz to 8.09 Hz for the unloaded scenario, a 2.41% decrease compared to the initial stage. A more significant decrease in the value of the fundamental frequency could be observed when the model was loaded with additional masses, the change being 31.21%.

4.3. Response of the model in accelerations

Fig. 14 presents the input versus recorded accelerations at the level of the shake table and at the top part of the walls for the model as an average value of the records given by accelerometers A_{x1} and A_{x2} (see Fig. 9). It can be observed that for the first series of tests (input frequency 1 Hz and different values for the acceleration amplitudes) the model behaves rigidly, with very small values of the relative accelerations computed as the difference between the absolute accelerations at the top of the walls and the absolute accelerations recorded at the

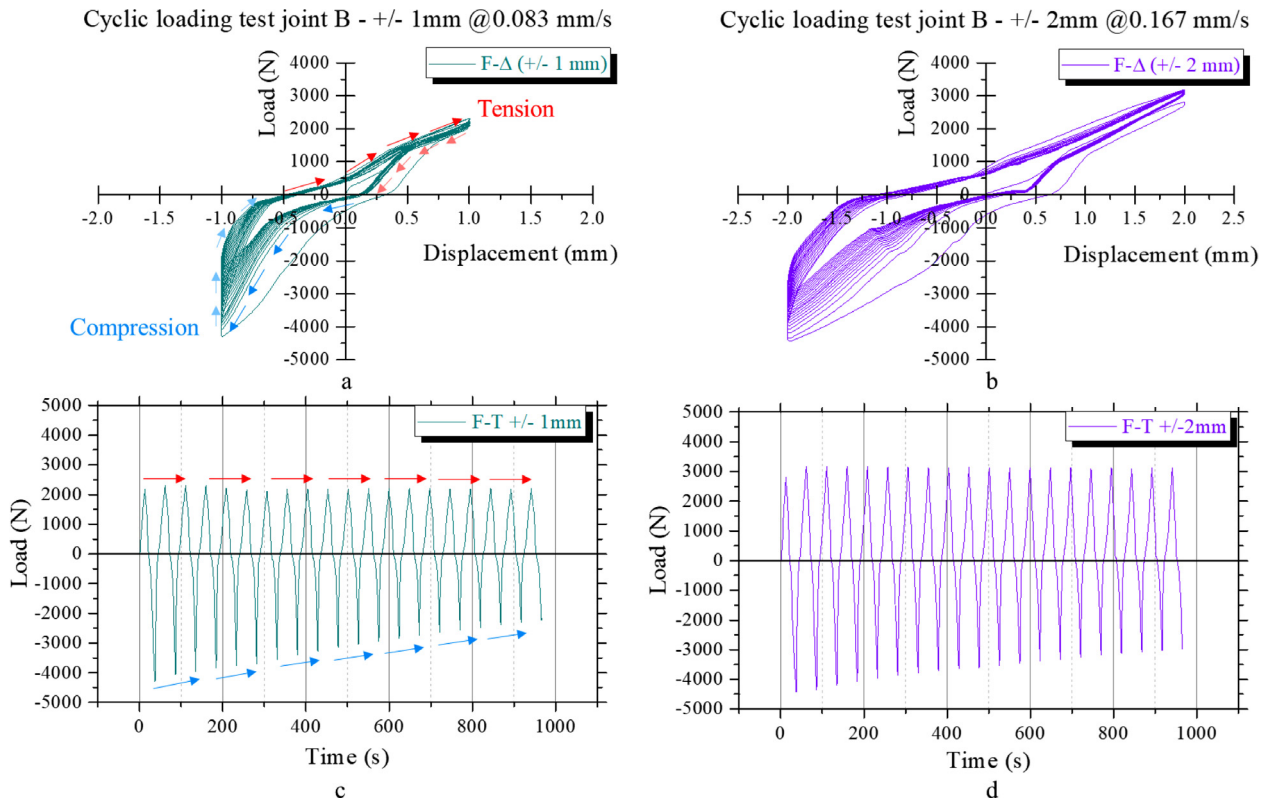

Fig. 12. Tension–Compression cyclic test results: (a) joint B +/−1 mm @0.083 mm/s; (b) joint B +/−2 mm @0.167 mm/s; (c) Load vs. time evolution of cyclic test with +/−1 mm; Load vs. time evolution of cyclic test with +/−2 mm.

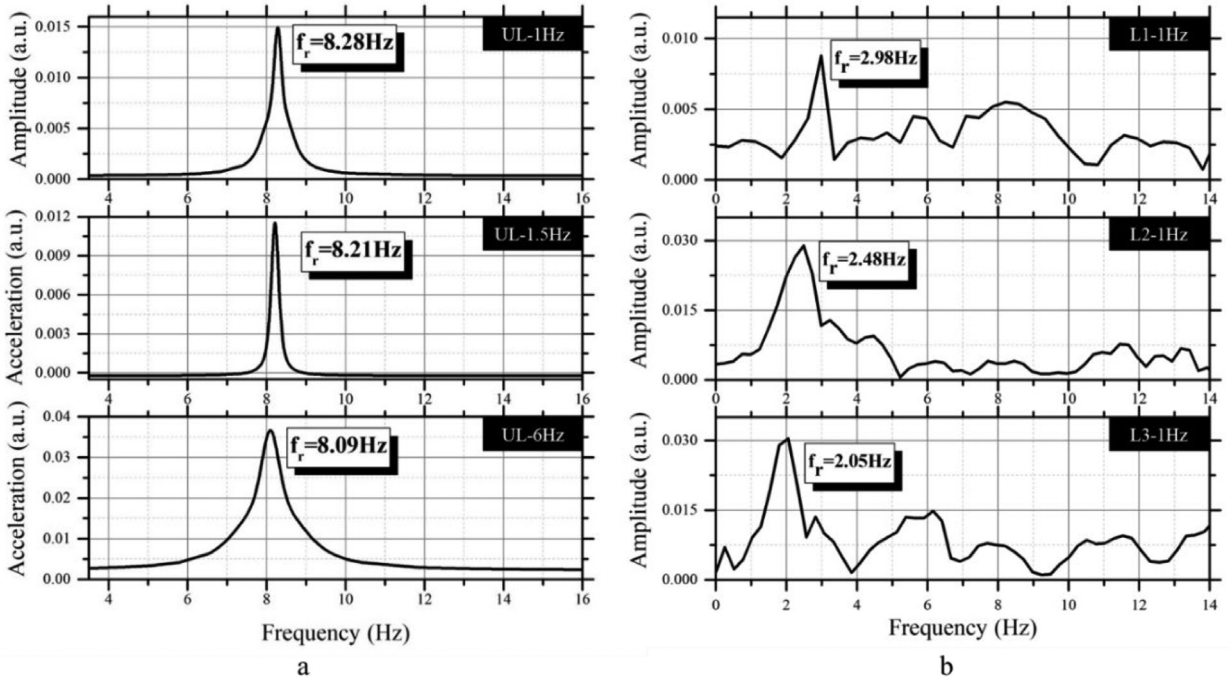

Fig. 13. Results of dynamic identification in terms of natural frequency (a) -Unloaded Model — UL; (b) Loaded Model — L..

level of the shake table. There is, however, an instance during test T3 when the maximum amplitude of the relative acceleration was 0.48 g.

Increasing the frequency of the input motion to 1.5 Hz did not result in significant change in the behavior of the model. It can be seen that the model and the shake table are in phase with one-another. The amplitude of the relative acceleration was reached a maximum of 0.34 g during test T5. From the data of the two series of tests it can be concluded that no significant amplifications were observed.

Increasing the frequency of the input motion to 6 Hz resulted in significant amplifications of the response. In test T9, even though the amplitude of the input motion was 0.33 g, the maximum relative acceleration was 1.76 g. This could be explained by the fact that the

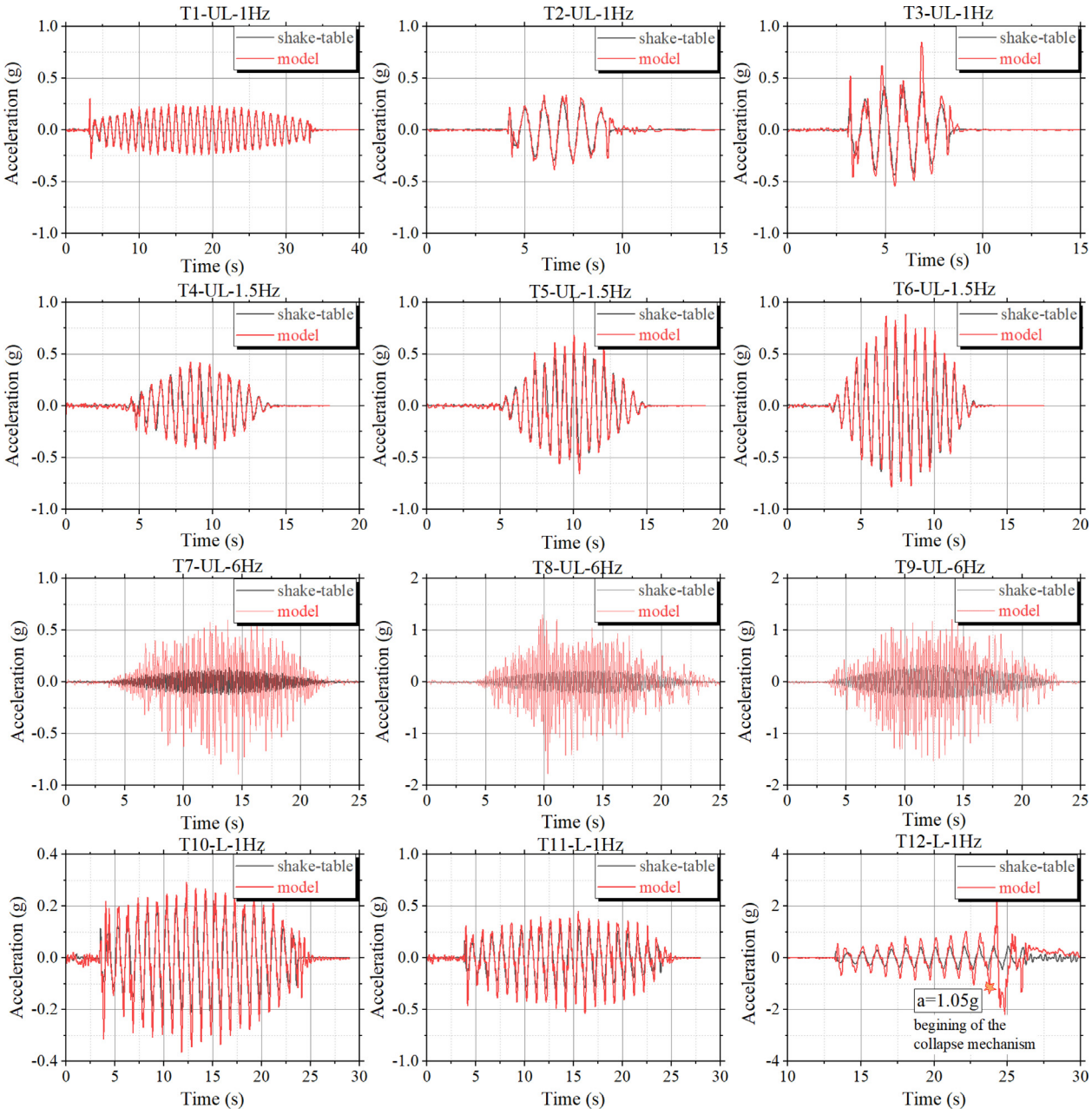

Fig. 14. Absolute acceleration vs. time of the experimental tests.

frequency of the input motion is closer to the fundamental frequency of vibration of the model and therefore significant amplifications of the response were observed.

When the model was loaded by additional masses, the amplitude of relative accelerations increased from 0.4 g in case of test T11 to 0.92 g in case of test T12 before the failure mechanisms started to develop. When the amplitude of the absolute acceleration of the model exceeded 1.05 g, the model failed, and the test was stopped. This can be seen from the last graph in Fig. 14 when the input and response motions are clearly out of phase and significant amplifications of the input amplitude were observed.

4.4. Relative lateral displacements

Fig. 15 presents the time histories of the relative lateral displacements computed as the difference between the average values measured by the displacement transducers D_{x2} and D_{x3} and the displacements recorded by D_{x1} (see Fig. 9).

The recorded data is consistent to what was presented in Fig. 14. Lower values of the relative lateral displacements were observed for the first two series of test with input frequencies of 1 Hz and 1.5 Hz, irrespective of the acceleration amplitudes. The maximum relative lateral displacement for the first series of tests was obtained for test T3, 2.99 mm, whereas for the second series the maximum relative displacement was 3.07 mm.

When the frequency of the input motion increased to 6 Hz, significant amplification of the response was observed during tests T8 and T9 for which the relative lateral displacements were 12.8 mm and 13.44 mm, respectively.

The loaded model exhibited significantly larger relative displacements from 22.75 mm for test T10 to 55.03 mm for test T12 before the failure mechanisms started to develop. A relative displacement of 283.14 mm was recorded when the collapse of the model occurred.

Table 4 summarizes the results in terms of fundamental frequencies of vibration as well as maximum amplitudes of relative accelerations and displacements.

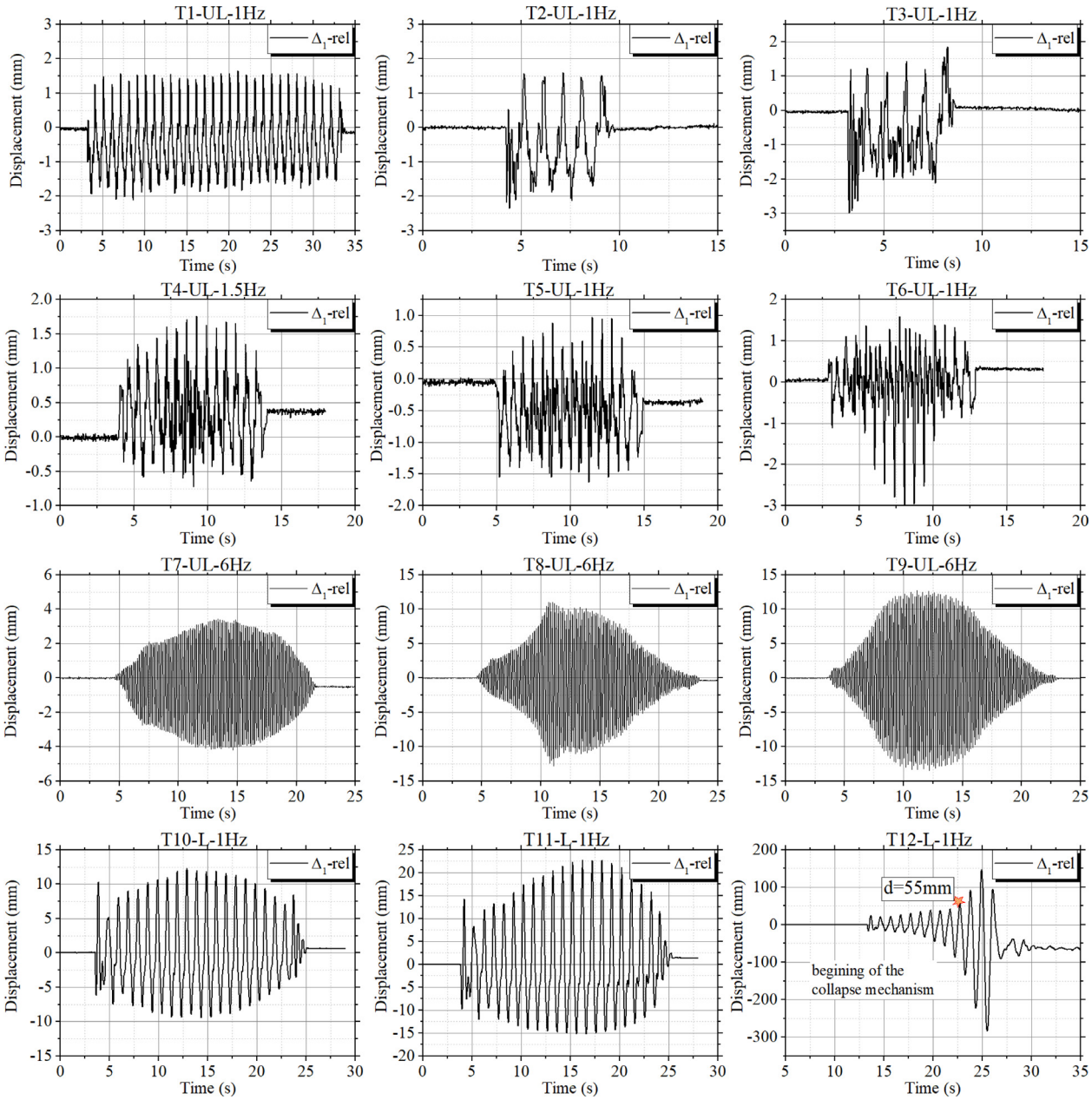

Fig. 15. Relative displacement vs. time: (a) Unloaded tests T3, T6, T9; (b) Loaded model tests T10, T11, T12.

4.5. Base shear–relative displacement curves

Fig. 16 presents the base shear–relative displacements curves for the tests of highest amplitude of the input motion in case of the bare frame model (T3, T6 and T9) as well as all three tests conducted on the loaded frame (tests T10–12).

According to the Romanian seismic design code, the maximum relative displacement in case of serviceability limit state (SLS) should be less than $0.005H$ where H is the height of the structure. For the model presented in this research work the maximum allowable displacement in case of SLS would be 10.5 mm.

$$d_r^{SLS} = 0.005H = 0.005 \cdot 2100 = 10.5 \text{ mm} \quad (1)$$

In case of ultimate limit state (ULS), the relative displacement should not exceed $d_r^{ULS} = 0.025H$, where H is the height of the structure. For the model presented in this research work the maximum allowable displacement in case of ULS is 52.5 mm.

$$d_r^{ULS} = 0.025H = 0.025 \cdot 2100 = 52.5 \text{ mm} \quad (2)$$

Analyzing the data presented in Fig. 16 it can be concluded that the scaled down model behaves linearly for the most part of the tests although in case of test T9 larger values were obtained for the relative lateral displacement which could mean that some of the joints exhibited larger deformations. For the loaded model, the relative displacement exceeds 20 mm in case of test T11 and a decrease in the overall stiffness can be observed. The values of the relative displacement become more significant during test T12, reaching 55.03 mm which represent the onset of the failure mechanisms.

4.6. Failure mechanisms

4.6.1. T-joints subjected to cyclic loading

The following failure mechanisms could be observed during the cyclic tests performed on the T-joints with 4.8 × 22 mm STS. Their order of development is presented in Fig. 17. Due to the cyclic loading the screw, which can be assumed as a small cantilever, tilts downwards due to the tensile force being applied, mechanism (a), almost at the

Table 4
Experimental test results.

Test no.	Test label	Natural frequency *(Hz)*	A_{TX} PGA abs shake table *(g)*	A_x abs. max structure (g)	A_x rel. max (g)	$\Delta_{1max} = D_{x3} - D_{x1}$ *(mm)*	$\Delta_{2max} = D_{x4} - D_{x1}$ *(mm)*
1	F0-UL-1Hz – F.D.T*	8.285	-	-		-	-
2	T1-UL-1Hz	-	0.21	0.30	0.25	2.11	2.47
3	T2-UL-1Hz	-	0.31	0.38	0.21	2.35	3.05
4	T3-UL-1Hz	-	0.43	0.84	0.48	2.99	5.06
5	F1-UL-1Hz – F.D.T	8.28	-	-		-	-
6	T4-UL-1.5Hz	-	0.36	0.42	0.27	1.76	1.39
7	T5-UL-1.5Hz	-	0.51	0.68	0.34	1.63	2.15
8	T6-UL-1.5Hz	-	0.71	0.88	0.25	3.07	3.40
9	F2-UL-1.5Hz – F.D:T	8.21	-	-		-	-
10	T7-UL-6Hz	-	0.14	0.89	0.77	4.18	5.01
11	T8-UL-6Hz	-	0.23	1.77	1.72	12.80	17.05
12	T9-UL-6Hz	-	0.33	1.52	1.76	13.44	18.48
13	F3-UL-6Hz – F.D.T	8.09	-	-		-	-
14	F4-L-1Hz – F.D.T	2.98	-	-		-	-
15	T10-L-1Hz	-	0.22	0.36	0.23	12.33	14.87
16	F5-L-1Hz – F.D:T	2.48	-				
17	T11-L-1Hz FEM correlation	-	0.31	0.53	0.40	22.75	27.78
18	F6-L-1Hz – F.D.T	2.05	-				
19	T12-L-1Hz collapsed	-	0.46	1.05 3.54**	0.92 2.17**	55.03 283.14**	86.04 294.82**

*F.D.T – frequency determination test
** near collapse

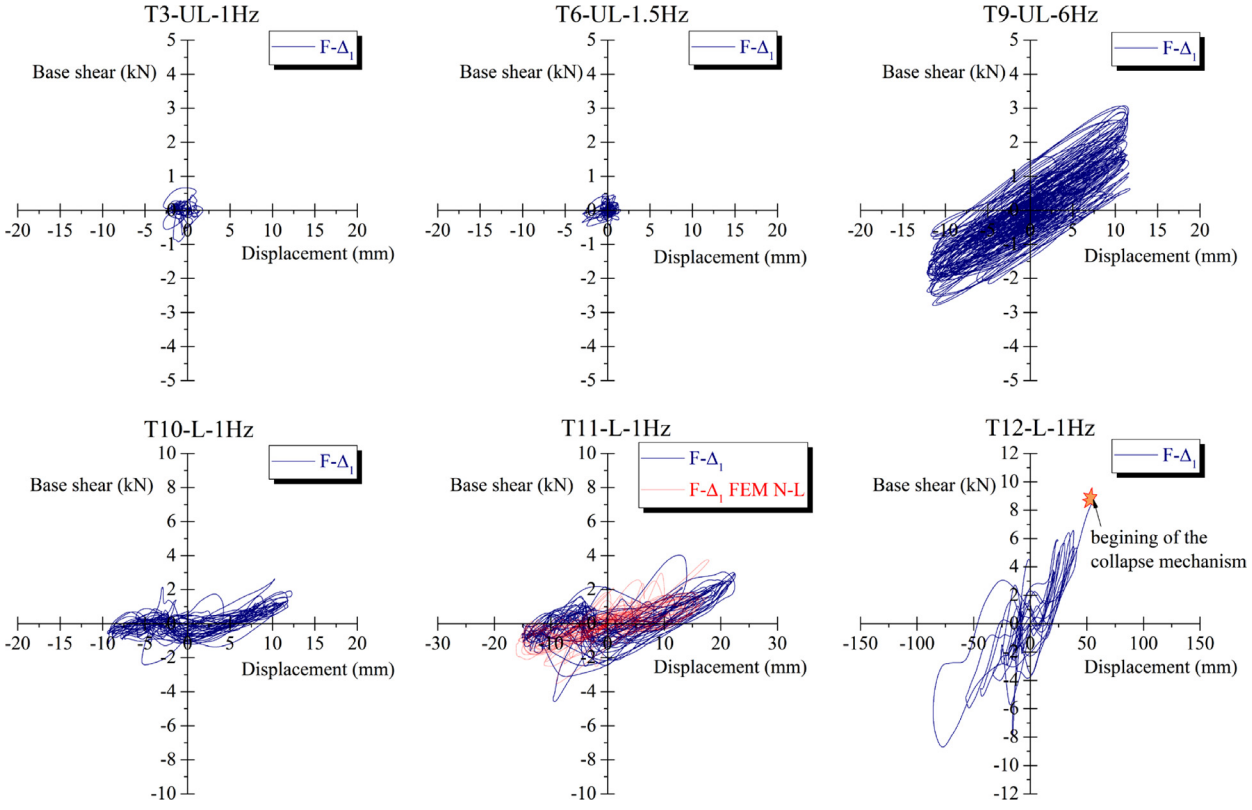

Fig. 16. Base shear vs. displacement graphs.

same time with the onset of plastic deformations of the edges of the pre-drilled holes, mechanism (b). The wall of the clipped steel profile (the chord) is subjected to bending and rotates outwards creating a gap between the chords and the strut during the application of the tensile load, mechanism (d). The excessive rotation is restrained due to the contacts between the chord and the strut. At the same time, the gap the occurs between the steel profiles lowers the friction force and leads to the unscrewing of the STS, mechanism (c).

4.6.2. Bare steel frame model subjected to seismic actions

After the first two series of tests were conducted at frequencies of 1 Hz and 1.5 Hz, no visible deformations could be observed at the joints between the CFS profiles, especially at the ends of the diagonal elements (the most loaded ones). When the frequency of the shaking motion increased to 6 Hz, significant amplifications of the response were recorded in terms of accelerations and relative displacements. The model was inspected once again and no visible damages could be detected for the elements and the joints of the framing in X direction.

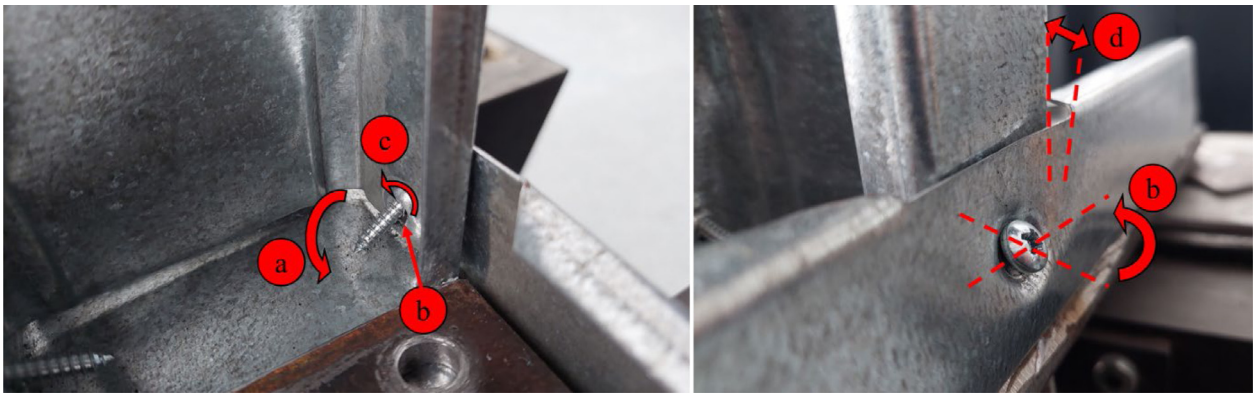

Fig. 17. Failure mechanism in joints during cyclic tests.

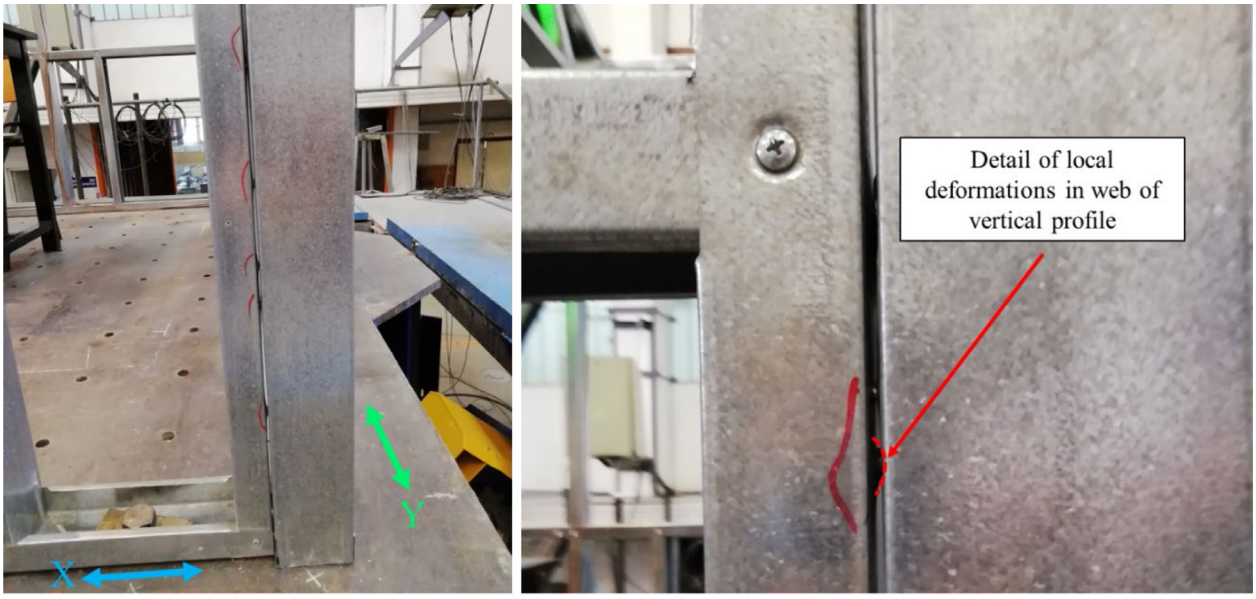

Fig. 18. Deformations of the joints between panels: (a) panel intersection; (b) detail of the deformation.

However, local deformation could be observed at the joints between the framing panels in X and Y directions, as shown in Fig. 18.

During test T11, after the model was loaded with additional masses, the maximum recorded relative displacements was 22 mm. There were still no other visible damages than the ones already identified during the previous tests. During test T12 the model exhibited a relative displacement of 55.03 mm which represented the onset of the failure mechanism, almost at the same time for all 6 locations presented in Fig. 19.

The exact order of the failure mechanisms occurrence in Fig. 19 could not clearly be established because of the extremely short time interval between their occurrences. In case of mechanism **1**, local buckling of the lower chord of the wall framing was observed on both East and West walls (see Fig. 5) which could be caused due to the fixing of the model onto the shake table coupled with the eccentricities between the centerline of the struct and the diagonal element. The axial force it the joint between the diagonal element and the lower chord produced normal stresses that exceeded the yield strength of the material leading to excessive plastic deformations and pulling out of the screw.

Mechanism **2** occurred at the upper end of the diagonal element adjacent to the door gap in the East wall along axis X2 (see Fig. 9). The failures occurred due to the local buckling of the horizontal element connecting the diagonal element and the vertical one forming the door gap. A similar failure mechanism was identified on the opposite side of the door gap. The 3rd failure mechanisms occurred at the joint between the vertical element and the lower end of the upper diagonal in the East wall. Both the vertical and horizontal elements failed due to local buckling because the joint between the diagonal element and the vertical one was stronger than the other joints due to the presence of an additional screw.

Mechanism **4** occurred in the upper part of the door gap, in the vertical element due to torsional buckling. The presence of the truss system to stiffen the upper part of the door gap led to significant differences in lateral stiffness which may have triggered the failure mechanism 4.

Mechanism **5** occurred due to local buckling of the horizontal element at the top of the door gap in Eastern wall coupled with pulling out of the screw. Mechanism **5** may have influenced the occurrence of mechanism **4** due to the fact that the upper left panel of the door gap lost its in-plane stability.

Mechanism **6** occurred in the Western, at the top end of the lower diagonal element from the panel located between the two windows opening. The failure occurred due to the tearing of the material in the diagonal element.

There were also other local damages identified throughout the model in the form of local crushing of the steel sheet at the edges of

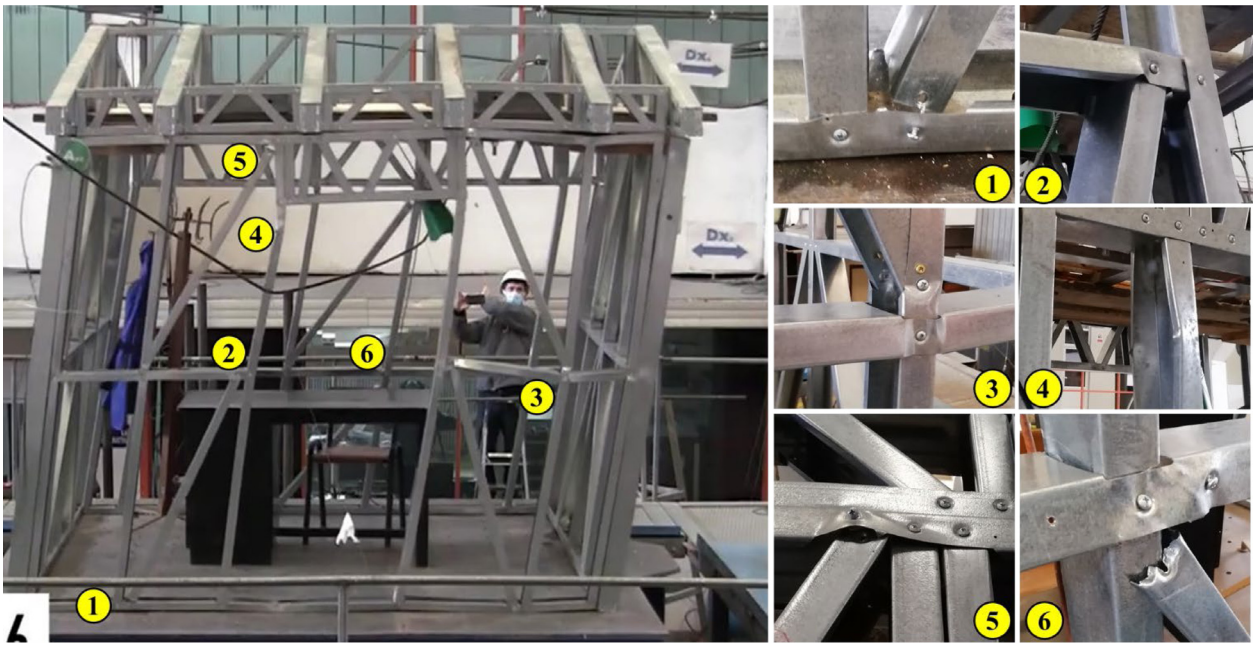

Fig. 19. Failure details mechanisms captured from video recording of the experiment.

the holes of local deformation at the joints between the walls (corners of the model) but without pulling out of the screws.

5. Numerical modeling

5.1. General considerations

The numerical modeling of CFS structures can be accomplished by means of two frequently used approaches aimed at accurately simulating the real behavior of the structure. One of the frequently met approaches in the scientific literature [55–60] consists in using 2D or even 3D elements. Coupled with a non-linear material behavior, this approach leads to very accurate results, but it requires expensive hardware and a lot of time to run the simulations especially in case of complex structures.

On the other hand, the approach presented in the design codes [3, 61,62] suggests that the joints are the most vulnerable components of the CFS structures. The numerical investigations conducted in case of such an approach should take into account the second order effect and the real stiffness of the joints. The latter can be obtained from experimental testing. The numerical models presented in this paper consist in linear and non-linear models with infinitely (1) rigid joints and (2) semi-rigid joints. The rigidity of the latter was considered as constant or having a parabolic variation.

Starting from previously published results [46] and considering the results obtained through cyclic tests on T-joints, the finite element structural model based on 1D-beam pin-connected elements was used to simulate the behavior of the experimental model subjected to a similar loading scenario as in test T11.

5.2. The numerical model

Robot Structural Analysis Professional was used to generate the numerical model [63]. Depending on the type of analysis, linear or non-linear, the joints may be defined by means of their axial stiffness k_x depending on the considered scenario:

1. For the bare frame model:
    a. Linear with joints defined with elastic option $k_x = 5650$ N/mm and simple supports;
    b. Linear with rigid joints defined by $k_x = \infty$ and simple supports;
    c. Nonlinear with $k_x = 5650$ N/mm — parabolic and uplift supports.
2. For the loaded model (additional masses considered):
    a. Linear with joints defined with elastic option $k_x = 5650$ N/mm and simple supports;
    b. Linear with rigid joints defined by $k_x = \infty$ and simple supports;
    c. Nonlinear with $k_x = 2300$ N/mm — parabolic and uplift supports.

Fig. 20a presents the conceptual design/definition of the joint in the local coordinate system of each bar element. Based on the experimentally obtained data from direct tensile tests, Fig. 20b, and cyclic tests, Fig. 20c, the values of the joint stiffness both in tension and compression were assessed as a mean value of 2300 N/mm. The program allows the user to choose from several options on how to define the end releases for each degree of freedom as: fixed (fully restrained, infinite rigidity), fixed values of rigidity or by means of a parabolic variation [63]. Fig. 21 presents the numerical model highlighting the bar ends at the joints.

The geometry of the numerical model was generated based on the exact dimensions of the experimental model, including the eccentricities of the elements at the joints. Rigid joints were considered between the walls. The support conditions were chosen as pin supports at the location of the bolts fixing the model on the shake table. In the case of the non-linear numerical model, FEM N-L, additional uplift support conditions were generated on the surface of the lower chord of the wall framing. Such support conditions have a restrained displacement in the negative direction of the global Z axis (downwards) but the upward displacement was allowed. A graphical representation of the location of supports is presented in Fig. 22. Table 5 summarizes the characteristics of each numerical model considered in the paper.

Newmark method was used for the Time History Analysis (THA) for which the Rayleigh Damping coefficients were computed based on $\omega_1 = 14.72, \xi_1 = 0.02$ and $\omega_2 = 25.54, \xi_2 = 0.02$. The resulting values were $\alpha = 0,3735$ and $\beta = 0,00099$. A 0.02 s time step size was considered which was similar to the time interval for data acquisition during the

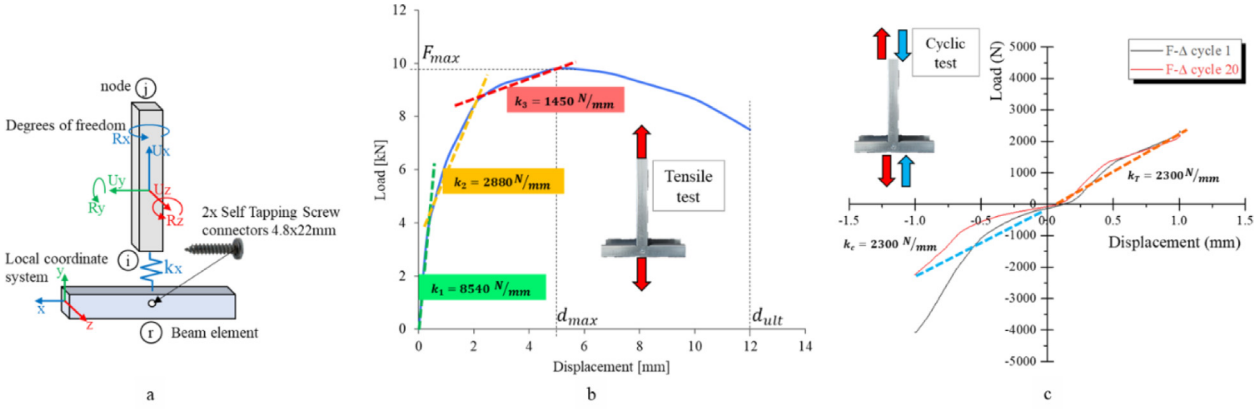

Fig. 20. Definition of beam element end-releases in Robot Structural Analysis (a) joint of beam FEM schematic concept; (b) load–displacement experimental monotonic data test; (c) load–displacement cyclic data test.

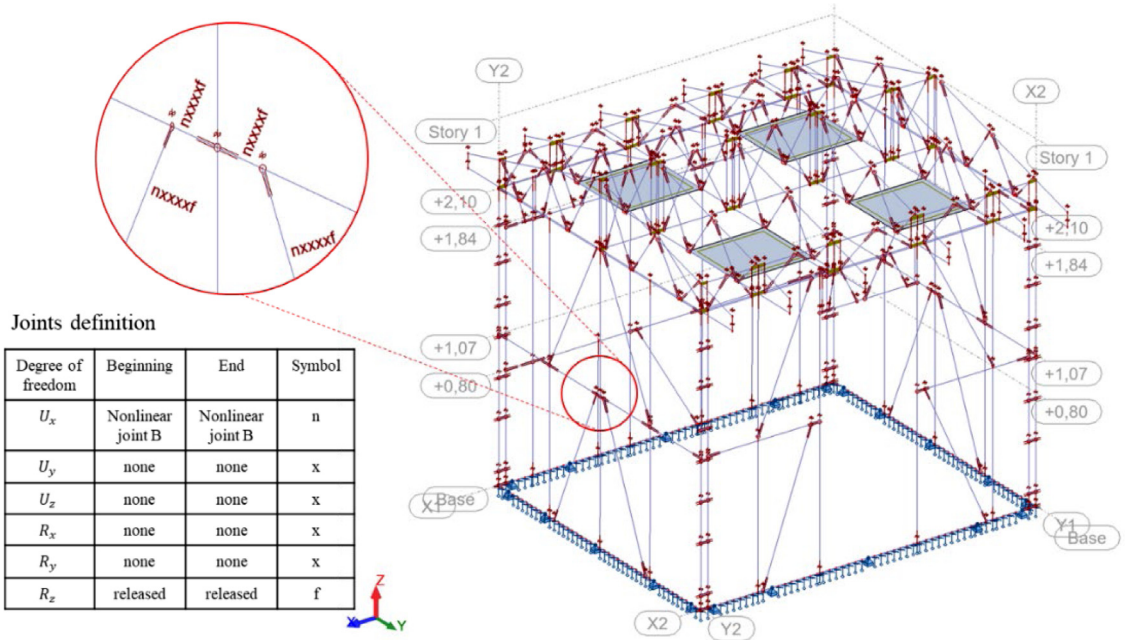

Fig. 21. Numerical model FEM N-L with beam elements and joints definition.

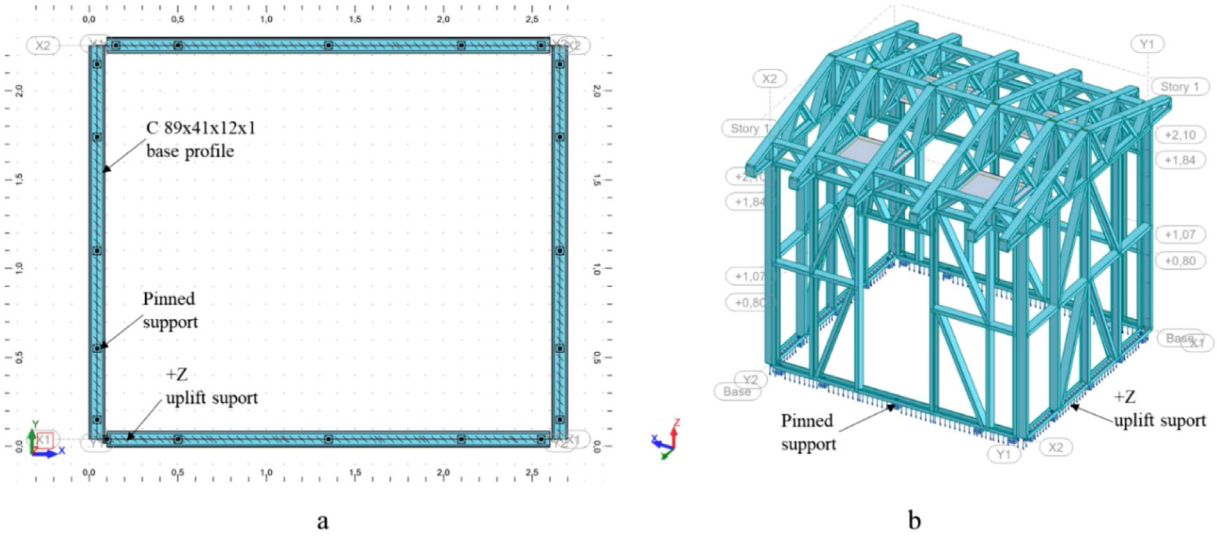

Fig. 22. Numerical model FEM N-L geometry (a) base plan view with supports; (b) 3D spatial model.

Table 5
Numerical models characteristics.

Model analysis type	Number of nodes	Number of bars	Bar finite elements	Rigid links	Releases	Non-linear releases	Supports	Unidirectional supports (uplift +Z)	Static degree of freedom	Time-History analysis method
Linear $k_x = 2300$ N/m	1193	312	897	105	256	–	200		6920	Modal decomposition
Linear $k_x = \infty$	1193	312	897	105	256	–	200		6920	Modal decomposition
Nonlinear $k_x = 2300$ N/mm	1193	312	897	105	–	256	200	181	7101	Newmark method

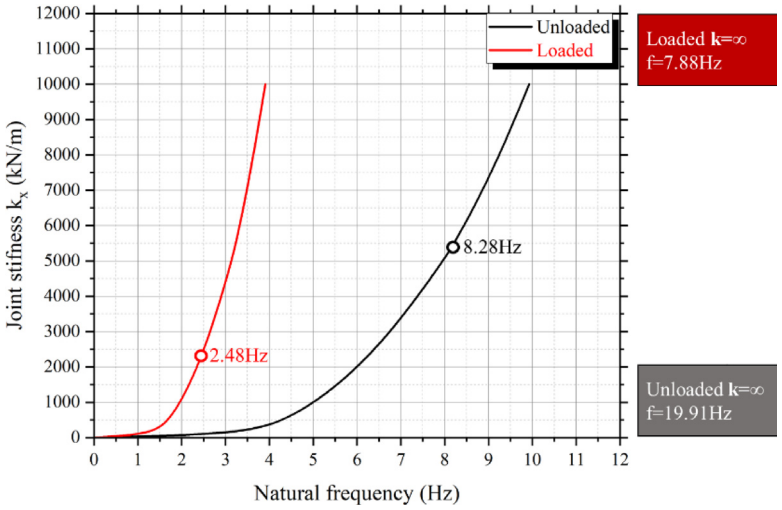

Fig. 23. Joint stiffness vs. natural frequency of the FEM Nonlinear model.

experimental program. The accelerograms used in the numerical model were the ones recorded at the level of the shake table, in both X and Y directions, during test T11-L-1 Hz.

5.3. Dynamic properties of the model

In order to calibrate the model from the point of view of the fundamental frequency of vibration, a set of modal analyses were conducted for which the main parameter was the axial stiffness at the joints. The considered range was between 100 N/mm up to 10000 N/mm. Fig. 23 presents the variation of the fundamental frequency with the change of the axial stiffness at the joints (end of bars). It can be observed that the values of the axial stiffness for which the fundamental frequency of the numerical model matched the experimental data, in both bare/unloaded and loaded frame configurations, were 5650 N/mm and 2300 N/mm, respectively. The axial rigidities exhibited lower values compared to the ones obtained by means of direct tensile tests but similar to the ones obtained during the cyclic tests. For the case of bare/unloaded structure, the considered value of the stiffness should be the one corresponding to the linear elastic range. In case of the loaded structure, already subjected to a three series of seismic motions, the axial rigidity at the joints should be reduced because of the innate displacements that may occur in the joint areas The results obtained from the numerical investigations suggested that the axial rigidity at the joints should be equal to the average value of the secant stiffness obtained from the cyclic tests and presented in Fig. 20c.

Fig. 24 presents the first two mode shapes of the bare/unloaded structural model. It can be observed that both mode shapes are translational ones in X and Y directions, respectively. Fig. 25 presents the first two mode shapes for the loaded structure.

Table 6 summarizes the results obtained from the modal analyses for all considered scenarios. From the presented data it can be observed that for the numerical model for which the joints were considered to have infinite axial rigidity, the obtained dynamic characteristics of the model differ significantly from the experimental results. It can, therefore, be concluded that this approach would lead to erroneous results.

5.4. Time history analyses

A similar accelerogram to the one corresponding to experimental test T11-L-1 Hz was considered in the numerical model. Both linear and non-linear analyses were run.

Fig. 26 present the response of the model in terms of accelerations and displacements. For comparative purposes, the experimentally obtained results and the numerical ones for different types of THA analyses were plot on the same graph. The output for the numerical model was considered to be at node 65 which corresponds to A_{x1} and D_{x3} on the real model (see Fig. 9).

It can be observed that there are significant differences between the results obtained from each of the two numerical models for which linear analysis was considered. The difference between the two models consisted in the way the axial rigidity was considered at the joints: infinite axial rigidity and finite axial rigidity with a value of 2300 N/mm. At the same time, the numerical model for which a non-linear analysis was considered, lead to similar results as the linear analysis case but with axial rigidity at the nodes defined based on the experimental data. For both graphs presented in Fig. 26, the numerical results are very close to the experimental data during the first 10 s on the THA. After that, the experimental model started to exhibit local damages which could not be captured in the numerical model. For this to happen, nonlinear material behavior should also be considered in the numerical simulations which would lead to a more demanding calculation effort.

Fig. 27 presents the deformed shape of the structure in each of the considered scenarios for the THA: (a) nonlinear with $k_x = 2300$ N/mm

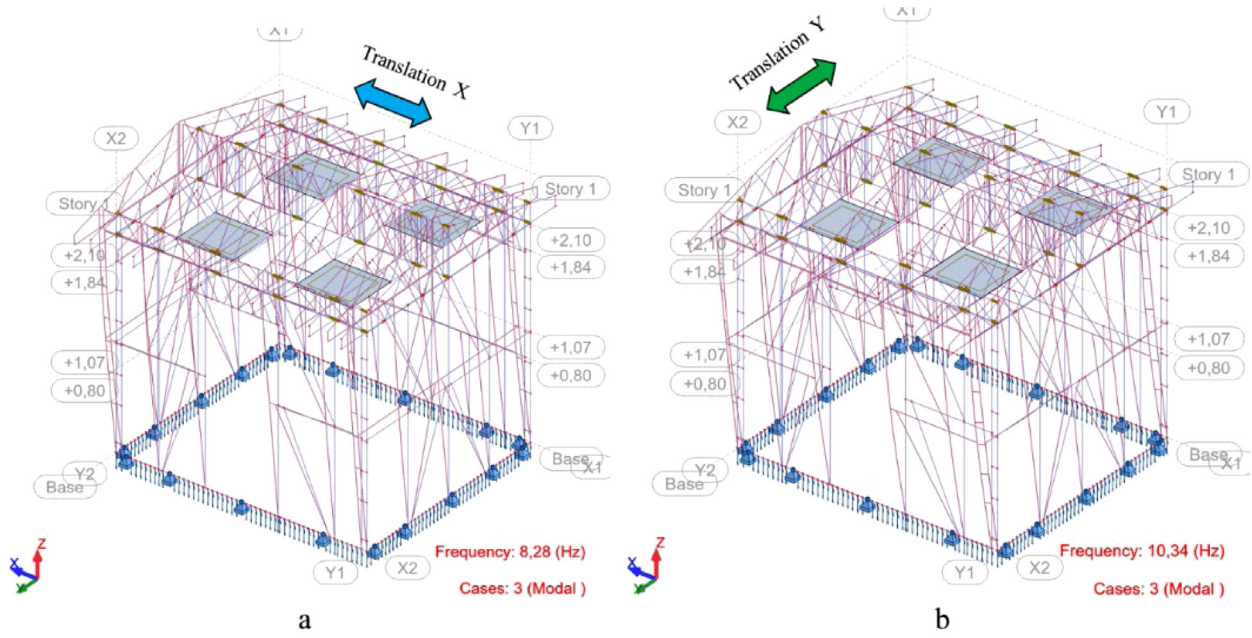

Fig. 24. Vibration modes of nonlinear unloaded-UL model: (a) 1st mode — translation in X direction; (b) 2nd mode — translation in Y direction.

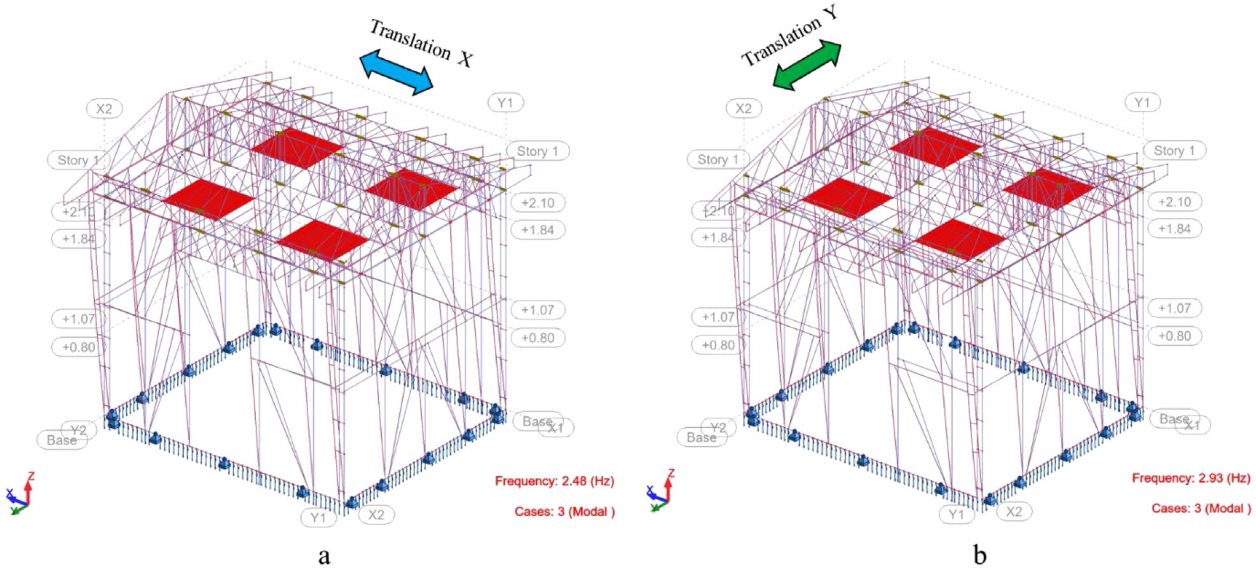

Fig. 25. Vibration modes of nonlinear loaded-L model: (a) 1st mode — translation in X direction; (b) 2nd mode — translation in Y direction.

Table 6
Dynamic analysis results.

Model	Mode	Frequency (Hz)	Period (sec)	Current mass Ux (%)	Current mass Uy (%)	Total mass (kg)	Pulsation	Damping
Unloaded	1	8.28	0.12	83.78	0.01	293	52.05	0.01
FEM k_x = 5650 N/mm	2	10.34	0.10	0.02	84.40	293	64.97	0.01
Unloaded	1	19.93	0.06	85.10	0.01	293	112.04	0.04
FEM k_x=inf	2	26.14	0.05	0.01	84.48	293	125.09	0.04
Unloaded Experimental	1	8.28	0.12	–	–	293	52.05	0.01
Loaded	1	2.48	0.40	96.44	0.05	1496	16.21	0.01
FEM k_x = 2300 N/mm	2	2.73	0.37	0.07	96.66	1496	18.34	0.01
Loaded	1	7.88	0.13	96.89	0	1496	49.54	0.04
FEM k_x = inf	2	10.45	0.10	0	96.78	1496	65.67	0.04
Loaded Experimental	1	2.48	0.40	–	–	1496	15.58	0.02

(b) linear with k_x = 2300 N/mm and (c) linear with k_x = ∞. The maximum intensity of the axial force obtained during the THA for the three considered scenarios is shown in Fig. 28.

It can be observed that the lateral displacements of the linear and nonlinear models with k_x = 2300 N/mm are much larger than in the case of infinite rigidity at the nodes. At the same time, the obtained

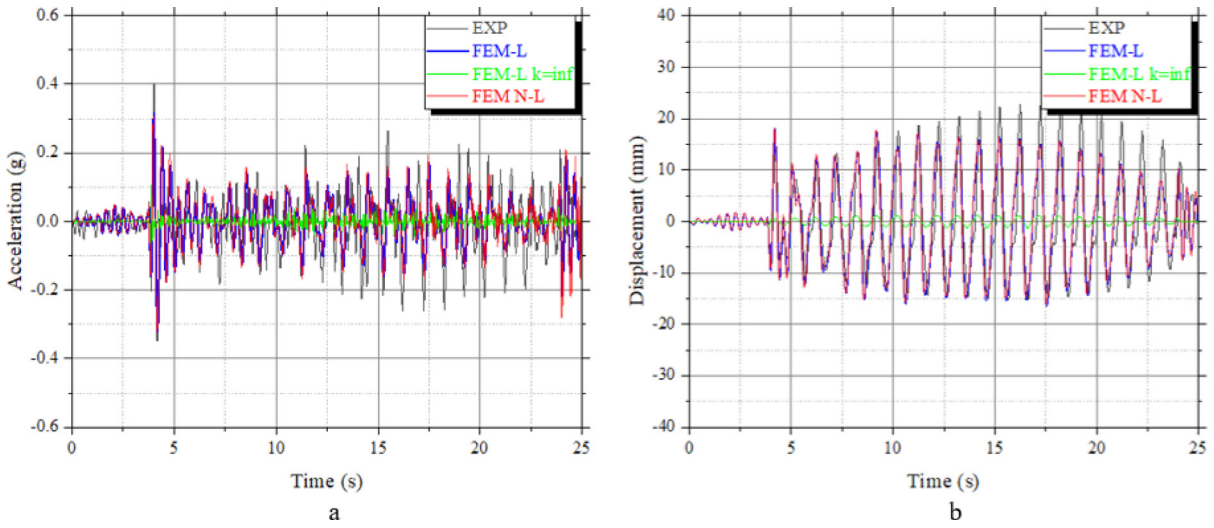

Fig. 26. Results on Loaded-L model, test T11 actions: (a) accelerations; (b) displacements.

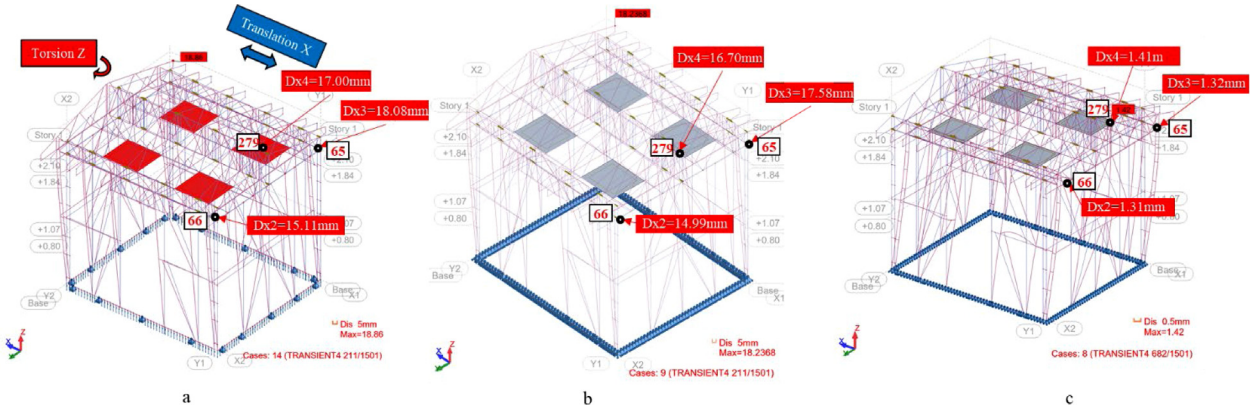

Fig. 27. Time History analysis maximum displacements: (a) Nonlinear model-k_x = 2300 N/mm; (b) linear model-k_x = 2300 N/mm; (c) linear model k_x = inf.

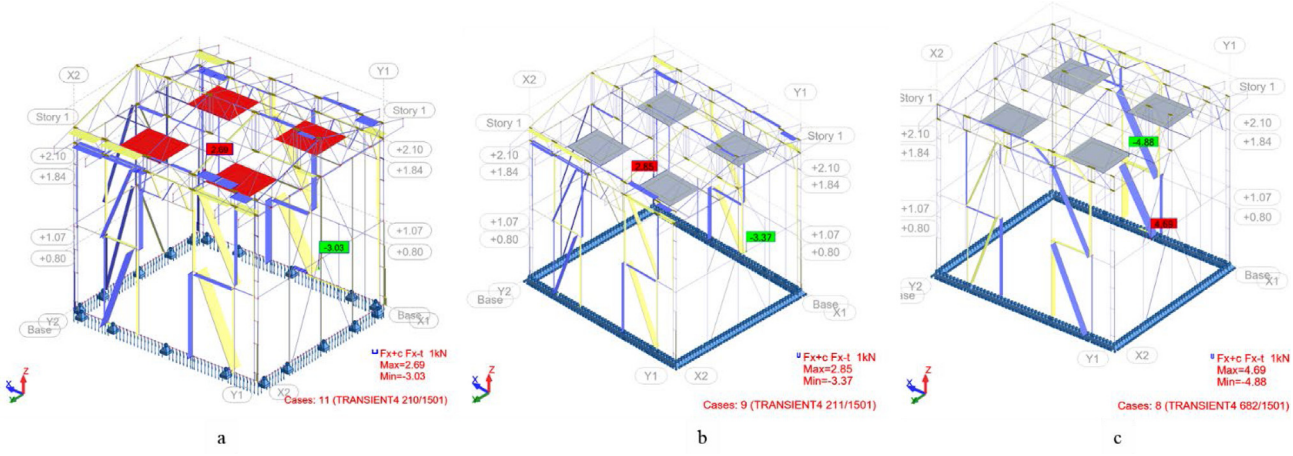

Fig. 28. Maximum axial forces (a) Nonlinear model-k_x = 2300 N/mm; (b) linear model-k_x = 2300 N/mm; (c) linear model k_x = inf.

values of the lateral displacements at node 66, located at the same level as node 65 but on the opposite wall, are different than the ones obtained at node 65 which suggests that a torsional movement was also present. Considering the geometry of the model and the locations for the door and windows openings, this torsional effect was somehow expected.

The maximum intensity of the axial force, 3.03 kN, occurred in the diagonal element of the lower central panel belonging to West wall where window openings were located. For comparison, in case of the model with infinite axial rigidity at the nodes, the corresponding axial force was 4.69 kN.

6. Discussions

Laboratory cyclic tests conducted on the T-joints showed that they have a lower bearing capacity and a lower stiffness compared to the values obtained from direct tensile tests. Even though on the compression side of the cyclic test the initial tendency of the joint was to behave more rigidly compared to the tensile side, the rigidity in compression was significantly reduced after 20 loading cycles and becomes similar to the one in tension. Similar behavior was observed during the experimental tests on the shake table. The obtained results for the axial rigidity of the joints were used in calibrating the numerical model.

The shaking motions at low frequencies of 1 Hz and 1.5 Hz did not produce significant damages into the structure and resulted in an almost rigid body motion response from the model. Very low values of relative accelerations and displacements were obtained even though the amplitude of the input acceleration was increased up to 0.71 g in case of T6. One possible explanation could be the fact that the frequency of the input motion was far away from the fundamental frequency of vibration of the model, 8.28 Hz. However, based on the determined fundamental frequency after each series of tests, it resulted those slight damages could be present in the model since the fundamental frequency decreased to 8.21 Hz, a 0.8% decrease. This small difference may also be due to the inherent measurement errors.

When the frequency of the input motion increased to 6 Hz, larger lateral displacements could be observed. However, the model was still in the linear elastic range of material behavior and the decrease in the fundamental frequency of vibration to 8.09 Hz after the third series of tests could be attributed to the small displacements starting to occur at the joints. This would lead to a more flexible model. The maximum relative displacements increased to 13.44 mm and the relative acceleration reached 1.76 g. The large amplification of the shaking motion, especially in terms of accelerations, could be explained by the ratio of 0.8 between the frequency of the input motion and the fundamental frequency of the model.

The model was loaded with additional masses which would amount to an equivalent load of 1.80 kN/m^2. The increased weight resulted in a 63% decrease in the value of the fundamental frequency from 8.09 Hz to 2.98 Hz. For the loaded model, only a sine beat input motion with a frequency of 1 Hz was selected but with different amplitudes of the input signal. It was observed that during test T11 the relative displacement increased to 22 mm which exceeded the maximum values for ULS by 100%. The fundamental frequency of the model decreased by 16.8% to 2.48 Hz.

During the test T12 the response of the structure was significantly amplified due to damages in the elements and joints and possible resonance phenomenon on higher modes of vibration. After 20 s the relative displacement exceeded 86 mm and failure mechanisms started to develop. This led to further amplification in the response of the structure due to the fact that the fundamental frequency of the model dropped below 2 Hz and became very close to the frequency of the input motion.

The experimental program revealed a complex failure mechanism which can be considered as:

- Global Rocking — a slight uplift of the lower chords of the framing walls between the connection points between the model and the shake table;
- Local buckling of compressed elements such as diagonal elements and even vertical ones near the joints;
- Local buckling of horizontal elements;
- Plastic deformations at the edges of the pre-drilled holes in the CFS profiles;
- Tilting and pulling out of the screws at the joints;
- Tearing of elements in the joint area corresponding to the net cross-sectional area of CFS profile.
- Unfasten of screws at the joints.
- The overall stiffness of the whole structure during the tests decreased due to damages located in general in connections between structural elements. The level of energy absorption is low.

The information collected during the experimental program serves as the starting point for a new series of experiments on similar models with different cladding options such as OSB or gypsum boards. They also served as calibration data for the numerical model developed within the framework of the present research.

The numerical investigation included both linear and non-linear analyses with finite values of axial stiffness at the end of the bar elements determined from cyclic tests. It was observed that for a value of the axial stiffness of 2300 N/mm the results obtained by means of FEA matched the experimental ones very well. Moreover, the values of the relative displacements and accelerations were very close to the ones obtained during the shake table tests. However, the fact that the numerical model did not consider any material non-linearities, only geometrical ones, resulted in quite large differences between the obtained results especially after the experimental model started to exhibit damages due to repeated shaking motions.

7. Conclusions

The paper presents the results obtained after a complex experimental program coupled with numerical simulations on a scaled-down model, 1/1.2 scale, of a CFS structure made of 89 × 41×12× x1 mm lipped channel elements. It represents a replica of constructive solutions for ground floor or ground floor and one or two storeys structures that are frequently met in South-East Europe, including highly active seismic areas.

The main purpose of the research program is to gather both quantitative but more importantly, accurate information in terms of structural response to dynamic actions characterized by input accelerations equal in amplitude to the maximum values specified in seismic design codes, PGA=0.40 g. Comparing both experimental and numerical results obtained for the relative displacements with the maximum allowed values specified in the code for ULS (0.005H) and SLS (0.025H) it can be concluded that the overall stiffness of the structure is able to fulfill the imposed conditions. It was observed that the small values of damping from 0.01 to 0.02 for such structural systems without cladding materials, means they have low energy dissipation capabilities.

The damage of the joints and the reduction in the structural stiffness due to cyclic loads, such as the ones produced by earthquakes, change the eigen period of the structure and has a significant influence on the response of the structure to seismic actions. Larger gravitational loads lead to more extensive damage to the joints.

The developed numerical model based on the experimentally determined connection axial rigidity is able to offer accurate results in terms of the fundamental frequency of vibration, relative accelerations and displacements. This accuracy can be obtained even by running simple linear static and THA analyses, without the need for complex and computationally intensive non-linear approaches. However, for a more accurate capturing of the local damages and onset of failure mechanisms, more complex numerical models are needed, which take into account non-linear material behavior.

The results presented in this paper serve as a starting point for future research works aimed at assessing the influence of the sheathing on the response of CFS structures to seismic actions. Additionally, research in the direction of improved joints with better energy dissipation properties is also pursued by the authors.

CRediT authorship contribution statement

George Taranu: Writing – original draft, Software, Project administration, Methodology, Investigation, Funding acquisition, Data curation, Conceptualization. **Viorel Ungureanu:** Writing – review & editing, Validation, Supervision, Conceptualization, Investigation, Writing – original draft. **Zsolt Nagy:** Writing – review & editing, Validation, Supervision, Investigation, Writing – original draft. **Mihai-Sergiu Alexa-Stratulat:** Methodology, Data curation. **Ionut-Ovidiu Toma:** Writing – original draft, Investigation, Methodology, Writing – review & editing. **Septimiu-George Luca:** Software, Formal analysis, Data curation.

Declaration of competing interest

The authors declare that they have no known competing financial interests or personal relationships that could have appeared to influence the work reported in this paper.

Data availability

Data will be made available on request.

Acknowledgments

The authors acknowledge the contribution of UNIC-ROTAREX, Romania, for supplying the materials, joints and accessories needed for conducting the laboratory investigations.

Additional information

Video shaking table experiment: https://youtu.be/IcGuz9mW8l4
Video Time History vs. Experiment: https://youtu.be/tZVaSpgGxy4
Video of direct tensile tests on T-joints: https://youtu.be/v0yRbs4fWvM
Video of cyclic tests on T-joints: https://youtu.be/eujWg-R-O2U

References

[1] EN 1998-1, Eurocode 8: Design of Structures for Earthquake Resistance – Part 1: General Rules, Seismic Actions and Rules for Buildings, CEN, Brussels, Belgium, 2004.
[2] P100/2013-1, Seismic Design Code - Part I: Design Rules for Buildings, M.D.L.P.A Romania, 2013, (in Romanian).
[3] EN 1993-1-3, Eurocode 3: Design of Steel Structures, Part 1.3: General Rules, Supplementary Rules for Cold-Formed Thin Gauge Members and Sheeting, CEN, Brussels, Belgium, 2006.
[4] EN 1993-1-5, Eurocode 3: Design of Steel Structures-Part 1-5: Plated Structural Elements, CEN, Brussels, Belgium, 2006.
[5] S.K. Naman, B.J. Goodno, Seismic evaluation of a low rise steel building, Eng. Struct. 8 (1986) 9–16, http://dx.doi.org/10.1016/0141-0296(86)90014-3.
[6] R.T. Severn, D.P. Stoten, Y. Tagawa, The contribution of shaking tables to earthquake engineering, in: 15 WCEE, 2012.
[7] B.W. Schafer, D. Ayhan, J. Leng, P. Liu, D. Padilla-Llano, K.D. Peterman, M. Stehman, S.G. Buonopane, M. Eatherton, R. Madsen, B. Manley, C.D. Moen, N. Nakata, C. Rogers, C. Yu, Seismic response and engineering of cold-formed steel framed buildings, Structures 8 (2016) 197–212, http://dx.doi.org/10.1016/j.istruc.2016.05.009.
[8] K.D. Peterman, M.J.J. Stehman, R.L. Madsen, S.G. Buonopane, N. Nakata, B.W. Schafer, Experimental seismic response of a full-scale cold-formed steel-framed building. I: System-level response, J. Struct. Eng. 142 (2016) http://dx.doi.org/10.1061/(asce)st.1943-541x.0001577.
[9] B.W. Schafer, Cold-formed steel structures around the world, Steel Constr. 4 (2011) 141–149, http://dx.doi.org/10.1002/STCO.201110019.
[10] N. Nakata, B.W. Schafer, R.L. Madsen, Seismic design of multi-story cold-formed steel buildings: The CFS-NEES archetype building, in: Structures Congress 2012 - Proceedings of the 2012 Structures Congress, 2012, http://dx.doi.org/10.1061/9780784412367.134.
[11] K.D. Peterman, R.L. Madsen, B.W. Schafer, Experimental seismic behavior of the CFS-NEES building: System- level performance of a full-scale two-story light steel framed building, in: 22nd International Specialty Conference on Recent Research and Developments in Cold-Formed Steel Design and Construction, 2014.
[12] P. Liu, K.D. Peterman, C. Yu, B.W. Schafer, Cold-formed steel shear walls in ledger-framed buildings, in: Structural Stability Research Council Annual Stability Conference, 2012.
[13] X. Wang, T.C. Hutchinson, Evolution of modal characteristics of a mid-rise cold-formed steel building during construction and earthquake testing, Int. J. Earthq. Eng. Struct. Dyn. 49 (2020) 1539–1558, http://dx.doi.org/10.1002/EQE.3316.
[14] R. Landolfo, O. Iuorio, L. Fiorino, Experimental seismic performance evaluation of modular lightweight steel buildings within the ELISSA project, Earthq. Eng. Struct. Dyn. 47 (2018) http://dx.doi.org/10.1002/eqe.3114.
[15] V. Macillo, L. Fiorino, R. Landolfo, Seismic response of CFS shear walls sheathed with nailed gypsum panels: Experimental tests, Thin-Walled Struct. 120 (2017) 161–171, http://dx.doi.org/10.1016/j.tws.2017.08.022.
[16] L. Fiorino, V. Macillo, R. Landolfo, Shake table tests of a full-scale two-story sheathing-braced cold-formed steel building, Eng. Struct. 151 (2017) 633–647, http://dx.doi.org/10.1016/j.engstruct.2017.08.056.
[17] R. Landolfo, A. Campiche, O. Iuorio, L. Fiorino, Seismic performance evaluation of CFS strap-braced buildings through experimental tests, Structures 33 (2021) http://dx.doi.org/10.1016/j.istruc.2021.05.098.
[18] S. Shakeel, B. Bucciero, A. Campiche, T. Pali, L. Fiorino, R. Landolfo, Shake table testing and numerical modelling of LWS strap-braced structures for seismic performance evaluation, in: AIP Conference Proceedings, 2019, http://dx.doi.org/10.1063/1.5114270.
[19] A. Campiche, S. Shakeel, B. Bucciero, T. Pali, L. Fiorino, R. Landolfo, Seismic behaviour of strap-braced LWS structures: Shake table testing and numerical modelling, in: IOP Conference Series: Materials Science and Engineering, 2019, http://dx.doi.org/10.1088/1757-899X/473/1/012032.
[20] M.T. Terracciano, B. Bucciero, T. Pali, V. Macillo, L. Fiorino, R. Landolfo, Shake table tests of structures with CFS strap-braced stud walls, Key Eng. Mater. 763 (2018) http://dx.doi.org/10.4028/www.scientific.net/KEM.763.432.
[21] V. Macillo, A. Campiche, S. Shakeel, B. Bucciero, T. Pali, M.T. Terracciano, L. Fiorino, R. Landolfo, Seismic behaviour of sheathed CFS buildings: Shake-Table testing and numerical modelling, Key Eng. Mater. 763 (2018) http://dx.doi.org/10.4028/www.scientific.net/KEM.763.584.
[22] A. Campiche, S. Shakeel, V. Macillo, M.T. Terracciano, B. Bucciero, T. Pali, L. Fiorino, R. Landolfo, Seismic behaviour of sheathed CFS buildings: Shake table tests and numerical modelling, Ingen. Sismica 35 (2018).
[23] D. Dubina, Behavior and performance of cold-formed steel-framed houses under seismic action, J. Construct. Steel Res. 64 (2008) 896–913, http://dx.doi.org/10.1016/J.JCSR.2008.01.029.
[24] L.A. Fülöp, D. Dubina, Performance of wall-stud cold-formed shear panels under monotonic and cyclic loading: Part II: Numerical modelling and performance analysis, Thin-Walled Struct. 42 (2004) 339–349, http://dx.doi.org/10.1016/S0263-8231(03)00064-8.
[25] D. Dubina, L. Fülöp, V. Ungureanu, I. Szabo, Z. Nagy, Cold-Formed Steel Structures for Residential and Non-Residential Buildings, Timisoara, 2000.
[26] D. Dubina, L.A. Fülöp, A. Aldea, S. Demetriu, Z. Nagy, Seismic performance of cold-formed steel framed houses, in: Proceedings of 5th International Conf. on Behaviour of Steel Structures in Seismic Areas (STESSA), Yo1kohama, 2006, pp. 429–435.
[27] D. Dubina, A. Stratan, A. Ciutina, L. Fulop, Z. Nagy, Strength, stiffness and ductility of cold-formed steel bolted connections, in: International Workshop on Connections in Steel Structures V, Behaviour, Strength & Design, 2004.
[28] V. Ungureanu, I. Both, M. Burca, B. Radu, C. Neagu, D. Dubina, Experimental and numerical investigations on built-up cold-formed steel beams using resistance spot welding, Thin–Walled Struct. 161 (2021) http://dx.doi.org/10.1016/j.tws.2021.107456.
[29] O. Senkardesler, G. Goler, S. Soyoz, Dynamic and cyclic response of a full-scale 2-storey cold-formed steel structure with and without infill materials, Bull. Earthq. Eng. 15 (2017) 3207–3226, http://dx.doi.org/10.1007/s10518-016-0042-1.
[30] C. Hui, L. Gardner, D.A. Nethercot, Moment redistribution in cold-formed steel continuous beams, Thin-Walled Struct. 98 (2016) 465–477, http://dx.doi.org/10.1016/J.TWS.2015.10.009.
[31] P. Kyvelou, L. Gardner, D.A. Nethercot, Composite Action Between Cold-Formed Steel Beams and Wood-Based Floorboards, vol. 15, 2015, http://dx.doi.org/10.1142/S0219455415400295.
[32] J. Wang, W. Wang, Y. Xiao, B. Yu, Cyclic test and numerical analytical assessment of cold-formed thin-walled steel shear walls using tube truss, Thin-Walled Struct. 134 (2019) 442–459, http://dx.doi.org/10.1016/J.TWS.2018.09.038.
[33] X. Wang, T.C. Hutchinson, G. Hegemier, Seismic behavior of cold-formed steel shear walls during full-scale building shake table tests, in: Wei-Wen Yu International Specialty Conference on Cold-Formed Steel Structures 2018 - Recent Research and Developments in Cold-Formed Steel Design and Construction, 2018.
[34] C. Wang, Z. Yang, Z. Zhang, R. Qi, Experimental study on shear behavior of cold-formed steel shear walls with bracket, Structures 32 (2021) 448–460, http://dx.doi.org/10.1016/j.istruc.2021.03.064.
[35] Y. Zou, X. Zhou, Y. Shi, Z. Wang, K. Ke, Z. Zhang, Y. Guan, Shear resistance of cold-formed thin-walled steel inter-story connections, J. Construct. Steel Res. 183 (2021) http://dx.doi.org/10.1016/j.jcsr.2021.106757.

[36] A. Singh, X. Wang, S. Torabian, T.C. Hutchinson, K.D. Peterman, B.W. Schafer, Seismic performance of symmetric unfinished CFS in-line wall systems, in: Structures Congress 2020 - Selected Papers from the Structures Congress 2020, 2020, http://dx.doi.org/10.1061/9780784482896.058.

[37] H.J. Kim, D.H. Shin, Shake table test program of cold-formed steel in-plane partition walls, Structures 30 (2021) http://dx.doi.org/10.1016/j.istruc.2021.01.026.

[38] Y. Guan, X. Zhou, X. Yao, Y. Shi, Seismic performance of prefabricated sheathed cold-formed thin-walled steel buildings: Shake table test and numerical analyses, J. Construct. Steel Res. 167 (2020) http://dx.doi.org/10.1016/j.jcsr.2019.105837.

[39] J. Jing, G.C. Clifton, K. Roy, J.B.P. Lim, Three-storey modular steel building with a novel slider device: Shake table tests on a scaled down model and numerical investigation, Thin-Walled Struct. 155 (2020) 106932, http://dx.doi.org/10.1016/J.TWS.2020.106932.

[40] L. Jiang, K. Yu, J. Ye, Y. Hu, L. Jiang, Seismic damage assessment and shaking-table test validation of midrise cold-formed steel composite shear wall buildings, J. Struct. Eng. 148 (2022) 04022093, http://dx.doi.org/10.1061/(ASCE)ST.1943-541X.0003387.

[41] Y. Hu, L. Jiang, J. Ye, X. Zhang, L. Jiang, Seismic responses and damage assessment of a mid-rise cold-formed steel building under far-fault and near-fault ground motions, Thin-Walled Struct. 163 (2021) 107690, http://dx.doi.org/10.1016/J.TWS.2021.107690.

[42] L. Jiang, J. Ye, Redundancy of a mid-rise CFS composite shear wall building based on seismic response sensitivity analysis, Eng. Struct. 200 (2019) 109647, http://dx.doi.org/10.1016/J.ENGSTRUCT.2019.109647.

[43] L. Jiang, J. Ye, Quantifying the effects of various uncertainties on seismic risk assessment of CFS structures, 18, 2020, pp. 241–272, http://dx.doi.org/10.1007/s10518-019-00726-w.

[44] I.-O. Toma, M. Budescu, G. Albu, Seismic behaviour of an experimental model made of thin-walled cold formed steel profiles - Hardell structures, in: The Bulletin of the Polytechnic Institute of Jassy, Construction. Architecture Section, vol. 67, 2009.

[45] A. Firouzianhaij, N. Usefi, B. Samali, P. Mehrabi, Shake table testing of standard cold-formed steel storage rack, Appl. Sci. 2021 (2021) 1821, http://dx.doi.org/10.3390/app11041821.

[46] G. Taranu, I.O. Toma, Experimental investigation and numerical simulation of c-shape thin-walled steel profile joints, Buildings 11 (2021) http://dx.doi.org/10.3390/buildings11120636.

[47] TR Group, Self Drilling Screw, DIN 7504N ~ISO 15481. (n.d.). https://www.trfastenings.com/Products/Catalogue/Screws-and-Bolts/Self-Drilling-Screws/Pan-Head/Cross-Recess-H-Drive (accessed May 4, 2022).

[48] TR Group, Screws Mechanical Properties ISO 898-1 EN 20898-1, (n.d.). https://www.trfastenings.com/products/knowledgebase/steel-fasteners/screws-and-bolts-mechanical-properties (accessed May 4, 2022).

[49] TR Group, Self Tapping Screw, DIN 7981C ~ISO 7049. (n.d.). https://www.trfastenings.com/Products/Catalogue/Screws-and-Bolts/Self-Tapping-Screws/Pan-Head/Cross-Recess-H-Drive/Form-C (accessed May 4, 2022).

[50] P.D. Moncarz, Helmut Krawinkler, Theory and Application of Experimental Model Analysis in Earthquake Engineering, Stanford, California, 1981.

[51] P. Candeias, A. Campos Costa, E. Coelho, Shaking TableTests of 1:3 Reduced Scale Models of Four Story Unreinforced Masonry Buildings, in: 3 Th World Conference on Earthquake Engineering S, 2004.

[52] Mapping Europe's earthquake risk | Research and Innovation, (n.d.), https://ec.europa.eu/research-and-innovation/en/horizon-magazine/mapping-europes-earthquake-risk (accessed April 1, 2022).

[53] ISO 12106:2017(E) - Metallic materials-fatigue testing - Axial-strain-controlled method, 2017.

[54] ASTM E606/E606M-12 - Standard Test Method for Strain-Controlled Fatigue Testing, 2012, http://dx.doi.org/10.1520/E0606-04E01.

[55] M. Kotełko, J. Grudziecki, V. Ungureanu, D. Dubina, Ultimate and post-ultimate behaviour of thin-walled cold-formed steel open-section members under eccentric compression. Part I: Collapse mechanisms database (theoretical study), Thin-Walled Struct. 169 (2021) 108366, http://dx.doi.org/10.1016/J.TWS.2021.108366.

[56] Ł. Borkowski, J. Grudziecki, M. Kotełko, V. Ungureanu, D. Dubina, Ultimate and post-ultimate behaviour of thin-walled cold-formed steel open-section members under eccentric compression. Part II: Experimental study, Thin-Walled Struct. 171 (2022) 108802, http://dx.doi.org/10.1016/J.TWS.2021.108802.

[57] N. Usefi, P. Sharafi, H. Ronagh, Numerical models for lateral behaviour analysis of cold-formed steel framed walls: State of the art, evaluation and challenges, Thin-Walled Struct. 138 (2019) 252–285, http://dx.doi.org/10.1016/J.TWS.2019.02.019.

[58] I. Shamim, C.A. Rogers, Numerical modelling and calibration of CFS framed shear walls under dynamic loading, in: 21st International Specialty Conference on Cold-Formed Steel Structures - Recent Research and Developments in Cold-Formed Steel Design and Construction, 2012.

[59] A.A. Kasimzade, S. Tuhta, G. Atmaca, S. Ozdemir, Analytical and experimental modal analysis of a model cold formed steel (CFS) structures using microtremor excitation, in: Seismic Isolation, Structural Health Monitoring, and Performance Based Seismic Design in Earthquake Engineering: Recent Developments, 2018, http://dx.doi.org/10.1007/978-3-319-93157-9_9.

[60] A. Campiche, L. Fiorino, R. Landolfo, Numerical modelling of CFS two-storey sheathing-braced building under shaking-table excitations, J. Construct. Steel Res. 170 (2020) http://dx.doi.org/10.1016/j.jcsr.2020.106110.

[61] EN 1993-1-8, Eurocode 3: Design of steel structures - Part 1-8: Design of joints, CEN, Brussels, Belgium, 2005.

[62] EN 1993-1-1, Eurocode 3: Design of Steel Structures - Part 1-1: General Rules and Rules for Buildings, CEN, Brussels, Belgium, 2005.

[63] Robot Structural Analysis Professional, (n.d.). https://www.autodesk.com/products/robot-structural-analysis/overview (accessed January 13, 2022).

applied sciences

MDPI

Article

Experimental Investigations on the Long Term Material Properties of Rubberized Portland Cement Concrete

Ionut-Ovidiu Toma *, Sergiu-Mihai Alexa-Stratulat, Petru Mihai, Ana-Maria Toma and George Taranu

Faculty of Civil Engineering and Building Services, The Gheorghe Asachi Technical University of Iasi, 700050 Iași, Romania; sergiu-mihai.alexa-stratulat@staff.tuiasi.ro (S.-M.A.-S.); petru.mihai@academic.tuiasi.ro (P.M.); ana-maria.toma@academic.tuiasi.ro (A.-M.T.); george.taranu@academic.tuiasi.ro (G.T.)

* Correspondence: ionut.ovidiu.toma@tuiasi.ro; Tel.: +40-232-701-455

Featured Application: The use of rubberized concrete in structural applications demands the assessment of its strength and elastic properties. The evolution of these properties in time is important for making pertinent predictions related to the safety of structural elements.

Abstract: The paper presents the results of a research work aimed at assessing the long-term strength and elastic properties of rubberized concrete. The parameters of the research were the rubber replacement of fine aggregates and the age of testing the specimens. Compressive and splitting tensile strength of concrete cylinders were obtained at the age of 5 years, coupled with the static and dynamic modulus of elasticity of all concrete specimens. Additionally, the material damping coefficient was assessed by means of non-destructive tests. The density of the rubberized concrete decreases with the percentage replacement of natural sand by rubber aggregates. A significant drop in the values of density after 5 years was observed for specimens made with rubberized concrete. The static and the dynamic moduli of elasticity decrease with the increase in rubber content. A similar trend is observed for the compressive and tensile splitting strength.

Keywords: long term properties; dynamic modulus of elasticity; material damping; rubberized concrete; compressive strength

Citation: Toma, I.-O.; Alexa-Stratulat, S.-M.; Mihai, P.; Toma, A.-M.; Taranu, G. Experimental Investigations on the Long Term Material Properties of Rubberized Portland Cement Concrete. *Appl. Sci.* **2021**, *11*, 10868. https://doi.org/10.3390/app112210868

Academic Editor: Muhammad Junaid Munir

Received: 26 October 2021
Accepted: 15 November 2021
Published: 17 November 2021

1. Introduction

Concrete, one of the most used construction materials, has been intensively studied due to the complex phenomena governing its behavior from an early age to the long term [1]. Despite its many uncontested advantages as a construction material, concrete also has some drawbacks that prompted an overwhelming research effort to either mitigate or eliminate them entirely. However, perhaps one of the biggest advantages of concrete is its ability to incorporate a variety of wastes from different sources: power plants [2], steel manufacturing processes [3], construction and demolition wastes, municipal wastes, etc.

The latest report of ETRMA (European Tyre and Rubber Manufacturers' Association) shows that in 2019, a total of 3.55 million tons of tires reached their end of life in Europe alone. Most of them, 95%, according to the same report, were treated through either material or energy recovery (cement kilns, urban heating and power plants) techniques. The application of ELT (end of life tires) derived materials in civil engineering, public works and backfilling amounted to a total of 112 thousand tons, a significant 18% increase compared to 2018.

In view of the continuously stricter regulations in terms of environmental protection and abiding by the concept of circular economy, the construction industry has looked for alternatives in terms of reducing the carbon footprint and preserving the raw materials. The use of rubber crumbs from ELTs as partial substitutes of fine and small coarse aggregates was investigated for the past 25 years. From the early works of Fattuhi and Clark [4] up

to the recent research of Wang et al. [5], much effort was invested in understanding the behavior of this new type of concrete.

From the very beginning, it was clear that adding rubber aggregates to concrete resulted in a decrease in the values of mechanical properties [6]. Since strength and elastic properties are the main parameters considered in the design process of structural elements, rubberized concrete has seen limited application in this direction unless special confining solutions were applied [7–9]. However, significant deformability was achieved for a material that is inherently brittle [10]. This fact, coupled with the proven ability of rubberized concrete to dampen vibrations, resulted in it being used for various purposes, from road crush barriers to non-structural elements designed to reduce the traffic vibrations or to have enhanced soundproofing properties. Moreover, the durability of concrete incorporating rubber aggregates was found to be higher [11], especially in the case of sulfate corrosion [12].

However, the data presented in the scientific literature focused on the short-term values of the mechanical properties of Portland cement concrete containing rubber aggregates. This is completely understandable given the fact that all design guidelines refer to the strength values and modulus of elasticity obtained by means of standardized tests at the age of 28 days. This allows for a quick and unified approach to assess whether a certain type of concrete is suitable for structural or non-structural applications.

On the other hand, the long-term strength and elastic properties of concrete are rarely investigated, and it is generally assumed they increase in time, provided that there are no deleterious agents acting upon the material. Accelerated durability tests are able to offer information on the ability of concrete to keep its integrity when subjected to chemical attacks and environmental factors (freeze-thaw).

The paper presents the results of a research work aimed at assessing the long-term strength and elastic properties of rubberized concrete. The parameters of the research were the rubber replacement of fine aggregates and the age of testing the specimens. Compressive and splitting tensile strength of concrete cylinders were obtained at the age of 5 years, coupled with a static and dynamic modulus of elasticity of all concrete specimens. Additionally, the material damping coefficient was assessed by means of non-destructive tests.

The significance of the conducted research work relies on the fact that it puts forward data for the material properties of rubberized concrete (RuC) well beyond the standard testing time of 28 days. The main objective was to determine the values of the modulus of elasticity, compressive and tensile splitting strength and their evolution after a significantly longer time interval compared to the standard testing time. Material damping was another important factor considered in the research since it offers an insight into the damping properties of RuC. On the other hand, the data are limited by the number of selected mix proportions, type of aggregate that was replaced by rubber particles as well as storage conditions of the specimens.

2. Materials and Methods

2.1. Materials

The target concrete strength class considered in the research was C30/37. The specimens were cast as part of the FP7-ANAGENNISI (ENV.2013.6.3-1: 603722) project, where large sets of data were obtained for statistical analysis in terms of concrete compressive strength. The target compressive strength for RuC was 20 MPa so that it would actually be used in structural applications. Since replacing natural aggregates with rubber aggregates would result in a decrease of the compressive strength, several strength classes were considered at that time for the reference concrete mix. Based on the experimental data obtained, at the age of 28 days, the C30/37 concrete proved to be the most economical solution in terms of cement consumption. It would lead to the desired compressive strength for the rubberized concrete derived from it at the standard testing age of 28 days.

A CEM I 42.5R type of cement, readily available on the market, was used. The choice of the cement type was based on the fact that high early age compressive strength was sought

during the initial experimental plan. River aggregates with rounded edges were used as natural aggregates. The rounded edges prevent the occurrence of stress concentrations and the initiation of early cracking.

The rubber aggregates (Figure 1) came from a local supplier and were obtained from shredding and grinding of the tires from commercial vehicles. The surface texture of the aggregates, as a result of the shredding process, is shown in Figure 1a. Figure 1b gives an overview of the maximum particle size. The rubber aggregates were sorted according to their maximum size and cleaned from any impurities before being delivered in bulk. The impurities refer to any steel parts and/or textiles resulting from the shredding process. The particle size distribution is shown in Figure 1c.

(**a**)

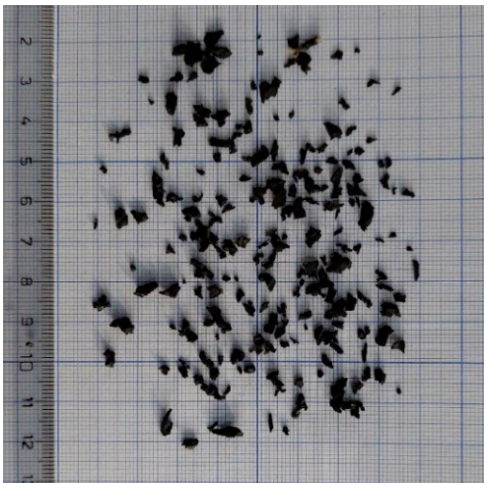

(**b**)

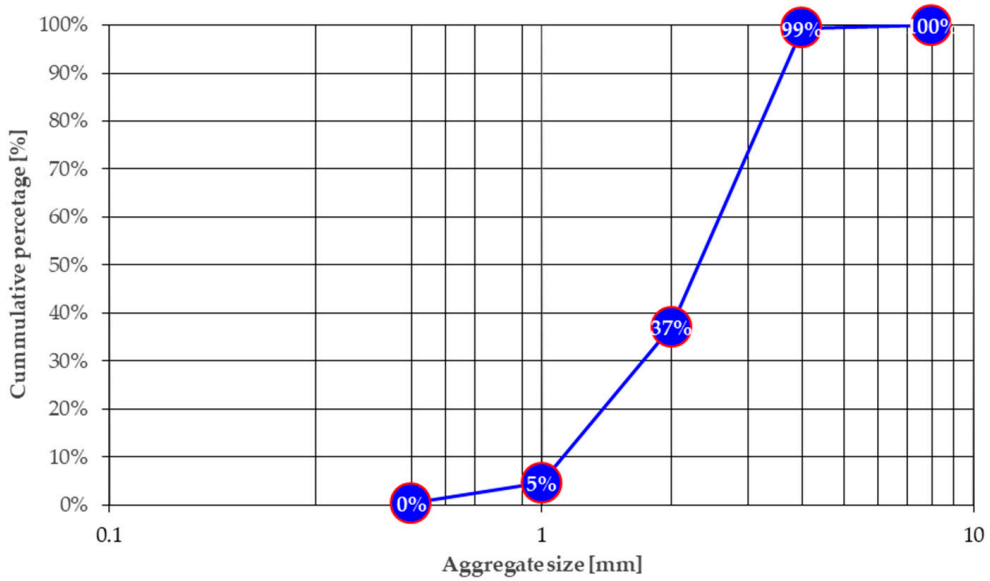

(**c**)

Figure 1. Rubber aggregates from worn tyres. (**a**) Surface texture; (**b**) Rubber aggregates; (**c**) Particle size distribution.

2.2. Methods

The mix proportion considered at the beginning of the experimental program is shown in Table 1 [6]. The water to cement ratio was kept constant to 0.47 for all mix proportions. The mix proportions were denoted as Ref, for the reference mix without any rubber aggregates, and RuC for rubberized concrete, followed by a number showing the replacement percentage, by volume, of sand by rubber aggregates. The data were converted to mass units when preparing the mix proportions, as presented in Table 1.

Table 1. Mix proportions used in the research.

Mix Designation	Cement (C) CEM I 42.5R	Water (W)	W/C	Aggregates			
				Sand	Rubber	Sort 4–8 mm	Sort 8–16 mm
	[kg/m^3]	[kg/m^3]	-	[kg/m^3]	[kg/m^3]	[kg/m^3]	[kg/m^3]
Ref	489	230	0.47	582	-	388	647
RuC40				532	50		
RuC60				514.8	67.2		
RuC80				492.4	89.6		

The rubber aggregates were set to replace the natural sand, with a maximum dimension of 4 mm. The replacement percentages, by volume, were 40%, 60% and 80%. The apparent density of the rubber aggregates was experimentally determined, 506 kg/m^3, and was found to be in line with similar reported data in the scientific literature [13].

A total number of 20 cylinders (ϕ100 $\times$ 200 mm) were cast, resulting in a total number of 80 specimens. The specimens were demolded at 24 h after casting and cured in water for 28 days. At the age of 28 days, a cylindrical specimen of each mix proportion was cut in 30 mm thick slices to assess the distribution of the rubber aggregates within the concrete mix, as shown in Figure 2. After 28 days, the samples were kept in laboratory conditions (23 $\pm$ 2 °C and relative air humidity of 40–50%) until the day of testing, 5 years later.

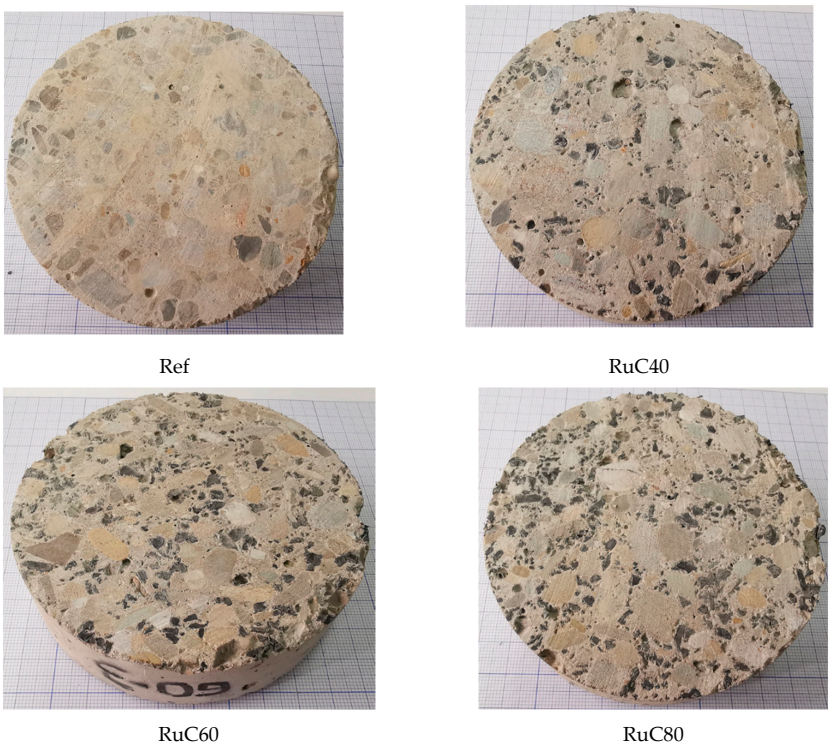

Figure 2. Distribution of rubber aggregates in concrete specimens at the age of 28 days.

The static longitudinal modulus of elasticity was assessed in accordance with specifications of SR EN 12390:13 [14]. Cyclic loading was applied within limits mentioned in the code, and three individual values were obtained for each specimen. One cylinder was loaded in compression until failure in order to set the correct upper and lower limits of the loading cycles, as shown in Figure 3a. Therefore, the static longitudinal modulus of elasticity was assessed for 19 specimens only, with 3 distinct measurements for each specimen. The experimental setup is shown in Figure 3b. A hinge was used between the loading platens of equipment and the concrete cylinder in order to ensure an even distribution of the compressive load.

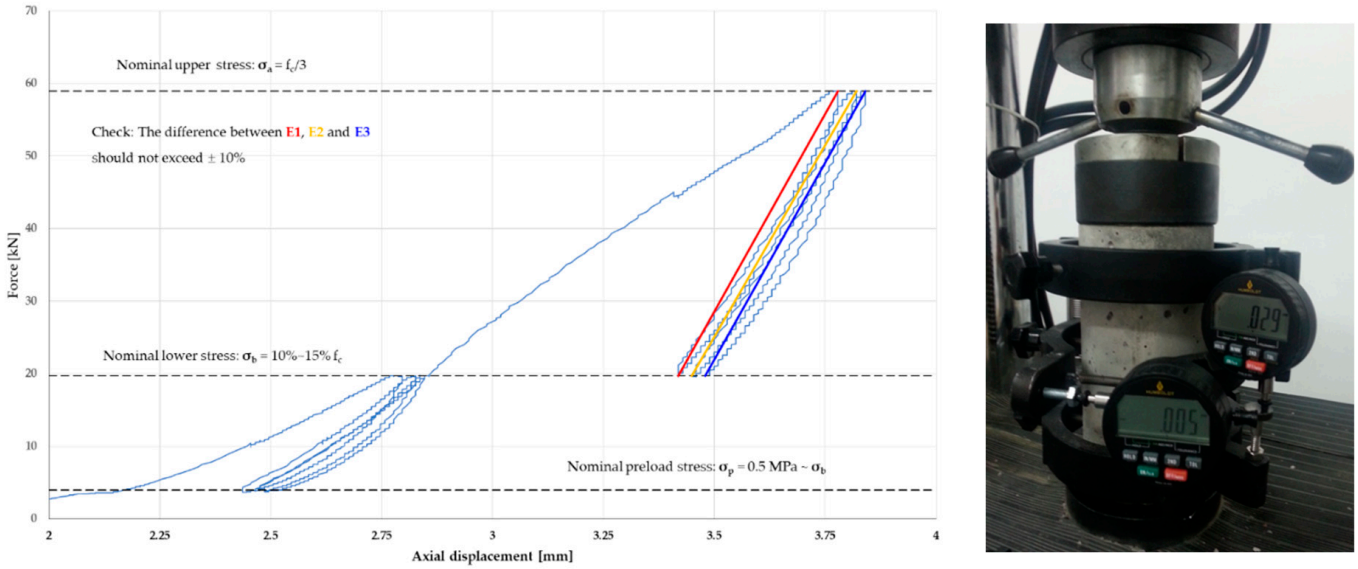

(**a**) (**b**)

Figure 3. Assessment of the static modulus of elasticity. (**a**) Standard loading scenario; (**b**) Experimental setup.

The compressive and splitting tensile strengths were determined in accordance with SR EN 12390:3 [15] and SR EN 12390:6 [16], respectively. The considered loading rate for determining the compressive strength was 0.6 MPa/s (4.71 kN/s), whereas, for the tensile splitting strength, a loading rate of 0.05 MPa/s (0.4 kN/s) was adopted.

The dynamic longitudinal modulus of elasticity, E_d, was assessed following the guidelines of ASTM C215:14 [17] and was based on the first resonant frequency (FRF) obtained from the Impact Echo Method. The experimental setup is shown in Figure 4. An accelerometer was placed at one end of the concrete cylinder along the longitudinal axis of the specimen to record the response of the sample when subjected to a small impact load at the opposite end. The signal was recorded on a computer via a data acquisition system. The dynamic modulus of elasticity for the cylindrical specimens was computed as shown in Equation (1):

$$E_d = D \cdot m \cdot f_{ln}^2 \quad (1)$$

where m is the mass of the sample [kg], f_{ln} is the fundamental frequency of vibration [Hz] and D is a coefficient that depends on both the diameter and the length of the cylinder (Equation (2)):

$$D = 5.093 \cdot \frac{L}{d^2} \quad (2)$$

where L is the length of the cylinder [m] and d is the diameter [m].

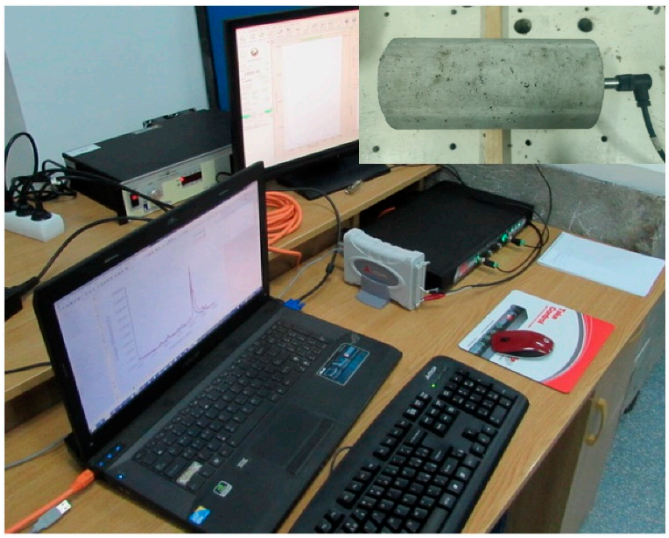

Figure 4. Assessment of the dynamic modulus of elasticity.

The material damping properties were assessed by means of the decaying rate function obtained from the damped free vibrations response of the specimens.

3. Results and Discussions

3.1. Density

Figure 5 presents the variation in density with the age of specimens using as reference the values obtained at the standard curing age of 28 days [6]. The presented data are the average value of 20 measurements for the age of 5 years and 30 measurements for the early age.

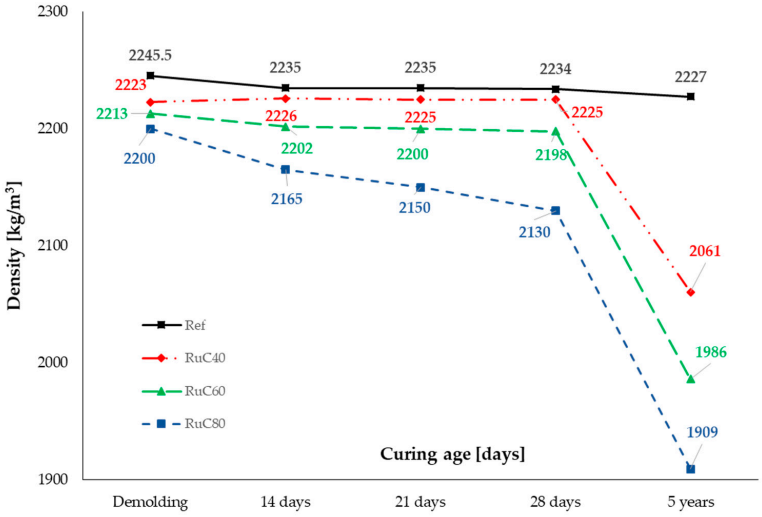

Figure 5. Variation in density with age of specimens.

It can be observed that even though all specimens were kept in the same conditions, the reference kept its value for the density as compared to 28 days. The change from 28 days to 5 years was less than 1%. On the other hand, all three mixes of RuC exhibited a much larger decrease in the density by as much as 12% for RuC80. A possible explanation could be that, even though the same water/cement ratio was used for all mixes, due to the hydrophobic nature of rubber particles, the excess water available for the hydration of the cement paste evaporated due to the storage conditions. Since the amount of cement was the same for all mixes (Table 1) and the curing and storing conditions were identical, it was

thought that the rate of hydration was similar for all mixes, and therefore the excess water was lost by evaporation.

According to a recent study on rubberized concrete [18], the porosity and density of micro-cracks in RuC increased with the curing age, although the determined pore radius decreased. All other chemical reactions and rate of strength increase were similar to normal concrete. Earlier findings [19] showed that keeping concrete specimens in hot and, especially, dry conditions would result in overall lower values of the strength and elastic properties that are closely related to the density of the material.

In a similar study [20], it was concluded that the addition of rubber particles increased the number of cracks inside the concrete, which favors the migration of chemically unbound water, weakened the ITZ between the rubber aggregate and cement paste, and entrained more air during the mixing process. As a direct, immediate consequence, the density of rubberized concrete decreased compared to the normal concrete.

The presented trend is in line with data available in the scientific literature and with the general consensus that adding rubber to the concrete mix leads to a decrease in the density of rubberized concrete compared to the equivalent reference mix [11].

3.2. Static Modulus of Elasticity

As previously mentioned, the static modulus of elasticity in compression was determined in accordance with currently available standards [14]. The results are presented in Figure 6 as the average values of 19 determinations each of these individual values were, in turn, obtained as the average of three measurements, as shown in Figure 3.

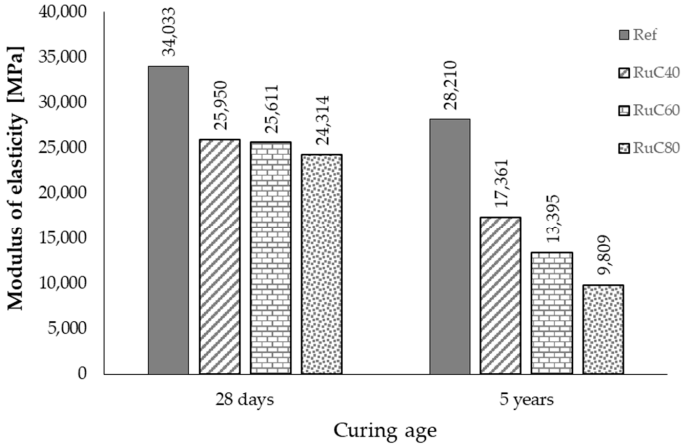

Figure 6. Variation in the static modulus of elasticity in time.

It can be observed that irrespective of the mix, there is a decrease in the values of the static modulus of elasticity. The decrease ranged from 17% for the reference mix up to 60% for RuC80. Small variations in the values of modulus of elasticity were reported in the literature for concrete with fly ash, but the curing and exposure conditions were different compared to the present study [21]. The storage conditions of the specimens presented in this study favored the loss of water by evaporation through pores and capillaries.

Rubberized concrete specimens were most affected by this due to the fact that the presence of rubber aggregates favor the occurrence of weak links at the interface between the cement paste and rubber particles, thus favoring migration of water towards the surface of the specimens. A similar decrease in the values of mechanical and elastic properties of RuC was reported in the scientific literature, although for much smaller replacement percentages [22].

The decrease in the values of the static modulus of elasticity ranged from 38.6% for RuC40 to 65.23% for RuC80 mix compared to the reference mix.

3.3. Dynamic Modulus of Elasticity

The determination of the dynamic modulus of elasticity was based on the first resonant frequency of the cylindrical specimen, which was determined by means of the impact echo method. The free vibration response of all specimens (20 for each of the mix proportions presented in Table 1) was recorded, as shown in Figure 7a for the Ref mix, using the experimental setup presented in Figure 4. The Fast Fourier Transform (FFT) was applied to the recorded signal so that to obtain the response spectrum of the specimens, as shown in Figure 7b, from which the fundamental frequency of vibration was identified. For each cylindrical specimen, there were considered at least four measurements from which the fundamental frequency of vibration was calculated, as shown in Figure 8. The different scales used for the vertical axis of the graph were necessary since the response spectrum amplitude varied from one impact to another because the impact energy was different. The use of a single scale for the vertical axis would result in some of the response spectra being displayed with very small peaks. However, the fundamental longitudinal frequency of vibration did not vary by much, proving the consistency of the obtained data.

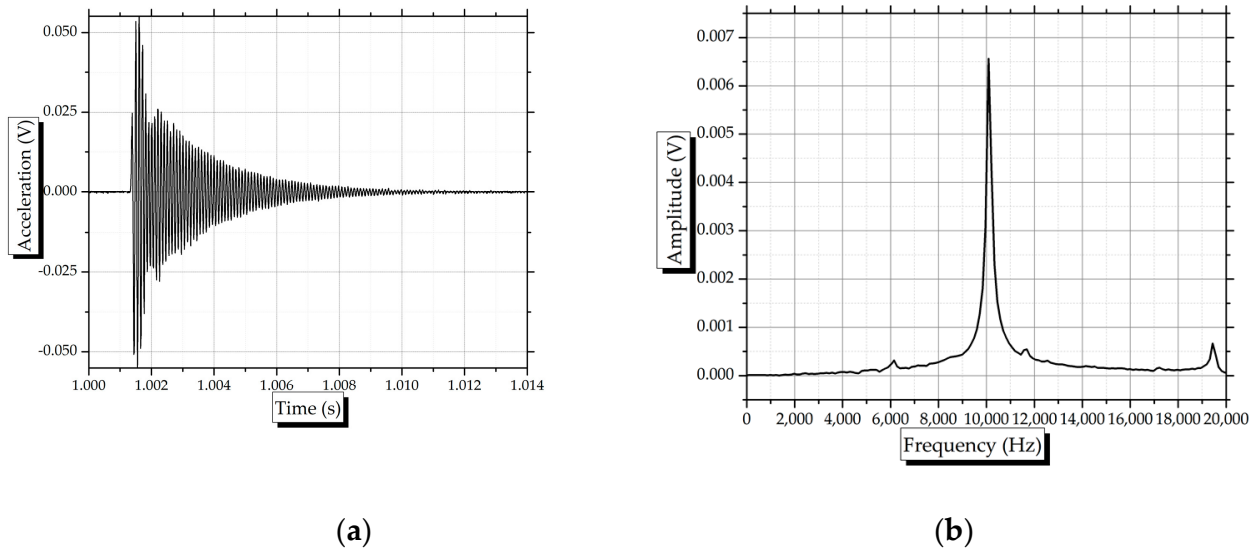

Figure 7. Assessment of the fundamental frequency of vibration. (**a**) Damped free vibrations; (**b**) Response spectrum (FFT).

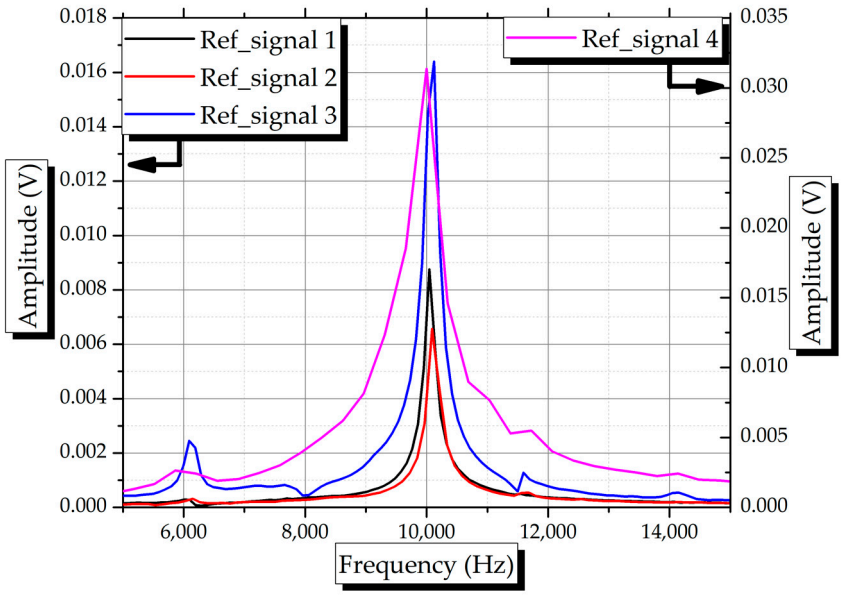

Figure 8. Multiple measurements for the fundamental frequency of vibration.

By applying Equations (1) and (2), the dynamic modulus of elasticity was obtained for all specimens belonging to the considered mix proportions. The data are summarized in Table 2, where the presented values are the averaged ones from all the measurements.

Table 2. Dynamic modulus.

Mix	Length	Diameter	Mass	Freq of Vibration	E_d
	[m]	[m]	[kg]	[Hz]	[MPa]
Ref	0.2	0.1	3.51	10,019	35,863
RuC40	0.199	0.1	3.23	8278	22,381
RuC60	0.2	0.1	3.13	7339	17,128
RuC80	0.199	0.1	3.01	6343	12,298

By taking a look at the data presented in Table 2, it can be observed that the higher the rubber content, the lower the fundamental frequency of vibration (Figure 9). The vertical axis represents the amplitude of the signal, whereas the horizontal axis represents the frequency. Since the amplitude of the peak does not provide valuable information, the unit of measure was not converted into units of measure for acceleration. The information that was relevant for the purpose of the research was the one given on the horizontal axis, the fundamental frequency of vibrations and the downward shift of this frequency with the increase in the content of rubber replacement. Additionally, the lower mass of the cylinders, owing to smaller densities of RuC (Figure 5), leads to lower values for the dynamic modulus of elasticity. The decrease was 37.6% for 40% replacement of sand and reached 65.7% for 80% replacement, similar decrease rates to the static modulus of elasticity.

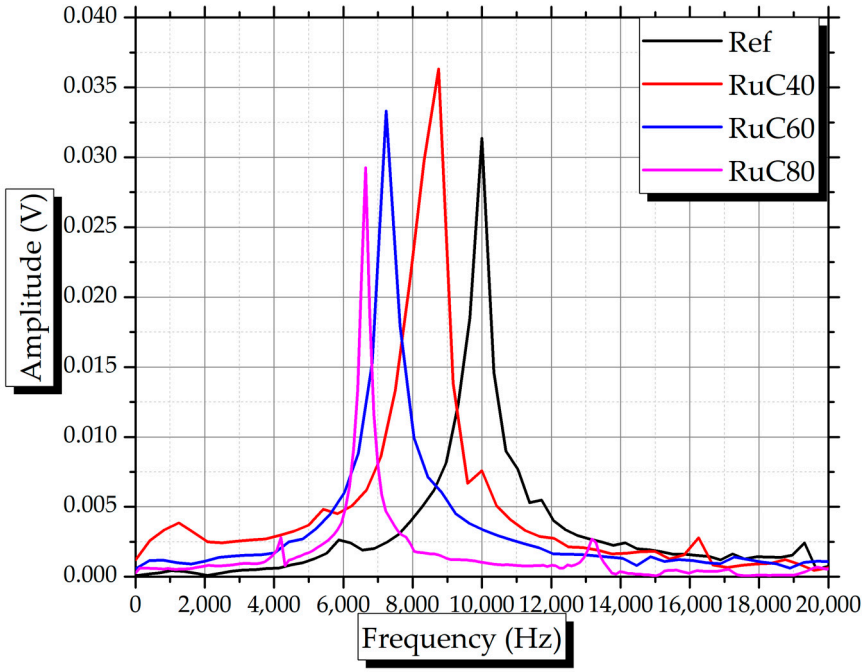

Figure 9. Shift of the fundamental frequency of vibration as a function of rubber content.

3.4. Conversion Equations from Dynamic to Static Modulus of Elasticity

The assessment of the dynamic modulus of elasticity has the advantage that involves a non-destructive method, and it can be performed, in general, directly on site. Since, for design and technical assessment purposes, the values of the static modulus of elasticity are considered, conversion equations were proposed. This section is dedicated to checking whether the readily available equations could also be suitable for rubberized concrete.

The considered equations are the one proposed by Popovics [23] (Equation (3)), the equation proposed by Lydon and Balendran [24] (Equation (4)) and the equation available in BS EN 1992-1-1:2004 [25] (Equation (5)).

$$E_c = \frac{446.09 \times E_d^{1.4}}{\rho_c} \quad (3)$$

$$E_c = 0.83 \times E_d \quad (4)$$

$$E_c = 1.25 \times E_d - 19 \quad (5)$$

where E_c is the static modulus of elasticity (GPa), E_d is the dynamic modulus of elasticity [GPa] and ρ_c is the density of concrete (kg/m^3). The obtained results are summarized in Figure 10.

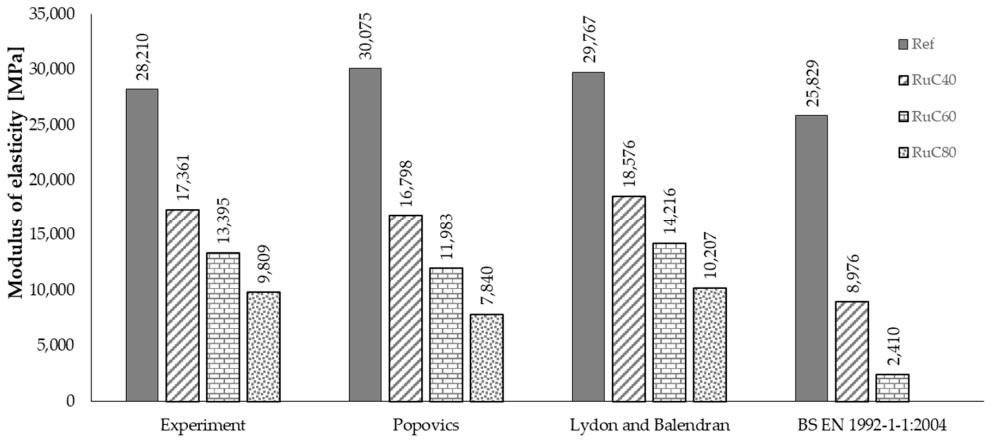

Figure 10. Prediction of the dynamic modulus of elasticity.

It can be observed that both Equations (3) and (4) give quite accurate results in terms of the predicted value of the static modulus of elasticity of the reference mix, although they tend to slightly overestimate the experimental results by 6.6% and 5.5%, respectively. When it comes to RuC mixes, Equation (3) underestimates the experimental results by 3.3% for RuC40 up to 20.1% for RuC80. On the other hand, Equation (4) tends to slightly overestimate the experimental results by almost 7% for RuC40 and improve its accuracy with only 4.1% overestimation for RuC80.

Based on the obtained results, it can be concluded that even though Equations (3) and (4) were developed for regular concrete, they are both accurate for 40% replacement of sand by rubber aggregates with Equation (4), keeping its accuracy even for 80% replacement. Equation (5) is very conservative when it comes to the reference mix and quite inaccurate for rubberized concrete.

3.5. Material Damping

One of the key features of rubberized concrete is its ability to dampen vibrations. For this purpose, the material damping was determined by means of the signal decaying function.

From the analysis of the experimental data, it was observed that the recorded signal consisted of a transient part, right after the impact, and a steady-state part. The steady-state part of the signal was fitted by means of a SineDamp equation, as shown in Figure 11. The material damping, ξ, was computed by means of Equation (6):

$$\xi = \frac{\lambda}{\sqrt{\lambda^2 + \omega^2}} \quad (6)$$

where λ is the signal rate of decay and ϖ is the pulsation of the signal. Both the rate of decay and the pulsation were extracted from the SineDamp function used to fit the steady-state response.

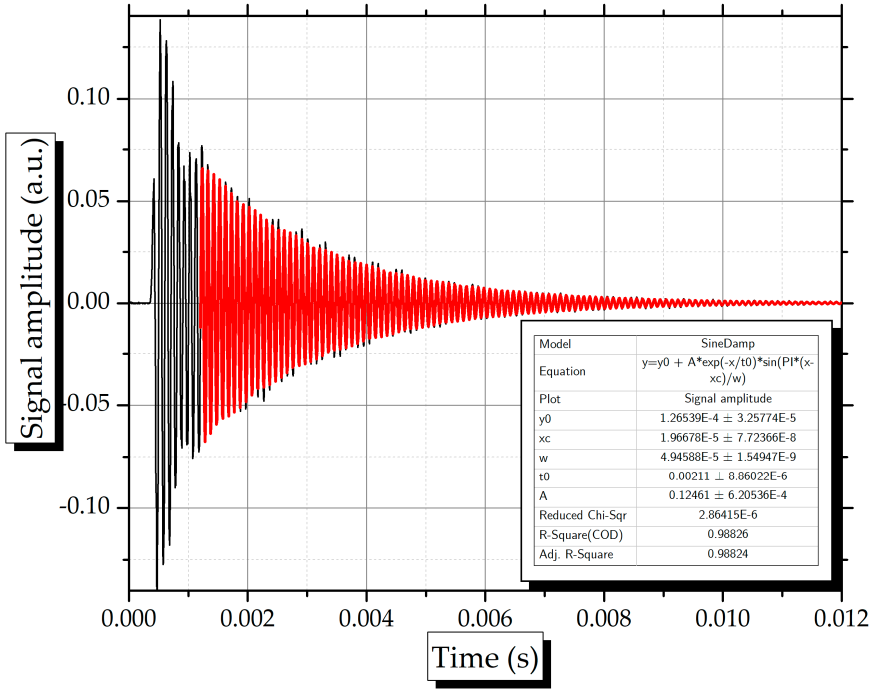

Figure 11. SineDamp function for fitting the steady-state response of the specimen.

The obtained values for the material damping ratio are summarized in Table 3. It can be observed that the replacement of natural sand by rubber particles leads to a three-fold increase in the material damping.

Table 3. Material damping.

Mix	Vibration Decay, λ	Pulsation	ξ
	[Hz]	[Hz]	[%]
Ref	471	10,019	0.75
RuC40	1561	8278	3.00
RuC60	1260	7339	2.73
RuC80	1072	6343	2.69

Contrary to what was expected, higher percentages of rubber replacement did not necessarily mean better damping. The explanation may lie in the interfacial transition zone (ITZ) between the rubber particles and the cement matrix. A recent study [26] indicated that even for lower replacement percentages of sand by rubber aggregates, up to 15% replacement, the ITZ exhibited a higher concentration of voids and weaker bonding. The presence of voids was also reflected in lower values for the fundamental frequency of vibration, and further research should be dedicated to this topic.

3.6. Compressive Strength

The compressive strength was measured on 10 cylinders in accordance with SR EN 12390-3 [15]. The load was applied at a constant rate of 0.6 MPa/s (4.71 kN/s). The obtained values are shown in Figure 12.

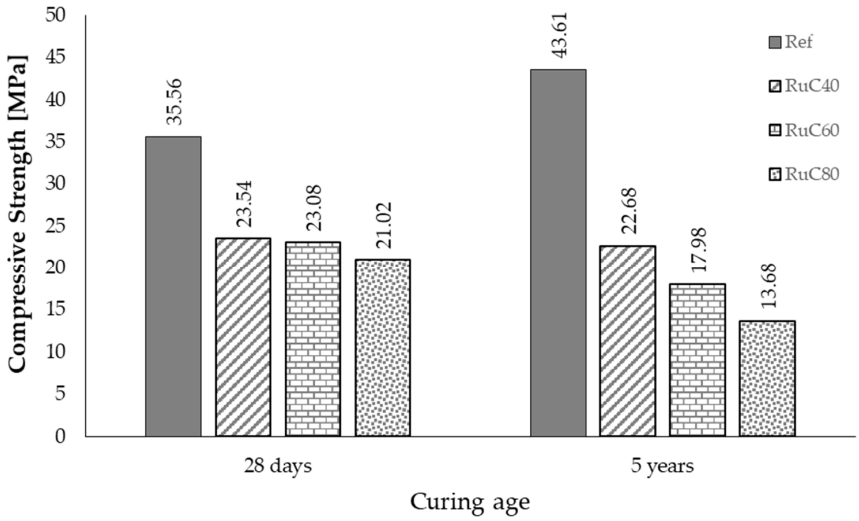

Figure 12. Compressive strength of Ref and RuC mixes.

Compared to the data from [6], the compressive strength of the reference mix increased by 22.64% from 35.56 MPa to 43.61 MPa. However, all other concrete mixes, the ones involving rubber aggregates, showed a decrease in the values of the compressive strength with an almost 35% decrease for RuC80. Only a 3.65% decrease was observed for RuC40. The obtained results are in line with the decreased values of both the static and the dynamic moduli of elasticity and the decrease in the values of the material damping with the increase in the replacement percentage.

A possible explanation may reside in the higher number of voids present at the ITZ level for concrete mixes with large volumes with rubber particles.

The conversion equations from compressive strength to static modulus of elasticity were checked for accuracy and suitability of being applied to rubberized concrete, although they were not specifically developed and proposed for this purpose. Hence, the equation given by Eurocode 2 [27] (Equation (6)) and the equation given in ACI 318-14 [28] (Equation (7)) were investigated. The obtained results are summarized in Table 4.

$$E_{cm} = 22 \times \left(\frac{f_{cm}}{10}\right)^{0.3}, \text{ where } f_{cm} = f_{ck} + 8[\text{MPa}] \quad (7)$$

$$E_c = 4.7\sqrt{f_c'} \quad (8)$$

where f_c' and f_{ck} are the compressive strength of concrete obtained from laboratory investigations [MPa], E_c and E_{cm} are the static moduli of elasticity [MPa].

Table 4. Predicted values for the static modulus of elasticity as function of the compressive strength.

Mix	Ec (Eurocode 2, Equation (6))	Exp/Ec,6	Ec (ACI 318-14, Equation (7))	Exp/Ec,7
	[MPa]	[%]	[MPa]	[%]
Ref	35,995	78.37	28,825	90.89
RuC40	30,795	56.38	22,711	77.56
RuC60	29,296	45.72	20,978	67.21
RuC80	27,749	35.35	19,180	56.43

It can be observed that the best prediction for the reference mix was given by Equation (7). Equation (6) overestimated the experimental results by as much as 22%. All equations significantly overestimated the experimental results with the increase in the rubber content. The data are in line with the results reported in previous studies [6] and underline

the limitation of currently available equations in predicting the modulus of elasticity of rubberized concrete with large volumes of rubber aggregates. Therefore, further studies should be conducted with the aim of proposing accurate prediction equations in view of the increasing use of rubberized concrete in the construction industry.

3.7. Tensile Splitting Strength

The tensile splitting strength was determined on 10 samples in accordance with SR EN 12390:6 [16]. The specimens were loaded by a loading rate of 0.05 MPa/s (0.4 kN/s). The obtained results are shown in Figure 13. It can be seen that the tensile splitting strength decreases with the increase in rubber content. The prediction equation presented in ACI 318:14 [28] was used to check whether or not it can be used in the case of rubberized concrete. The data are summarized in Table 5.

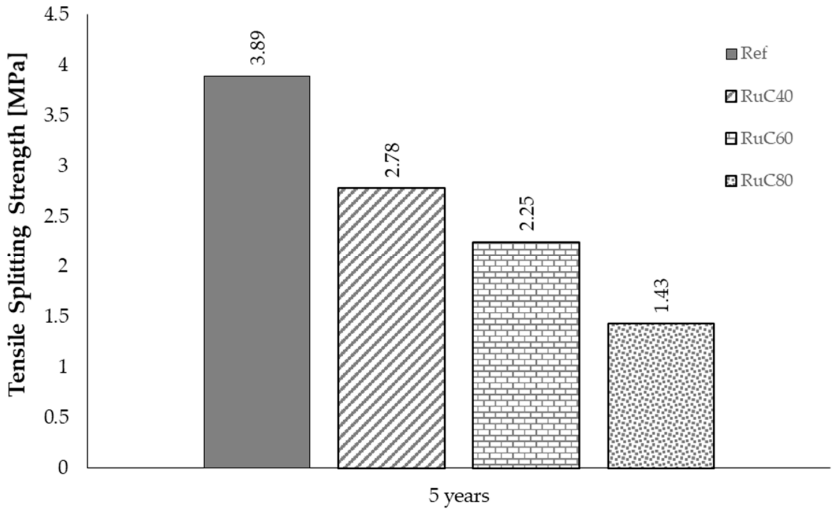

Figure 13. Tensile splitting strength of Ref and RuC mixes.

Table 5. Predicted values for the tensile splitting strength as function of the compressive strength.

Mix	Ec (ACI 318-14)	Exp/Ec
	[MPa]	-
Ref	3.70	1.051
RuC40	2.67	1.041
RuC60	2.37	0.949
RuC80	2.07	0.691

From the obtained results, it can be concluded that the equation can accurately predict the tensile splitting strength of both the reference mix and the rubberized concrete mixes with replacement percentages of sand from 40% to 60%. However, it tends to overestimate the values of the tensile splitting strength of RuC80 by 31.9%.

4. Discussions

The obtained results were also investigated from a statistical point of view, namely the spread of the data with respect to the average value. The data are summarized in Table 5 in terms of density, modulus of elasticity and strength values. The coefficient of variation (COV) was used to assess the dispersion of data with respect to the average value obtained from different data set sizes. The static and dynamic moduli of elasticity were determined from 19 specimens, whereas the compressive and tensile splitting strength was from a set of 10 samples each.

It can be observed that the values for the density of all concrete mixes exhibit a very small spread with respect to the median. This proves that the changes in the dimensions of

the specimens, as well as the weight of specimens within the same mix proportion, were equally influenced by the storing conditions.

A larger spread of the results was observed for the values of the modulus of elasticity, especially for RuC60 and RuC80 mixes. This could be attributed to the higher content of rubber particles which leads to a larger number of micro-cracks. There is, however, not enough data on this issue, and further research should be conducted in this direction.

The dynamic modulus of elasticity exhibits larger values of COV compared to those obtained for the density but with an almost uniform distribution among the concrete mixes. Taking into account the fact that the vibrations induced by using the Impact Echo Method to assess the fundamental frequency of the specimens have to travel through the material to reach the opposite side and be recorded by the accelerometer, any defect within the material structure would impact the response of the specimens.

Since all cylinders were stored in the same relatively dry environment that favored the evaporation of free water from the concrete pores, this had a direct influence on the material structure, which led to overall lower values for material properties.

By observing the data from Table 6, there is no clear trend in the values of COV as a function of rubber replacement for sand in concrete. This is mainly due to the heterogeneous structure of concrete in general. However, if the values of COV were judged together with the values obtained for the standard deviation with respect to the average values for each investigated material characteristic, the calculated values for COV are in line with those reported in similar research works [29].

Table 6. Characterization of the experimentally obtained data at the age of 5 years.

Reference Mix (Ref)					
	Density	Modulus of Elasticity	Dynamic Modulus of Elasticity	Compressive Strength	Tensile Splitting Strength
	[kg/m^3]	[MPa]	[MPa]	[MPa]	[MPa]
Value	2227	28,210	35,863	43.61	3.89
Standard deviation	8.558	456.54	937.57	1.865	0.12
Coefficient of Variation [%]	0.38	1.62	2.61	4.28	3.09
RuC40					
	Density	Modulus of Elasticity	Dynamic Modulus of Elasticity	Compressive Strength	Tensile Splitting Strength
	[kg/m^3]	[MPa]	[MPa]	[MPa]	[MPa]
Value	2061	17,361	22,381	22.68	2.78
Standard deviation	5.376	240.92	948.37	0.71	0.086
Coefficient of Variation [%]	0.26	1.39	4.24	3.13	3.09
RuC60					
	Density	Modulus of Elasticity	Dynamic Modulus of Elasticity	Compressive Strength	Tensile Splitting Strength
	[kg/m^3]	[MPa]	[MPa]	[MPa]	[MPa]
Value	1986	13,395	17,128	17.98	2.25
Standard deviation	13.539	1047.3	371.54	0.305	0.091
Coefficient of Variation [%]	0.68	7.82	2.17	1.69	4.06
RuC80					
	Density	Modulus of Elasticity	Dynamic Modulus of Elasticity	Compressive Strength	Tensile Splitting Strength
	[kg/m^3]	[MPa]	[MPa]	[MPa]	[MPa]
Value	1909	9809	12,298	13.68	1.43
Standard deviation	10.748	590.94	305.26	0.968	0.083
Coefficient of Variation [%]	0.56	6.02	2.48	7.08	5.76

5. Conclusions

The paper presents an experimental program aimed at assessing the long-term material properties of rubberized Portland cement concrete. Based on the obtained results, the following conclusions can be drawn:

A significant drop in the values of density after 5 years is observed for specimens made with rubberized concrete, whereas the density of the reference mix changes by a very small amount.

The values of the static modulus of elasticity decrease after 5 years compared to the standard value obtained at 28 days, mainly due to the fact that the specimens were kept indoors, in laboratory conditions and in a relatively dry environment. Therefore, the excess water slowly evaporated during the 5 years. Since the presence of rubber creates a larger amount of excess water, its evaporation left behind voids in the concrete specimens that ultimately leads to lower values of the modulus of elasticity.

Since the dynamic modulus of elasticity is influenced both by the mass of the specimen and by its fundamental longitudinal frequency of vibration, any trend observed for the two parameters is reflected in the evolution in time for this material property. The voids inside the RuC specimens lead to lighter concrete and to lower values for the frequency of vibration. The conversion equations from dynamic modulus to static modulus of elasticity cannot be directly applied to rubberized concrete. Further investigations are deemed necessary in this direction.

Material damping is strongly influenced by the rubber content in concrete. A 40% replacement of sand by rubber aggregates leads to a three-fold increase in the value of the material damping. However, further increase of the replacement percentage has an opposite effect on the damping properties due, primarily, to the occurrence of voids at the ITZ level between rubber particles and cement matrix.

Both compressive and tensile splitting strength are adversely affected by the presence of rubber aggregates. The use of currently available conversion equations from the compressive strength of concrete to the values of the elastic modulus is not applicable to rubberized concrete.

By considering the phenomena observed during the experimental program, further research is necessary, especially at the material level, for a better understanding of the long-term behavior of rubberized concrete. The authors have already taken the first steps in this direction, and a set of SEM and XRD investigations are being conducted. Porosity and absorption assessments are also considered. This may help shed some light on the material structure of normal and rubberized concrete after five years from casting and may provide explanations on the observed behavior pattern.

The structural application of rubberized concrete is currently limited. Based on the obtained data, it can be considered that a 40% replacement of natural sand by rubber aggregates, without any prior surface treatment, leads to acceptable values of the compressive strength after five years of storage in a relatively dry environment. However, the starting mix proportion should be for a higher concrete strength class so that the values obtained for the material properties, after using rubber aggregates, still warrant the use of rubberized concrete in structural applications. Additionally, the large deformation capacity of such concrete should be carefully investigated and considered during the design process as it strongly influences the behavior of connecting elements in a structure. The recommendations are still limited to the mixed proportions used in this research. Other mixes could be considered after careful investigation of their elastic and mechanical properties.

Author Contributions: Conceptualization, I.-O.T., P.M. and G.T.; methodology, I.-O.T., S.-M.A.-S., P.M. and A.-M.T.; formal analysis, P.M., G.T. and A.-M.T.; investigation, I.-O.T. and S.-M.A.-S.; resources, G.T. and A.-M.T.; writing—original draft preparation, S.-M.A.-S., A.-M.T. and G.T.; writing—review and editing, I.-O.T. and P.M.; funding acquisition, I.-O.T. All authors have read and agreed to the published version of the manuscript.

Funding: The APC was funded by The "Gheorghe Asachi" Technical University of Iasi under the Publications grant GI/P12/2021.

Institutional Review Board Statement: Not applicable.

Informed Consent Statement: Not applicable.

Data Availability Statement: The data reported in this research is available upon request from the corresponding author.

Conflicts of Interest: The authors declare no conflict of interest.

References

1. Gasch, T.; Eriksson, D.; Ansell, A. On the behaviour of concrete at early-ages: A multiphase description of hygro-thermo-chemo-mechanical properties. *Cem. Concr. Res.* **2019**, *116*, 202–216. [CrossRef]
2. Asaad, M.; Morcous, G. Evaluating Prediction Models of Creep and Drying Shrinkage of Self-Consolidating Concrete Containing Supplementary Cementitious Materials/Fillers. *Appl. Sci.* **2021**, *11*, 7345. [CrossRef]
3. Correia, V.; Gomes Ferreira, J.; Tang, L.; Lindvall, A. Effect of the Addition of GGBS on the Frost Scaling and Chloride Migration Resistance of Concrete. *Appl. Sci.* **2020**, *10*, 3940. [CrossRef]
4. Fattuhi, N.I.; Clark, L.A. Cement-based materials containing shredded scrap truck tyre rubber. *Constr. Build. Mater.* **1996**, *10*, 229–236. [CrossRef]
5. Wang, Z.; Hu, H.; Hajirasouliha, I.; Guadagnini, M.; Pilakoutas, K. Tensile stress-strain characteristics of rubberised concrete from flexural tests. *Constr. Build. Mater.* **2020**, *236*, 117591. [CrossRef]
6. Toma, I.O.; Ţăranu, N.; Banu, O.M.; Budescu, M.; Mihai, P.; Ţăran, R.G. The effect of the aggregate replacement by waste tyre rubber crumbs on the mechanical properties of concrete. *Rev. Rom. Mater. Rom. J. Mater.* **2015**, *45*, 394–401.
7. Son, K.S.; Hajirasouliha, I.; Pilakoutas, K. Strength and deformability of waste tyre rubber-filled reinforced concrete columns. *Constr. Build. Mater.* **2011**, *25*, 218–226. [CrossRef]
8. Youssf, O.; ElGawady, M.A.; Mills, J.E. Static cyclic behaviour of FRP-confined crumb rubber concrete columns. *Eng. Struct.* **2016**, *113*, 371–387. [CrossRef]
9. Oprişan, G.; Enţuc, I.-S.; Mihai, P.; Toma, I.-O.; Ţăranu, N.; Budescu, M.; Munteanu, V. Behaviour of Rubberized Concrete Short Columns Confined by Aramid Fibre Reinforced Polymer Jackets Subjected to Compression. *Adv. Civ. Eng.* **2019**, *2019*, 1360620. [CrossRef]
10. Raffoul, S.; Garcia, R.; Escolano-Margarit, D.; Guadagnini, M.; Hajirasouliha, I.; Pilakoutas, K. Behaviour of unconfined and FRP-confined rubberised concrete in axial compression. *Constr. Build. Mater.* **2017**, *147*, 388–397. [CrossRef]
11. Liu, H.; Wang, X.; Jiao, Y.; Sha, T. Experimental Investigation of the Mechanical and Durability Properties of Crumb Rubber Concrete. *Materials* **2016**, *9*, 172. [CrossRef]
12. Yung, W.H.; Yung, L.C.; Hua, L.H. A study of the durability properties of waste tire rubber applied to self-compacting concrete. *Constr. Build. Mater.* **2013**, *41*, 665–672. [CrossRef]
13. Xue, J.; Shinozuka, M. Rubberized concrete: A green structural material with enhanced energy-dissipation capability. *Constr. Build. Mater.* **2013**, *42*, 196–204. [CrossRef]
14. ASRO (Romanian Standards Association). *SR EN 12390-13/2013, Testing Hardened Concrete. Part 13: Determination of Secant Modulus of Elasticity in Compression*; National Standardisation Body (Organismul National de Standardizare): Bucuresti, Romania, 2013.
15. ASRO (Romanian Standards Association). *SR EN 12390-3/2009, Testing Hardened Concrete. Part 3: Compressive Strength of Test Specimens*; National Standardisation Body (Organismul National de Standardizare): Bucuresti, Romania, 2009.
16. ASRO (Romanian Standards Association). *SR EN 12390-6/2010—Testing Hardened Concrete. Part 6: Tensile Splitting Strength of Test Specimens*; National Standardisation Body (Organismul National de Standardizare): Bucuresti, Romania, 2010.
17. ASTM International. *ASTM C215-14—Standard Test Method for Fundamental Transverse, Longitudinal, and Torsional Resonant Frequencies of Concrete Specimens*; ASTM International (American Society for Testing and Materials): Philadelphia, PA, USA, 2014.
18. Wang, J.; Guo, Z.; Yuan, Q.; Zhang, P.; Fang, H. Effects of ages on the ITZ microstructure of crumb rubber concrete. *Constr. Build. Mater.* **2020**, *254*, 119329. [CrossRef]
19. Kustermann, A.; Thienel, K.C.; Keuser, M. Influence of curing methods on the formation of microcracks in high-strength concrete. In Proceedings of the 7th International Symposium on the Utilization of High-Strength/High-Performance Concrete, Washington, DC, USA, 20–24 June 2005; pp. 1281–1293.
20. Zhu, H.; Wang, Z.; Xu, J.; Han, Q. Microporous structures and compressive strength of high-performance rubber concrete with internal curing agent. *Constr. Build. Mater.* **2019**, *215*, 128–134. [CrossRef]
21. Kou, S.C.; Poon, C.S. Long-term mechanical and durability properties of recycled aggregate concrete prepared with the incorporation of fly ash. *Cem. Concr. Compos.* **2013**, *37*, 12–19. [CrossRef]
22. Romanazzi, V.; Leone, M.; Tondolo, F.; Fantilli, A.P.; Aiello, M.A. Bond strength of rubberized concrete with deformed steel bar. *Constr. Build. Mater.* **2021**, *272*, 121730. [CrossRef]
23. Popovics, S. Verification of relationships between mechanical properties of concrete-like materials. *Matériaux Constr.* **1975**, *8*, 183–191. [CrossRef]
24. Lydon, F.D.; Balendran, R.V. Some observations on elastic properties of plain concrete. *Cem. Concr. Res.* **1986**, *16*, 314–324. [CrossRef]
25. BSI (British Standards Institute). *BS EN 1992-1-1—Structural Use of Concrete. Code of Practice for Special Circumstances*; BSI (Brithis Standards Institute): London, UK, 2004; ISBN 0-580-14490-9.
26. Khan, R.B.N.; Khitab, A. Enhancing Physical, Mechanical and Thermal Properties of Rubberized Concrete. *Eng. Technol. Q. Rev.* **2020**, *3*, 33–45.

27. EN1992-1-1:2004. *Eurocode 2: Design of Concrete Structures—Part 1-1: General Rules and Rules for Buildings*; 2004; European Union: Brussel, Belgium.
28. ACI (American Concrete Institute). *ACI CODE-318-14: Building Code Requirements for Structural Concrete and Commentary*; ACI (American Concrete Institute): Farmington Hills, MI, USA, 2014.
29. Pacheco, J.; de Brito, J.; Chastre, C.; Evangelista, L. Experimental investigation on the variability of the main mechanical properties of concrete produced with coarse recycled concrete aggregates. *Constr. Build. Mater.* **2019**, *201*, 110–120. [CrossRef]